ABSTRACT

Development and Characterization of High-Efficiency, High-Specific Impulse Xenon Hall Thrusters

by

Richard Robert Hofer

Chair: Associate Professor Alec D. Gallimore

This dissertation presents research aimed at extending the efficient operation of 1600 s specific impulse Hall thruster technology to the 2000-3000 s range. While recent studies of commercially developed Hall thrusters demonstrated greater than 4000 s specific impulse, maximum efficiency occurred at less than 3000 s. It was hypothesized that the efficiency maximum resulted as a consequence of modern magnetic field designs, optimized for 1600 s, which were unsuitable at high-specific impulse. Motivated by the industry efforts and mission studies, the aim of this research was to develop and characterize xenon Hall thrusters capable of both high-specific impulse and high-efficiency operation. The research divided into development and characterization phases.

During the development phase, the laboratory-model NASA-173M Hall thrusters were designed with plasma lens magnetic field topographies and their performance and plasma characteristics were evaluated. Experiments with the NASA-173M version 1 (v1) validated the plasma lens design by showing how

changing the magnetic field topography at high-specific impulse improved efficiency. Experiments with the NASA-173M version 2 (v2) showed there was a minimum current density and optimum magnetic field topography at which efficiency monotonically increased with voltage. Between 300-1000 V, total specific impulse and total efficiency of the NASA-173Mv2 operating at 10 mg/s ranged from 1600-3400 s and 51-61%, respectively. Comparison of the thrusters showed that efficiency can be optimized for specific impulse by varying the plasma lens design.

During the characterization phase, additional plasma properties of the NASA-173Mv2 were measured and a performance model was derived accounting for a multiply-charged, partially-ionized plasma. Results from the model based on experimental data showed how efficient operation at high-specific impulse was enabled through regulation of the electron current with the magnetic field. The decrease of efficiency due to multiply-charged ions was minor. Efficiency was largely determined by the current utilization, which suggested maximum Hall thruster efficiency has yet to be reached. The electron Hall parameter was approximately constant with voltage, decreasing from an average of 210 at 300 V to an average of 160 between 400-900 V, which confirmed efficient operation can be realized only over a limited range of Hall parameters.

Development and Characterization of High-Efficiency, High-Specific Impulse Xenon Hall Thrusters

by

Richard Robert Hofer

A dissertation submitted in partial fulfillment
of the requirements for the degree of
Doctor of Philosophy
(Aerospace Engineering)
in The University of Michigan
2004

Doctoral Committee:

Associate Professor Alec D. Gallimore, Chair

Professor Iain D. Boyd

Professor Ronald M. Gilgenbach

Professor Yue Ying Lau

"Ben, if I teach you anything, it's this:
don't build an airplane you don't believe in.
Don't prostitute yourself for bucks."

Clarence "Kelly" Johnson
Skunk Works, pp. 292
By Ben Rich and Leo Janos

Acknowledgements

Having started my undergraduate studies in the fall of 1993, I have spent just over a decade at the University of Michigan. My years in Ann Arbor have been so immensely rewarding that it would be impossible to express my full appreciation for the opportunities this place has made possible. Nonetheless, I would like to take a few moments to try and thank just some of those that have been a part of my life here at the University as well as those that have supported this research.

First, I would like to thank my research advisor, Assoc. Prof. Alec Gallimore, for his unwavering support and guidance through the successes and the setbacks. By always believing that, "things will work out, they always do," Gallimore-Sensei's optimism and trust in my abilities has been a major contributor to my success. I cannot imagine having a better guide for this journey. Thank you.

In addition, I would like to thank the rest of my dissertation committee: Prof. Iain Boyd, Prof. Ron Gilgenbach, and Prof. Y. Y. Lau, for their time and assistance in refining this work. Any errors that remain are my own.

The Department of Aerospace Engineering is filled with people dedicated to the success of its students. I would like to thank each of my professors for teaching me what I know about aerospace engineering. I would also like to thank the department for its generous financial support while I have been a graduate student. In addition, I would like to express my sincere gratitude to Margaret Fillion, the

department's graduate student services coordinator, for her tireless devotion and commitment to every one of the students under her care. Moreover, I would like to thank machinist Terry Larrow for not only building me quality parts, but for teaching me a thing or two about fabrication at the same time.

PEPL has been a great place to learn and to live. While PEPL's world-class facilities give it the means to be the special place that it is, its most valuable resource are the graduate students that work there. It has been a privilege and an honor to work with each of you. In particular, I would like to thank Dr. Brian Beal, Dr. Frank Gulczinski, Dr. James Haas, Dan Herman, Peter Peterson, Dr. Tim Smith, and Mitchell Walker. Each of your have been a big part of making life at PEPL both fun and rewarding through your friendship and the many stimulating conversations we have had about all things related to magnetic fields, Hall thrusters, and plasmas. The contributions that Peter and Mitchell made to the design and subsequent troubleshooting of the NASA-173Mv1 are greatly appreciated. Thanks to Frank and James for being gracious enough to teach me during my first year what they knew about the lab and all the various vagaries of conducting research. James, who bore the brunt of my ignorance, gets a special thank-you, for putting up with the hundreds of questions I must have asked him.

My decision to stay at Michigan for graduate school is the second smartest thing I have ever done (the first of course, was marrying my wife). I truly think the opportunities that came my way while here were of the "once in a lifetime" variety. In my second year, Peter and I began working with a small group of dedicated, talented engineers at the On-Board Propulsion Branch at the NASA Glenn Researcher Center (GRC). These individuals were the Hall thruster team leader Rob Jankovsky (now branch chief) and fellow engineers David Manzella and David

Jacobson (now team leader). Our initial collaborations were made possible by the NASA Graduate Student Researchers Program that supported me financially and a grant from GRC that funded our experiments. I am extremely grateful for this support. Along the way, I was offered part-time work as a contractor at GRC that eventually led to full-time employment. At GRC, not only did I have access to the world's best facilities for conducting electric propulsion research, I was also given every resource I needed and the freedom to explore the ideas that ultimately led to the design of the NASA-173Mv2. I am extremely grateful for the opportunity to have conducted this research, and humbled by the amount of responsibility that has at times been afforded to me.

I would also like to thank all the other outstanding engineers and technicians at NASA that have offered valuable advice and/or supported my experiments: Lynn Arrington, Kevin Blake, Glenn Bowers, Howard Eakin, Eli Green, Chris Griffiths, Stan Grisnik, Tom Haag, Hardy Hartman, George Jacynycz, Terry Jansen, Steve Oleson, Resty Palad, Eric Pencil, Luis Pinero, and Vince Rawlin. I owe a special debt of gratitude to Chris Griffiths for his efforts in improving the mechanical design of the NASA-173Mv2. It has been an extremely rewarding and valuable experience to work with Chris; he is a true professional and a top-notch designer.

I also want to thank everyone in my family for all of their love and support throughout my education. My mother's unending love and encouragement have been a constant source of support. I would also like to thank my father for his love and support, especially during the undergraduate years. Moreover, to my sister, thank you for loving me unconditionally and for being a great friend. Lastly, thanks to my uncle, Dr. John Hofer, for setting such a fine example for me and for being someone that I could share my experiences with during the graduate years.

Most importantly, to my wife Anya, I want you to know how much I have appreciated you for simply being there to listen to me when I was frustrated, celebrating with me when things were going well, and for showing me that there is indeed life after research. Thank you for being with me on this wonderful journey.

RRH
Ann Arbor, MI
December 2003

Table of Contents

List of Figures

List of Tables

List of Appendices

Nomenclature

Constants

g	gravitational acceleration, 9.80665	[m/s^2]
e	electron charge, 1.6022 x 10^{-19}	[C]
k	Boltzmann's constant, 1.3807x10^{-23}	[J/K]
m_e	electron mass, 9.1094x10^{-31}	[kg]
m_{xe}	mass of a xenon atom, 2.18 x 10^{-25}	[kg]
ε_o	permittivity of free space, 8.8542x10^{-12}	[F/m]
μ_o	permeability of free space, 1.25664x10^{-6}	[H/m]

Variables

A	cross-sectional area, typically of the discharge chamber	[m^2]
A_c	current collection area of the ExB probe or RPA	[m^2]
A_g	effective gap area of the C-core magnetic circuit	[m^2]
A_m	cross-sectional area of the C-core magnetic circuit	[m^2]
A_s	cross-sectional area of a section of a magnetic circuit	[m^2]
$\vec{B}$	magnetic flux density vector	[T]
B	magnitude of the magnetic field (magnetic flux density)	[T]
B_g	gap magnetic flux density	[T]
B_m	C-core magnetic circuit magnetic flux density	[T]

B_o	magnetic field normalization constant	[T]
B_r	radial component of the magnetic field	[T]
$B_{r,anode}$	radial magnetic field at the anode on the channel centerline	[T]
$B_{r,max}$	maximum radial magnetic field on the channel centerline	[T]
B_z	axial component of the magnetic field	[T]
c	effective exit velocity	[m/s]
c_a	anode effective exit velocity	[m/s]
c_t	total effective exit velocity	[m/s]
d	distance between the plates of an ExB probe	[m]
$d\vec{l}$	differential vector along a closed boundary	[m]
dS	differential area of a surface	[m^2]
$\vec{E}$	electric field vector	[V/m]
E	magnitude of the electric field	[V/m]
E_r	radial component of the electric field	[V/m]
E_z	axial component of the electric field	[V/m]
$\vec{F}$	force vector of a charged particle	[N]
F_{mmf}	magnetomotive force	[A]
f_b	breathing-mode frequency	[Hz]
$f(V)$	ion voltage distribution function	[s/m]
$\vec{H}$	magnetic intensity vector	[A/m]
H_m	magnetic intensity of the C-core magnetic circuit	[A/m]
I_b	ion beam current	[A]
I_b^+	ion beam current of a singly-charged plasma	[A]
I_c	current through an electromagnetic coil	[A]

I_d	discharge current	[A]
I_e	axial electron current	[A]
I_e^+	electron current of a singly-charged plasma	[A]
I_i	current of the i^{th} ion species	[A]
I_{ic}	current supplied to the inner coil	[A]
I_{oc}	current supplied to the outer coil(s)	[A]
I_{probe}	current collected by the RPA	[A]
$I_{probe,i}$	current collected by the ExB probe from the i^{th} ion species	[A]
I_{sp}	specific impulse	[s]
$I_{sp,a}$	anode specific impulse	[s]
$I_{sp,t}$	total specific impulse	[s]
I_t	total impulse	[N·s]
i	ion charge-state index (1, 2, 3, etc.)	[-]
$\vec{j}$	current density vector	[A/m^2]
j_b	ion current density	[A/m^2]
j_{ez}	axial electron current density	[A/m^2]
$j_{e\theta}$	azimuthal electron current density	[A/m^2]
K_c	cathode flow fraction	[-]
K_{mag}	electromagnetic coil power fraction	[-]
L	characteristic length scale of the closed-drift region	[m]
L_a	length of the acceleration zone	[m]
L_b	axial distance between anode and location of $B_{r,max}$	[m]
L_g	gap length across the C-core magnetic circuit	[m]
L_i	length of the ionization zone	[m]

L_m	mean length of the C-core magnetic circuit	[m]
L_s	mean length of a section of a magnetic circuit	[m]
$\vec{M}$	magnetization vector	[A/m]
$M(t)$	instantaneous spacecraft mass	[kg]
M_f	final spacecraft mass	[kg]
M_o	initial spacecraft mass	[kg]
M_p	total propellant mass	[kg]
M_{pl}	spacecraft payload mass	[kg]
M_{pp}	power plant mass of a propulsion system	[kg]
$\dot{m}$	mass flow rate of propellant	[kg/s]
$\dot{m}_a$	anode mass flow rate	[kg/s]
$\dot{m}_b$	ion beam mass flow rate	[kg/s]
$\dot{m}_b^+$	ion beam mass flow rate of a singly-charged plasma	[kg/s]
$\dot{m}_c$	cathode mass flow rate	[kg/s]
$\dot{m}_i$	mass flow rate of the i^{th} ion species	[kg/s]
$\dot{m}_n$	neutral mass flow rate	[kg/s]
$\dot{m}_n^+$	neutral mass flow rate of a singly-charged plasma	[kg/s]
$\dot{m}_t$	total mass flow rate of propellant through the thruster	[kg/s]
N	total number of ion species	[-]
N_c	total number of turns of an electromagnetic coil winding	[-]
N_{ic}	total number of turns of the inner coil	[-]
N_{oc}	total number of turns of the outer coil(s)	[-]
$\hat{n}$	unit normal vector	[-]

n_b	ion beam number density	[m^{-3}]
n_b^+	ion beam number density of a singly-charged plasma	[m^{-3}]
n_e	electron number density	[m^{-3}]
n_i	number density of the i^{th} ion species	[m^{-3}]
n_n	neutral number density	[m^{-3}]
n_n^+	neutral number density of a singly-charged plasma	[m^{-3}]
n_o	reference electron number density	[m^{-3}]
n_t	total particle density	[m^{-3}]
P_{aux}	auxiliary power for cathode heater or keeper	[W]
P_d	discharge power	[W]
P_{DCIU}	digital control and interface unit power	[W]
P_{jet}	jet (or beam) power in the exhaust of a rocket	[W]
P_{mag}	electromagnetic coil power	[W]
P_{PPU}	PPU power	[W]
P_{sys}	power required by a complete propulsion system	[W]
P_t	total input power (from the PPU to the thruster)	[W]
P_{XFC}	xenon flow control system power	[W]
p	plasma pressure	[Pa]
p_b	base pressure on air	[Torr]
p_c	xenon corrected pressure	[Torr]
p_e	electron pressure	[Pa]
p_i	indicated ionization gauge pressure	[Torr]
q_i	charge of the i^{th} ion species	[C]
R_b	ion gyroradius (Larmor radius)	[m]

R_{bp}	reluctance of the back pole piece	[H^{-1}]
R_{dc}	reluctance across the discharge chamber	[H^{-1}]
R_e	electron gyroradius (Larmor radius)	[m]
R_{ic}	reluctance of the inner coil	[H^{-1}]
R_{ifp}	reluctance of the inner front pole piece	[H^{-1}]
R_{is}	reluctance of the inner magnetic screen	[H^{-1}]
R_{ofp}	reluctance of the outer front pole piece	[H^{-1}]
R_{og}	reluctance of the outer guide pole piece	[H^{-1}]
R_{os}	reluctance of the outer magnetic screen	[H^{-1}]
R_s	reluctance of a section of a magnetic circuit	[H^{-1}]
r	radial coordinate direction	[-]
r_{avg}	average radius of the discharge chamber	[m]
r_{in}	inner radius of the discharge chamber wall (plasma side)	[m]
r_{out}	outer radius of the discharge chamber wall (plasma side)	[m]
T	thrust	[N]
T^+	thrust of a singly-charged plasma	[N]
T_e	electron temperature	[K]
$T_{e,D}$	electron temperature controlling divergence	[K]
$T_{e,S}$	electron temperature at the sonic transition in the channel	[K]
t	time	[s]
t_p	thrusting time over which propellant mass M_p is consumed	[s]
$U(t)$	instantaneous spacecraft velocity	[m/s]
U_f	final spacecraft velocity	[m/s]
U_o	initial spacecraft velocity	[m/s]

V_a	average acceleration voltage	[V]
$V_{a,i}$	average acceleration voltage of the ith ion species	[V]
V_a^+	average acceleration voltage of a singly-charged plasma	[V]
V_{acc}	acceleration-stage voltage	[V]
$V_{c\text{-}g}$	cathode voltage with respect to ground	[V]
V_d	discharge voltage	[V]
V_f	floating potential	[V]
$V_{div,i}$	loss voltage due to divergence of the ith ion species	[V]
$V_{ion,i}$	loss voltage due to ionization location of the ith ion species	[V]
V_l	average loss voltage	[V]
$V_{l,i}$	average loss voltage of the ith ion species	[V]
V_l^+	average loss voltage of a singly-charged plasma	[V]
V_{loss}	loss voltage as measured by the RPA	[V]
V_{mp}	most-probable ion voltage	[V]
V_p	plasma potential	[V]
V_{probe}	voltage of the ExB probe or RPA	[V]
$V_{probe,i}$	pass voltage of the ith ion species through an ExB probe	[V]
V_{rpa}	uncorrected ion voltage from the RPA	[V]
V_{true}	true, or corrected ion voltage from the RPA	[V]
$\vec{v}$	particle velocity vector	[m/s]
v	particle speed	[m/s]
$\left\langle v_b^+ \right\rangle$	average ion velocity of a singly-charged plasma	[m/s]
v_c	characteristic speed of a propulsion system	[m/s]
v_{ez}	axial electron velocity	[m/s]

v_{ExB}	ExB drift velocity	[m/s]
$\langle v_i \rangle$	average velocity of the ith ion species	[m/s]
$\langle v_l^+ \rangle$	average ion defect velocity of a singly-charged plasma	[m/s]
$\langle v_n \rangle$	neutral thermal velocity	[m/s]
$v_{th,e}$	electron thermal velocity	[m/s]
W_i	ion energy	[J or eV]
$\dot{w}$	propellant weight flow rate	[kgf/s]
$\dot{w}_t$	total propellant weight flow rate	[kgf/s]
Z	charge-state of a particle	[-]
Z_i	charge-state of the ith ion species	[-]
z	axial coordinate direction	[-]
z_a	centroid position of the acceleration zone	[m]
z_{anode}	axial location of the anode	[m]
z_i	centroid position of the ionization zone	[m]
z_{max}	axial location of Br,max	[m]
α	specific power of a complete propulsion system	[W/kg]
α_{ano}	anomalous (Bohm-like) electron transport coefficient	[-]
$\beta_{0.95}$	95% plume divergence half-angle	[degrees]
χ_m	magnetic susceptibility	[-]
ε	electron current fraction	[-]
ε^{+}	electron current fraction of a singly-charged plasma	[-]
ϕ	plasma potential	[V]
γ	index denoting a magnetic field line	[-]

γ_i	species-dependent secondary electron emission yield	[electrons/ion]
η_a	anode efficiency	[-]
η_a^+	anode efficiency of a singly-charged plasma	[-]
η_b	current utilization efficiency	[-]
η_b^+	current utilization efficiency of a singly-charged plasma	[-]
η_c	cathode efficiency	[-]
η_d	ion velocity dispersion efficiency	[-]
η_{mag}	electromagnetic coil efficiency	[-]
η_m	mass utilization efficiency	[-]
η_m^+	mass utilization efficiency of a singly-charged plasma	[-]
η_{PPU}	PPU efficiency	[-]
η_q	charge utilization efficiency	[-]
η_{sys}	efficiency of a complete propulsion system	[-]
η_v	voltage utilization efficiency	[-]
η_v^+	voltage utilization efficiency of a singly-charged plasma	[-]
η_t	total thruster efficiency (excluding PPU)	[-]
μ	magnetic permeability	[H/m]
μ_{ez}	axial electron mobility	[$m^2/V \cdot s$]
μ_m	permeability of the C-core magnetic material	[H/m]
μ_s	permeability of a section of a magnetic circuit	[H/m]
ν	collision frequency	[s^{-1}]
ν_e	electron collision frequency	[s^{-1}]
ν_{ee}	electron-electron collision frequency	[s^{-1}]
ν_{eff}	effective electron collision frequency	[s^{-1}]

ν_{ei}	electron-ion collision frequency	[s^{-1}]
ν_{en}	electron-neutral collision frequency	[s^{-1}]
ν_{wall}	electron-wall collision frequency	[s^{-1}]
ν_{turb}	turbulent electron collision frequency	[s^{-1}]
θ	azimuthal coordinate direction	[-]
ω_b	breathing-mode frequency	[s^{-1}]
ω_c	cyclotron frequency	[s^{-1}]
ω_{cb}	ion cyclotron frequency	[s^{-1}]
ω_{ce}	electron cyclotron frequency	[s^{-1}]
ξ	exchange ratio	[-]
ψ	unit vector directed along a magnetic field line	[-]
ζ_i	fraction of the i^{th} ion species	[-]
ΔU	spacecraft velocity increment	[m/s]
Φ	magnetic flux	[Wb]
ϑ	dimensionless $\langle \nabla_z B_r \rangle$	[-]
Θ	ionization fraction	[-]
Θ^+	ionization fraction of a singly-charged plasma	[-]
Ω	Hall parameter	[-]
Ω_b	ion Hall parameter	[-]
Ω_e	electron Hall parameter	[-]
Ω_i	current fraction of the i^{th} ion species	[-]
$\Omega_{probe,i}$	current fraction of the i^{th} ion species collected by the ExB probe	[-]
$\nabla_z B_r$	axial gradient of the centerline radial magnetic field	[T/m]
$\langle \nabla_z B_r \rangle$	average, axial gradient of the centerline radial magnetic field	[T/m]

Acronyms

AIAA	American Institute of Aeronautics and Astronautics
Al_2O_3	Alumina
AFRL	Air Force Research Laboratory
BaO	Barium Oxide
BN	Boron Nitride
DCIU	Digital Control and Interface Unit
ESA	ElectroStatic energy Analyzer
ETC	External Trim Coil
FEEP	Field Emission Electric Propulsion
FWHM	Full Width at Half-Maximum
GEO	Geosynchronous Earth Orbit
GRC	Glenn Research Center, Cleveland, OH
HARP	High-speed Axial Reciprocating Probe positioning system
IC	Inner Coil
ITC	Internal Trim Coil
KeRC	Keldysh Research Center, Moscow, Russia
LaB_6	Lanthanum hexaboride
LEO	Low Earth Orbit
LVTF	Large Vacuum Test Facility
LVDT	Linear Voltage Displacement Transducer
MLT	Magnetic Layer Thruster
MPDT	MagnetoPlasmaDynamic Thruster
NASA	National Aeronautics and Space Administration
NSTAR	Nasa Solar electric propulsion Technology Applications Readiness

NRO	National Reconnaissance Office
OC	Outer Coil(s)
PEPL	Plasmadynamics and Electric Propulsion Laboratory
PPT	Pulsed Plasma Thruster
PPU	Power Processing Unit
SCCM	Standard Cubic Centimeter per Minute
SBIR	Small Business Innovation Research
SEE	Secondary Electron Emission
SiC	Silicon Carbide
SiH_4	Silane
SiO_2	Silicon dioxide
SMART	Small Missions for Advanced Research and Technology
SPT	Stationary Plasma Thruster
STEX	Space Technology Experiment Satellite
TAL	Anode Layer Thruster
TsNIMMASH	Central Scientific Research Institute of Machine Building, Korolev, Moscow
T/P	Thrust-to-Power ratio
UM	University of Michigan
VF5	Vacuum Facility 5 (at NASA GRC)
VF12	Vacuum Facility 12 (at NASA GRC)
VIPS	Variable Specific ImPulse
XFC	Xenon Flow Control system

Part I

Background

Chapter 1

Introduction

1.1 Problem statement

Most often regarded as a moderate specific impulse (1600 s) space propulsion technology, the Hall effect thruster has benefited from considerable theoretical and experimental research since the 1960's [1-3]. Deriving from research on magnetrons and other cross-field plasma sources, the first working devices were reported by Americans beginning in 1962 [4-10],[1] but ultimately the technology was developed in the former Soviet Union.[2] Hall thrusters were first flown in space when the Russian design bureau Fakel launched a pair of SPT-60 magnetic layer thrusters with the Soviet Meteor satellite in December 1971 [18]. Since that pioneering flight, over one hundred thrusters have flown on Earth orbiting spacecraft, primarily for station keeping and orbit maintenance tasks [14, 15, 19-22]. In the early 1990's, the technology was exported to western countries as the Cold War between the Soviet

[1] In Chapter 3, the two major variants of the Hall thruster are discussed. These are the magnetic layer thruster (MLT) and the anode layer thruster (TAL). The MLT is also called the stationary plasma thruster (SPT), but that convention will be avoided to differentiate thrusters of this type from those marketed by Fakel (*e.g.*, the SPT-100). The first magnetic layer thruster experiments were reported in Ref. [4-6] and the first anode layer thruster experiments were reported in Ref. [7, 8].

[2] Although the first experiments were reported by Americans, in the late 1950's and early 1960's the ideas that would lead to the Hall thruster were developed simultaneously in the United States and Soviet Union. At the end of 1963, Hall thruster experiments began in the Soviet Union, which were, it seems fair to say, partly in response to the 1962 American experiments. This seems to be the case since the earliest Soviet journal articles on Hall thruster theory [11-13] reference the American experiments [4, 5, 9, 10] and it has been reported that Fakel, the leading Soviet design bureau, began work on magnetic layer thrusters in 1963 [14-16]. Regardless, the Soviets are properly credited for the development efforts that led to the first spaceflights using Hall thrusters, which is an achievement that certainly outweighs the early American ground experiments. Sometime around 1970, Americans abandoned Hall thrusters in favor of the gridded ion thruster, partly because they were unable to achieve the efficiencies that had been demonstrated by ion thrusters. Ironically, the Soviets pursued Hall thrusters in part because they were unsuccessful in developing the grids necessary for ion thrusters [17].

Union and the United States ended [23]. After extensive investigations of Russian Hall thruster technology in the west (mostly of Fakel's 1.35 kW SPT-100) [21, 24-45], several countries worldwide, most-prominently the United States and France, have emerged with their own versions of the technology spanning the power range of 0.1 to 100 kW [46-59]. On October 23, 1998, a D-55 anode layer thruster built by the Russian research institute TsNIIMASH was fired for the first time on-board the STEX spacecraft and thus became the first use of Russian Hall thruster technology on a western satellite [19, 40, 60, 61]. On September 28, 2003, the first Hall thruster used for primary, interplanetary propulsion began as the European Space Agency's SMART-1 spacecraft started its journey to the moon using a 1.35 kW PPS-1350 (a SPT-100 derivative) [51, 62]. Fakel's 0.66 kW SPT-70 and 1.35 kW SPT-100 continue to fly on Russian communication satellites [22]. Several companies in the United States and France have integrated Hall thrusters on communication satellites (or are in the process of doing so) with launches scheduled in the near future [50, 51].

Ironically, development of the Hall thruster has been hindered in some ways by its success as a flight technology. The notion of the Hall thruster as a 1600 s specific impulse technology is so prevalent in today's literature that it is accepted practice to specify a thruster's properties simply by referring to the rated thruster power.[3] However, there is no fundamental reason that Hall thrusters must operate at 1600 s specific impulse. This range was probably arrived at for flight thrusters because it optimized, at the time, thruster engineering issues and spacecraft mission

[3] While Fakel's efforts have primarily been devoted to 1200-1600 s magnetic layer thrusters, as late as the 1980's TsNIIMASH was investigating 3000-8000 s anode layer thrusters for application to high-power, interplanetary missions [63]. As it became clear that the promise of space-based nuclear power sources was never going to be realized, TsNIIMASH began to focus on low-power, 1600-3000 s specific impulse anode layer thrusters. However, at the time of this writing there have been no published results of a Hall thruster operating much above 1600 s specific impulse in space.

requirements. The Russians were successful with this approach, finding the right balance between the performance, stability, thermal and lifetime issues that an efficient, simple, and robust technology emerged that was well suited for Earth orbiting spacecraft.

Several trends in electric propulsion in general and Hall thruster technology in particular are requiring that the traditional notions of the Hall thruster be re-examined. These include, at least:

1. new materials and fabrication technologies that are improving thruster designs,
2. computer simulations that are delving deeper into thruster physics,
3. the rapid rise in spacecraft power that is allowing more capable thrusters to be deployed, and
4. new spacecraft missions requiring propulsion systems with larger operating envelopes, longer lifetimes, and greater efficiencies [23, 49, 64-66].

The results of these trends are improvements to existing designs or expansion of the operating envelope to greater specific impulse and/or power. **While influenced by all of these trends, this dissertation is concerned with the extension of Hall thruster technology to a higher range of specific impulse.**

Western interest in Russian Hall thruster technology developed in the 1990's because the specific impulse of flight hardware was between arcjets (less than 1000 s) and ion thrusters (greater than 3000 s) [1, 23]. After the SPT-100 met western flight qualification standards in the mid-1990's, interest in expanding the specific impulse range quickly developed, mostly towards 3000 s, so that the Hall thruster could more fully bridge the 1000-3000 s specific impulse gap. As discussed in

Chapter 2, these activities were motivated by studies indicating the substantial mission benefits for Earth orbiting and interplanetary spacecraft if Hall thrusters could operate at higher specific impulses.

In 1999, a focused research program to operate modern, xenon Hall thrusters above 3000 s specific impulse was started and initially met with mixed results. As discussed in Chapter 3, several thrusters were developed by industry and performance tested through sponsorship by the NASA Glenn Research Center. Specific impulse in excess of 3000 s was demonstrated at greater than 50% efficiency. However, it was found that efficiency maximized at less than 3000 s. This was a source of some concern since decreasing thruster efficiency may also affect the thermal robustness, stability, and lifetime of high-specific impulse Hall thrusters.

Although several engineering issues likely contributed, the research presented in this dissertation was based on the hypothesis that the efficiency maximum resulted as a consequence of modern magnetic field designs, which have been optimized for 1600 s specific impulse, that were unsuited for high-specific impulse operation. Motivated by the limited success of these industry efforts, a central theme of this research concerns the effects of magnetic field topography on Hall thruster efficiency at high-specific impulse.

Combined with the mission studies, this hypothesis was the basis for the development of a new series of Hall thrusters designed to extend the efficient operating range of 1600 s specific impulse Hall thruster technology to the 2000-3000 s range of specific impulse.

1.2 Research aim and contributions

The central aim of the research described here was to develop and characterize xenon Hall thrusters capable of both high-specific impulse and high-efficiency operation. The research was divided into development and characterization phases.

During the development phase, the laboratory-model NASA-173M Hall thrusters were designed incorporating plasma lens magnetic field topographies and evaluated in terms of their performance and plasma characteristics. Experiments with the first thruster, the NASA-173M version 1 (v1), validated the plasma lens design by showing how changing the magnetic field topography at high-specific impulse improved efficiency. The follow-on thruster, the NASA-173M version 2 (v2), incorporated design improvements suggested by its predecessor. Experiments with the NASA-173Mv2 showed there was a minimum current density and optimum magnetic field topography at which efficiency monotonically increased with voltage. Between 300-1000 V and an anode mass flow rate of 10 mg/s, the total specific impulse of the NASA-173Mv2 ranged from 1600-3400 s with a corresponding total efficiency of 51-61%. Thus, the NASA-173Mv2, by virtue of its improvements, achieved both high-efficiency and high-specific impulse operation. Performance comparisons between the thrusters also demonstrated that efficiency could be optimized for specific impulse by varying the plasma lens design.

During the characterization phase, a series of plasma diagnostics were deployed with the NASA-173Mv2 to improve the understanding of the competing mechanisms affecting performance at high-specific impulse. The NASA-173Mv2 was chosen for these studies since this thruster had demonstrated high-efficiency operation at high-specific impulse. To aid in the interpretation of experimental

data, a phenomenological Hall thruster performance model accounting for the effects of a multiply-charged, partially-ionized plasma was also derived as a function of the utilization efficiencies of current, mass, voltage, and charge.

Using experimental data as inputs, the performance model was used to compute the utilization efficiencies of the NASA-173Mv2. With increasing discharge voltage, the net decrease of the anode efficiency due to the increasing fraction of multiply-charged ions was shown to be minor. The electron current was also shown to be approximately constant with increasing discharge voltage, while the ion current increased due to the increased fraction of multiply-charged ions. The results of this analysis confirmed how efficient operation at high-specific impulse was enabled through regulation of the electron current with the magnetic field. Further analysis revealed that anode efficiency was largely determined by the current utilization efficiency, which suggested that the maximum efficiency of Hall thrusters has yet to be reached. Finally, it was shown that the electron Hall parameter was nearly constant with voltage, which confirmed that efficient operation can be realized only over a limited range of Hall parameters.

1.3 Organization

This dissertation is organized into three major parts: background, thruster development, and thruster characterization.

Chapters 2-5 discuss the background information that motivated this research and lays the foundation for understanding the thruster development and characterization efforts. In Chapter 2, the mission studies motivating the development of high-specific impulse Hall thrusters are reviewed. Chapter 3 discusses the basic operating principles of Hall thrusters and shows how controlling

the electron current is critical to maintaining efficiency. Recent studies of Hall thrusters are then reviewed that have shown maximum efficiency occurred at less than 3000 s specific impulse. Combined with the mission studies, the results from these studies led directly to the development of the NASA-173M Hall thrusters. In Chapter 4, a phenomenological Hall thruster performance model that allows for a multiply-charged, partially-ionized plasma is derived. It is shown how the model can be used to weigh the relative importance of electron current and multiply-charged ions on performance. In Chapter 5, magnetic circuits and plasma lens focusing are discussed. Some early experiments that attempted to improve the focusing of a Hall thruster are presented. These experiments provided the insight necessary to design a high-specific impulse Hall thruster.

Chapters 6-9 discuss the development phase of the NASA-173M Hall thrusters. Chapter 6 describes the vacuum facilities and diagnostics that were used during the development phase experiments. Chapter 7 discusses the development of the NASA-173Mv1. Chapter 8 discusses the development of the NASA-173Mv2 and it is shown how the NASA-173Mv2 achieved the intended goal of high-efficiency, high-specific impulse operation. In Chapter 9, the performance characteristics of the two thrusters are compared.

Chapters 10-12 discuss the characterization phase of the plasma properties of the NASA-173Mv2. Chapter 10 describes the vacuum facilities and diagnostics that were used during the characterization phase experiments. In Chapter 11, the results of experiments that measured discharge chamber and far-field plasma properties are described. In Chapter 12, the results from the NASA-173Mv2 plasma characterization are analyzed and the performance model derived in Chapter 4 is used to compute the utilization efficiencies of the NASA-173Mv2.

Finally, in Chapter 13, the major conclusions from this dissertation are summarized and suggestions concerning the future development of high-specific impulse Hall thrusters are proposed.

Chapter 2

The need for high-specific impulse Hall thrusters

The high-specific impulse Hall thruster yields benefits to a number of Earth orbital and interplanetary missions that other electric propulsion technologies do not provide. To show why this is the case, this chapter begins by reviewing the performance of space propulsion systems, discusses the different types of electric propulsion, and demonstrates how the optimum specific impulse for a mission is not solely governed by the rocket equation. The second half of this chapter reviews studies showing how mission benefits such as greater payloads, launch vehicle step downs, reduced trip times, or lower required power are demonstrating a need for high-specific impulse Hall thrusters.

2.1 Performance of space propulsion systems

A space propulsion system (*i.e.*, any rocket, be it chemical, electric, or otherwise) accelerates a spacecraft by applying a thrust force, usually through the expulsion of propellant mass at high velocity [67]. Consider the one-dimensional flight of a rocket-propelled spacecraft as a function of time t with mass $M(t)$ and velocity $U(t)$ in the absence of gravitational forces. From conservation of momentum, the acceleration of the spacecraft results from the application of the

thrust T, given by the product of the mass flow rate $\dot{m}$ and effective exit velocity c (relative to the rocket) of the propellant

$$M(t)\frac{d}{dt}U(t) = T = \dot{m}c\,. \tag{2-1}$$

The effective exit velocity accounts for any unbalanced pressure forces and the non-uniform distribution of exhaust velocities over the exit cross-section of the rocket.

The expulsion of propellant by the rocket reduces the mass of the spacecraft over time. If the mass flow rate of propellant is constant, the spacecraft mass is

$$M(t) = M_o - \dot{m}t\,, \tag{2-2}$$

where M_o is the initial mass of the spacecraft. Differentiating Eqn. 2-2 and then substituting into Eqn. 2-1 yields the differential equation

$$M\frac{dU}{dt} = -\frac{dM}{dt}c\,. \tag{2-3}$$

Canceling the time differentials and integrating over some initial to final spacecraft velocity and mass

$$\int_{U_o}^{U_f} dU = -c\int_{M_o}^{M_f}\frac{dM}{M}\,, \tag{2-4}$$

an expression for the ratio of final to initial vehicle mass is obtained as a function of the velocity increment ΔU and effective exit velocity

$$\frac{M_f}{M_o} = e^{-\frac{\Delta U}{c}}\,. \tag{2-5}$$

Eqn. 2-5 was first derived by Konstantin Tsiolkovskii in 1895 [68]. Also known as the rocket equation, Eqn. 2-5 illustrates the impact of exhaust velocity on the mass ratio of a spacecraft. In the authoritative words of ion propulsion pioneer Ernst Stuhlinger, the rocket equation "has been ever since the basis of all theoretical work on rocket propulsion [68]." The rocket equation implies that exhaust velocity should be on the order of the velocity increment to deliver a useful mass fraction at the destination. Exhaust velocity is often used as a first-order criterion in space vehicle design. However, as shown in section 2.3, other competing criteria can diminish the importance of exhaust velocity such that the technology with the highest exhaust velocity is not always the optimum choice for a particular mission.

Before considering those situations, a few more definitions are needed. The total impulse delivered to a spacecraft is the thrust integrated over time

$$I_t = \int_0^t T\, dt\,. \tag{2-6}$$

Total impulse has units of Newton-seconds (N·s) and is often used to report rocket lifetime. For example, the lifetime of a rocket with a total impulse capability of 3×10^6 N·s and a constant thrust of 83 mN would be about 10,000 hours.

The specific impulse is the total impulse per unit weight of propellant given by

$$I_{sp} = \frac{\int_0^t T\, dt}{g\int_0^t \dot{m}\, dt}, \tag{2-7}$$

where the weight of the propellant is defined by the sea-level acceleration of gravity on Earth (g = 9.80665 m/s^2) [67]. Specific impulse has units of seconds, but is really force per unit weight flow rate, that is, specific impulse is a measure of how effectively propellant is converted into useful thrust. If the thrust and mass flow rate are constant over the thrust time, specific impulse reduces to

$$I_{sp} = \frac{T\int_0^t dt}{g\dot{m}\int_0^t dt} = \frac{T}{g\dot{m}} = \frac{T}{\dot{w}} = \frac{c}{g}. \qquad \textbf{(2-8)}$$

Specific impulse (in seconds) is then roughly one-tenth of the effective exit velocity (in m/s). The two quantities can be used interchangeably in the rocket equation (Eqn. 2-5) via Eqn. 2-8. However, specific impulse should not be interpreted as the exit velocity divided by some (seemingly) arbitrary constant. Unfortunately, Eqn. 2-8 has led some investigators, usually in the absence of reliable thrust measurements, to report specific impulse from measurements of the propellant ion velocity alone. This can significantly overestimate specific impulse if the rocket produces only a very small amount of ions from the propellant or if the ions significantly diverge from the thrust axis. Therefore, using the ion velocity to estimate specific impulse should be avoided.

Besides producing thrust, a rocket can also be thought of as an energy converter, since producing thrust requires the conversion of a source of potential energy to kinetic energy. For example, in a chemical rocket potential energy stored in molecular bonds is released to heat propellant gas and converted to kinetic energy by accelerating the gas through a nozzle. In electric propulsion, the potential energy is provided by an external power source. Some fraction of the input power from this

external source is converted into the axially directed kinetic power of the exhaust, or jet power, given by

$$P_{jet} = \frac{1}{2}\dot{m}c^2 = \frac{1}{2}Tc\,. \qquad \textbf{(2-9)}$$

Due to the second law of thermodynamics, the efficiency of producing the jet power is less than perfect. To characterize the losses of the conversion, the total system efficiency (of the power source and thruster) is defined as the ratio of the jet power to the system input power provided by the spacecraft bus

$$\eta_{sys} = \frac{P_{jet}}{P_{sys}} = \frac{\frac{1}{2}Tc}{P_{sys}} = \frac{1}{2}gI_{sp}\frac{T}{P_{sys}}\,. \qquad \textbf{(2-10)}$$

Eqn. 2-10 shows that the performance of a space propulsion system can be described by specifying the system efficiency, system input power, specific impulse, and thrust. These quantities are collectively referred to as the **system performance parameters**.

2.2 Electric propulsion

Hall thrusters belong to a larger family of propulsion technologies that are collectively known as electric propulsion. Jahn defined electric propulsion as "the acceleration of gases for propulsion by electrical heating and/or by electric and magnetic body forces [69]." Unlike a chemical rocket, which relies on the stored internal energy in the molecular bonds of its propellant, in an electric rocket the energy is obtained from an external power source. This is the main advantage of electric over chemical propulsion, since the amount of energy that can be externally applied is limited only by available technology. In a chemical rocket, the dependence on internal energy limits the maximum specific impulse to about 450 s, whereas in

electric rockets specific impulses of over 17,000 s have been obtained in the laboratory [70, 71].[4]

Since external power sources are required, the high-specific impulse capabilities of electric propulsion come at the expense of power and mass. This limited the application of electric propulsion on-board spacecraft until the 1980's as spacecraft power finally began to increase to meet the growing needs of communication satellites [72].[5] The so-called "power supply penalty" [69] places a premium on maximizing the specific power (in W/kg) of power supplies used for electric propulsion systems. Other design constraints, such as launch vehicle selection, mission time, and payload further complicate the situation. As shown in section 2.3, the result is that the highest attainable specific impulse is not always the optimum choice.

The different electric propulsion technologies were first categorized by Stuhlinger [68] and Jahn [69]. Adopting the definitions of Jahn [69], the thruster categories are:

1. **Electrothermal propulsion:** acceleration of a propellant gas by electrical heat addition and expansion through a convergent/divergent nozzle. Examples include resistojets and arcjets.
2. **Electrostatic propulsion:** acceleration of an ionized propellant gas by the application of electric fields. Examples include gridded ion thrusters, colloid thrusters, and field emission electric propulsion (FEEP).

[4] Current flight hardware operates around 330 s for hydrazine chemical rockets, 500 s for arcjets, 1600 s for Hall thrusters, and 3000 s for gridded ion thrusters [67].
[5] One is left to wonder what Dire Straits the field of electric propulsion would be in otherwise [73].

3. **Electromagnetic propulsion:** acceleration of an ionized propellant gas by the application of both electric and magnetic fields. Examples include Hall thrusters, pulsed plasma thrusters (PPT), and magnetoplasmadynamic thrusters (MPDT).

Descriptions of the thruster types, flight programs, and development trends can be found in Ref. [69, 70, 74-76] and the September-October 1998 issue of the AIAA Journal of Propulsion and Power (Vol. 14, No. 6). The mission studies discussed in section 2.4 primarily compare the merits of using electrostatic ion thrusters versus electromagnetic Hall thrusters. The characteristics of Hall and ion thrusters make them well suited for a number of energetic Earth orbital and interplanetary missions of interest for commercial, military, and space science applications.

In the ion thruster, propellant is usually ionized in a discharge chamber through bombardment with magnetically confined electrons [77, 78]. A set of biased grids on one side of the discharge chamber extracts and electrostatically accelerates ions. Because electrons are excluded from the gap between the grids, the beam current is space-charge limited. As a result, ion thrusters have relatively low thrust densities. However, the specific impulse, efficiency, and lifetime are high with values greater than 3000 s, 60%, and 10,000 h, respectively, being common.

Hall thrusters, which are discussed in more detail in Chapter 3, ionize and accelerate propellant in a quasineutral plasma without the use of a dedicated ionization chamber and accelerating grids [1-3]. Instead, an annular discharge chamber with crossed electric and magnetic fields trap electrons in an azimuthal ExB drift. The trapped electrons ionize the propellant and, in order to maintain current continuity, a sharp rise in the electric field is forced to occur that accelerates

the ions (which are unaffected by the magnetic field due to their greater mass). Hall thrusters are sometimes called "gridless" for this reason, but the implied association with ion thrusters is misleading since the basic operating principles of a Hall thruster, the use of magnetic fields for ionization and acceleration, leads to a substantially different physical situation. Hall thrusters accelerate ions in a quasineutral plasma such that current density (*i.e.*, thrust density) is limited only by material and thermal limitations. Hall thrusters achieve thrust densities on the order of 1.0 mN/cm^2 compared to about 0.1 mN/cm^2 for ion thrusters. Compared to ion thrusters, Hall thrusters also have higher specific power because they require fewer power supplies, have a lower part count, and less stringent voltage isolation requirements.[6] However, the specific impulse, efficiency, and lifetime (typically 1600 s, 50%, and 7000 h, respectively) are usually lower for Hall thrusters.

In summary, when compared to a Hall thruster of equivalent power an ion thruster will be more massive (because of lower specific power), physically larger (because of lower thrust density), and produce less thrust (because higher specific impulse means a lower thrust-to-power ratio) but will have higher specific impulse, efficiency, and lifetime. The benefits of higher specific power and thrust-to-power ratio can be advantageous for missions in certain situations.

2.3 Optimum flight performance

Since all thruster technologies presumably benefit from the same pool of power technology, specific power mainly depends on the relative complexity of the propulsion system's power handling requirements. Specific power can be modeled as

[6] Specific powers on the order of 50-200 W/kg are possible and are expected to increase because of near-term technology advancements [67]. However, specific power is highly dependent on the available technology, the relative development of a thruster, and the mission. Both Hall and ion thrusters draw from the same technology pool so advances are almost equally applied. The end result is that Hall thrusters generally have a higher specific power than ion thrusters.

$$\alpha = \frac{P_{sys}}{M_{pp}}, \tag{2-11}$$

where M_{pp} is the mass of the power plant, the thruster, and all other equipment to supply power and propellant to the thruster (*e.g.*, a power processing unit, cabling, propellant tank, gimbals, etc.). The initial mass of the spacecraft is

$$M_o = M_p + M_{pl} + M_{pp}, \tag{2-12}$$

where M_p is the propellant mass and M_{pl} is the payload mass. (As defined, the payload mass includes the dry mass of the spacecraft except for the power plant.) If the system efficiency and mass flow rate are constant over a thrusting time t_p that consumes the propellant mass M_p, Eqn. 2-11 can be expressed as

$$P_{sys} = \alpha M_{pp} = \frac{M_p c^2}{2 t_p \eta_{sys}}. \tag{2-13}$$

Combining Eqns. 2-5, 2-11, 2-12, and 2-13 the payload mass fraction is

$$\frac{M_{pl}}{M_o} = e^{-\Delta U/c} - \left(1 - e^{-\Delta U/c}\right)\left(\frac{c}{v_c}\right)^2, \tag{2-14}$$

where a characteristic speed v_c has been defined as [79]

$$v_c = \sqrt{2\alpha t_p \eta_{sys}}. \tag{2-15}$$

Note that the characteristic speed depends only on the mission time for a given thruster (since the thruster choice sets the specific power and efficiency).[7] If the

[7] Mission time is left unspecified in this example. However, note that long mission times have penalties in terms of higher costs (to maintain mission operations) and the possiblity of failure (the longer the mission, the more likely something will break).

payload ratio is specified, solutions to Eqn. 2-14 exhibit a single maxima represented by the line [67]

$$\frac{c}{\Delta U}\left(e^{\Delta U/c}-1\right)-\frac{1}{2}\left(\frac{v_c}{c}\right)^2-\frac{1}{2}=0\,. \qquad \textbf{(2-16)}$$

Figure 2-1 plots solutions to Eqns. 2-14 and 2-16 when the velocity increment and effective exit velocity are normalized by the characteristic speed in Eqn. 2-15. For a given payload fraction and characteristic speed, there is always an optimum choice of the effective exit velocity (*i.e.*, the specific impulse) that maximizes the velocity increment. In this example, the optimum occurs in the range $\Delta U/v_c \leq 0.805$ and $0.505 \leq c/v_c \leq 1.0$ [67]. The optimum exists because the mass of the power plant grows with exit velocity but the propellant mass decreases. The optimum in Figure 2-1 is also rather broad, so small decreases to the payload fraction can be traded for specific impulse at a fixed velocity increment. This example problem is actually under constrained (the mission time and payload fraction are free parameters), but still demonstrates how space mission design utilizing electric propulsion goes far beyond the simple implications of the rocket equation. More advanced analysis of space mission optimization can be found in the literature [80].

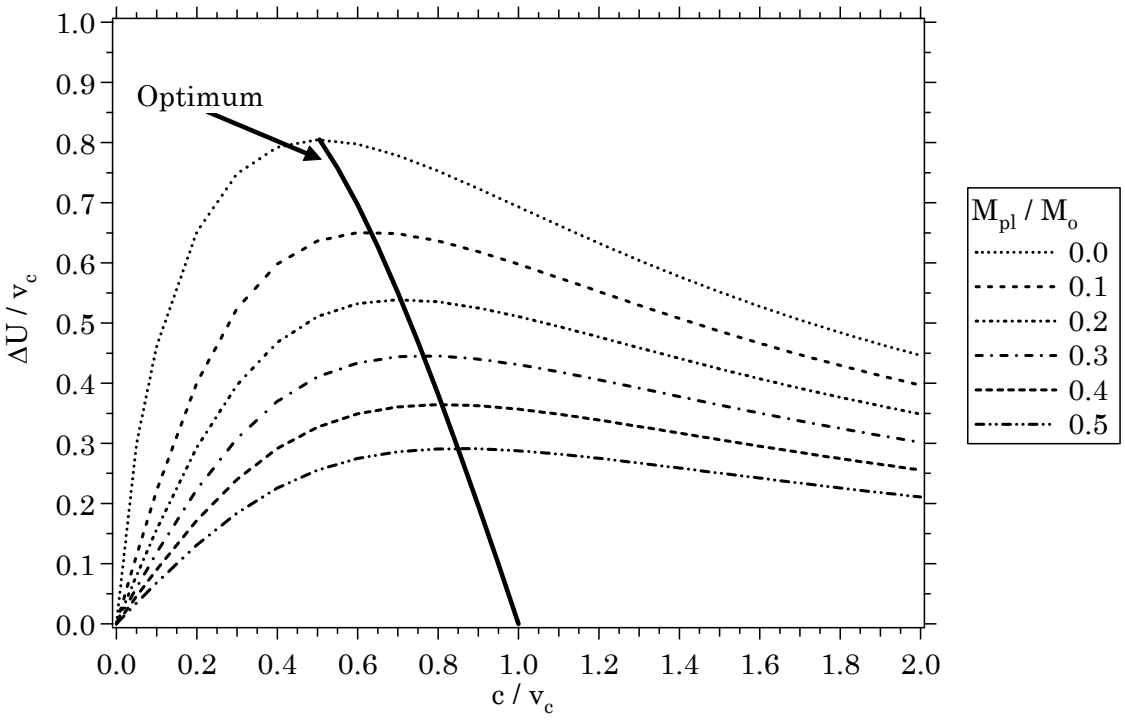

Figure 2-1 Normalized velocity increment versus normalized effective exit velocity as a function of the payload mass fraction. The line of optimum solutions from Eqn. 2-16 is also shown.

2.4 Mission studies

The previous section showed that specific impulse is a necessary, but not sufficient criterion for choosing a thruster technology. In this section, studies are reviewed that have demonstrated how high-specific impulse Hall thrusters can provide substantial benefits to Earth orbital and interplanetary missions.

In general, electric propulsion used on Earth orbiting satellites can provide a cost benefit, typically by delivering more payload or by allowing for a launch vehicle step down, when chemical propulsion systems used for station keeping and orbit transfers are replaced or augmented [23, 72, 75, 81-92]. For example, studies of low earth orbit (LEO) constellation missions by Oleson [83] have shown that the use of 1600 s Hall thrusters or 2500 s ion thrusters for beginning-of-life orbit transfer and end-of-life de-orbit decreased the required number of launch vehicles from fourteen

for an all-chemical spacecraft to eleven. Geosynchronous earth orbit (GEO) communications satellite mission studies by Oleson, *et al.* [72] have also shown that the use of 1600 s Hall thrusters or 2500 s ion thrusters provided a 13% increase in payload mass if used only for north-south station keeping and as much as a 20-45% if used for portions of beginning-of-life orbit transfers .

In either Ref. [83] or [72], 2500 s ion thrusters marginally outperformed 1600 s Hall thrusters, if at all. When the specific impulse of the Hall thruster is increased to the domain of the ion thruster, the performance improvements can be substantial [23, 82, 84-86]. For example, a study by Gulczinski and Spores [82] of trip time constrained orbit transfer missions showed significant benefits when high-specific impulse Hall thrusters were used. Results of one case from Ref. [82] are shown in Figure 2-2, Figure 2-3, and Figure 2-4 for LEO-GEO orbit transfers with trip times of 180, 270, and 360 days, respectively. In Figure 2-2, 180 day trips with 2500 s Hall thrusters delivered 38% higher payload mass fractions (0.33 versus 0.24) than 3200 s ion thrusters. When the trip time was relaxed to 360 days (Figure 2-4), the same Hall thrusters delivered payload fractions of 0.49 and ion thrusters delivered 0.47. In other words, only when trip times were relaxed could the lower specific power and high-specific impulse of the ion thruster match the high-specific power and lower specific impulse of the Hall thruster. Since it is usually the case that the trip time must be minimized (the satellite is not useful until it reaches GEO), high-specific impulse Hall thrusters outperform ion thrusters for these missions.

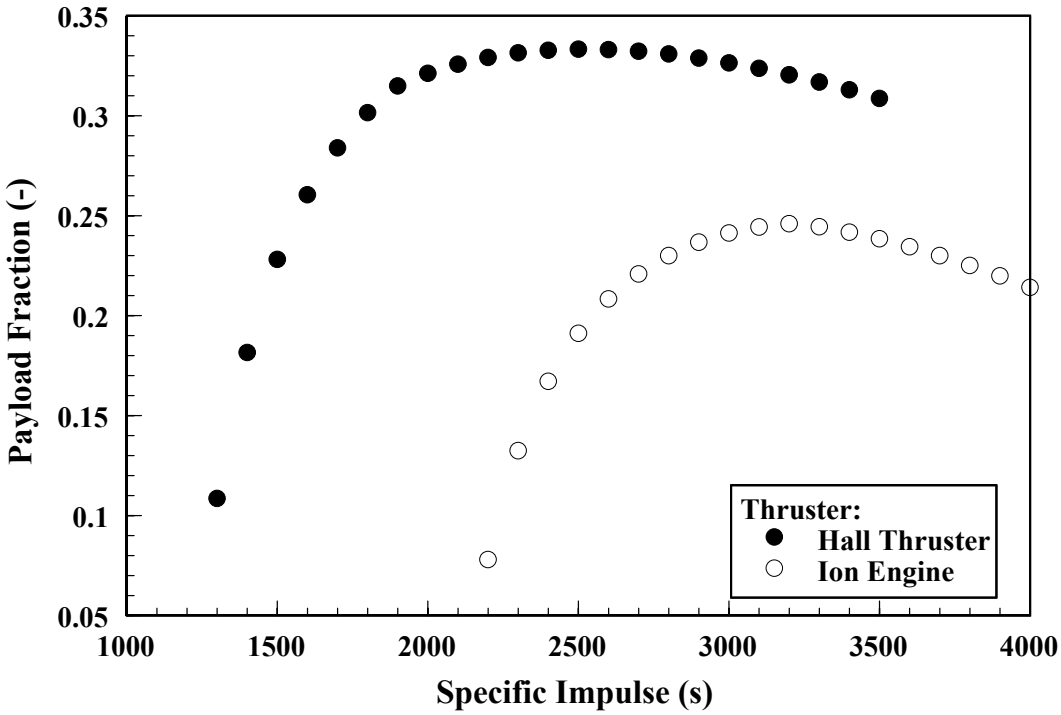

Figure 2-2 **Payload mass fraction versus specific impulse (180 day trip time) for the LEO-to-GEO orbit transfer mission in Ref. [82].**

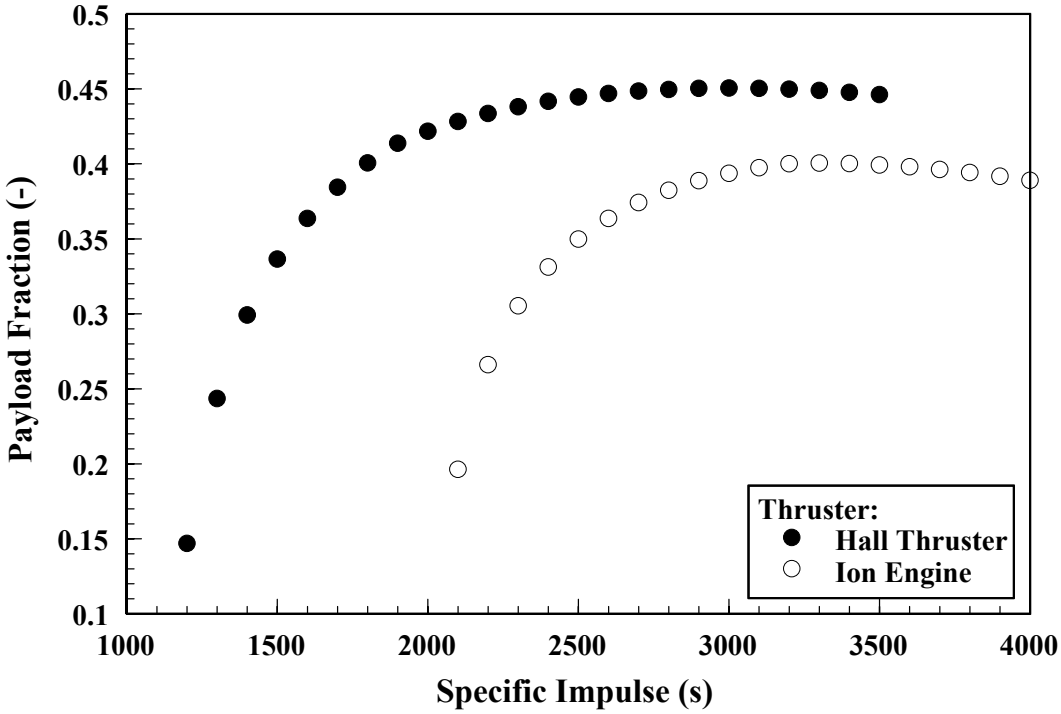

Figure 2-3 **Payload mass fraction versus specific impulse (270 day trip time) for the LEO-to-GEO orbit transfer mission in Ref. [82].**

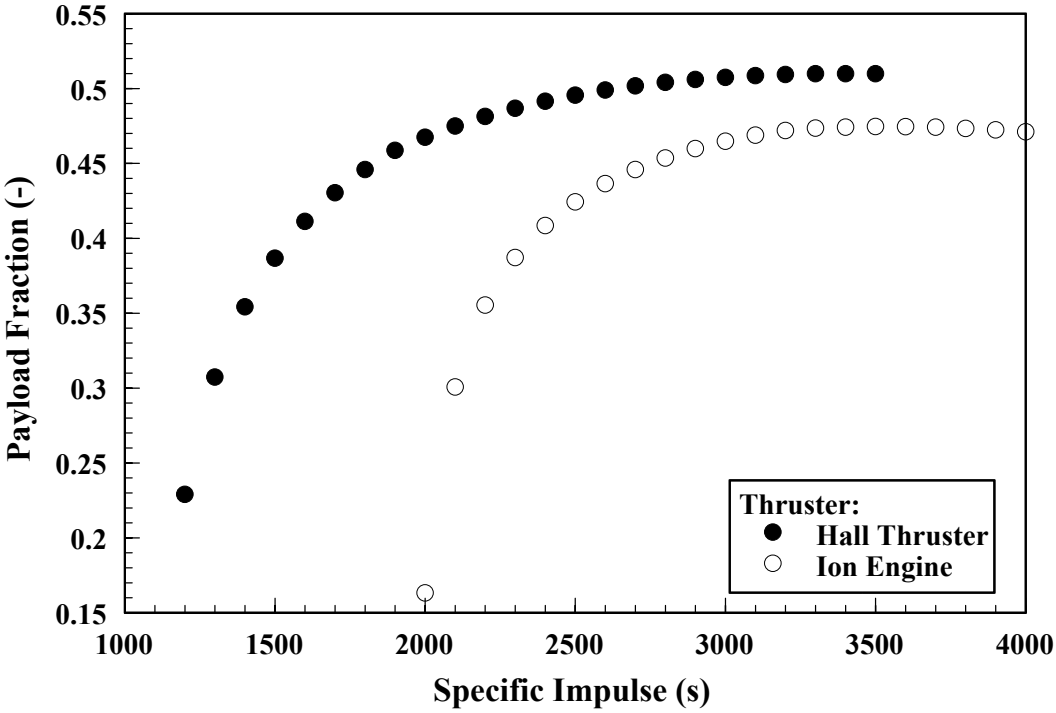

Figure 2-4 Payload mass fraction versus specific impulse (360 day trip time) for the LEO-to-GEO orbit transfer mission in Ref. [82].

Ref. [82] considered fixed orbit transfer trip times but allowed the power level to vary. In contrast, Oleson [84] studied missions with fixed power levels and variable trip times for Hall thruster specific impulses of 1800 or 2400 s relative to 3000 s ion thrusters. Oleson's results [84], which were essentially the same as Ref. [82], showed that the higher specific power of the Hall thruster operating at high-specific impulse always outperformed the ion thruster, with the more significant gains again being for shorter trip times. For trip times greater than 60 days, launch vehicle step downs were possible for either Hall or ion thrusters.

Additional benefits can be realized if Hall and ion thrusters are designed for variable specific impulse (VIPS) operation [86, 87]. Sometimes referred to as bi-modal or multi-mode operation, VIPS usually describes constant power operation for at least two different specific impulses. The first set point is a low-specific impulse

(1000-2000 s), high-thrust mode suitable for rapid orbit transfers. The second set point is a high-specific impulse (3000-4000 s), low thrust mode suitable for station keeping and interplanetary maneuvers. Oleson [86] considered LEO-to-GEO orbit insertion and station keeping, LEO-to-GEO reusable tug missions, and an interplanetary mission for a Europa orbiter. For both LEO-to-GEO missions, Hall thrusters slightly outperformed the ion thruster and for the Europa orbiter both technologies showed similar results. To achieve VIPS operation a need was identified with both technologies to overcome lifetime issues. In the case of the ion thruster, operation as low as 1800 s was required, where space-charge limitations are known to enhance grid erosion due to beamlet defocusing [1, 77, 93]. For the Hall thruster, operation above 3000 s was needed, where the higher energy of the ions can enhance discharge chamber wall erosion [2].

The competitiveness of the Hall thruster in Ref. [86] for interplanetary missions defies the popular belief that ion thrusters optimize for these mission types. Other interplanetary mission studies that have considered Hall thrusters have shown similar or additional benefits [93-97]. In a concept for piloted Mars missions using solar power alone, Gefert, *et al.* [96] and later Dudzinski, *et al.* [94] specified 2000-2500 s Hall thrusters primarily because the required power of 0.8 MW was much less than the 4-8 MW needed with 4000-7000 s ion thrusters. Fiehler and Oleson [95], using performance data derived from the NASA-173Mv2 Hall thruster (see Chapter 8), considered scenarios for a Mars orbiter. While delivering nearly equivalent payloads for the same trip times, it was concluded that 3200 s Hall thrusters outperformed 4000 s ion thrusters because the required power was lower for the Hall thruster system. These benefits were realized because the higher

specific power of the Hall thruster reduced the system mass, allowing equivalent payload mass to be delivered at lower power levels.

2.5 Conclusions

When choosing an electric propulsion technology for a space mission, the ratio of the mission velocity increment and specific impulse is a useful means to down select initially from available thrusters. Other considerations, especially specific power, must be factored in to the analysis in order to maximize mission performance. Several studies of Earth orbital and interplanetary scenarios have shown that increasing the specific impulse of Hall thrusters to 2000-3000 s can yield benefits that its closest competitor, the ion thruster, cannot match. These benefits have included greater payloads, launch vehicle step downs, reduced trip times, or lower required power. Since the realization of these benefits depends on high-specific impulse Hall thrusters, a clear need exists to explore the development challenges of such technology enhancements.

Chapter 3

The high-specific impulse Hall thruster

Studies have demonstrated the mission benefits of high-specific impulse Hall thrusters. This chapter discusses the basic operating principles of Hall thrusters and shows how controlling the electron current is critical to maintaining efficiency. Next, the development history of high-specific impulse Hall thrusters is reviewed with an emphasis on the investigations that have motivated this dissertation. These recent investigations have demonstrated 4000 s specific impulse with modern Hall thrusters, but it was found that maximum efficiency occurred at less than 3000 s. The research presented in this dissertation was based on the hypothesis that the efficiency peak was a consequence of modern magnetic field designs, which have been optimized for 1600 s specific impulse, that were unsuited for high-specific impulse operation. Combined with the mission studies, this hypothesis was the basis for the development of a new series of Hall thrusters designed specifically for high-efficiency, high-specific impulse operation.

3.1 Hall thruster operating principles

This section describes how coaxial Hall thrusters are constructed and provides an overview of their basic operating principles most relevant to high-specific impulse operation. In Chapter 4, a Hall thruster performance model is discussed and Chapter 5 describes how magnetic fields affect thruster operation.

Additional details concerning Hall thruster physics can be found in the literature [1-3, 98, 99].

3.1.1 Physical description

Figure 3-1 is a schematic of a single-stage Hall thruster with a coaxial, ceramic discharge chamber, also known as a magnetic layer thruster (MLT) or as a stationary plasma thruster (SPT). Figure 3-2 is a schematic of a two-stage anode layer thruster (TAL), which is a Hall thruster that uses a metallic discharge chamber separated into an ionization and acceleration stage by an intermediate electrode. There will be more to say about two-stage thrusters in general and anode layer thrusters in particular later in this chapter. However, unless noted the focus throughout is on single-stage magnetic layer thrusters. Photographs of the two thruster types are shown in Figure 3-3 and Figure 3-4, respectively. Geometries other than the coaxial discharge chamber, such as linear [100-102], cylindrical [103-105], or racetrack [46, 57] configurations, are not considered here.

Hall thrusters are usually constructed from four major components: discharge chamber, anode, cathode, and magnetic circuit. As shown in Figure 3-1, the ceramic walls of the discharge chamber house an anode through which a neutral propellant gas is injected. The ratio of the discharge chamber axial length to radial width is usually greater than one.[8] The walls are typically made from boron nitride (BN) or are mixed with silicon dioxide (SiO_2) into a compound called borosil (BN-SiO_2). There have been attempts to use other materials such as alumina (Al_2O_3) or silicon carbide (SiC) [109-117]. Although these materials may exhibit lower erosion under ion bombardment than boron nitride, their secondary electron emission

[8] In an anode layer thruster, the discharge chamber is usually much shorter, with a length to width ratio of less than one. However, to insure uniform propellant distribution and to enhance stability in the shorter discharge chamber, the anode is typically hollow and long [99, 106-108].

characteristics result in enhanced electron transport that lowers thruster efficiency [109].

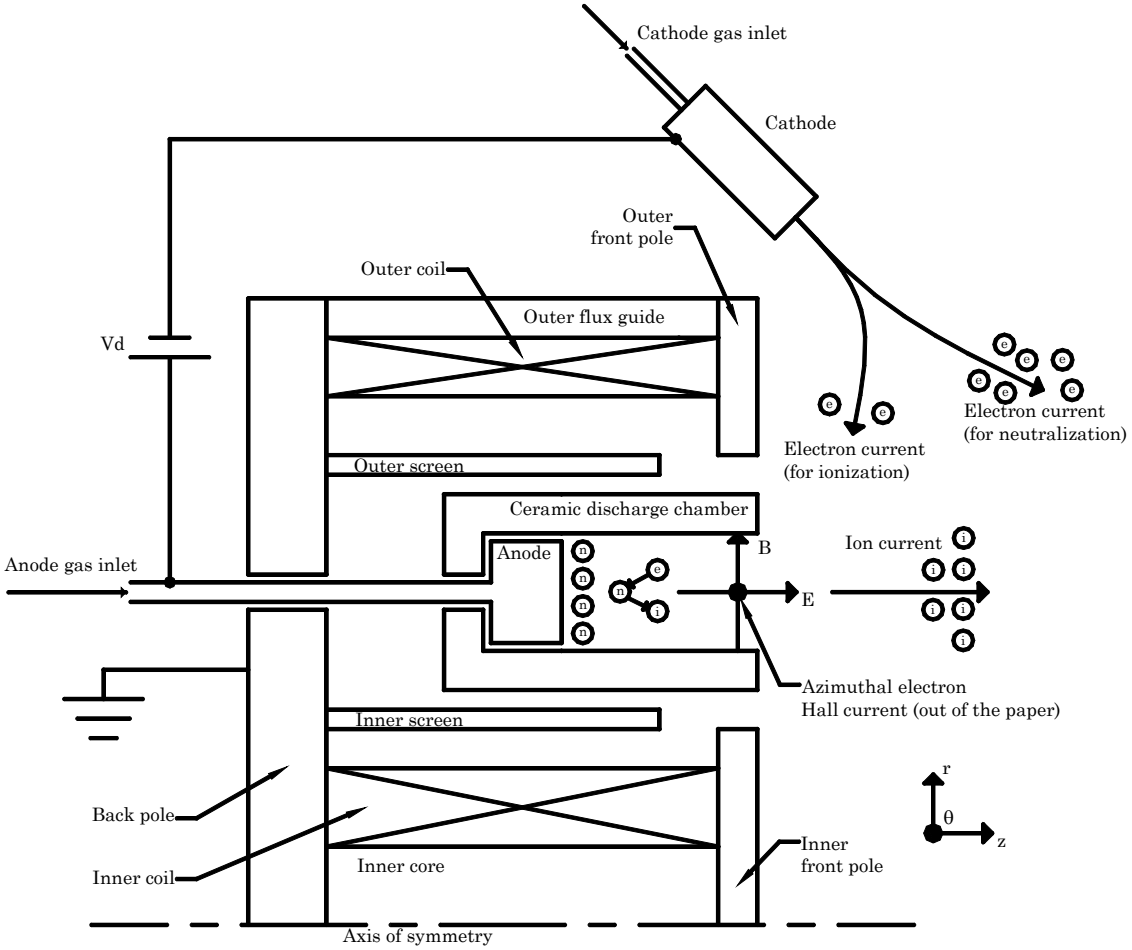

Figure 3-1 Cross-sectional schematic of a single-stage magnetic layer Hall thruster with a coaxial, ceramic discharge chamber (not to scale). Electrons (*e*) from the cathode are trapped in an azimuthal drift by the electric (*E*) and magnetic fields (*B*). Neutral (*n*) propellant gas is injected through the anode into the discharge chamber, where collisions with electrons create ions (*i*) that are accelerated by the electric field producing thrust.

In a single-stage thruster, the anode acts both as the positive electrode for the applied voltage V_d and the gas distributor for the propellant gas, which is typically xenon (krypton is currently being considered for high-power thrusters [48,

112, 118-120]).[9] The anode is fabricated to ensure that the azimuthal distribution of neutral propellant gas is uniform. This is usually accomplished through a series of equally spaced injection ports around the circumference of the anode [123-125]. Some designs, usually sub-kilowatt models [126], separate the anode and gas distributor into separate components.

In a two-stage thruster, an intermediate electrode separates the ionization and acceleration stages. In the ionization stage the applied potential, usually dubbed the discharge voltage, is typically five to ten times the ionization potential of the propellant [106]. The applied potential in the acceleration stage, usually dubbed the acceleration-stage voltage, accelerates ions created in the ionization stage. (Note that the applied voltage in a single-stage thruster, which is used for both ionization and acceleration, is always referred to as the discharge voltage.) A two-stage thruster potentially offers performance benefits over a single-stage thruster, primarily by improving the ionization efficiency. However, these benefits come at the expense of complexity due to the additional electrode. In a magnetic layer thruster, it turns out that the benefits of a two-stage design only begin to outweigh the drawbacks when the acceleration potential is on the order of several kilovolts. This is mainly because sub-kilovolt magnetic layer thrusters, when properly designed, efficiently ionize the propellant without the encumbrances of an ionization stage. In an anode layer thruster, the electron temperature is higher than in a magnetic layer thruster (see section 3.1.3.3). This means that, in order to maintain thruster efficiency, the two-stage approach in an anode layer thruster becomes necessary at lower voltages than in the magnetic layer thruster. The cross-over

[9] Hall thrusters have been operated on a multitude of propellants, including at least: all of the noble gases, hydrogen, helium, lithium, nitrogen, oxygen, sodium, potassium, cesium, bismuth, lead, cadmium, thallium, barium, mercury, methane, and silane (SiH_4) [63, 98, 99, 106, 121, 122].

depends on several variables, but is apparently in the range of 500-800 V (less than 3000 s specific impulse) [127].

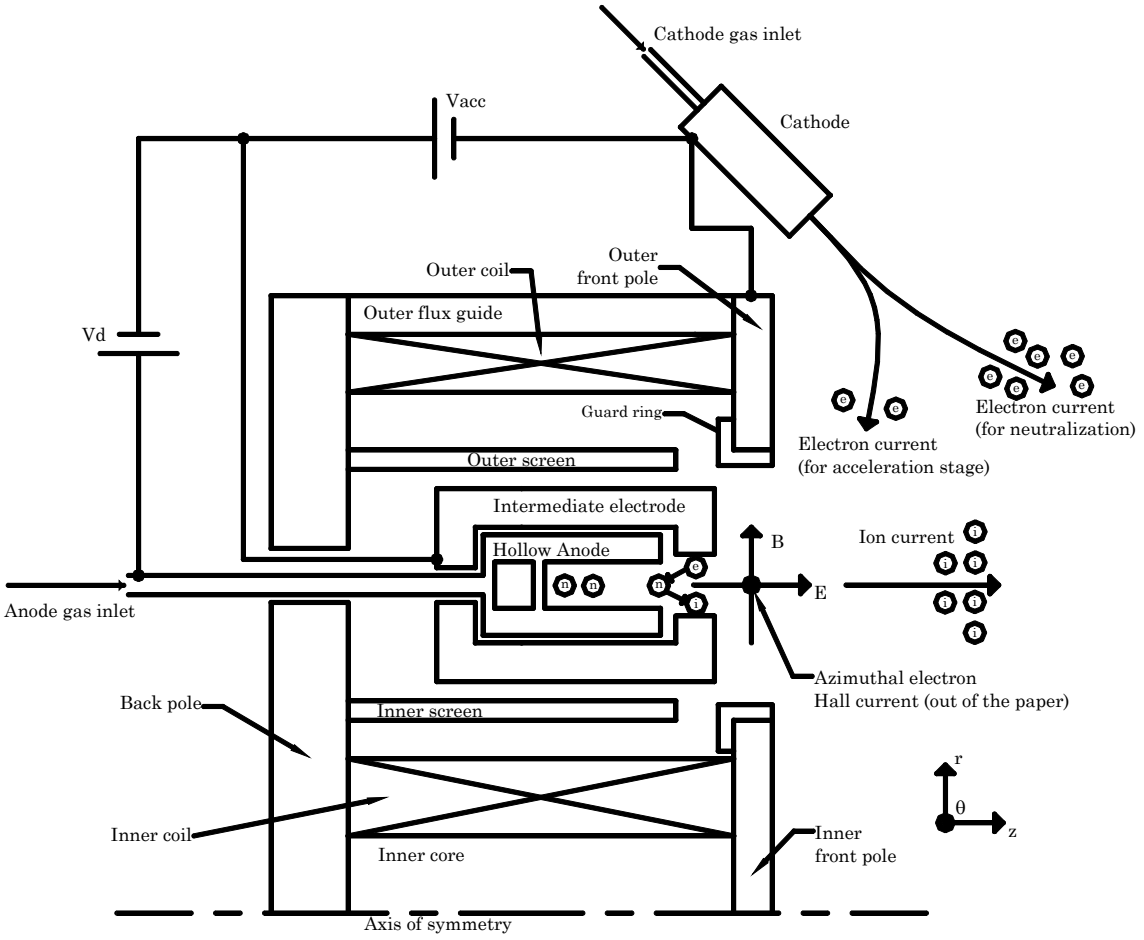

Figure 3-2 Cross-sectional schematic of a two-stage anode layer Hall thruster with a coaxial, metallic discharge chamber (not to scale). The discharge voltage (V_d) is applied between the hollow anode and intermediate electrode, creating the ionization stage. The acceleration-stage voltage (V_{acc}) is applied between the intermediate electrode and the cathode, creating the acceleration stage. The thruster body is usually maintained at cathode potential.

The cathode supplies electrons to the discharge for ionization and to the plume for neutralization of the ion exhaust. While emitting filaments are sometimes used, an orificed hollow cathode is the electron source of choice. In a hollow cathode, additional propellant gas is passed over a thermionic emitter, such as lanthanum hexaboride (LaB_6) or porous tungsten impregnated with oxides (*e.g.*, barium oxide

(BaO)), which when heated emits electrons and initiates a plasma breakdown via electron-neutral collisions [128, 129]. Electrons are extracted through a small orifice using a positively biased electrode called a keeper. Modern cathodes are usually capable of heaterless and keeperless operation after the initial plasma breakdown occurs. Cathodes are usually mounted outside the thruster as shown in Figure 3-4, but can also be mounted on thruster centerline if the inner core is hollow. Such an approach is used with the NASA-457M shown in Figure 3-3 (the cathode is not shown in the photograph).

Figure 3-3 Photograph of the NASA Glenn Research Center series of magnetic layer thrusters. From left to right are the 2 kW NASA-120Mv2, 5 kW NASA-173Mv2 [130], and 50 kW NASA-457M [47, 131].

The magnetic circuit supplies the magnetic field that confines the plasma in the discharge chamber and acts as the support structure for the other thruster components. Several configurations are possible, but the basic design is composed of a collection of electromagnetic coils used to generate the magnetic flux and magnetic pole pieces used to channel the magnetic flux into the discharge chamber. The configuration shown in Figure 3-1 employs concentric inner and outer coil windings.

The more traditional design, (*e.g.*, the D-80 shown in Figure 3-4) uses individual coil windings for the outer portion of the circuit. Magnetic circuits are discussed more in Chapter 5.

Figure 3-4 Photograph of a Hall thruster with a metallic discharge chamber, also known as an anode layer thruster. The thruster shown is the TsNIIMASH D-80, which is capable of single- and two-stage operation [132, 133].

3.1.2 Basic theory of operation

As depicted in Figure 3-1, Hall thrusters are cross-field plasma sources in which an axial electric field E_z and a radial magnetic field B_r are used to confine electrons and accelerate ions [1-3, 98, 99].[10] Electrons migrating upstream from the negatively-biased cathode towards the positively-biased anode encounter the radial magnetic field. For purposes of stability, the axial gradient of the applied radial magnetic field $\nabla_z B_r$ is positive along the discharge chamber, with the minimum magnetic field at the anode and the maximum near the exit plane (see section 5.2.2) [134]. The magnitude of the magnetic field near the exit plane is sufficient to

[10] There are significant off-axis deviations of the electric and magnetic fields from these orientations. Chapter 5 discusses how magnetic fields can be shaped to improve Hall thruster performance by using radial and axial magnetic fields to form a plasma lens.

magnetize electrons and the cross-field configuration forces electrons to execute closed, azimuthal ExB drifts, forming a Hall current.[11] Thus, the axial electron mobility is severely restricted, which increases the electron residence time in the channel so that electrons can be effectively used to ionize neutral propellant injected through the anode. The restriction of the axial electron mobility is also responsible for establishing the self-consistent electric field, which must sharply rise in the region of maximum magnetic field intensity in order to maintain current continuity. This means then that the electric field profile can be approximated from the magnetic field profile. The portion of the discharge chamber where the electron ExB drift is greatest is referred to here as the closed-drift region.

Due to their much greater mass, ions are unimpeded by the magnetic field but are accelerated by the electric field to produce thrust. The mixture of electrons and ions in the closed-drift region means that the plasma is electrically neutral, and as such, the ion current density is not space-charge limited as in an ion thruster. The conditions in the closed-drift region therefore satisfy

$$n_e \approx n_b, \tag{3-1}$$

$$R_e << L << R_b, \tag{3-2}$$

$$\Omega_b << 1 << \Omega_e, \tag{3-3}$$

where R_e is the electron gyroradius based on the electron thermal velocity

$$R_e = \frac{v_{th,e}}{\omega_{ce}} = \sqrt{\frac{kT_e}{m_e}}\frac{m_e}{eB}, \tag{3-4}$$

[11] The azimuthal Hall current is where the thruster derives its most common name. Hall thrusters with annular discharge chambers are also sometimes called closed-drift thrusters, to distinguish them from linear configurations where the electron drifts are open [100-102].

R_b is the ion gyroradius based on the ion drift velocity gained from electrostatic acceleration (see section 4.3.3)

$$R_b = \frac{\left\langle v_b^+ \right\rangle}{\omega_{cb}} = \sqrt{\frac{2eV_a^+}{m_{xe}}}\frac{m_{xe}}{eB}, \tag{3-5}$$

Ω is the Hall parameter, given by ratio of the cyclotron frequency ω_c and the collision frequency ν

$$\Omega = \frac{\omega_c}{\nu}, \tag{3-6}$$

and L is a length scale characteristic of the closed-drift region. The length scale is usually taken as the length of the acceleration region $L \approx L_a$, *i.e.*, the portion of the discharge chamber over which the electric field is positive and large.

The Hall parameter characterizes the number of azimuthal orbits that a particle executes before being perturbed by particle collisions, collisions with the walls, or plasma fluctuations. The high value of the electron Hall parameter, being much greater than unity but not infinite, means that electrons undergo enough ionizing collisions on their way to the anode to sustain the plasma discharge while still maintaining a bulk azimuthal current that is several times larger than the axial current. **Therefore, it is reasonable to expect that efficient Hall thruster operation can only be realized over a limited range of electron Hall parameters.** By extension, this also implies that there always exists an optimum magnetic field strength. This has been confirmed by experiments, which have shown that the electron Hall parameter attains a value of several hundred in the closed-drift region [2, 135, 136] when the magnetic field strength is optimized for maximum thruster efficiency. Outside of the closed-drift region, wall collisions and

plasma turbulence can drive the electron Hall parameter to the Bohm value (*i.e.*, 16).

To optimize the efficiency of a Hall thruster it is critical to minimize the axial electron current by controlling the strength and shape of the magnetic field. The discharge current supplied to the thruster is the sum of the ion beam current I_b and the counter streaming electron current I_e

$$I_d = I_b + I_e . \tag{3-7}$$

As discussed in Chapter 4, the current utilization efficiency, which largely determines the overall thruster efficiency, is given by

$$\eta_b \equiv \frac{I_b}{I_d} = \frac{1}{1 + \left(I_e \middle/ I_b \right)} . \tag{3-8}$$

For constant discharge current, Eqn. 3-8 shows how minimizing the electron current improves the current utilization efficiency by maximizing the ion yield. The electrons also largely determine the ionization efficiency (through their average temperature) and the acceleration efficiency (by establishing the self-consistent electric field). **Thus, an understanding of the electron dynamics is of great importance in the study of Hall thrusters**.

The complex physical processes determining the electron current in a Hall thruster is a seemingly intractable problem that has plagued modelers and theoreticians for decades. Fortunately, while a complete understanding of electron dynamics is currently unavailable, it is known that the electron dynamics can be influenced by controlling the shape and strength of the magnetic field. At least in

this sense, it is fair to say that **the magnetic field is the most important aspect of Hall thruster design**.

Other factors affecting thruster efficiency are discussed in Chapter 4 and methods to focus ions and control the electrons with magnetic fields are discussed in Chapter 5. The next section discusses some important aspects of the electron dynamics in a Hall thruster.

3.1.3 Hall thruster electron dynamics

Neglecting the electron inertia, the axial electron current density is related to the Hall parameter through the steady-state, one-dimensional electron momentum equation [137, 138]

$$\nu_e n_e v_{ez} m_e + e n_e E_z + j_{e\theta} B_r + \frac{dp_e}{dz} = 0, \tag{3-9}$$

where ν_e is the electron collision frequency, v_{ez} is the axial electron velocity, $j_{e\theta}$ is the azimuthal electron current density, $p_e = n_e k T_e$ is the electron pressure, and the rest of the symbols have their usual meaning. Neglecting the electron inertia in the azimuthal electron momentum equation yields a relationship between the azimuthal and axial current densities and the electron Hall parameter [137]

$$j_{e\theta} = j_{ez} \Omega_e. \tag{3-10}$$

With this relation, Eqn. 3-9 can be solved for the axial current density

$$j_{ez} = \mu_{ez} \left(- e n_e E_z - \frac{dp_e}{dz} \right), \tag{3-11}$$

which shows that the axial electron current density is given by the product of the axial electron mobility

$$\mu_{ez} = \frac{e}{\nu_e m_e}\left(\frac{1}{1+\Omega_e^2}\right), \tag{3-12}$$

and the terms inside the brackets of Eqn. 3-11, which are due to the momentum gained from the electric field and by diffusion, respectively.

3.1.3.1 Anomalous electron mobility

In the closed-drift region, the electrons are strongly magnetized so the axial mobility simplifies to [139, 140]

$$\mu_{ez} \approx \frac{e}{\nu_e m_e \Omega_e^2} = \frac{\nu_e m_e}{e B_r^2} \quad , \tag{3-13}$$

which shows that the mobility is given by the ratio of the collision frequency and the square of the magnetic field.

Measurements of the electron current have shown that the effective electron collision frequency in an SPT-100 is on the order of 10^7-10^8 s^{-1} [138-140]. A collision frequency based off "classical" collisions between the electrons and the heavy particles cannot account for this high a value of collision frequency. Estimates inferred from global measurements of the electron current [138-140], as well as calculations based directly from internal plasma measurements [135, 141], show that the classical collision frequency is on the order of 10^6-10^7 s^{-1}. Thus, additional "anomalous" transport mechanisms must be present that enhance the cross-field electron mobility.

The two leading candidates that could be responsible for anomalous transport are collisions with the walls and turbulent plasma fluctuations. Determining which of these mechanisms is dominant has been the subject of considerable debate since the 1960's. However, a review of past experimental, numerical simulation, and

theoretical research [109, 110, 135-150], shows that it is likely that both mechanisms each play a role in different regions of the discharge chamber and at different thruster operating conditions. Including these effects in the mobility can be accomplished by using an effective electron collision frequency that is sometimes modeled as

$$\nu_e = \nu_{eff} = \nu_{en} + \nu_{wall} + \nu_{turb}, \tag{3-14}$$

where ν_{en} is the electron-neutral collision frequency, ν_{wall} is the collision frequency of the electrons with the walls, and ν_{turb} is a collision frequency due to turbulent plasma fluctuations (*i.e.*, anomalous Bohm-like diffusion). It is worth noting that the electron-electron collision frequency ν_{ee} and the electron-ion collision frequency ν_{ei} are absent from Eqn. 3-14. This is because these collision frequencies, which are typically an order of magnitude less than the electron-neutral collision frequency [135], are usually neglected for the sake of computational expediency [139].

Morosov, *et al.* [145] first suggested that wall collisions have a role in enhancing cross-field transport by introducing the concept of a so-called "near-wall conductivity." In this view, the walls act essentially as a macroparticle on which primary electrons also collide. Non-specular reflection of primary electrons and the emission of low-energy secondary electrons from the walls act to enhance the bulk electron conductivity by untrapping electrons from magnetic field lines. Near-wall conductivity has been extensively studied experimentally, in numerical simulations, and theoretically [109, 110, 138-140, 146, 147]. This research has shown that near-wall conductivity plays a role in enhancing the effective collision frequency.

The experiments of Janes and Lowder [148] were the first to demonstrate that azimuthal fluctuations in the electric field correlated with density gradients

could account for anomalous diffusion via adiabatic ExB drifts. Anomalous diffusion of this sort was found to agree closely with Bohm-like mobility, which scales as the inverse of the magnetic field. Meezan, *et al.* [149, 150] have also studied the effects of field fluctuations in a low-voltage (100-200 V) Hall discharge with alumina walls and a long channel and also found that Bohm-like mobility could explain the observed cross-field transport. However, as pointed out by Ahedo *et al.* [138], Bohm-like diffusion likely dominates at low-voltage because the electron temperature is much lower, thereby reducing the wall collision rate.[12] Anomalous Bohm-like diffusion can be included in the expression for the effective collision frequency (Eqn. 3-14) by supposing

$$\nu_{turb} = \alpha_{ano}\omega_{ce}, \tag{3-15}$$

where α_{ano} is a fitting parameter that can be adjusted so that the necessary amount of diffusion results. In the case of classic Bohm diffusion, α_{ano} would be equal to 1/16 (*i.e.*, if Bohm transport dominates the Hall parameter would be $\Omega_e = \alpha_{ano}^{-1} = 16$). If Bohm-like diffusion were the dominant mechanism, the electron mobility would then be given by

$$\mu_{ez} \approx \frac{\nu_{turb} m_e}{eB_r^2} = \frac{\alpha_{\text{ano}}}{B_r} \ . \tag{3-16}$$

[12] The device used by Janes and Lowder [148] was operated at a discharge voltage of 400 V, which seemingly contradicts this statement. However, it should be noted that their accelerator had an excessively long channel and used quartz as the wall material. Such a device does not share much in common with modern thrusters. The results of Janes and Lowder should therefore be viewed as a worse case scenario. In other words, it is important for studies of anamolous electron diffusion to be conducted on "efficient" Hall thrusters operating at voltages and ion current densities where flight designs are used (at least greater than 200 V and on the order of 100 mA/cm^2) in order for the results to be relevant to flight hardware. Examples of such studies can be found in the publications of Haas and Gallimore [135, 142, 143] and Bishaev and Kim [136].

In practice, assuming only near-wall conductivity or Bohm-like diffusion throughout the channel is not justified by the available data. This was shown from experiments by Haas [135] and computations by Choueiri [141] (using Bishaev and Kim's data [136]). Haas' experiments were conducted using the P5 Hall thruster (see section 5.3.1). The P5 was operated at a discharge voltage of 300 V, a discharge current density of 85 mA/cm^2, and greater than 50% thrust efficiency. Haas showed that the effective Hall parameter in the closed-drift region can approach that given by classical collisions alone, but falls to the Bohm value near the anode or downstream of the exit plane.[13] This strongly suggests that a mixed-mobility, accounting for both Bohm-like and wall collisionality effects, is more appropriate. Fife was among the first to adopt such an approach in numerical simulations, by accounting for classical scattering and Bohm-like diffusion in a simulation of the SPT-70 [144]. Fife found that a value of $\alpha_{ano}^{-1} = 107$ yielded the necessary amount of cross-field transport. Ahedo, *et al.* [138] has also found acceptable results when $\alpha_{ano}^{-1} = 100$ in a mixed-mobility approach that accounted for classical scattering, wall collisions, and Bohm-like diffusion. The value of α_{ano}^{-1} used by Fife and Ahedo, *et al.* agree (within an order of magnitude) with those found experimentally, which have shown that the electron Hall parameter attains a value of several hundred in the closed-drift region [2, 135, 136]. In Chapter 12, it will be shown that the electron Hall parameter in a high-efficiency, high-specific impulse Hall thruster averaged 160 over a voltage range of 400-900 V. Others have adopted similar mixed-mobility

[13] Haas includes a factor of two in the electron Hall parameter that is not included in Eqn. 3-10. Without this factor of two, the effective Hall parameter in the channel never rises above the Hall parameter derived from classical collisions alone and the maximum Hall parameter in the closed-drift region would be 850. As shown by Fife [144], the measurements of Bishaev and Kim [136] show the same trends as Haas' data. The electron Hall parameter computed by Choueri [141], from Bishaev and Kim's data [136], averaged about 290 in the closed-drift region.

approaches that have differed by which of the terms shown in Eqn. 3-14 are included in their simulations [110, 139, 147].

3.1.3.2 Diffusion by electron heating

The importance of the electron pressure, or more explicitly, the electron temperature can be shown if Eqn. 3-11 is expanded

$$j_{ez} = \mu_{ez}\left(-en_e E_z - \frac{dp_e}{dz}\right) = \mu_{ez}\left(-en_e E_z - n_e \frac{dkT_e}{dz} - kT_e \frac{dn_e}{dz}\right). \qquad \textbf{(3-17)}$$

Thus, if either the electron temperature or its gradient are very large, the axial electron current density increases via diffusion (or similarly for the number density, but these situations are usually not encountered in magnetic layer thrusters). Since the electrons gain energy from the electric field as they migrate towards the anode, the relative importance of diffusion depends mostly on the discharge voltage. The energy imparted to the electrons from the electric field is regulated primarily by losses due to inelastic collisions and wall collisions, which leads us back to the primary difference between magnetic layer thrusters (ceramic walls) and anode layer thrusters (metallic walls).

3.1.3.3 Wall effects and secondary electron emission

The choice of wall material strongly influences the average electron temperature in the channel because of secondary electron emission (SEE) effects [151-153]. When a primary electron from the channel collides with the walls, a flux of low-energy secondary electrons are released. Because of their lower temperature, the secondary electrons act in effect to cool the plasma, which in a magnetic layer thruster regulates the electron temperature to approximately 10% of the discharge

voltage ($T_e \propto 0.1 V_d$) [136, 143, 149, 154]. Regulating the electron temperature benefits the ionization efficiency, since the ionization cross-section of xenon by electron impact maximizes with electron temperature in the range of 40-90 eV [155]. The magnitude of the cooling effect depends on several factors, but most importantly, it depends on the choice of wall material.

For the ceramic walls of a magnetic layer thruster, the cooling effect is significant because the secondary electron emission coefficient is large compared to metals. This moderates the electron temperature and allows for a gradual increase in the potential along the channel. In contrast, the metallic walls of an anode layer thruster have a much lower yield of secondary electrons and the walls are usually kept at the cathode potential to repel electrons. This means that in the anode layer thruster that the electrons liberate their energy only through inelastic collisions (*e.g.*, ionization). Thus, the electron temperature in an anode layer thruster will typically be much higher than in a magnetic layer thruster [156]. Because electrons conserve their energy as the anode is approached, a sharp increase in the plasma potential is forced to occur, which is also where the anode layer thruster derives its name. The higher electron temperatures encountered in anode layer thrusters has partly led to the development of two-stage models [63, 106, 107, 157]. When properly designed, the intermediate electrode in a two-stage thruster aids in regulating the electron temperature in the ionization stage, which can improve the ionization efficiency in thrusters where the electron temperature would otherwise surpass the maximum in the ionization cross-section.

3.2 Development history of high-specific impulse Hall thrusters

After the 1970's, Hall thruster research languished in the United States and flourished in the Soviet Union. Zhurin, *et al.* [3] estimate that the number of scientists and engineers working on electric propulsion (of any kind) was about 2000 in the Soviet Union in the 1980's compared to about 200 in the United States during the 1970's. This substantially larger investment in electric propulsion, especially in Hall thruster research, allowed Soviet researchers to explore almost every thruster design imaginable, ultimately leading to the development of several flight thrusters. The early research considered important design variables such as the thruster type (magnetic versus anode layer), operating point (discharge voltage and current), discharge chamber geometry, magnetic field topography, propellant type, and wall material. In the next two sections, the focus will be on the trends that have influenced the development of high-voltage (high-specific impulse) Hall thrusters. The discussion is logically divided into the development efforts during the Cold War (pre-1990) and the research that has occurred since Hall thrusters were re-introduced to western countries in the 1990's.

3.2.1 Development from 1960-1990

Since its beginnings, Hall thruster researchers have been divided into two camps based on those that favored the magnetic layer thruster and those that extolled the virtues of the anode layer thruster. The purpose here is to highlight the major development efforts that have occurred. Several review articles and textbooks provide considerably more detail than will be discussed here [1-3, 14, 15, 19, 20, 63, 98, 99, 106, 107, 157-162].

Magnetic layer thruster development in the former Soviet Union benefited from the majority of research investigations. This was because early efforts to optimize magnetic layer thrusters revealed that they were well suited as single-stage thrusters operating below one kilovolt, making them an attractive option for satellite station keeping missions [2, 19, 159]. Multi-stage configurations have been reported [145], but were never developed extensively [99]. This was probably because the electron temperatures encountered at discharge voltages below one kilovolt (T_e < 100 eV) can be effectively used to ionize the propellant, making the added complexity of a two-stage design unnecessary [1]. Magnetic layer thrusters have also been operated in pulsed and quasi-steady operating modes at discharge voltages of several kilovolts and megawatt power levels [159, 162, 163]. However, interest in these operating modes quickly waned as the focus shifted to the needs of flight hardware. Magnetic layer thrusters gradually evolved into 200-300 V models that were successfully flown in space for the first time in 1971 [18]. As a result, the bulk of magnetic layer thruster research was focused on low-voltage models from the 1970's until well into the 1990's.

Anode layer thrusters developed in the former Soviet Union were never flown in space because the kilowatt- to megawatt-class missions that they were being developed for were never brought to fruition [63, 160]. The earliest attempts at optimizing anode layer thrusters revealed that they were well suited as two-stage thrusters operating at discharge voltages of several kilovolts. Bismuth propelled thrusters were extensively investigated at TsNIIMASH from 1960-1985 at power levels in excess of 100 kW, specific impulse of 3000-8000 s, and efficiencies approaching 80% [63, 157]. These thrusters were usually operated in a so-called "vacuum mode" [99, 122], which is related to a Penning discharge [164]. Such a

mode of operation is a qualitatively different type of discharge than that encountered in modern anode layer or magnetic layer thrusters. In vacuum mode thrusters, the ionization stage typically operates at ion current densities common to today's thrusters. In the acceleration stage, however, the ion current density is only about 10-20% of the value of a modern thruster and the quasineutrality condition is violated ($n_e >> n_b$). A vacuum-mode discharge will transition to quasineutrality above a critical neutral pressure, which has been reported to be on the order of the pressures encountered in modern thrusters. A peculiar aspect of vacuum mode thrusters is that they are apparently incapable of operation below some critical voltage, which is usually on the order of 1-2 kV. As the critical voltage is approached, vacuum-mode thrusters also become grossly inefficient (<20%). For these reasons, there are some fundamental differences between the designs of vacuum-mode anode layer thruster and modern thrusters that are not applicable to the present work. The interested reader is directed to the literature for more details [13, 63, 99, 106, 107, 122, 157, 161, 165-169]. In the 1970's, as it became increasingly clear that spaceflights using high-power electric propulsion were decades away, TsNIIMASH began to develop sub-kilovolt, 1-10 kW anode layer thrusters that operated at the current densities of modern thrusters [161].

3.2.2 Development from 1990-present

As discussed in Chapter 1, the end of the Cold War made it possible for Hall thruster technology from the former Soviet Union to be exported to western countries. The early efforts focused on 1.35 kW models: the Fakel SPT-100, the TsNIIMASH D-55, and KeRC T-100 [23]. Hall thrusters gradually gained acceptance in the western electric propulsion community due to the success of these

investigations and since that time Hall thruster research has flourished worldwide. After the initial flight qualification efforts, the community quickly became interested in expanding the capabilities of Hall thrusters in terms of their operating power and specific impulse. These trends were motivated by the rapid growth of available power on-board Earth orbiting satellites and studies indicating the benefits of high-specific impulse Hall thrusters (see Chapter 2). Hall thrusters are now being investigated worldwide at power levels of 0.1 to 100 kW and specific impulses of 1000-5000 s [49, 51, 52, 66].

In the United States, on-going Hall thruster research is being pursued by industry, academia, and several government entities [49, 50, 53, 66]. The largest government programs are currently implemented by the Air Force Research Laboratory (AFRL) at Edwards Air Force Base, CA and the NASA Glenn Research Center (GRC) in Cleveland, OH. Major portions of both the AFRL and GRC programs are concerned with investigating high-power (10-100 kW) Hall thrusters [47-49, 64-66, 131, 170-173]. In addition, GRC has funded or directly implemented several investigations of high-specific impulse Hall thrusters [130, 132, 133, 169, 174-180]. Other organizations, mostly in Russia at TsNIIMASH and Fakel, have also explored high-specific impulse operation during the 1990's [51, 52, 106, 107, 127, 156, 181-185].

3.2.2.1 NASA's high-specific impulse Hall thruster program

In 1999, motivated by the mission studies described in Chapter 2, NASA GRC initiated a focused high-specific impulse Hall thruster program.[14] This

[14] Although not explicitly stated at the time, the high-specific impulse program also naturally emerged from on-going research at high-power [65]. The high-power programs had already begun to expand the specific impulse operating range of Hall thrusters beyond 2000 s [131, 172, 173]. As NASA GRC began in-house development of its own high-

program was divided into two major phases. Phase one consisted of feasibility studies through thruster development contracts with industry [174-176]. Phase two was an extended research and development effort that included a collaboration with the University of Michigan along with in-house thruster development. The phase two efforts, which are the subject of this dissertation, are discussed beginning in Chapter 6.

In phase one, contracts were awarded to industry with the goal of demonstrating the feasibility of operating modern, xenon Hall thrusters at specific impulses greater than 3000 s [174-176]. Specifically, proposals were solicited for thrusters that were to operate at 2.3 kW discharge power while producing 3200 s specific impulse and 100 mN thrust. These targets were similar to the nominal operating conditions of the 2.3 kW NSTAR ion thruster that had recently flown on Deep Space 1 [186]. Three thrusters were developed in phase one, two of which were delivered to GRC for evaluation. The thrusters delivered to GRC were the D-80 from TsNIIMASH under sub-contract to Boeing and the SPT-1 from Fakel under sub-contract to the Atlantic Research Corporation. The third thruster was the BHT-HD-1000 from the Busek Company, which was developed under a NASA funded SBIR program. The major results from each of these thruster development efforts are described below, followed by a brief discussion.

The D-80 was an anode layer thruster that was operated in both single- and two-stage configurations. A photograph of the D-80 is shown in Figure 3-4. Performance in the two-stage configuration showed little or no benefit over single-stage operation (not shown, see Ref. [133]). In the single-stage configuration, the

---

power thrusters [47], the high-specific impulse program, which focussed on mid-power thrusters (1-10 kW), evolved into a means to investigate high-specific impulse divorced from the challenges of high-power operation.

thruster was operated at discharge voltages ranging from 300 to 1700 V with corresponding anode specific impulses of 1600-4100 s. Figure 3-5 shows the anode specific impulse versus discharge voltage at anode mass flow rates between 4-8 mg/s. At constant voltage, the propellant utilization increased with flow rate resulting in higher specific impulse.[15] Figure 3-6 shows the anode efficiency versus discharge voltage. The efficiency also benefited from improved propellant utilization at higher flow rates. However, it was found that maximum efficiency occurred between 600-800 V, depending on the mass flow rate. This range of voltage roughly corresponded to specific impulses less than 3000 s. Figure 3-7 shows the current-voltage characteristic. A slight downward trend in the current was observed with increasing voltage. Between 700 and 800 V the discharge current increased regardless of the mass flow rate, which also corresponded with an increase in specific impulse and efficiency.

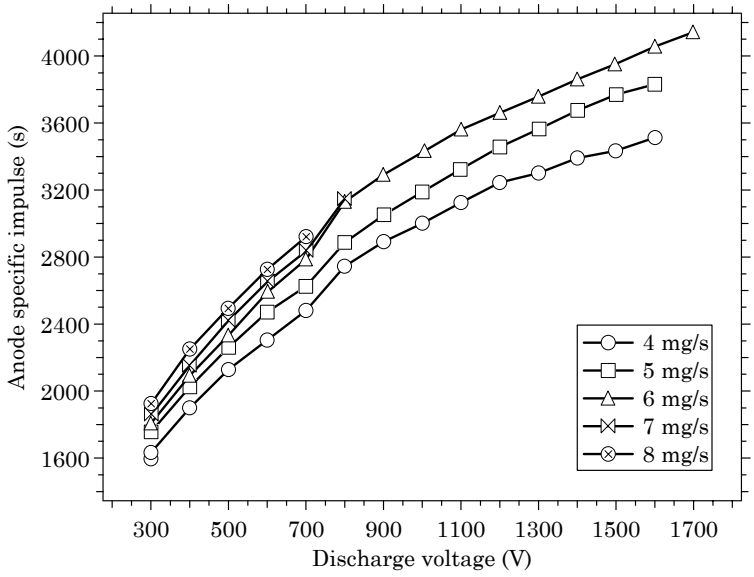

Figure 3-5 Anode specific impulse versus discharge voltage of the TsNIIMASH D-80 (single-stage configuration) from Ref. [133].

[15] The so-called "anode" performance parameters of specific impulse and efficiency neglect the power to the electromagnets and the mass flow rate supplied to the cathode. The anode performance parameters are formally defined in section 4.2. The mass utilization, defined in section 4.3.2, is the ratio of the mass flow rate of ions to the mass flow rate of neutral propellant through the anode.

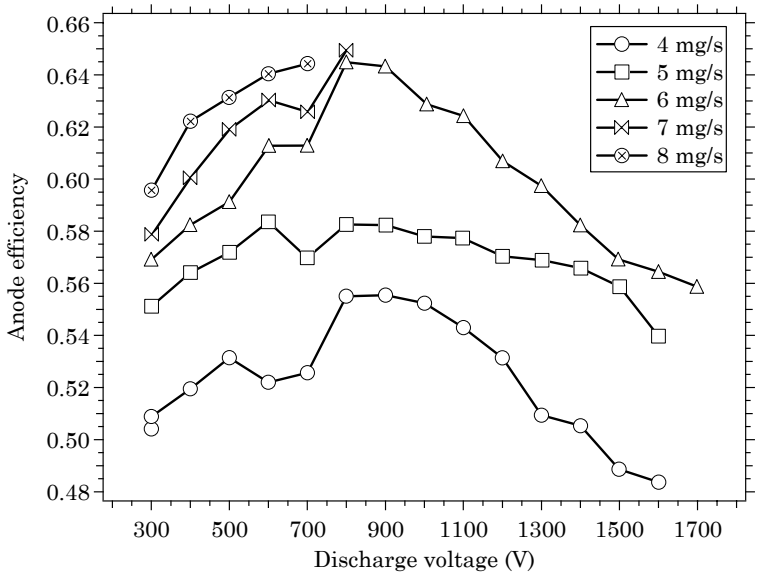

Figure 3-6 Anode efficiency versus discharge voltage of the TsNIIMASH D-80 (single-stage configuration) from Ref. [133].

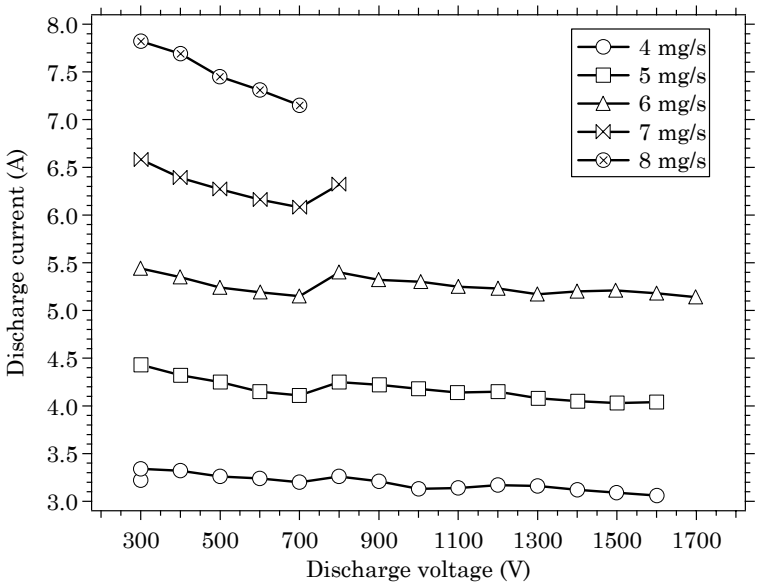

Figure 3-7 Discharge current versus discharge voltage of the TsNIIMASH D-80 (single-stage configuration) from Ref. [133].

The D-80 was later subjected to a 1200 hour erosion characterization at NASA GRC while operating in single-stage mode at 700 V and 4 A [174]. Although guard ring erosion exposed the magnet poles sometime after 600-900 hours of

operation, the thruster continued to operate normally up to 1200 hours when the test was voluntarily terminated.

A follow-on version of the D-80 was fabricated by TsNIIMASH with NASA GRC support. This thruster was reported to show performance benefits over single-stage operation when operated in two-stage mode at high-voltage [132]. The primary change in the new version of the D-80 was a decrease in length of the acceleration stage, *i.e.*, the axial length between the downstream surfaces of the intermediate electrode and the guard rings (see Figure 3-2) [181]. Unfortunately, these claims have yet to be verified in NASA vacuum facilities. After NASA program support ended with the fabrication of the new D-80, TsNIIMASH later evaluated its erosion characteristics independently [181]. Although the efficiency was greater in the two-stage mode, the erosion of the intermediate electrode was greater than the erosion while operating in single-stage mode.

The SPT-1 was a single-stage, magnetic layer thruster of hybrid design [176]. A metallic anode was used for a portion of the discharge chamber with a dielectric at the exit as in conventional magnetic layer thrusters. The thruster was operated at discharge voltages ranging from 300 to 1250 V with corresponding anode specific impulses of 1600-3700 s. Figure 3-8 shows the anode specific impulse versus discharge voltage at anode mass flow rates between 2.4-5.4 mg/s. Figure 3-9 shows the anode efficiency versus discharge voltage. Like the D-80, at constant voltage both the specific impulse and efficiency increased with flow rate due to improved mass utilization. A peak in the efficiency with voltage was also measured, that again depended on the mass flow rate, over the range of 500-700 V. This range of voltages roughly corresponded to specific impulses of less than 3000 s. Figure 3-10

shows the current-voltage characteristic. The slope of the characteristic was found to increase near the discharge voltage that also corresponded to maximum efficiency.

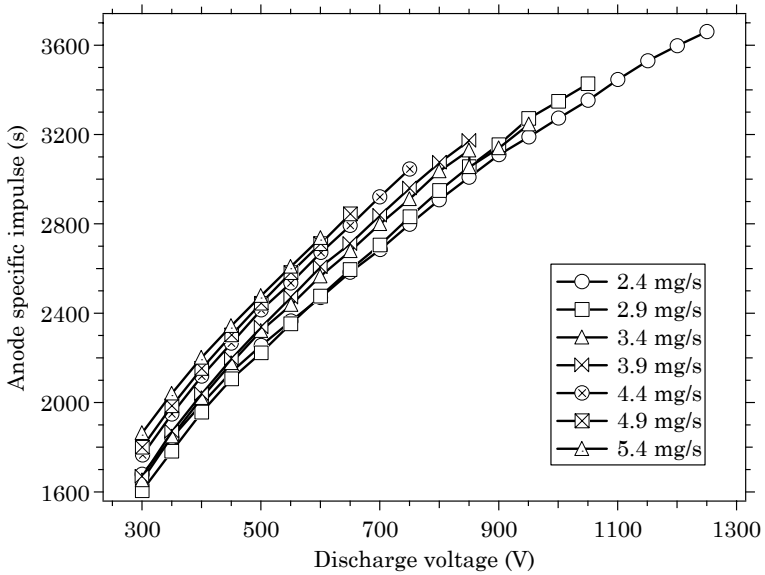

Figure 3-8 Anode specific impulse versus discharge voltage of the Fakel SPT-1 from Ref. [176].

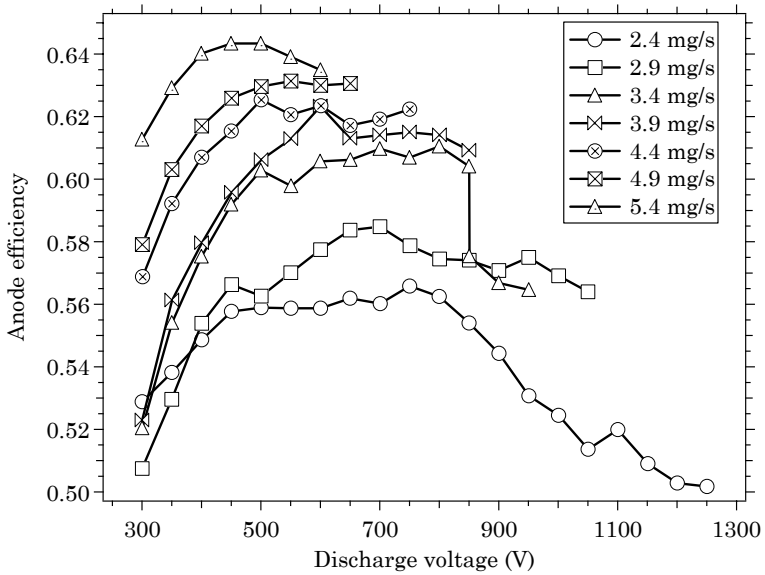

Figure 3-9 Anode efficiency versus discharge voltage of the Fakel SPT-1 from Ref. [176].

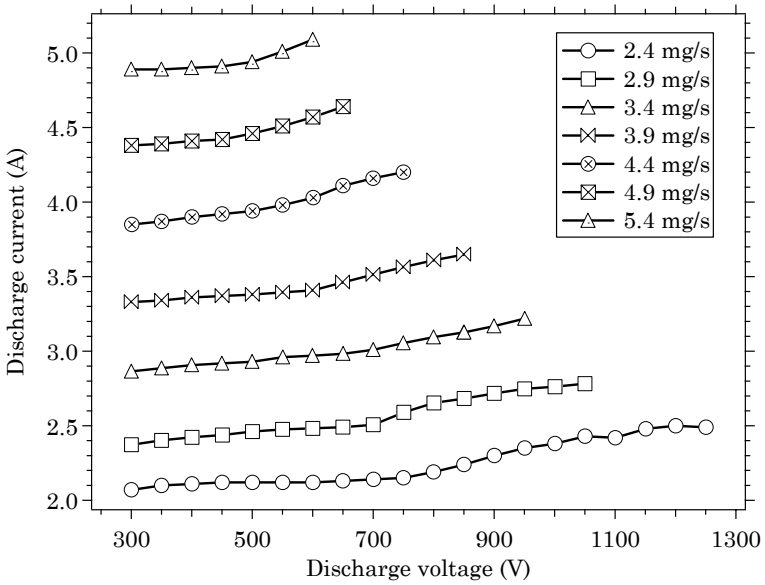

Figure 3-10 Discharge current versus discharge voltage of the Fakel SPT-1 from Ref. [176].

Similar to the SPT-1, the BHT-HD-1000 was also a magnetic layer thruster of hybrid design [175]. The BHT-HD-1000 was operated in both single- and two-stage configurations. As with the D-80, performance in the two-stage configuration showed little or no benefit over single-stage operation (not shown, see Ref. [175]). In the single-stage mode, the thruster was operated at discharge voltages ranging from 300 to 1000 V with corresponding anode specific impulses of 1600-3200 s. Figure 3-11 shows the anode specific impulse versus discharge voltage at anode mass flow rates between 2.5-3.0 mg/s. Figure 3-12 shows the anode efficiency versus discharge voltage. Thermal limitations restricted the performance evaluation to the flow rates that were investigated. As with the D-80 and SPT-1, at constant voltage both the specific impulse and efficiency of the BHT-HD-1000 increased with flow rate due to improved mass utilization. A peak in the efficiency was also measured at 500 V for each flow rate tested. This voltage corresponded to a specific impulse of about 2400 s. Figure 3-13 shows the current-voltage characteristic. The slope of the

characteristic was found to increase near 500 V where maximum efficiency occurred. Above 600 V, the current reached a maximum then decreased. NASA sponsored studies of the BHT-HD-1000 are on-going [187-189].

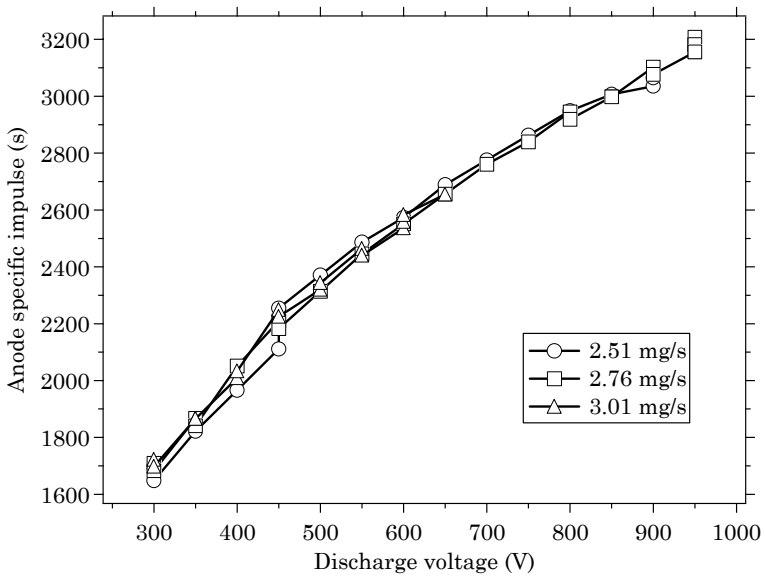

Figure 3-11 Anode specific impulse versus discharge voltage of the Busek BHT-HD-1000 (single-stage configuration) from Ref. [175].

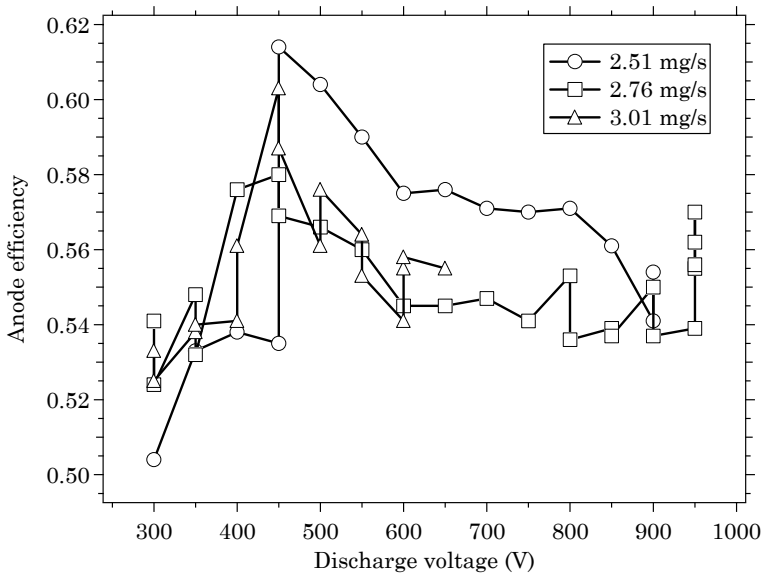

Figure 3-12 Anode efficiency versus discharge voltage of the Busek BHT-HD-1000 (single-stage configuration) from Ref. [175].

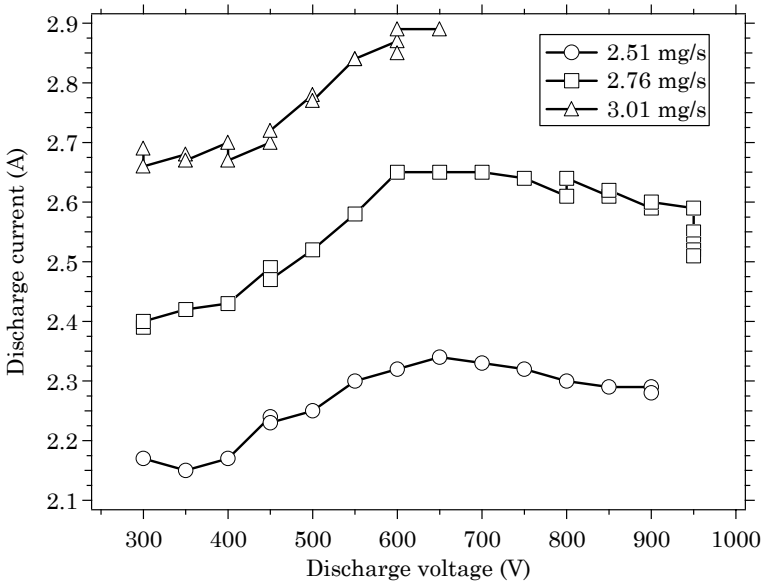

Figure 3-13 Discharge current versus discharge voltage of the Busek BHT-HD-1000 (single-stage configuration) from Ref. [175].

In summary, each of the thrusters in phase one successfully demonstrated operation of modern, xenon Hall thrusters at greater than 3000 s specific impulse. Above 3000 s specific impulse, anode efficiencies were maintained above 50% for a wide range of voltages and flow rates. However, maximum efficiency was limited to less than 3000 s specific impulse. The maximum efficiency occurred between 500-800 V depending on the mass flow rate and the thruster design. This was a source of some concern since decreasing thruster efficiency may also affect the thermal robustness, stability, and lifetime of high-specific impulse Hall thrusters. Understanding the causes of the efficiency peak therefore required additional study.

Since the investigations in Ref. [133, 175, 176] were limited to performance measurements alone, it was not possible to precisely identify the physical mechanisms causing the efficiency peak. However, based on the available data the authors in Ref. [175, 176] considered two possible explanations:

1. electron current leakage across the transverse magnetic field and
2. increased production of multiply-charged ions.

Although not explicitly stated in Ref. [175, 176], either of these effects could be the likely outcome of increased electron temperature, which is expected with increased discharge voltage.

When analyzing these possibilities, Manzella *et al.* [176] observed that the efficiency peak in the SPT-1 closely coincided with the increased slope of the current-voltage characteristic, from which, it was concluded that enhanced axial electron current was the dominant mechanism lowering efficiency. Pote and Tedrake [175] applied a performance model to the BHT-HD-1000 data, and similarly concluded that enhanced electron transport was the likely cause of the efficiency trends.[16] While a precise mechanism for the increased electron current was not offered in these analyses, the authors of Ref. [175, 176] all concluded that **there was a clear need to investigate magnetic field effects on electron transport in magnetic layer thrusters**. Although the electron transport in magnetic layer thrusters is a poorly understood process (see section 3.1.3), it is clear that the interaction of the plasma with the walls and the magnetic field strongly influence the cross-field electron mobility. As shown in later chapters, it is possible to control wall effects partially by properly designing the magnetic field. In conclusion, the phase one results revealed a strong need for further study of the role of the magnetic field in influencing Hall thruster performance.[17]

[16] The model used by Pote and Tedrake [175], which did not include the effects of multiply-charged ions, was a simplified version of the model discussed in Chapter 4.
[17] NASA GRC has also investigated wall material effects in other studies [113, 190]. The orientation of the magnetic field is known to influence the erosion rate in 300 V Hall thrusters [113].

In contrast to the SPT-1 or BHT-HD-1000, the slope of the D-80 current-voltage characteristic was slightly negative. Since the efficiency still peaked in the D-80, this trend suggests that the mechanism limiting efficiency in anode layer thrusters may be (much) different than in magnetic layer thrusters. A possible explanation for this phenomenon is proposed here as follows. Recalling the discussion of electron dynamics in section 3.1.3, it may be that the higher electron temperatures encountered in anode layer thrusters lowers the ionization rate enough that the ion current actually decreases with voltage. If this were the case, it would be possible for the discharge current to remain constant while the ion current decreased and the electron current increased (as shown by Eqn. 3-11, if the electron temperature increases with voltage, the electron current can increase via diffusion). This hypothesis is supported by electron current measurements that were made on the TsNIIMASH D-100 in Ref. [156]. In those experiments, the current-voltage characteristic of the D-100 was constant, the electron current increased with voltage and the efficiency was found to peak at less than 3000 s specific impulse. As first noted in section 3.1.3.3, it therefore seems necessary to transition to two-stage operation at lower voltages in an anode layer thruster than in a magnetic layer thruster. Because of the added system complexity of a two-stage design, this may make anode layer thrusters undesirable for sub-kilovolt operation. This conclusion later provided strong justification for pursuing magnetic layer thrusters in the development of 2000-3000 s specific impulse Hall thrusters.

The phase one studies led to the basic hypothesis of this dissertation. While several engineering issues (*e.g.*, thermal margin) likely contributed, the research presented in this dissertation was based on the hypothesis that the efficiency peak was a consequence of modern magnetic field designs, which

have been optimized for 1600 s specific impulse, that were unsuited for high-specific impulse operation. This hypothesis led directly to the thruster development and characterization efforts that would occupy the bulk of the phase two efforts and became the subject of the work presented here.

3.2.2.2 Related high-specific impulse research

In the late 1990's there have been several other investigations of high-specific impulse Hall thrusters that are related to studies described in the previous section. The studies related to anode layer and magnetic layer thrusters are briefly reviewed in this section.

High-specific impulse anode layer thrusters developed by TsNIIMASH are discussed in Ref. [106, 127, 131, 156, 181, 182]. While some of the thrusters described in these references do not exhibit an efficiency peak (or at least show asymptotic behavior at high-voltage), it is interesting to examine the review of anode layer thrusters in Ref. [127]. In that reference, a compilation of efficiency data from the D-55, TAL-110, D-150, and TM-50 shows a clear trend towards maximum efficiency occurring below 3000 s specific impulse.[18] This suggests that the efficiency trends observed in the D-80 are generally shared by other anode layer thrusters.

Magnetic layer thrusters developed by companies in the United States and Russia are discussed in Ref. [172, 173, 183-185]. The 500 V, 10 kW T-220 was developed by Space Power Inc. (now Pratt & Whitney) with NASA GRC sponsorship to investigate high-power operation [172]. The T-220 has shown an increasing efficiency up to a maximum tested voltage of 600 V (see section 4.5.3). The 1000 hour erosion characterization reported in Ref. [173] showed that the volumetric

[18] These thrusters span a power range of 1-25 kW.

erosion rate of the 500 V T-220 was only slightly higher than the 300 V SPT-100. This has obvious significance for the prospects of developing long-lived, high-specific impulse Hall thrusters.

Fakel, through various collaborations, has also explored high-specific impulse operation of the SPT-80, SPT-115, SPT-140, and the SPT-290. The SPT-80 was reported to have a flat current-voltage characteristic and increasing efficiencies up to 850 V at several flow rates [185]. However, these trends were not repeated in the SPT-115, SPT-140, SPT-290, or the SPT-1. The efficiencies reported for the SPT-115 and SPT-140 exhibit current-voltage characteristics with a positive slope and some evidence of a peak efficiency with voltage (the efficiencies often leveled off with voltage) [184]. Some thermal design issues were also reported in the SPT-140 operating at high-voltage. The SPT-290 generally showed increasing current and efficiency up to a maximum tested voltage of 600 V [183]. Some thermal issues were also reported in the SPT-290. In general, the existing Fakel SPT designs seem to exhibit either a peak or asymptotic efficiency-voltage characteristic at high-voltage. However, the overall trends in erosion and efficiency of magnetic layer thrusters in general lend additional support for their continued development at high-specific impulse.

3.3 Conclusions

Minimizing the axial electron transport in Hall thrusters is critical to achieving high efficiency. Since electron current is controlled by the magnetic field distribution in the discharge chamber, the magnetic field topography is very important in Hall thruster design.

Phase one efforts of NASA's high-specific impulse program have demonstrated that greater than 3000 s specific impulse is possible at more than 50% thrust efficiencies in modern, xenon Hall thrusters. However, maximum efficiency was limited to less than 3000 s specific impulse. Analysis of the phase one results indicated that enhanced axial electron transport across the transverse magnetic field was the likely cause of the peak efficiency. **Combined with the mission studies showing the benefits of high-specific impulse Hall thrusters, the phase one studies motivated the development of the NASA-173M series of Hall thrusters.** Part II discusses efforts to develop the NASA-173M Hall thrusters.

In the next chapter, a Hall thruster performance model that includes the effects of a multiply-charged, partially-ionized plasma is discussed. Such a model is an important tool in the analysis of Hall thruster performance at high-specific impulse. The model is used in Chapter 12 to weigh the relative importance of electron current and multiply-charged ions on the performance of Hall thrusters.

Chapter 4

Phenomenological Hall thruster performance model

A phenomenological Hall thruster performance model is derived as a function of the utilization efficiencies of current, mass, voltage, and charge. The model allows for a partially-ionized plasma consisting of either singly- or multiply-charged ions. Trends in the performance parameters from the model are discussed for certain limiting cases and it is demonstrated how a simplified version of the model bounds Hall thruster performance over a wide range of operating conditions. As a motivation for its use in Chapter 12, it is shown how the model can provide insight on thruster processes by providing a means to correlate thruster performance with the plasma parameters. The model is especially useful in weighing the relative importance of electron current and multiply-charged ions on performance.

4.1 Hall thruster performance models

A complete model of Hall thruster physics has thus far defied description due to the complexity of the physical processes involved, most of which are not very well understood. Although significant progress has been made in recent years [138-140, 144, 147, 191-194], there presently are no analytic or numerical models of Hall thrusters that can accurately predict the performance parameters over a wide range of operating conditions.

The dearth of analytic or numerical solutions has led to the development of several semi-empirical Hall thruster performance models [46, 58, 59, 98, 195-198]. While the depth of the models has varied, they have all been based on simple physical arguments, scaling relations, or correlations with existing data used to describe the dependence of the performance parameters with operating condition (*e.g.*, voltage, current, mass flow rate, geometry, etc.). Since the models have relied on experiments to determine various constants, their predictive value is limited by the available data. However, the models have proven useful in judging the relative performance of thrusters, for example, against large databases of thruster performance [198], or to derive dimensionless scaling laws that can guide new designs [195, 196].

A series of models discussed in Ref. [46, 58, 59, 197] have all been similarly based. McLean, *et al.* [58] and Pote, *et al.* [46] developed nearly identical two-parameter models for a fully-ionized, singly-charged plasma and found good agreement with individual thrusters. Hofer and Jankovsky [197] expanded these models to include the effects of a fully-ionized, multiply-charged plasma so that the performance of high-voltage, high-power thrusters could be analyzed. Including the effects of multiply-charged ions was later shown to be a useful tool in interpreting the performance trends of the 50 kW NASA-457M Hall thruster [47]. Hruby, *et al.* [59] have also expanded the model of Pote, *et al.* [46] by including additional physics and geometric effects related to thruster scaling. While the models in Ref. [46, 58, 59, 197] were capable of capturing the experimentally measured performance trends, most of the models neglected multiply-charged ions [46, 58, 59], and all of these models assumed a fully-ionized plasma (*i.e.*, 100% propellant mass utilization). These modeling approaches are too restrictive considering that Hall thrusters

operate efficiently over a wide range of voltages and flow rates where these simplifying assumptions are no longer valid. To address these shortcomings, the model presented here extends the work of Ref. [197] by allowing for a partially-ionized, multiply-charged plasma. System level considerations are also added to the model to aid in future mission analyses. When combined with measurements of thruster performance and plasma parameters, the model can be used to compute thruster properties (*e.g.*, electron current) that are difficult to measure directly using probe-based techniques.

4.2 Hall thruster performance parameters

The system performance parameters defined in section 2.1 can be applied to space propulsion systems in general. In this section, system and thruster level equations for the performance of a Hall thruster are presented. Differences between the magnetic and anode layer Hall thrusters are neglected throughout this analysis. Although differences do exist between magnetic and anode layer thrusters, their performance is similar for thrusters with the same power rating [32, 198].

In a Hall thruster, thrust may be developed by the mixture of particle species present in the discharge chamber. The different particles include electrons, neutral propellant, and each ion species (*e.g.*, Xe^{+}, Xe^{2+}, Xe^{3+}). The ion momentum flux dominates over the electrons and neutrals because of the large disparity in mass and velocity, respectively. Thus, the thrust produced by a Hall thruster is given by

$$T = \sum_{i=1}^{N} \dot{m}_i \langle v_i \rangle , \tag{4-1}$$

where the index i indicates the charge-state of each ion species, N is the total number of ion species, and $\dot{m}_i$ and $\langle v_i \rangle$ are the mass flow rate and average velocity

of the i^{th} ion species, respectively. Second-order effects that can artificially increase thrust, such as ingestion of neutrals from the cathode [176, 199] or the background gases in a vacuum facility [200], are not included in Eqn. 4-1 or throughout this analysis.

The system efficiency depends on the total mass flow rate of propellant supplied to the thruster, which includes the flow through the anode and cathode

$$\dot{m}_t = \dot{m}_a + \dot{m}_c \,, \tag{4-2}$$

where t, a, and c indicate total, anode, or cathode quantities, respectively. The cathode flow rate for thrusters with discharge powers greater than 1 kW is typically 5-10% of the anode flow rate [34, 56, 58, 131, 172]. If the cathode flow fraction is defined as

$$K_c \equiv \frac{\dot{m}_c}{\dot{m}_a} \,, \tag{4-3}$$

and a cathode efficiency is defined as

$$\eta_c \equiv \frac{\dot{m}_a}{\dot{m}_t} = \frac{1}{1+K_c} \,, \tag{4-4}$$

then the total mass flow rate can be expressed as

$$\dot{m}_t = \dot{m}_a + \dot{m}_c = \left(1+K_c\right)\dot{m}_a = \frac{\dot{m}_a}{\eta_c} \,. \tag{4-5}$$

The total effective exit velocity is defined as the average velocity at which the propellant is expelled based on the total mass flow rate

$$c_t \equiv \frac{T}{\dot{m}_t} = \frac{T}{\dot{m}_a}\frac{1}{\left(1+K_c\right)} = \frac{T}{\dot{m}_a}\eta_c \,. \tag{4-6}$$

The total specific impulse is defined as the thrust per unit total weight flow rate of propellant

$$I_{sp,t} \equiv \frac{T}{\dot{w}_t} = \frac{T}{\dot{m}_t g} = \frac{T}{\dot{m}_a g}\eta_c = \frac{c_t}{g}. \quad \textbf{(4-7)}$$

The total power input to the thruster is

$$P_t = P_d + P_{mag} + P_{aux}, \quad \textbf{(4-8)}$$

where $P_d = V_d \times I_d$ is the discharge power, P_{mag} is the power to run the electromagnetic coils, and P_{aux} accounts for any auxiliary power requirements (*e.g.*, a heater or keeper on the cathode). Most modern thrusters use heaterless and keeperless cathodes, so P_{aux} will be zero for the remainder of this analysis.[19]

The power input to the electromagnets is typically 1% of the discharge power for flight models [55], but can vary from about 0.5-4% of the discharge power depending on the magnetic circuit design and operating point. If the electromagnet power fraction is defined as

$$K_{mag} \equiv \frac{P_{mag}}{P_d}, \quad \textbf{(4-9)}$$

and an electromagnet efficiency is defined as

$$\eta_{mag} \equiv \frac{P_d}{P_t} = \frac{1}{1 + K_{mag}}, \quad \textbf{(4-10)}$$

then the total thruster power is

[19] The cathode heater and keeper are still used during start-up on modern thrusters.

$$P_t = P_d + P_{mag} + \overbrace{P_{aux}}^{=0} = \left(1 + K_{mag}\right)P_d = \frac{P_d}{\eta_{mag}}. \tag{4-11}$$

The total thrust efficiency is the ratio of jet power in the exhaust to the total input power

$$\eta_t = \frac{P_{jet}}{P_t} = \frac{\frac{1}{2}Tc_t}{\left(P_d + P_{mag}\right)} = \frac{T^2}{2\dot{m}_a P_d}\frac{1}{\left(1 + K_c\right)}\frac{1}{\left(1 + K_{mag}\right)} = \frac{T^2}{2\dot{m}_a P_d}\eta_c\eta_{mag}. \tag{4-12}$$

A Hall thruster propulsion system is usually composed of four major components: the power processing unit (PPU), a xenon flow control (XFC) system, a digital control and interface unit (DCIU), and the thruster. The PPU converts the spacecraft bus power into the appropriate voltages and currents needed by the system components (including the power to run the PPU). Power conversion efficiencies of modern PPU's are typically 90-95% [56, 201, 202]. The PPU and system efficiency are defined as

$$\eta_{PPU} \equiv \frac{P_t}{P_{sys}}, \tag{4-13}$$

$$\eta_{sys} \equiv \eta_{PPU}\eta_t, \tag{4-14}$$

where P_{sys} is the power input to the PPU from the spacecraft bus and is the sum of the power requirements of each system component

$$P_{sys} = P_{PPU} + P_{XFC} + P_{DCIU} + P_t. \tag{4-15}$$

As defined, the PPU power includes the power to run the PPU as well as power lost as waste heat during the power conversion process.

The focus in this chapter is on thruster-level, rather than system-level, performance. Neglecting the PPU efficiency, the combination of total thruster efficiency, total thruster power, total specific impulse, and thrust define the **thruster performance parameters**. To account for thrusters of varying degrees of development (*e.g.*, a laboratory versus a flight thruster), the parasitic system losses not directly associated with the production of useful thrust should also be excluded. These include the cathode efficiency (η_c) and the electromagnet efficiency (η_{mag}). This is necessary due to the variability of different thruster designs, *i.e.*, some thrusters have more optimized cathodes[20] or more efficient magnetic circuits. Neglecting these losses defines the aptly named "anode" quantities for the effective exit velocity, specific impulse, and efficiency

$$c_a = \frac{c_t}{\eta_c} = \frac{T}{\dot{m}_a}, \tag{4-16}$$

$$I_{sp,a} = \frac{I_{sp,t}}{\eta_c} = \frac{T}{\dot{m}_a g}, \tag{4-17}$$

$$\eta_a = \frac{\eta_t}{\eta_c \eta_{mag}} = \frac{T^2}{2\dot{m}_a P_d}. \tag{4-18}$$

The combination of the anode efficiency, discharge power, anode specific impulse, and thrust define the **anode performance parameters**. For a given thruster design, the anode performance parameters characterize how thruster operation is affected by changes to the voltage and mass flow rate. Deviation of the anode quantities from ideal scaling can be used to assess how thruster processes are

[20] Implicit to neglecting the cathode flow is the assumption that it is not much greater than 10% of the total flow rate. This is necessary so that neutrals from the cathode do not significantly contribute to the thrust (through ingestion into the discharge chamber where they can be ionized and accelerated) [176, 199]. A similar argument holds for the background pressure. If the vacuum facility pumping speed is too low for the mass flow rate, the ingestion of neutrals from the high background pressure can artificially increase the thrust [200].

affected by changing the operating point. Unless noted otherwise, the focus in subsequent sections is on the "anode" rather than the "total" performance parameters. The "total" quantities are easily recovered with Eqns. 4-16 to 4-18 and the system efficiency with Eqn. 4-14.

4.3 Performance model for a singly-charged plasma

In the literature, it is common to assume that the Hall thruster exhaust is composed only of singly-charged ions [46, 58]. This is a fair approximation for first order analyses; however, the Hall thruster exhaust is known to contain multiply-charged propellant ions that should be accounted for in certain situations, especially at high-voltage. Typical ion species fractions for 300 V, xenon Hall thrusters are 4-11% Xe^{2+} and 1% Xe^{3+} [203, 204]. In section 11.2, the Xe^{2+} species fraction of the NASA-173Mv2 is shown to vary from 3% at 300 V to 16% at 900 V. In this section, a model that predicts the performance parameters is derived assuming a partially-ionized plasma of singly-charged ions. The singly-charged model serves as a reference case to assess the relative importance of multiply-charged ions on performance, which will be included in section 4.4.

Thruster performance is determined by the efficiency of the ionization and acceleration processes. The ionization and acceleration of a singly-charged Hall thruster plasma can be characterized by the conversion efficiency of three distinct processes:

1. the fraction of ion current contained in the discharge current, that is, the current utilization efficiency,
2. the conversion of mass flow rate into ion current, that is, the mass utilization efficiency, and

3. the conversion of voltage into axially directed ion velocity, that is, the voltage utilization efficiency.

A fourth important process, the charge utilization efficiency, will be added in section 4.4 for a multiply-charged plasma. Before considering the performance parameters, expressions for each utilization efficiency are expressed in terms of measurable thruster properties. A plus sign (+) is used to denote that the defined quantities correspond to a plasma of singly-charged ions.

4.3.1 Current utilization efficiency

In the Hall thruster discharge chamber, the net current flow (*i.e.*, the discharge current) is composed of the ion (or beam) current used to produce thrust and the electron current that ionizes the propellant. Applying Kirchoff's Law, the discharge current is the sum of the ion and electron current

$$I_d = I_b^+ + I_e^+ . \tag{4-19}$$

If the electron current fraction is defined as

$$\varepsilon^+ \equiv \frac{I_e^+}{I_d}, \tag{4-20}$$

and the current utilization efficiency is defined as the ratio of the ion beam current to the discharge current

$$\eta_b^+ \equiv \frac{I_b^+}{I_d}, \tag{4-21}$$

then the dimensionless version of Eqn. 4-19 is

$$\eta_b^+ = 1 - \varepsilon^+ . \tag{4-22}$$

The current utilization efficiency characterizes how effectively the electrons are used to ionize the propellant. Hall thrusters operating above 200 V typically have current utilization efficiencies of 70-80% [2], which is usually the lowest of the utilization efficiencies composing the anode efficiency. As a result, considerable effort is devoted to minimizing the electron current in Hall thruster design, but a practical limit must exist since the electrons are needed to sustain the discharge.

4.3.2 Mass utilization efficiency

Neglecting any ingestion from the cathode or the vacuum facility, the anode mass flow rate is the propellant supply used to produce ions. The anode mass flow rate can be decomposed as the sum of the flow rates of beam ions and neutrals

$$\dot{m}_a = \dot{m}_b^+ + \dot{m}_n^+ . \tag{4-23}$$

where the ion mass flow rate is related to the ion and discharge currents by

$$\dot{m}_b^+ = \frac{m_{xe} I_b^+}{e} = \frac{m_{xe} \eta_b^+ I_d}{e} , \tag{4-24}$$

and a useful parameter, usually called the exchange ratio, is defined as

$$\xi \equiv \frac{m_{xe} I_d}{\dot{m}_a e} . \tag{4-25}$$

The mass utilization efficiency can then be defined as the ratio of the mass flow rate of ions to the anode mass flow rate[21]

[21] Occasionally, the mass utilization efficiency is confused as the ratio of the ion current to the current equivalent of the neutrals (by converting the neutral mass flow rate into a "neutral current"). Since there is no such thing as a neutral current this can distress some readers, so it should be duly noted that the mass utilization efficiency defined here is the ratio of the mass flow rates of ions (a very real quantity) to neutrals. A similar definition is used when multiply-charged ions are added to the mix.

$$\eta_m^+ \equiv \frac{\dot{m}_b^+}{\dot{m}_a} = \frac{m_{xe}\eta_b^+ I_d}{\dot{m}_a e} = \xi\eta_b^+ . \tag{4-26}$$

The mass utilization efficiency characterizes how effectively the flux of neutrals through the anode is converted into an ion flux and is often misinterpreted as the ionization fraction. This is far from the case due to the large disparity in velocity between the ions and neutrals. If the total particle density is defined as the sum of the particle densities of neutrals and ions

$$n_t \equiv n_n^+ + n_b^+ , \tag{4-27}$$

then it can be shown that the ionization fraction Θ^+, defined as the ratio of the ion particle density to the total particle density, is given by

$$\Theta^+ \equiv \frac{n_b^+}{n_t} = \frac{n_b^+}{n_n^+ + n_b^+} = \frac{1}{1 + \left(\frac{1-\eta_m^+}{\eta_m^+}\right)\frac{\langle v_b^+ \rangle}{\langle v_n \rangle}} . \tag{4-28}$$

(Note that only when the singly-charged mass utilization efficiency reaches 100% is the ionization fraction of a singly-charged plasma also 100%.) This definition of the ionization fraction is valid near the exit plane, downstream of the ionization and acceleration regions and assumes that the area over which the neutrals and ions flow are equal. Because of the breathing-mode ionization instability (see section 6.3.3), it is possible for the instantaneous ionization fraction to reach 100% over portions of the discharge chamber. Therefore, like all of the quantities used to characterize the global thruster properties, the ionization fraction defined in Eqn. 4-28 should be interpreted as a characteristic, or average, ionization fraction. In a 300 V Hall thruster operating at greater than 50% efficiency, a typical value of the singly-charged mass utilization efficiency is around 90%, the ion velocity is about 20

km/s and the neutral velocity is about 0.4 km/s. Applying Eqn. 4-28, these conditions equate to an ionization fraction of only 15%, which is in good agreement with the ionization fraction computed by Haas [135] from probe measurements.

4.3.3 Voltage utilization efficiency

Ideally, ions would be accelerated over a potential drop equal to the discharge voltage. However, cathodes typically float between 10-20 V below spacecraft ground [32, 58, 172] and the plasma potential several thruster diameters downstream of the exit can still be 5-10 V above spacecraft ground (*e.g.*, see Ref. [205, 206] or section 11.3). Both of these effects lower the maximum accelerating potential that an ion can be accelerated through to produce thrust (see Figure 10-12 for more). Further, because ions are created in the discharge chamber at different axial locations, the plasma exhaust has a spread in ion velocities [29, 207, 208], as each ion is accelerated by the voltage drop corresponding to where it was created. The average, axial exit velocity for the thruster as a whole is also affected by the ionization potential of the propellant, wall losses, ion charge-state, radial beam divergence, and plasma oscillations. To take into account all of these factors, an average accelerating voltage V_a and a loss voltage V_l are defined.[22] The acceleration and loss voltages are related through the discharge voltage by

$$V_d \equiv V_a^+ + V_l^+ . \qquad \textbf{(4-29)}$$

The voltage utilization efficiency (sometimes called the acceleration efficiency) is defined as the ratio of the acceleration voltage to the discharge voltage

[22] Despite all the possible loss mechanisms, the average ion energy of a Hall thruster is only 25-50 V below the discharge voltage. See, for example, Ref. [28, 207] or the results in section 11.4.

$$\eta_v^+ \equiv \frac{V_a^+}{V_d}. \tag{4-30}$$

In a Hall thruster, ion acceleration can be attributed to the axial electric field through an electrostatic process [2], or equivalently by an electromagnetic interaction of the azimuthal electron current and radial magnetic field [135]. From the electrostatic viewpoint, the average exit velocity of the ions can be computed by applying energy conservation

$$eV_a^+ = \tfrac{1}{2} m_{xe} \left\langle v_b^+ \right\rangle^2. \tag{4-31}$$

The average exit velocity of the ions can then be expressed as

$$\left\langle v_b^+ \right\rangle = \sqrt{\frac{2eV_a^+}{m_{xe}}} = \sqrt{\frac{2e\eta_v^+ V_d}{m_{xe}}} = \sqrt{\frac{2e\left(V_d - V_l^+\right)}{m_{xe}}}, \tag{4-32}$$

and a defect velocity based on the loss voltage [46] can also be defined as

$$\left\langle v_l^+ \right\rangle \equiv \sqrt{\frac{2eV_l^+}{m_{xe}}}. \tag{4-33}$$

4.3.4 Performance

With the utilization efficiencies defined, it is now possible to write down equations for the performance parameters. From Eqn. 4-1, thrust is the product of the mass flow rate and average exit velocity of ions

$$T^+ = \dot{m}_b^+ \left\langle v_b^+ \right\rangle = \eta_b^+ I_d \sqrt{\frac{2m_{xe}\eta_v^+ V_d}{e}} = \eta_b^+ I_d \sqrt{\frac{2m_{xe}\left(V_d - V_l^+\right)}{e}}. \tag{4-34}$$

Thrust is therefore proportional to the discharge current (or power), *i.e.*, the thruster size. Instead of the thrust, the thrust-to-power ratio will be used, since this quantity

removes the dependence on thruster size from the model. The thrust-to-power ratio based on the discharge power is

$$\frac{T^+}{P_d} = \eta_b^+ \sqrt{\frac{2m_{xe}\eta_v^+}{eV_d}} = \frac{\eta_b^+}{V_d}\sqrt{\frac{2m_{xe}\left(V_d - V_l^+\right)}{e}}\,. \tag{4-35}$$

From Eqn. 4-17 the anode specific impulse is

$$I_{sp,a}^+ = \frac{T^+}{\dot{m}_a g} = \frac{\eta_m^+}{g}\sqrt{\frac{2e\left(V_d - V_l^+\right)}{m_{xe}}}\,. \tag{4-36}$$

Combining the equations for the defect velocity and anode specific impulse yields an alternative form of the thrust-to-power ratio

$$\frac{T^+}{P_d} = \frac{2\eta_m^+\eta_b^+}{gI_{sp,a}^+}\frac{1}{1+\left(\dfrac{\left\langle v_l^+\right\rangle\eta_m^+}{gI_{sp,a}^+}\right)^2}\,. \tag{4-37}$$

Inspection of Eqn. 4-37 shows that the maximum thrust-to-power ratio is at the specific impulse corresponding to

$$I_{sp}^+ = \frac{\left\langle v_l^+\right\rangle\eta_m^+}{g}\,, \tag{4-38}$$

and maximum thrust-to-power ratio is therefore,

$$\left(\frac{T^+}{P_d}\right)_{\max} = \frac{\eta_b}{\left\langle v_l^+\right\rangle}\,. \tag{4-39}$$

Lastly, from Eqn. 4-18 the anode efficiency is

$$\eta_a^+ = \frac{\left(T^+\right)^2}{2\dot{m}_a P_d} = \eta_b^+\eta_m^+\eta_v^+ = \left(1-\varepsilon\right)^2\xi\left(1-\frac{V_l^+}{V_d}\right). \tag{4-40}$$

Eqn. 4-40 shows that the anode efficiency of a Hall thruster is given by the product of the three utilization efficiencies of current, mass, and voltage when the plasma consists of only singly-charged ions. In the limit of both high-voltage ($\eta_v^+ \approx 1$) and a fully-ionized plasma ($\eta_m^+ = 1$), Eqn. 4-40 shows how the anode efficiency asymptotically approaches the current utilization efficiency.

4.4 Performance model for a multiply-charged plasma

The performance model in section 4.3 considered the utilization efficiency of current, mass, and voltage for a plasma of singly-charged ions. This is not always adequate to describe Hall thruster performance, especially at high mass flow rates and voltages when the effects of multiply-charged ions can no longer be neglected. A fourth important conversion process in a Hall thruster, the fraction of multiply-charged ions in the plasma, that is, the charge utilization efficiency, requires several new definitions and modifications to the singly-charged model. Other researchers have considered, under certain limiting assumptions, the effects of multiply-charged ions on the performance of ion thrusters [209] and on Hall thrusters [197, 203, 208]. The model presented here makes none of these assumptions by generalizing to the case of a partially-ionized plasma consisting of any number of multiply-charged ion species.

4.4.1 Current utilization efficiency

A multiply-charged ion transports more current than a singly-charged ion because of the higher charge-state and velocity of the ion (the additional current is proportional to $Z^{3/2}$ when accelerated through the same potential as a singly-charged ion). Consider an ion beam consisting of N charged species (*e.g.*, Xe^+, Xe^{2+}, Xe^{3+}, …, Xe^{N+}). The total beam number density is the sum of each ion species number density

$$n_b = \sum_{i=1}^{N} n_i \,. \tag{4-41}$$

(From this point on, all summations will also be for each ion species, i, from 1 to N.) The species fraction of the i^{th} ion species is defined as

$$\zeta_i \equiv \frac{n_i}{n_b}, \tag{4-42}$$

where,

$$\sum \zeta_i = 1 \,. \tag{4-43}$$

The total ion current is the sum of each of the ion species currents

$$I_b = \sum I_i \,, \tag{4-44}$$

and the current of the i^{th} ion species is

$$I_i = A n_i q_i \langle v_i \rangle = A n_i e Z_i \sqrt{\frac{2eZ_i V_a}{m_{xe}}} = A n_b e^{3/2} \sqrt{\frac{2V_a}{m_{xe}}} \xi_i Z_i^{3/2} \,, \tag{4-45}$$

where the accelerating potential V_a and the cross-sectional area of the discharge chamber A are taken as constants for each ion species. Section 4.4.3 justifies the use of a constant accelerating potential. Using the same area for each ion species seems reasonable, since the majority of the ionization occurs upstream of the exit plane. Even if the area for each ion species differs (perhaps due to sheath effects or ionization downstream of the exit plane), it is unlikely that the areas would differ substantially and are therefore taken as constant for each ion species.

The beam current can now be expanded as

$$I_b = \sum I_i = Ae^{3/2} n_b \sqrt{\frac{2V_a}{m_{xe}}} \sum \xi_i Z_i^{3/2} \,. \tag{4-46}$$

The current fraction of the i^{th} species is defined as the ratio of species current to the beam current

$$\Omega_i \equiv \frac{I_i}{I_b} = \frac{\zeta_i Z_i^{3/2}}{\sum \zeta_i Z_i^{3/2}}, \tag{4-47}$$

where,

$$\sum \Omega_i = 1 \,. \tag{4-48}$$

The current utilization efficiency is still defined as the ratio of the beam to discharge current

$$\eta_b \equiv \frac{I_b}{I_d} \,. \tag{4-49}$$

Whether or not the current utilization efficiency of a multiply-charged plasma differs from the singly-charged case depends on the how the models are used. Since the models are best used to compare with experimental data, it will usually be the case that the beam current is held constant between the singly- and multiply-charge models (*i.e.*, $\eta_b = \eta_b^+$). The discharge current is always the same in either model. Section 4.5 discusses applications of the singly- and multiply-charged models further.

4.4.2 Mass utilization efficiency

To account for multiply-charged ions, the expression for anode mass flow rate given by Eqn. 4-23 needs to be modified. The mass flow rate of the i^{th} ion species is

$$\dot{m}_i = \frac{m_{xe}}{e}\frac{I_i}{Z_i} = \frac{m_{xe} I_b}{e}\frac{\Omega_i}{Z_i}, \tag{4-50}$$

and the mass flow rate of all the beam ions is

$$\dot{m}_b = \sum \dot{m}_i = \frac{m_{xe} I_b}{e}\sum \frac{\Omega_i}{Z_i}. \tag{4-51}$$

The anode mass flow rate can then be expressed as

$$\dot{m}_a = \dot{m}_b + \dot{m}_n = \frac{m_{xe} I_b}{e}\sum \frac{\Omega_i}{Z_i} + \dot{m}_n. \tag{4-52}$$

With the anode mass flow rate modified for multiply-charged ions, the mass utilization efficiency becomes

$$\eta_m \equiv \frac{\dot{m}_b}{\dot{m}_a} = \frac{m_{xe}\eta_b I_d}{\dot{m}_a e}\sum \frac{\Omega_i}{Z_i} = \xi\eta_b \sum \frac{\Omega_i}{Z_i}. \tag{4-53}$$

In the literature, the mass utilization efficiency is based, almost without exception, on the singly-charged plasma definition given by Eqn. 4-26. Under the singly-charged definition, Hall thruster mass utilization efficiencies are usually greater than 90%. If the ion species fractions were actually 90% Xe^+ and 10% Xe^{2+}, the "true" mass utilization efficiency would be 79%.

When comparing the singly- or multiply-charged models, the beam current is usually held constant (see section 4.5), which then makes the current utilization efficiencies equal

$$\eta_b = \eta_b^+ \quad \left(\text{if } I_b = I_b^+\right), \tag{4-54}$$

and which means the mass utilization efficiencies are related by

$$\eta_m = \xi \eta_b^+ \sum \frac{\Omega_i}{Z_i} = \eta_m^+ \sum \frac{\Omega_i}{Z_i} \quad \left(\text{if } I_b = I_b^+\right). \tag{4-55}$$

Further, if the loss voltage and beam current are set equal to that of a singly-charged plasma, the ionization fraction of a multiply-charged plasma is

$$\begin{aligned} \Theta &= \frac{1}{1 + \left(\frac{1-\eta_m}{\eta_m}\right)\frac{\langle v_b^+ \rangle}{\langle v_n \rangle}\sum \xi_i Z_i^{1/2}} \\ &= \frac{1}{1 + \left(\frac{1-\eta_m^+ \sum (\Omega_i / Z_i)}{\eta_m^+ \sum (\Omega_i / Z_i)}\right)\frac{\langle v_b^+ \rangle}{\langle v_n \rangle}\sum \xi_i Z_i^{1/2}} \quad \left(\text{if } I_b = I_b^+, V_l = V_l^+\right) \end{aligned}, \tag{4-56}$$

where the terms in the summations account for the effects of multiply-charged ions. Eqn. 4-56 reduces to Eqn. 4-28 if the plasma is singly-charged. Recall from section 4.3.2 that the ionization fraction based on the assumption of a singly-charged plasma was 15%. If the singly-charged mass utilization efficiency is 90%, the ion species fractions of Xe^+ and Xe^{2+} are 90% and 10%, respectively, and the singly-charged ion and neutral velocities are 20 and 0.4 km/s respectively, then the ionization fraction given by Eqn. 4-56 is only 6%. In other words, under typical operating conditions for 300 V Hall thrusters, the characteristic ionization fraction is much less than one.

4.4.3 Voltage utilization efficiency

Accounting for multiply-charged ions, the average, axial exit velocity for each species is

$$\langle v_i \rangle = \sqrt{\frac{2eV_{a,i}}{m_{xe}}}\sqrt{Z_i}\,, \tag{4-57}$$

where the accelerating voltage of the i^{th} species $V_{a,i}$ is related to the discharge voltage and species-dependent loss voltage $V_{l,i}$ through the discharge voltage

$$V_d \equiv V_{a,i} + V_{l,i} \,. \tag{4-58}$$

The average accelerating voltage of each species can differ by a few volts if the locations where the ion species are created are spatially separated along the axial direction of the discharge chamber. Since a Xe^+ ion would begin to accelerate downstream after being created, differences in the average accelerating voltage would result if the ionization occurs through any multi-step process (*i.e.*, as opposed to a single electron collision with sufficient energy to create a multiply-charged ion). If multiply-charged ions are created sufficiently far downstream, the divergence angle of each species would also differ, since the solid angle through which an ion could escape the discharge chamber without colliding with the wall increases the further downstream from the anode that the ion is created. Kim and King [204, 208] have observed, using different types of energy analyzers, that the species-dependent energy-to-charge ratios (*i.e.*, the average ion voltage, $V_{a,i} = W_i/q_i$) were different by a few tens of volts and that the divergence angle of multiply-charged ions was greater than the singly-charged ions.[23] In addition, both Kim and King observed that the voltage difference between each species was on the order of the ionization potential.[24] For present purposes, assume then that the species-dependent loss voltage can be modeled as

$$V_{l,i} \equiv V_{div,i} + V_{ion,i} \,, \tag{4-59}$$

[23] If the ionization process resulting in multiply-charged ions is through multiple electron impacts, it should be the case that the ordering (from highest to lowest) of the W_i/q_i ratio would be: Xe^+, Xe^{2+}, Xe^{3+}. Both Kim and King observed an ordering that was usually: Xe^+, Xe^{3+}, Xe^{2+}, which suggests that the process creating multiply-charged ions is more complicated than multiple electron impacts.

[24] The ionization potentials are 12 eV from Xe to Xe^+, 21 eV from Xe^+ to Xe^{2+}, and 32 eV from Xe^{2+} to Xe^{3+}.

where $V_{div,i}$ accounts for the loss of axially directed ion velocity due to the species-dependent divergence angle, and $V_{ion,i}$ accounts for the difference in potential between the discharge voltage and the location where the ion is created. A reasonable estimate for $V_{ion,i}$ is the total ionization potential (*i.e.*, from a ground state neutral atom) of the i^{th} ion species (12 eV for Xe^{+}, 33 eV for Xe^{2+}, and 65 eV for Xe^{3+}).

Even though the loss voltages should be greater for the multiply-charged ions than the singly-charged ions, the change in the effective exit velocity is relatively minor because singly-charged ions account for the vast majority of the ions (even at high-voltage, see section 11.2). Allowing for species-dependent loss voltages, the effective exit velocity can be expressed as

$$c = \eta_m^+ \sum \left(\frac{\Omega_i}{\sqrt{Z_i}} \sqrt{\frac{2e\left(V_d - V_{l,i}\right)}{m_{xe}}} \right), \qquad \textbf{(4-60)}$$

where the species current fractions appearing in the equation above would be redefined to account for the species-dependent loss voltages. Using typical values of $\eta_m^+ = 90\%$, species fractions of (ξ_1, ξ_2, ξ_3 = 90%, 9%, 1%), and estimating the loss voltages by the ionization potentials ($V_{l,1}$, $V_{l,2}$, $V_{l,3}$ = 12, 33, 65 V), the effective exit velocity would be 17 km/s for a discharge voltage of 300 V. In order to match this effective velocity with a constant loss voltage for each species, the loss voltage would need to be 13 V, which is only 1 V more than the species-dependent loss voltage of Xe^{+}. While this example illustrates that the singly-charged ions largely determine the effective exit velocity, the more important result is that a constant loss voltage for all species may be used in the performance model without a significant loss of accuracy. This turns out to be desirable from the standpoint of measurable

quantities, since most energy diagnostics measure the energy-to-charge ratio of the ions, which is equivalent to measuring the average loss voltage over all species.

With the considerations above, the loss voltage will be taken as a constant for all ion species. This modifies Eqn. 4-57 such that the ion velocity will depend only on the charge-state of the ion

$$\langle v_i \rangle = \sqrt{\frac{2eV_a}{m_{xe}}}\sqrt{Z_i}\,. \tag{4-61}$$

The discharge voltage and voltage utilization efficiency can then be expressed, respectively, as

$$V_d = V_a + V_l\,, \tag{4-62}$$

and

$$\eta_v \equiv \frac{V_a}{V_d}\,. \tag{4-63}$$

4.4.4 Performance

With the modifications to the utilization efficiencies, the performance parameters of a multiply-charged plasma can now be written down. The thrust produced by a multiply-charged plasma is

$$T = \sum \dot{m}_i \langle v_i \rangle = \eta_b I_d \sqrt{\frac{2m_{xe}\eta_v V_d}{e}} \sum \frac{\Omega_i}{\sqrt{Z_i}}\,. \tag{4-64}$$

The thrust-to-power ratio is more useful since it is independent of thruster size (see section 4.3.4). The thrust-to-power ratio based on the discharge power is

$$\frac{T}{P_d} = \eta_b \sqrt{\frac{2m_{xe}\eta_v}{eV_d}} \sum \frac{\Omega_i}{\sqrt{Z_i}}. \tag{4-65}$$

The anode specific impulse for a multiply-charged plasma is

$$I_{sp,a} = \frac{T}{\dot{m}_a g} = \frac{\eta_m}{g} \sqrt{\frac{2e\eta_v V_d}{m_{xe}}} \frac{\sum \frac{\Omega_i}{\sqrt{Z_i}}}{\sum \frac{\Omega_i}{Z_i}} = \frac{\eta_b \xi}{g} \sqrt{\frac{2e\eta_v V_d}{m_{xe}}} \sum \frac{\Omega_i}{\sqrt{Z_i}}, \tag{4-66}$$

Finally, the anode efficiency for a multiply-charged plasma is

$$\eta_a = \frac{T^2}{2\dot{m}_a P_d} = \eta_b \eta_v \eta_m \frac{\left(\sum \Omega_i / \sqrt{Z_i} \right)^2}{\sum \Omega_i / Z_i} = \eta_b \eta_v \eta_m \eta_q, \tag{4-67}$$

where the charge utilization efficiency has been defined as

$$\eta_q \equiv \frac{\left(\sum \Omega_i / \sqrt{Z_i} \right)^2}{\sum \Omega_i / Z_i}. \tag{4-68}$$

Eqn. 4-67 resembles the singly-charged efficiency given by Eqn. 4-40 except for the addition of the charge utilization efficiency. Thus, when allowing for a partially-ionized, multiply-charged plasma, the anode efficiency of a Hall thruster is given by the product of the four utilization efficiencies of current, voltage, mass, and charge.

The mass utilization in Eqn. 4-67 still includes a term due to multiply-charged ions. Substituting Eqn. 4-53 into Eqn. 4-67 yields an alternate form of the anode efficiency given by

$$\eta_a = \eta_b^2 \eta_v \xi \left(\sum \frac{\Omega_i}{\sqrt{Z_i}} \right)^2 = (1-\varepsilon)^2 \xi \left(1 - \frac{V_l}{V_d} \right) \left(\sum \frac{\Omega_i}{\sqrt{Z_i}} \right)^2 . \quad \textbf{(4-69)}$$

In the limit of both high-voltage ($\eta_v \approx 1$) and a fully-ionized plasma ($\eta_m = 1$), the anode efficiency asymptotically approaches

$$\lim_{\eta_v \eta_m \to 1} \eta_a = \eta_b \eta_q . \quad \textbf{(4-70)}$$

It turns out that the charge utilization efficiency remains above 90% for reasonable values of the species fractions. As an extreme example, for species fractions of 50% Xe^+, 25% Xe^{2+}, 15% Xe^{3+}, and 10% Xe^{4+}, the charge utilization efficiency is still 93.5%. Therefore, it is still accurate to say that the anode efficiency of a Hall thruster is primarily limited by the current utilization efficiency.

4.5 Model applications

To use the performance model requires that the system, thruster, and plasma parameters are available (see Table 4-1). The system parameters are the PPU efficiency and the power required by the XFC and DCIU. The thruster parameters are the discharge voltage and current, the anode and cathode mass flow rates, and electromagnet power. The plasma parameters are the loss voltage, electron current (or beam current), and species fractions (multiply-charged model only). If the model is used to compute one of the plasma parameters, then the performance parameters are needed: thrust, specific impulse, and efficiency. Regardless of how the models are used and unless noted otherwise, the system and thruster parameters are considered constants between the singly- and multiply-charged versions of the model. Whether the plasma or performance parameters are constant depends on how the model is used.

Table 4-1 Parameters needed by the model to compute performance.

System Parameters	Thruster Parameters	Plasma Parameters
η_{PPU}, P_{XFC}, P_{DCIU}	V_d, I_d, $\dot{m}_a$, $\dot{m}_c$, P_{mag}	V_l, ε, ζ_i

When the model is used to compute performance, the plasma parameters are needed. Since in most cases the plasma parameters are not known for each thruster or have never been measured (most of the literature is devoted to 300 V, 1 kW thrusters), the model cannot be used to find universal performance trends for Hall thrusters unless curve fitting is used. Due to the number of free variables involved in the model, this can lead to inaccurate estimates of the plasma parameters. This is probably why Ref. [46, 58] considered models with only two free parameters (loss voltage and electron current). Excluding the effects of mass utilization and multiply-charged ions from those models led to overestimates of the loss voltage and beam current from the "true" values. Ref. [197] partially improved the situation by adding multiply-charged ions, but was still limited to a single set of species fractions, fully-ionized plasmas, and voltage-independent electron current and loss voltage.

However, the best use of the model is not to universally describe Hall thruster performance, but as a means to study the performance of individual designs. When the performance and plasma parameters for a specific thruster are available, the model can be used to correlate changes in performance with operating conditions and the plasma parameters. In Chapter 12, the model is used to compute the electron current from measurements of the loss voltage, species fractions, and performance parameters. An analysis of the utilization efficiencies is then used to correlate changes in the measured performance to specific plasma parameters (*e.g.*, the electron Hall parameter).

Before concluding this chapter, a few example cases illustrating how multiply-charged ions affect performance are discussed. These examples are meant to highlight the major trends that can be expected when the model is used in Chapter 12. Three cases are considered in sections 4.5.1-4.5.3:

1. $I_b > I_b^+$, $\eta_m = \eta_m^+$ – The multiply-charged beam current is greater than the singly-charged beam current (recall that $\dot{m}_a = \dot{m}_a^+$). Just how much greater is arbitrary, but for the sake of comparison the mass utilization efficiencies are set equal ($\eta_m = \eta_m^+$).

2. $I_b = I_b^+$, $\eta_m < \eta_m^+$ – The beam current is the same in either model. In this case, adding multiply-charged ions to the current decreases the mass utilization since the anode mass flow rate is also constant ($\dot{m}_a = \dot{m}_a^+$).

3. $I_b = I_b^+$, $\eta_m = \eta_m^+$ – The beam current and the mass utilization are the same in either model. To satisfy this condition, the anode mass flow rate from the multiply-charged model must be less than the singly-charged model ($\dot{m}_a < \dot{m}_a^+$). This case is a generalization of the model in Ref. [197], which was limited to a fully-ionized plasma (100% mass utilization).

For each of the cases above, the loss voltage and species fractions also need to be specified. For the purposes of comparison, the species fractions can be considered as known values. Since the multiply-charged model uses an average loss voltage over all species, it is also the case that the singly- and multiply-charged loss voltages are approximately equal

$$V_l \approx V_l^+ . \tag{4-71}$$

This is a valid approximation as long as singly-charged ions dominate the flow, which is apparently the case for sub-kilovolt discharge voltages (see section 11.2).

4.5.1 Constant mass utilization efficiency

The first case adds multiply-charged ions to the beam while the mass utilization remains constant

$$\eta_m = \eta_m^+ . \tag{4-72}$$

Constant mass utilization means that the beam current increases due to multiply-charged ions according to

$$I_b = \frac{I_b^+}{\sum \frac{\Omega_i}{Z_i}} . \tag{4-73}$$

Since the discharge current is constant, the current utilization also increases

$$\eta_b = \frac{\eta_b^+}{\sum \frac{\Omega_i}{Z_i}} . \tag{4-74}$$

Taking $V_l = V_l^+$ and assuming that the species fractions are known, the performance parameters are related by

$$\frac{T}{P_d} = \left(\frac{T}{P_d}\right)^+ \frac{\sum \frac{\Omega_i}{\sqrt{Z_i}}}{\sum \frac{\Omega_i}{Z_i}} \Rightarrow \frac{T}{P_d} > \left(\frac{T}{P_d}\right)^+ , \tag{4-75}$$

$$I_{sp,a} = I_{sp,a}^{+} \frac{\sum \frac{\Omega_i}{\sqrt{Z_i}}}{\sum \frac{\Omega_i}{Z_i}} \Rightarrow I_{sp,a} > I_{sp,a}^{+}, \tag{4-76}$$

$$\eta_a = \eta_a^{+} \left(\frac{\sum \frac{\Omega_i}{\sqrt{Z_i}}}{\sum \frac{\Omega_i}{Z_i}} \right)^2 \Rightarrow \eta_a > \eta_a^{+}. \tag{4-77}$$

The terms due to multiply-charged ions are always greater than one. **Therefore, if the mass utilization is constant, the performance parameters of a multiply-charged plasma are always greater than those of a singly-charged plasma.**

4.5.2 Constant beam current

The second case adds multiply-charged ions to the beam for constant beam current

$$I_b = I_b^{+}. \tag{4-78}$$

Since the discharge current is constant, the current utilization is also constant

$$\eta_b = \eta_b^{+}. \tag{4-79}$$

Constant beam current means that the mass utilization decreases due to multiply-charged ions according to

$$\eta_m = \xi \eta_b \sum \frac{\Omega_i}{Z_i} = \eta_m^{+} \sum \frac{\Omega_i}{Z_i}. \tag{4-80}$$

The quantity given by the summation in Eqn. 4-80 is always less than one. Therefore, if the beam current is constant, the mass utilization efficiency of a multiply-charged plasma is always less than that of a singly-charged plasma. Note

that if the multiply-charged mass utilization is 100% and the anode mass flow rate is constant, then the singly-charged mass utilization will exceed 100% by an amount given by Eqn. 4-80.

Taking $V_l = V_l^+$ and assuming that the species fractions are known, the performance parameters are related by

$$\frac{T}{P_d} = \left(\frac{T}{P_d}\right)^+ \sum \frac{\Omega_i}{\sqrt{Z_i}} = \Rightarrow \frac{T}{P_d} < \left(\frac{T}{P_d}\right)^+, \tag{4-81}$$

$$I_{sp,a} = I_{sp,a}^+ \sum \frac{\Omega_i}{\sqrt{Z_i}} \Rightarrow I_{sp,a} < I_{sp,a}^+, \tag{4-82}$$

$$\eta_a = \eta_a^+ \left(\sum \frac{\Omega_i}{\sqrt{Z_i}} \right)^2 \Rightarrow \eta_a < \eta_a^+. \tag{4-83}$$

The terms due to multiply-charged ion are always less than one. **Therefore, for constant beam current, the performance parameters of a multiply-charged plasma are always less than those of a singly-charged plasma.**

4.5.3 Constant beam current and mass utilization efficiency

The third case adds multiply-charged ions to the beam if the beam current and mass utilization both remain constant

$$I_b = I_b^+. \tag{4-84}$$

$$\eta_m = \eta_m^+. \tag{4-85}$$

Since the discharge current is constant, the current utilization is also constant

$$\eta_b = \eta_b^+. \tag{4-86}$$

Constant mass utilization at constant beam current requires that the anode mass flow rate of the multiply-charged model decrease according to

$$\dot{m}_a = \dot{m}_a^+ \sum \frac{\Omega_i}{Z_i}. \tag{4-87}$$

Taking $V_l = V_l^+$ and assuming that the species fractions are known, the performance parameters are related by

$$\frac{T}{P_d} = \left(\frac{T}{P_d}\right)^+ \sum \frac{\Omega_i}{\sqrt{Z_i}} \Rightarrow \frac{T}{P_d} < \left(\frac{T}{P_d}\right)^+, \tag{4-88}$$

$$I_{sp,a} = I_{sp,a}^+ \frac{\sum \frac{\Omega_i}{\sqrt{Z_i}}}{\sum \frac{\Omega_i}{Z_i}} \Rightarrow I_{sp,a} > I_{sp,a}^+, \tag{4-89}$$

$$\eta_a = \eta_a^+ \frac{\left(\sum \frac{\Omega_i}{\sqrt{Z_i}}\right)^2}{\sum \frac{\Omega_i}{Z_i}} \Rightarrow \eta_a < \eta_a^+. \tag{4-90}$$

In the equations above, the terms appearing due to multiply-charged ions are greater than unity for the thrust and efficiency, but less than unity for the specific impulse. **Therefore, for constant beam current and mass utilization efficiency, the thrust and efficiency of a multiply-charged plasma are always less than those of a singly-charged plasma while the specific impulse is greater.** By allowing for a partially-ionized plasma, this case can be considered a generalization of the model used in Ref. [197], which assumed a fully-ionized (100% mass utilization) plasma.

Although the approach had limitations, the results of Ref. [197] are an example of how the model can be practically implemented for studies of Hall thruster performance at various operating conditions. In Ref. [197], the plasma was assumed to be fully-ionized, the species fractions for the multiply-charged model were taken from experimental measurements of 300 V thrusters [29, 207], and the remaining plasma parameters (loss voltage and electron current) were assumed to be constant with discharge voltage. These approximations simplified the analysis, but at the cost of overestimating the loss voltage and electron current from their true values (see section 4.5). Despite these limitations, the results of Ref. [197] were still found to lend insight on the performance behavior of high-power Hall thrusters. It is very important to emphasize that the model in Ref. [197] was aimed specifically at high-power Hall thrusters so that the mass utilization efficiency could be approximated as 100%.

Under the assumptions of Ref. [197], the loss voltage and the electron current fraction were fit to data sequentially because the performance parameters of a fully-ionized plasma (with $\eta_m = \eta_m^+ = 1$) are given by

$$I_{sp,a} = \frac{1}{g}\sqrt{\frac{2e(V_d - V_l)}{m_{xe}}}\frac{\sum \frac{\Omega_i}{\sqrt{Z_i}}}{\sum \frac{\Omega_i}{Z_i}} = I_{sp}^+ \frac{\sum \frac{\Omega_i}{\sqrt{Z_i}}}{\sum \frac{\Omega_i}{Z_i}}, \tag{4-91}$$

$$\eta_a = (1-\varepsilon)\left(1 - \frac{V_l}{V_d}\right)\frac{\left(\sum \Omega_i / \sqrt{Z_i}\right)^2}{\sum \Omega_i / Z_i} = \eta_a^+ \frac{\left(\sum \Omega_i / \sqrt{Z_i}\right)^2}{\sum \Omega_i / Z_i}, \tag{4-92}$$

$$\frac{T}{P_d} = (1-\varepsilon)\sqrt{\frac{2m_{xe}(V_d - V_l)}{eV_d}}\sum \frac{\Omega_i}{\sqrt{Z_i}} = \left(\frac{T}{P_d}\right)^+ \sum \frac{\Omega_i}{\sqrt{Z_i}}. \tag{4-93}$$

Since the specific impulse was only a function of the loss voltage, plots of specific impulse versus discharge voltage were used to find the best fit for the loss voltage. With the loss voltage determined, plots of efficiency versus discharge voltage were used to find the best fit for the electron current fraction, which then allowed the thrust-to-power ratio to be computed. A loss voltage of 50 V and electron current fraction of 0.26 were found to fit the available data the best. Table 4-2 summarizes the species fractions that were used. Figures 4-1 through 4-3 show the variation of the performance parameters with discharge voltage from the singly- and multiply-charged models of Ref. [197]. Data from the NASA-457M [47], which were not available when Ref. [197] was originally published, are included here.

Table 4-2 Ion species fractions from Ref. [29, 207] used in the fully-ionized, multiply-charged plasma performance model of Ref. [197]. Species current fractions, and several terms used in the multiply-charged performance model are also shown.

	Species Fractions			Species Current Fractions			Important Summations			
	Xe+	Xe2+	Xe3+	Xe+	Xe2+	Xe3+	$\sum \frac{\Omega_i}{Z_i}$	$\sum \frac{\Omega_i}{\sqrt{Z_i}}$	$\frac{\sum \frac{\Omega_i}{\sqrt{Z_i}}}{\sum \frac{\Omega_i}{Z_i}}$	$\frac{\left(\sum \Omega_i / \sqrt{Z_i}\right)^2}{\sum \Omega_i / Z_i}$
SPT-100, King	0.888	0.110	0.002	0.734	0.257	0.009	0.866	0.921	1.064	0.980
P5, Gulczinski	0.925	0.068	0.007	0.802	0.167	0.032	0.896	0.938	1.047	0.982
Average	**0.907**	**0.089**	**0.005**	**0.767**	**0.213**	**0.020**	**0.880**	**0.929**	**1.056**	**0.981**

The model predictions from Ref. [197] could have benefited from including the mass utilization efficiency and by allowing for variable electron current. Adding these features would have improved the predictions of efficiency and thrust-to-power ratio, especially for the low-voltage data from the T-220 and the high-voltage data from the NASA-457M, but at the expense of adding free parameters to the model.

Two important results came from the model predictions:

1. The singly- and multiply-charged models bounded the experimental data reasonably well over a large range of voltage and power.

Although the plasma parameters were best-fit estimates, the ability to bound the performance with a simple model is a useful tool for thruster design and mission analysis.

2. Second, as the discharge power increased, performance was found to match the multiply-charged model more closely, especially at high-voltage. This was later confirmed in a performance characterization of the 50 kW NASA-457M [47] (some of the NASA-457M data from Ref. [47] are included here).

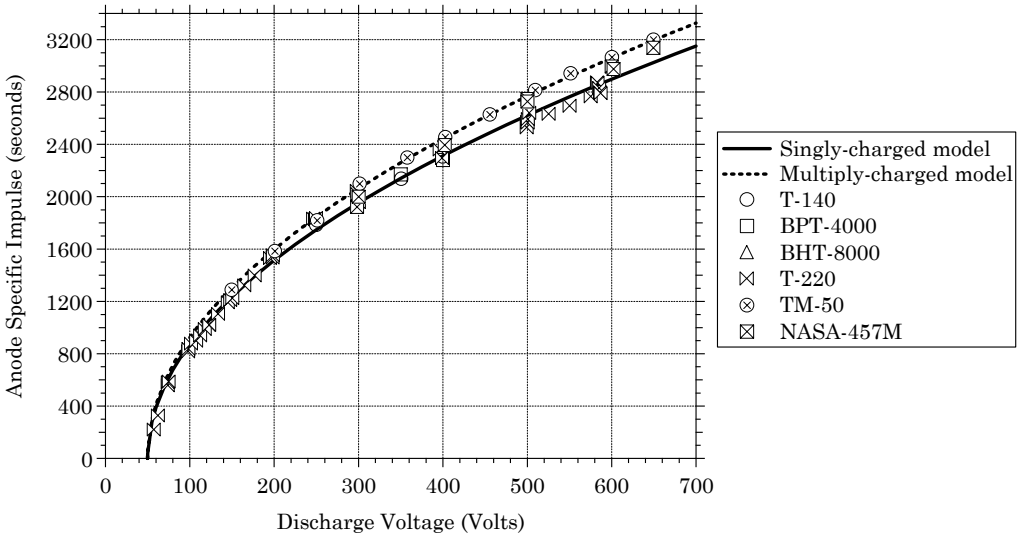

Figure 4-1 Anode specific impulse versus discharge voltage from the fully-ionized plasma performance model of Ref. [197]. The loss voltage was 50 V.

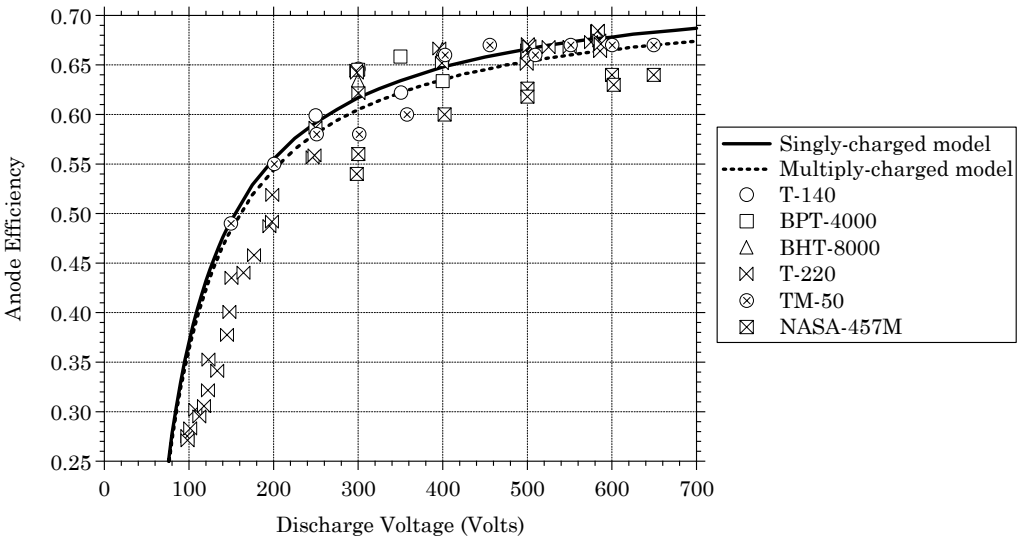

Figure 4-2 Anode efficiency versus discharge voltage from the fully-ionized plasma performance model of Ref. [197]. The loss voltage was 50 V, and the electron current fraction was 0.26.

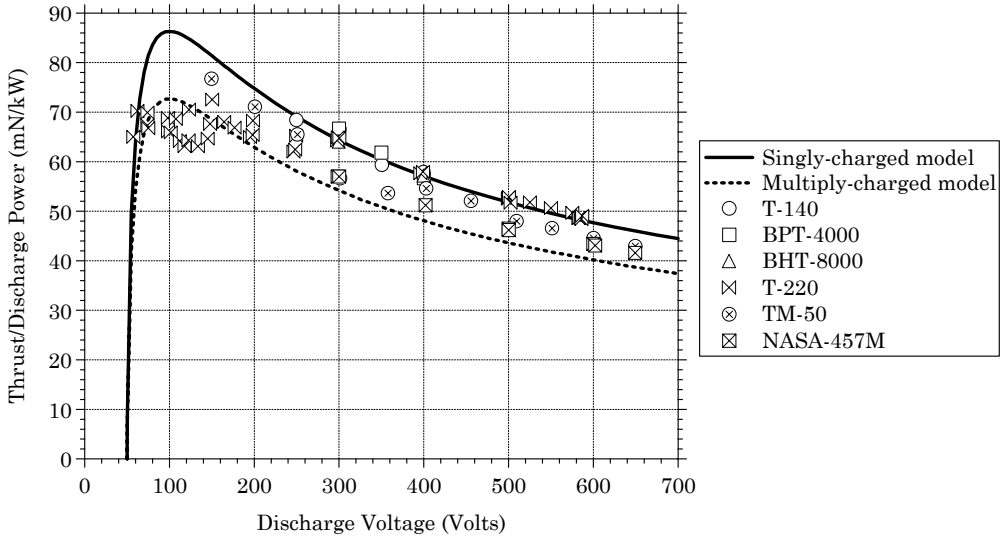

Figure 4-3 Thrust-to-power ratio versus discharge voltage from the fully-ionized plasma performance model of Ref. [197]. The loss voltage was 50 V, and the electron current fraction was 0.26.

4.6 Conclusions

A phenomenological Hall thruster performance model has been developed for the case of a partially-ionized, multiply-charged plasma accounting for the utilization efficiencies of current, mass, voltage, and charge. The model can be used to predict the system or thruster level performance of a Hall thruster provided that

the necessary inputs are available. A simplified version of the model that assumed a fully-ionized, multiply-charged plasma has been shown to bound Hall thruster performance over a wide range of operating conditions. The true utility of the model, however, is not in examining Hall thrusters in general, but in studying specific designs. When combined with plasma measurements from a thruster, the model can be used to gain considerable insight on internal thruster processes that would not otherwise be possible. In Chapter 12, the model is used to compute the utilization efficiencies and to assess how their relative variation with operating point correlate with changes to the plasma.

Chapter 5

Hall thruster magnetic field topography

In Chapter 3, a qualitative analysis of the electron dynamics showed the importance of the magnetic field in Hall thruster design. In this chapter, an overview of Hall thruster magnetic circuits is discussed to provide the necessary background for those unfamiliar with the subject. This is followed by a literature review of the magnetic field topography[25] in Hall thrusters that focuses on the key features common to efficient designs. In the last part of this chapter, an initial set of experiments are discussed that had as their goal to understand how the field line inclination and the axial gradient of the magnetic field affect plume divergence and focusing. The results of these early experiments indicated that a plasma lens magnetic field topography would be necessary for high-specific impulse Hall thrusters.

5.1 Magnetic circuits

5.1.1 Governing equations

Magnetic circuits are governed by two of Maxwell's equations [210]

$$\nabla \cdot \vec{B} = 0, \tag{5-1}$$

[25] Magnetic field topology is frequently confused in the literature with magnetic field topography. The root "topo-" is from the Greek "topos" which translates to "place." As defined in Webster's dictionary, topology is a "topographical study of a particular place." Topography is defined as "the configuration of a surface including its relief and the position of its natural and man-made features." That is, topology is the study of topography and a person that designs magnetic circuits is properly called a magnetic field topologist.

$$\nabla \times \vec{H} = \vec{j} + \varepsilon_o \frac{\partial \vec{E}}{\partial t}, \tag{5-2}$$

where $\vec{B}$ is the magnetic flux density, $\vec{H}$ is the magnetic intensity, $\vec{j}$ is the current density, $\vec{E}$ is the electric field, ε_o is the permittivity of free space, and t is time. The magnetization $\vec{M}$ of the ferromagnetic pole pieces is related to the magnetic intensity and the magnetic flux density by

$$\vec{M} = \chi_m \vec{H}, \tag{5-3}$$

$$\vec{B} = \mu_o\left(\vec{H} + \vec{M}\right) = \mu_o\left(1 + \chi_m\right)\vec{H} = \mu\vec{H}, \tag{5-4}$$

where χ_m is the susceptibility of the material, μ is its permeability, and μ_o is the permeability of free space.

In a Hall thruster, the self-magnetic field produced by the azimuthal electron current has a magnitude of only a few Gauss [143]. Since the applied magnetic field is on the order of a few hundred Gauss, self-fields from plasma currents can be neglected. The electric field and characteristic frequency of a Hall thruster plasma is on the order 20 V/mm and 20 kHz, respectively, resulting in a negligible contribution from the displacement current [142]. Under these conditions, Ampere's law (Eqn. 5-2) outside the magnetic circuit reads

$$\nabla \times \vec{H} = 0. \tag{5-5}$$

Inside the magnetic circuit, the coils are usually driven by steady electrical currents and Ampere's law reads

$$\nabla \times \vec{H} = \vec{j}. \tag{5-6}$$

When analyzing a magnetic circuit, the integral forms of Eqns. 5-1 and 5-2 are more convenient. These are obtained by applying Gauss' theorem to Eqn. 5-1

$$\iint \vec{B} \cdot \hat{n} dS = 0 . \tag{5-7}$$

and Stokes' theorem to Eqn. 5-6

$$\oint \vec{H} \cdot d\vec{l} = \iint \vec{j} \cdot \hat{n} dS . \tag{5-8}$$

5.1.2 C-core magnetic circuit

The typical C-core magnetic circuit shown in Figure 5-1 can be used to illustrate the major features of most magnetic circuits [211]. The circuit consists of a coil winding wrapped around a ferromagnetic core with a constant cross-sectional area A_m and mean length L_m. For present purposes, the core material is assumed to have a constant permeability $\mu_m = B_m / H_m$. A current I_c is supplied to the winding of N_c turns to produce a magnetic flux Φ. The core material guides the flux from the coil into the vacuum gap of length L_g and effective area A_g. The gap distance is assumed small enough that the flux density B_g across the gap can be assumed constant. The effective area is larger than the geometric area because of field fringing across the gap.

If flux leakage outside the core is neglected, applying Eqn. 5-7 across the interface between the core and the gap shows

$$B_m A_m = B_g A_g = \Phi = \text{constant} . \tag{5-9}$$

Applying the integral form of Ampere's law the magnetic flux density in the gap is given by

$$B_g = \frac{\mu_o N_c I_c}{\left(L_g + \frac{A_g}{A_m} \frac{\mu_o}{\mu_m} L_m \right)}. \qquad \textbf{(5-10)}$$

For a given magnetomotive force $F_{mmf} = N_c I_c$ supplied by the winding, Eqn. 5-10 shows that the flux density in the gap can be maximized by

1. minimizing the gap distance L_g and effective area A_g,
2. maximizing the cross-sectional area of the core A_m,
3. decreasing the length of the circuit L_m, and
4. using a core material with a large permeability μ_m.

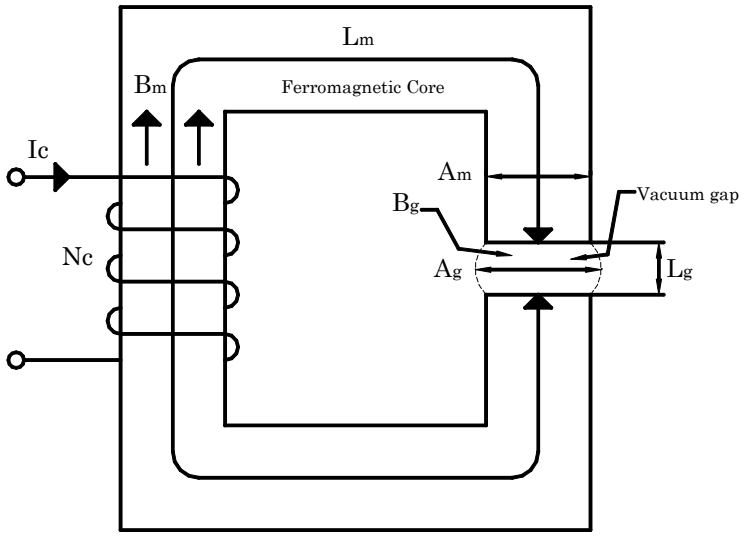

Figure 5-1 Schematic of a C-core magnetic circuit consisting of a coil winding, ferromagnetic core, and vacuum gap.

5.1.3 Hall thruster magnetic circuit

In a Hall thruster, the magnetic circuit design is a significantly more complex situation than the C-core discussed in the previous section. The circuit equivalent of the Hall thruster in Figure 3-1 is shown in Figure 5-2. Each section of the magnetic circuit is represented by an equivalent "resistance" given by a reluctance $R_s = L_s / \mu_s A_s$. The coils appear as "voltage" sources that supply a magnetomotive

force $N_c I_c$. The magnetic field topography in the discharge chamber is determined primarily by the reluctances across the inner and outer front poles and the inner and outer magnetic screens. The front pole pieces determine where most of the magnetic flux is applied across the gap. The screens shape the magnetic field topography in the channel by redirecting a portion of the magnetic flux. This serves to lower the magnitude of the magnetic field in the upstream portion of the discharge chamber, which increases the axial gradient of the radial magnetic field.

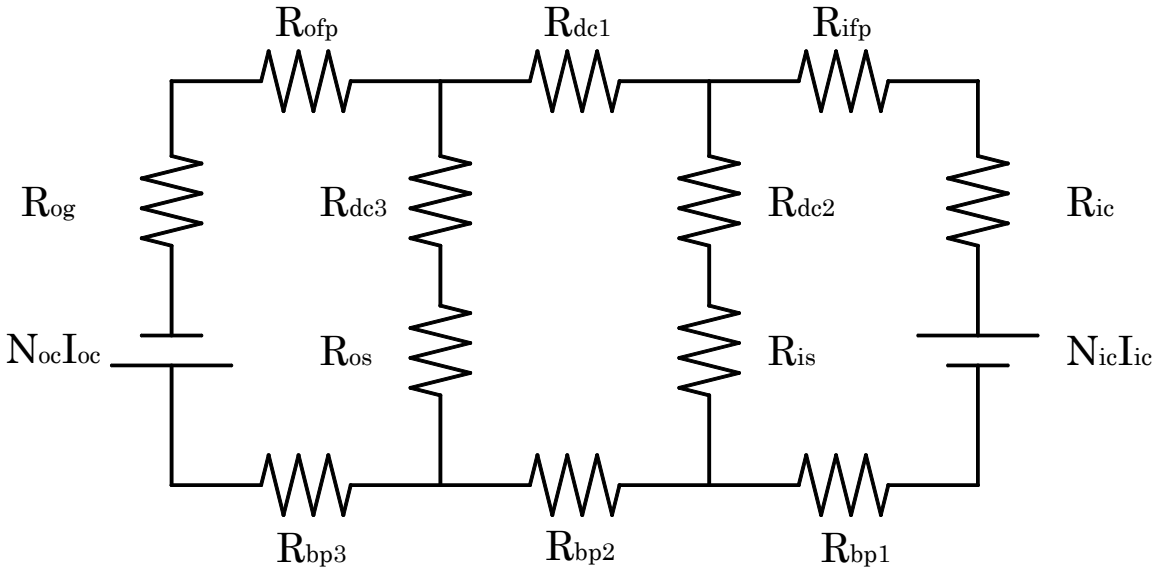

Figure 5-2 Electric circuit equivalent of the magnetic circuit from Figure 3-1.

As an example, the NASA-173Mv1 magnetic circuit produces the magnetic field topography shown in Figure 5-3. Axial profiles of the radial and axial components of the magnetic field are shown in Figures 5-4 and 5-5, respectively. Due to the magnetic screens, the radial magnetic field decreases from the exit plane to the anode which in turn decreases the radius of curvature of the field lines (*i.e.*, the concavity increases). In Chapter 7, the magnetic field topography of the NASA-173Mv1 is discussed further.

As in any engineering endeavor, the design of a magnetic circuit is constrained by the requirements of the particular application. The application is usually specified as a certain range of thruster operating conditions that dictate the shape and strength of the magnetic field. The resulting process of designing the magnetic circuit is an optimization problem that involves a large number of free variables governed by a set of non-linear equations, where the appropriate combination of materials, pole piece geometry, and coil design must be determined [211-213].

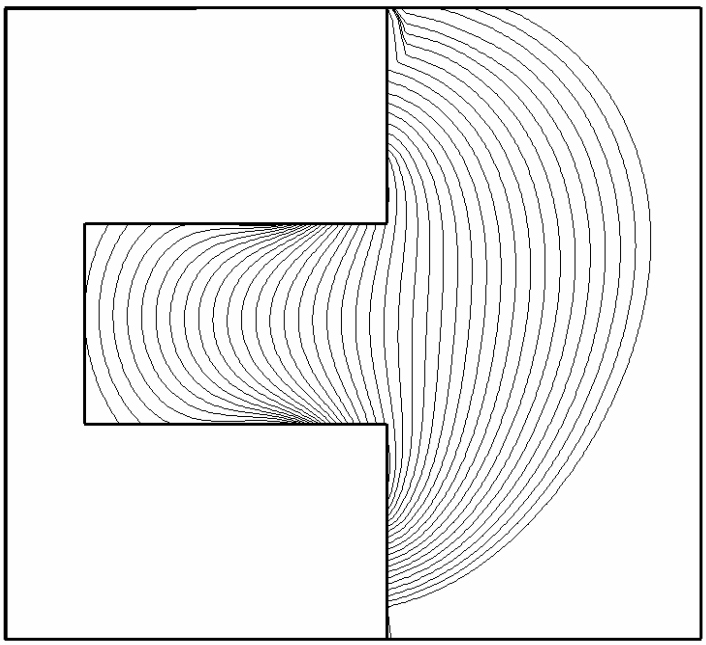

Figure 5-3 Magnetic field topography of the NASA-173Mv1. The field lines form what is commonly referred to as a plasma lens.

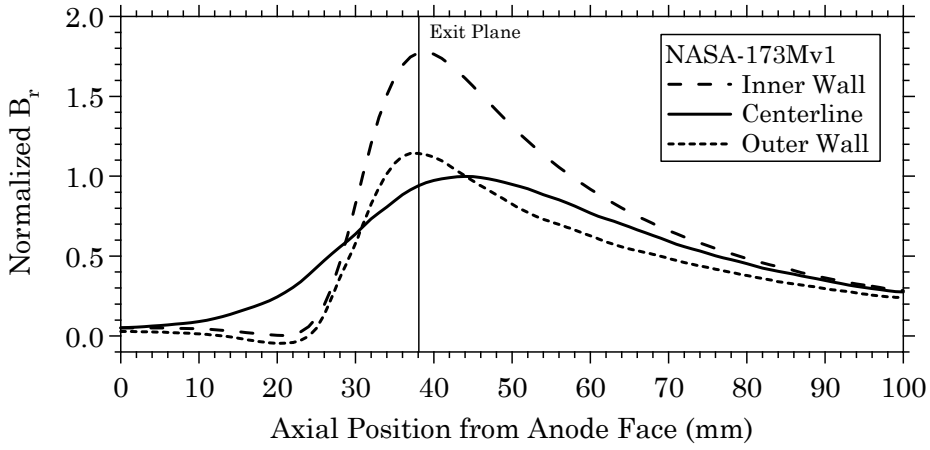

Figure 5-4 Radial magnetic field profiles of the NASA-173Mv1 normalized by the maximum value on centerline.

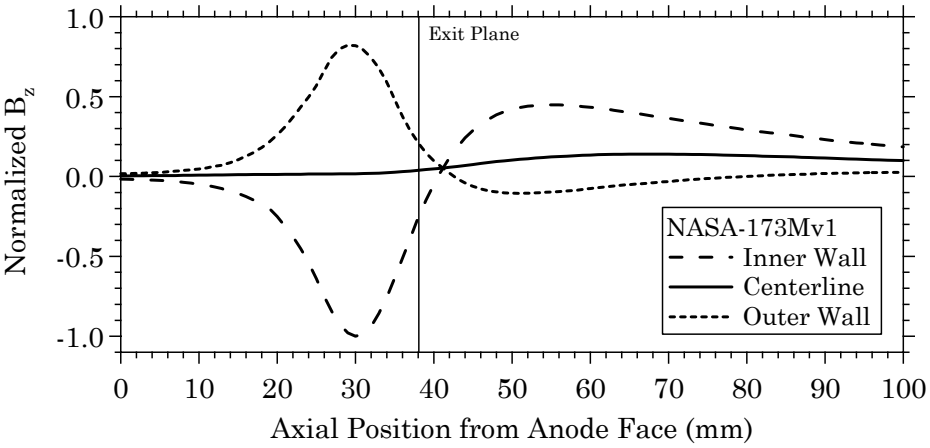

Figure 5-5 Axial magnetic field profiles of the NASA-173Mv1 normalized by the magnitude of the maximum field on the inner wall.

While it is possible to study the magnetic circuit analytically [214], the simplifications and assumptions that are required to make tractable progress result in solutions with a limited range of applicability. To obtain accurate results a computer simulation is typically employed. The three-dimensional, magnetostatic, finite-element solver Magnet 6 by Infolytica was used to design the NASA-173M Hall thrusters. The code allows the user to explore the design space of a given magnetic circuit through advanced parameterization methods, which has enabled the simulation of literally hundreds of different magnetic circuit configurations.

Repeated comparisons between predictions from Magnet and measurements of the magnetic field using a Hall probe connected to a Gaussmeter have shown agreement to within ±10%. The comparisons have shown that the uncertainty was determined primarily by positional and alignment errors of the Hall probe rather than the accuracy of Magnet. The agreement between Magnet and the fabricated thrusters has been confirmed on several NASA Hall thrusters, including the NASA-457M [47].

5.1.4 Trim coils

Figure 5-6 is a schematic of a Hall thruster that uses an internal trim coil (ITC) and an external trim coil (ETC). As defined here, a trim coil is any coil used in a Hall thruster besides the inner and outer coils. The NASA-173Mv1, discussed in Chapter 7, makes use of an internal trim coil. The NASA-173Mv2, discussed in Chapter 8, makes use of both an internal and external trim coil. Trim coils are used to provide additional control of the magnetic field topography beyond that afforded by the inner and outer coils. A more precise method for sculpting the field would be to change the pole pieces, but this is prohibitively time-consuming and expensive from the perspective of a research program. Trim coils are most useful in identifying an optimum magnetic field configuration that can be later used in follow-on versions of a thruster. Such an approach was adopted with the NASA-173Mv2, which is based on experiments with the internal trim coil in the NASA-173Mv1.

Trim coils have been used extensively in Hall thrusters for decades, dating back at least to the work of Morosov, *et al.* [134, 145] (see section 5.2.1-5.2.2). Recently, Kim has experimented with internal trim coils on xenon and krypton mixtures [118, 120]. Other implementations of internal trim coils are discussed in

Ref. [215-218]. Ref. [219] discusses the use of external trim coils and pole pieces to affect plume divergence and thrust vectoring in an SPT-100.

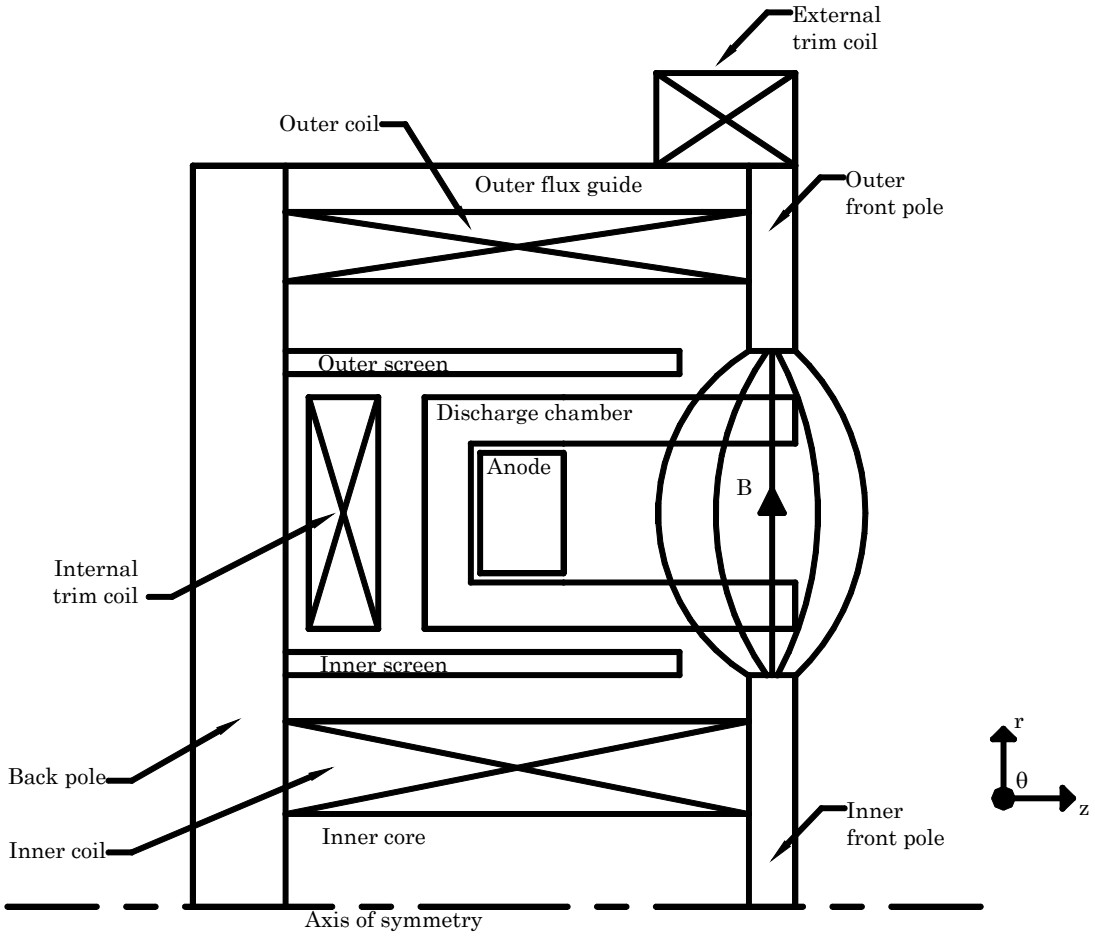

Figure 5-6 Cross-sectional schematic of a magnetic layer Hall thruster with internal and external trim coils (not to scale).

The internal trim coil shown in Figure 5-6 primarily affects the radial magnetic field in the discharge chamber. Depending on the direction of the coil current, the radius of curvature of the field lines (*i.e.*, the axial gradient of the magnetic field, $\nabla_z B_r$) can be altered. By convention, a negative current subtracts from the radial magnetic field and increases $\nabla_z B_r$. The effects of positive and negative current on the centerline profile of the radial magnetic field are shown in Figure 5-7. Note how the influence of the internal trim coil is greatest near the

anode. Figure 5-8 shows how a negative coil current decreases the radius of curvature of the field lines (*i.e.*, negative coil current increases the concavity) and Figure 5-9 shows how positive coil current has the opposite effect.

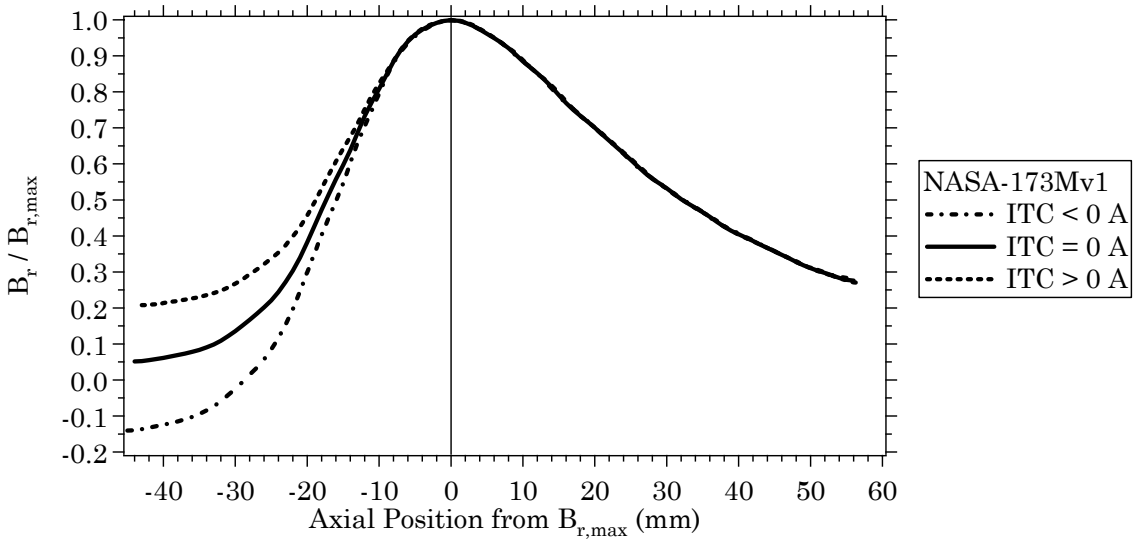

Figure 5-7 Radial magnetic field profiles of the NASA-173Mv1 showing the effects of the internal trim coil (ITC) on the axial gradient of the radial magnetic field.

The external trim coil shown in Figure 5-6 primarily affects the magnetic field outside of the thruster's magnetic circuit in the vicinity where the cathode is usually mounted (see Figure 3-1). Figure 5-10 shows the field lines around a Hall thruster without energizing the external trim coil (ETC = 0 A) and when a negative current is supplied to the external trim coil (ETC < 0 A). With a negative current on the external trim coil, the field line inclination is increased towards the radial direction in the figure.

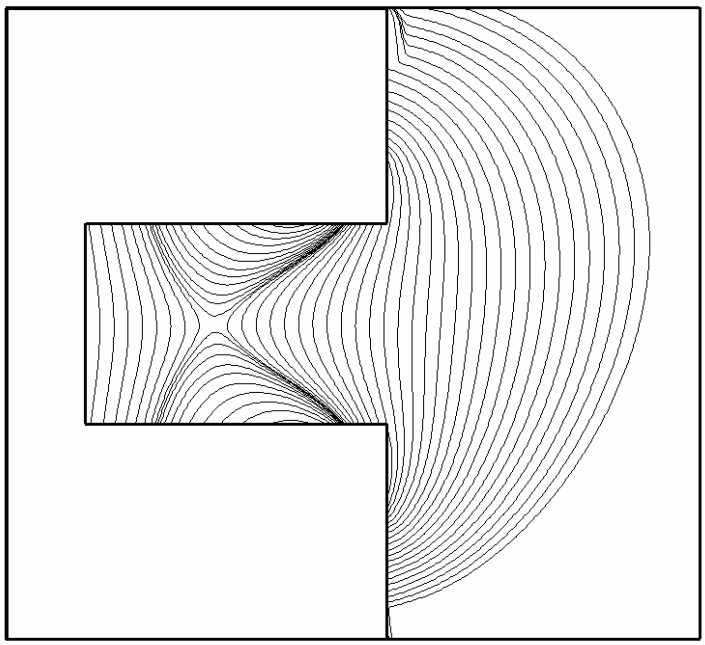

Figure 5-8 **Magnetic field topography of the NASA-173Mv1 when the internal trim coil is energized with a negative current. Negative current increases the concavity of the plasma lens from the configuration shown in Figure 5-3.**

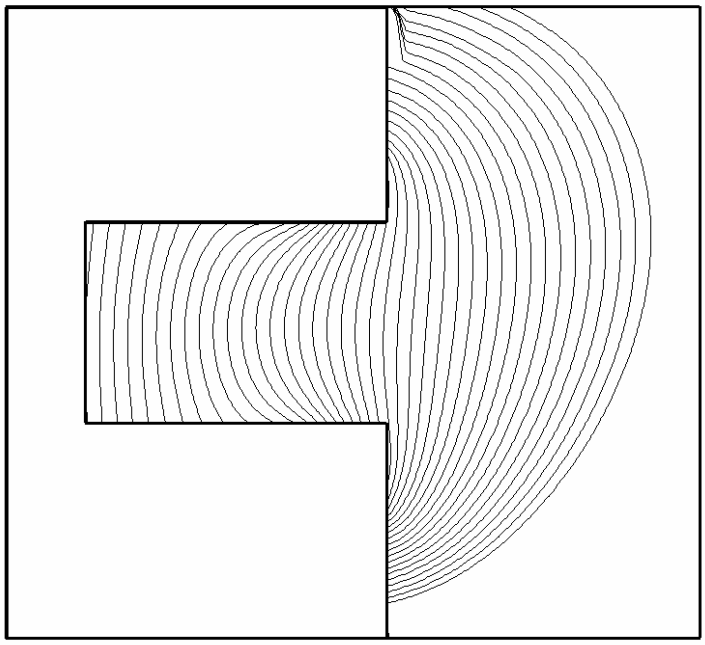

Figure 5-9 **Magnetic field topography of the NASA-173Mv1 when the internal trim coil is energized with a positive current. Positive current decreases the concavity of the plasma lens from the configuration shown in Figure 5-3.**

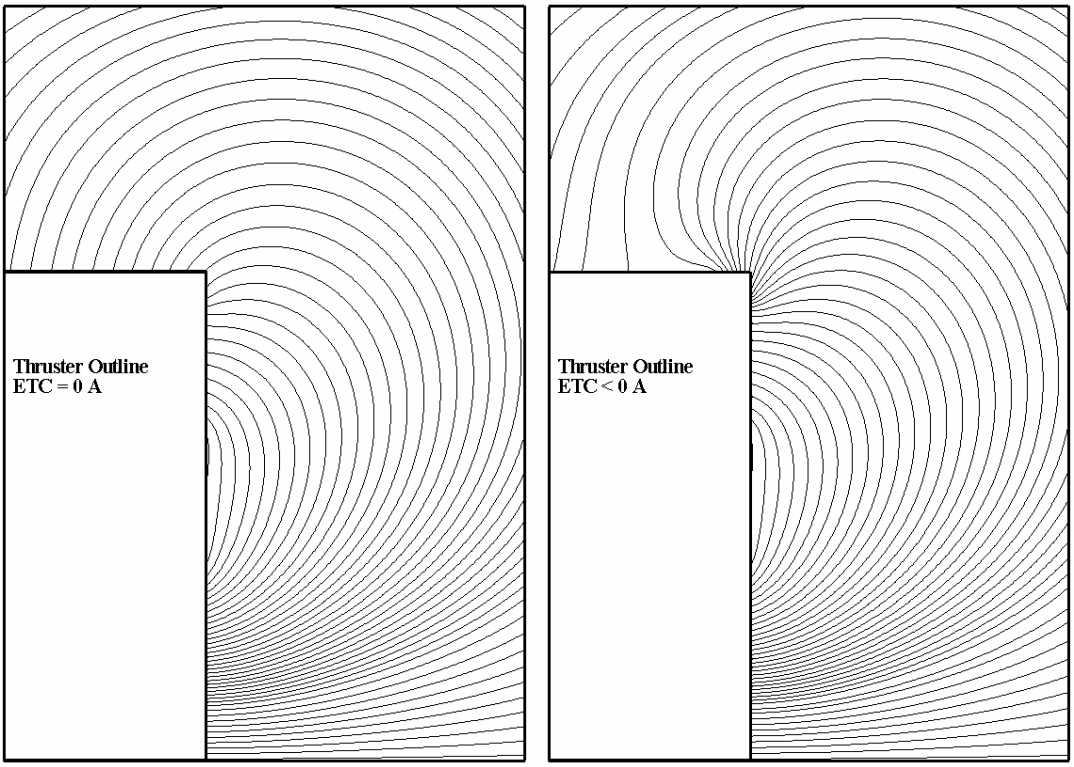

Figure 5-10 Effect of an external trim coil (ETC) on the magnetic field topography around a Hall thruster. Left – ETC current = 0 A. Right – ETC current < 0 A.

5.2 Review of Hall thruster magnetic field topography

The earliest Hall thrusters were designed so that the magnetic field was as radially uniform as possible across the channel, presumably in an attempt to minimize electron leakage to the anode [148]. This was a seemingly reasonable approach based on the fundamental operating principles of Hall thrusters (see section 3.1.2). However, it was quickly discovered that such designs were inherently unstable and inefficient (ironically, because of enhanced electron current). To achieve an efficient design, the shape of the magnetic field must also be considered.

In section 3.1.2, the existence of an optimum Hall parameter and magnetic field strength yielding maximum thruster efficiency was discussed. Magnetic field strength is important when considering basic scaling but fails to address the more

important effects of magnetic field shape on thruster efficiency. In this section, studies on Hall thruster magnetic field topography dating to the 1960's are reviewed. The seminal work of Morosov, *et al.* [11, 134, 145] first revealed how the magnetic field is instrumental in minimizing the electron current and focusing the ions. Research on magnetic field topography has been on-going ever since, mostly on 1600 s specific impulse Hall thrusters [2, 3, 121, 218, 220-222]. As shown in later chapters, these basic ideas are still valid at high-specific impulse when properly modified for the change in operating conditions.

5.2.1 Thermalized potential

The cross-field electron mobility is severely restricted in a Hall thruster by the application of a radial magnetic field (see section 3.1.3). However, due to field fringing across the discharge chamber, axial magnetic fields are present that give the magnetic field lines curvature. In this section, it is shown how the shape of the magnetic field lines can be exploited to control the electric field distribution.

In the direction normal to the field lines, the arguments from section 3.1.3 apply, that is, the electron cross-field mobility is reduced. However, parallel to the field lines the electrons are essentially unimpeded. Following Morosov, *et al.* [11, 145], the steady-state electron momentum equation along a magnetic field line neglecting the electron inertia and collisions is given by

$$-\frac{\partial \phi}{\partial \psi} = \frac{1}{e n_e}\frac{\partial p_e}{\partial \psi}. \qquad \textbf{(5-11)}$$

where ψ denotes the unit vector directed parallel to the line of force, ϕ is the plasma potential, and p_e is the electron pressure. If the electron temperature is constant along a magnetic field line designated by an index γ

$$T_e = T_e(\gamma), \tag{5-12}$$

then Eqn. 5-11 can be integrated to obtain an expression for the plasma potential along the field line

$$\phi = \phi(\gamma) + \frac{kT_e(\gamma)}{e}\ln\left(\frac{n_e}{n_o}\right), \tag{5-13}$$

where n_o is a reference density and $\phi(\gamma)$ is the so-called "thermalized potential." Since the thermalized potential is constant along a given field line, the plasma potential along a magnetic field line varies only by the logarithm of the density variation (the density varies roughly by a factor of five). Thus, to an accuracy on the order of the electron temperature (kT_e/e), magnetic field lines form equipotentials of the electric field. It turns out that the electron pressure cannot be neglected over large portions of the discharge chamber. Nonetheless, the idea that magnetic field lines influence the shape of the electric field has proven to be an invaluable tool in Hall thruster design for decades [3]. Numerical simulations have also made use of the thermalized potential [144, 147, 223].

5.2.2 Axial gradient of the radial magnetic field

In Ref. [134], Morosov *et al.* studied how the axial variation of the radial magnetic field affected thruster operation. Specifically, the axial gradient of the radial magnetic field $\nabla_z B_r$ was varied along the discharge chamber centerline (*i.e.*, along the average radius $r_{avg} = (r_{out}+r_{in})/2$, where r_{out} was defined as the radius of the outer wall and r_{in} was the radius of the inner wall. It is important that the field lines were also reported to be symmetric about r_{avg}. Three cases were considered:

1. $\nabla_z B_r > 0$ – (positive gradient) where the magnetic field increased from the anode and peaked near the exit (see Figure 5-7),
2. $\nabla_z B_r \approx 0$ – (uniform gradient) where the magnetic field was uniform from the anode to the exit, and
3. $\nabla_z B_r < 0$ – (negative gradient) where the magnetic field decreased from the anode towards the exit.

The study found that the electron current fraction (I_e/I_d) for the negative gradient was 0.85, for the uniform gradient, it was 0.5, and for the positive gradient, it was 0.35. The markedly higher electron transport for the negative gradient was attributed to an increase in plasma oscillations. The uniform gradient was apparently a marginally stable condition. The problem was also considered theoretically and it was shown how a plasma flow across a decreasing magnetic field is unstable. Largely because of this study, modern Hall thrusters satisfy the condition

$$\nabla_z B_r > 0 . \qquad \textbf{(5-14)}$$

5.2.3 Modern magnetic field topography

The work of Morosov, *et al.* established the importance of magnetic field topography in focusing ion trajectories and in minimizing electron current [11, 134, 145]. It was also recognized very early that a field line topography that is symmetric about the channel centerline was beneficial to thruster efficiency [2, 3]. When $\nabla_z B_r$ is positive and the field lines are symmetric about the channel centerline, the concavity of the field lines will tend to point downstream. Since field lines approximate equipotentials of the electric field, ion trajectories should focus on the channel centerline as a result. (Such a configuration is commonly referred to as a

plasma lens [2, 221].) However, the concavity and symmetry of the field lines alone are not sufficient to achieve adequate focusing. The value of $\nabla_z B_r$ is important in this respect. Studies have shown that the value of $\nabla_z B_r$ affects the focusing qualities of the magnetic field [2, 121, 224]. Specifically, it has been found that there is an optimum value of $\nabla_z B_r$ resulting in minimum plume divergence and maximum ion yield. The benefits of changing $\nabla_z B_r$ have been correlated to changes in the thickness and position of the ionization and acceleration zones, which have been found to be roughly separated at the point along the channel where $B_r = 0.8 \times B_{r,\max}$ [121]. Assuming that the field lines remain symmetric, then the focusing properties of the magnetic field can be characterized by the axial profile of the radial magnetic field along the channel centerline (see Figure 5-7), or more simply, by the average value of $\nabla_z B_r$.[26]

The "first generation" of magnetic layer thrusters from Fakel (the SPT series) had magnetic circuits that induced large radial ion velocities [222], which in turn resulted in high beam divergence, high erosion rates, and low efficiency. Apparently, this was because the magnetic circuits did not provide the required gradient in the magnetic field. It was not until as late as 1992 that the "second generation" SPT's were developed [16]. The major change with these thrusters appears to be the use of magnetic screens (see Figure 5-6) to increase $\nabla_z B_r$ and create a zone of zero magnetic field near the anode [121, 218]. Internal trim coils have also been used to control $\nabla_z B_r$ in the second generation thrusters [218]. These thrusters reportedly achieve a better correlation between magnetic field lines and equipotentials of the electric field [222]. The improved focusing decreases beam

[26] This is the reason that most of the Russian literature only show the centerline profile of the radial magnetic field.

divergence and erosion while improving thruster efficiency. The field line shape in one of these modern designs, the SPT-100ML, has only a moderate degree of curvature [215] (*i.e.*, the field lines are mostly radial, similar to Figure 5-12). Finally, it is worth noting that the lifetime of the modern day SPT-100 has demonstrated over 7000 hours of operation [24].

As discussed in Chapter 1, the majority of research in Russia has been concerned with the development of 1600 s specific impulse Hall thrusters resulting in magnetic circuit designs optimized for those operating conditions. The efficiency peak that was observed in the Fakel SPT-1 and other thrusters (see Chapter 3) strongly suggested that the magnetic field at high-specific impulse would need to be different from that at 1600 s in order to achieve efficient operation. Accordingly, the NASA-173M thrusters were developed to explore how magnetic field topography should be changed to improve efficiency at high-specific impulse. This was primarily done by increasing the concavity of the plasma lens from the nearly radial configuration that is used, for example, in the SPT-100ML [215] or the UM/AFRL P5 (see Figure 5-12).[27] There will be more to say about the plasma lens used in the NASA-173M thrusters in Chapter 7.

5.3 Preliminary plume focusing experiments

Prior to designing the NASA-173Mv1, a series of experiments that investigated possible improvements to the focal properties of the UM/AFRL P5 Hall thruster were conducted. These experiments provided the initial insight on how the design of a high-specific impulse Hall thruster should proceed. The major findings from these experiments are summarized below.

[27] It is unclear whether the SPT-100ML field line topography is indicative of all modern SPT's developed in Russia. For example, Ref. [121, 220] shows field lines with a high degree of curvature.

5.3.1 UM/AFRL P5 Hall thruster

The laboratory model P5 was developed by PEPL and AFRL to serve as a test-bed for new diagnostics and for investigating Hall thruster physics [135, 203, 225]. Depicted in Figure 5-11, the P5 has a discharge chamber outer diameter of 173 mm, a channel width of 25 mm, and a channel depth of 38 mm. While the nominal operating power of the P5 is 5 kW, the thruster has demonstrated sustained operation in excess of 9 kW. Most relevant to the present study is that the P5 magnetic field lines are directed primarily in the radial direction. The nominal field line configuration of the P5 is shown as Case 1 (Baseline) in Figure 5-12. A more detailed description of the thruster and its performance characteristics can be found in Ref. [135, 200, 203, 225].

Figure 5-11 Photograph of the UM/AFRL P5 Hall thruster.

Researchers at PEPL have subjected the P5 to a battery of diagnostics that have characterized the thruster performance and plasma properties. In particular, Ref. [207, 226] have concluded via laser induced fluorescence and ion energy diagnostics that the plume focal point was within a few tens of centimeters of the thruster exit plane. Ion current density measurements at 50 and 100 cm from the thruster exit plane have confirmed these conclusions by showing angular distributions with only a single maximum on thruster centerline. The 100 cm data

are shown in Figure 5-13 as Case 1. The 50 cm data are not shown here but can be found in Ref. [135].

Commercially developed thrusters such as the SPT-140 or BPT-4000 exhibit a double peak structure in the ion current density profiles at distances of 100 cm [55, 227]. (An example of a double peak profile is shown in Figure 7-37.) A double peak structure is usually attributed to the plasma jets emanating from either side of the annular discharge chamber. The double peak implies that the plume focal length of these thrusters is greater than 100 cm. It was decided to investigate whether the focal properties of the P5 could be improved by altering the magnetic field topography.

5.3.2 Experiments to extend the P5 plume focal length

A numerical and experimental investigation of the effect of magnetic field inclination on the P5 plume characteristics was conducted. The study employed a commercial 3D magnetostatic computer solver, Magnet 6 by Infolytica, and experimental measurements of the ion current density. Different magnetic circuits were investigated numerically and subsequently tested by modifying the P5 magnetic circuit and then operating the thruster in the LVTF at the University of Michigan (see section 6.2.1). The numerical solutions from Magnet and measurements using a Gaussmeter agreed to within ±10%. The ion current density measurements used a nude Faraday probe identical to the one used in Ref. [228] and similar to the probes described in section 6.3.2. The goal of these experiments was to determine whether the focal length and plume divergence of the P5 could be improved by altering the inclination of the magnetic field lines. A secondary goal

was to examine what effect the axial magnetic field gradient had on plume divergence.

The tested field line topographies are shown in Figure 5-12 as Case 1 through Case 4. Case 1 is the nominal, or baseline configuration of the P5. Note that the field line topography of Case 1 was mostly in the radial direction and is symmetric about the channel centerline over most of the discharge chamber. Case 2 considered field lines that were inclined towards thruster centerline in a convergent pattern. Case 3 considered a divergent field line pattern from thruster centerline. Note that Case 2 and 3 were not symmetric about the channel centerline. In Case 4, the field lines were mostly radial and symmetric like Case 1. However, for Case 4 the magnetic screens (see Figure 5-6) were removed from the P5. Removing the magnetic screens substantially decreased the axial gradient of the radial magnetic field. This is because the screens act to create a zone of low magnetic field near the anode. When the screens were removed, the magnetic field at the anode increased and the axial gradient of the magnetic field decreased.

To quantify the differences between the cases, the dimensionless magnetic field gradient defined by Eqn. 7-4 was calculated. Table 5-1 shows the dimensionless magnetic field gradient for Cases 1-4. Cases 1-3 were approximately the same, but Case 4 was 44% less than the baseline of Case 1. The similarity of the magnetic field gradients between Cases 1-3 meant that differences in the plume characteristics could be attributed to changes made to the field line inclination. Case 4 was tested to examine how the magnetic field gradient influenced the plume characteristics while maintaining a similar field line topography to Case 1.

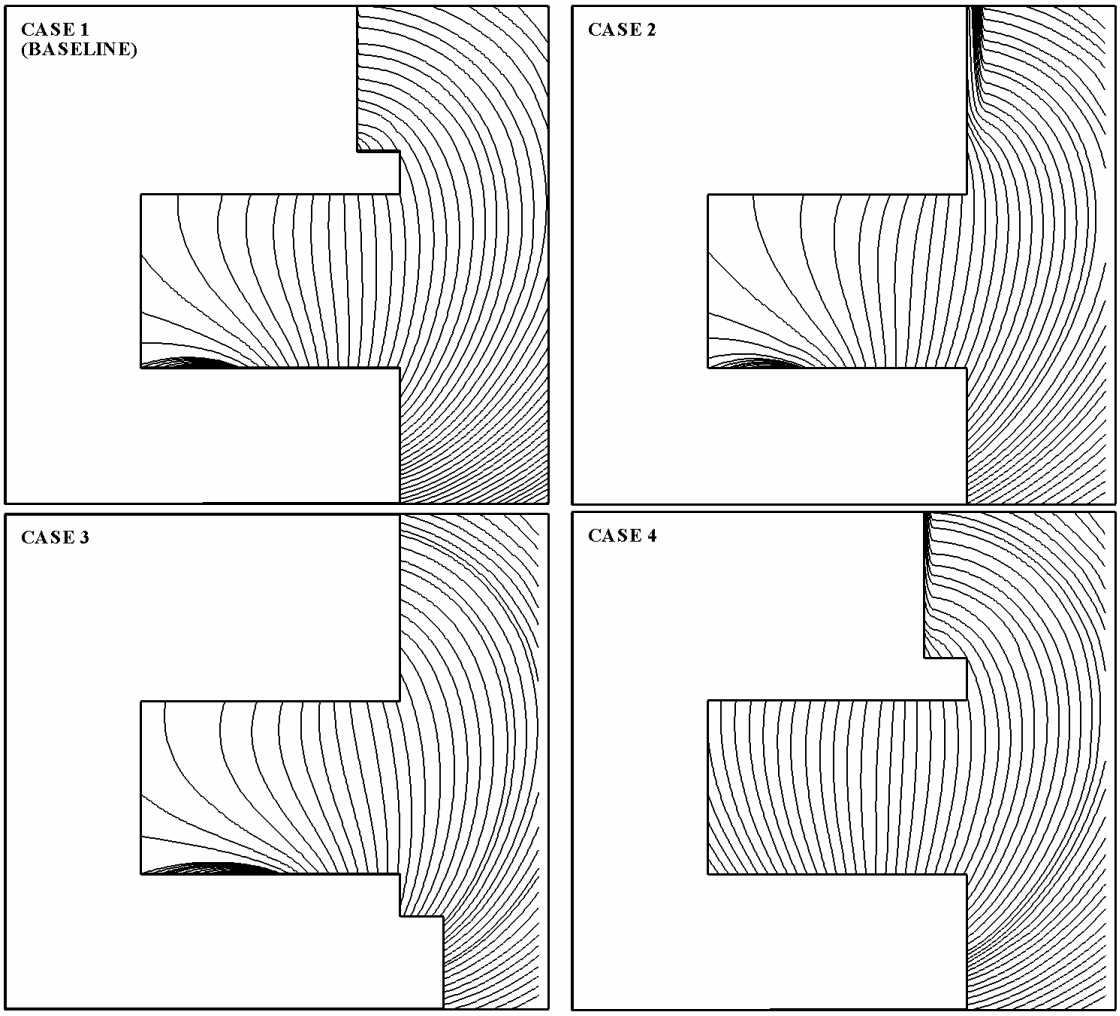

Figure 5-12 **Magnetic field topography for different magnetic circuit configurations of the P5. Case 1 – baseline configuration with field lines aligned radially, perpendicular to the thrust axis. Case 2 – convergent field lines. Case 3 – divergent field lines. Case 4 – field lines without magnetic screens.**

Table 5-1 **Dimensionless magnetic field gradient defined by Eqn. 7-4 of the P5 for each magnetic field topography shown in Figure 5-12.**

Case 1	Case 2	Case 3	Case 4
0.79	0.83	0.88	0.44

For each case, the P5 was operated at a constant 300 V discharge voltage and discharge currents of 5, 10, and 15 A. Profiles of the ion current density were measured for each case and operating condition. Figures 5-13 through 5-15 compare the ion current density profiles of Case 2, 3, and 4 to Case 1, respectively. There were substantial differences between Cases 2-4 with the baseline in Case 1, mostly due to higher current density at large angles from centerline. Case 4 also showed a much lower current density on centerline than Case 1. None of the cases resulted in a double peak profile in the current density profiles. This indicated that Case 2 and 3 were unsuccessful in extending the plume focal length beyond 100 cm.

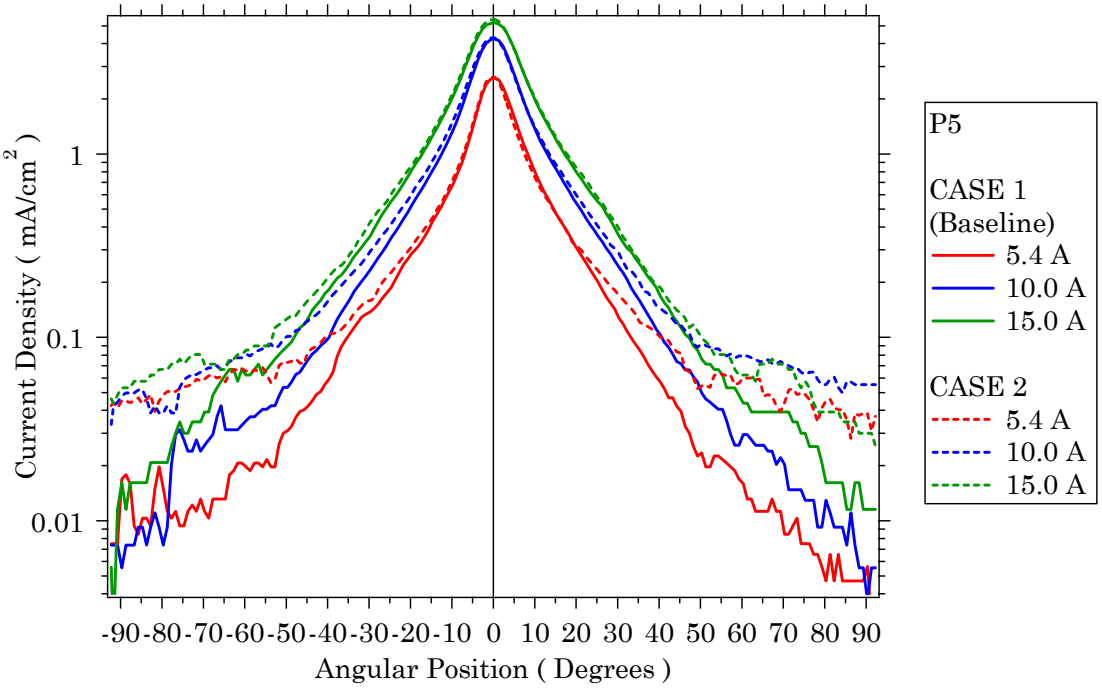

Figure 5-13 Ion current density versus angular position from thruster centerline for case 1 and case 2 of the P5 shown in Figure 5-12. (300 V discharge voltage)

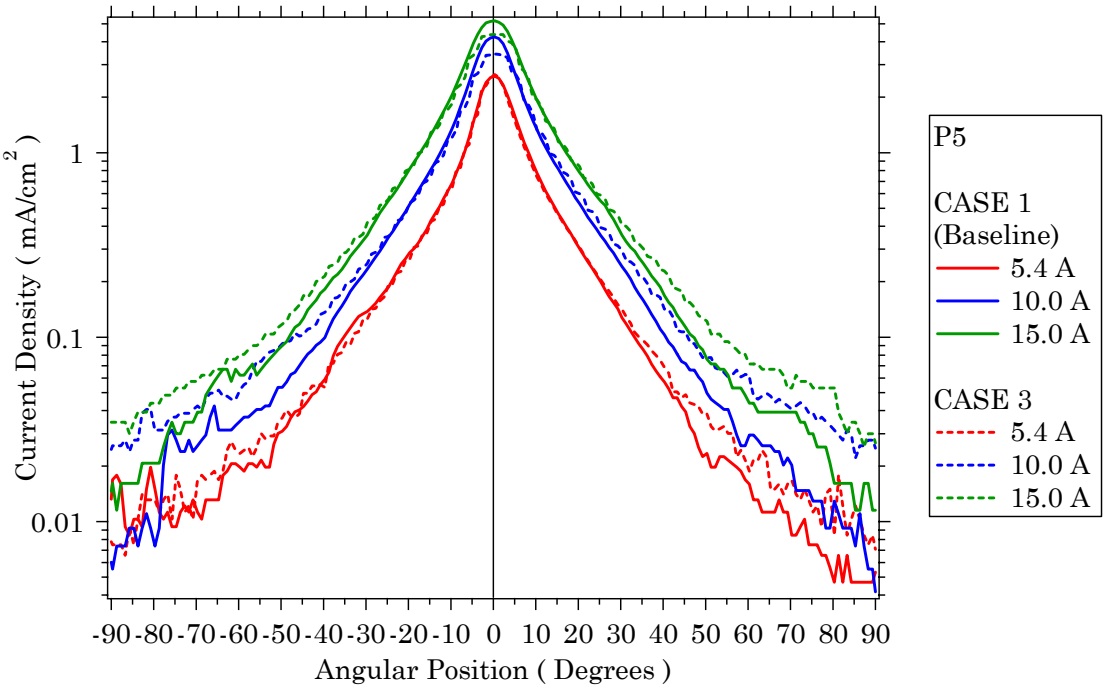

Figure 5-14 Ion current density versus angular position from thruster centerline for case 1 and case 4 of the P5 shown in Figure 5-12. (300 V discharge voltage)

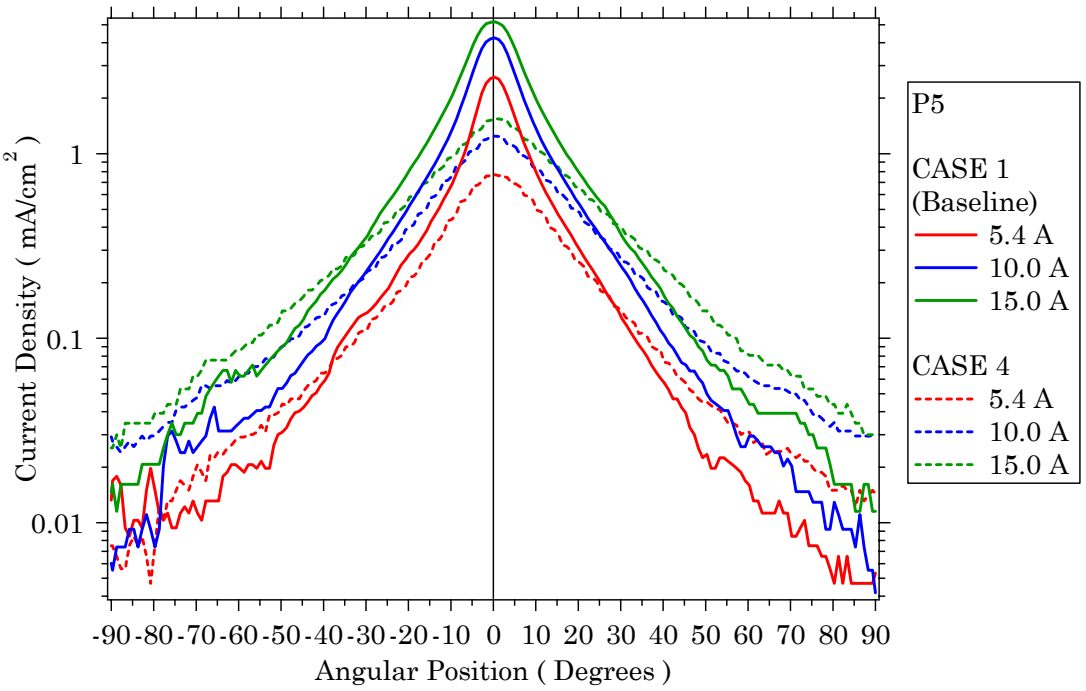

Figure 5-15 Ion current density versus angular position from thruster centerline for case 1 and case 4 of the P5 shown in Figure 5-12. (300 V discharge voltage)

To quantify the differences between each case, the 95% plume divergence half-angles (see section 6.3.2) were calculated from the ion current density profiles. The results of the calculations, shown in Figure 5-16, indicated that the baseline configuration (Case 1) resulted in the lowest plume divergence while Case 4 exhibited the highest plume divergence.

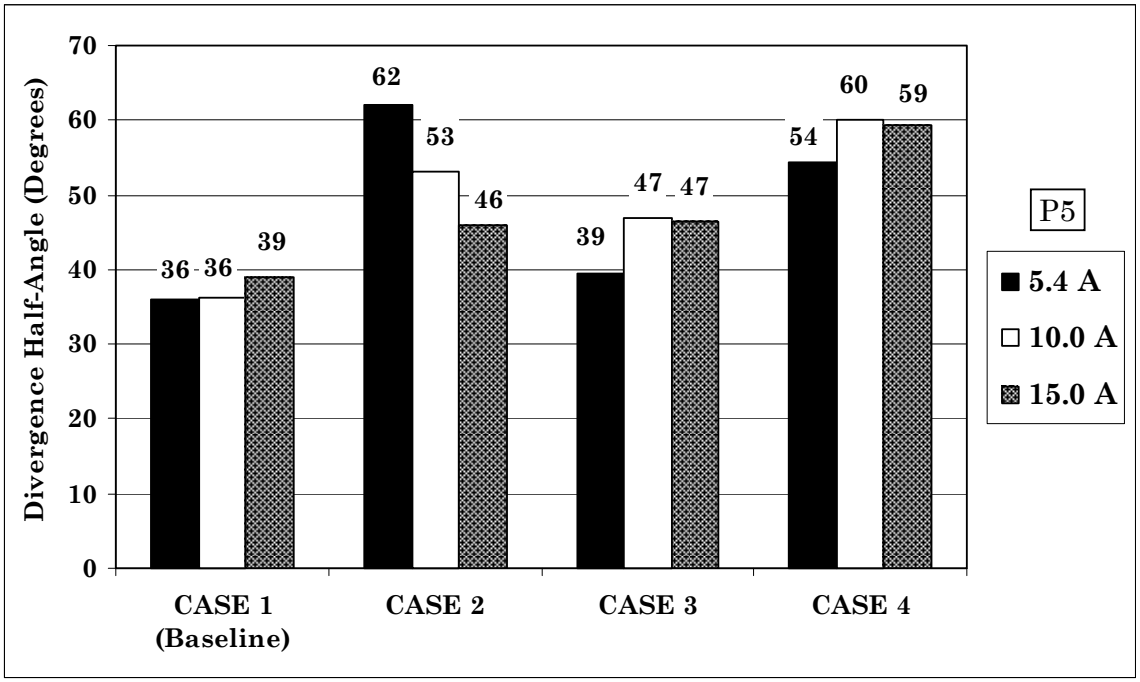

Figure 5-16 95% plume divergence half-angle of the P5 for the magnetic field configurations shown in Figure 5-12. (300 V discharge voltage)

From these results, two major conclusions were formulated:

1. The symmetry of magnetic field lines and the magnetic field gradient both have important roles in the focusing properties of a Hall thruster.
2. Although the symmetric, radially aligned field line topography resulted in the lowest plume divergence, the focal properties were still inferior to other thrusters. This strongly suggested that the concavity of the magnetic field lines needed to be increased in order to extend the plume focal distance.

These early experiments provided the insight necessary to begin the development of a high-specific impulse Hall thruster. It was decided that the new thruster would employ a plasma lens with curved magnetic field lines and flexibility in the magnetic circuit to alter the field line curvature during thruster operation.

5.4 Conclusions

The available literature concerning magnetic field topography in 1600 s specific impulse Hall thrusters have provided the basis for the design of a high-specific impulse Hall thruster. Successful designs have shown how the symmetry of the magnetic field lines about the channel centerline, the curvature of the magnetic field lines, and the axial magnetic field gradient all influence thruster operation. A series of experiments on the UM/AFRL P5 Hall thruster have confirmed the importance of field line symmetry and magnetic field gradient. The P5 experiments strongly suggested that the curvature of the field lines would be a critical aspect to improving the overall focal properties of the plume. It was concluded that the NASA-173Mv1 Hall thruster would allow for a plasma lens with curved magnetic field lines and flexibility in the magnetic circuit so that the field line curvature could be altered during high-specific impulse operation.

Part II

Development of High-Efficiency, High-Specific Impulse Xenon Hall Thrusters

Chapter 6

Experimental apparatus I

This chapter begins part II, which concerns the development phase of the NASA-173M Hall thrusters. The first thruster, designated the NASA-173M version 1 (v1), validated the magnetic field design [169]. The follow-on thruster, the NASA-173M version 2 (v2), was shown to achieve high-efficiency and high-specific impulse operation [130]. Chapter 7 discusses the development of the NASA-173Mv1 while Chapter 8 discusses the development of the NASA-173Mv2. In Chapter 9, the performance characteristics of the thrusters are compared.

The purpose of this chapter is to describe the experimental apparatus that were used during the development phase of the NASA-173M Hall thrusters. Several experiments were conducted in vacuum facilities at the University of Michigan and NASA GRC. This chapter describes those facilities and the diagnostics that were used. Experiment specific details, such as the thruster operating conditions, are presented in subsequent chapters.

6.1 Overview of facilities and diagnostics

The experiments described in Chapters 7-9 were conducted in two vacuum facilities using different diagnostics. Table 6-1 summarizes the diagnostics that were used for those experiments. The rest of this chapter discusses the facilities and diagnostics in detail.

Table 6-1 Diagnostics used to evaluate the NASA-173M Hall thrusters discussed in Chapters 7-9. For each thruster, the section where major results from each diagnostic are discussed is indicated.

	Location	Facility	NASA-173Mv1	NASA-173Mv2
Thrust stand (UM)	UM	LVTF	§7.5	-
Thrust stand (GRC)	GRC	VF12	§7.6.1-7.6.3	§8.4.1
Faraday Probe	GRC	VF12	§7.6.4	§8.4.2
Discharge current probe	GRC	VF12	§7.6.5	§8.4.3
Gaussmeter	GRC	VF12	§7.5.1, 7.6.6	§8.4.4

6.2 Vacuum facilities

This section describes the vacuum facilities and the support equipment that were used with the NASA-173M thrusters at the University of Michigan and NASA GRC.

6.2.1 Large Vacuum Test Facility at the University of Michigan

Experiments with the NASA-173Mv1 were conducted at the University of Michigan's Plasmadynamics and Electric Propulsion Laboratory (PEPL) in the Large Vacuum Test Facility (LVTF). A schematic of the LVTF is shown in Figure 6-1. The LVTF is a cylindrical, stainless steel vacuum chamber that is six meters in diameter and nine meters in length. A pair of 900 l/s blowers and four, 200 l/s mechanical pumps are used to evacuate the LVTF to moderate vacuum (30-100 mTorr). To reach high vacuum the LVTF is equipped with seven re-entrant cryopumps, each of which is surrounded by a liquid nitrogen baffle. The blowers and mechanical pumps are turned off once the cryopumps are activated. The cryopump system can be operated with any number of pumps in use.

During the experiments, chamber pressure was monitored using two hot-cathode ionization gauges as indicated in Figure 6-1. Pressure measurements from both gauges were corrected for xenon using the base pressure on air and a xenon correction factor of 2.87 according to [229]

$$p_c = \frac{p_i - p_b}{2.87} + p_b, \tag{6-1}$$

where p_c was the corrected pressure on xenon, p_b was the base pressure, and p_i was the indicated pressure when xenon was flowing into the vacuum chamber. The operating pressure in the LVTF was then calculated as the average from the corrected readings from the two gauges. With seven cryopumps operating, the base pressure was typically 2×10^{-7} Torr. After correcting the gauges with Eqn. 6-1 and then averaging, the background pressure in the LVTF with seven cryopumps operating was typically 4.6×10^{-6} Torr for a xenon flow rate of 5.5 mg/s.

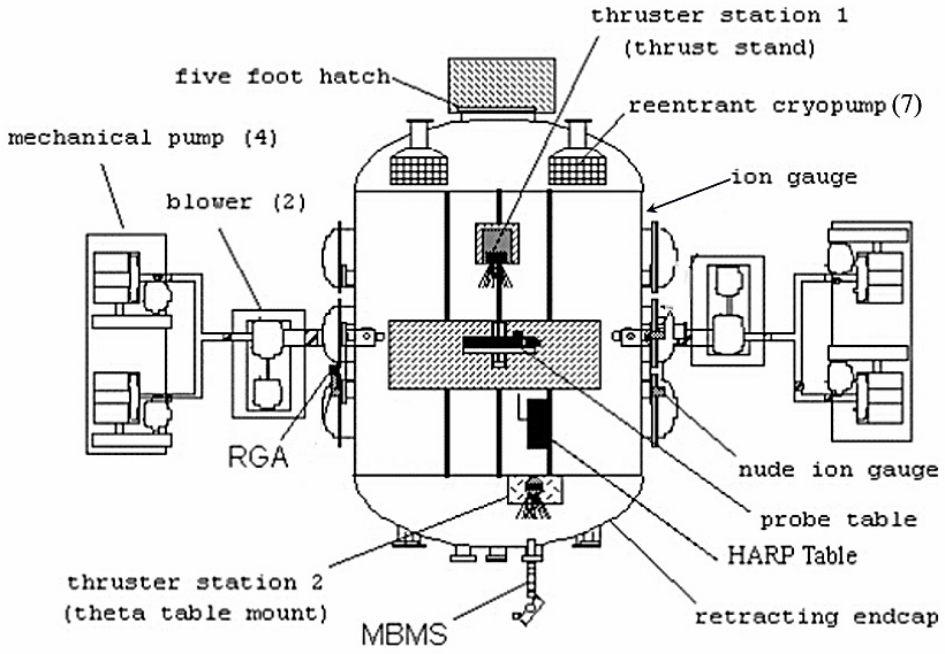

Figure 6-1 Schematic of the Large Vacuum Test Facility at the University of Michigan (not to scale).

Performance measurements in the LVTF have been characterized previously with the UM/AFRL P5 Hall thruster [200]. In that study, it was found that neutral ingestion from the ambient tank environment negligibly influenced thruster performance below the maximum tested pressure of 1.3×10^{-5} Torr.[28] Since all of the experiments reported here are below the maximum pressure from Ref. [200], no corrections were made to the measured thruster performance reported in section 7.4.

During the experiments described in section 7.4, the NASA-173Mv1 was mounted at thruster station 1 (see Figure 6-1) on the thrust stand described in section 6.3.1.1. The thruster was positioned near the centerline of the LVTF and was fired away from the cryopumps. At this position, the cryopumps were approximately two meters from the thruster and the thruster plume was allowed to expand approximately seven meters down the length of the chamber.

6.2.1.1 Power electronics and propellant delivery

Figure 6-2 is an electrical schematic of the power electronics used to run the NASA-173M Hall thrusters at the University of Michigan. The plasma discharge was powered by a matching pair of commercially available power supplies wired in series that provided a maximum output of 1200 V, 16 A. The discharge filter consisted of a 95 μF capacitor in parallel with the power supply outputs and a 1.3 Ω ballast resistor in series with the positive terminal of the power supply output. Other commercially available power supplies were used to power the magnet coils and the cathode heater and keeper.

[28] There are currently no rigorous standards for the maximum permissible tank pressure at which Hall thruster performance can be reliably measured without correcting for facility effects. As a general guideline, performance testing below a pressure of 2×10^{-5} Torr (corrected for xenon) is adequate to obtain reliable thrust measurements without correcting for neutral ingestion [200, 230].

Xenon (99.999% pure) was supplied through stainless steel feed lines with 20 and 200 SCCM mass flow controllers. The controllers were calibrated before each experiment using the ideal gas law, the time rate of change of the pressure and temperature in a known volume, and the compressibility of xenon. Based on the calibrations, the uncertainty was estimated as ±1.5% for the anode flow rate and ±2.5% for the cathode flow rate.

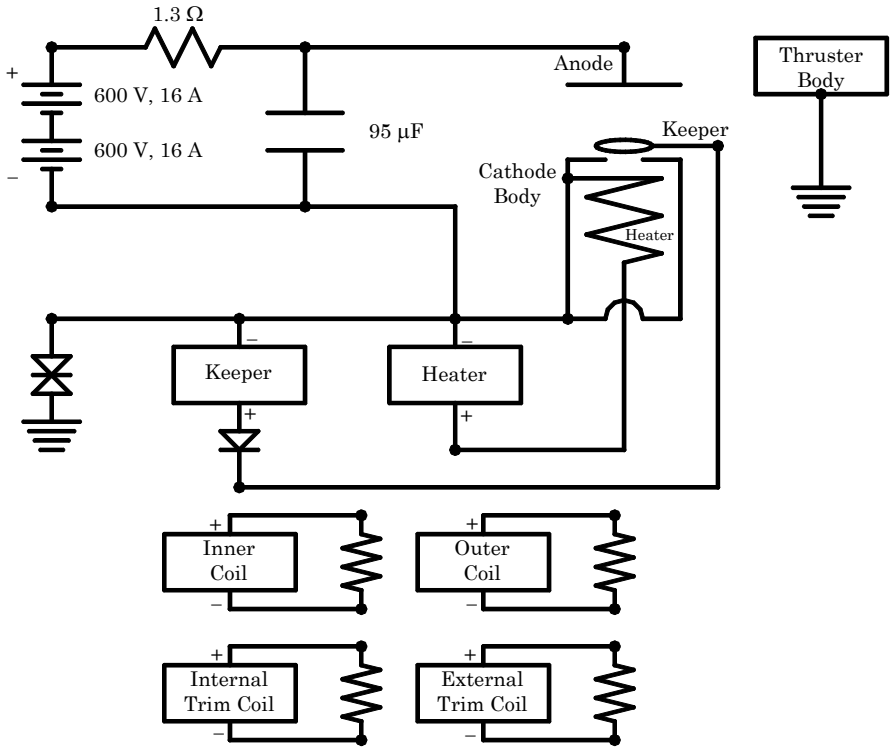

Figure 6-2 Electrical schematic of the power electronics used to run the NASA-173M Hall thrusters at the University of Michigan.

6.2.1.2 Thruster telemetry

Thruster telemetry were acquired using a 22-bit datalogger. Voltages were measured directly at the power supply outputs except for the discharge voltage, which was measured after the ballast resistor shown in Figure 6-2 using a calibrated voltage divider. Currents were measured with high-accuracy shunts with the exception of the discharge current, which was measured with a Hall current sensor.

The entire system was calibrated before each experiment. The uncertainty of the datalogger, as reported by the manufacturer, was ±0.004% of the indicated value. However, calibration of each channel using digital multimeters increased the uncertainty to ±0.05% for voltage and ±0.2% for each current except for the discharge current. The discharge current uncertainty was ±1% due to drift of the Hall sensor's zero offset over time.

6.2.2 Vacuum Facility 12 at NASA GRC

Experiments with both NASA-173M thrusters were conducted in Vacuum Facility 12 (VF12) at NASA GRC. A schematic of VF12 is shown in Figure 6-3. Photographs of the interior of VF12 are shown in Figure 6-4 and Figure 6-5. VF12 is a cylindrical, stainless steel vacuum chamber that is three meters in diameter and 9.6 meters in length. The facility is cryogenically pumped and backed by a 1,000 l/s turbomolecular pump for removal of non-condensable gases.

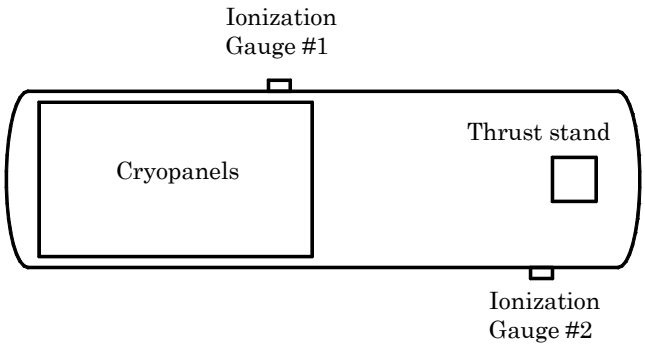

Figure 6-3 Schematic of Vacuum Facility 12 at NASA GRC (not to scale).

The NASA-173M was always mounted on the thrust stand indicated in Figure 6-3. In this position, the thruster was near the chamber's vertical centerline and fired 8.9 m down the length of the tank toward the cryopanels, which are located along the back half of the chamber. A pair of hot-cathode ionization gauges mounted

to the chamber wall measured pressure. Ionization gauge #1 was mounted approximately 0.4 m below the vertical chamber centerline, 5.2 m downstream of the thruster. The convention at GRC is to report the pressure from ionization gauge #1 as the chamber pressure. Ionization gauge #2 was mounted approximately 0.3 m above vertical chamber centerline, 0.8 m downstream of the thruster.

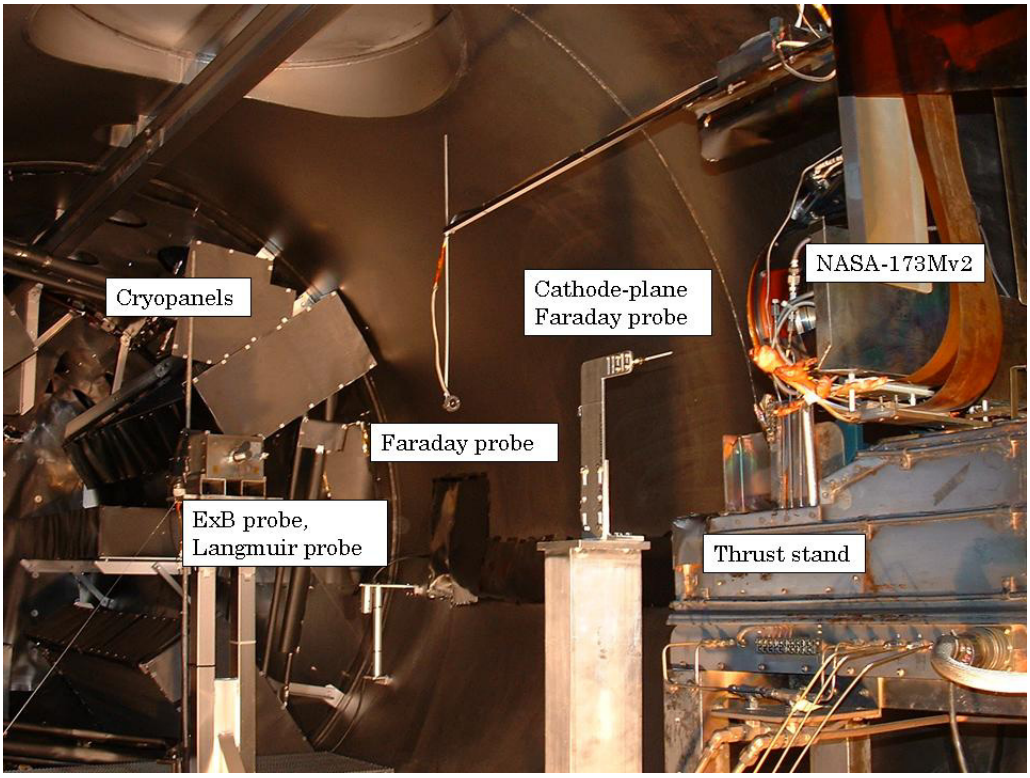

Figure 6-4 Photograph inside Vacuum Facility 12 at NASA GRC showing the NASA-173Mv2 mounted on the thrust stand, several plume diagnostics, and a portion of the cryopanels.

Figure 6-6 shows the background pressure in VF12 indicated from the ionization gauges as a function of xenon mass flow rate. The base pressure in VF12 was typically between 1-2x10^{-7} Torr. Pressure measurements were corrected for xenon using Eqn. 6-1. The majority of the experiments were conducted at a xenon flow rate of 11 mg/s. At this flow rate, the corrected pressures from ionization gauge #1 and #2 were 4.6x10^{-6} Torr and 1.1x10^{-5} Torr, respectively. The equivalent xenon

pumping speeds based on these pressures were 310,000 l/s and 130,000 l/s for ionization gauge #1 and #2, respectively.[29]

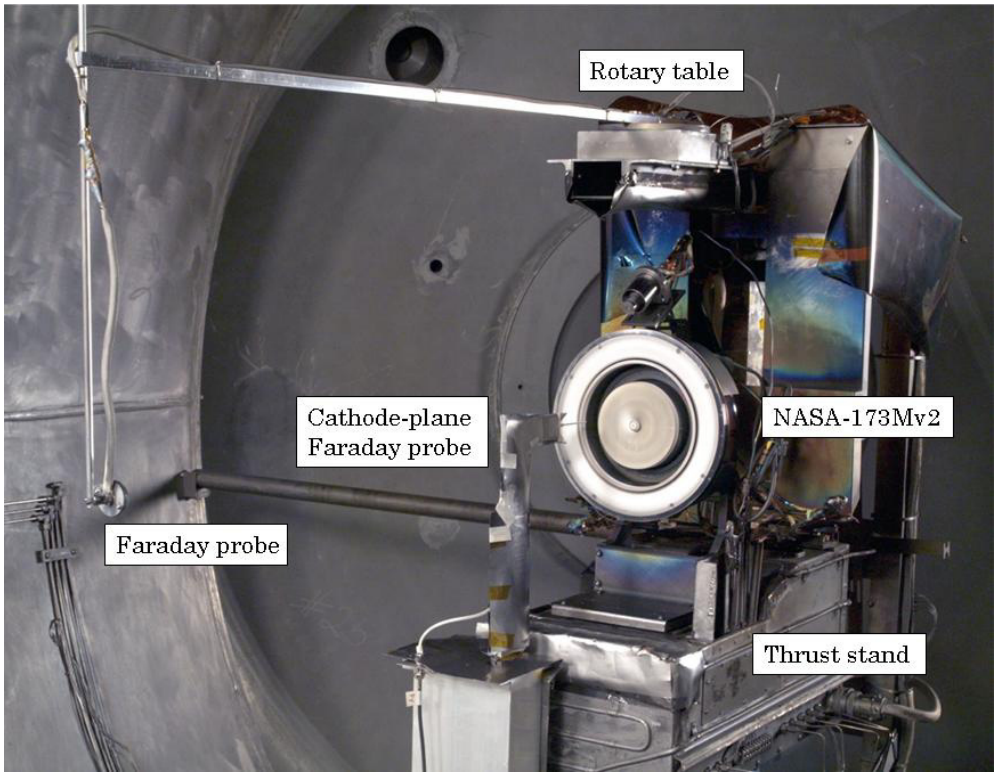

Figure 6-5 Photograph inside Vacuum Facility 12 at NASA GRC showing the NASA-173Mv2 mounted on the thrust stand and a pair of Faraday probes used to measure ion current density.

VF12 has been used in the past for several Hall thruster studies, most notably for erosion characterizations of the T-220 and D-80 [173, 174]. When considering possible facility effects on performance measurements, the T-220 is a convenient reference because thrust measurements have been taken with the T-220 in VF12 [173] and in the main volume of Vacuum Facility 5 (VF5) at NASA GRC [172]. VF5 has a xenon pumping speed in excess of 1,000,000 l/s and is 4.6 m in

[29] Ionization gauge #2 always indicated a higher background pressure than ionization gauge #1. Whether or not ionization gauge #2 is a more accurate measurement of the "background" pressure is debatable. On the one hand, ionization gauge #2 and the thruster were far from the cryopanels so a pressure reading higher than ionization gauge #1 would be expected. On the other hand, ionization gauge #2 was 0.8 m downstream of the thruster so the pressure reading may have been artificially high due to neutrals coming from the thruster. Regardless, as read by either ionization gauge, the background pressure in VF12 never exceeded the general guideline of 2×10^{-5} Torr discussed in footnote 28.

diameter and 19 m in length [231]. The facility has been used to evaluate the performance of the NASA-457M at xenon flow rates in excess of 100 mg/s [47]. Table 6-2 compares the performance of the T-220 in VF5 and VF12 when operating at xenon flow rates of 21.8-21.9 mg/s. Within the margin of error typical of performance measurements, the T-220 performance was equivalent in either facility. This result was consistent with a study of facility effects in the LVTF conducted with the UM/AFRL P5 Hall thruster [200]. That study concluded that neutral ingestion from the ambient tank environment has a negligible influence on performance measurements at similar tank pressures.

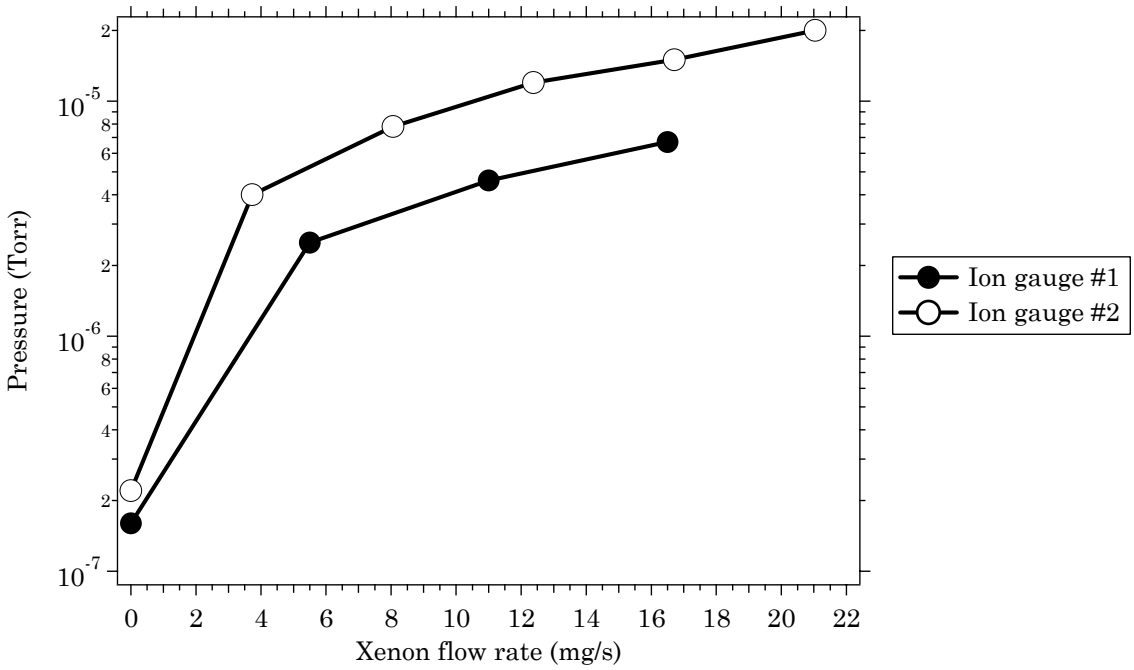

Figure 6-6 Background pressure, corrected for xenon, versus xenon mass flow rate of Vacuum Facility 12 at NASA GRC. The ionization gauge locations are shown in Figure 6-3.

The maximum xenon flow rate that was investigated in VF12 with the NASA-173M Hall thrusters was 16.5 mg/s (25% less than the T-220). At this flow rate, ionization gauge #1 and #2 read 6.7×10^{-6} Torr and 1.5×10^{-5} Torr, respectively. After considering the P5 and T-220 experiments [172, 173, 200], facility effects on

the performance measurements of the NASA-173M Hall thrusters in VF12 were judged to be negligible and no corrections were made to the measured thruster performance reported in sections 7.6.1-7.6.3 and 8.4.1.

Table 6-2 Comparison of the measured performance of the 10 kW T-220 from Vacuum Facility 5 (VF5) and Vacuum Facility 12 (VF12) at NASA GRC [172, 173].

T-220 Performance	VF5	VF12
Vd (V)	495	500
Id (A)	20.2	20
Anode flow (mg/s)	20.3	19.9
Cathode flow (mg/s)	1.5	2
Total Power (W)	10212	10384
Thrust (mN)	511	508
Total Specific Impulse (s)	2390	2370
Total Efficiency	0.59	0.57
Pressure (Torr-Xe)*	$2x10^{-6}$	$1x10^{-5}$
* Corrected for xenon from reported pressures		

6.2.2.1 Power electronics and propellant delivery

Figure 6-7 is an electrical schematic of the power electronics that were used to operate the NASA-173M Hall thrusters in VF12. The plasma discharge was powered by a matching pair of commercially available power supplies wired in series that provided a maximum output of 1200 V, 16 A. The discharge filter consisted of a 100 μF capacitor in parallel with the power supply outputs. Other commercially available power supplies were used to power the magnet coils and the cathode heater and keeper.

Xenon (99.999% pure) was supplied through stainless steel feed lines with 20 and 200 SCCM mass flow controllers. The controllers were calibrated before each experiment using the ideal gas law, the time rate of change of the pressure and temperature in a known volume, and the compressibility of xenon. Based on the

calibrations from several experiments, the uncertainty was on average ±0.8% for the anode flow rate and ±1.2% for the cathode flow rate.

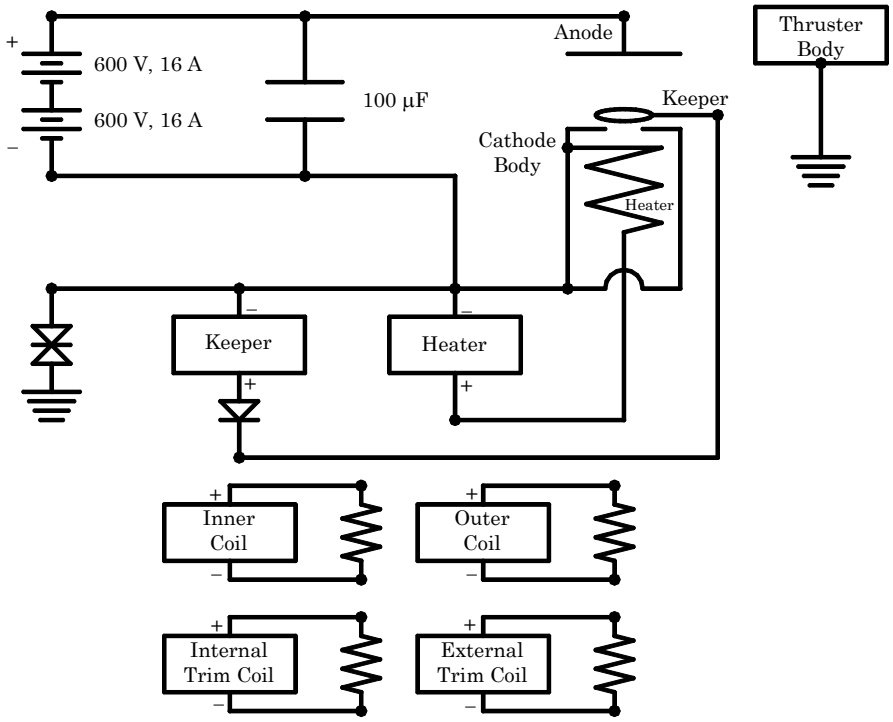

Figure 6-7 Electrical schematic of the power electronics used to run the NASA-173M Hall thrusters at NASA GRC.

6.2.2.2 Thruster telemetry

Thruster telemetry were acquired using a 22-bit datalogger. Voltages were measured at the power feedthrus on the vacuum chamber wall. All voltages were measured directly except for the discharge voltage and cathode keeper voltage, which were monitored using voltage dividers. Currents were measured with high-accuracy shunts. The entire system was calibrated before each experiment. The uncertainty of the datalogger, as reported by the manufacturer, was ±0.004% of the indicated value. However, calibration of each channel using digital multimeters increased the uncertainty to ±0.05% for voltage and ±0.2% for current.

6.3 Diagnostics

This section describes the diagnostics used to evaluate the NASA-173M Hall thrusters at the University of Michigan and NASA GRC during the development phase.

6.3.1 Thrust stands

6.3.1.1 Thrust stand at the University of Michigan

Thrust measurements of the NASA-173Mv1 were taken at the University of Michigan with a displacement-mode, inverted-pendulum type thrust stand, based on the NASA GRC design [232, 233]. Deflection of the pendulum was monitored by recording the output voltage from a linear voltage displacement transducer (LVDT) by the datalogger described in section 6.2.1.2. Inclination of the thruster was similarly recorded from the output voltage of an inclinometer. Corrections were later made to the data from a correlation between inclination and the LVDT. Calibrations were performed before and after thruster operation by deploying a series of known weights. To minimize thermal drift, a water-cooled shroud maintained at 10° C encompassed the thrust stand components. Upon initial exposure to vacuum, the thruster was operated for at least two hours to allow for outgassing of thruster components. Thrust measurements were typically conducted at constant voltage and flow rate, in intervals of about 30 minutes, following the outgassing procedure. A calibration was always performed before and after thruster operation. To account for thermal drift, the dependence of the calibrations was linearly interpolated over time as recorded by the datalogger. Using these methods, the uncertainty in the thrust measurements was estimated to be ±1.5% of the measured value.

From the measured thrust and other telemetry (voltage, current, flow rate, etc.) the anode performance parameters were calculated according to the definitions in section 4.2. The thrust-to-power ratio was computed based on the discharge power. Anode specific impulse was based on the anode mass flow rate. Anode efficiency was based on the anode mass flow rate and discharge power.

6.3.1.2 Thrust stand at NASA GRC

Thrust measurements of the NASA-173M Hall thrusters were taken at NASA GRC using a null-mode, inverted-pendulum thrust stand designed at GRC and used previously in VF12 with the 10 kW T-220 [173]. The basic principles of the thrust stand design are described in Ref. [232, 233]. Inclination was controlled by leveling the thrust stand via a stepper motor mechanism to maintain a constant inclinometer output. To minimize thermal drift, a water-cooled shroud that encompassed the thrust stand components was maintained at 10° C. Upon initial exposure to vacuum, the thruster was operated for at least two hours to allow for outgassing of thruster components. Thrust measurements were typically conducted at constant voltage and flow rate, in intervals of about 30 minutes, following the outgassing procedure. Thermal drift during a testing interval was equivalent to no more than 0.5 mN and was quantified between thruster shutdowns by recording the zero offset of the thrust stand output. Calibrations using a series of known weights were performed every two to four hours before and after several of these firings. Since the slope of the calibration curve was highly repeatable throughout testing, the zero offset recorded after each shutdown was used to obtain the calibration curve valid at the time of shutdown. Linear interpolation over time during each thruster firing yielded the zero offset and, thus, the true calibration curve for each data point as a

function of time. Using these methods, the uncertainty in the thrust measurements was estimated to be ±0.5 mN.

During testing, if the thruster had been off for more than a few minutes, an initial firing of at least 30 minutes was done before data were collected. This ensured that the thruster and thrust stand had equilibrated sufficiently to minimize thermal drift. Repeatability was quantified by returning to certain operating points over a given testing period and was influenced more by the thruster (*e.g.*, by returning to the same discharge current) than the thrust stand. Using these methods, variations in thrust for a given operating point were ±1% of the measured value, on average.

From the measured thrust and other telemetry (voltage, current, flow rate, etc.) the thruster performance parameters were calculated according to the definitions in section 4.2. Thrust-to-power ratios were computed based on either the discharge power or the total power. The total power included the power dissipated in the coils. Both "anode" and "total" quantities were computed for specific impulse and efficiency. Anode quantities included only the anode flow and discharge power. Total quantities added the cathode flow and the power required by the coils.

6.3.2 Faraday probe

After determining the coil currents that maximized thruster efficiency, ion current density measurements of the NASA-173M Hall thruster exhaust plumes were taken using a Faraday probe. Similar Faraday probes had been used previously at NASA GRC and characterized in other investigations [32, 173, 234]. Figure 6-8 shows a schematic and photograph of the Faraday probe. Table 6-3 summarizes the dimensions of the Faraday probe. The probe consisted of a 1.94 cm

diameter collection electrode enclosed within a guard ring that were both made from molybdenum and mounted to an alumina disk.

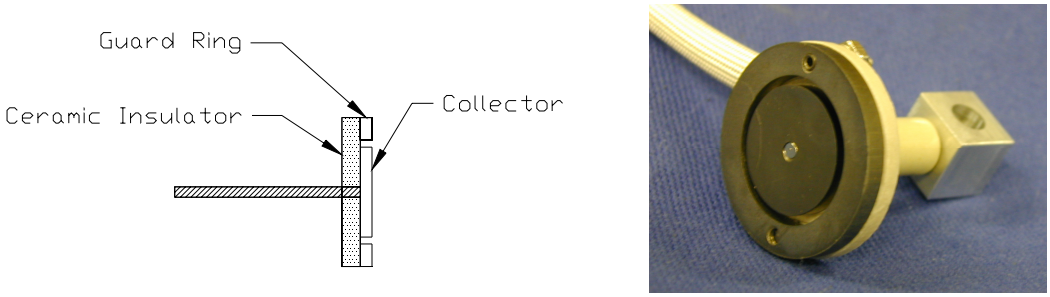

Figure 6-8 Schematic and photograph of the Faraday probe.

Table 6-3 Dimensions of the Faraday probe.

	Dimension (cm)
Collector	
Outer Diameter	1.94
Depth	0.32
Guard ring	
Inner Diameter	2.22
Outer Diameter	3.20
Depth	0.32
Alumina Insulator	
Outer Diameter	3.20
Depth	0.32

Figure 6-9 shows the Faraday probe electrical schematic. The collector and guard ring were biased –15 V below facility ground to repel electrons. Biasing the guard ring and collector to the same potential minimized edge effects around the collector by creating a flat, uniform sheath over the collection area. The collection area was taken as the geometric area of the collection electrode (2.96 cm^2). The probe face was aligned 98.5 ± 0.5 cm downstream of the exit plane, with the axis of rotation located on thruster centerline at the exit plane. An angular coordinate system was defined such that thruster centerline was referenced as zero degrees. When viewed downstream from the exit plane angles became increasingly positive when the probe was swept clockwise. Sweeps were performed from –100° to +100°

in 1° increments. At each location, 1000 data points were sampled at 1 kHz and averaged using a 16-bit data acquisition card and a 502 Ω resistor.

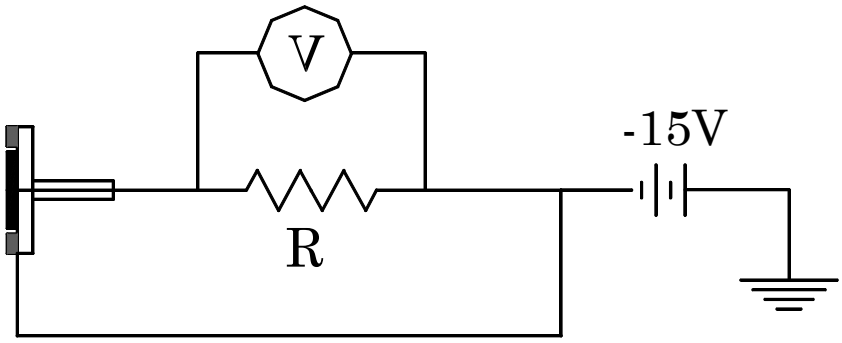

Figure 6-9 Faraday probe electrical schematic.

Angular profiles of the ion current density were used to compute the plume divergence angle. The plume divergence angle $\beta_{0.95}$ was defined as the half-angle from thruster centerline over which the ion current density integrated to 95% of the ion current density integrated over ±90°. No corrections to the measured ion current density were made for the charge-exchange plasma in the vacuum facility [234].

6.3.3 Discharge current probe

An 8-bit, 500 MHz oscilloscope and a 50 MHz current probe were used to measure discharge current oscillations after determining the coil currents that maximized thruster efficiency. The probe was located after the positive terminal of the capacitor shown in Figure 6-7 at the feedthru on the vacuum chamber wall. The oscilloscope sampled the discharge current at 250 kHz for 2 ms. Discharge current oscillations were quantified by calculating the standard deviation of the discharge current over the sampling period. To compare results at different discharge currents, the standard deviation was then expressed as a percentage of the mean discharge current.

Discharge current oscillations at frequencies of 10-30 kHz are usually attributed to the breathing-mode ionization instability [109, 110, 139, 141, 144]. Breathing-mode oscillations result from the periodic depletion of the neutral and ion density in the discharge chamber due to ionization events. A "predator-prey" model of breathing-mode oscillations [144] shows that their frequency scales as

$$2\pi f_b = \omega_b \sim \frac{\sqrt{\left\langle v_b^+ \right\rangle \left\langle v_n \right\rangle}}{L_i}, \tag{6-2}$$

where $\left\langle v_b^+ \right\rangle$ is the average ion velocity, $\left\langle v_n \right\rangle$ is the neutral thermal velocity, and L_i is the length of the ionization zone.

To study discharge current oscillations, the power spectral density of the discharge current was computed from the discrete Fourier transform with Parzen windowing. The breathing-mode ionization instability was identified as the frequency at which the magnitude of the power spectrum was greatest in the 10-30 kHz frequency range.

6.3.4 Hall probe and Gaussmeter

A commercially available three-axis Hall probe and a commercially available Gaussmeter were used to measure the magnetic field of the NASA-173M Hall thrusters at atmospheric conditions (no plasma). As reported by the manufacturer, the Hall probe had a linearity of 0.25% up to 10 kG. A photograph of the experimental setup used with the NASA-173Mv2 is shown in Figure 6-10. A similar setup was used with the NASA-173Mv1.

The Hall probe was connected to the Gaussmeter and positioned relative to the thruster using linear translation stages. The coils were energized using

commercially available power supplies and calibrated, digital multimeters were used to record the applied current. Before collecting data, the Hall probe and Gaussmeter were zeroed using a zero-Gauss chamber with the thruster coils off and the probe located 300 mm from the thruster exit plane. When the probe was placed near the thruster without the coils energized, the residual magnetic field from the thruster pole pieces was between 1-3 G. As with all Hall thrusters, the NASA-173M magnetic circuits were designed so that the azimuthal magnetic field was negligible compared to the radial and axial components. This provided a convenient means to align the Hall probe before collecting data. Accordingly, the Hall probe was oriented such that the indicated azimuthal magnetic field was minimized, which insured that the full magnitude of the radial magnetic field was being measured. The Hall probe was placed on the channel centerline at the axial location of the maximum radial magnetic field, which is near the exit plane in both thrusters.

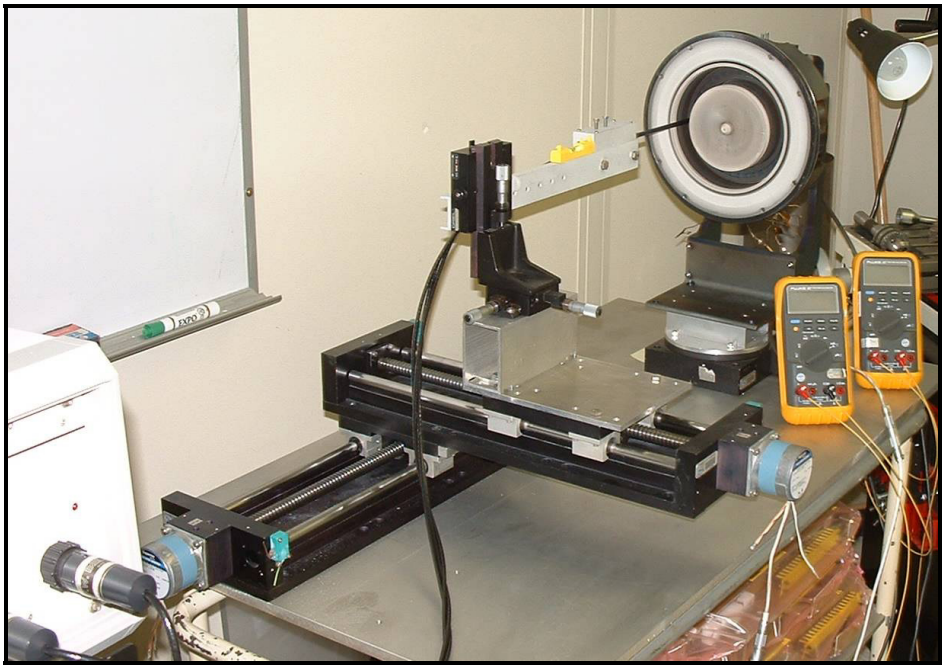

Figure 6-10 Photograph of the experimental configuration used to measure the magnetic field of the NASA-173Mv2. A similar setup was used with the NASA-173Mv1.

The uncertainty of the Hall probe position was estimated as ±1 mm. The uncertainty of the magnetic field measurements was conservatively estimated as ±10%, which was largely due to positional and alignment errors of the Hall probe (see the end of section 5.1.3 for more).

6.4 Summary

This chapter has described the vacuum facilities, support equipment, and diagnostics used during the development phase of the NASA-173M Hall thrusters. The next chapter describes the development of the NASA-173Mv1 Hall thruster, followed by the NASA-173Mv2 development in Chapter 8. Chapter 9 compares the relative merits of each thruster.

Chapter 7

Development of the NASA-173Mv1

This chapter describes the development of the laboratory-model NASA-173M version 1 (v1) Hall thruster. The NASA-173Mv1 was designed and fabricated by the University of Michigan (UM) and the NASA Glenn Research Center (GRC) for operation at high-specific impulse [169]. Experiments with the NASA-173Mv1 validated the magnetic field topography that was implemented to improve efficiency at high-specific impulse. The basis of the magnetic field design was a topography shaped in the form of a plasma lens.

In sections 7.1-7.3, the NASA-173Mv1 Hall thruster is described in terms of its design objectives and approach, physical description, and magnetic field topography. Section 7.4 reviews the early experiments with the NASA-173Mv1 that confirmed the plasma lens improved the focusing properties of the plasma exhaust. Section 7.5 discusses the results from a detailed study of the effects of magnetic field topography on thruster performance at high-specific impulse. Lastly, section 7.6 reports on a broader study of the operating characteristics of the NASA-173Mv1. A follow-on version of this thruster, the NASA-173Mv2, is discussed in Chapter 8. In Chapter 9, the relative merits of the two thruster designs are compared.

7.1 Design objectives and approach

Section 3.2.2.1 discussed the first phase of the NASA GRC high-specific impulse Hall thruster program [133, 175, 176]. The phase two objectives of the NASA GRC high-specific impulse Hall thruster program were to:

1. develop the necessary design tools to extend efficient operation beyond 3000 s specific impulse, and
2. identify the physical mechanisms controlling efficiency at high-specific impulse.

To aid in achieving these objectives, the University of Michigan collaborated with NASA GRC in the design and fabrication of the laboratory-model NASA-173Mv1 Hall thruster.

As the discharge voltage in a magnetic layer Hall thruster increases, the average electron temperature in the channel also increases as the ability of the walls to moderate the electron temperature decreases [109, 110]. Increasing electron temperature can grossly affect thruster efficiency by several mechanisms. As the electron temperature rises:

1. the ionization efficiency will eventually decrease because the ionization cross-section of xenon maximizes for electron temperatures between 40-90 eV [155],
2. the production of multiply-charged ions will increase as the number of electrons with sufficient energy to create multiply-charged ions increases, and
3. the axial transport of electrons will increase by thermal diffusion (see Eqn. 3-17).

It is also possible that electron transport could increase due to plasma instabilities that are not encountered in 1600 s specific impulse Hall thrusters.

The processes listed above are influenced in whole or in part by the magnetic field, the secondary electron emission from the discharge chamber walls, and the uniformity of the neutral propellant in the channel. Since boron nitride is a proven wall material for Hall thrusters, it was decided that wall material effects would not be explicitly studied with the NASA-173Mv1. Further, every effort was made to ensure that the neutral distribution in the channel was azimuthally uniform (see section 7.4 for more).

The design of the NASA-173Mv1 was based on the hypothesis that the efficiency peak observed with the phase one thrusters was actually a consequence of modern magnetic field designs that have been optimized for 1600 s specific impulse. Accordingly, the NASA-173Mv1 design was an attempt to improve efficiency through the implementation of a magnetic field topography intended for high-specific impulse operation.

7.2 Physical description

Shown in Figure 7-1, the NASA-173Mv1 is a single-stage, magnetic layer Hall thruster sized to operate nominally at discharge powers of 5 kW.[30] Figure 7-2 is a photograph of the thruster operating at 300 V, 15 A. The discharge chamber of the NASA-173Mv1 has an outer diameter of 173 mm, a channel width of 25 mm, and a channel depth of 38 mm. The thruster body has an outer diameter of 277 mm and an overall length of 96 mm.

[30] The first iteration of the NASA-173Mv1 included an intermediate electrode so that two-stage operation would be possible [169]. In Ref. [169], the NASA-173Mv1 was referred to as the P5-2 and was operated as a two-stage thruster. After a brief series of experiments revealed that two-stage operation resulted in higher thrust at the expense of efficiency, the intermediate electrode was removed. The thruster was then re-named the NASA-173Mv1 to reflect this change. For the results reported here, the NASA-173Mv1 was operated as a single-stage thruster.

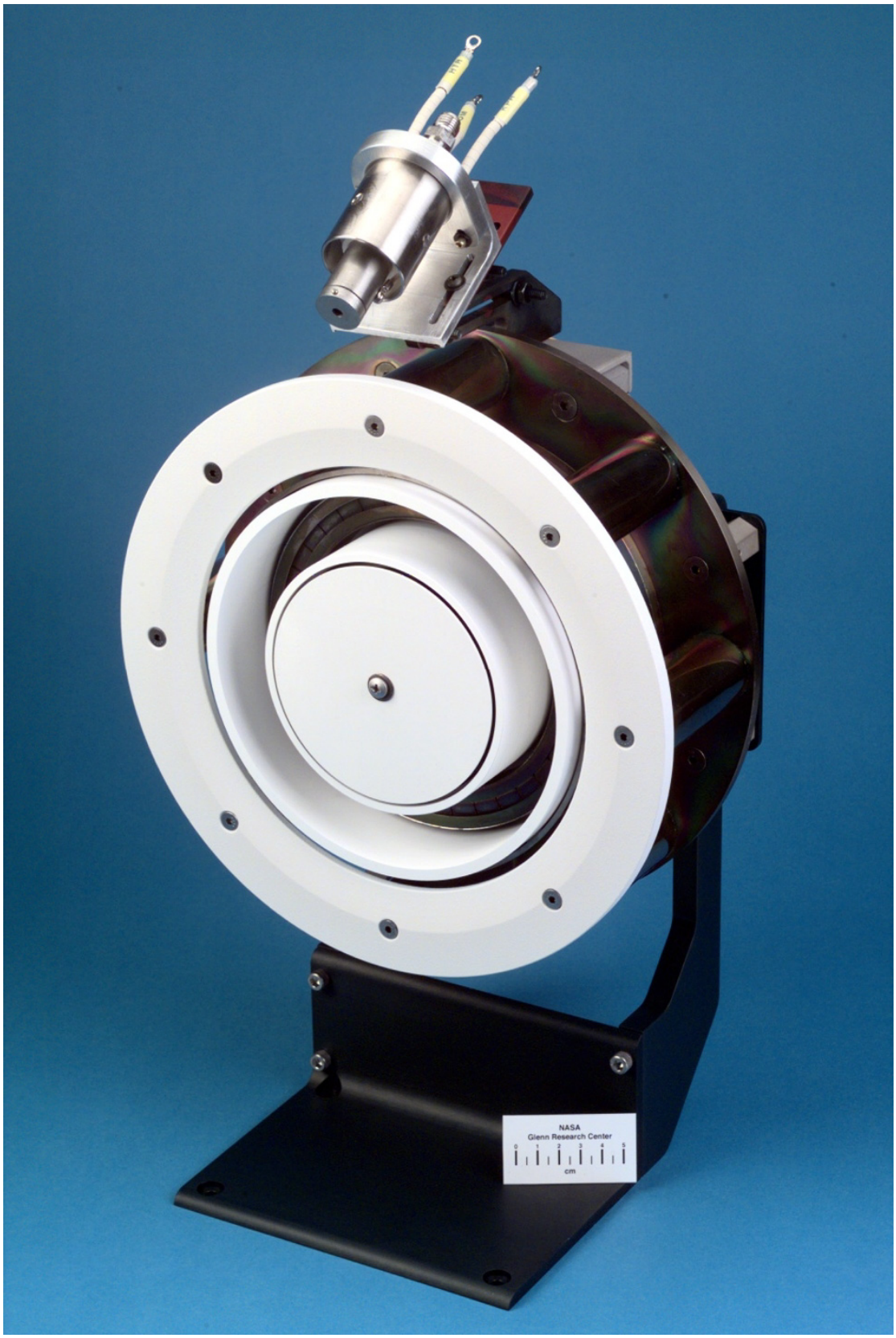

Figure 7-1 Photograph of the laboratory-model NASA-173Mv1 Hall thruster.

The NASA-173Mv1 uses a laboratory-model hollow cathode from NASA GRC that is capable of emission currents up to 20 A. As shown in Figure 7-1, the cathode is positioned above the thruster. Several experiments were conducted to improve thruster operation with respect to cathode position. Consideration was given to the cathode coupling voltage with respect to ground $V_{c\text{-}g}$, the magnitude of discharge current oscillations, thruster efficiency, and the shape and luminescence of the plume. The best position was found to be with the cathode orifice located approximately 25 mm downstream of the exit plane and 25 mm radially away from the outer radius of the outer front pole piece at an inclination of 30° from thruster centerline.

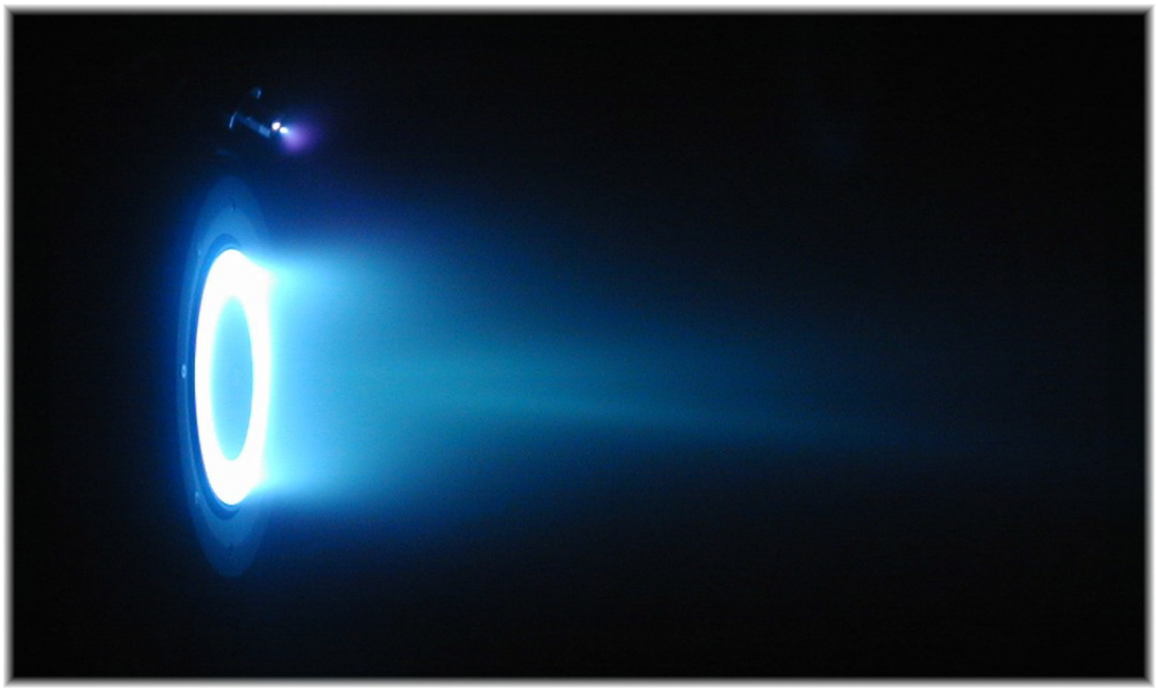

Figure 7-2 Photograph of the NASA-173Mv1 operating at 300 V, 15 A.

The design of the NASA-173Mv1 was partly based on the UM/AFRL P5 Hall thruster that was described in section 5.3.1. The primary characteristics of the P5 that are maintained in the NASA-173Mv1 are:

1. the channel geometry (outer diameter, width, length),
2. discharge chamber walls made from boron nitride,[31] and
3. the gas injection scheme of the anode.

The major difference between the P5 and NASA-173Mv1 is the magnetic field topography. **Retaining the other characteristics listed above allowed for differences in the performance and plume characteristics between the thrusters to be attributed to changes in the magnetic field topography.**

7.3 Magnetic field topography

7.3.1 Magnetic circuit

The primary magnetic circuit of the NASA-173Mv1 consists of a fixed structure of magnetic poles pieces, an inner coil (IC), and eight outer coils (OC). Fine control of the magnetic field is provided with an internal trim coil (ITC). The magnetic circuit configuration of the NASA-173Mv1 is similar to the generic schematic shown in Figure 5-6 except that eight outer coils are used (instead of a single azimuthal coil) and the thruster does not have an external trim coil.

7.3.2 Axial gradient of the radial magnetic field

Figure 5-7 shows the axial profile of the radial magnetic field on the channel centerline for the P5 and the NASA-173Mv1. The axial coordinate was referenced from the location of the maximum, centerline radial magnetic field $B_{r,max}$ so that the curvature of the axial profiles could be compared. As shown in Figure 5-7, the axial gradient of the radial magnetic field $\nabla_z B_r$ of the NASA-173Mv1 is nearly the same as the P5. To quantify the differences between the thrusters, the dimensionless

[31] The discharge chamber of the P5 is 50% boron nitride and 50% silicon dioxide. The NASA-173Mv1 uses a ceramic that is 94% boron nitride and uses calcium borate as a binder. Differences in thruster performance between grades of boron nitride are known to be minor.

magnetic field gradient ϑ defined by Eqn. 7-4 was calculated. In the P5, ϑ has a value of 0.79, while the value of ϑ in the NASA-173Mv1 has a value of 0.95. The differences are driven by a lower magnetic field at the anode in the NASA-173Mv1. In the P5, $B_{r,max}$ is upstream of the exit plane while in the NASA-173Mv1, $B_{r,max}$ is downstream of the exit plane. Locating $B_{r,max}$ downstream of the exit plane is known to increase thruster lifetime at the expense of higher plume divergence [2]. The location of $0.8*B_{r,max}$ was placed upstream of the exit plane because it has been shown in 1600 s specific impulse thrusters that there is a correlation between the position of $0.8*B_{r,max}$ and the location of the ionization zone [121, 135]. Locating $0.8*B_{r,max}$ inside the bounds of the ceramic wall aids in moderating the electron temperature and enhances the ionization efficiency.

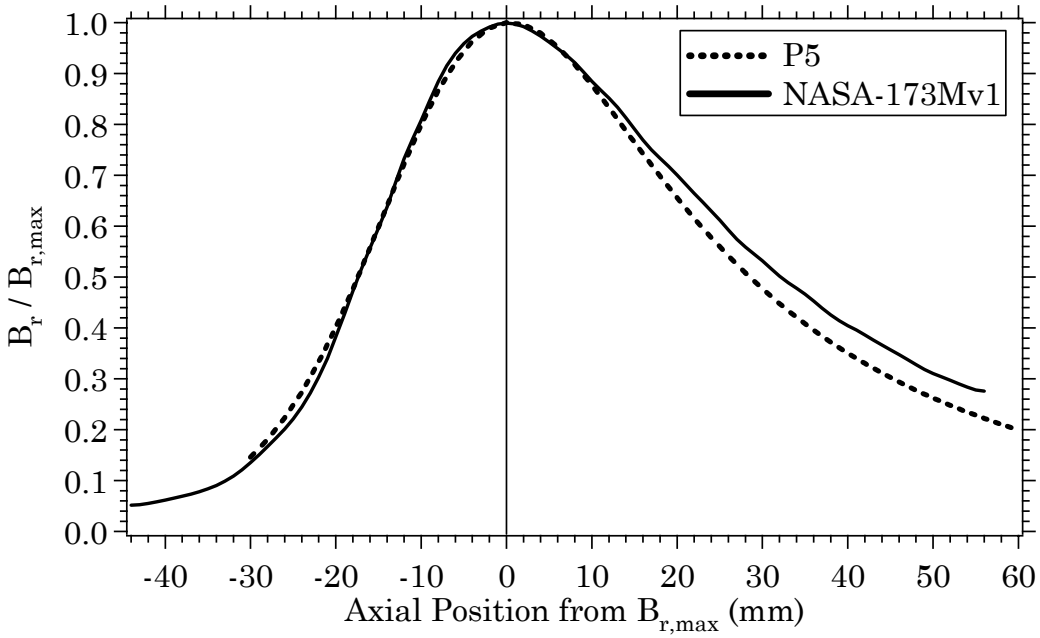

Figure 7-3 Axial variation of the centerline, radial magnetic field in the P5 and the NASA-173Mv1.

7.3.3 Plasma lens focusing

The experiments discussed in section 5.3 with the P5 suggested that concave magnetic field lines would be necessary to improve the focusing of the plume.

Accordingly, the NASA-173Mv1 uses a plasma lens magnetic field topography and an internal trim coil that allow for variations of the magnetic field not possible with the inner and outer coils alone.

A plasma lens magnetic field topography significantly departs from the radial field line configuration used in the P5 (see Case 1 in Figure 5-12). Figure 7-4 shows the NASA-173Mv1 plasma lens and Figures 7-5 and 7-6 show the corresponding axial profiles of the radial and axial magnetic fields, respectively. On centerline, the axial fields are approximately zero and both the radial and axial fields nearly vanish at the anode. Along the discharge chamber walls, the plasma lens has regions of significant axial fields. The magnetic field profiles result in a plasma lens with concave field lines that are symmetric about the channel centerline. Ref. [220] discusses how a symmetric plasma lens minimizes discharge current and plume divergence.

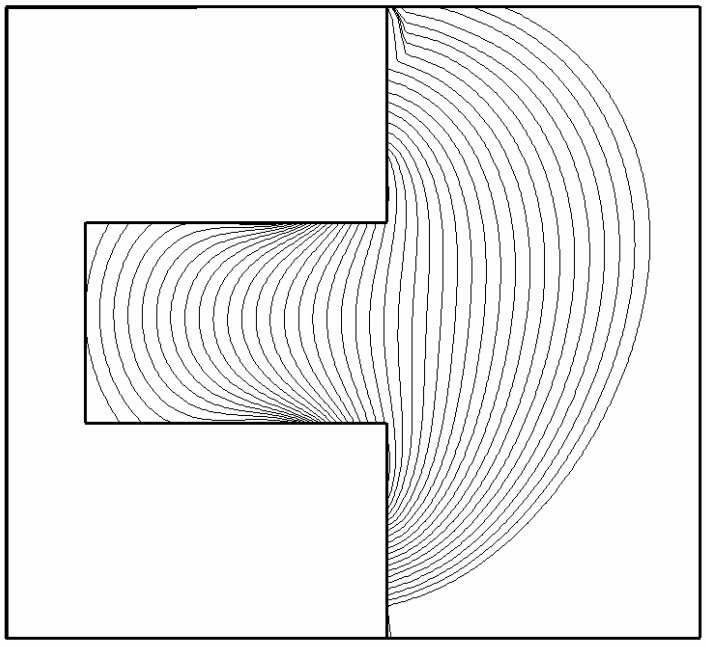

Figure 7-4 The plasma lens magnetic field topography of the NASA-173Mv1.

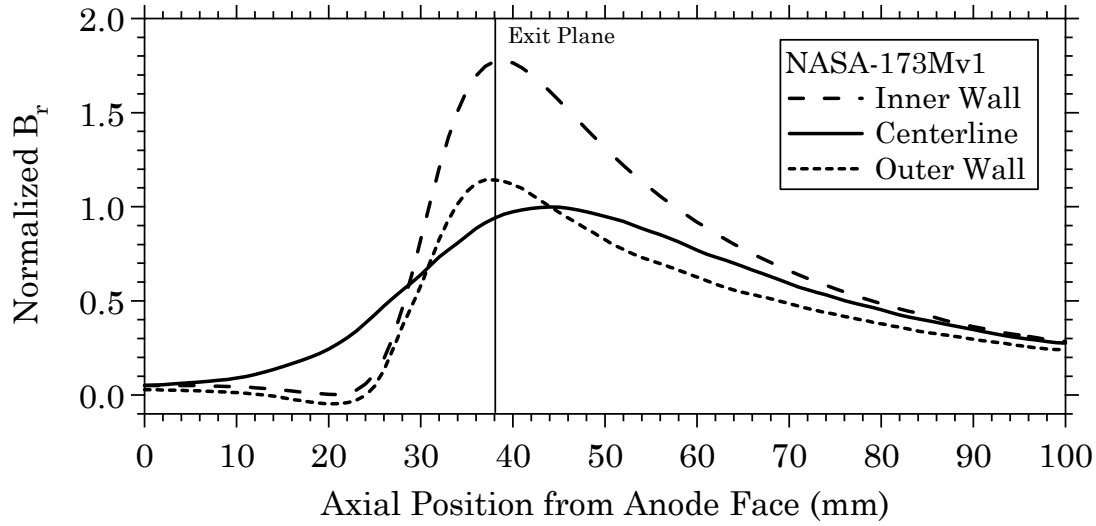

Figure 7-5 Radial magnetic field profiles of the NASA-173Mv1 normalized by the maximum value on centerline.

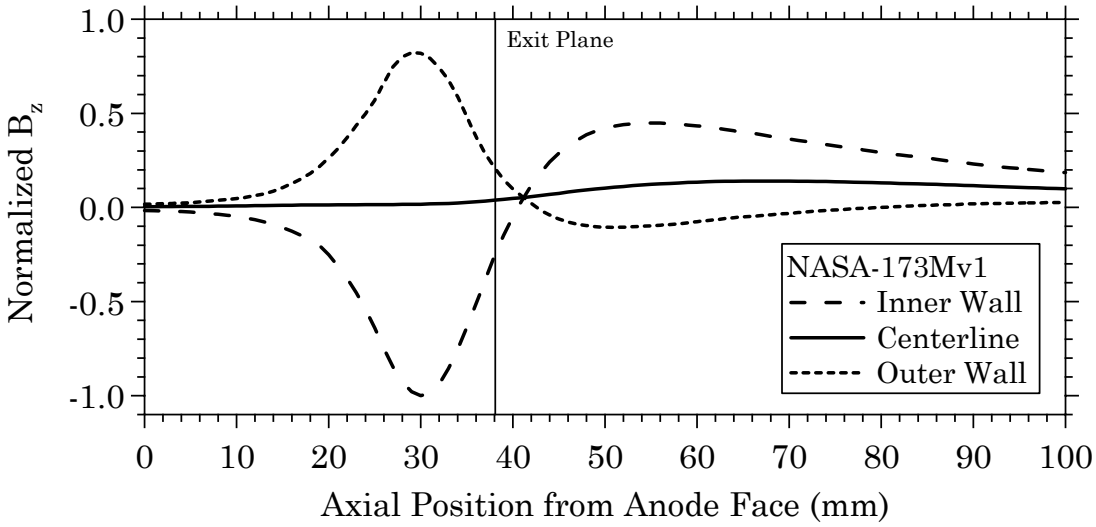

Figure 7-6 Axial magnetic field profiles of the NASA-173Mv1 normalized by the magnitude of the maximum field on the inner wall.

Figure 7-5 shows that the maximum radial fields along the discharge chamber walls are greater than the maximum value on channel centerline. Such a configuration increases the magnetic insulation of the plasma from the walls because the plasma location tends towards regions of low magnetic field. This is

illustrated with the radial component of the single-fluid MHD approximation given by

$$\frac{\partial}{\partial r}\left(p + \frac{B^2}{2\mu_0} \right) = 0 \,. \qquad \textbf{(7-1)}$$

Eqn. 7-1 shows that a balance between the pressure and the magnetic field governs the plasma location [135]. Thus, creating a minimum in the magnetic field profile across the channel radius tends to locate the plasma on centerline.

A plasma lens affects thruster operation primarily by:

1. Increasing the magnetic insulation of the ions from the wall. This effect should be greatest for ions born in weak electric fields before the ions are significantly accelerated. The field line curvature preferentially directs ions towards the channel centerline away from the walls, which increases efficiency and lifetime while decreasing plume divergence and thermal loads.
2. Increasing the path length (*i.e.*, the residence time) of electrons trapped on a given field line thereby increasing the ionization efficiency and decreasing the axial electron current. Field lines terminating at the walls in regions of high magnetic field create a mirror effect on all but the most energetic electrons, reflecting the low-energy electrons back into the discharge chamber. The high-energy electrons penetrate both the magnetic field and the wall sheath potential and impact the walls, which in turn releases secondary electrons from the wall that decrease the average electron temperature in the channel.

7.3.4 Internal trim coil

Section 5.1.4 discussed the effects of the internal trim coil on the magnetic field topography of the NASA-173Mv1. The internal trim coil primarily affects the radial magnetic field in the discharge chamber. When the coil is energized, the radius of curvature of the plasma lens (*i.e.*, the axial gradient of the magnetic field, $\nabla_z B_r$) can be changed, depending on the direction of the coil current. By convention, a negative current subtracts from the magnetic field and increases $\nabla_z B_r$.

7.3.5 Response of the magnetic circuit to applied coil current

The response of the NASA-173Mv1 magnetic circuit to the inner coil (IC), outer coils (OC), and internal trim coil (ITC) was characterized using the Hall probe and Gaussmeter described in section 6.3.4. The Hall probe was placed on the channel centerline at the axial location of the maximum radial magnetic field.

Figure 7-7 shows the maximum, radial magnetic field on channel centerline versus coil current for the inner and outer coils. The measured values (indicated as "exp" in the figure) were normalized by an arbitrary constant B_o. The radial magnetic field as a function of coil current was recorded for each coil without the other coil being energized. In a Hall thruster, if the magnetic circuit is below saturation (*i.e.*, the magnetic field increases linearly with coil current), the total magnetic field for arbitrary coil currents can be computed by linear superposition. As an example, the total magnetic field for equal coil currents from the inner and outer coils was computed (indicated as "comp" in the figure). Section 8.3.5 discusses results that have experimentally verified the validity of this method to compute the total magnetic field.

Figure 7-8 shows the maximum, radial magnetic field on channel centerline versus coil current for the internal trim coil. The measured values were normalized by an arbitrary constant B_o. The response of the magnetic circuit to the internal trim coil was linear over the range of coil currents that were tested. A zero offset at zero applied current was measured due to the residual magnetism of the magnetic circuit. The offset is also present in Figure 7-7, but is less apparent due to the scale.

Over the range of coil currents that were tested, the magnetic field produced by the magnetic circuit of the NASA-173Mv1 linearly increased. To study the scaling of the magnetic field with discharge voltage, data from Figure 7-7 and Figure 7-8 were used to compute the total magnetic field for specific operating points of the thruster (see sections 7.5.1.1 and 7.6.6). When computing the total magnetic field, the residual magnetism was included in the contribution from the inner coil and subtracted from the other coils (so that it was not counted more than once).

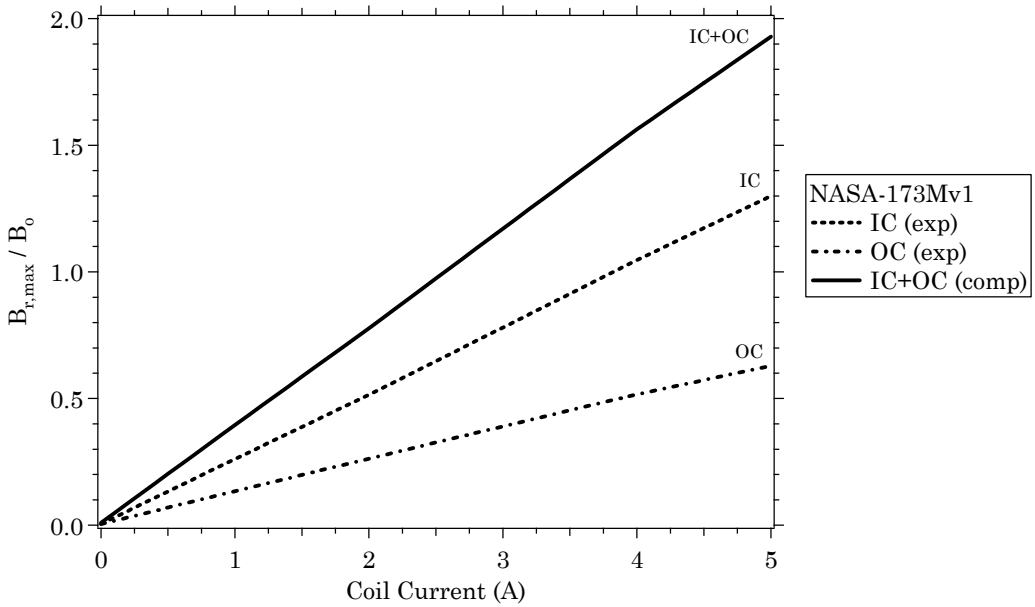

Figure 7-7 Maximum, radial magnetic field on channel centerline versus coil current for the inner coil (IC) and outer coils (OC) of the NASA-173Mv1. (exp = measured data, comp = computed data)

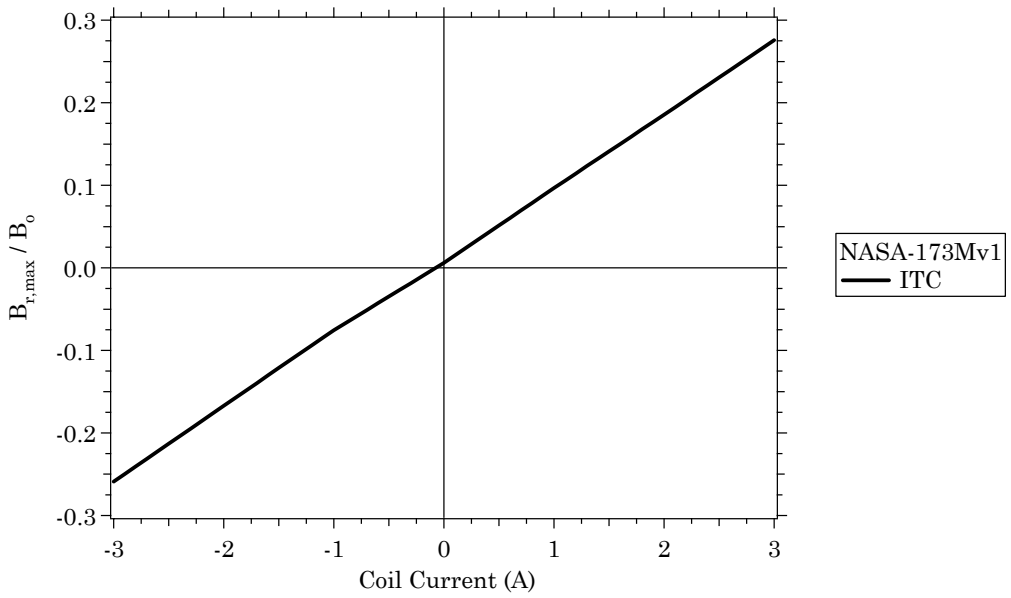

Figure 7-8 Maximum, radial magnetic field on channel centerline versus coil current for the internal trim coil (ITC) of the NASA-173Mv1.

7.4 Effects of the plasma lens on plume focusing

The first experiments with the NASA-173Mv1 were reported in Ref. [169, 228]. During these experiments, the thruster design was still evolving.[32] Only the most important results from these early experiments are discussed here.

Figure 7-9 shows the ion current density measured in the plume of the NASA-173Mv1 during the experiments described in Ref. [228]. The thruster was operated at 300 and 500 V, at mass flow rates of 5.3 and 10.0 mg/s, and only the inner and outer coils were energized. A Faraday probe was used to measure ion current density, similar to the one described in section 6.3.2, that was 100 cm from the thruster exit plane. Two important conclusions emerged from the profiles shown in Figure 7-9:

[32] That is, several thruster components failed due to thermal expansion or voltage isolation problems. During this time, the internal trim coil shorted, the discharge chamber cracked, and the anode suffered from asymmetric flow distribution. While the trim coil and discharge chamber were replaced (after modifying their designs to avoid further failures), the anode was not replaced until after the experiments in section 7.5. This period is fondly referred to as our "time of learning." The problems were eventually remedied with better engineering.

1. Unlike the P5 Hall thruster (see section 5.3), the plume of the NASA-173Mv1 exhibited a "double peak" in the ion current density profile. **This confirmed that the focusing of the plasma exhaust plume of a Hall thruster could be improved using a plasma lens.**

2. The ion current density profiles were asymmetric and the double peak profile was only evident at 10 mg/s. This indicated that the azimuthal distribution of the neutral propellant through the anode was asymmetric. This anode is referred to as anode #1.

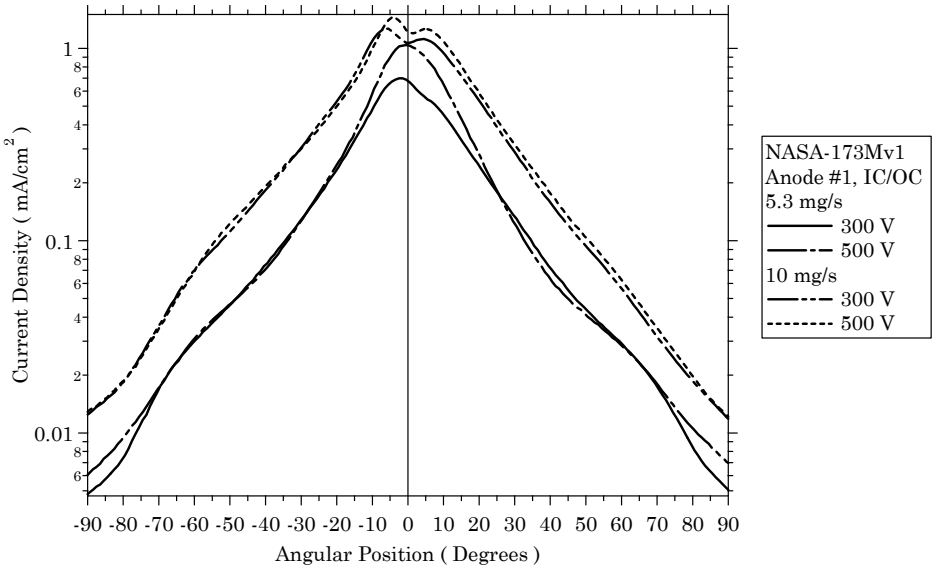

Figure 7-9 Ion current density versus angular position from thruster centerline with anode #1 of the NASA-173Mv1. Azimuthal non-uniformity of the neutral propellant resulted in asymmetric plume profiles. The problem was corrected with anode #2 (see Figures 7-37 to 7-41).

Thruster efficiency also decreased because of the asymmetric gas distribution from anode #1 (see section 7.6.1). Unfortunately, circumstances did not permit anode #1 to be replaced until after the study described in section 7.5. **While anode #1 decreased performance, the performance trends discussed in section 7.5 were still observed in the NASA-173Mv1 after anode #1 was replaced with anode #2. Further, the efficiency-voltage characteristic of the NASA-**

173Mv2 at 5 mg/s shows the same trends (see Figure 9-7). Thus, the general trends and conclusions drawn from the experiments in section 7.5 were still judged valid.

Anode #1 was replaced with anode #2 for the performance characterization described in section 7.6. Anode #2 corrected the problems with anode #1 by changing the fabrication method (the gas injection scheme was still the same). Section 7.6.1 discusses the improvements in the performance and plume characteristics that resulted when anode #2 was installed in the NASA-173Mv1.

7.5 The role of magnetic field topography

Despite the initial challenges with the design of the NASA-173Mv1, the early experiments confirmed that the plasma lens improved the focusing of the ion beam. This section describes a study that investigated the effects of magnetic field topography on thruster performance at high-specific impulse. The goal of the experiments was to determine whether performance improvements could be realized by changing the magnetic field topography using the internal trim coil.

7.5.1 Results

This section reports on a performance evaluation of the NASA-173Mv1 at voltages of 300-1000 V and a constant mass flow rate of 5 mg/s. At each voltage, the internal trim coil current was varied to determine whether efficient operation could be achieved by changing the magnetic field topography. Numerical simulations of the magnetic field were also conducted in order to correlate changes made to the magnetic field with thruster performance.

The experiments used the setup described for the LVTF in section 6.2.1 and the thrust stand described in section 6.3.1.1. As discussed in section 7.4, the

thruster was operated with anode #1. The NASA-173Mv1 had been previously operated for over 40 hours before performance data were collected. The pressure in the LVTF at an anode and cathode flow rate of 4.98 mg/s and 0.52 mg/s, respectively, was 4.5×10^{-6} Torr when corrected for xenon using Eqn. 6-1. Performance data are tabulated in Tables B-1 and B-2 in Appendix B.

7.5.1.1 Performance with the inner and outer coils

Performance measurements were collected in two sets of experiments. In the first set of experiments, the influence of the inner coil (IC) and the outer coils (OC) on performance was studied. This series was conducted over a voltage range of 300-1000 V in 100 V increments at a constant anode mass flow rate of 5 mg/s.[33] The cathode was operated at 0.5 or 1.0 mg/s, which was varied to minimize thruster oscillations. No systematic dependence of cathode flow rate with the operating point was ever determined, and a majority of the data were taken at the lower flow rate.

At each voltage, data were acquired by setting the inner coil current and varying the outer coil current so that different coil current ratios (IC/OC) could be examined. At least three thrust measurements were made at different inner coil currents, typically in increments of 0.5 A around a medial value of the inner coil current that roughly minimized discharge current and oscillations, while increasing plume focusing and thrust. At each inner coil current, the coil current ratio was varied over the range of 0.75–2.0, typically in increments of 0.2. By the time the experiments progressed to the 500 V series, it became evident that coil current

[33] The asymmetric flow distribution from anode #1 influenced the flow rate choice. At discharge powers in excess of 5 kW, the thruster tended to overheat due to hotspots in the discharge chamber that developed as a result of anode #1's flow asymmetries. Thus, the 5 mg/s flow rate was chosen so that the discharge power would be 5 kW at 1000 V (the nominal power rating of the NASA-173Mv1). Limiting the power to 5 kW minimized the risk of thermally induced failure. After anode #2 was replaced, the thermal problems with the thruster were resolved. To date, the NASA-173Mv1 has been operated at up to 8.5 kW with anode #2.

ratios of about 1.0 were resulting in peak performance. Subsequent data at coil current ratios of 0.75–1.25 were taken at increments of about 0.1. Data above coil current ratios of 1.25 were still taken but at increments as large as 0.5. The performance data were later analyzed to determine which coil currents resulted in maximum thruster efficiency. In general, the coil current ratio corresponding to maximum efficiency was found to be close to unity.

Thruster operation over the range of 300-800 V was stable. At 900 and 1000 V, oscillations in the discharge current were severe unless the inner and outer coil currents were increased to 5 A. Below 5 A, oscillations would grow until the plasma would eventually extinguish. At 5 A, the oscillations were substantially reduced and the thruster behaved similar to the 300-800 V cases.

7.5.1.2 Performance with the internal trim coil

In the second series of experiments, the effect of the internal trim coil on thruster performance was evaluated to determine if improvements over the experiments in section 7.5.1.1 could be realized. The thruster was operated at the same voltages and flow rates as the experiments in section 7.5.1.1. The inner coil currents from section 7.5.1.1 that yielded maximum efficiency were used and the coil current ratio was 1.0. At fixed discharge voltage and inner and outer coil current, a test would begin by starting at zero internal trim coil current and then the internal trim coil current was increased to larger negative values. Testing at a given discharge voltage was halted when it became evident that applying more negative internal trim coil current was resulting in unstable or inefficient operation. A cursory examination revealed that positive internal trim coil current always resulted in decreasing efficiency (not shown).

The results from the internal trim coil current study are presented in Figures 7-10 through 7-18. Discharge current, thrust, anode specific impulse, and anode efficiency versus internal trim coil current at constant inner and outer coil current, discharge voltage, and flow rate are shown in each figure. At 800 V, in addition to testing the optimum coil currents from the first series of experiments, the inner and outer coil currents were increased by 1.0 A. Figures 7-15 and 7-16 show 800 V data at 3.5 and 4.5 A, respectively, on the inner and outer coils. The data for 800 V and 4.5 A on the coils shows an additional 0.5% improvement in the efficiency over the 3.5 A case.

Figure 7-19 plots the internal trim coil current that resulted in maximum efficiency at each discharge voltage. Two data points are shown for 800 V, corresponding to 3.5 or 4.5 A on the inner and outer coils. Note the large change in the required internal trim coil current as the inner and outer coil currents were increased from 3.5 to 4.5 A.

Figures 7-20 through 7-24 present discharge current, thrust, thrust-to-power ratio, anode specific impulse, and anode efficiency, respectively, versus discharge voltage. In each figure, two curves are shown corresponding to operation with zero internal trim coil current and operation with the internal trim coil currents shown in Figure 7-19. Changing the magnetic field with the internal trim coil improved thruster performance over the entire voltage range.

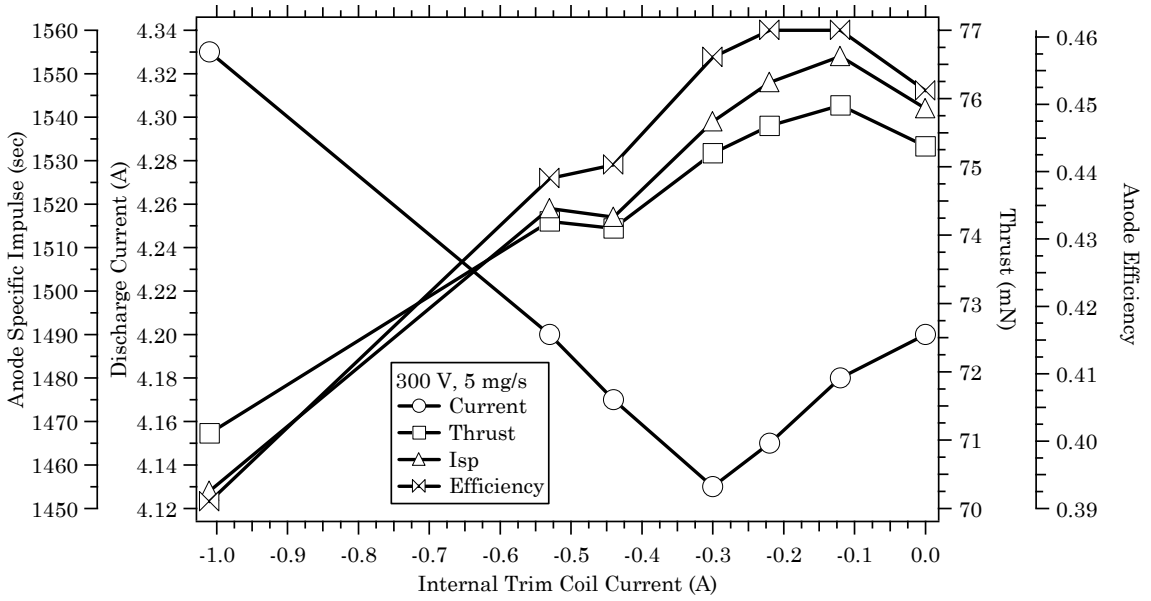

Figure 7-10 Performance of the NASA-173Mv1 versus internal trim coil current at 300 V, 5 mg/s. (Anode #1)

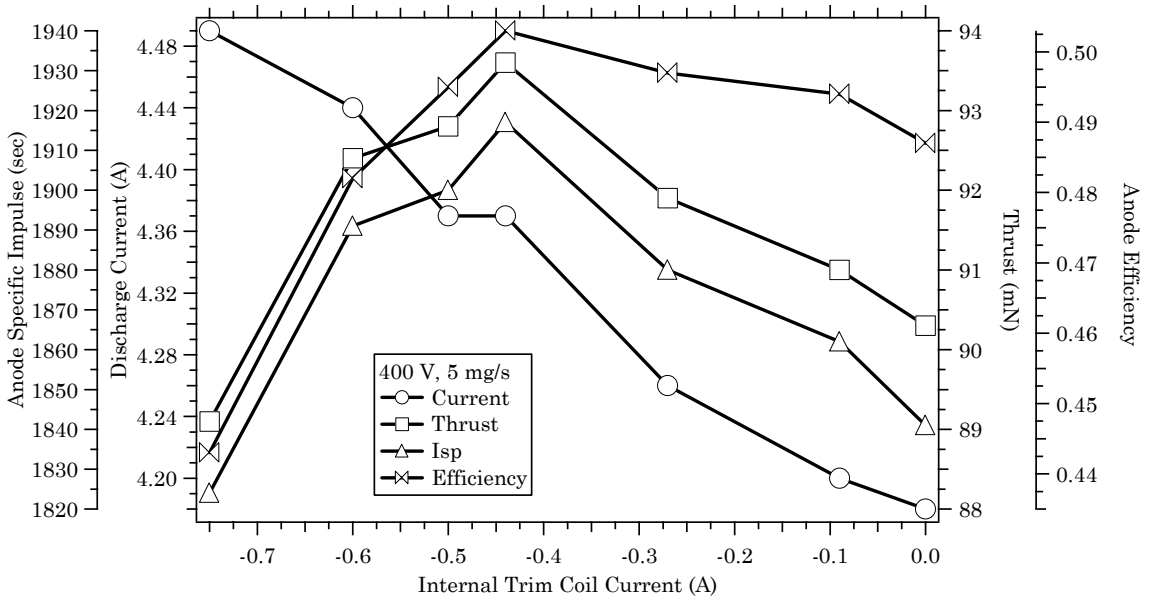

Figure 7-11 Performance of the NASA-173Mv1 versus internal trim coil current at 400 V, 5 mg/s. (Anode #1)

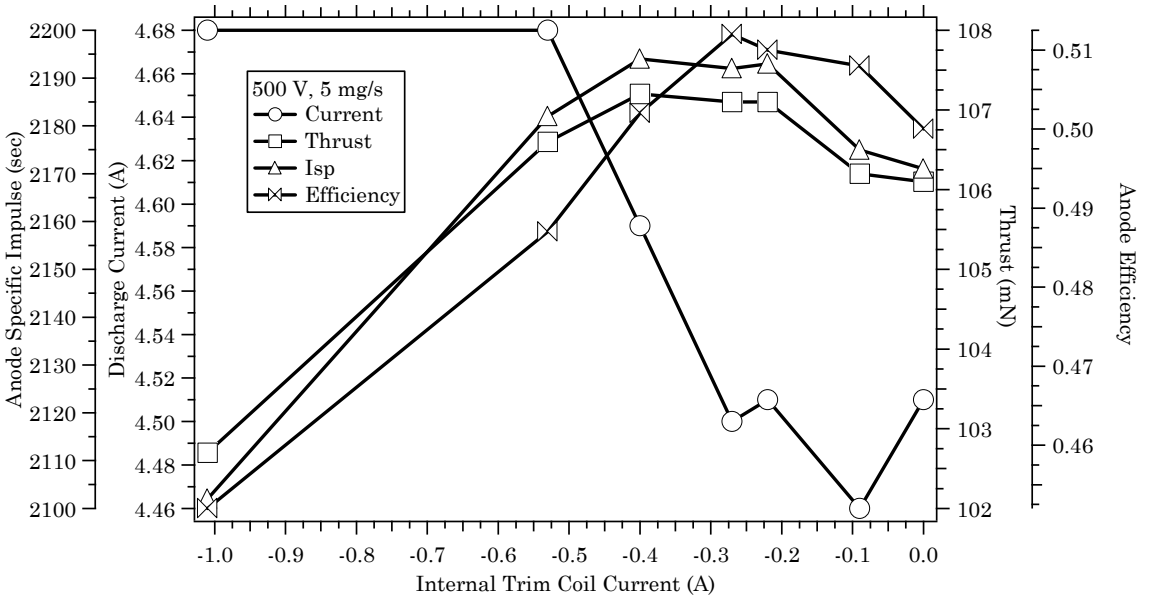

Figure 7-12 Performance of the NASA-173Mv1 versus internal trim coil current at 500 V, 5 mg/s. (Anode #1)

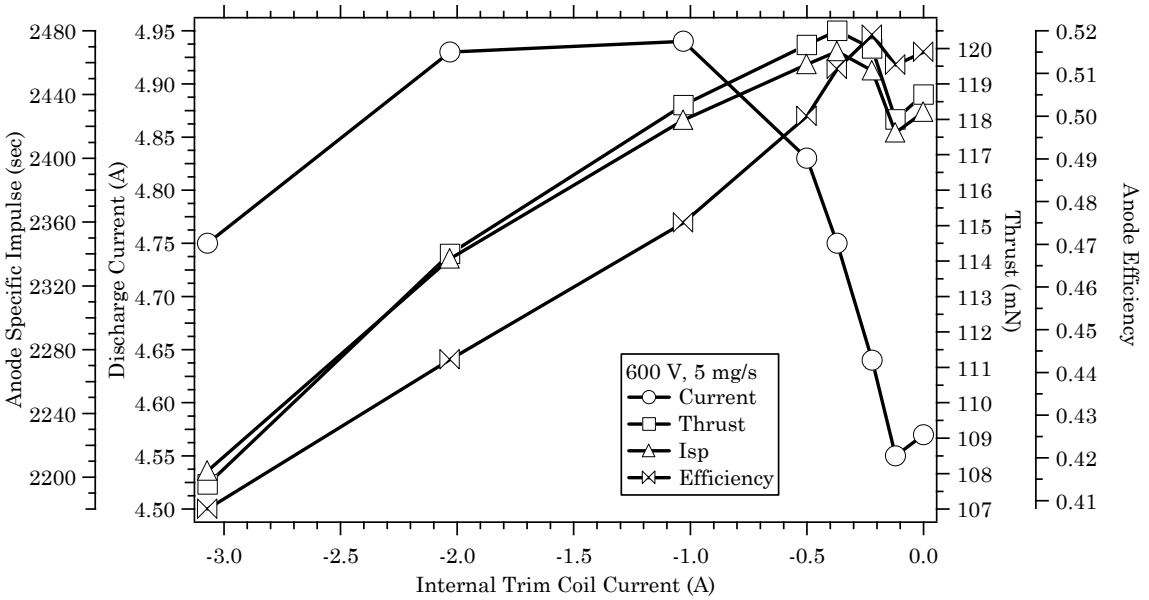

Figure 7-13 Performance of the NASA-173Mv1 versus internal trim coil current at 600 V, 5 mg/s. (Anode #1)

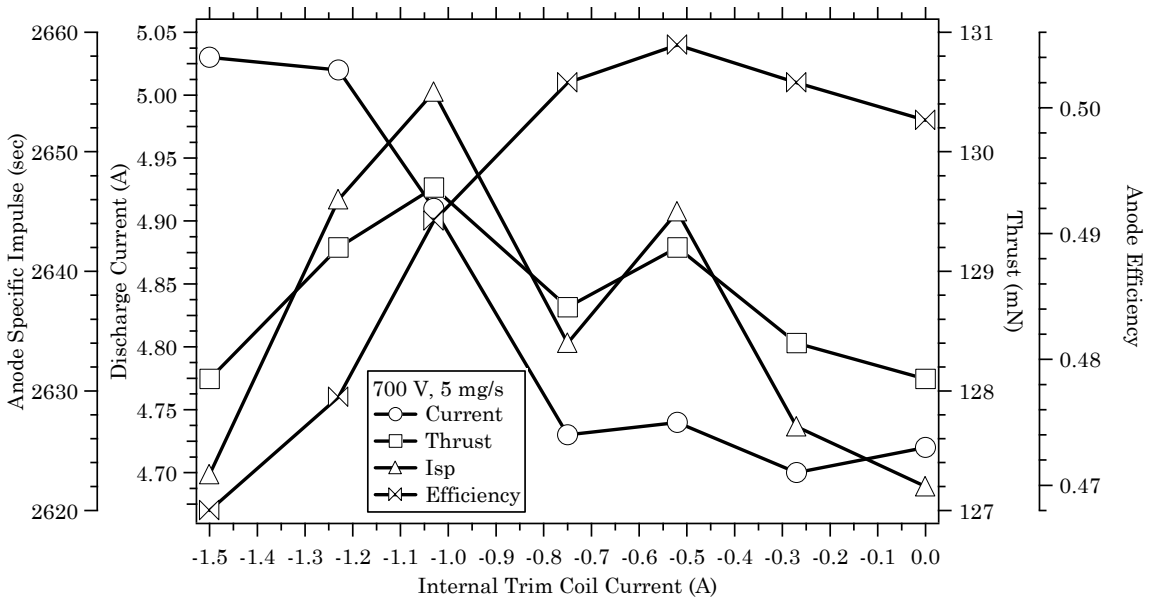

Figure 7-14 Performance of the NASA-173Mv1 versus internal trim coil current at 700 V, 5 mg/s. (Anode #1)

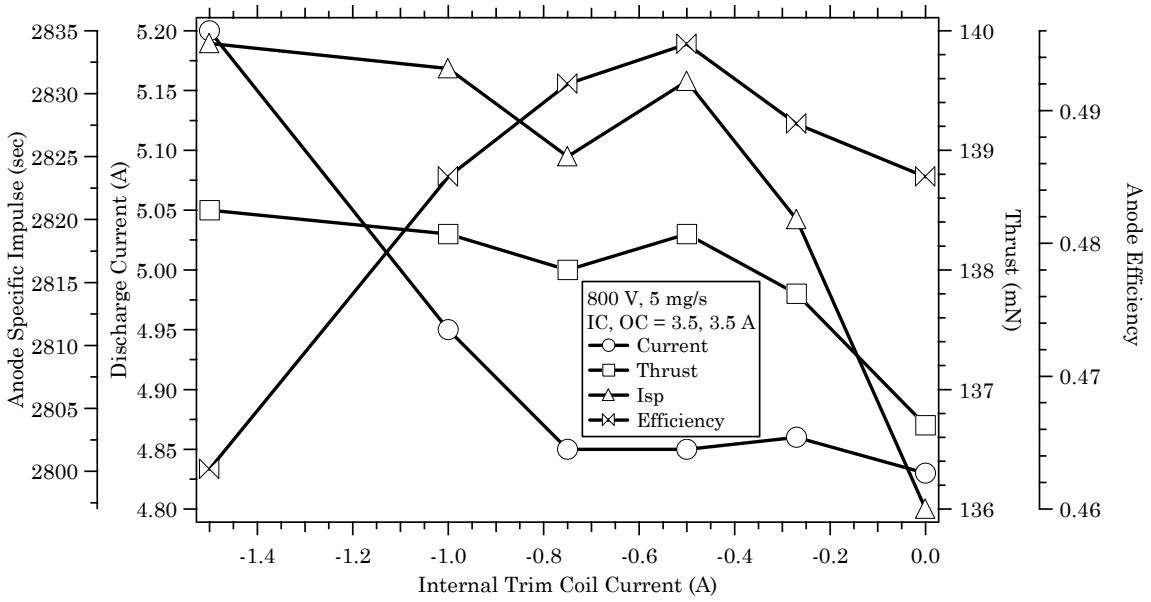

Figure 7-15 Performance of the NASA-173Mv1 versus internal trim coil current at 800 V, 5 mg/s with the inner and outer coils at 3.5 A. (Anode #1)

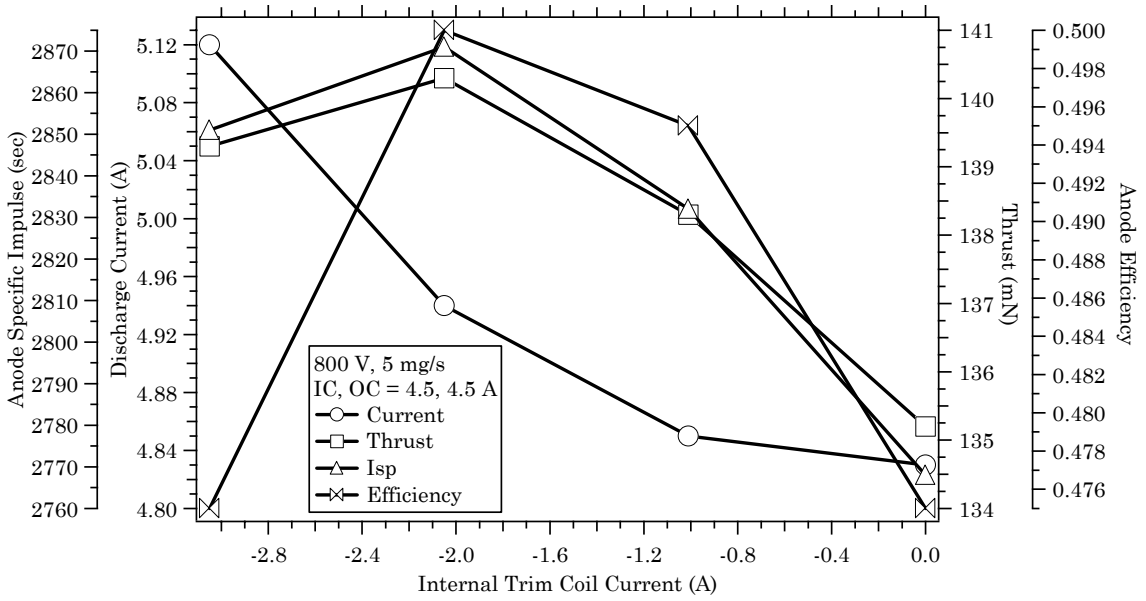

Figure 7-16 Performance of the NASA-173Mv1 versus internal trim coil current at 800 V, 5 mg/s with the inner and outer coils at 4.5 A. (Anode #1)

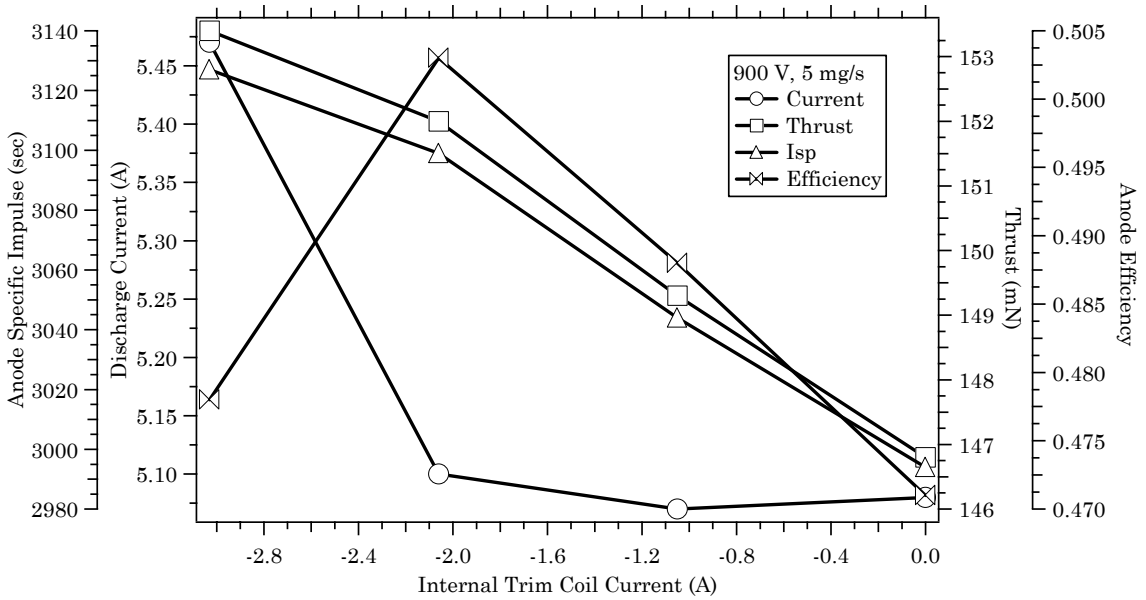

Figure 7-17 Performance of the NASA-173Mv1 versus internal trim coil current at 900 V, 5 mg/s. (Anode #1)

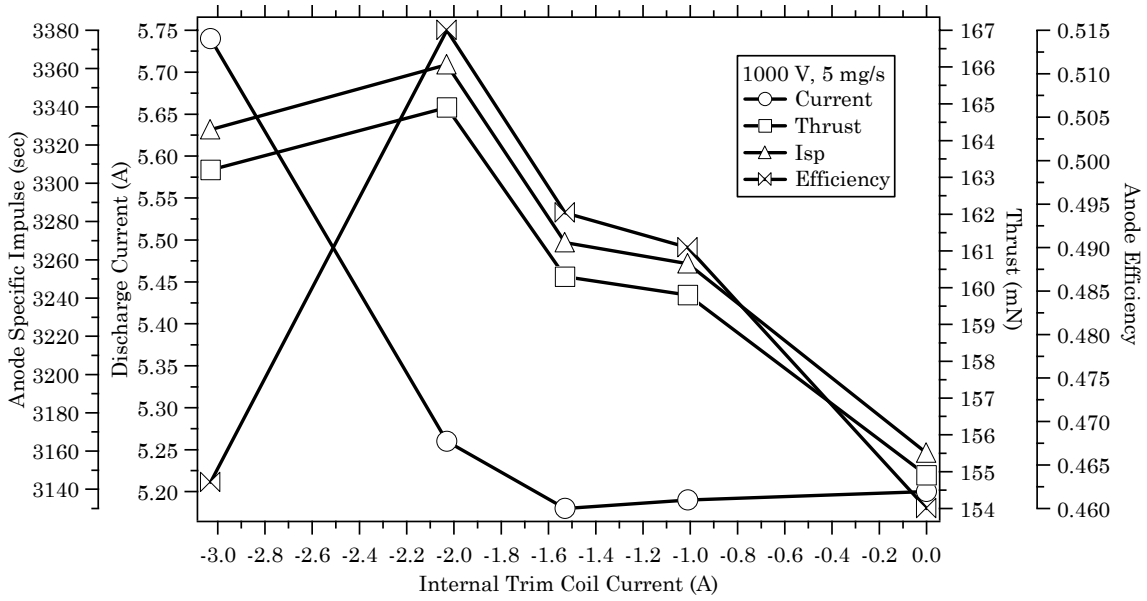

Figure 7-18 Performance of the NASA-173Mv1 versus internal trim coil current at 1000 V, 5 mg/s. (Anode #1)

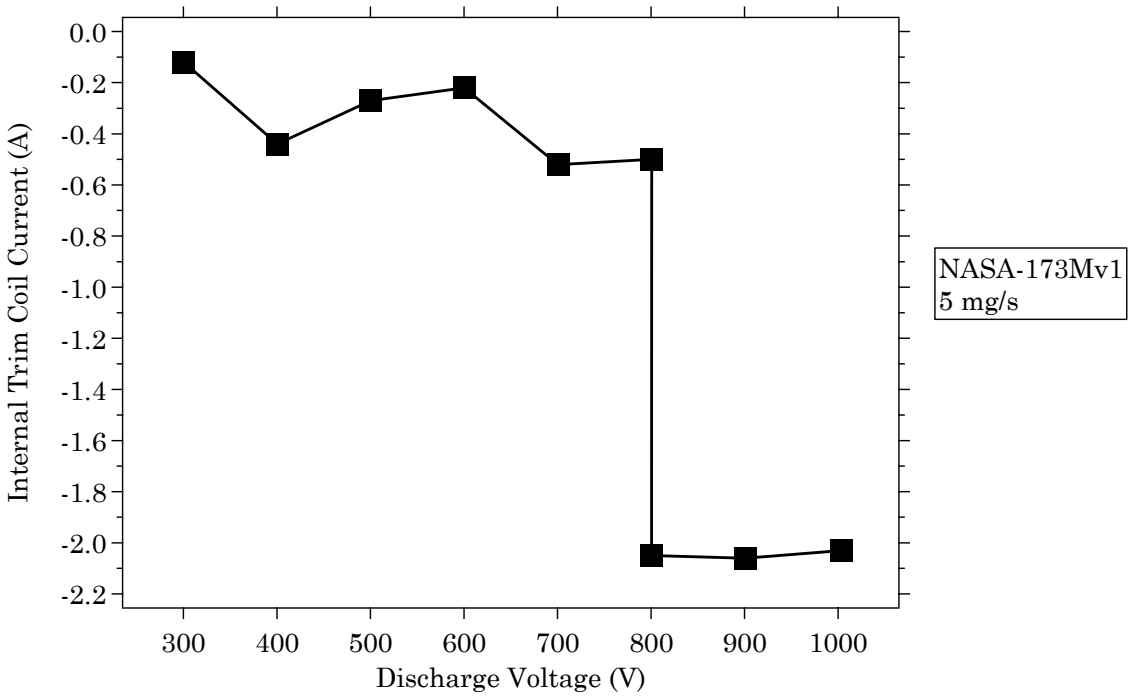

Figure 7-19 Internal trim coil current versus discharge voltage of the NASA-173Mv1 at 5 mg/s. (Anode #1)

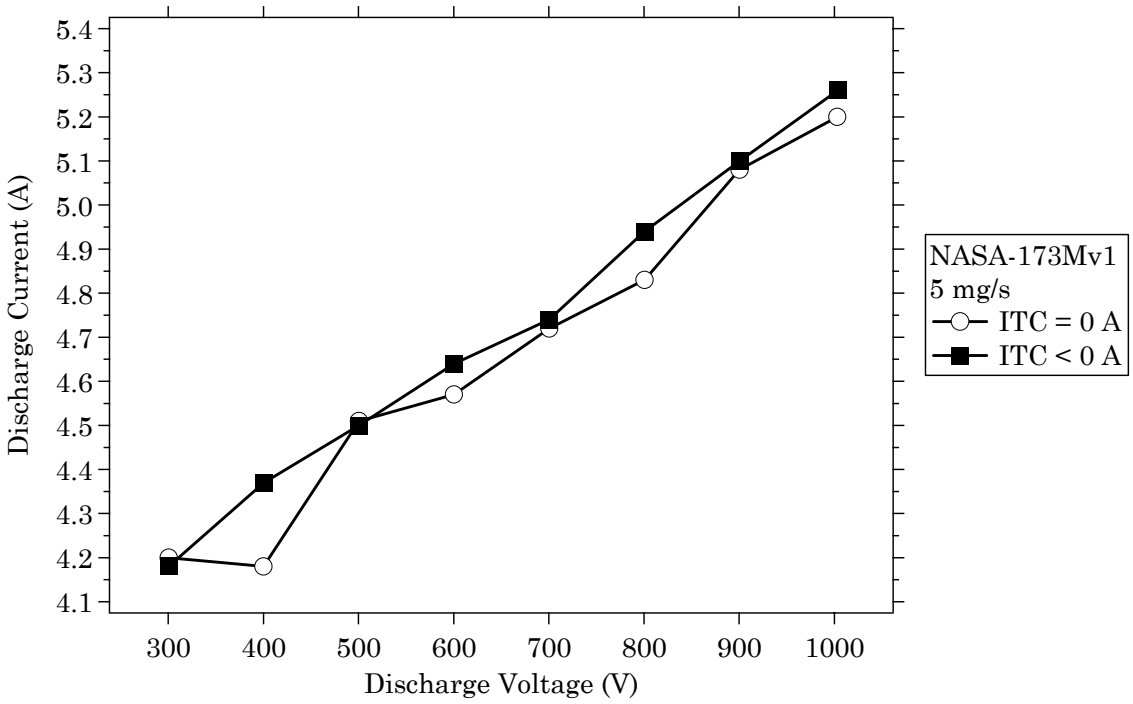

Figure 7-20 Discharge current versus discharge voltage of the NASA-173Mv1 at 5 mg/s. (Anode #1)

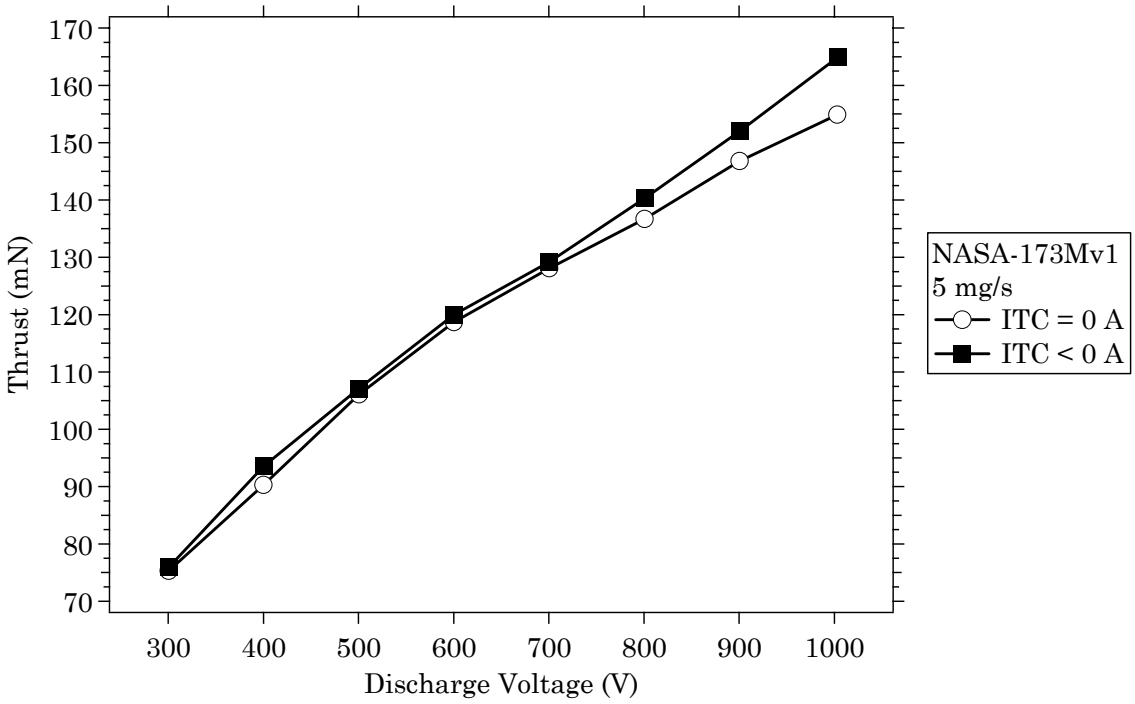

Figure 7-21 Thrust versus discharge voltage of the NASA-173Mv1 at 5 mg/s. (Anode #1)

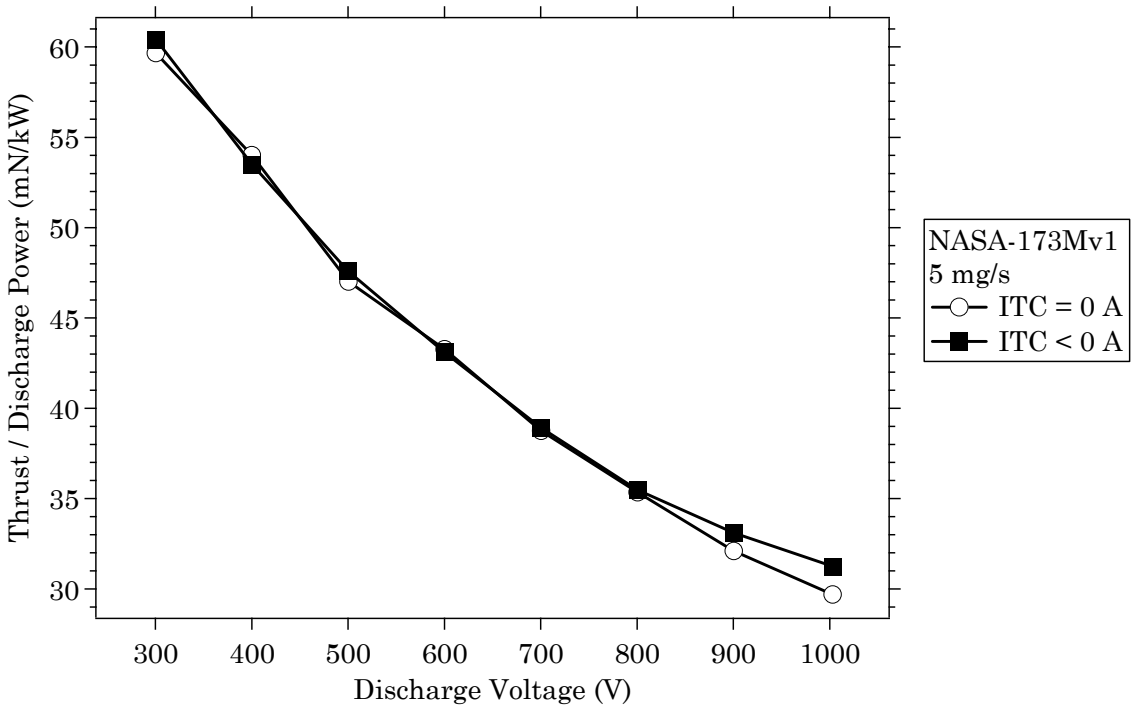

Figure 7-22 Thrust-to-discharge power ratio versus discharge voltage of the NASA-173Mv1 at 5 mg/s. (Anode #1)

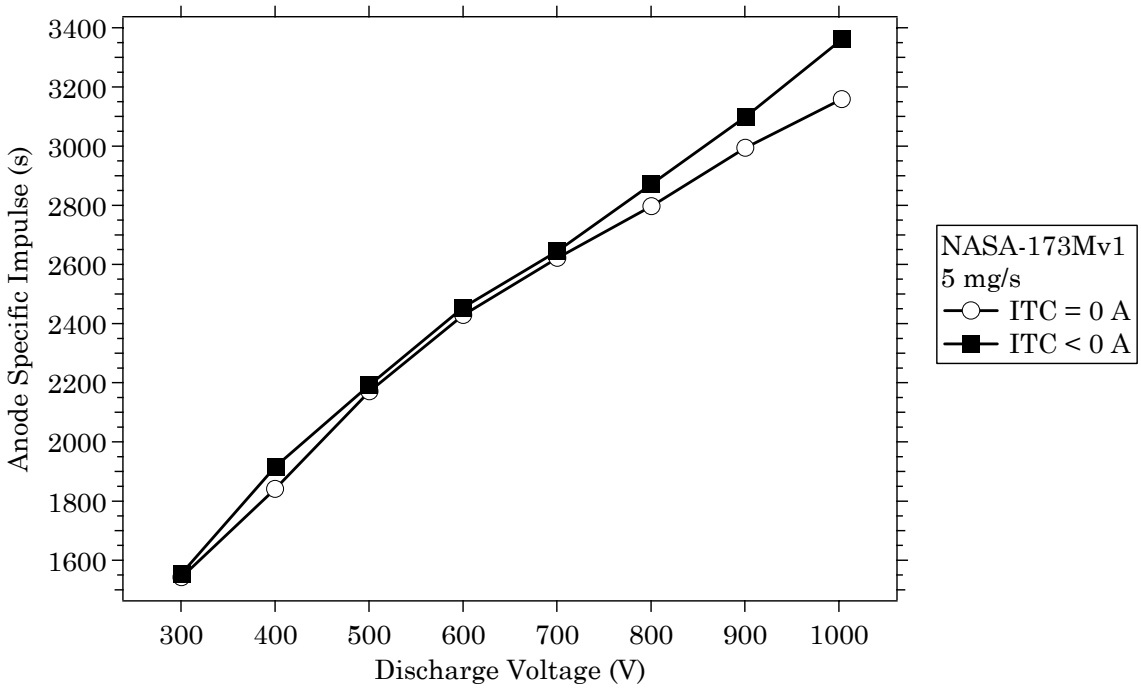

Figure 7-23 Anode specific impulse versus discharge voltage of the NASA-173Mv1 at 5 mg/s. (Anode #1)

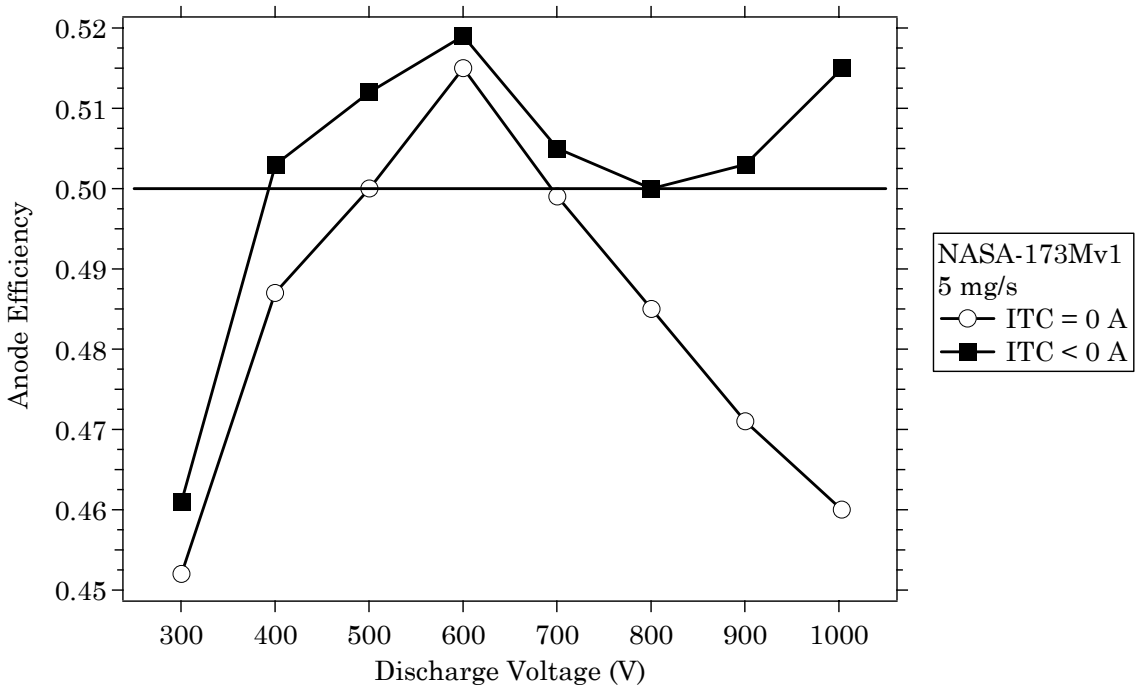

Figure 7-24 Anode efficiency versus discharge voltage of the NASA-173Mv1 at 5 mg/s. (Anode #1)

7.5.1.3 Magnetic field measurements

The relative change in the maximum radial magnetic field on channel centerline, normalized by an arbitrary constant B_o, is shown in Figure 7-25. In the figure, two curves are shown corresponding to operation with zero internal trim coil (ITC) current and operation with the internal trim coil current corresponding to maximum efficiency, as discussed below. The magnetic field was nearly constant from 300 to 500 V and then increased for discharge voltages greater than 500 V. The relative increase of the magnetic field over discharge voltages of 300 to 1000 V was 2.7 without the internal trim coil and 2.5 when the internal trim coil was used.

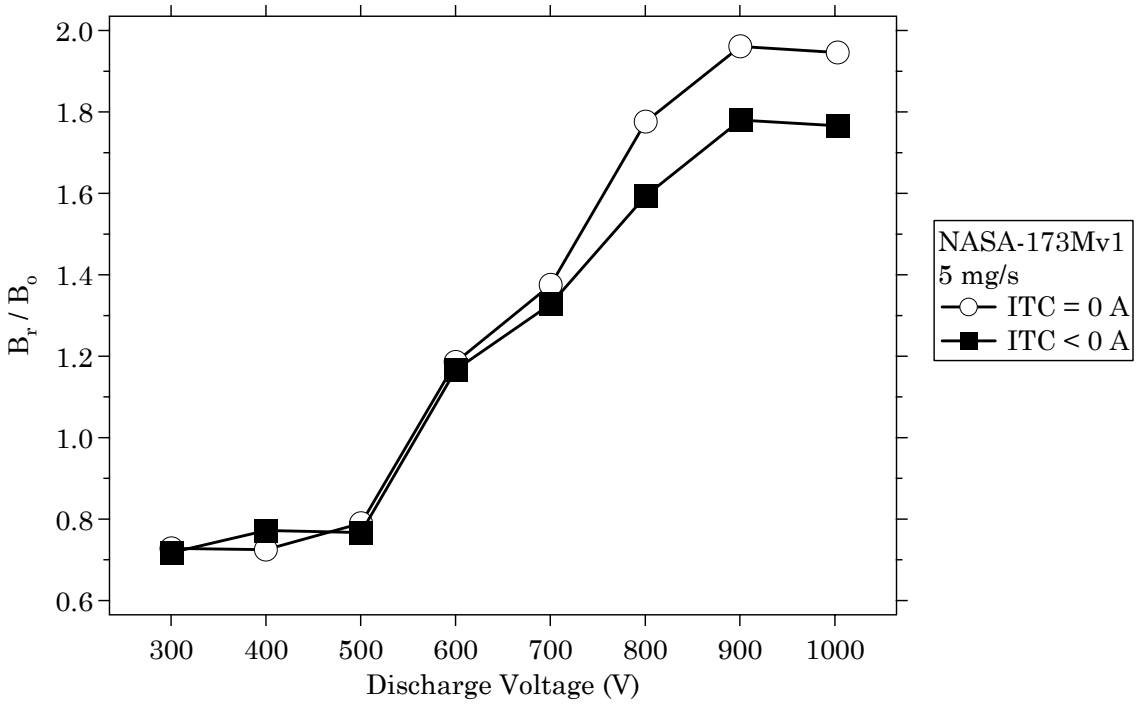

Figure 7-25 Maximum radial magnetic field on channel centerline versus discharge voltage of the NASA-173Mv1. (Anode #1)

7.5.1.4 Measurement uncertainty

While the absolute error from any experiment can be large, the relative error between data points can be much less depending on how data were collected. Recall that thrust data with the internal trim coil were taken at constant voltage and mass flow rate. Uncertainty in the thrust, mass flow rate, current, and voltage would therefore be a constant offset to the data. An error analysis estimated the average relative error at a given voltage to be 0.7 mN, 15 s, and 0.3%, for the thrust, specific impulse, and efficiency, respectively.

Since the efficiency increased on average by 2% when the internal trim coil was used (a maximum of 5.5% was observed at 1000 V), it was concluded that the trends shown in the figures at fixed discharge voltage were not a result of relative measurement error. The average increase in specific impulse and thrust was 70 s and 3 mN, respectively, which were greater than the relative error estimates. The

maximum increase in the specific impulse and thrust was 200 s and 10 mN, respectively, both of which occurred at 1000 V.

The error between data at different voltages would be quantified best by the absolute error. The absolute error was largely determined by the uncertainty in the thrust and anode flow controller. Analysis has shown the average uncertainty for both the thrust and anode flow controller to be ±1.5% of the measured value (see sections 6.2.1.1 and 6.3.1.1).

7.5.1.5 Numerical simulations of the magnetic field

A series of numerical simulations using the three-dimensional, magnetostatic solver, Magnet 6 by Infolytica, were conducted at each of the coil currents from the experiments described in sections 7.5.1.1-7.5.1.2. Repeated comparisons between predictions from Magnet and measurements of the magnetic field using a Hall probe connected to a Gaussmeter have shown agreement to within ±10%. The comparisons have shown that the uncertainty was determined primarily by positional and alignment errors of the Hall probe rather than the accuracy of Magnet.

Figure 7-26 shows the magnetic field topography for a series of cases corresponding to a 1000 V discharge voltage. Specifically, the inner and outer coil currents were each set to 5 A and the internal trim coil current was set to 0, -1, -2, and -3 A. The 0 A internal trim coil current case is representative of the magnetic field topography at other discharge voltages where the internal trim coil was not used. In general, at voltages of 300-700 V, the optimum internal trim coil current was lower than at 1000 V. So for voltages of 300-700 V, the increase in the field line curvature more closely resembled the -1 A case in Figure 7-26 (or less depending on the particular internal trim coil current). At 800-1000 V, -2 A internal trim coil

current was the optimum determined in the experiments, but note that 800 V optimized at the slightly lower value of 4.5 A for the inner and outer coil.

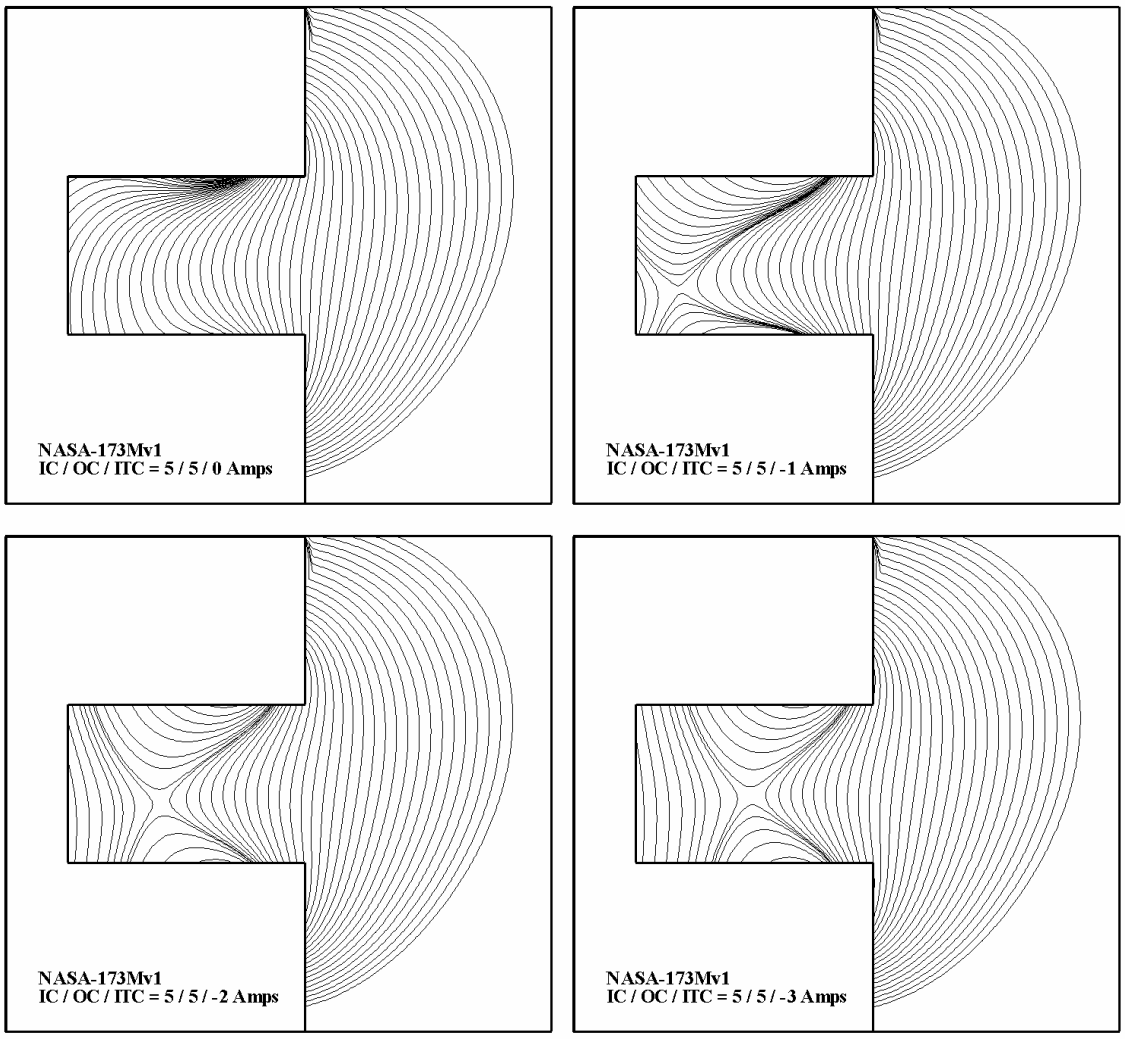

Figure 7-26 Magnetic field topography of the NASA-173Mv1 at several internal trim coil (ITC) currents and constant inner (IC) and outer coil (OC) currents of 5 A. (Anode #1)

7.5.2 Discussion

7.5.2.1 Effects of the magnetic field at the walls

The results in section 7.5.1.1 showed that coil current ratios (IC/OC) near 1.0 resulted in maximum thruster efficiency. Since magnetic field simulations have shown that the plasma lens was most symmetric about the channel centerline for

coil current ratios near 1.5, it was unexpected to find that thruster efficiency was greater at ratios of 1.0. This may have been the result of the higher outer wall magnetic fields that occurred at the lower coil current ratios since the plasma location is governed by Eqn. 7-1. Eqn. 7-1 implies that when the radial magnetic field profile across the channel is greater at the walls than the channel center, the plasma density will be greatest away from the walls at the minimum magnetic field.

As the coil current ratio decreased in the NASA-173Mv1 towards 1.0, the outer coils provided more of the magnetic flux to the channel and the magnetic field at the outer walls increased. At coil current ratios of 1.5 and 1.0, the maximum outer wall to centerline magnetic field ratio was 1.13 and 1.22, respectively. This may indicate a need to modify the fixed magnetic structure of the NASA-173Mv1 so that higher outer wall fields are possible for symmetric field line topographies.

In general, the performance began to decrease at coil current ratios less than 1.0. This was attributed to shifting the plasma lens far enough off centerline that other inefficiencies resulting from the asymmetry began to dominate. For example, changes in the magnetic field could alter the distribution and location of the Hall current, which would impact the ionization and acceleration efficiency, as well as thruster stability.

The magnetic field topographies shown in Figure 7-26 also support these conclusions. At 1000 V, as the internal trim coil current became more negative, the magnetic field topography gradually became more symmetric about the channel centerline while the ratio of the outer wall to centerline magnetic field remained approximately constant. However, it was not concluded that the performance benefits of the internal trim coil were solely the result of the plasma lens symmetry being restored. This was because the use of the internal trim coil at voltages of 300-

600 V only marginally shifted the plasma lens back to centerline. Other contributing factors to the performance benefits due to the internal trim coil are discussed in section 7.5.2.5.

7.5.2.2 Magnetic field scaling

Figure 7-25 shows that the magnetic field increased by a factor of 2.7 between 300 and 1000 V without the internal trim coil, and by a factor of 2.5 when the internal trim coil was used. These results demonstrate that merely increasing the magnetic field intensity is not a sufficient condition to maintain an increasing efficiency with voltage. Changing the magnetic field topography with the internal trim coil (with respect to the topography used at 1600 s specific impulse), was required to improve efficiency at high voltage. In Chapter 8, it is shown how changing the magnetic field topography in the NASA-173Mv2 resulted in a monotonically increasing efficiency characteristic with increasing discharge voltage.

7.5.2.3 Performance trends at constant discharge voltage

The variations in thruster performance when the internal trim coil was used in Figures 7-10 through 7-18 displays a remarkable level of complexity. In the following, only the most important trends will be discussed. First, consider the 300 V data shown in Figure 7-10. As the internal trim coil current was made more negative, an increase in thrust was accompanied by a decrease in the discharge current. The result was an increase in the specific impulse and efficiency. At some point, maximum thrust was reached but the discharge current continued to decrease. Since efficiency scales with the thrust squared, the decrease in thrust caused the specific impulse and efficiency also to decrease. Eventually, a minimum

in the discharge current was reached. Performance continued to decrease as the internal trim coil current was increased past the discharge current minimum.

Many of the same trends at 300 V are repeated at the other discharge voltages in Figures 7-11 through 7-18. In general, the thrust would initially increase, reach a maximum, and then continually decrease. Some notable exceptions are at 600 V, 800 V (IC,OC=3.5 A), and 900 V. At 600 V, a small decrease was initially measured, after which a maximum occurred. At 800 V (IC,OC=3.5 A) and 900 V, the thrust was still increasing at the last data point taken with the internal trim coil but the efficiency was decreasing probably because of increased electron current.

The general trend for the discharge current was to either initially decrease with internal trim coil current or remain approximately constant. Only the 400 V case continually increased with the use of the internal trim coil. There was usually a critical internal trim coil current after which the discharge current quickly increased. This was attributed to an increase in the field line curvature that shorted some of the electrons to the anode and rapidly increased the electron current.

Since the discharge current is the sum of the ion and electron current, simply knowing the relative change in discharge current was not always sufficient to determine whether it was the ions or electrons that were being affected the most when the discharge current changed. Following the trends in the thrust and the efficiency aids in this determination, but there were still inconclusive cases. Measurements of the ion current (and hence, electron current) are needed to better understand these trends. A method to compute the electron current from other thruster properties is demonstrated in Chapter 12.

The results at 800 V shown in Figures 7-15 and 7-16 suggest that further improvements in the efficiency may be achieved at other voltages. In Figure 7-15, the inner and outer coil currents were 3.5 A, and in Figure 7-16 these were set to 4.5 A. This method of increasing the coil currents was not systematically investigated at other voltages. The 3.5 A case had the highest efficiency without the internal trim coil, but a lower maximum efficiency than at 4.5 A when the internal trim coil was energized. This was probably due to the relative reduction in the magnetic field from using the internal trim coil. Using higher inner and outer coil currents with the internal trim coil maintains the magnetic field intensity at the magnitude of the lower inner and outer coil currents without the internal trim coil. Taken together, the results at 800 V highlight the importance of both the magnitude and shape of the magnetic field in achieving maximum thruster performance.

7.5.2.4 Overall performance trends

The data comparing operation with and without the internal trim coil in Figures 7-20 through 7-24 show several important trends. In Figure 7-20, the discharge current increased by more than 1 A as the voltage was increased from 300 to 1000 V whether or not the internal trim coil was used. At each voltage and at the optimum internal trim coil current, the discharge current was essentially unchanged from operation without the internal trim coil (the average increase was only 0.05 A). In Figure 7-21, thrust always increased at the optimum current for the internal trim coil, which resulted in a corresponding increase in the specific impulse (see Figure 7-23). Since, at the optimum internal trim coil current, the thrust increased while the discharge current was constant, it was likely that the electron current simultaneously decreased. However, measurements of the ion current and the ion

species fractions would be needed to reach further conclusions. A method to compute the electron current from other thruster properties is demonstrated in Chapter 12.

Trends in the discharge current and thrust are brought together in the efficiency characteristic shown in Figure 7-24. Without the internal trim coil, the efficiency maximized at 600 V and then continually decreased. This same behavior was observed in the thrusters discussed in section 3.2.2.1. The results with the internal trim coil indicated there was always some performance benefit to altering the magnetic field topography. Above 400 V, efficiencies were maintained above 50% while using the internal trim coil. Beyond 600 V, operation with the internal trim coil initially decreased efficiency, then another minimum was reached at 800 V, after which the efficiency increased at 900 and 1000 V. The largest gains in performance were observed at 1000 V, where the thrust, specific impulse, and efficiency improved by 10 mN, 200 s, and 5.5%, respectively, to 165 mN, 3360 s, and 51.5%. **Overall, the performance trends demonstrated that the peak in the efficiency characteristic observed without the internal trim coil could be mitigated when the magnetic field topography was tailored for operation at high-specific impulse.**

7.5.2.5 Correlating performance with magnetic field topography

To quantify which changes in the magnetic field topography were influencing the performance trends the most, results from the numerical simulations of the magnetic field were analyzed. Other than field line shape, this analysis indicated that the two most important aspects of the plasma lens characterizing changes in

the magnetic field were the magnitude of the magnetic field at the anode and the variation of the axial gradient of the radial magnetic field.

A vanishing magnetic field at the anode is desirable because this lowers the fall voltage in the anode sheath that is required to maintain current continuity. Moreover, it is undesirable for large electric fields (resulting from the fall voltage) to persist at the anode as this increases the likelihood of ions being accelerated into the channel walls. While avoiding anode falls should improve performance, this does not explain the benefits observed at 800 V (4.5 A) and above. At those voltages, because the internal trim coil current was so large, the radial magnetic field reversed direction and increased in magnitude. At 800 V (4.5 A) and with the internal trim coil energized, the magnitude of the radial magnetic field at the anode on centerline $|B_{r,anode}|$ was about 14% of the maximum radial field on centerline $B_{r,max}$. In comparison, without the internal trim coil $|B_{r,anode}|$ was about 6% of $B_{r,max}$, and for voltages of 800 V (3.5 A) or less, this was reduced to only 2% (when the internal trim coil was energized). The tendency then was for the internal trim coil to drive the anode field towards zero except for the data that utilized the most negative values of the internal trim coil current. From these observations, it was concluded that the anode field was not the only factor improving performance.

As discussed in sections 5.2.2 and 5.2.3, the axial gradient of the radial magnetic field strongly influences performance [2, 121, 224]. In the Russian literature, the approach has usually been to define an average value of the gradient based on the inverse of the scale length of variation of the radial magnetic field. It appears that this length scale was defined either as the distance from the anode to $B_{r,max}$, or as the distance from $B_{r,max}$ to the position where the field falls to $0.80*B_{r,max}$.

When applied to the magnetic fields from these experiments, there was no strong correlation between either of these definitions for the length scale and the operating point. It was concluded that a dimensionless axial gradient might be more applicable. To define this number, the average gradient of the centerline radial magnetic field was defined as

$$\left\langle \nabla_z B_r \right\rangle \equiv \frac{B_{r,\max} - B_{r,anode}}{z_{\max} - z_{anode}}, \tag{7-2}$$

where z_{max} was the axial coordinate of $B_{r,max}$, and z_{anode} was the axial coordinate of the anode. In order to non-dimensionalize the average gradient, a characteristic length scale and magnetic field were needed. $B_{r,max}$ was chosen for the magnetic field and the scale length was chosen as the distance from $B_{r,max}$ to the anode

$$L_B \equiv z_{\max} - z_{anode}. \tag{7-3}$$

With these choices, the average, dimensionless gradient of the centerline radial magnetic field was defined as

$$\vartheta \equiv \frac{L_B}{B_{r,\max}} \times \left\langle \nabla_z B_r \right\rangle = 1 - \frac{B_{r,anode}}{B_{r,\max}}. \tag{7-4}$$

The definition of ϑ, while arbitrary, removed the dependence of the channel in the calculation. This seemed appropriate because modern Hall thrusters are designed with $B_{r,max}$ located at or near the exit plane [2].

For a given channel length, the value of ϑ yields additional information about $B_{r,anode}$. When ϑ is equal to unity, $B_{r,anode}$ is zero. Values less than one correspond to a positive value of $B_{r,anode}$ and values greater than one correspond to a negative value of $B_{r,anode}$. Figure 7-27 plots the value of ϑ at each discharge voltage from these

experiments. Without the internal trim coil, ϑ was a constant value of 0.94. For moderate values of the internal trim coil current (300-800 V [3.5 A]), the value of ϑ was on average 1.00. When the internal trim coil current was large (800 [4.5 A]-1000 V), the value of ϑ increased to an average of 1.14.

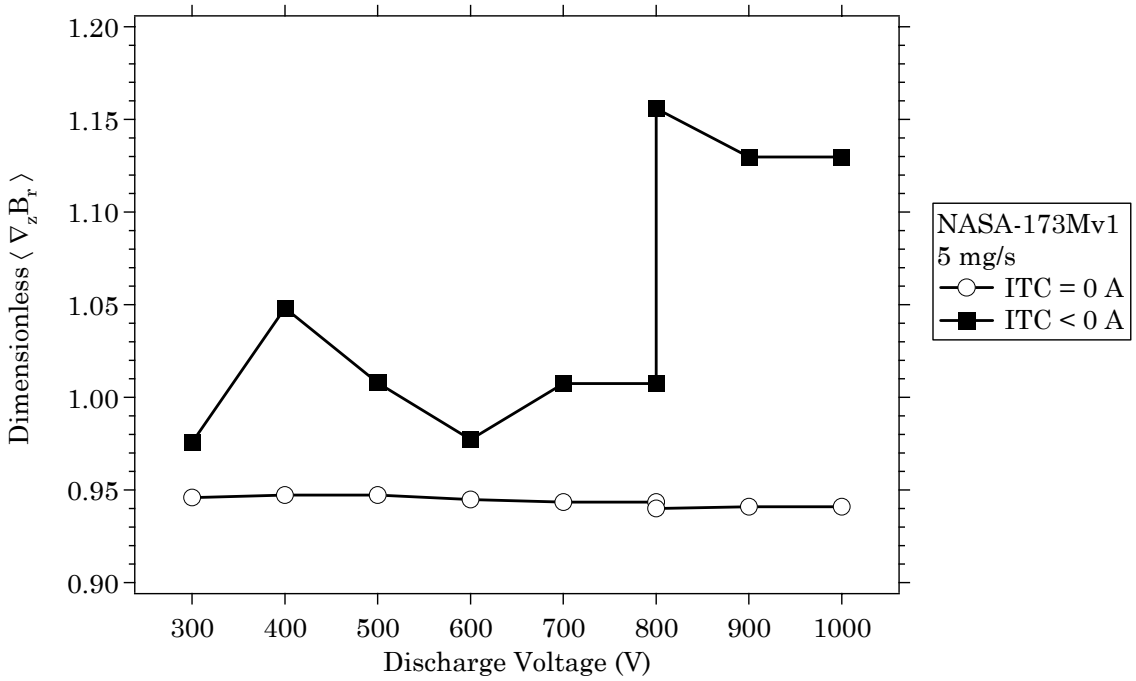

Figure 7-27 Dimensionless gradient of the radial magnetic field versus discharge voltage of the NASA-173Mv1 at 5 mg/s. (Anode #1)

These results implied that high-specific impulse thrusters operating at low current densities might benefit from short channel lengths and steep gradients in the magnetic field. Accordingly, the performance of the NASA-173Mv1 at flow rates of 5 mg/s and at voltages above 800 V may see further improvements if the anode is repositioned to the point where the centerline radial field vanishes. This point closely corresponds to the saddle point shown in the field lines of Figure 7-26.

Studies of channel length dependence have been hindered in the past because they usually did not change the magnetic field gradient along the length of the channel or the gas distributor [235, 236]. So long as the magnetic field is properly

modified, the real challenge of a short channel is maintaining uniform flow distribution. Apparently, these difficulties have been largely overcome in the BPT-4000, which employs a channel width to length ratio of 2:1 [217]. A long, narrow anode may also be a viable solution. Such a configuration might resemble the anode design typically used in anode layer thrusters (see Figure 3-2) [133].

7.5.3 Summary of results from section 7.5

The NASA-173Mv1 was operated at 300-1000 V and 5 mg/s to investigate whether performance improvements could be realized by changing the magnetic field topography with the internal trim coil. Without the internal trim coil, maximum thruster efficiency occurred at a discharge voltage of 600 V. With the internal trim coil energized, there was always some performance benefit to altering the magnetic field topography. Above 400 V, efficiencies greater than 50% were maintained and above 900 V greater than 3000 s specific impulse was demonstrated. The largest gains in performance were observed at 1000 V, where the thrust, specific impulse, and efficiency improved by 10 mN, 200 s, and 5.5%, respectively, to 165 mN, 3360 s, and 51.5%. **The results demonstrated that the peak in the efficiency characteristic observed without the internal trim coil could be mitigated when the magnetic field topography was tailored for high-specific impulse.** Further, the results validated the design approach of the NASA-173Mv1, which was based on the hypothesis that the magnetic field topography of a high-specific impulse Hall thruster would be different than at 1600 s specific impulse.

Analysis of the magnetic field identified several factors that contributed to the performance benefits gained by altering the magnetic field topography. These factors were:

1. the symmetry of the magnetic field lines,
2. the concavity of the magnetic field lines,
3. the magnitude of the radial magnetic field at the anode face, and
4. the dimensionless axial gradient of the centerline, radial magnetic field.

Other factors that were common to high-specific impulse operation with or without the internal trim coil were:

1. the ratio of the radial magnetic field at the discharge chamber walls to the centerline value, and
2. the magnitude of the magnetic field.

The magnetic field analysis suggested several ways to improve the magnetic field of the NASA-173Mv1. These changes were later integrated into the follow-on thruster, the NASA-173Mv2. The performance trends also demonstrated a need for a rigorous examination of high-specific impulse Hall thrusters through probe-based diagnostics. This study is the subject of part III of this dissertation, which begins with Chapter 10.

7.6 Operating characteristics

This section describes the operating characteristics of the NASA-173Mv1 after anode #1 was replaced with anode #2. The experiments in section 7.4 and 7.5 used anode #1. To quantify how the asymmetric neutral flow from anode #1 affected thruster performance, section 7.6.1 begins by comparing the thruster characteristics

with the different anodes. Next, to quantify how the plasma lens in the NASA-173Mv1 improved performance, section 7.6.2 compares the NASA-173Mv1 to the P5. Lastly, sections 7.6.3 through 7.6.6 discuss the results from a performance and plasma characterization of the NASA-173Mv1. In Chapter 9, the results from sections 7.6.3 through 7.6.6 are compared to results discussed in Chapter 8 for the NASA-173Mv2.

All experiments described in this section were conducted in Vacuum Facility 12 (VF12) at NASA GRC. VF12 is described in section 6.2.2 and the various diagnostics that were used are described in section 6.3. The NASA-173Mv1 had been previously operated with anode #2 for over sixty hours before the experiments described in this section began.

In the experiments, the thruster was operated at discharge voltages spanning 300-900 V and anode flow rates of 5-15 mg/s. Only data for anode flow rates of 10 mg/s span the entire voltage range of 300-900 V.[34] The cathode flow rate was 10% of the anode flow rate to ensure that there was a sufficient supply of electrons for neutralization and ionization. The thruster was stable and capable of sustained operation during the period when data at a given operating point were recorded. The specific thruster operating points are described at the beginning of each of the sub-sections that follow.

The general method for taking thrust data was to set the voltage and flow rate and then the effects of each coil on discharge current, plasma oscillations, and

[34] The experiments with the NASA-173Mv1 presented in this section were less complete (in terms of the voltages that were tested and the amount of time spent optimizing performance at each operating point) than those discussed in Chapter 8 for the NASA-173Mv2. This was because the NASA-173Mv2 had been fabricated and characterized before the NASA-173Mv1 could be characterized with anode #2. There was then less of a need to perform a full characterization of the NASA-173Mv1 since the NASA-173Mv2 design had already demonstrated high-efficiency, high-specific impulse operation. Regardless, the NASA-173Mv1 experiments proved to be very useful in showing how changes to the magnetic field in the NASA-173Mv2 resulted in superior performance at high-specific impulse (see Chapter 9).

anode efficiency were investigated. In this way, coil currents were identified that were near maximum thruster efficiency. At some operating points, the internal trim coil showed little or no benefit to thruster performance. Maximum efficiency was generally realized where the discharge current and oscillations were minimized.

Plume measurements and plasma oscillation data were collected concurrently after determining coil currents for a given voltage and flow rate from the performance measurements. Similarly, the magnetic field was computed from Gaussmeter measurements after the performance characterization.

7.6.1 Effects of neutral gas distribution

When the neutral gas distribution entering the discharge chamber of a Hall thruster is azimuthally non-uniform, localized regions of intense ionization are created around the circumference of the discharge chamber that create azimuthal gradients of the plasma density. These density gradients can induce azimuthal electric fields, which when coupled with the magnetic field, result in ExB particle drifts into the walls and anode that increase thermal loads and decrease the current utilization efficiency. As the thruster temperature rises, there is usually some point where the discharge current will begin to increase rapidly. Shortly thereafter, the plasma discharge will unexpectedly extinguish. The cumulative effects of asymmetric propellant distribution are decreased thruster efficiency and limitations of the thruster power range.

Replacing anode #1 with anode #2 in the NASA-173Mv1 substantially increased thermal margin, plume symmetry, and thruster performance. After the anode was replaced, the thruster could be operated in excess of the previous limit of 5 kW (to date, the thruster has been operated at 8.5 kW without incident).

Improvements to the symmetry of the ion current density profiles were also evident (*e.g.*, compare Figure 7-9 for anode #1 to Figures 7-37 through 7-41 for anode #2). At all mass flow rates, the double peak profile was clearly defined and much more symmetric about thruster centerline with anode #2.

Figures 7-28 through 7-31 highlight changes to thruster performance after replacing the anode. The figures compare data collected with anode #2 to data from section 7.5 collected with anode #1 when the thruster was operated at 5 mg/s.

Figure 7-28 shows the variation of the current-voltage characteristic of the NASA-173Mv1 with the different anodes. At constant voltage, replacing the anode generally decreased the discharge current. Without the internal trim coil, between 300-400 V the current dropped by only 0.02 A on average, but at 500-600 V the current dropped by 0.16 A on average. Figure 7-29 shows how the thrust increased by an average of 8 mN after replacing the anode. Expressed as a percentage of the thrust at each voltage, thrust increased by an average of 8%. Since discharge current decreased while thrust increased, replacing the anode must have decreased the electron current to the anode and improved the focusing of ions exiting the discharge chamber. The result was a substantial increase in thruster efficiency. As shown in Figure 7-30, the anode efficiency increased by an average of 10% (absolute) after replacing the anode.

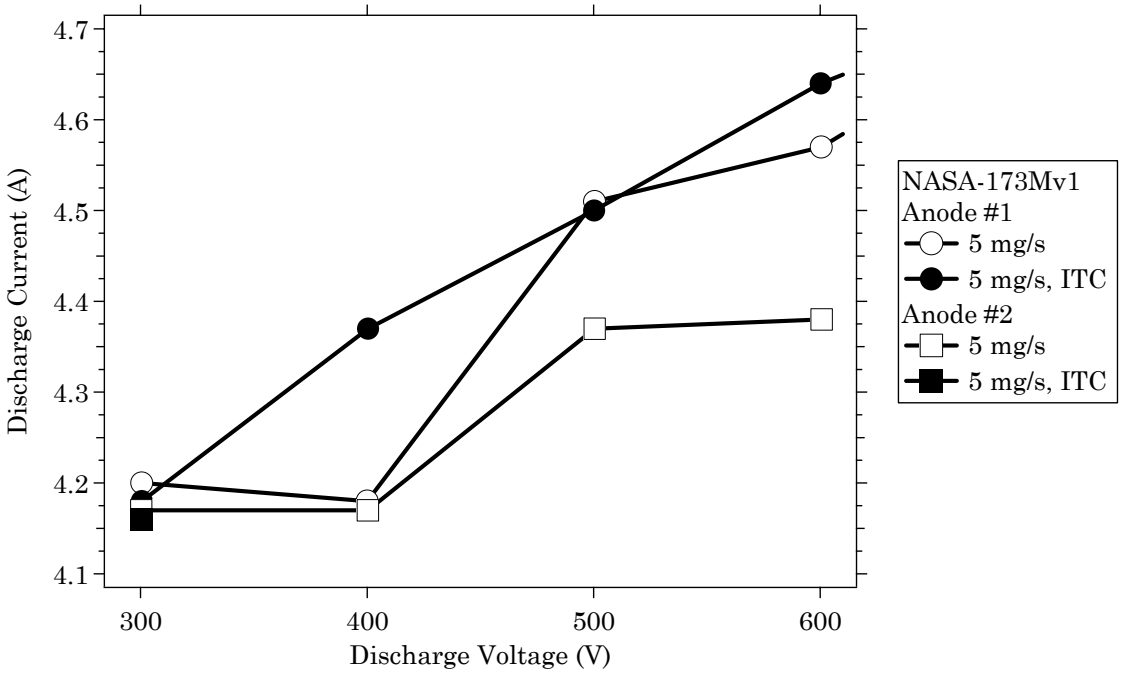

Figure 7-28 Discharge current versus discharge voltage for anode #1 and anode #2 of the NASA-173Mv1. At constant voltage, replacing the anode decreased the discharge current.

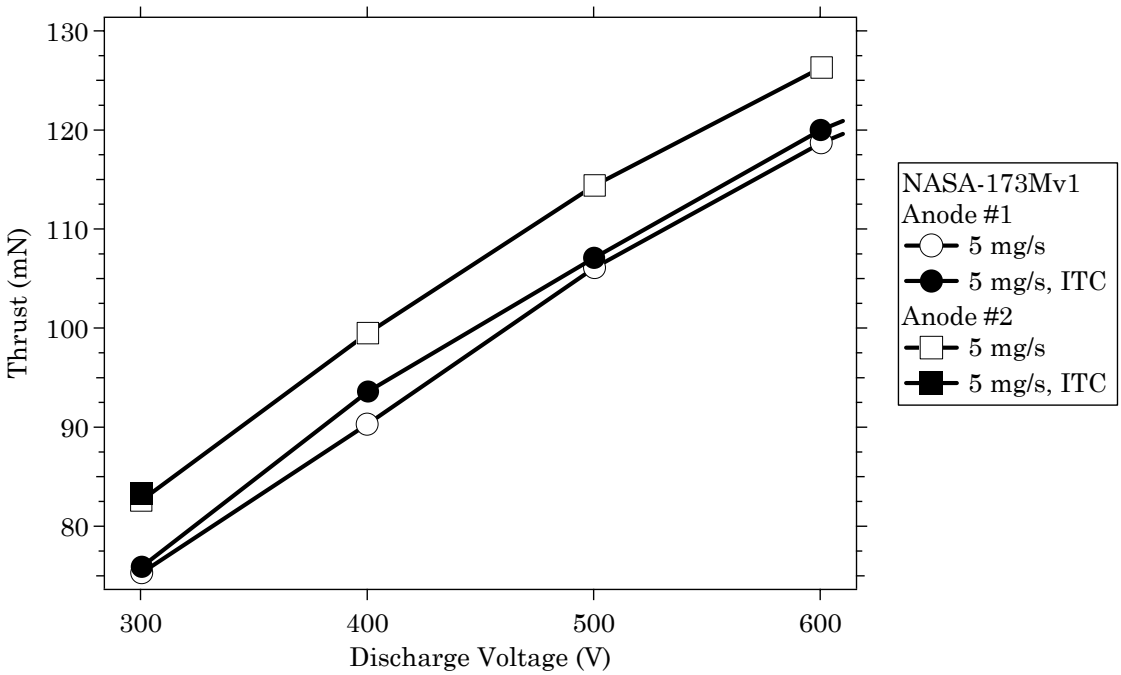

Figure 7-29 Thrust versus discharge voltage for anode #1 and anode #2 of the NASA-173Mv1. Replacing the anode resulted in an average increase in thrust of 8%.

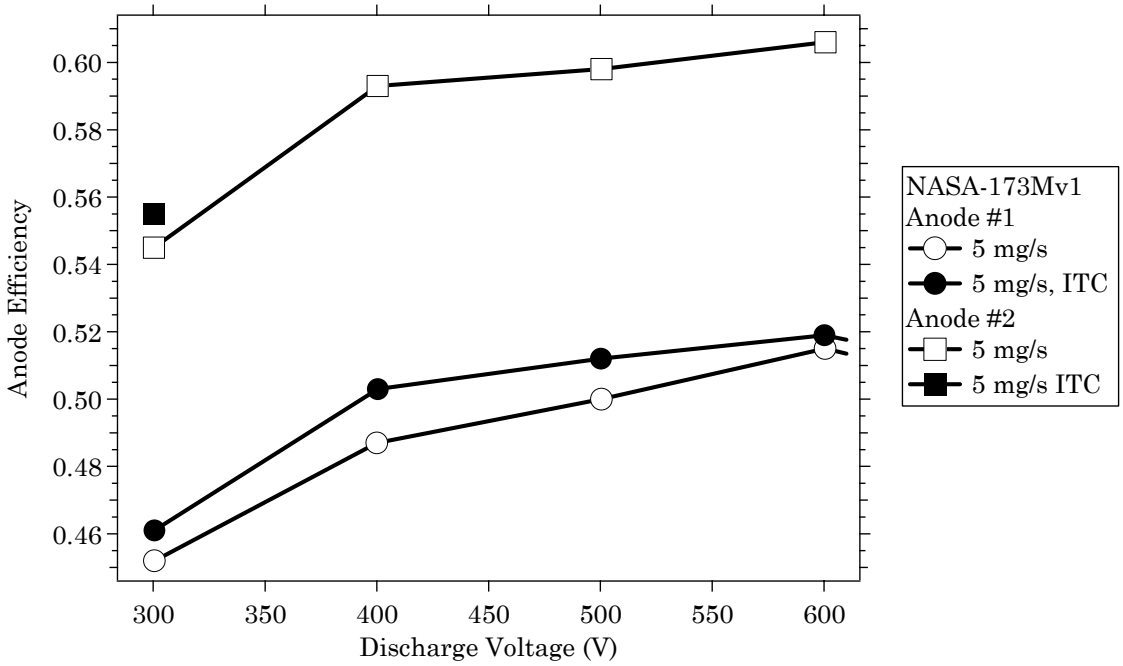

Figure 7-30 Anode efficiency versus discharge voltage for anode #1 and anode #2 of the NASA-173Mv1. Replacing the anode resulted in an average increase in efficiency of 10% (absolute).

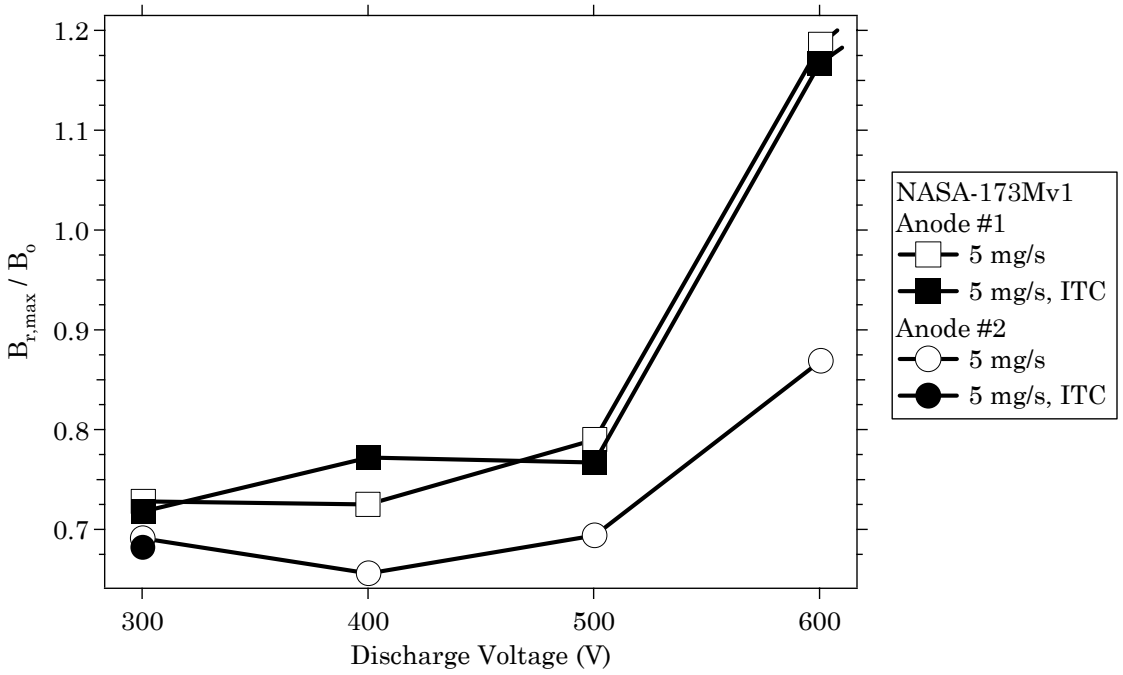

Figure 7-31 Radial magnetic field versus discharge voltage for anode #1 and anode #2 of the NASA-173Mv1. Replacing the anode decreased the required magnetic field at each voltage.

Figure 7-31 shows the magnetic field at each voltage for the different anodes. After replacing the anode, the required magnetic field decreased by an average of 7% between 300-500 V and by 32% at 600 V. Recall that maximum efficiency occurred at 600 V with anode #1 (see Figure 7-24). A decrease in magnetic field was not unexpected, as this would tend to decrease the elevated axial electron current resulting from the asymmetries. In effect, the thruster has to "fight" the electrons harder when the asymmetries opened up "electron highways" through the dense regions of the plasma.

7.6.2 Performance comparison to the UM/AFRL P5

After replacing the NASA-173Mv1 anode, thruster performance was compared to the UM/AFRL P5 Hall thruster. The NASA-173Mv1 was based on several aspects of the P5 design, with the notable exception of the magnetic field topography (see section 7.2). Thus, differences in the performance and plume characteristics were attributed to changes in the magnetic field.

Figure 7-32 compares the anode efficiency of the P5 and the NASA-173Mv1 at several discharge voltages and mass flow rates. To ensure the most accurate comparison, the NASA-173Mv1 data were collected at the same mass flow rates as the performance characterization of the P5 in Ref. [200]. The NASA-173Mv1 was only operated at 300 and 500 V for this particular comparison. The P5 data are included as Table A-1 in Appendix A. The NASA-173Mv1 data are included as Table B-3 in Appendix B.

At all operating points, the efficiency of the NASA-173Mv1 was substantially greater than the P5. For example, at 300 and 500 V and 14.5 mg/s, the efficiency of the NASA-173Mv1 was 18% and 10% greater (in absolute scale) than the P5,

respectively. This was a marked improvement in thruster efficiency, which was simply the result of changing the magnetic field topography.

The performance of the NASA-173Mv1 was also found to be comparable to the performance of the 4.5 kW SPT-140 and the 4.5 kW BPT-4000 (not shown) [55, 56, 227, 237]. A similar statement can be made for the NASA-173Mv2 discussed in Chapter 8. Table B-5 in Appendix B and Table C-4 in Appendix C include data used to compare with the SPT-140 and BPT-4000 for the NASA-173Mv1 and v2, respectively.

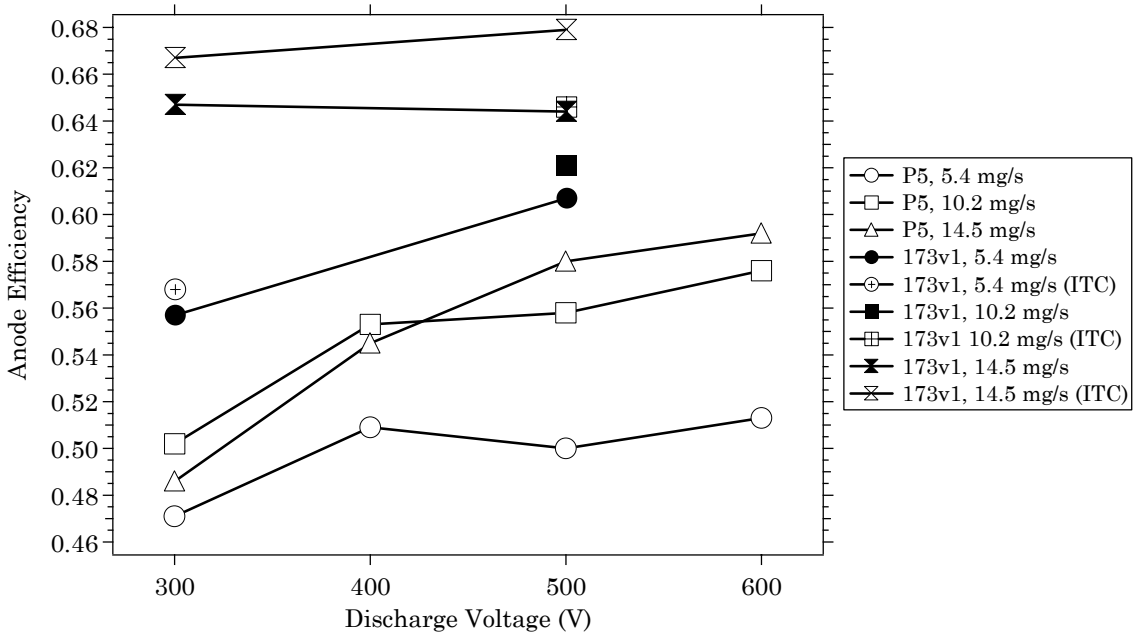

Figure 7-32 Comparison of the anode efficiency versus discharge voltage of the P5 and the NASA-173Mv1 at 5.4-14.5 mg/s.

7.6.3 Performance (5-15 mg/s)

This section presents results from a performance characterization of the NASA-173Mv1. The NASA-173Mv1 was tested at anode flow rates of 5, 10, and 15 mg/s. By testing at constant flow rates, current density was held approximately constant as the voltage increased, which was equivalent to increasing the power

density. The data collected at 10 mg/s covered the largest range of discharge voltages. Performance data are tabulated in Table B-4 in Appendix B.

The different thruster operating points are shown in the current-voltage characteristic plotted in Figure 7-33. The discharge current slowly increased with the discharge voltage. At a fixed voltage, changing the magnetic field with the internal trim coil decreased the discharge current. Note that at 10 mg/s that the discharge current was approximately constant between 600-900 V.

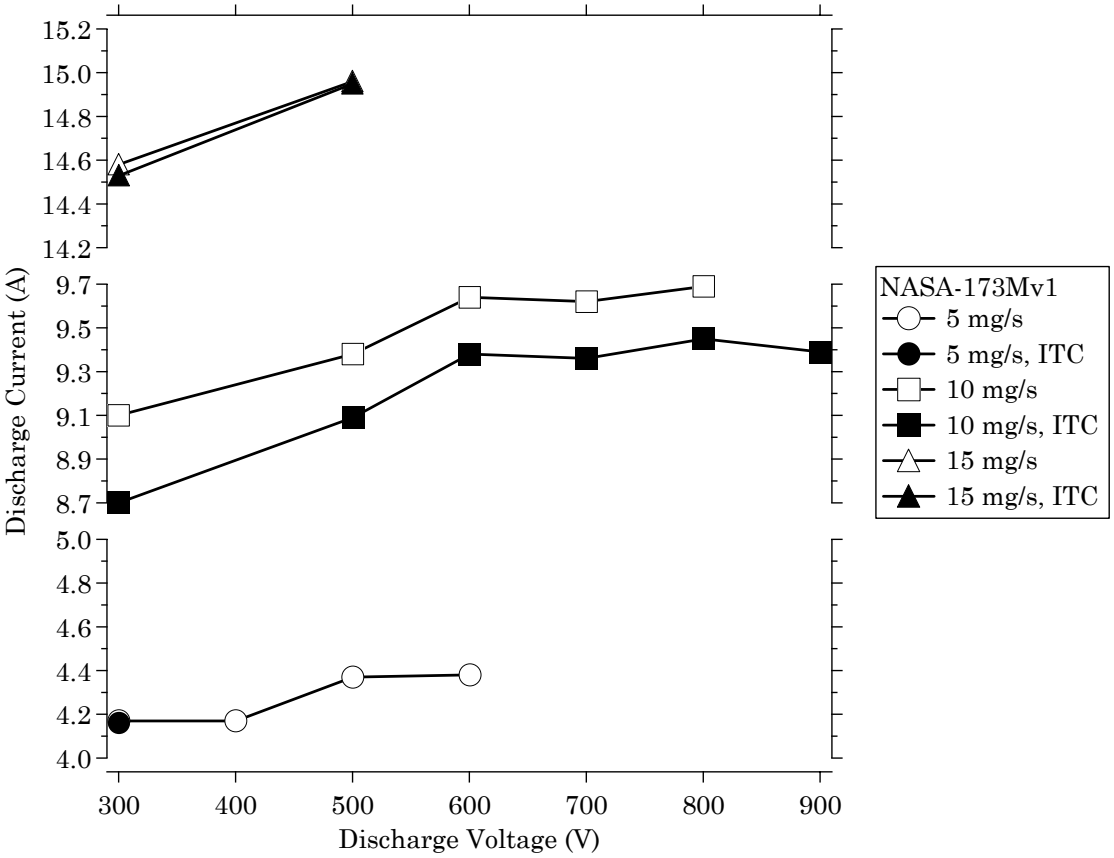

Figure 7-33 Discharge current versus discharge voltage of the NASA-173Mv1 at 5-15 mg/s.

The thrust-to-total power ratio, total specific impulse, and total efficiency at each of the operating points that were tested are shown in Figures 7-34 through 7-36, respectively. Over the entire range of operating conditions, the thrust-to-power ratio varied from 38-68 mN/kW, thrust (not shown) varied from 83-392 mN,

total specific impulse varied from 1530-3030 s, and total efficiency varied from 48.8-61.5%.

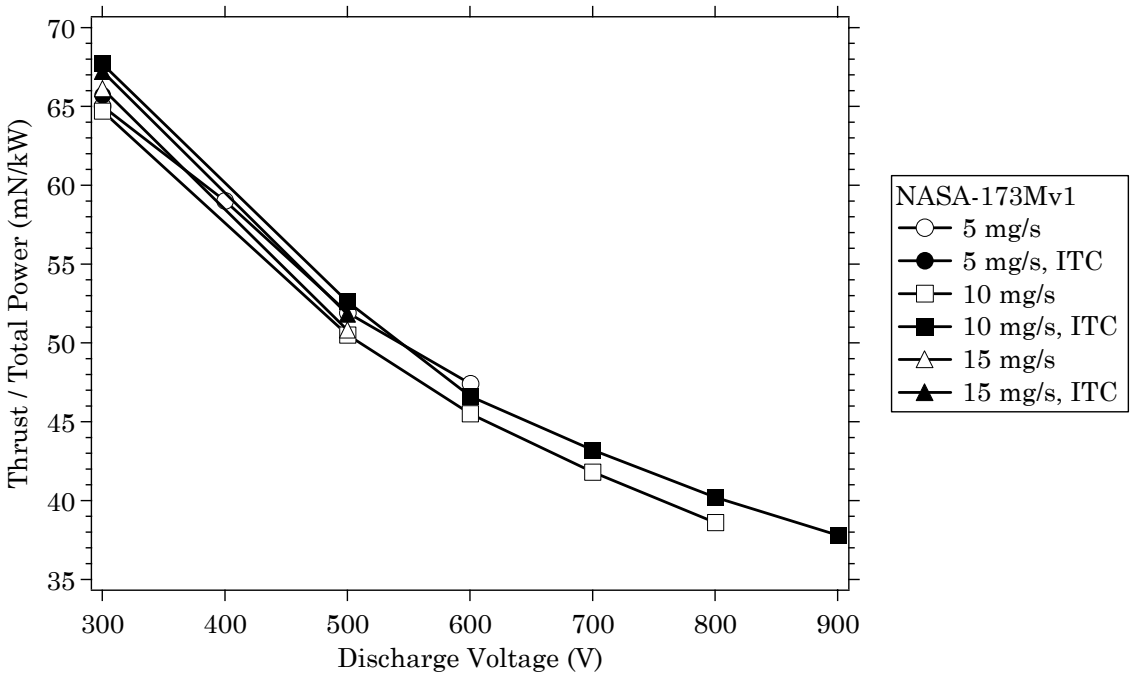

Figure 7-34 Thrust to total power ratio versus discharge voltage of the NASA-173Mv1 at 5-15 mg/s.

In a cursory examination of the effects of the internal trim coil at 5 mg/s, efficiency increased at 300 V and only marginally improved performance between 400-600 V (no data are shown for 400-600 V for this reason). This was still consistent with the experiments in section 7.5, which showed the largest improvements to performance at voltages greater than 600 V.

Benefits from the internal trim coil were measured at flow rates of 10 and 15 mg/s. The performance benefit resulted from an increase in thrust and a decrease in discharge current when the internal trim coil was energized. Note that at 10 mg/s that the efficiency was approximately constant between 600-900 V when the internal trim coil was energized. The efficiency characteristic at 10 mg/s still indicated a maximum around 500-600 V. This showed that additional changes to the magnetic

field topography were still required to eliminate the efficiency peak. Such changes were integrated in the design of the NASA-173Mv2 (see Chapter 8).

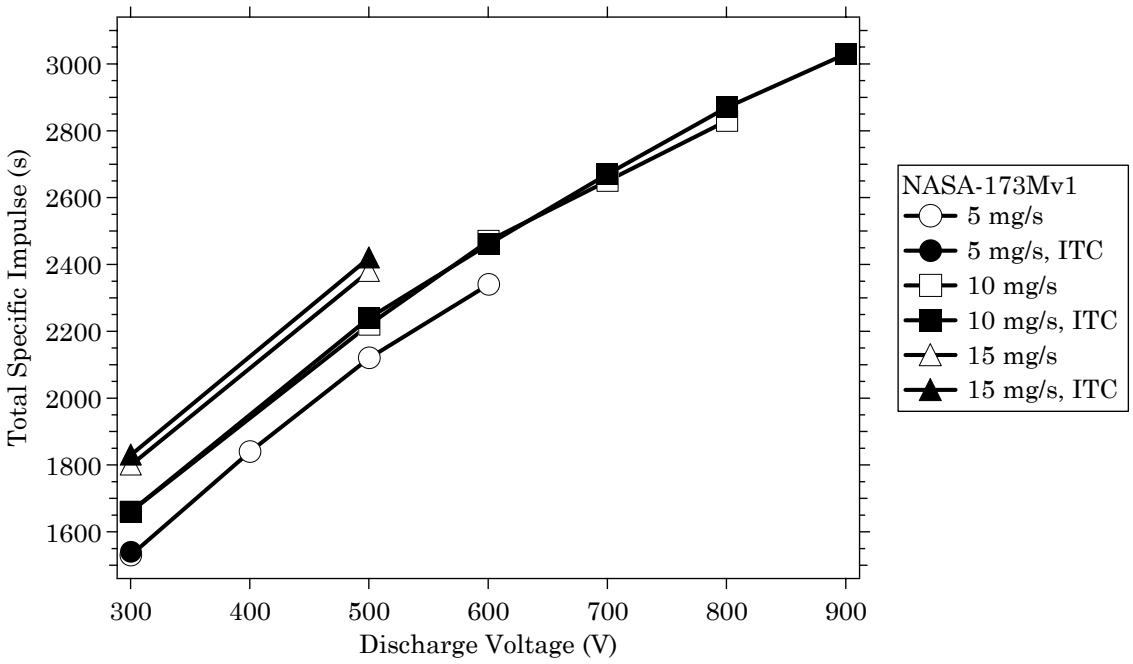

Figure 7-35 Total specific impulse versus discharge voltage of the NASA-173Mv1 at 5-15 mg/s.

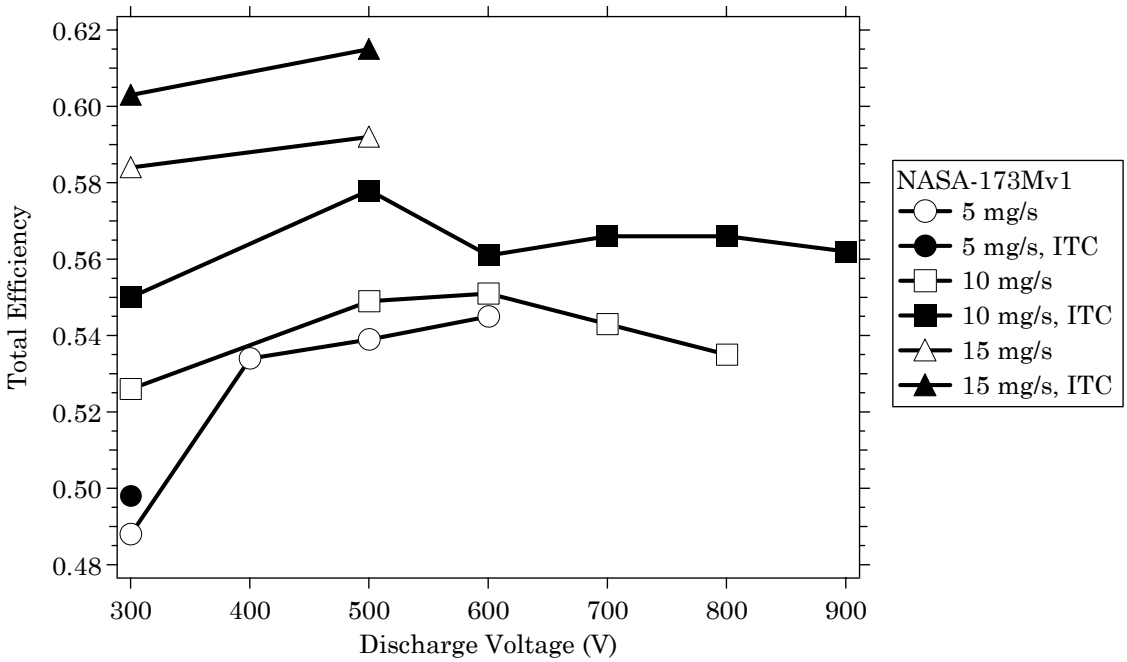

Figure 7-36 Total efficiency versus discharge voltage of the NASA-173Mv1 at 5-15 mg/s.

7.6.4 Ion current density (5-15 mg/s)

This section presents results from measurements of the ion current density in the plume of the NASA-173Mv1. The NASA-173Mv1 was tested at anode flow rates of 5, 10, and 15 mg/s and discharge voltages of 300 and 500 V. Coil currents were chosen from performance measurements discussed in section 7.6.3 and presented as Table B-4 in Appendix B. Plume profiles were measured with the inner and outer coils alone and with the addition of the internal trim coil (if the internal trim coil benefited performance). Figures 7-37 through 7-39 show the ion current density at constant flow rate while Figures 7-40 and 7-41 show the ion current density at constant discharge voltage. Differences in the plume profiles as a function of flow rate, voltage, and magnetic field (due to using the internal trim coil) were quantified by calculating the plume divergence (see section 6.3.2). Figures 7-42 and 7-43 show the 95% plume divergence half-angle as a function of anode mass flow rate and discharge voltage, respectively.

In general, the ion current density profiles shown in Figures 7-37 through 7-39 were symmetric about the thruster centerline (zero degrees) and showed a double peak profile near centerline at each of the operating points. The symmetry of the ion current density profiles compared to those shown in Figure 7-9 was attributed to replacing anode #1 with anode #2 (see section 7.6.1). The double peak structure was attributed to the annular ion beam that results from the discharge chamber geometry. Additionally, the double peaks were taken as an indication that the ion beam was well-focused due to the plasma lens magnetic field topography (see section 7.4).

The ion current density profiles also show a change in slope beginning around 50º. Experiments and numerical simulations on a number of different Hall thrusters

have shown that the slope change results from the charge-exchange plasma present in all vacuum facilities due to the finite backpressure [32, 191, 234, 238, 239]. No attempts were made to correct for the effects of the charge-exchange plasma.

Changing the magnetic field topography with the internal trim coil markedly affected the shape of the ion current density profiles and the plume divergence. In general, when the internal trim coil was energized, a higher ion current density was measured near centerline while a decrease was measured at high angles from centerline. The net result was a decrease in plume divergence when the internal trim coil was energized. The decrease in plume divergence was greatest at 10 mg/s, where the divergence decreased by 6º at 300 V and by 4º at 500 V due to changing the magnetic field with the internal trim coil. Expressed as a percentage, the internal trim coil decreased plume divergence by 18% at 300 V and by 10 % at 500 V for a flow rate of 10 mg/s. The percentage decrease at 300 V, 5 mg/s was 3% and at 300 and 500 V, 15 mg/s the decrease was 6%.

Figure 7-42 shows that the plume divergence increased with increased discharge voltage, while Figure 7-43 shows that the plume divergence showed a general decrease with increased mass flow rate. However, the trend with voltage may be misleading because of the coarseness of the voltage interval. Shown in Figure 8-15, the plume divergence of the NASA-173Mv2 reached a maximum at 400 V and then continually decreased up to 1000 V. Additional measurements are needed to determine if a similar trend occurs with the NASA-173Mv1.

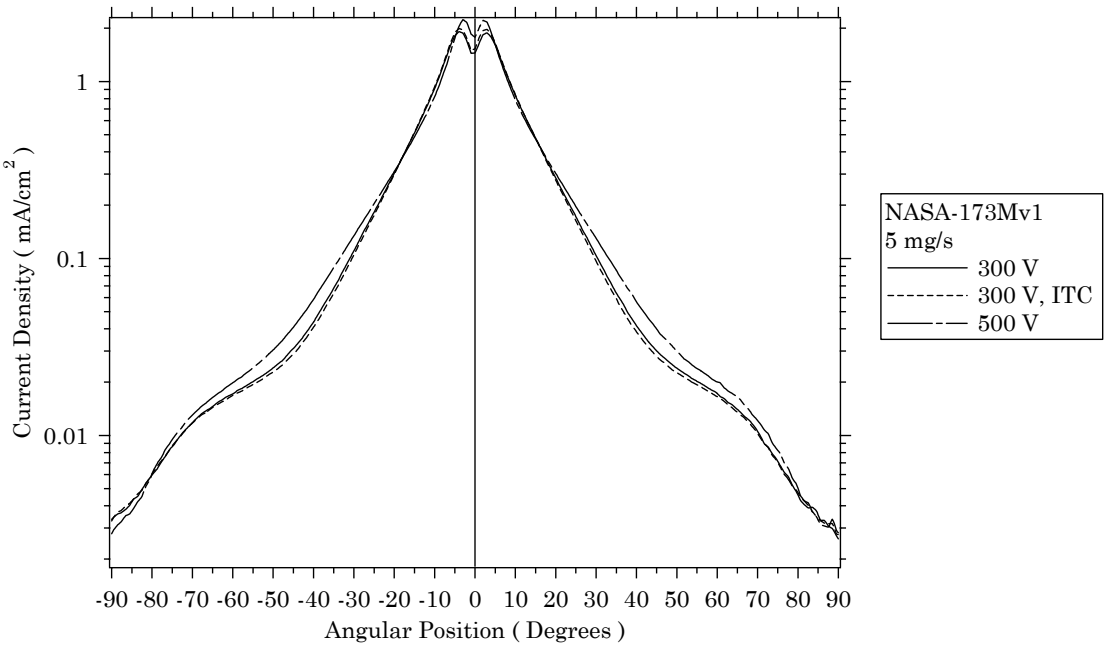

Figure 7-37 Ion current density in the plume of the NASA-173Mv1 versus angular position from thruster centerline at 5 mg/s.

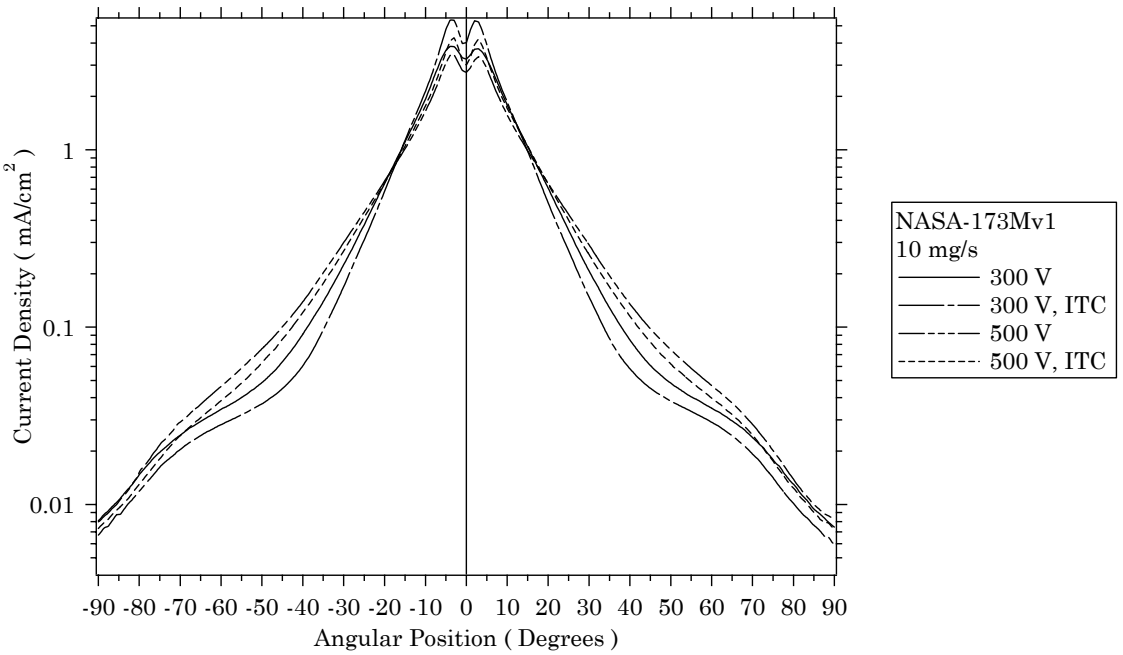

Figure 7-38 Ion current density in the plume of the NASA-173Mv1 versus angular position from thruster centerline at 10 mg/s.

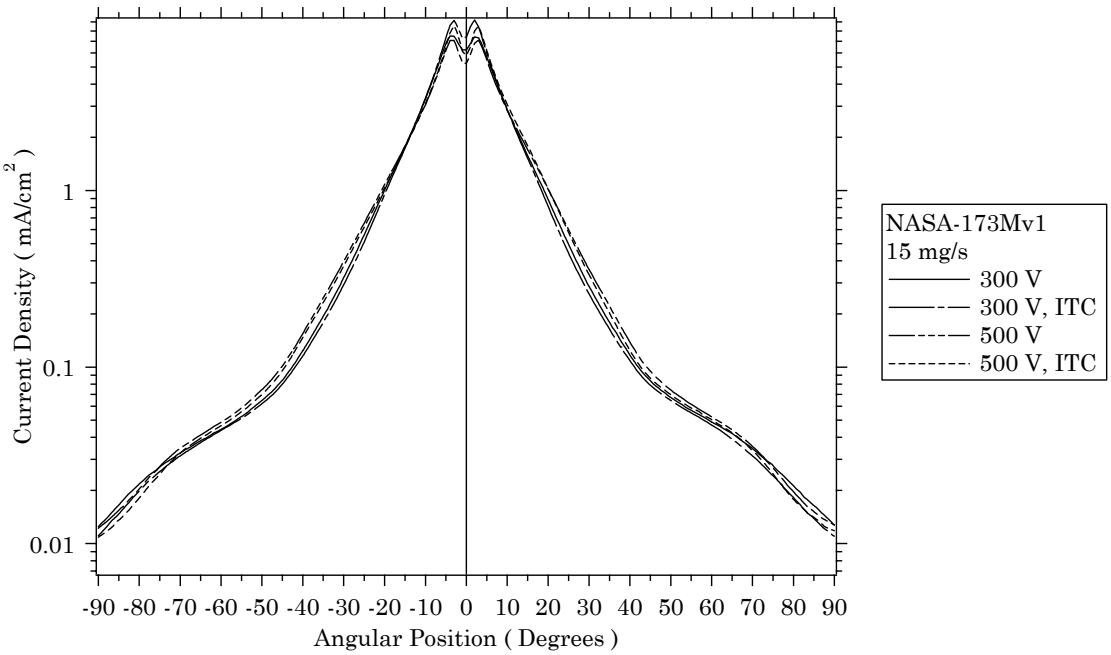

Figure 7-39 Ion current density in the plume of the NASA-173Mv1 versus angular position from thruster centerline at 15 mg/s.

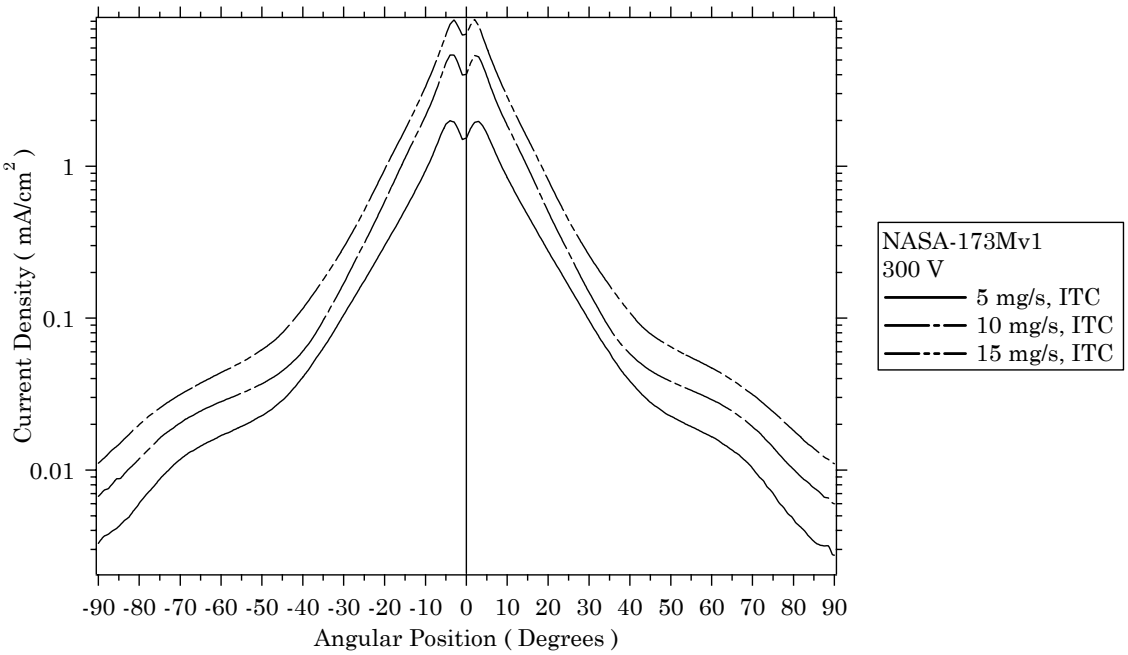

Figure 7-40 Ion current density in the plume of the NASA-173Mv1 versus angular position from thruster centerline at 300 V.

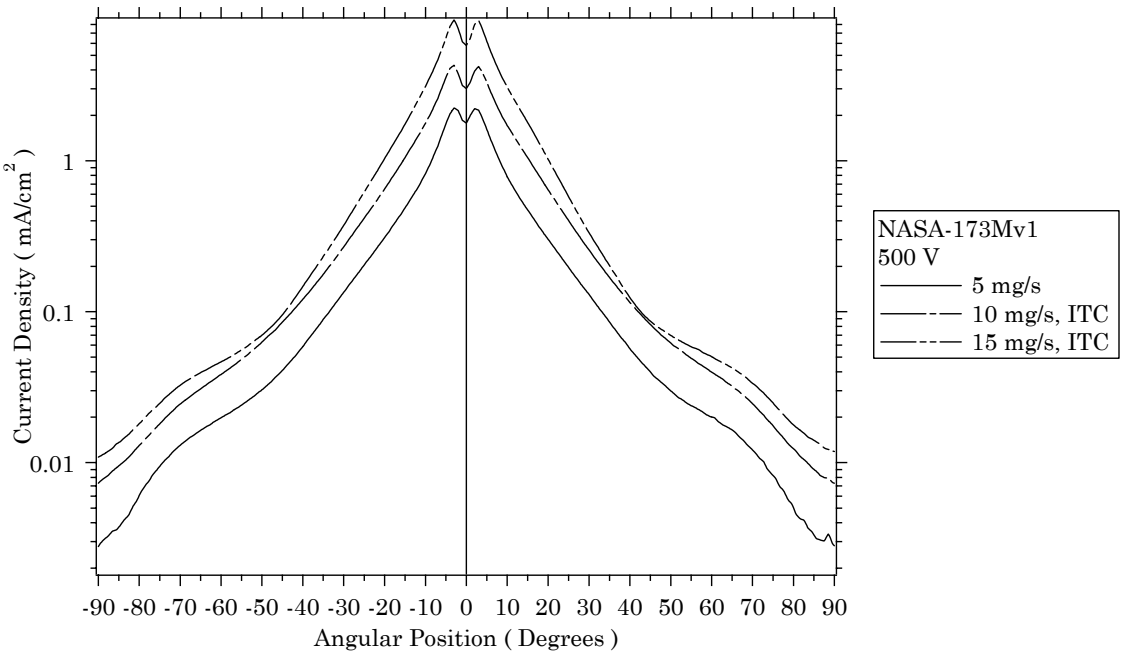

Figure 7-41 Ion current density in the plume of the NASA-173Mv1 versus angular position from thruster centerline at 500 V.

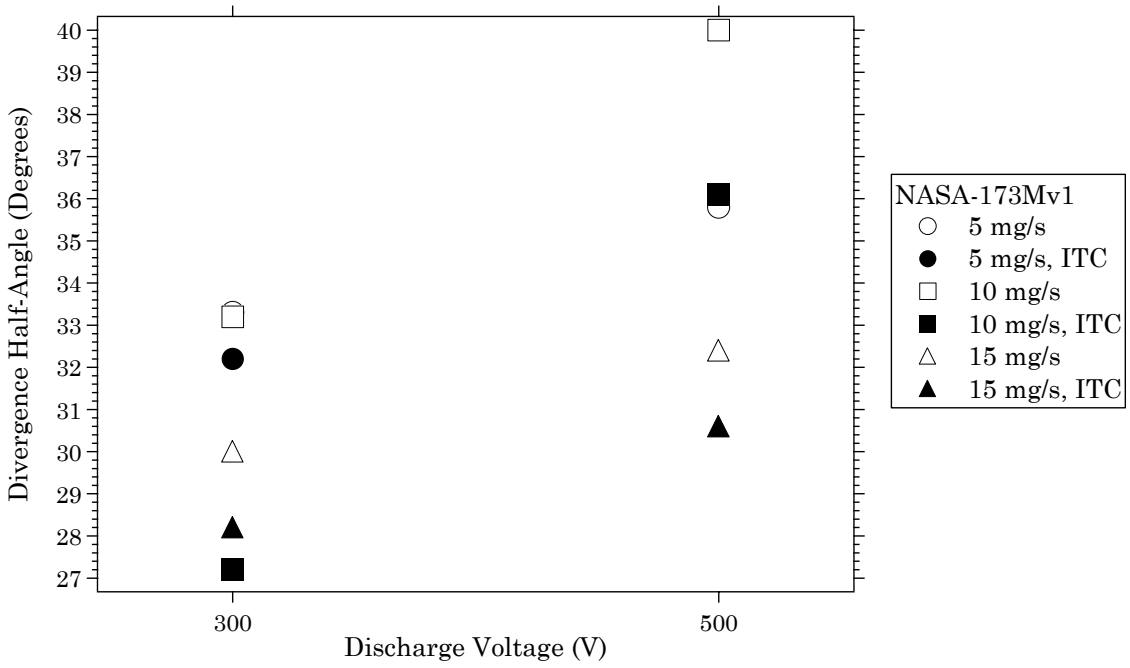

Figure 7-42 95% plume divergence half-angle versus discharge voltage of the NASA-173Mv1 at 5-15 mg/s.

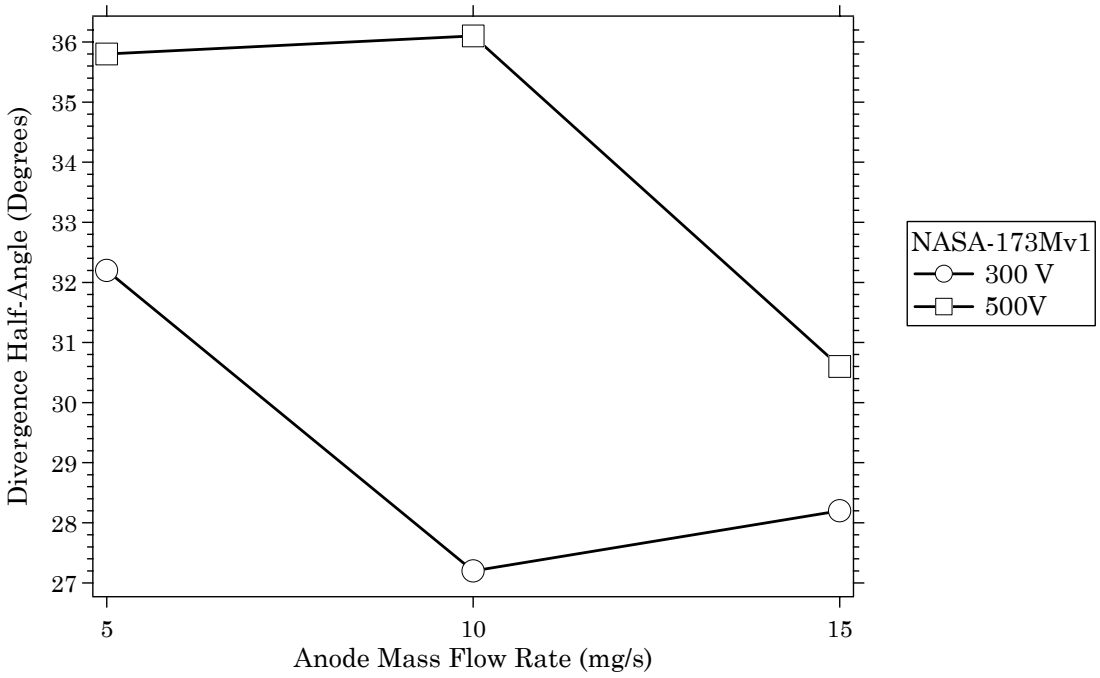

Figure 7-43 95% plume divergence half-angle versus anode mass flow rate of the NASA-173Mv1 at 300 and 500 V. The internal trim coil was energized except at 300 V, 5 mg/s.

7.6.5 Discharge current oscillations (10 mg/s)

This section presents results from measurements of discharge current oscillations of the NASA-173Mv1. Discharge current oscillations were measured at an anode flow rate of 10 mg/s and discharge voltages of 300 and 500 V. Coil currents were chosen from performance measurements discussed in section 7.6.3 and presented as Table B-4 in Appendix B. Measurements were taken with the inner and outer coils alone and with the addition of the internal trim coil. The power spectral density, breathing-mode frequency, and the standard deviation of the oscillations (expressed as a percentage of the mean discharge current) were computed from the data. Figures 7-44 and 7-45 show the power spectra at 300 and 500 V, respectively. At each voltage, the breathing-mode frequencies are shown in Figure 7-46 and the standard deviation of the oscillations are shown in Figure 7-47.

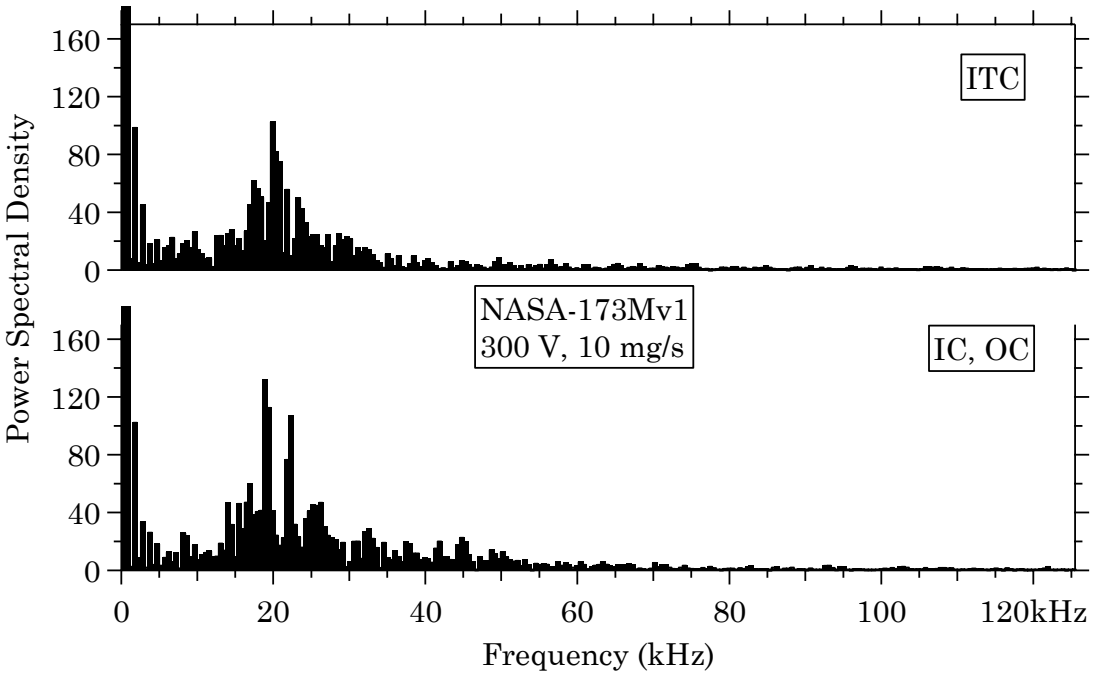

Figure 7-44 Discharge current power spectra of the NASA-173Mv1 at 300 V, 10 mg/s.

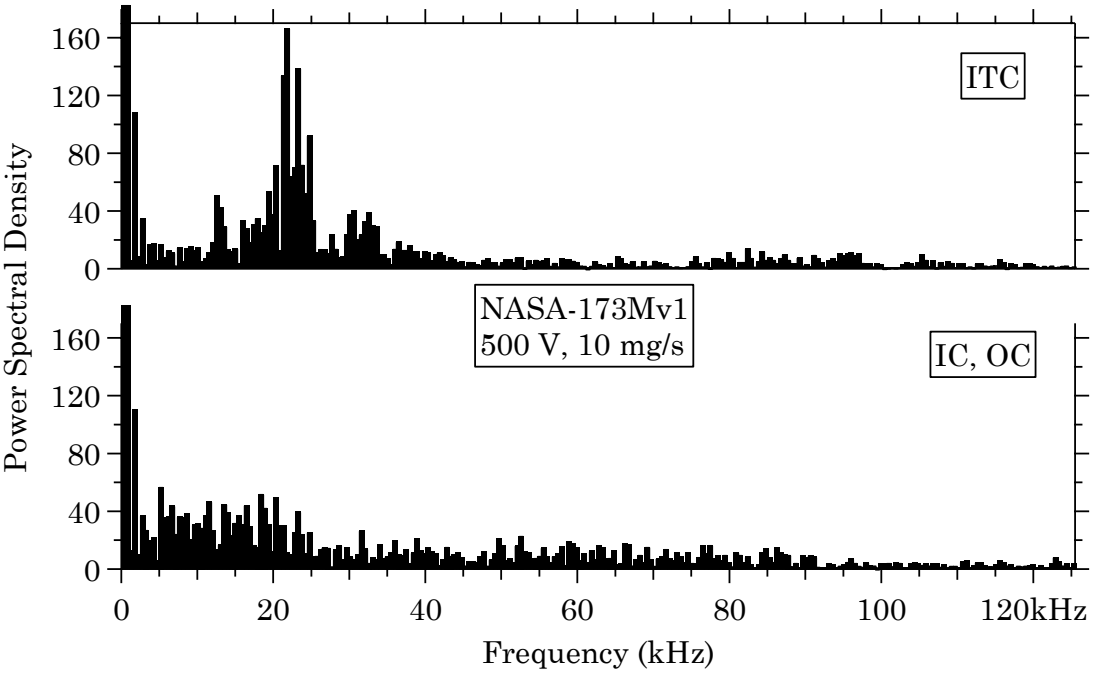

Figure 7-45 Discharge current power spectra of the NASA-173Mv1 at 500 V, 10 mg/s.

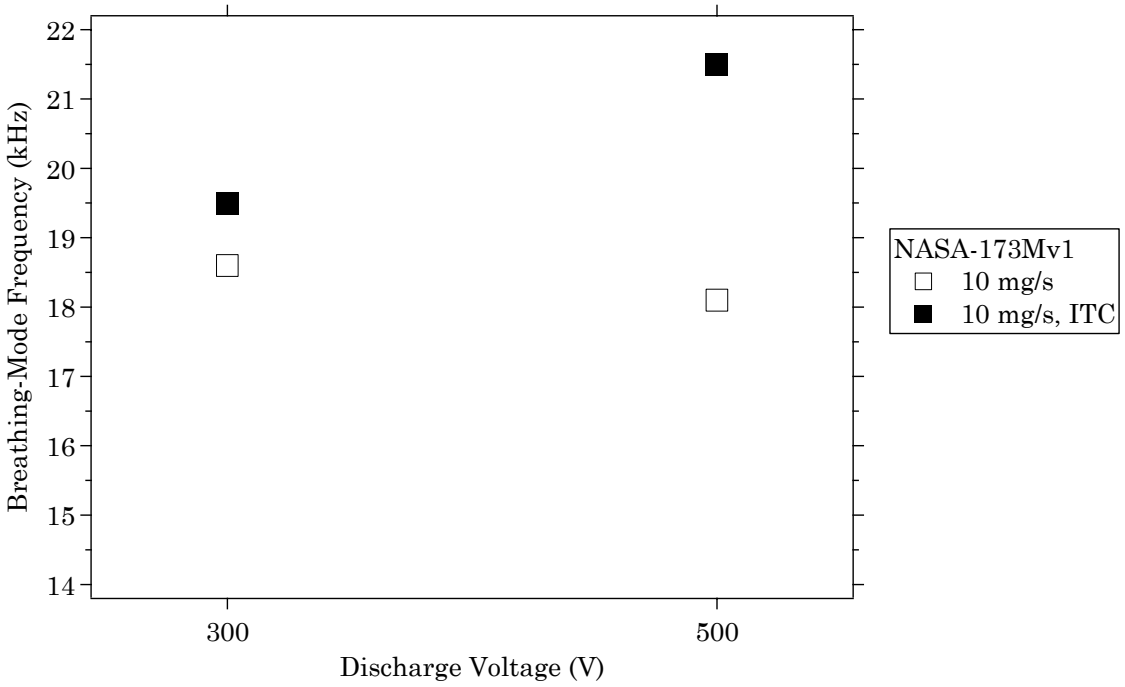

Figure 7-46 Breathing-mode frequency versus discharge voltage of the NASA-173Mv1 at 10 mg/s.

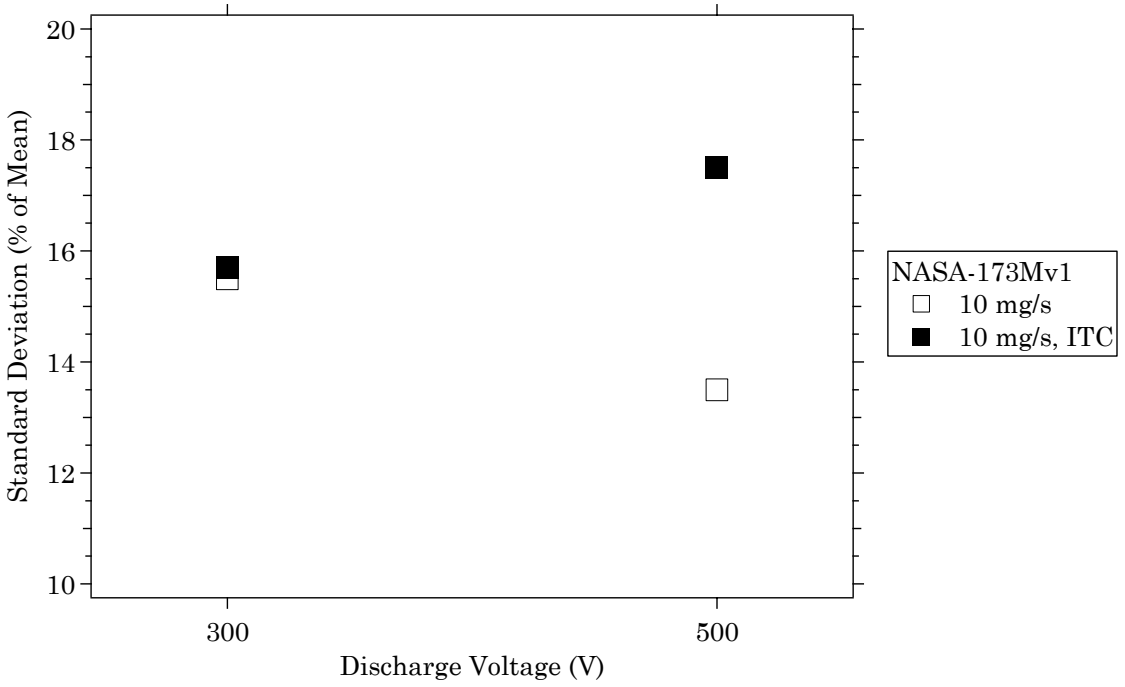

Figure 7-47 Standard deviation of the discharge current oscillations versus discharge voltage of the NASA-173Mv1at 10 mg/s.

The general effect of the internal trim coil on discharge current oscillations was to concentrate more of the energy of the power spectrum into a narrower band of frequencies centered on the breathing-mode frequency. This was most evident at 500 V (Figure 7-45), where the broadband distribution of the power spectrum was replaced by a much stronger peak when the internal trim coil was used while the magnitude of the oscillations (Figure 7-47) increased by only 4% (absolute). In addition, the breathing-mode frequency marginally increased when the internal trim coil was used. The breathing-mode frequency, which varied between 18.1-21.5 kHz for all of the operating conditions, was in the expected range for a Hall thruster [141].

7.6.6 Magnetic field (5-15 mg/s)

In this section, magnetic field measurements of the NASA-173Mv1 are presented. As shown in Figure 7-48, the maximum, radial magnetic field on the channel centerline of the NASA-173Mv1 was computed for each of the thruster operating points investigated in section 7.6.3 using the magnetic field data shown in Figure 7-7 and Figure 7-8. The magnetic field was calculated by finding the contribution from each coil based on the coil currents from the various operating points. The total magnetic field was then given by the sum of the magnetic field provided by each coil. This method was valid because the magnetic circuit of the NASA-173Mv1 exhibited a linear response to coil current up to 5 A (see sections 7.3.5 and 8.3).

In general, the required magnetic field was found to increase with increased mass flow rate or discharge voltage (while holding the other constant). The internal trim coil decreased the magnetic field when it was used. At 10 mg/s, the magnetic

field decreased between 500 and 600 V, and then linearly increased between 600-900 V. The magnetic field increased by a factor of 2.0 between 300-900 V at a flow rate of 10 mg/s.

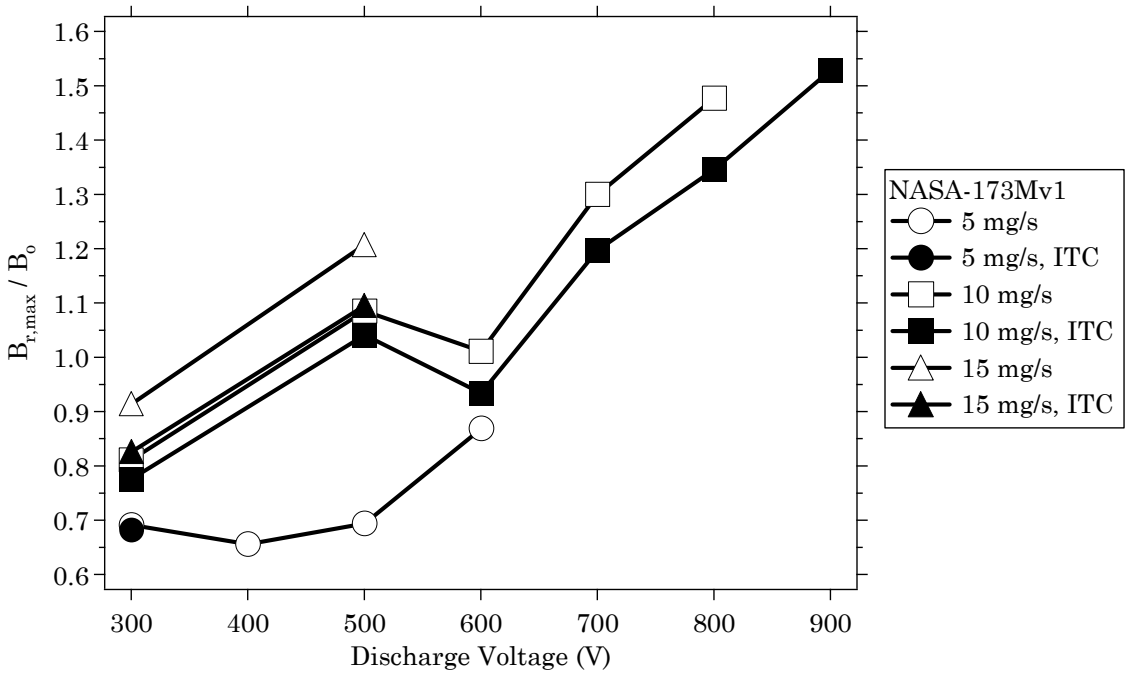

Figure 7-48 Radial magnetic field versus discharge voltage of the NASA-173Mv1 at 5-15 mg/s.

7.7 Conclusions

Designed and fabricated in a joint effort between the University of Michigan and NASA Glenn Research Center, the laboratory-model NASA-173Mv1 Hall thruster was conceived in order to understand the design challenges and physical mechanisms determining performance at high-specific impulse. The design approach of the NASA-173Mv1 was that changes to the magnetic field topography would be required for efficient operation above 1600 s specific impulse. The basis of these changes was a magnetic field topography shaped in the form of a plasma lens. The magnetic circuit also incorporated an internal trim coil to allow for additional flexibility in shaping the magnetic field with operating point.

Experiments with the NASA-173Mv1 established the validity of the magnetic field design. In a performance study at low current density, changes to the magnetic field topography at high-specific impulse were shown to be critical to achieving efficient operation. Analysis of the magnetic field identified several factors that contributed to the performance benefits gained by altering the magnetic field topography.

Additional experiments with the NASA-173Mv1 operating at nominal current densities demonstrated that efficiency could be improved when the magnetic field topography was tailored for high-specific impulse. However, the efficiency-voltage characteristic of the NASA-173Mv1 still showed a maximum and was found to asymptote at high-specific impulse.

The NASA-173Mv1 experiments validated the plasma lens design and suggested several ways to refine the magnetic field topography. The follow-on version, the GRC-developed NASA-173Mv2 discussed in the next chapter, incorporated design improvements suggested by its predecessor. In Chapter 9, the relative merits of the two thruster designs are compared.

Chapter 8

Development of the NASA-173Mv2

This chapter describes the development of the laboratory-model NASA-173M version 2 (v2) Hall thruster. The NASA-173Mv2 was designed and fabricated for operation at high-specific impulse at the NASA Glenn Research Center while the author was employed as a NASA support service contractor with QSS Group, Inc. [130]. The experiments described in Chapter 7 validated the design of the NASA-173Mv1 and suggested several ways to refine the magnetic field for the NASA-173Mv2 design. Additionally, other means to improve on the NASA-173Mv1 design became evident as the authors experience grew in designing, fabricating, and operating Hall thrusters.[35]

In sections 8.1-8.3, the NASA-173Mv2 Hall thruster is described in terms of its design objectives and approach, physical description, and magnetic field topography. Section 8.4 describes a characterization of the NASA-173Mv2 that considered the effects of current density and magnetic field topography on thruster efficiency at high-specific impulse. These experiments demonstrated that changes to the magnetic field of the NASA-173Mv2 resulted in a Hall thruster that was optimized for high-specific impulse operation. In Chapter 9, the characteristics of the NASA-173Mv1 and v2 thrusters are compared.

[35] The design of the NASA-173Mv2 followed the development of the 50 kW NASA-457M [47]. The magnetic circuits of the NASA-457M and NASA-173Mv2 were designed by the author while employed as a contractor with QSS Group, Inc. at NASA GRC. The mechanical design of the NASA-173Mv2 was also significantly improved through a collaboration between the author and NASA support service contractor Chris Griffiths of Zin Technologies.

8.1 Design objectives and approach

The NASA-173M Hall thrusters were conceived in order to understand the design challenges and physical mechanisms determining performance at high-specific impulse (see section 7.1). The thrusters were designed based on the hypothesis that the magnetic field topography required for efficient, high-specific impulse operation would differ from that employed at 1600 s specific impulse. Experiments with the NASA-173Mv1 described in Chapter 7 demonstrated that efficient operation could be improved when the magnetic field topography was tailored for high-specific impulse. However, the efficiency characteristic of the NASA-173Mv1 still showed a maximum and was found to asymptote at high-specific impulse. The NASA-173Mv1 experiments validated the design and suggested several ways to refine the magnetic field topography. Accordingly, the GRC-developed NASA-173Mv2 incorporated the design improvements suggested by its predecessor. The goal with the NASA-173Mv2 was to eliminate the efficiency peak completely and to obtain an efficiency characteristic that continuously increased with specific impulse.

As with the NASA-173Mv1, wall effects and neutral flow uniformity were not explicitly studied. The design of the NASA-173Mv2 was an effort to improve on the performance of the NASA-173Mv1 by implementing changes to the magnetic field topography.

8.2 Physical description

Shown in Figure 8-1, the NASA-173Mv2 is a single-stage, magnetic layer Hall thruster sized to operated nominally at a discharge power of 5 kW. Figure 8-2 is a photograph of the thruster operating at 300 V, 10 mg/s. The thruster body has

an outer diameter of 270 mm and an overall length of 87 mm. Like the NASA-173Mv1, the discharge chamber of the NASA-173Mv2 has an outer diameter of 173 mm, a channel width of 25 mm, and a channel depth of 38 mm.

The NASA-173Mv2 uses a laboratory-model hollow cathode from NASA GRC that is capable of emission currents up to 20 A. As shown in Figure 8-1, the cathode is positioned above the thruster. Cathode positioning is similar to the NASA-173Mv1 (see section 7.2). To date, no attempts have been made to optimize performance by changing the cathode position. For the experiments described here, the cathode orifice was located approximately 30 mm downstream of the exit plane and 30 mm radially away from the outer radius of the outer front pole piece at an inclination of 30° from thruster centerline.

The NASA-173Mv2 is an evolved version of the NASA-173Mv1 that was described in Chapter 7. The primary characteristics of the NASA-173Mv1 that are maintained in the NASA-173Mv2 are:

1. the channel geometry (outer diameter, width, length),
2. discharge chamber walls made from boron nitride, and
3. the gas injection scheme of the anode.

Although qualitatively similar, the major difference between the NASA-173M thrusters is the shape of the plasma lens magnetic field topography. Other improvements have been made to the thermal design, assembly scheme, and mass of the NASA-173Mv2. **Since these changes were not relevant to quantifying differences in thruster performance, differences in the performance and plume characteristics between the NASA-173M thrusters were attributed to changes in the magnetic field topography.**

Figure 8-1 Photograph of the laboratory-model NASA-173Mv2 Hall thruster.

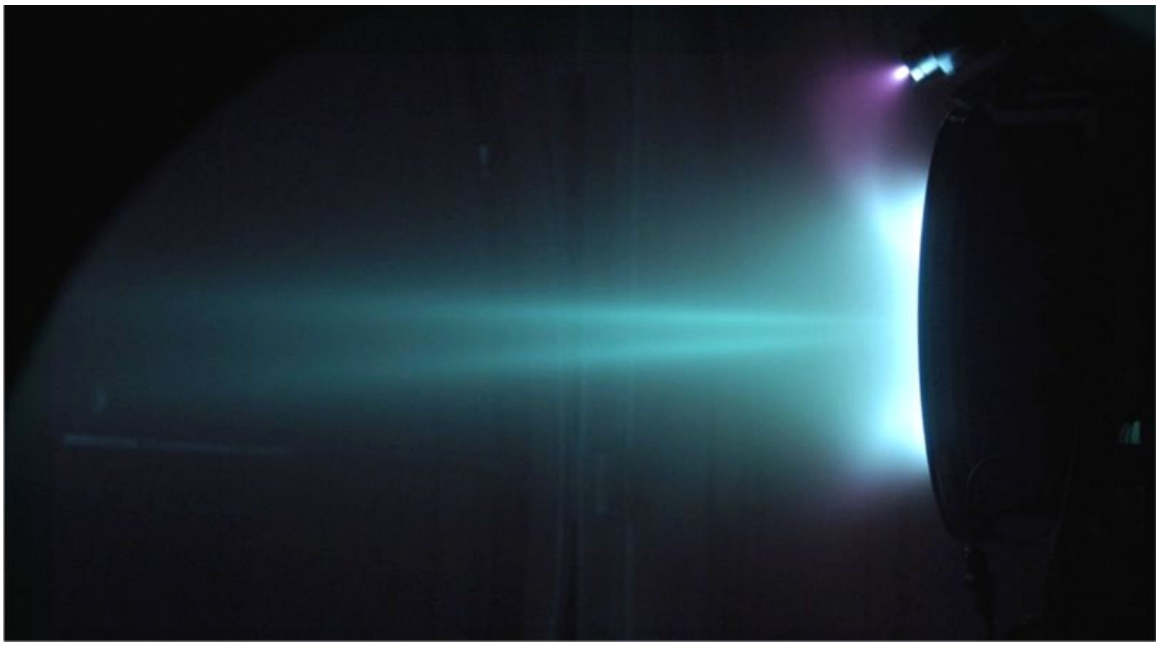

Figure 8-2 Photograph of the NASA-173Mv2 operating at 300 V, 10 mg/s.

8.3 Magnetic field topography

8.3.1 Magnetic circuit

The primary magnetic circuit of the NASA-173Mv2 consists of a fixed structure of magnetic poles pieces, an inner coil (IC), and an outer coil (OC). Fine control of the magnetic field is provided with an internal trim coil (ITC) and an external trim coil (ETC). The magnetic circuit configuration of the NASA-173Mv2 is similar to the generic schematic shown in Figure 5-6.

8.3.2 Plasma lens focusing

The magnetic field topography in the discharge chamber of the NASA-173M Hall thrusters employ what is commonly referred to as a plasma lens (see section 7.3.3). The plasma lens in the NASA-173Mv2 is qualitatively similar to that of the NASA-173Mv1. However, improvements to the lens curvature and symmetry were incorporated in the NASA-173Mv2. The changes were inspired by experiments with the NASA-173Mv1 that suggested a means to improve performance at high-specific

impulse without the use of trim coils. Since the exact changes are considered proprietary to the On-Board Propulsion Branch at the NASA Glenn Research Center, they will not be discussed here.

8.3.3 Internal trim coil

The internal trim coil primarily affects the radial magnetic field in the discharge chamber (see section 5.1.4). When the coil is energized, the concavity of the plasma lens (*i.e.*, the axial gradient of the magnetic field, $\nabla_z B_r$) can be changed depending on the direction of the coil current. By convention, a negative coil current subtracts from the radial magnetic field, increases the value of $\nabla_z B_r$, and increases the concavity of the plasma lens.

8.3.4 External trim coil

As shown in Figure 8-1, the external trim coil is an azimuthal coil located on the outer radius of the thruster body. An external trim coil alters the magnetic field downstream of the exit plane and near the cathode (see section 5.1.4). As shown in Figure 5-10, with a negative current on the external trim coil, the field line inclination is increased towards the radial direction.

8.3.5 Response of the magnetic circuit to applied coil current

The response of the NASA-173Mv2 magnetic circuit to the inner coil (IC), outer coil (OC), and internal trim coil (ITC) was characterized using the Hall probe and Gaussmeter described in section 6.3.4. The Hall probe was placed on the channel centerline at the axial location of the maximum radial magnetic field. The external trim coil was not tested for these measurements because this coil does not affect the magnetic field in the discharge chamber. Other measurements with the external trim coil have confirmed that it was operating as designed (not shown).

Figure 8-3 shows the maximum, radial magnetic field on channel centerline versus coil current for the inner and outer coils. The measured values (indicated as "exp" in the figure) were normalized by an arbitrary constant B_o. The radial magnetic field as a function of coil current was recorded for each coil without the other coil being energized. In a Hall thruster, if the magnetic circuit is below saturation (*i.e.*, the magnetic field increase is linear with coil current), the total magnetic field for arbitrary coil currents can be computed by linear superposition. To demonstrate this, measurements were taken with both the inner and outer coils energized to the same coil current by wiring the inner and outer coils in series on the same power supply. The total magnetic field for equal coil currents from the inner and outer coils was also computed (indicated as "comp" in the figure). Comparison of the computed data showed excellent agreement with the experimental data.

Figure 8-4 shows the maximum, radial magnetic field on channel centerline versus coil current for the internal trim coil. The measured values were normalized by an arbitrary constant B_o. The response of the magnetic circuit to the internal trim coil was linear over the entire range of coil currents. A zero offset at zero coil current was measured due to the residual magnetism of the magnetic circuit. The offset is also present in Figure 8-3, but is less apparent due to the scale.

Over the range of coil currents that were tested, the magnetic field produced by the magnetic circuit of the NASA-173Mv2 linearly increased. To study the scaling of the magnetic field with discharge voltage, data from Figures 8-3 and 8-4 were used to compute the total magnetic field for specific operating points of the thruster (see section 8.4.4). When computing the total magnetic field, the residual magnetism was included in the contribution from the inner coil and subtracted from the other coils (so that it was not counted more than once).

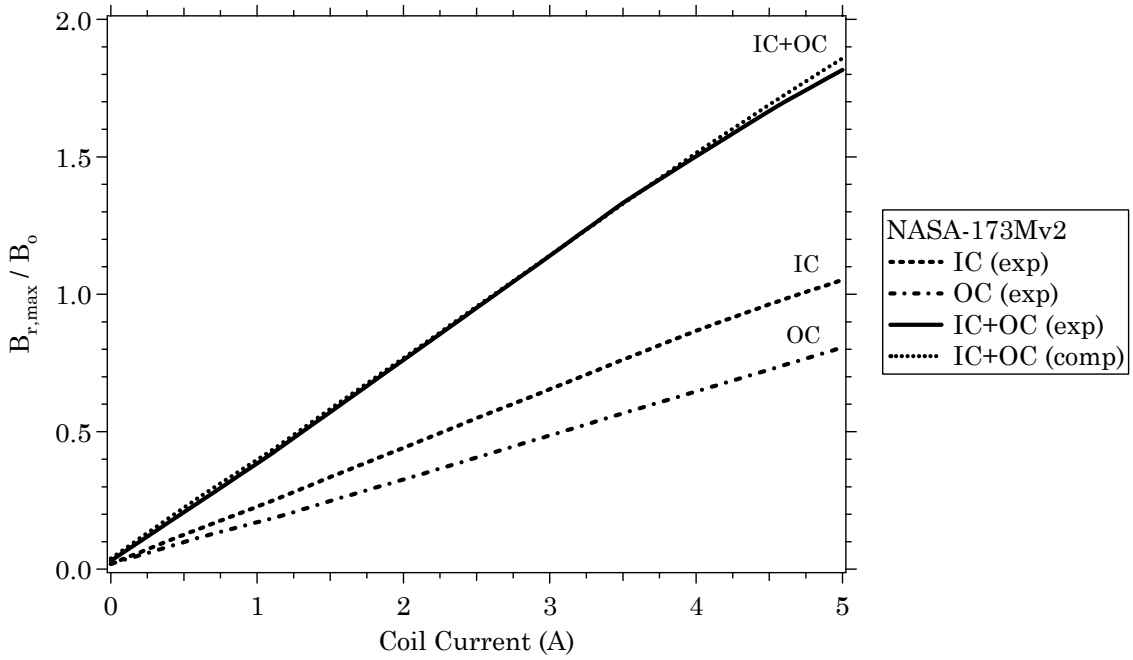

Figure 8-3 Maximum, radial magnetic field on channel centerline versus coil current for the inner coil (IC) and outer coil (OC) of the NASA-173Mv2. (exp = measured data, comp = computed data)

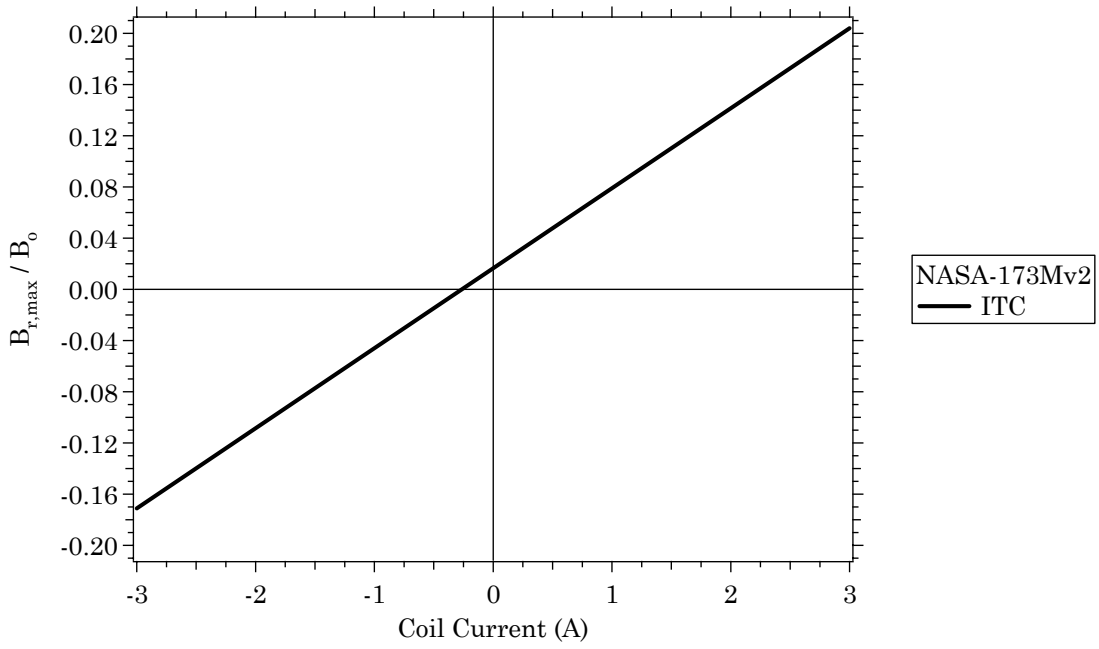

Figure 8-4 Maximum, radial magnetic field on channel centerline versus coil current for the internal trim coil (ITC) of the NASA-173Mv2.

8.4 Operating characteristics

This section describes the operating characteristics of the NASA-173Mv2. Section 8.4.1 discusses a performance evaluation that was conducted to quantify the effects of current density and magnetic field topography on thruster efficiency at high-specific impulse. Additional experiments were conducted to measure the ion current density of the plume (§8.4.2), discharge current oscillations (§8.4.3), and the magnetic field (§8.4.4). In Chapter 9, results from this section are compared to the NASA-173Mv1 from experiments discussed in section 7.6.

All experiments discussed in this section were conducted in Vacuum Facility 12 (VF12) at NASA GRC. VF12 is described in section 6.2.2 and the various diagnostics that were used are described in section 6.3. The NASA-173Mv2 had been previously operated for over 25 hours before these experiments began.

The effects of changing the magnetic field topography on thruster operation were investigated by energizing the thruster coils in different combinations. These coil combinations are labeled in the figures as:

1. IC, OC – only the inner and outer coils were energized,
2. ITC – the internal trim coil was energized in addition to the inner and outer coils
3. ITC, ETC – both trim coils were energized in addition to the inner and outer coils
4. ETC – the external trim coil was energized in addition to the inner and outer coils.

Performance of the NASA-173Mv2 was mapped while varying the discharge voltage from 300–1000 V at an anode flow rate of 5–10 mg/s and 300–600 V at an anode flow rate of 15 mg/s. The cathode flow rate was always 10% of the anode flow

rate. Ion current density and discharge current oscillation data were also collected at an anode flow rate of 10 mg/s. Lastly, the magnetic field was computed based on the coil currents that were used during the performance characterization.

The thruster was stable and capable of sustained operation during the period when data at a given operating point were recorded. Additional details specific to each experiment are described at the beginning of each of the sub-sections that follow.

8.4.1 Performance (5-15 mg/s)

8.4.1.1 Methods and observations

The performance of the NASA-173Mv2 was evaluated over 300–1000 V at 5 and 10 mg/s and 300–600 V at 15 mg/s. Performance data are tabulated in Tables C-1 through C-3 in Appendix C. The different thruster operating points are shown in the current-voltage characteristic plotted in Figure 8-5. By testing at constant flow rates, current density was held approximately constant as the voltage increased, which was equivalent to increasing the power density. The maximum power at which the thruster could be safely operated was determined to be 10 kW, so no data were generated beyond this power level.

The cathode flow rate was maintained at 10% of the anode flow rate to ensure there was a sufficient supply of electrons for neutralization and ionization. No attempts were made to optimize the cathode flow, cathode position, or to minimize the power dissipation of the coils. Minor improvements to the total specific impulse and total efficiency should be possible if the cathode and coils are later optimized.

The general method for taking data was to set the voltage and flow rate and then investigate the effects of each coil on discharge current, plasma oscillations,

and anode efficiency. It was observed that the effects of the internal and external trim coils on performance were nearly independent. It was therefore decided to record data first with the internal trim coil energized, then with both trim coils. This method was used only when both trim coils were beneficial to efficiency. For example, if the internal trim coil showed no benefit, only external trim coil data were collected.

After determining the general range of coil currents yielding near-optimum efficiency, data were recorded at several coil currents in this range to ensure that performance was indicative of the optimum. Only data at the coil currents resulting in maximum performance are reported here. Maximum performance was generally realized where the discharge current and oscillations were minimized. However, there were cases when the discharge current would increase with efficiency when the trim coils were energized.

The thruster was stable and capable of sustained operation (from tens of minutes to hours) during the period when data at a given operating point were recorded. At voltages greater than 300 V, the thruster became unstable for 10–30 minutes after the voltage was increased. This was attributed to instabilities associated with movement of the plasma towards the anode. Internal probe measurements have confirmed the movement of the plasma with voltage (see section 11.1). If the voltage was increased rapidly, oscillations would sometimes cause the discharge to extinguish.

Movement of the plasma resulted in a gradual lengthening of the discharge chamber erosion band. A "burn-off" period at 600 V or more first confirmed this. This burn-off was qualified by visually observing the erosion layer glowing orange-red at its upstream boundary. Burn-off was observed only above 600 V, but it most

likely occurred to a lesser extent at all voltages. The burn-off was quantified by an increase in the discharge current and a decrease in efficiency. The thruster was unstable during burn-off unless the coil currents were increased by a few Amperes (typically by 0.5-2.0 A above the currents shown in Appendix C). After the burn-off period at each voltage, which lasted 10–30 minutes, the coil currents could be reduced and the thruster returned to a stable operating mode. Discharge current also decreased after burn-off and the efficiency increased. Additionally, after burn-off the voltage could be decreased and increased back to the burn-off voltage as quickly as the power supply could accommodate the change.

8.4.1.2 Results and discussion

In this section, results from the performance evaluation of the NASA-173Mv2 are presented and discussed. Figures 8-5 through 8-8 show how changing the magnetic field with the trim coils affected thruster operation. Specifically, Figure 8-5 shows the current-voltage characteristics and Figures 8-6 through 8-8 plot the total efficiency versus voltage. Figures 8-9 through 8-12 show the performance quantities from the coil combinations in Figures 8-6 through 8-8 that maximized total efficiency at each operating point. Over the entire range of operating conditions, thrust varied from 81-442 mN, the thrust-to-total power ratio varied from 31-66 mN/kW, total specific impulse varied from 1510-3390 s, and total efficiency varied from 47.1-63.5%.

The functional relationship of the discharge voltage and current is depicted in Figure 8-5 for flow rates of 5, 10, and 15 mg/s, respectively. At constant flow rate, the current was found to increase slowly with voltage. At a fixed discharge voltage, energizing the trim coils generally reduced the discharge current and increased

thrust. Exceptions to this trend were at 700-1000 V at 10 mg/s. At these operating points, changing the magnetic field with the trim coils increased the discharge current and thrust. In Chapter 12, it is shown that the rise in discharge current with voltage at 10 mg/s was primarily due to increased ion current while the electron current remained nearly constant.

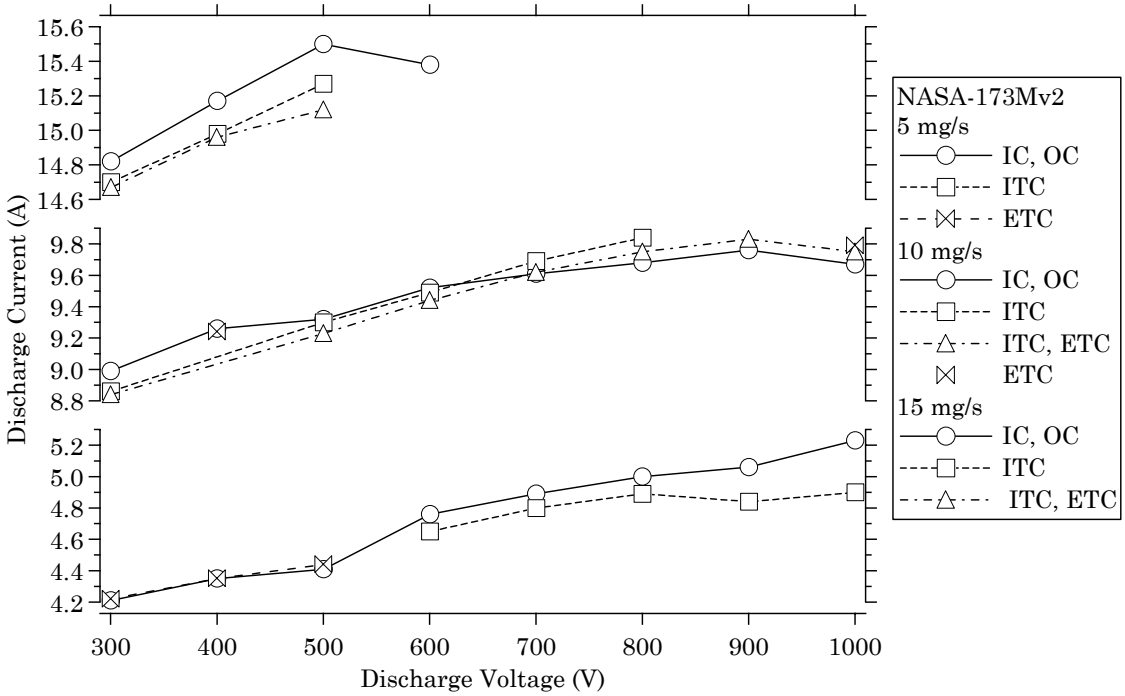

Figure 8-5 Discharge current versus discharge voltage of the NASA-173Mv2 at 5-15 mg/s.

Figures 8-6 through 8-8 show total efficiency versus discharge voltage for flow rates of 5, 10, and 15 mg/s, respectively. At a given flow rate and voltage, efficiency was improved or remained unchanged by using the trim coils. When efficiency was unchanged, there were still performance benefits since thrust usually increased.

In Figure 8-6, the efficiency at 5 mg/s shows trends that are very similar to the NASA-173Mv1 data shown in Figure 7-24. When the internal trim coil benefited

performance, a positive coil current was applied (*i.e.*, the concavity of the plasma lens was reduced). The implications of these results are discussed further in section 9.4.1. Total efficiency at 5 mg/s spanned the range of 47.1% at 300 V to 52.1% at 1000 V.

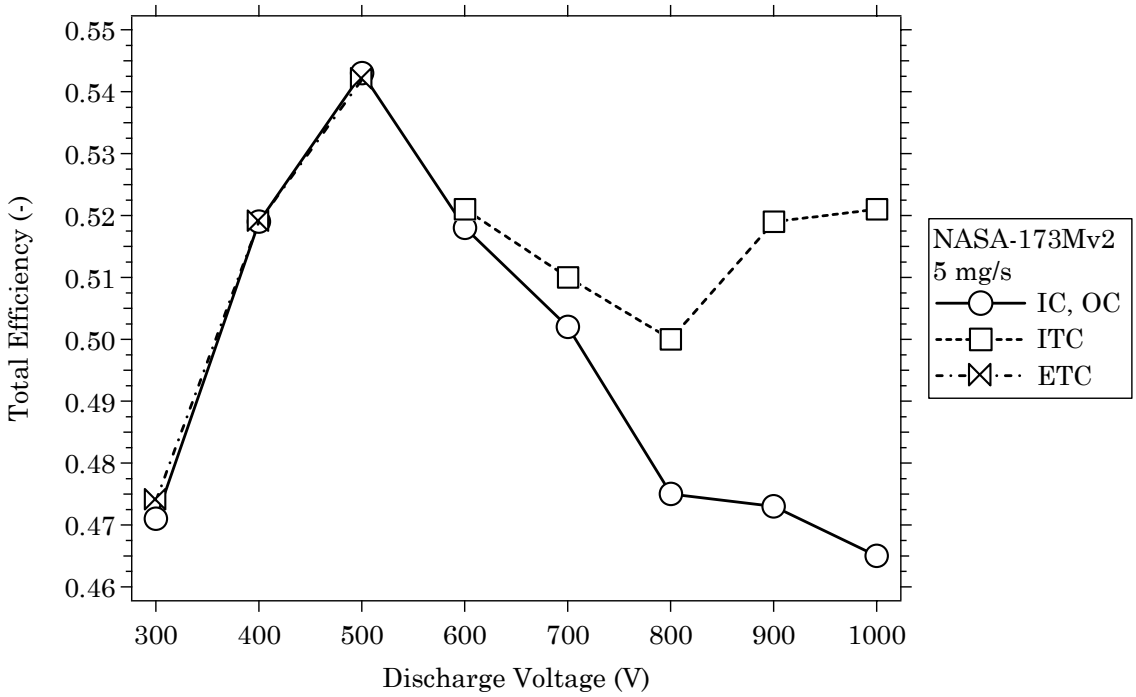

Figure 8-6 Total efficiency versus discharge voltage of the NASA-173Mv2 at 5 mg/s.

Figure 8-7 shows that total efficiency at 10 mg/s increased monotonically with voltage. Total efficiency at 10 mg/s spanned the range of 52.7% at 300 V to 60.8% at 1000 V. Although 1000 V, 10 mg/s operation was near the power limit of 10 kW, the thruster was operated for one hour at this setting. **The efficiency at 10 mg/s increased with voltage whether or not the trim coils were used, which indicated improvements to the magnetic field topography in the NASA-173Mv2 with respect to the NASA-173Mv1 were near the optimum required for high-specific impulse operation.** Unlike the data at 5 mg/s in Figure 8-6 that shows efficiency improved by as much as 5.6% (absolute), using trim coils at 10

mg/s improved efficiency by an average of only 0.8% (absolute) and the maximum increase was 1.6% (absolute). **Overall, differences between the 5 and 10 mg/s efficiency data imply there is a minimum current density necessary for high-efficiency operation of the NASA-173Mv2.**

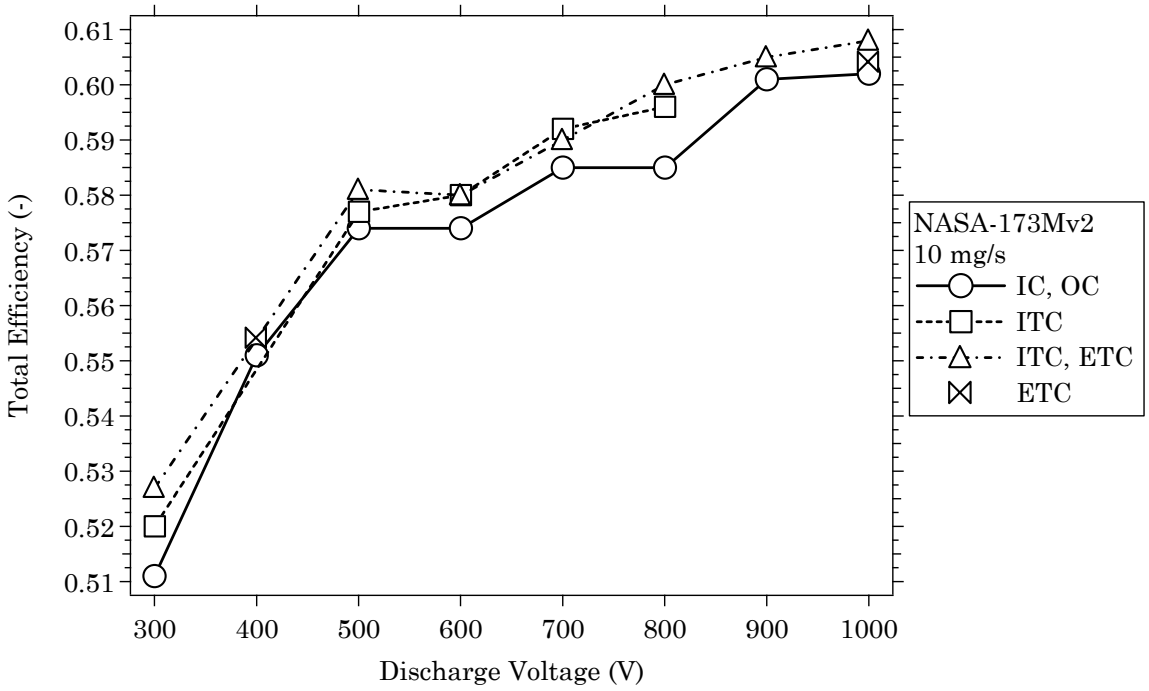

Figure 8-7 Total efficiency versus discharge voltage of the NASA-173Mv2 at 10 mg/s.

In Figure 8-8, the efficiency at 15 mg/s shows trends that are similar to Figure 8-7, albeit at higher efficiencies. Total efficiency at 15 mg/s spanned the range of 59.0% at 300 V to 63.3% at 1000 V. Anode efficiencies exceeded 70% at 500–600 V. As noted earlier, operation at 600 V, 15 mg/s was close to the 10 kW power limit of the thruster. It was difficult to maintain the discharge at 600 V for more than twenty minutes, which did not allow time to experiment with the trim coils.[36] Difficulties sustaining the discharge seemed to be driven more by the

[36] During the course of writing this dissertation, a thermal characterization of the NASA-173Mv2 was conducted at NASA GRC by the author. While the results of this characterization are not included here, it is worthy to note that the thruster was successfully run to thermal steady-state at 600 V, 15 A. This operating condition was reached after

combined influence of current and power density—rather than the power density alone—since the thruster was operated for an hour at 1000 V, 10 mg/s.

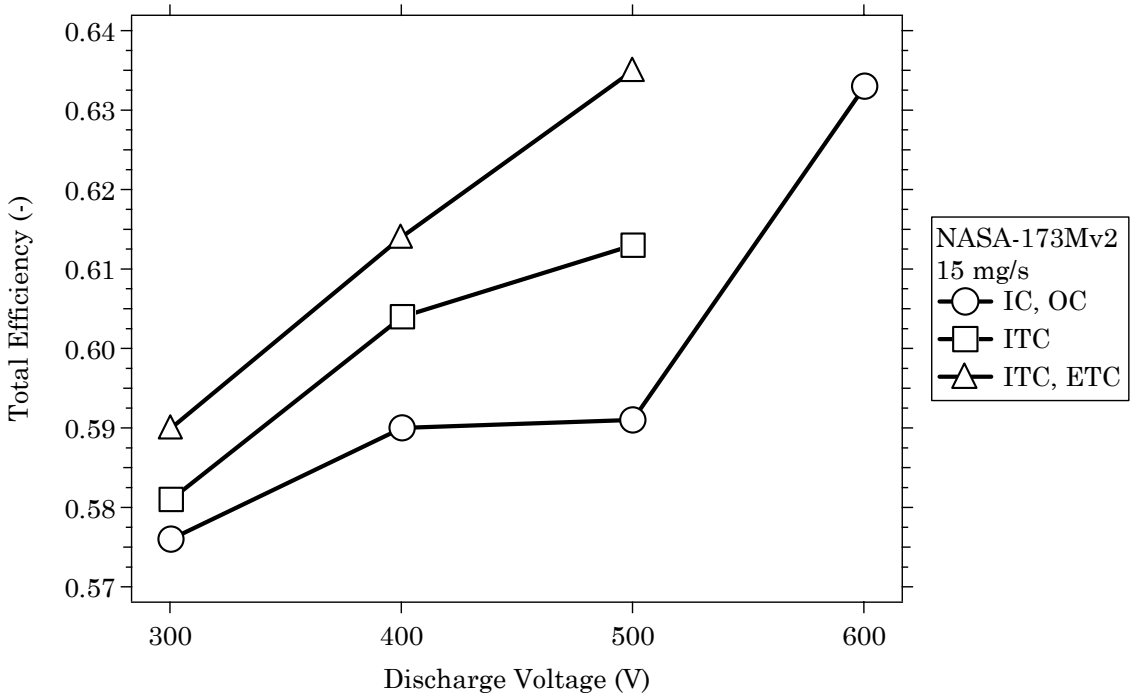

Figure 8-8 Total efficiency versus discharge voltage of the NASA-173Mv2 at 15 mg/s.

Thrust, total efficiency, total specific impulse, and the thrust-to-total power ratio T/P_t, for flow rates of 5, 10, and 15 mg/s are shown in Figures 8-9 through 8-12. At each operating point, the coil combinations corresponding to maximum thruster efficiency from Figures 8-6 through 8-8 are shown.

Figure 8-9 shows the thrust produced by the NASA-173Mv2 at each voltage and flow rate that were investigated. As expected, thrust increased with both increased mass flow rate and voltage.

spending several hours at 600 V, 10 A then increasing the discharge current slowly to 15 A over the course of several more hours. These results indicated that the maximum current and power density of the thruster has not yet been found. Nonetheless, operation at elevated current and power densities is still a tricky business, so the observations and conclusions made from the performance characterization described here are still thought to be generally valid.

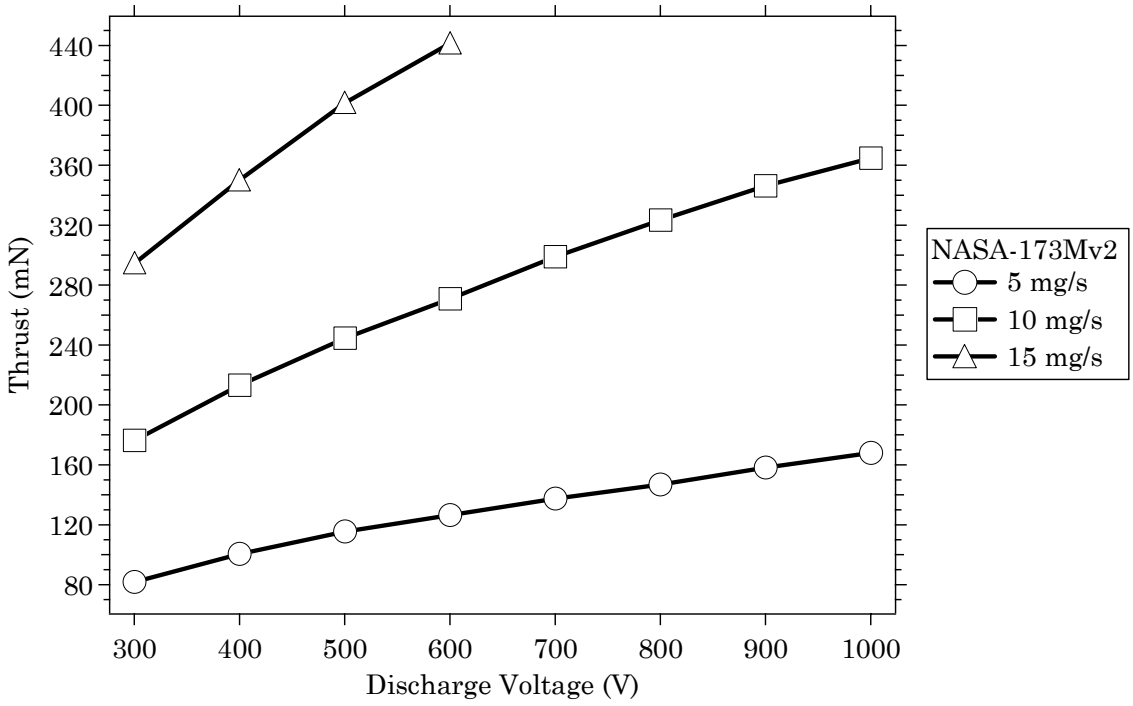

Figure 8-9 Optimized thrust versus discharge voltage of the NASA-173Mv2 at 5-15 mg/s.

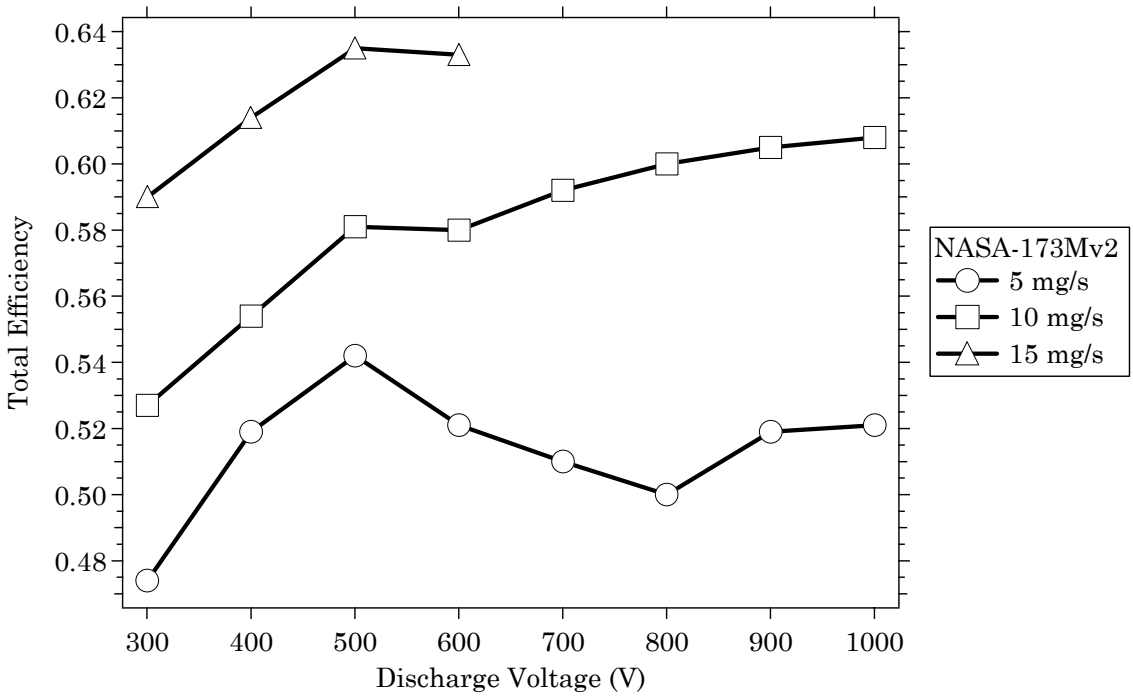

Figure 8-10 Optimized total efficiency versus discharge voltage of the NASA-173Mv2 at 5-15 mg/s.

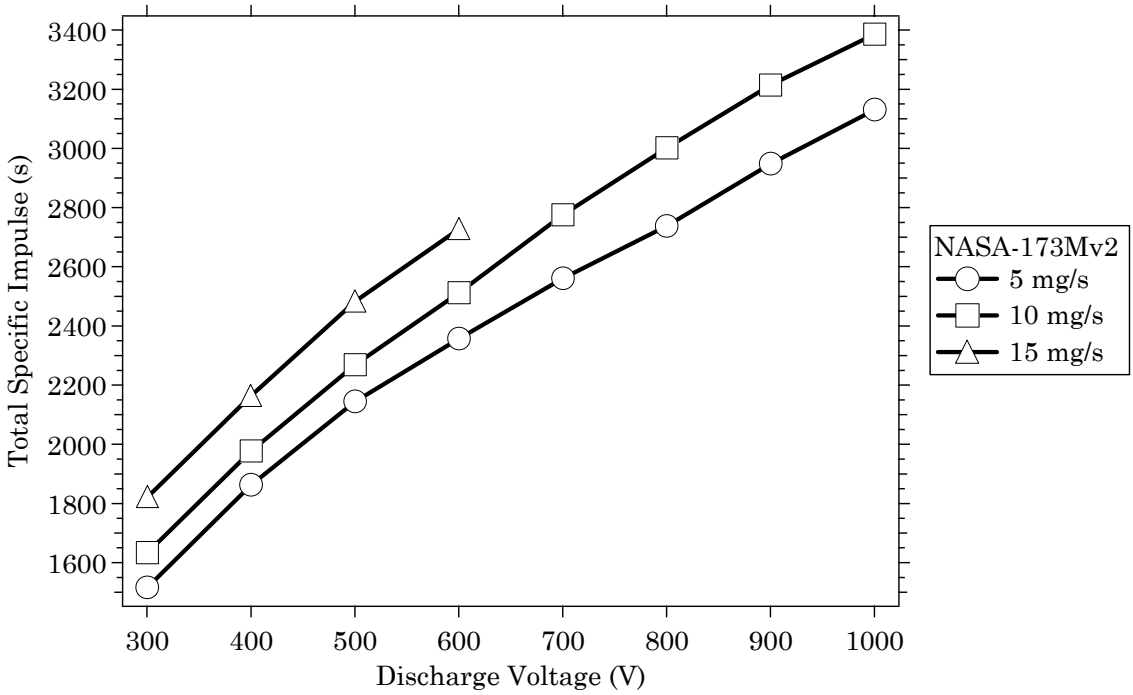

Figure 8-11 Optimized total specific impulse versus discharge voltage of the NASA-173Mv2 at 5-15 mg/s.

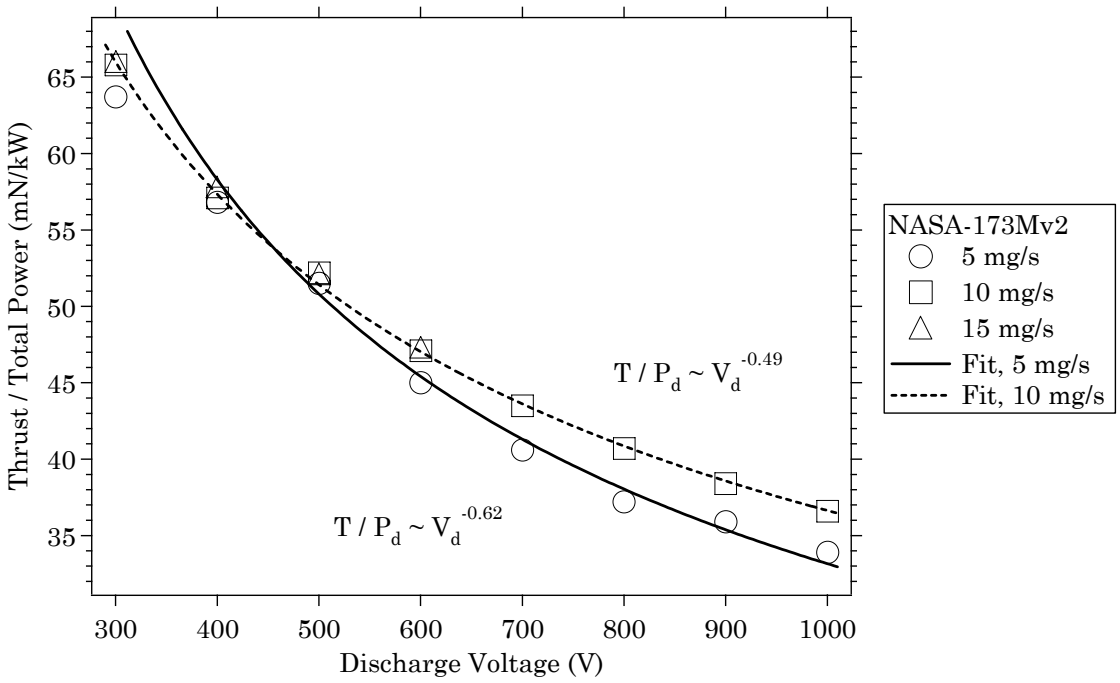

Figure 8-12 Optimized thrust-to-total power ratio versus discharge voltage of the NASA-173Mv2 at 5-15 mg/s.

Figure 8-10 shows the total efficiency at each flow rate. At a flow rate of 10 mg/s, total efficiency exceeded 60.0% at 800 V. The maximum total efficiency was 63.5% at 500 V, 15 mg/s. Trends in total efficiency emphasize the importance of current density in achieving optimal performance. At a fixed voltage, efficiency improved at each higher flow rate because mass utilization is known to increase with current density. At fixed mass flow rate, current density also has a role in optimizing efficiency with increasing voltage, as shown by the contrasting efficiency characteristics at 5 and 10 mg/s (see section 9.4 for more).

Figure 8-11 shows the total specific impulse at each flow rate. At 10 mg/s, greater than 3000 s total specific impulse was demonstrated at 800 V. The maximum total specific impulse was 3390 s at 1000 V, 10 mg/s. The specific impulse also increased, like efficiency, with current density at a fixed voltage because of improved mass utilization. However, unlike efficiency, the specific impulse always increased with voltage at constant mass flow rate. This was because thrust always increased with voltage (see Figure 8-9), and the thrust and specific impulse ideally scale with discharge voltage as $T \propto I_{sp} \propto V_d^{1/2}$.

Trends in efficiency and specific impulse are best understood by considering the T/P_t ratio, shown in Figure 8-12. The T/P_t ratio showed a weak dependence with current density at 300–500 V. At 600 V or above, the T/P_t ratio at 5 mg/s decreased faster than at 10 mg/s, which corresponded to the decrease in efficiency shown in Figure 8-10. The drop in efficiency can be understood by considering the scaling of the T/P_t ratio with voltage. At a constant flow rate, efficiency scales as $\eta \propto T^2/P_t \propto T/P_t * V_d^{1/2}$. Thus, if the T/P_t ratio scales with voltage at a power of less than –½, the efficiency will decrease. A power law curve fit to the 5 mg/s data in

Figure 8-12 shows that $T/P_t \propto V_d^{-0.62}$, while the 10 mg/s data scales as $T/P_t \propto V_d^{-0.49}$. **This result shows that the decrease in efficiency that was observed at 5 mg/s was most likely due to increased electron current, rather than a decrease in ion current or a large increase in multiply-charged ions.**

Overall, the performance and operating characteristics of the NASA-173Mv2 highlight the challenges of operating Hall thrusters over a large range of current and power densities. Depending on the application, the challenge is maintaining efficient operation without exceeding current and power density limitations. In a constant current application, throttling from 300 to 1000 V requires an increase in the power density by more than a factor of three. However, this may not be an issue since data at 10 mg/s has shown the NASA-173Mv2 was stable over these power densities. In constant power applications, however, problems may arise if the throttling range is beyond the thermal capabilities of the thruster. This is because at the highest voltage, the thruster should be sized to yield acceptable efficiency. Throttling at constant power to a lower voltage will then increase the current density. Recall that operation of the NASA-173Mv2 at 600 V, 15 mg/s was only sustained for twenty minutes as opposed to 1000 V, 10 mg/s, which was sustained for an hour. Both of these operating points are nearly the same power density, but current density is 50% higher at 15 mg/s than at 10 mg/s. This underscores the importance of current and power density considerations that could limit the throttling range in constant power applications.

8.4.2 Ion current density (10 mg/s)

Ion current density measurements in the plume of the NASA-173Mv2 and discharge current oscillation data (see section 8.4.3) were collected concurrently

after determining optimum coil currents from the performance characterization discussed in section 8.4.1. Ion current density measurements were made at 10 mg/s at voltages of 300–1000 V. At each voltage, plume profiles with the inner and outer coil alone were measured. At 300–600 V, the internal trim coil and the combined influence of both trim coils were documented. At 700–1000 V, only data with both trim coils energized were collected, with the exception of 1000 V, which included a data set with the external trim coil.

Figure 8-13 shows results from 300–600 V and Figure 8-14 includes data from 700–1000 V. Both figures include only data with both trim coils energized. Differences in the plume profiles with the other coils were quantified by calculating the plume divergence. Figure 8-15 shows the 95% plume divergence half-angle versus voltage for all of the coil combinations that were investigated. (See section 6.3.2 for how plume divergence was defined.) Figure 8-15 shows divergence reached a maximum of 38° at 400 V and a minimum of 28° at 1000 V.

The double peak structure of the ion current density profiles in Figures 8-13 and 8-14 was attributed to the annular geometry of the discharge chamber. The current density peaks were more pronounced as the voltage increased; indicating more of the ion current was located near centerline. It is likely that the asymmetry in the profiles was the result of azimuthal non-uniformity of the neutral gas distribution. In section 7.6.1, the effects of neutral asymmetries substantially lowered the efficiency of the NASA-173Mv1 with anode #1. **However, based on the favorable performance and thermal margin of the NASA-17Mv2, asymmetries in the plume profiles were judged to affect thruster operation only marginally.**

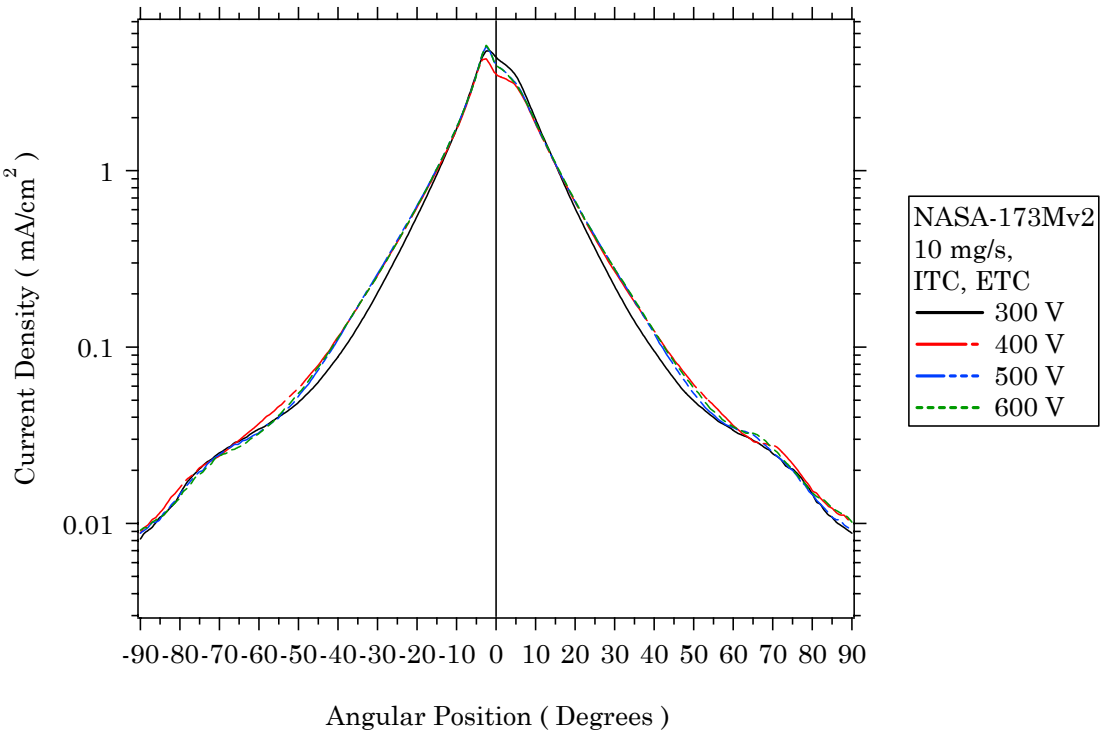

Figure 8-13 Ion current density in the plume of the NASA-173Mv2 versus angular position from thruster centerline at 10 mg/s, 300-600 V.

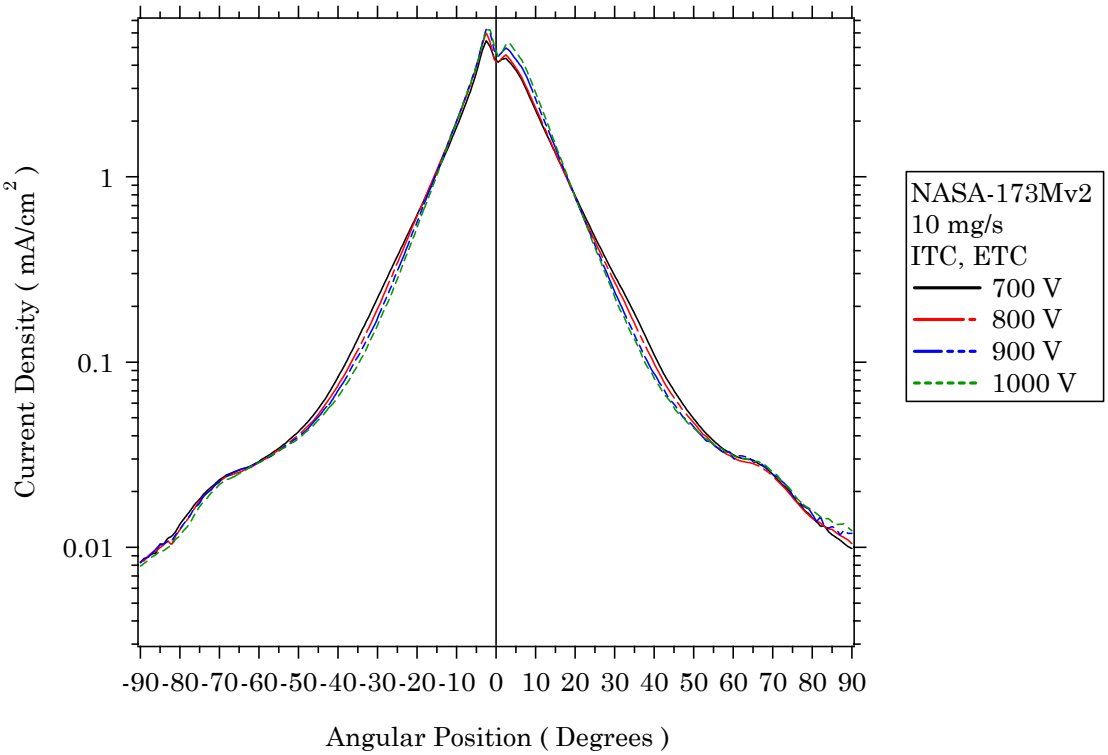

Figure 8-14 Ion current density in the plume of the NASA-173Mv2 versus angular position from thruster centerline at 10 mg/s, 700-1000 V.

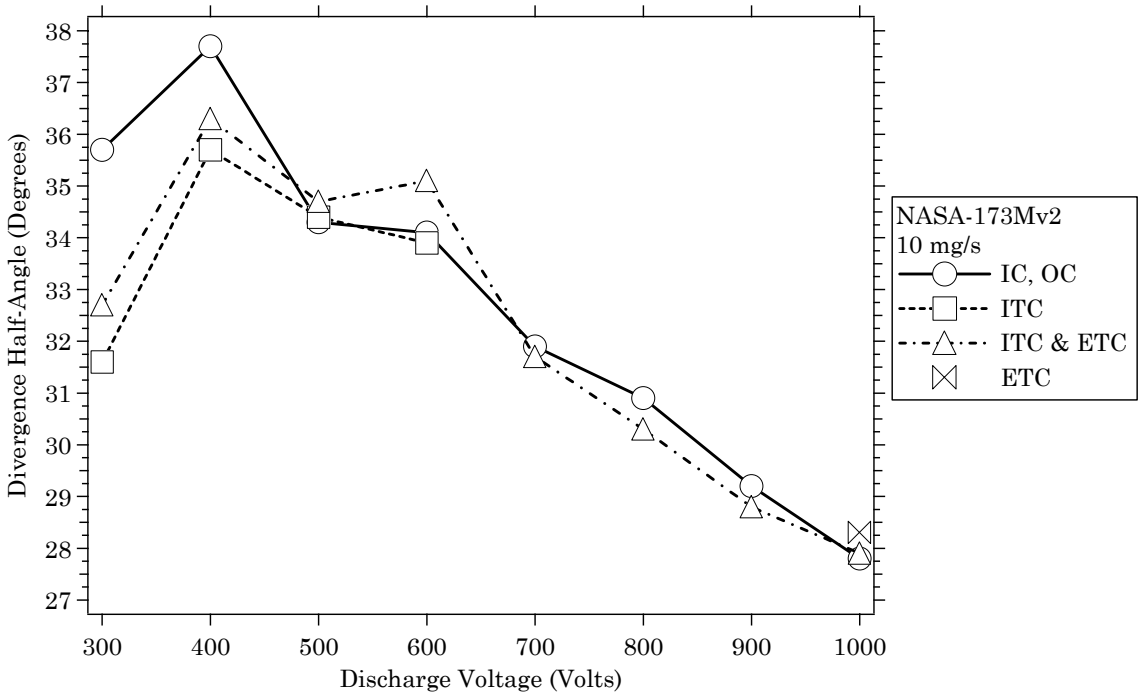

Figure 8-15 95% plume divergence half-angle versus discharge voltage of the NASA-173Mv2 at 10 mg/s.

Plume divergence is determined by a number of processes, including: radial electric fields in the acceleration zone, the axial location of the acceleration zone, thermal spreading at the ion acoustic velocity, particle collisions in the plume and even plasma oscillations [2, 141, 240, 241]. How these processes scale, and which ones dominate, is not completely understood, but divergence should scale as the ratio of radial to axial ion velocity if the influence of plume collisions and plasma oscillations can be neglected. Thus, a decreasing divergence angle with voltage would imply that axial velocities are increasing at a faster rate than radial velocities.

As shown in Figure 8-15, plume divergence increased between 300–400 V, followed by a continual decrease. The initial increase was attributed to a large increase in plasma oscillations (see Figure 8-19). Excluding the 300 V data, divergence was found to decrease from 400–1000 V as $\beta_{0.95} \propto V_d^{-0.08}$. Assuming that

radial electric fields and thermal expansion dominate the radial expansion, it can be shown that the electron temperature controlling divergence was scaling as $T_{e,D} \propto V_d^{0.84}$. Numerical simulations (with zero wall losses) by Ahedo are in close agreement, which suggested the electron temperature at the ion sonic transition in the discharge chamber scales as $T_{e,S} \propto V_d$ [242].

Figure 8-15 shows that the external trim coil increased divergence, while the internal trim coil decreased divergence. For example, at 1000 V the external trim coil increased divergence, but when the internal trim coil was added, a drop was observed. Data at 300–600 V also shows that the divergence decreased with the internal trim coil and then increased when the external trim coil was added. Further, the cathode potential data shown in Table C-2 of Appendix C, which is a measure of the electron coupling with the discharge, shows that the external trim coil increased the cathode potential (*i.e.*, decreased the magnitude with respect to ground). **Taken together, the divergence and cathode potential trends indicate that the external trim coil improved efficiency by acting primarily on the electrons.**

The effects of the internal trim coil are more complex than the external trim coil because the internal trim coil alters the magnetic field inside the discharge chamber. Figure 8-15 shows that the internal trim coil decreased divergence while the data in Table C-2 of Appendix C shows (with few exceptions) that the cathode potential became more negative, the discharge current decreased and the thrust increased. **The changes in cathode potential and discharge current implied the internal trim coil decreased the axial electron current, while the**

increase in thrust suggested that the ion focusing was improved when the internal trim coil was used.

8.4.3 Discharge current oscillations (10 mg/s)

Discharge current oscillations at 300–1000 V, 10 mg/s were measured at the same coil combinations as the ion current density in section 8.4.3. The power spectral density, breathing-mode frequency, and the standard deviation of the oscillations (expressed as a percentage of the mean discharge current) were computed from the data. Representative plots of the power spectra at 300 and 1000 V are shown in Figures 8-16 and 8-17, respectively. In Figures 8-18 and 8-19, the voltage dependence of the breathing-mode frequency and the standard deviation of the oscillations are shown, respectively.

As shown in Figures 8-16 and 8-17, energizing the trim coils affected the power spectra at 300 and 1000 V. Figure 8-16 at 300 V shows how the broadband distribution without trim coils was replaced by a much stronger peak when the trim coils were used. This peak is usually associated with the breathing-mode ionization instability (see section 6.3.3). Adding the external trim coil to the internal trim coil broadened the distribution, but there was still less broadening than when both trim coils were not used. The dependence of the standard deviation (see Figure 8-19) when the trim coils were energized was weak at 300 V, indicating that more of the energy was being concentrated into a narrower band of frequencies.

Figure 8-17 shows the power spectra at 1000 V. In this figure, note that operation with only the external trim coil, and then the combined influence of both trim coils are shown. The external trim coil data at 1000 V showed broadening similar to when the external trim coil was added to the internal trim coil at 300 V

(see Figure 8-16). A primary difference between 300 and 1000 V was the presence of a new oscillatory mode in the 80–90 kHz frequency band. This mode was present at all voltages between 500–1000 V and overall the external trim coil excited the mode, while the internal trim coil dampened the mode.

Gascon, *et al.* considered discharge current oscillations in the SPT-100ML in an experimental study spanning discharge voltages between 100–600 V [109]. In that study, between 340-520 V, high-frequency harmonics of the 20-25 kHz breathing-mode frequency were measured between 45-55 kHz and 70-80 kHz, and at voltages of 540-600 V, the breathing-mode frequency suddenly decreased to 15 kHz while the high-frequency harmonics were replaced with broadband noise between 10-60 kHz. (As shown in Figure 8-18, a similar decrease of the breathing-mode frequency was not observed in the NASA-173Mv2.) In a companion paper to Ref. [109], Barral, *et al.* attributed the decrease in the breathing-mode frequency to space-charge saturation of the wall sheaths due to the effects of intense secondary electron emissions from the walls [110]. At this time, it is not known if the high-frequency modes measured by Gascon, *et al.* are the same as those measured with the NASA-173Mv2. Choueiri has also considered plasma oscillations in the 25–100 kHz range, but his analysis was restricted primarily to the effects of the magnetic field at constant voltage [141]. Additional studies are needed to reach further conclusions regarding the nature of the oscillations in the 50-100 kHz frequency band with the NASA-173Mv2.

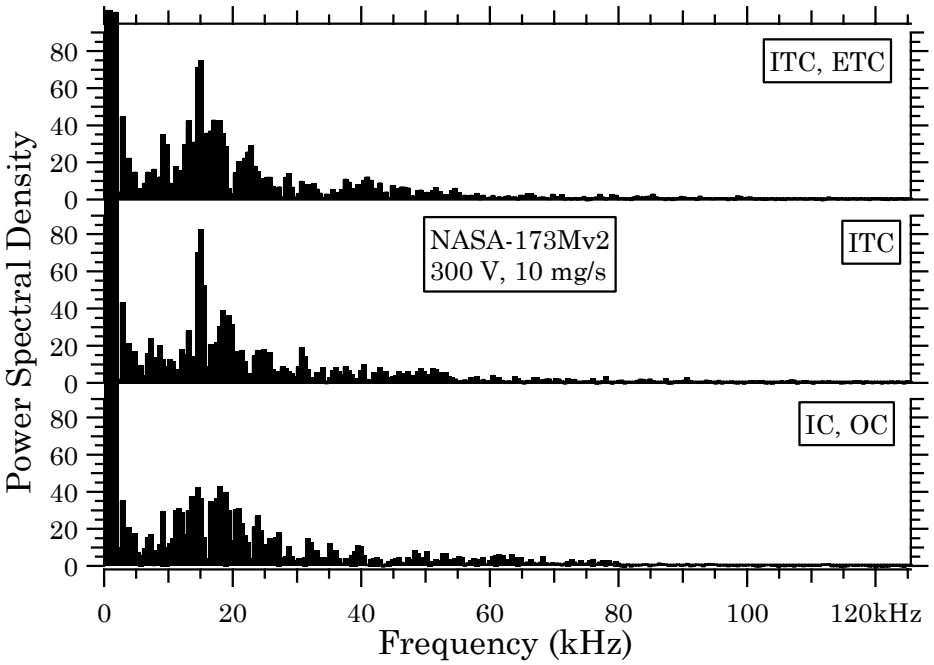

Figure 8-16 Discharge current power spectra of the NASA-173Mv2 at 300 V, 10 mg/s.

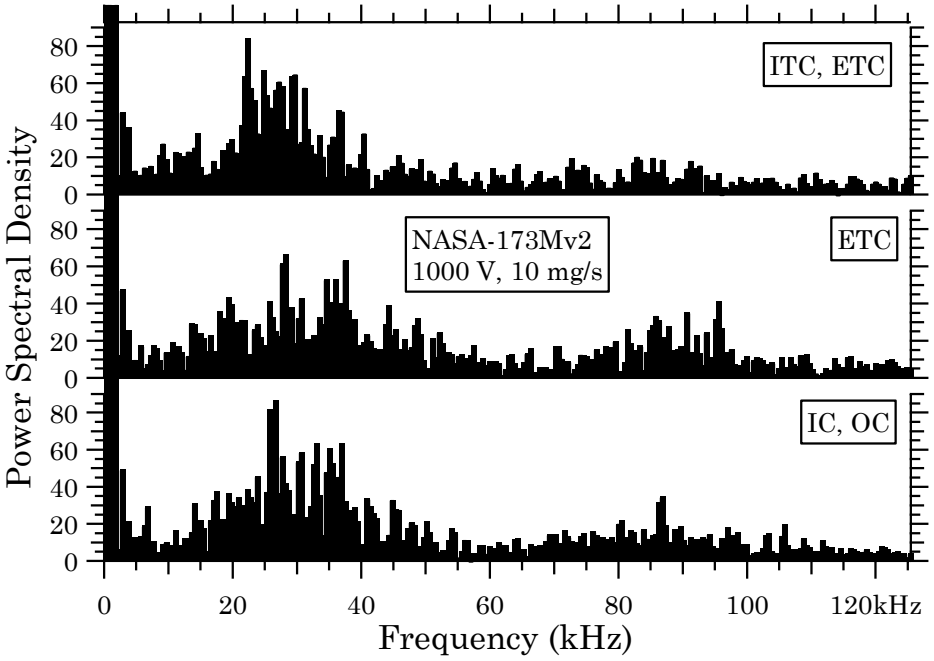

Figure 8-17 Discharge current power spectra of the NASA-173Mv2 at 1000 V, 10 mg/s.

As shown in Figure 8-18, there was a gradual shift to higher frequencies of the breathing-mode frequency, from 14.5 kHz at 300 V to 22 kHz at 1000 V. The

breathing-mode frequency was in the expected range for a Hall thruster [141]. The trim coils generally lowered the breathing-mode frequency at each voltage. For example, at 300 V the breathing-mode frequency decreased from 17.5 kHz to 14.5 kHz when the trim coils were used. At 1000 V, the breathing-mode frequency marginally increased from 26.5 kHz to 28 kHz with the external trim coil, then dropped to 22 kHz when the internal trim coil was energized.

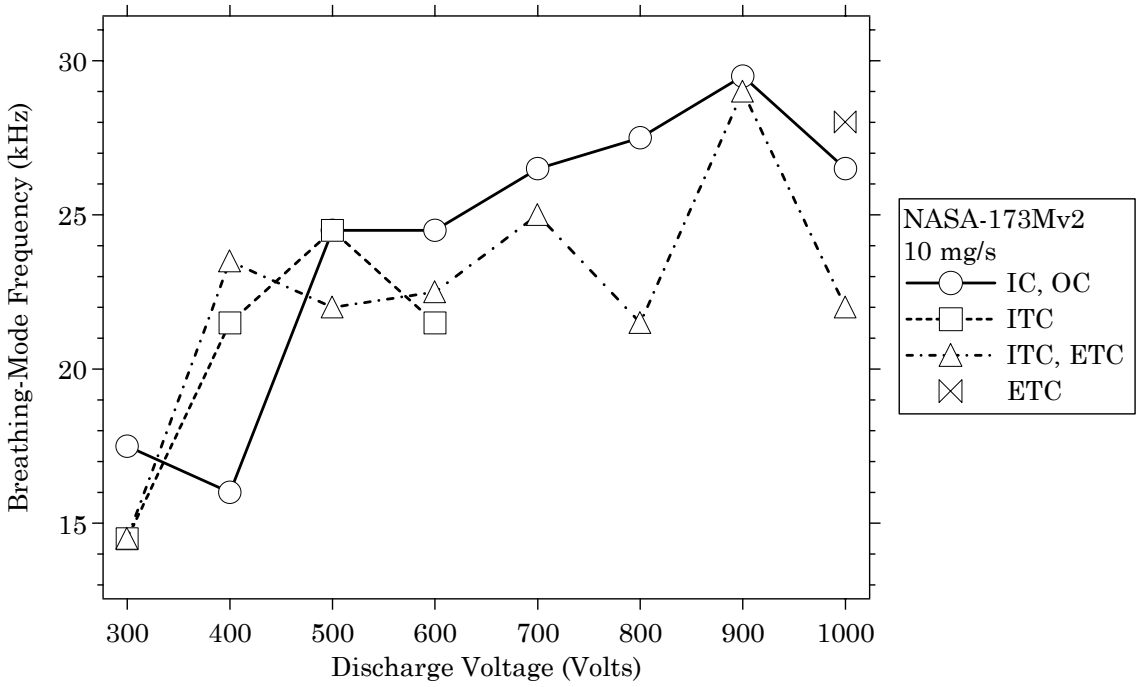

Figure 8-18 Breathing-mode frequency versus discharge voltage of the NASA-173Mv2 at 10 mg/s.

As shown in Figure 8-19, a large increase in the standard deviation of the discharge current oscillations was measured between 300 and 400 V, which persisted until 600 V. Between 700–1000 V, the standard deviation dropped again to another plateau. In general, the trim coils decreased the magnitude of oscillations at a fixed voltage.

The increased oscillations roughly coincided with the range of voltages where efficiency peaked in the NASA-173Mv1 and other Hall thrusters (*i.e.*, 500–800 V)

[133, 175, 176]. It may be that efficiency begins to decrease in other thrusters at a critical voltage due to increased discharge current oscillations related to the rapid onset of space-charge saturation of the wall sheaths [109, 110]. This is thought to be an indication that plasma oscillations and wall effects are playing a significant role determining efficiency with increasing voltage. **Apparently, the magnetic field in the NASA-173Mv2 is effective at controlling oscillations (and by extension, the axial electron current) above 600 V so that efficiency does not begin to decrease.**

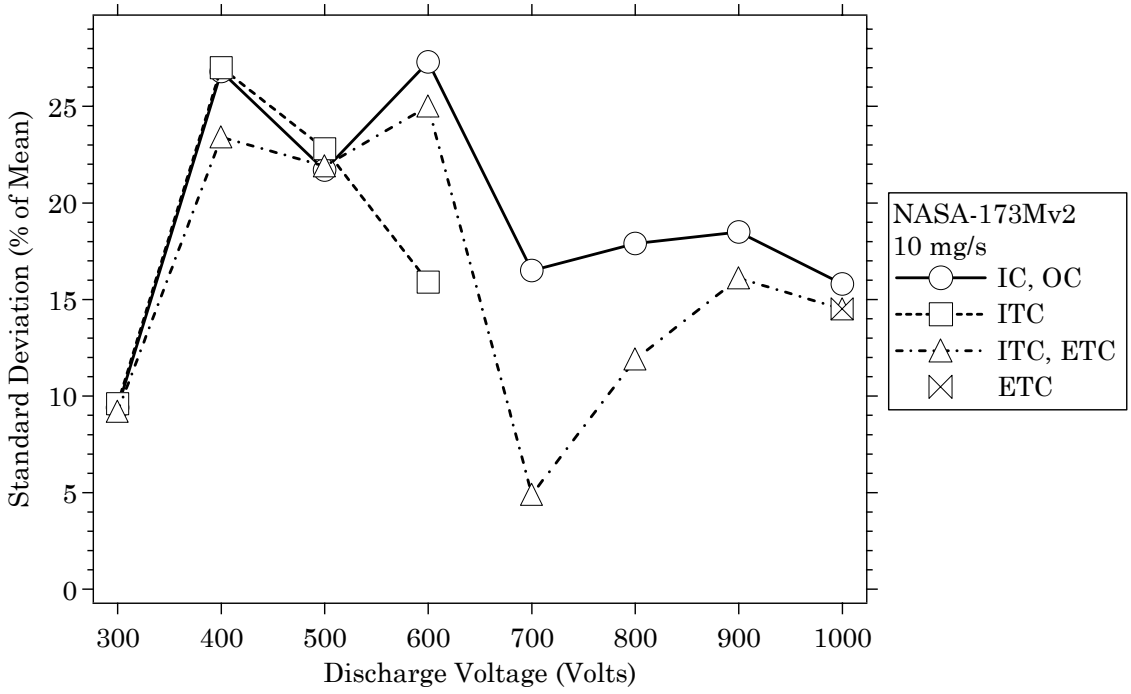

Figure 8-19 Standard deviation of the discharge current oscillations versus discharge voltage of the NASA-173Mv2 at 10 mg/s.

8.4.4 Magnetic field (5-15 mg/s)

In this section, magnetic field measurements of the NASA-173Mv2 are presented. As shown in Figure 8-20, the maximum, radial magnetic field on the channel centerline of the NASA-173Mv2 was computed for each of the thruster operating points investigated in section 8.4.1 using the magnetic field data shown in

Figures 8-3 and 8-4. Since the external trim coil does not affect the magnetic field in the discharge chamber, there are no data shown explicitly for the operating points that made use of the external trim coil. The magnetic field was calculated by finding the contribution from each coil based on the coil current from the various operating points. The total magnetic field was then given by the sum of the magnetic field provided by each coil. This method was valid because the magnetic circuit of the NASA-173Mv2 exhibited a linear response to coil currents up to 5 A (see section 8.3).

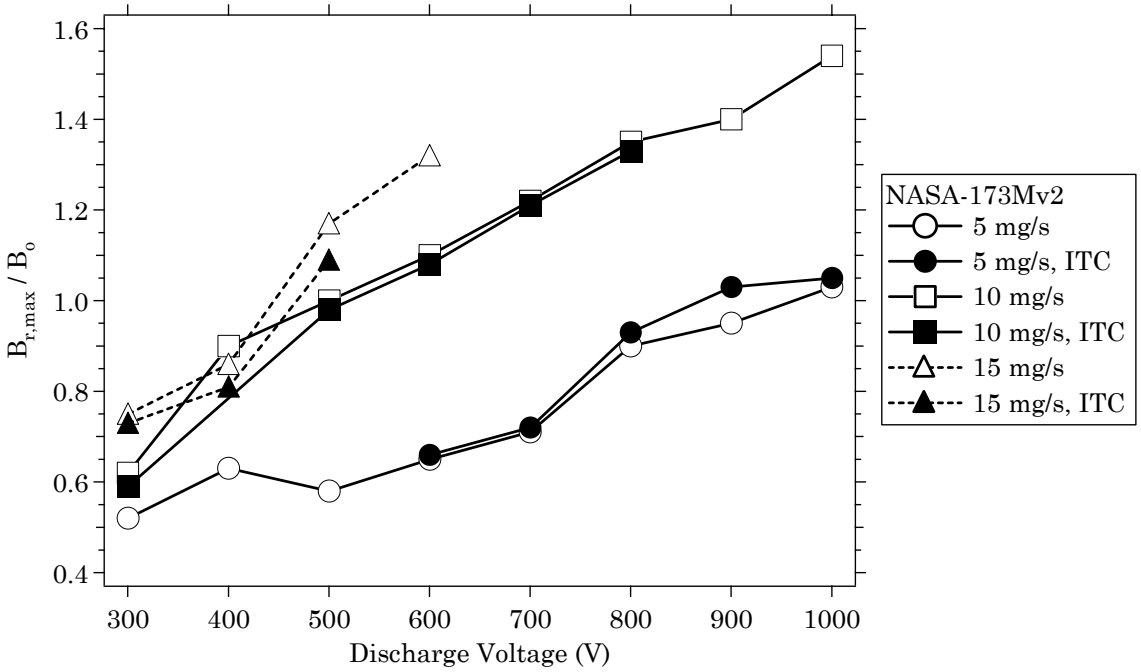

Figure 8-20 Radial magnetic field versus discharge voltage of the NASA-173Mv2 at 5-15 mg/s.

In general, the magnetic field increased with increased mass flow rate or discharge voltage. For constant mass flow rates, the magnetic field increase was nearly linear with voltage. At 10 mg/s, the magnetic field abruptly increased between 300-400 V and then linearly increased between 400-1000 V. Recall that plume divergence and discharge current oscillations also increased between 300-400 V (see Figures 8-15 and 8-19). The magnetic field increased by a factor of 1.5

between 300-400 V and by a factor of 1.7 between 400-1000 V at 10 mg/s. Overall, the magnetic field increased by a factor of 2.6 between 300-1000 V at 10 mg/s.

8.5 Conclusions

The laboratory-model NASA-173Mv2 was conceived in order to understand the design challenges and physical mechanisms determining the performance of high-specific impulse Hall thrusters. While experiments with the NASA-173Mv1 established the validity of the plasma lens magnetic field design, the NASA-173Mv1 still showed a maximum in the efficiency at high-specific impulse. With the NASA-173Mv2, the goal was to obtain a continuously increasing efficiency with increasing specific impulse. A performance characterization of the NASA-173Mv2 has confirmed that this goal was met.

Experiments with the NASA-173Mv2 have documented the influence of current density and magnetic field topography on the performance, plume divergence and plasma oscillations of high-specific impulse Hall thrusters. The key results and conclusions include:

1. The maximum in the efficiency-voltage characteristic observed in other xenon Hall thrusters, including the NASA-173Mv1, has been eliminated with the NASA-173Mv2. A performance mapping of the NASA-173Mv2 at voltages up to 1000 V and at several current densities showed there was a minimum current density and optimum magnetic field topography at which efficiency monotonically increased with voltage.
2. While enhancing performance overall, **trim coils were not required to obtain a continuously increasing efficiency-voltage**

characteristic. This demonstrated that traditional magnetic circuits can still be used if the fixed magnetic field topography is properly designed.

3. Between 300-1000 V and an anode mass flow rate of 10 mg/s, the total specific impulse of the NASA-173Mv2 ranged from 1600-3400 s with a corresponding total efficiency of 51-61%.
4. The use of trim coils to modify the magnetic field improved performance while decreasing plume divergence and the frequency and magnitude of plasma oscillations. This may ultimately prove to be the greatest utility of trim coils, since controlling divergence and oscillations is critical to extending thruster lifetime.
5. Plume divergence was shown to decrease over the range of 400–1000 V from a maximum of 38° to a minimum of 28°. An increase in divergence from 300 to 400 V was attributed to plasma oscillations.
6. The breathing-mode frequency steadily increased with voltage, from 14.5 kHz at 300 V to 22 kHz at 1000 V.
7. It was shown that the trim coils influenced the magnitude and frequency content of discharge current oscillations. Using the external trim coil broadened the power spectrum while the effect of the internal trim coil was to localize the energy to a narrower band of frequencies.
8. The emergence of additional oscillatory modes in the 80–90 kHz frequency band when the discharge voltage exceeded 500 V has been

reported. Modifying the magnetic field with the trim coils has also been shown to affect this frequency band.

9. At optimum thruster efficiency, a nearly linear increase of the magnetic field was measured with increasing discharge voltage. Between 300-1000 V, the magnetic field increased by a factor of 2.6 at mass flow rates of 10 mg/s.

Chapter 9

Discussion I - Comparison of the NASA-173M Hall thrusters

Experiments with the NASA-173M Hall thrusters established that efficient operation at high-specific impulse is possible if a minimum current density is maintained and the magnetic field topography is properly shaped. In this chapter, the characteristics of the two thrusters are compared in terms of ion current density, discharge current oscillations, magnetic field, and efficiency. Due to the limited data at 5 and 15 mg/s, the discussion is focused mostly on results at 10 mg/s.

9.1 Ion current density

Figures 9-1 and 9-2 compare the plume profiles of the NASA-173M Hall thrusters at an anode flow rate of 10 mg/s and discharge voltages of 300 and 500 V, respectively. Plume divergence angles computed from the ion current density profiles are compared in Figure 9-3. Data from the NASA-173Mv1 were limited to 300 and 500 V, while the NASA-173Mv2 data spans the range of 300-1000 V. At each operating condition, the data shown corresponds to the coil combination that yielded maximum efficiency. For both thrusters, maximum efficiency was obtained when the trim coils were energized.

At 300 V, the plume profile of the NASA-173Mv1 was substantially narrower than the NASA-173Mv2. While the centerline current densities were nearly the

same, the NASA-173Mv1 profile at high angles from centerline decayed faster than the NASA-173Mv2, which resulted in a large difference in plume divergence between the thrusters. At 300 V, the plume divergence angle was 27º with the NASA-173Mv1 and 33º with the NASA-173Mv2.

At 500 V, the plume profiles were nearly the same for the thrusters over all angles. One noticeable difference is the shape of the NASA-173Mv1 profile at high angles. Unlike the NASA-173Mv2, which exhibits a large change in slope around 60º, the change in slope with the NASA-173Mv1 was much less pronounced. Differences between the plume profiles were minor at 500 V, as evidenced by the computed plume divergence. At 500 V, the plume divergence angle was 36º with the NASA-173Mv1 and 35º with the NASA-173Mv2.

The effects of changing the magnetic field with the trim coils affected the plume divergence more with the NASA-173Mv1 than the NASA-173Mv2. This is shown by comparing effects of the trim coils on the plume divergence angles at 300 and 500 V, 10 mg/s in Figures 7-42 and 8-15. With the NASA-173Mv1, divergence decreased by 6º at 300 V and by 4º at 500 V when the internal trim coil was used. With the NASA-173Mv2, divergence decreased by 4º at 300 V and was unchanged at 500 V when the internal trim coil was used. Except for 300 V, plume divergence was only changed by an average of 0.2º (sometimes, the trim coils increased divergence) with the NASA-173Mv2 over 400-1000 V, whereas with the NASA-173Mv1 plume divergence was increased by an average of 3º at all voltages and flow rates that were tested.

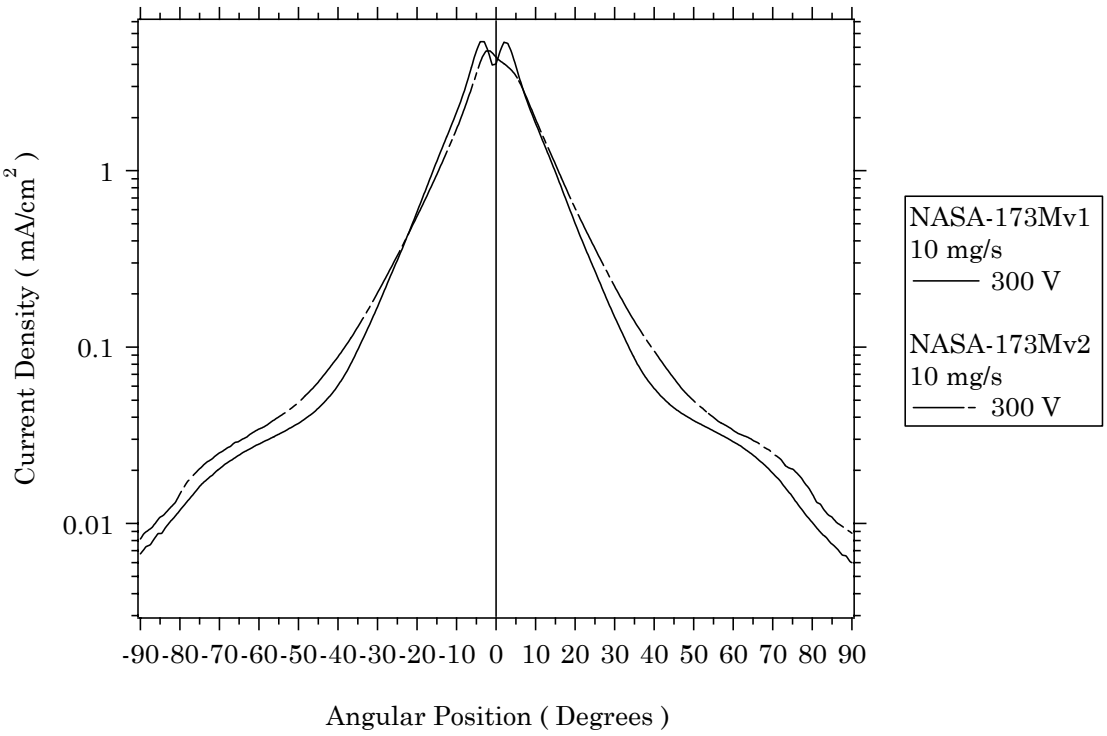

Figure 9-1 Ion current density in the plume of the NASA-173M Hall thrusters versus angular position from thruster centerline at 10 mg/s, 300 V.

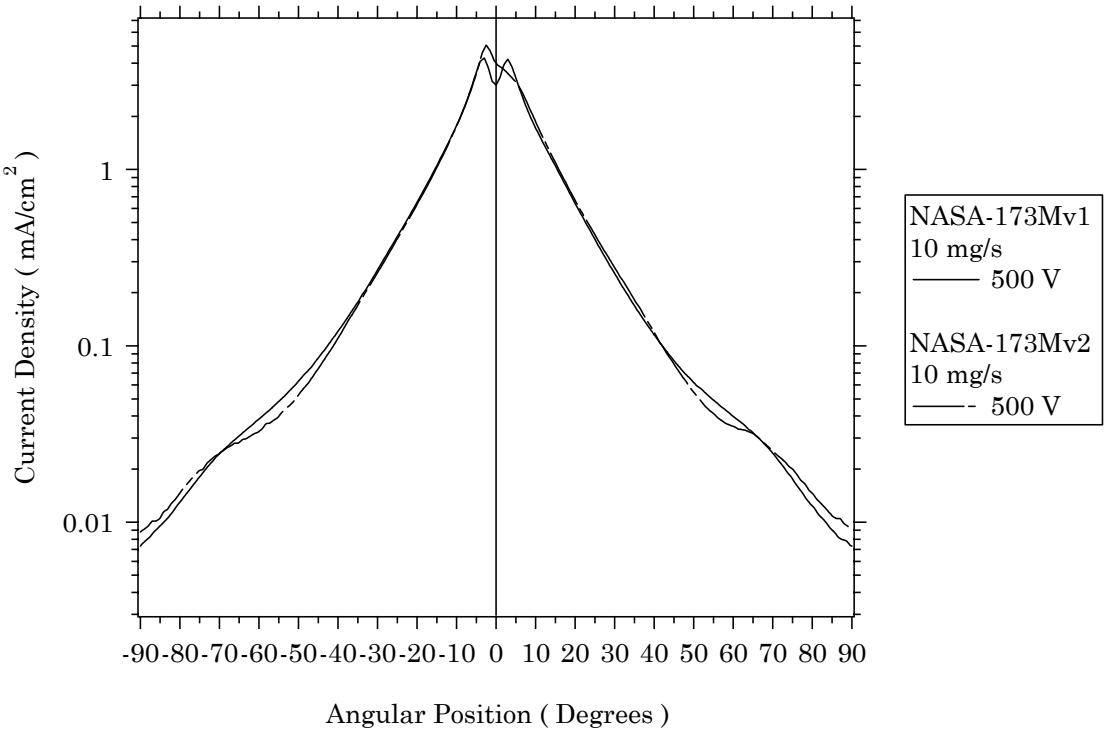

Figure 9-2 Ion current density in the plume of the NASA-173M Hall thrusters versus angular position from thruster centerline at 10 mg/s, 500 V.

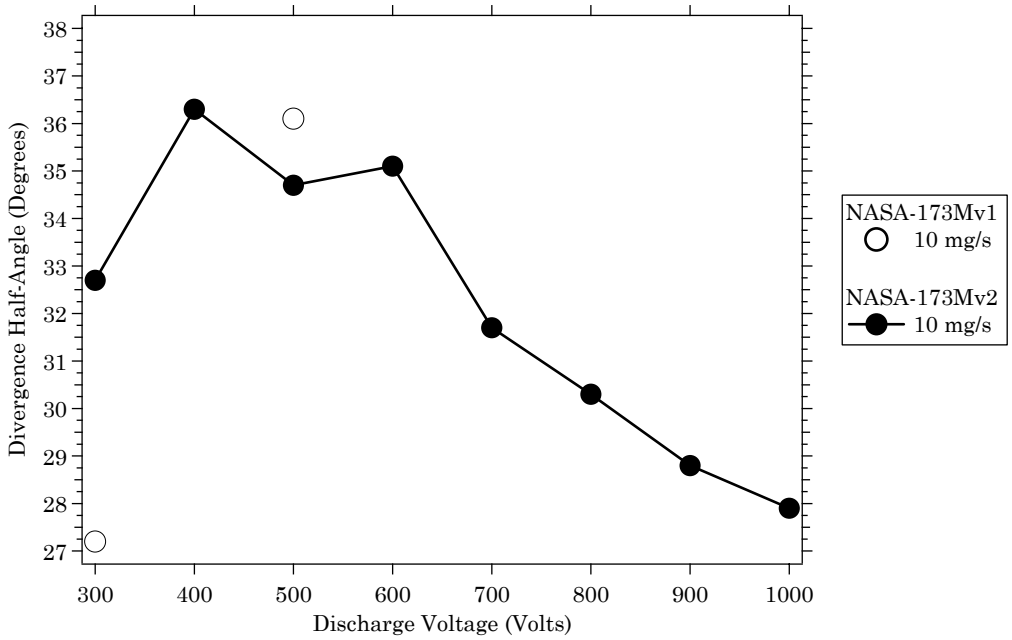

Figure 9-3 95% plume divergence half-angle versus discharge voltage of the NASA-173M Hall thrusters at 10 mg/s.

At least at 300 and 500 V, the relatively minor change in the plume divergence of the NASA-173Mv2 caused by the trim coils indicated that the plume focusing was already near the optimum with the magnetic field supplied by the inner and outer coils alone. This conclusion correlated with the observed change in thruster efficiency when using trim coils. In the NASA-173Mv1, using the internal trim coil improved efficiency by an average of 2.3% at 300-800 V, 10 mg/s (see Figure 7-36), whereas with the NASA-173Mv2, efficiency improved by an average of only 0.8% at 300-1000 V, 10 mg/s (see Figure 8-7).

9.2 Discharge current oscillations

Figures 9-4 and 9-5 compare the breathing-mode frequency and the standard deviation of the discharge current oscillations, respectively, of the NASA-173M Hall thrusters at an anode flow rate of 10 mg/s. At each operating condition, the data shown corresponds to the coil combination that yielded maximum efficiency. For

both thrusters, maximum efficiency was obtained when the trim coils were energized. Data from the NASA-173Mv1 were limited to 300 and 500 V, while the NASA-173Mv2 data spans the range of 300-1000 V.

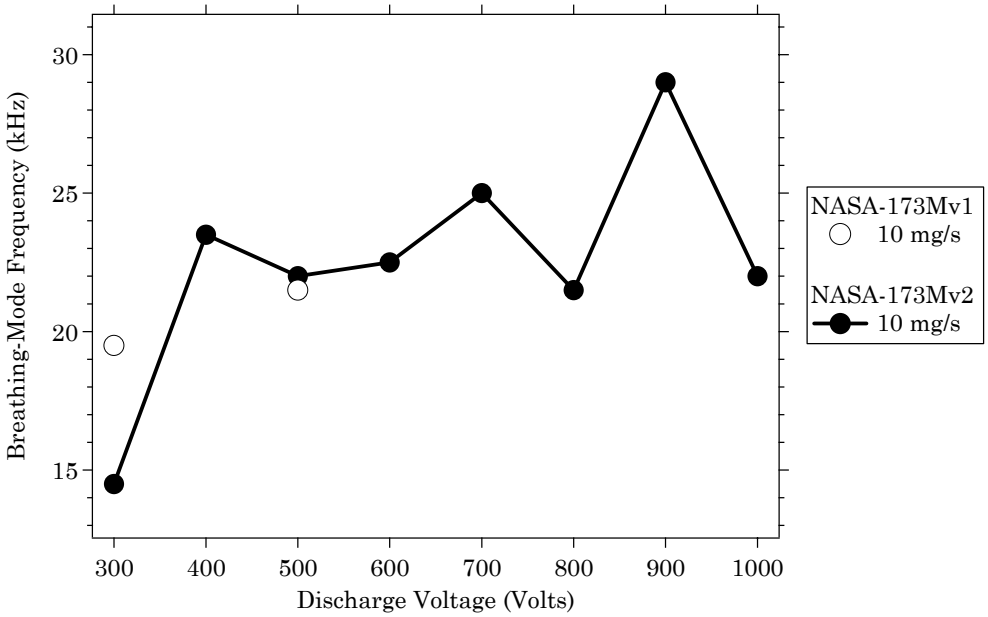

Figure 9-4 Breathing-mode frequency versus discharge voltage of the NASA-173M Hall thrusters at 10 mg/s.

At 300 and 500 V, there were only minor differences between the thrusters for either the breathing-mode frequency or the magnitude of the discharge current oscillations. However, for the NASA-173Mv1 at 500 V it may be significant that the discharge current oscillations were nearly the same as at 300 V. In the NASA-173Mv2, a large increase in oscillations was observed between 300-400 V that persisted until 600 V. Since the current oscillations were nearly constant with the NASA-173Mv1 between 300-500 V, this may be an indication that the NASA-173Mv1 magnetic field topography is better suited for operation at 300-500 V. Such a conclusion is consistent with the comparison of efficiency for the thrusters shown in Figure 9-8. Additional discharge current measurements with both thrusters,

especially the NASA-173Mv1, are needed to establish the connection between discharge current oscillations and thruster efficiency further.

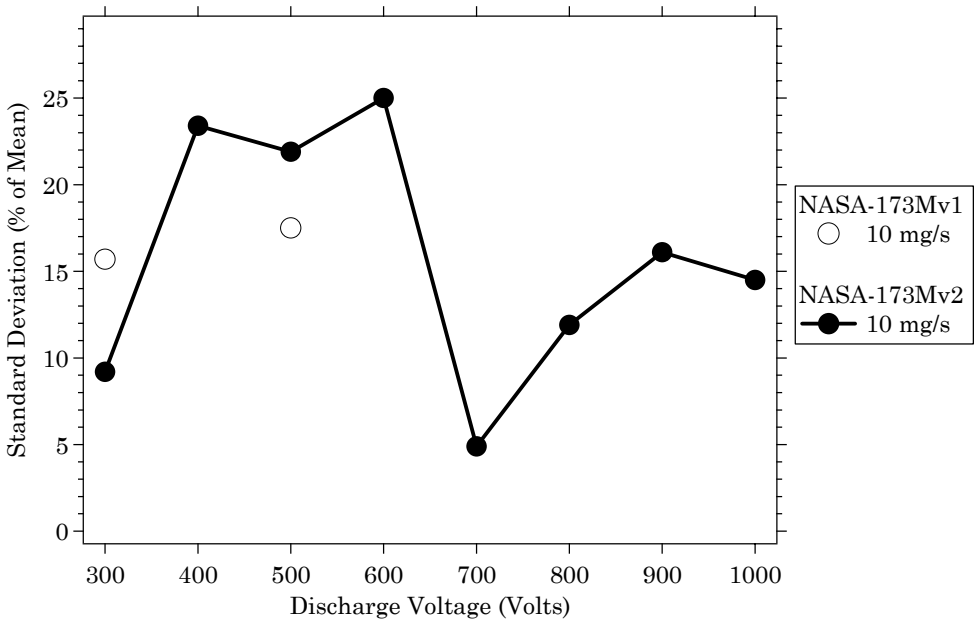

Figure 9-5 Standard deviation of the discharge current oscillations versus discharge voltage of the NASA-173M Hall thrusters at 10 mg/s.

9.3 Magnetic field

Figure 9-6 compares the maximum radial magnetic field on channel centerline for the NASA-173M Hall thrusters at anode flow rates of 5, 10, and 15 mg/s. At each operating condition, the data shown corresponds to the coil combination that yielded maximum efficiency. For both thrusters, maximum efficiency was obtained when the trim coils were energized.

At constant flow rate, Figure 9-6 shows that the magnitude of the magnetic field and the scaling of the magnetic field with voltage were nearly the same between the thrusters. **Since the magnitude of the magnetic field was nearly the same, but the efficiency was not (see Figure 9-8), the shape of the magnetic field was concluded to be more critical than its magnitude.** Further, it is significant that the magnetic field could not be increased enough (at

fixed voltage) to maintain thruster efficiency at 5 mg/s in either thruster. At 5 mg/s, neither changes to the magnitude or shape of the magnetic field (with the trim coils) could keep efficiency from decreasing (with either thruster, efficiency reached an asymptote at high-voltage). A possible explanation for the efficiency trend at 5 mg/s is proposed in section 9.4.1.

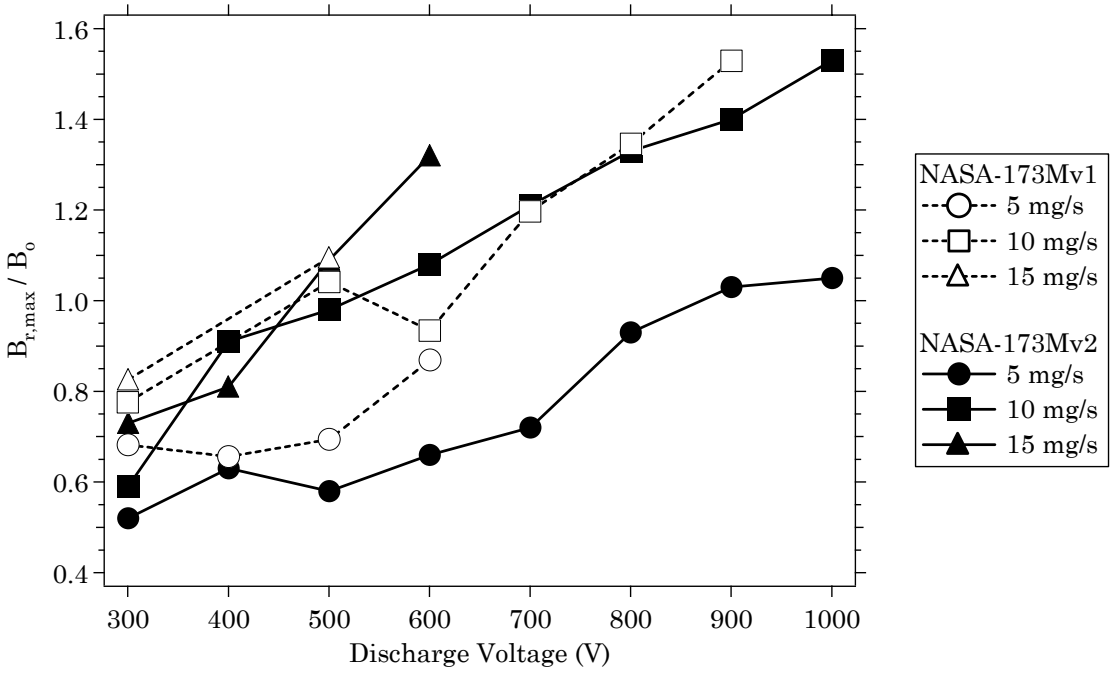

Figure 9-6 Radial magnetic field versus discharge voltage of the NASA-173M Hall thrusters at 5-15 mg/s.

Depending on the approach that is taken, theoretical considerations predict that the scaling of the magnetic field with voltage should go either as the square root ($B_r \propto V_d^{1/2}$) [2, 3] or be linear ($B_r \propto V_d$) [175, 243]. At constant flow rate, the magnetic field scaling of the NASA-173M Hall thrusters generally approached linearity, especially at 10 mg/s. However, the change in magnetic field with voltage did show differences over certain voltages and flow rates. For example, for the NASA-173Mv2 at 5 mg/s, there was a noticeable increase in the slope of the magnetic field variation between 300-700 V and 700-1000 V. In addition, the

magnetic field sharply increased between 300-400 V with the NASA-173Mv2 at 10 mg/s, then increased at a nearly linear rate between 400-1000 V. In general, while the variation of the magnetic field with voltage approached linearity with either thruster, additional measurements at smaller voltage intervals are needed to compute the magnetic field scaling with voltage more accurately.

9.4 Efficiency

In this section, the efficiency of the NASA-173M Hall thrusters at anode flow rates of 5, 10, and 15 mg/s over a voltage range of 300-1000 V is discussed. At each operating condition and unless noted otherwise, the data shown in this section corresponds to the coil combinations that yielded maximum efficiency. For both thrusters, maximum efficiency was obtained when the trim coils were energized.

9.4.1 Effects of current density

To illustrate the importance of current density in achieving efficient operation at high-specific impulse, trends in the anode efficiency of the NASA-173M Hall thrusters at 5 mg/s are discussed in this section. Figure 9-7 compares the anode efficiency of the thrusters at 5 mg/s when anode #1 was used with the NASA-173Mv1. For the NASA-173Mv1, data taken with anode #1 are used for comparison since these data spanned 300-1000 V (data with anode #2 only spanned 300-600 V). Anode efficiency is shown in Figure 9-7 since some of the data taken with the NASA-173Mv1 using anode #1 varied the cathode flow fraction. Since anode #1 decreased efficiency due to neutral asymmetries (see section 7.6.1), the focus in this section is on the relative change in efficiency with voltage rather than on absolute numbers. For reference, the total efficiency of the thrusters is compared (with anode #2 for the NASA-173Mv1) in Figure 9-8.

At 5 mg/s, the anode efficiency of the NASA-173Mv2 shows trends that are very similar to the NASA-173Mv1. Both thrusters reached a maximum efficiency, despite the use of trim coils, which occurred at 500 V in the NASA-173Mv2 and 600 V in the NASA-173Mv1 for anode #1. Above the maximum efficiency, trim coils improved efficiency but at best the efficiency reached an asymptote with increased voltage.

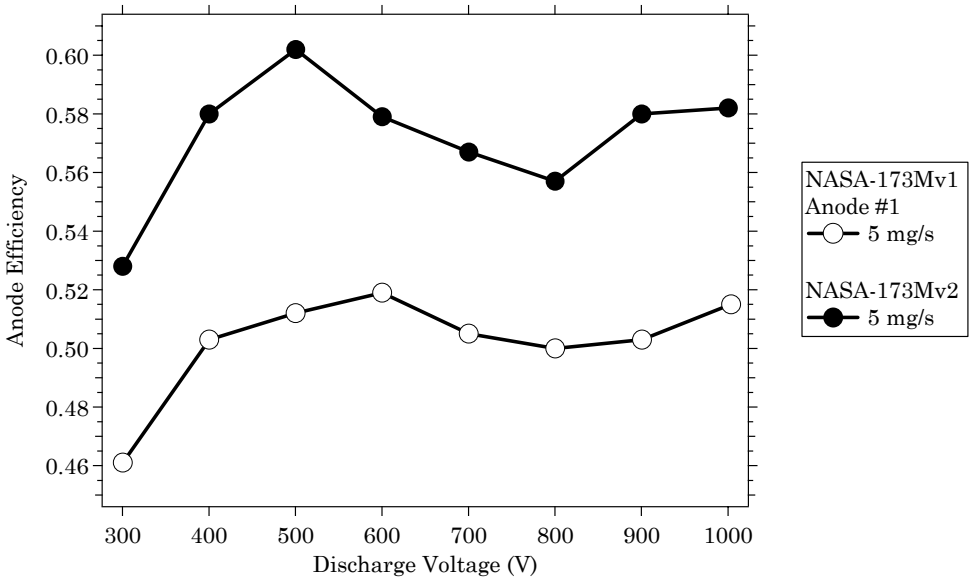

Figure 9-7 Anode efficiency versus discharge voltage of the NASA-173M Hall thrusters at 5 mg/s. The data shown for the NASA-173Mv1 was taken with anode #1 (see section 7.6.1).

Additionally, when trim coils were used at 5 mg/s the gain to efficiency was greatest at the highest voltages. For example, for the NASA-173Mv2 at 300 V trim coils improved efficiency by 0.6% while at 1000 V efficiency increased by 5.6% (see Figure 8-6). The NASA-173Mv2 showed no improvement with the internal trim coil at 500 V or less; only the external trim coil was effective. Above 500 V, only the internal trim coil increased efficiency in the NASA-173Mv2. Further, positive internal trim coil currents were found to improve efficiency in the NASA-173Mv2 at 5 mg/s, while negative currents were always beneficial in the NASA-173Mv1. Recall

that positive internal trim coil current decreases $\nabla_z B_r$ along the channel. **Since $\nabla_z B_r$ is greater in the NASA-173Mv2 than the NASA-173Mv1, this implies there is an optimum value of $\nabla_z B_r$ at 5 mg/s, which can be determined by comparing the magnetic fields in both thrusters.**

While an optimum magnetic field can be inferred from the data, it is significant that the relative variation of the anode efficiency at 5 mg/s was nearly identical between the thrusters despite the fact that the magnetic field topographies were different. This strongly suggested that current density was the dominant factor determining efficiency at 5 mg/s. (At 10-15 mg/s, the magnetic field was thought to be more important since at these higher flow rates the efficiency maximum was eliminated in the NASA-173Mv2 but not in the NASA-173Mv1, see Figure 9-8). A possible explanation for the efficiency trends at 5 mg/s is proposed in the following.

Regardless of the flow rate, as the discharge voltage is increased the challenge is to minimize electron back streaming and multiply-charged ion production while maintaining an average electron temperature that allows for efficient ionization (see sections 3.1.3, 3.2.2.1, and 7.1). Thus, efficient operation can be achieved by controlling the electron current with the magnetic field and by regulating the electron temperature. Electron temperature is primarily regulated by inelastic collisions with the walls and neutrals.

The data at 5 mg/s suggests that electron collisions with the walls and neutrals must both be at a sufficiently high rate if the electron temperature is to remain low enough that the ionization efficiency does not suffer and thermal diffusion does not dominate. The magnetic field is

clearly important in controlling wall collisions; however, at 5 mg/s the data suggests that the influence of the plasma lens on neutral collisions is second-order. At low flow rates, it is thought that electron temperature is poorly regulated since the plasma density is too low to sustain a neutral collision rate that can keep the electron temperature within acceptable limits.[37] In short, current density and magnetic field topography both have important roles in achieving efficient operation at high-specific impulse.

9.4.2 Combined effects of magnetic field and current density

Figure 9-8 compares the total efficiency for the NASA-173M Hall thrusters at anode flow rates of 5, 10, and 15 mg/s. The data shows that thruster efficiency can be maximized by controlling both current density and magnetic field topography.

Current density was shown to affect efficiency in two ways. First, as is well-known with Hall thrusters [2, 3], as the flow rate is increased at constant voltage, the ionization rate will increase and improve the propellant utilization, and hence, the overall efficiency. As shown in Figure 9-8, at constant voltage the efficiency of both thrusters benefited from increased propellant utilization as the flow rate increased. Second, current density also plays a critical role with the variation of efficiency with voltage. This is shown in the data from the NASA-173Mv2, which demonstrates that thruster efficiency monotonically increased at 10 mg/s, while at 5 mg/s a peak efficiency was observed.

However, current density was not the only factor responsible for eliminating the efficiency peak. Magnetic field topography also played a crucial role. This was shown by considering the variation of efficiency with voltage for both thrusters at 10

[37] The opposite is thought to occur in anode layer thrusters. In an anode layer thruster, wall collisions are not present to cool electrons, only inelastic collisions with neutrals can regulate the electron temperature (see section 3.2.2.1).

mg/s. With the NASA-173Mv1 at 10 mg/s, efficiency still showed evidence of a maximum at 500 V, and then at higher voltages, efficiency was relatively constant. In contrast, the efficiency of the NASA-173Mv2 at 10 mg/s monotonically increased with increasing voltage. **Since the major difference between the thrusters was the magnetic field topography, it was concluded that changes made to the magnetic circuit of the NASA-173Mv2 were responsible for eliminating the efficiency peak.** That is, the NASA-173Mv2 achieved the intended goal of optimizing the magnetic field topography for operation at high-specific impulse.

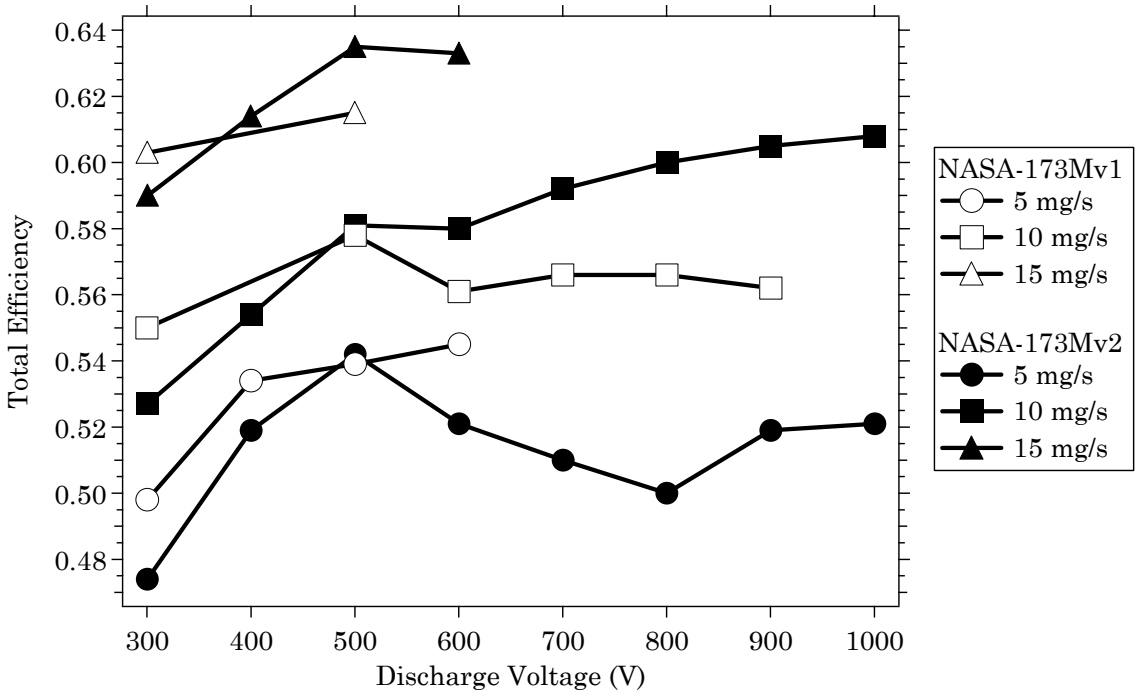

Figure 9-8 Total efficiency versus discharge voltage of the NASA-173M Hall thrusters at 5-15 mg/s.

These results have also shown that thruster efficiency can be optimized for specific discharge voltages by changing the plasma lens design. At 10 mg/s, the efficiency of the NASA-173Mv2 was higher than the NASA-173Mv1 for discharge voltages greater than 500 V. At 5 and 15 mg/s, the NASA-173Mv1 efficiency showed the same trend of being more efficient at low voltages (although data were limited at

these flow rates). **Thus, differences in the magnetic field topography of the NASA-173M Hall thrusters have shown how thruster efficiency can be optimized for a particular voltage and flow rate by changing the plasma lens.**

While these results have shown how current density and magnetic field work in tandem to maintain thruster efficiency at high-specific impulse, it is important to emphasize that there are practical limits to the current and power density that a given thruster design can sustain (see section 8.4.1.2). Power density limitations are determined by the thermal constraints of the thruster materials, the associated decrease in lifetime, and the potential loss of thruster stability. With the NASA-173M Hall thrusters, high-specific impulse operation at 10 mg/s has proven to be an acceptable balance between performance, thermal margin, and stability (no attempts have yet been made to assess lifetime). Accordingly, in part III the focus is on characterizing the thruster properties at 10 mg/s.

9.5 Conclusions

The efforts to develop the NASA-173M Hall thrusters have shown how current density and magnetic field topography are critical to achieving efficient operation at high-specific impulse. An extensive effort to characterize the plume, discharge current oscillations, magnetic field, and performance of the thrusters has revealed how each thruster optimizes over a certain range of specific impulse that depends primarily on the magnetic field topography. Since the NASA-173Mv2 has demonstrated high-efficiency, high-specific impulse operation, this thruster was chosen as the subject of the investigations described in part III, which begins with the next chapter.

Part III

Characterization of a High-Efficiency, High-Specific Impulse Xenon Hall Thruster

Chapter 10

Experimental apparatus II

Through design and experiment, the development of the NASA-173M Hall thrusters established that Hall thrusters can operate efficiently at high-specific impulse if a minimum current density is maintained and the magnetic field topography is properly shaped. This chapter begins part III, which concerns experiments that continued to characterize the NASA-173Mv2 Hall thruster.

While the NASA-173Mv2 can be operated efficiently at high-specific impulse, a need still exists to improve understanding of the relationship between the thruster design and the plasma properties. This is necessary to further increase the performance, thermal margin, stability, and lifetime of future thrusters designed for near-Earth and interplanetary missions. To that end, a series of plasma diagnostics were deployed to help improve the understanding of the competing mechanisms affecting Hall thruster performance at high-specific impulse.

The purpose of this chapter is to describe the experimental apparatus that were used during the extended plasma characterization of the NASA-173Mv2. Several experiments were conducted in vacuum facilities at the University of Michigan and NASA GRC. This chapter describes those facilities and the diagnostics that were used. Experiment specific details, such as the thruster operating conditions, are presented in subsequent chapters. Chapter 11 presents results from the experiments conducted with the diagnostics described in this

chapter. In Chapter 12, the results from the NASA-173Mv2 plasma characterization are analyzed and discussed.

10.1 Overview of facilities and diagnostics

The experiments described in Chapter 11 were conducted in two vacuum facilities using several diagnostics. Table 10-1 summarizes the diagnostics that were used for those experiments.

Table 10-1 Diagnostics used during the extended plasma characterization of the NASA-173Mv2.

	Location	Facility	Section
Floating potential probe	UM	LVTF	§11.1
ExB probe	GRC	VF12	§11.2
Langmuir probe	GRC	VF12	§11.3
RPA	GRC	VF12	§11.4

10.2 Vacuum facilities

Vacuum facilities at the University of Michigan and NASA GRC were used during the experiments discussed in Chapter 11. Since both vacuum facilities were described in section 6.1, in the following sub-sections only those details specific to the experiments in Chapter 11 are discussed.

10.2.1 Large Vacuum Test Facility at the University of Michigan

Internal floating potential measurements of the NASA-173Mv2 were taken at the University of Michigan in the Large Vacuum Test Facility (LVTF). A schematic of the LVTF is shown in Figure 6-1. The LVTF is equipped with seven re-entrant

cryopumps. For the floating potential measurements described in section 11.1, the LVTF was operated with four cryopumps.

Chamber pressure was monitored using two hot-cathode ionization gauges (see Figure 6-1). With four cryopumps operating, the base pressure was 2.5×10^{-7} Torr. After correcting the pressure measurements from both gauges with Eqn. 6-1 and then averaging, the background pressure in the LVTF with four cryopumps operating was 1.3×10^{-5} Torr for a xenon flow rate of 11 mg/s.

For the floating potential measurements, the NASA-173Mv2 was mounted at the "probe table" location shown in Figure 6-1. The thruster was positioned near the centerline of the LVTF and was fired away from the cryopumps. At this position, the cryopumps were approximately five meters away from the thruster and the thruster plume was allowed to expand approximately four meters down the length of the chamber.

The power electronics and propellant delivery systems were the same as those described in section 6.2.1.1. Thruster telemetry were acquired using the data acquisition system described in section 6.2.1.2.

10.2.2 Vacuum Facility 12 at NASA GRC

Experiments with an ExB probe, a Langmuir probe, and a RPA were conducted with the NASA-173Mv2 in Vacuum Facility 12 (VF12) at NASA GRC. A schematic of VF12 is shown in Figure 6-3. Photographs of the interior of VF12 are shown in Figures 6-4 and 6-5.

A pair of hot-cathode ionization gauges measured the background pressure (see Figure 6-3). The base pressure in VF12 was 1×10^{-7} Torr. Pressure measurements were corrected for xenon using Eqn. 6-1. All of the experiments

described in sections 11.2-11.4 were conducted at a xenon flow rate of 11 mg/s. At this flow rate, the corrected pressures from ionization gauge #1 and #2 were 4.6×10^{-6} Torr and 1.1×10^{-5} Torr, respectively.

In Chapter 12, data from the performance characterization (§8.4.1) and the probe measurements (§11.2-11.4) are used to derive other thruster properties such as the ion and electron current. The data from these experiments were not taken on the same days. However, the setup was nearly identical for all of the experiments. The NASA-173Mv2 was always mounted on the thrust stand indicated in Figure 6-3 and the thrust stand pendulum was locked down during the probe measurements so that the thruster position was fixed. In this position, the thruster was near the chamber's vertical centerline and fired 8.9 m down the length of the tank.

For the measurements in sections 11.2-11.4, the probes were added to the setup used during the performance characterization by adding the probes two meters downstream of the thruster exit plane on the thruster centerline. Every effort was also made to ensure that the thruster was operated under identical operating conditions (*e.g.*, flow rate, discharge voltage, magnet current). The power electronics and propellant delivery systems were the same as those described in section 6.2.2.1. Thruster telemetry were acquired using the data acquisition system described in section 6.2.2.2. The thruster was operated for four hours after initial exposure to vacuum conditions to allow for outgassing of the chamber walls. Upon subsequent thruster shutdowns and restarts or a change in the discharge voltage, the thruster was operated for at least 30-60 minutes before data were acquired. This procedure allowed enough time for the discharge current to reach a steady-state value. In these ways, any differences in thruster operation between the data sets were judged to have a negligible influence on the computations in Chapter 12.

10.3 Diagnostics

10.3.1 Floating potential probe

Measurements of the plasma floating potential were taken inside the discharge chamber and downstream of the exit plane of the NASA-173Mv2 (see section 11.1). All data were collected using a planar probe in conjunction with a high-speed translation stage in order to minimize probe-induced thruster perturbations.

10.3.1.1 Design

A schematic of the planar probe that was used to measure floating potential is shown in Figure 10-1. The probe consisted of a 1.54 mm diameter tungsten electrode flush with one end of a 99.8%-pure alumina jacket. The outer diameter and length of the alumina jacket were 3.24 and 75 mm, respectively. Based on plasma measurements in Ref. [143], the Debye length was estimated to range from 0.04–0.08 mm over the measurement domain, which was much less than the electrode diameter. Thus, the effective collection area was taken as the geometric area. Similar probe designs have been used to study the plasma downstream of the exit plane of the D-55 and SPT-100 [45, 208].

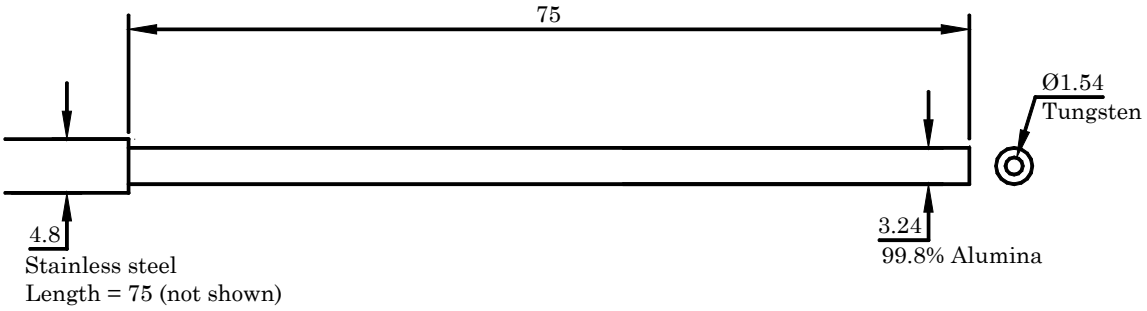

Figure 10-1 Schematic of the floating potential probe. Units are in millimeters.

10.3.1.2 Theory of operation

If the goal is to examine relative changes to the plasma rapidly, the relative simplicity of a floating potential probe has advantages over using failure-prone emissive probes to measure the plasma potential. Esipchuk, Bishaev, Raitses and Kim have used measurements of the floating potential to gain insight on the acceleration process [118, 136, 244, 245]. It has been shown that transient fluctuations of the floating potential were followed by the plasma potential and that the stationary values of the two quantities follow very similar trends [118, 244].

In an unmagnetized, quiescent, Maxwellian plasma, the floating potential V_f is related to the plasma potential V_p by

$$V_f = V_p - \frac{kT_e}{e}\frac{1}{2}\left[1 - \ln\left(\frac{2\pi m_e}{m_{xe}}\right)\right], \qquad \textbf{(10-1)}$$

where T_e is the electron temperature, k is the Boltzmann constant, e is the elementary charge, m_e is the electron mass and m_{xe} is the mass of xenon [246]. This is an important relationship because it is the plasma potential, or more specifically, the electric field derived from it, that accelerates the ions in a Hall thruster. The presence of magnetic fields, streaming ions and non-Maxwellian velocity distributions inside the discharge chamber complicates the relationship between the floating and plasma potential, such that Eqn. 10-1 is not strictly valid. However, the error is on the order of the electron temperature ($T_e \approx$ 10–40 eV in a 300 V Hall thruster [143]) so the floating potential profile is still a useful, albeit inexact, representation of the plasma potential.

The accuracy of a floating potential measurement in the presence of magnetic fields is determined by two important factors: the ratio of the electron or ion Larmor

radius to the probe radius and the orientation of the probe with respect to the magnetic field lines [246]. To achieve acceptable results, the probe radius should be less than the electron Larmor radius and oriented such that the magnetic field lines are nearly perpendicular to the collection electrode. This orientation allows particles to flow freely to the probe.

As a basic operating principle of Hall thrusters (see section 3.1.2), the magnetic field and channel dimensions are chosen so that only the electrons are magnetized [2, 3]. The relationship between the ion and electron Larmor radii therefore satisfies

$$R_e << L << R_b, \tag{10-2}$$

where L is the length of the closed-drift region in the discharge chamber. Since the electrons are magnetized while the ions are essentially unperturbed by the magnetic field, the probe radius should be smaller than the electron Larmor radius. For these experiments, the electron Larmor radius was estimated to range from 1–5 mm, while the probe radius was 0.77 mm. While the accuracy of the measurement would improve with a smaller probe, the error was deemed acceptable for the present application.

The probe was oriented with the collection electrode parallel to the radial direction. While the magnetic field lines on the centerline were essentially radial, an axial magnetic field component was always present that canted the field lines. This fact, combined with inaccuracies of aligning the probe, implied there was always a flux of electrons that freely streamed to the probe. It was also likely that anomalous diffusion of the electrons across magnetic field lines enhanced the flux of electrons to the probe, even in regions of negligible axial magnetic field.

With these considerations, the measurement uncertainty of the floating potential was conservatively estimated as ±10%. This estimate included the effects of probe-induced thruster perturbations (see section 11.1.1). To make the measurements, the electrode was isolated from ground and allowed to float. A 100X, 10 MΩ voltage probe connected to a 500 MHz oscilloscope was used to measure the floating potential with respect to ground. Combined with a simultaneous measurement of the cathode potential with respect to ground $V_{c\text{-}g}$, the floating potential of the probe with respect to the cathode was then computed.

10.3.1.3 Probe positioning system

Figure 10-2 shows the experimental setup used to measure the floating potential inside the discharge chamber of the NASA-173Mv2. The probe measurements were performed in the horizontal plane on thruster centerline. Three translation stages were used to position the floating potential probe with respect to the NASA-173Mv2. The thruster was mounted on a two-axis positioning system that primarily provided radial positioning. (These stages are indicated as the "probe table" in Figure 6-1.) Axial sweeps of the probe were done with the probe attached to PEPL's High-speed Axial Reciprocating Probe (HARP) positioning system. Figure 6-1 shows the approximate position of the HARP relative to the "probe table" where the thruster was mounted.

A full description of the HARP's capabilities can be found in Ref. [135, 142, 143, 247]. The HARP was used to move the probe rapidly in and out of the thruster discharge chamber in order to minimize probe-induced thruster perturbations. The total sweep time (in and out) averaged 300 ms over an axial length of 254 mm. Thruster perturbations always began inside the cathode plane (see section 11.1.1).

The sweep time in one direction from the cathode plane to 10 mm from the anode (58 mm total) ranged from 38–41 ms. Thus, the probe never spent more than 82 ms in this region of the thruster.

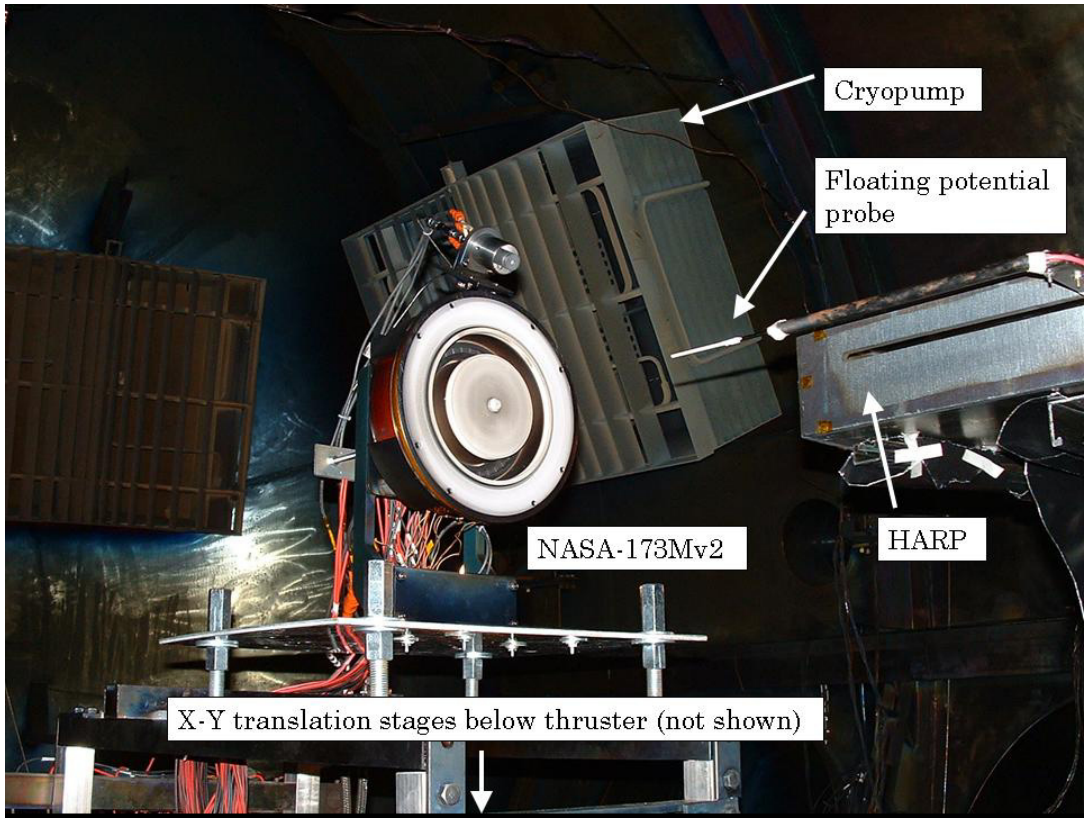

Figure 10-2 Photograph inside the LVTF showing the experimental setup used to measure the floating potential inside the discharge chamber of the NASA-173Mv2.

Figure 10-3 is a schematic of the NASA-173Mv2 showing the coordinate system that was used and the positions where floating potential was measured. Axial positions were referenced from the exit plane, with the anode at z = -38 mm and the cathode plane at z = +30 mm. Radial positions were referenced from thruster centerline, with the discharge chamber centerline at r = 73.7 mm and the outer radius of the thruster body at r = 135 mm. Floating potential was measured on discharge chamber centerline (r = 73.7 mm) along a line extending from z = -28.1 : +61.9 mm.

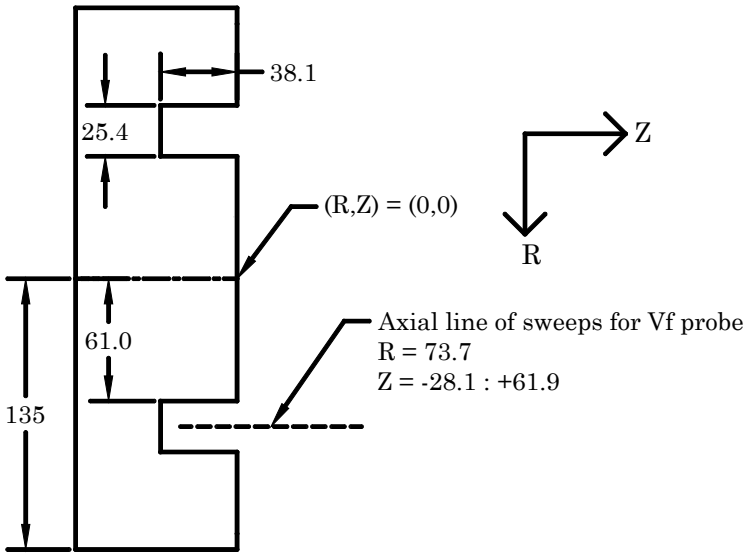

Figure 10-3 Schematic of the NASA-173Mv2 showing the axial line where floating potential was measured. Units are in millimeters.

10.3.2 ExB probe (Wien filter)

An ExB probe is a plasma diagnostic that selectively filters charged particles according to their velocities [27, 208, 209, 248-256]. Because multiply-charged ions in Hall thrusters will have velocities proportional to the square root of their charge-state $\sqrt{Z_i}$ (see Eqn. 4-57), an ExB probe can discriminate between distinct ion species. Examination of the relative height of the ion current peaks from the probe can then be used to compute the ion species fractions.

10.3.2.1 Theory of operation

The classical dynamics of a beam of charged particles in electric and magnetic fields are governed by the Lorentz force equation

$$\vec{F} = eZ(\vec{E} + \vec{v} \times \vec{B}). \qquad \textbf{(10-3)}$$

An ExB probe, also known as a Wien filter, selects particles with a particular velocity by balancing the electric and magnetic fields such that there is no net force acting on those particles

$$0 = eZ(\vec{E} + \vec{v} \times \vec{B}) . \tag{10-4}$$

If the ExB probe is constructed with the electric and magnetic field perpendicular to each other and the particle velocity

$$\begin{aligned} \vec{E} &= (0, E, 0) \\ \vec{B} &= (0, 0, B) , \\ \vec{v} &= (v, 0, 0) \end{aligned} \tag{10-5}$$

then Eqn. 10-4 becomes

$$v = -\frac{E}{B} . \tag{10-6}$$

Eqn. 10-6 shows that the particle velocity can be chosen by adjusting the electric and magnetic fields. In practice, a constant magnetic field is usually applied with permanent magnets. To establish the electric field, two parallel plates are usually biased to a potential V_{probe} and separated by a gap distance d such that the electric field between them is given by

$$E = -\frac{V_{probe}}{d} . \tag{10-7}$$

Thus, the velocity pass condition in an ExB probe is

$$v = \frac{V_{probe}}{Bd} . \tag{10-8}$$

Particles that satisfy Eqn. 10-8 pass through the ExB field region and reach a collection electrode where they are recorded as current. The resulting current-

voltage characteristic is therefore related to the velocity distribution function. It is important to note that an ExB probe is a velocity selector because the charge-state and particle mass do not appear in Eqn. 10-6. Thus, an ExB probe will not detect signatures due to charge-exchange collisions but will detect elastic collisions through signal broadening.

In a Hall thruster, each ion species is accelerated electrostatically to a velocity given by Eqn. 4-57. Substituting Eqn. 4-57 into Eqn. 10-8 and solving for the plate voltage yields an expression in terms of the effective accelerating potential of each ion species and charge-state (*i.e.*, the ion energy, $W_i = eZ_iV_{a,i}$)

$$V_{probe,i} = \sqrt{\frac{2eZ_iV_{a,i}}{m_{xe}}}(Bd). \tag{10-9}$$

The accelerating potential that each charge-state experiences in a Hall thruster differs only by a few tens of volts (see section 4.4.3). Thus, the ion charge-states will appear in an ExB current-voltage characteristic approximately at multiples of $\sqrt{Z_i}$ above the singly-charged peak.

10.3.2.2 Design and experimental setup

Figure 10-4 is a photograph of the ExB probe used to measure the ion species fractions of the NASA-173Mv2. The ExB probe was based on previous designs used to study ion thrusters [256]. Kim's ExB probe [27, 208], which was the first to be used on a Hall thruster, was also based on these designs. Shown schematically in Figure 10-5, the probe used with the NASA-173Mv2 consisted of three main sections: the entrance collimator, ExB test section, and exit collimator. The entrance collimator was 127 mm in length and had two circular orifices at either end

that were 0.5 and 1.0 mm in diameter. In the 127 mm long test section, the magnetic field was applied with permanent magnets that provided a magnetic field strength at the test section center of 0.16 T. The electric field was established with a pair of aluminum plates machined from channel stock. The bias plates were separated by a distance of d=42.5 mm with legs used to minimize electric field fringing that were $d/4$ in length [248, 254]. The exit collimator was 127 mm long and had an exit orifice diameter of 3.2 mm. A 23 mm diameter tungsten collection electrode was placed at the end of the exit collimator. Before installing the ExB probe in VF12, the entrance and exit collimator orifices were aligned using a laser. The acceptance angle of the probe was 0.7°. Probe resolution was conservatively estimated as 7% of the ion energy [208].

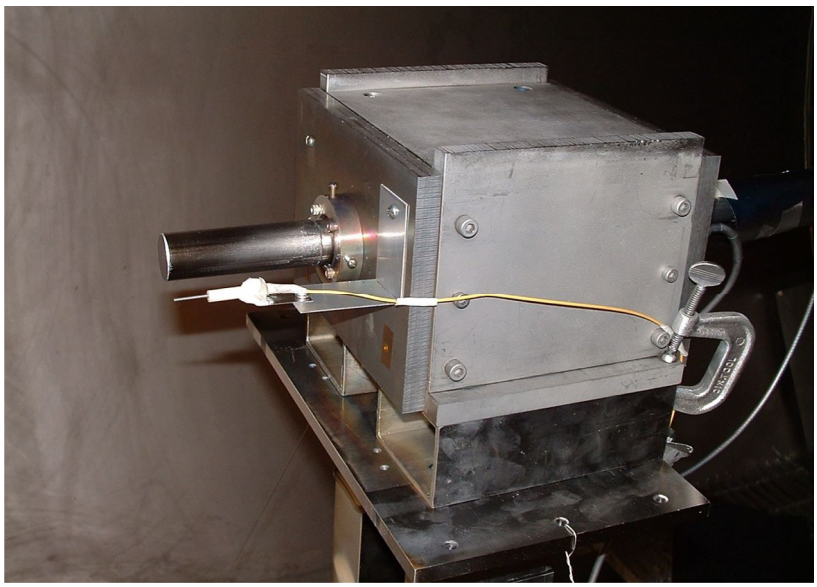

Figure 10-4 Photograph of the ExB probe and cylindrical Langmuir probe in VF12.

Figure 6-4 is a photograph of the experimental setup used with the ExB probe during testing with the NASA-173Mv2 in VF12. The entrance orifice of the ExB probe was placed two meters downstream of the thruster exit plane on thruster

centerline, within an accuracy of ±0.5 cm in both the axial and radial directions. Using a laser, the entrance and exit collimators were aligned perpendicular to the thruster exit plane to an accuracy of ±0.5°.

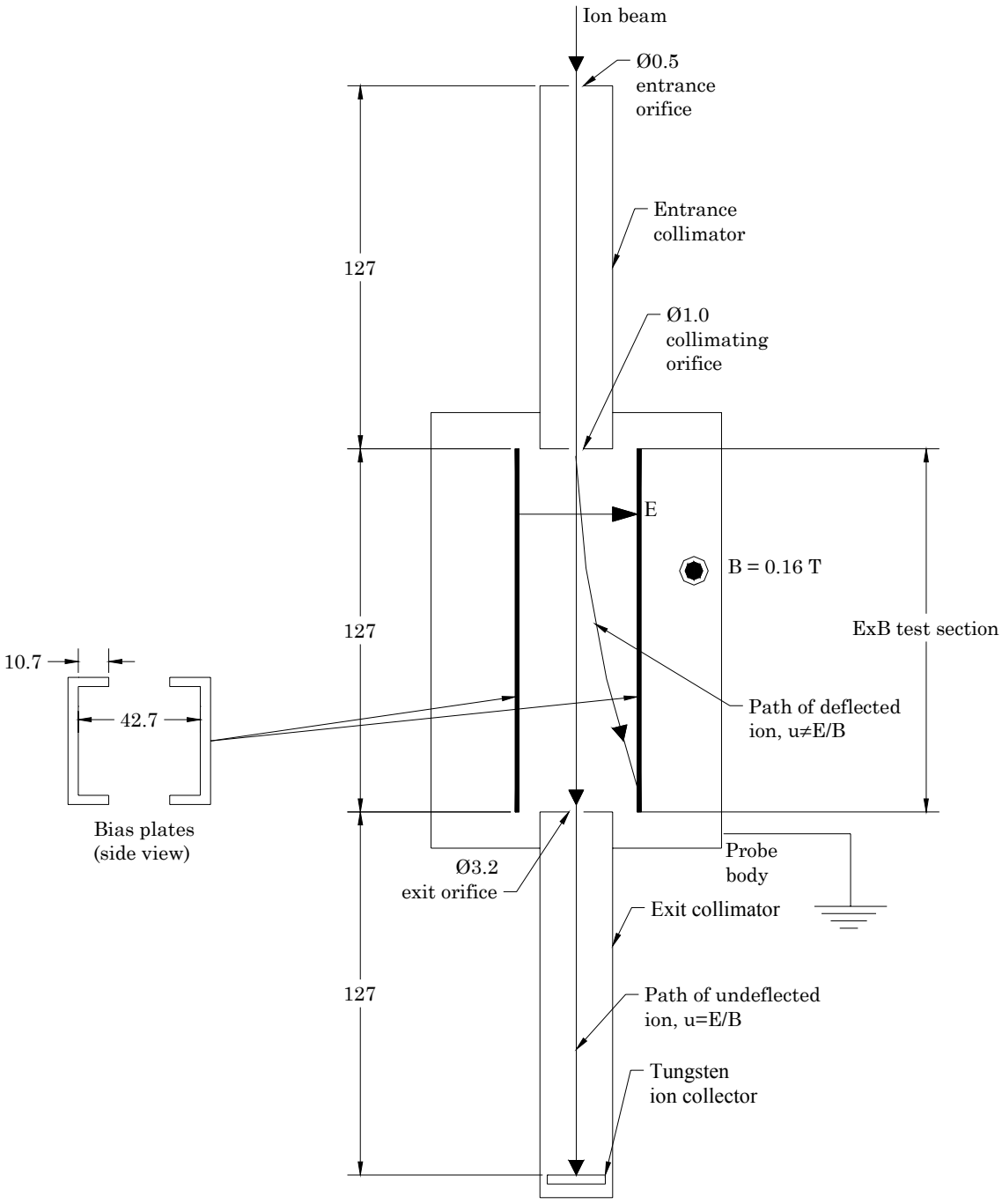

Figure 10-5 Schematic of the ExB probe. Dimensions are in millimeters.

Figure 10-6 shows the electrical schematic of the ExB probe. The plate bias was applied with a commercially available power supply and was swept over a range of voltages in two volt increments. For a given thruster operation condition, each voltage sweep was repeated 3-5 times and then averaged together to reduce measurement uncertainty. The supply outputs were biased with respect to ground using a pair of 1 MΩ resistors so that the potential at the mid-point of the plates was held near facility ground. Current from the collection electrode was measured with a picoammeter through 50 Ohm, shielded coaxial cable. The probe body was grounded to the vacuum facility.

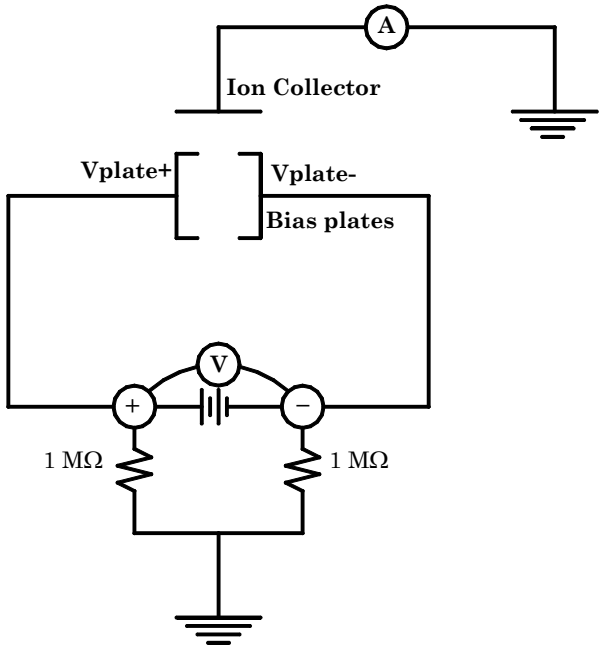

Figure 10-6 Electrical schematic of the ExB probe.

10.3.2.3 Data analysis

Since the goal of the experiments with the ExB probe was to obtain the ion species fractions as a function of the discharge voltage, data analysis consisted of interpreting the peak heights measured by the probe. The Xe^{+} and Xe^{2+} peaks were easily identified for all operating conditions. Signal broadening due to elastic

collisions and probe resolution limitations resulted in the Xe^{2+} and Xe^{3+} signals overlapping at discharge voltages of 500-800 V. In those cases, the Xe^{3+} ion current was taken where the first derivative of the ion current crossed, or nearly crossed, zero. The voltage where this occurred always closely corresponded to $\sqrt{3}V_{probe,1}$. Some discharge voltages showed evidence of Xe^{4+}, but the signal never represented a significant fraction of the total signal. For example, if the Xe^{4+} signal at 900 V (where Xe^{4+} was most evident, see Figure 11-7 in section 11.2) were included in the species fractions calculations, then the Xe^{4+} fraction would have been 0.001. Because the signal was so small, Xe^{4+} was not included in the calculations.

Using the peak heights to calculate the species fractions was equivalent to approximating the ion energy distribution function as a monoenergetic beam. In a Hall thruster, the beam has a distribution with a finite width of energies, since ions are produced along the length of the discharge chamber at different accelerating potentials. Kim [27, 208] accounted for these effects by including a model of the ion energy distribution function and found reasonable agreement with other mass analyzers [29, 203, 204, 207]. While modeling the distribution is a more rigorous approach that should reduce uncertainty, it requires that probe-induced signal broadening is much less than collisional broadening. The ExB probe used in these experiments had an energy resolution of 7% (compared to 1% with Kim's probe [208]), which was too high to neglect probe broadening. As a result, it was concluded that modeling the distribution would introduce more uncertainty to the calculations than using the peak heights. While using the peak heights introduced additional uncertainty, the computed species fractions were still comparable to mass analyzers used with other Hall thrusters (see section 11.2). A conservative estimate of the

uncertainty that included the effects of using the peaks heights is discussed in section 10.3.2.4.

The ion current of each species from the probe traces was expressed as

$$I_{probe,i} = eZ_i n_i \langle v_i \rangle A_c (1 + \gamma_i), \quad \textbf{(10-10)}$$

where A_c was the current collection area of the ExB probe, γ_i was the species-dependent secondary electron emission yield of the tungsten collector (given in electrons per ion), and n_i was the number density of the i^{th} ion species. The secondary electron emission yield was taken from data in Ref. [257] for xenon bombardment on tungsten which showed that γ_i was on average 0.018, 0.216, and 0.756 for Xe^+, Xe^{2+}, and Xe^{3+}, respectively, over the range of ion energies in these experiments.

From the ion current collected by the ExB probe, the probe current fractions were computed as

$$\Omega_{probe,i} = \frac{I_{probe,i}}{\sum I_{probe,i}} \quad i = 1,2,3, \quad \textbf{(10-11)}$$

where

$$\sum \Omega_{probe,i} = 1. \quad \textbf{(10-12)}$$

The ion species fractions were given by

$$\zeta_i = \frac{n_i}{\sum n_i} \quad i = 1,2,3, \quad \textbf{(10-13)}$$

where

$$\sum \zeta_i = 1. \quad \textbf{(10-14)}$$

Equations 4-61, 10-10, and 10-13 were then substituted into Eqn. 10-11 to obtain an expression relating the current fractions measured by the probe and the actual species fractions given by

$$\Omega_{probe,i} = \frac{Z_i^{3/2}\zeta_i(1+\gamma_i)}{\sum\left(Z_i^{3/2}\zeta_i(1+\gamma_i)\right)}, \quad \textbf{(10-15)}$$

where it was assumed that the collection area and effective acceleration potential of each species were the same (see section 4.4.3). Solving the system of equations defined by Eqns. 10-14 and 10-15 yielded the ion species fractions. Note that the actual ion current fractions are different from the probe ion current fractions defined in Eqn. 10-15 because of the effects of secondary electron emission on the collected ion current. The actual ion current fractions can be computed from the species fractions by applying Eqn. 4-47.

10.3.2.4 Measurement uncertainty

To estimate the measurement uncertainty, the sensitivity of each ion species fraction was analyzed by considering: the uncertainty in the probe voltage and current identified for each species, probe misalignment and resolution, the variation in accelerating potential with ion species, whether the secondary electron emission yield was included, the loss of ions through charge-exchange collisions over the two meter path length,[38] and the effects of using the peak heights to identify the species

[38] It is important to note that the Xe^+ species fraction is actually a conservative estimate since the effect of charge-exchange collisions in the plume is to remove Xe^+ at a higher rate than Xe^{2+} or Xe^{3+}. This is because the cross-sections for charge-exchange collisions is greater for Xe^+ than Xe^{2+} or Xe^{3+} [258] and the fact that particles experiencing a charge-exchange collision that results in two charged particles (*e.g.*, $Xe^{2+} + Xe^{3+} \rightarrow 2Xe^{2+}$) are still collected by an ExB probe according to their pre-collision state (since the ExB probe is a velocity filter). Also, note that an ExB probe yields ion species fractions that are a closer indication of the species fractions at the exit plane than mass spectrometers that filter ions based on energy [29, 203, 204, 207]. This is true as long as the tank pressure is low enough that the loss of Xe^+ through charge-exchange is small. Such conditions were met in these experiments and accounted for in the estimate of measurement uncertainty.

current fractions. Based on this analysis, the absolute uncertainty in the species fractions was estimated to be ±0.04, ±0.02, and ±0.01 for Xe^{+}, Xe^{2+}, and Xe^{3+}, respectively. At 300 V, this equated to a percentage uncertainty of ±4%, ±50%, and ±100% for the species fractions of Xe^{+}, Xe^{2+}, and Xe^{3+}, respectively.

10.3.3 Cylindrical Langmuir probe

Figure 10-4 is a photograph of the cylindrical Langmuir probe used to measure the plasma potential V_p with respect to facility ground of the NASA-173Mv2. As shown in Figure 10-4, the Langmuir probe was mounted on the ExB probe discussed in section 10.3.2. However, the plasma potential was actually measured in order to correct data taken with the RPA discussed in section 10.3.4.

Shown schematically in Figure 10-7, the Langmuir probe consisted of a tungsten electrode held by an alumina tube. To minimize edge effects, the length to diameter ratio of the electrode was greater than ten. The length of the probe was aligned parallel to the ion flow, with the mid-point located 200 ± 1 cm downstream of the thruster exit plane and 6.0 ± 0.5 cm radially from thruster centerline. This location meant that the Langmuir probe sampled the plasma at a slightly different radial location than the RPA. Data from the P5 Hall thruster [203] (the P5 is described in section 5.3.1), has shown that the plasma potential varies only by a few volts over large angular positions from centerline. Based on the P5 data, the uncertainty due to the Langmuir probe not having been in the same position as the RPA was estimated to be less than one volt.

The magnetic field leaking from the permanent magnets in the ExB probe was about 1-2 Gauss. This was sufficiently small that magnetic field effects could be neglected in the analysis of the Langmuir probe characteristic.

As shown by the sample probe trace in Figure 10-8, the plasma potential was found from the maximum in the first derivative of the electron current. This method was easily automated in the data analysis, but tended to underestimate the plasma potential when compared to graphical analysis using curve fitting [259]. Comparisons between the different methods on a few test cases showed that the derivative method was consistently lower than the graphical method by a value on the order of a volt. Considering all the error sources described above, the uncertainty in the plasma potential was estimated to be +2/-1 V.

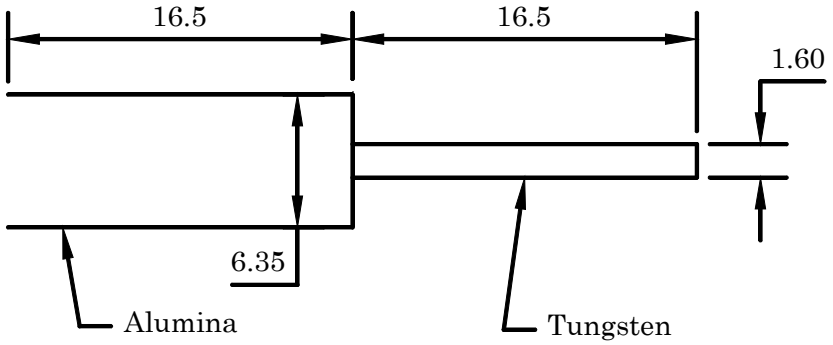

Figure 10-7 Schematic of the cylindrical Langmuir probe. Units are in millimeters.

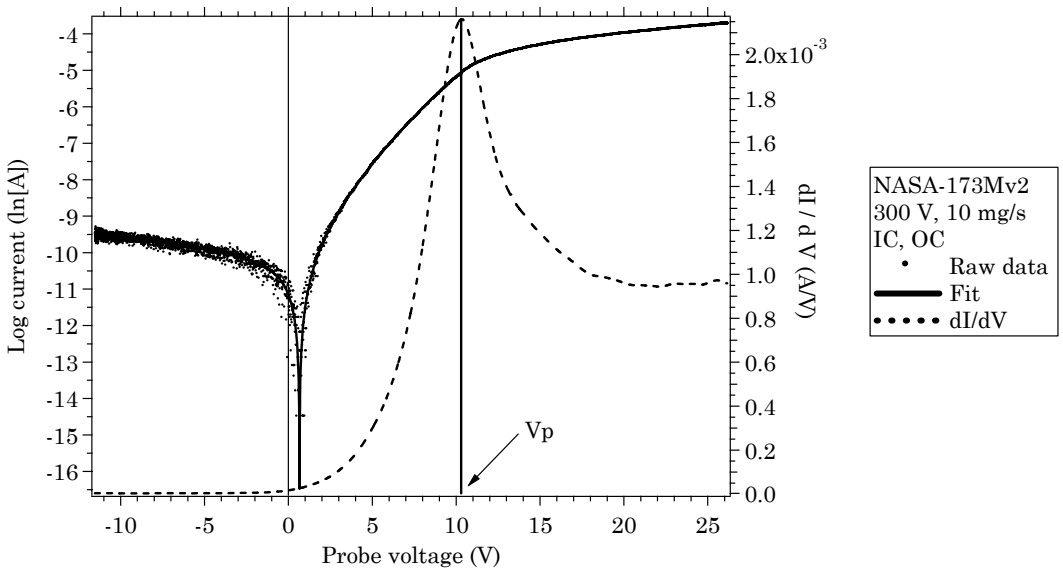

Figure 10-8 Sample Langmuir probe data illustrating the method used to compute the plasma potential.

10.3.4 Retarding potential analyzer (RPA)

10.3.4.1 Theory of operation

A retarding potential analyzer (RPA) selectively filters ions by applying a retarding potential across an inlet grid [204, 246, 260, 261]. The probe acts as a high-pass filter by allowing only ions with voltages (*i.e.*, energy-to-charge ratios, $V_i = W_i/q_i$) greater than the grid voltage to pass and reach a collection electrode. The derivative of the resulting current-voltage characteristic is proportional to the ion voltage distribution function $f(V)$

$$\frac{dI_{probe}}{dV_{probe}} = -\frac{Z_i^2 e^2 n_i A_c}{m_{xe}} f(V), \qquad \textbf{(10-16)}$$

where Z_i is the charge-state of the ion, e is the elementary charge, n_i is the ion density, A_c is the probe collection area, and m_{xe} is the mass of a xenon ion [204].

A RPA measures the ion energy distribution function only if the plasma is composed of ions of the same mass and charge. This is not the case for xenon Hall thrusters, which for 300 V discharges are composed of 4-11% Xe^{2+} and 1% Xe^{3+} [203, 204]. Further, the Xe^{2+} fraction of the NASA-173Mv2 was measured with the ExB probe to vary from 3% at 300 V to 16% at 900 V (see section 11.2). When used with Hall thrusters, a RPA therefore measures the ion voltage distribution function unless a time-of-flight method, such as the one described in Ref. [260], is used to discriminate the individual charge-state of the ions.

10.3.4.2 Design and experimental setup

The RPA was provided by Dr. James Haas of the Air Force Research Laboratory, Edwards Air Force Base, CA. Shown schematically in Figure 10-9, the three-grid RPA design was based on the multi-gridded energy analyzer in Ref. [246].

Relevant dimensions are summarized in Table 10-2. The outer body of the RPA was constructed of 316 stainless steel tubing and was grounded to the vacuum facility. A phenolic sleeve placed inside the body provided electrical isolation of the grids. All grids were made from 316 stainless steel, photochemically machined sheet with a thickness of 0.1 mm. The grid openings were 0.3 mm diameter with a total open area fraction of 38%. Grid spacing was achieved using glass-mica ceramic washers and the ion collector was a copper disk. Electrical connections were accomplished by spot welding stainless steel wire to each grid. The wires were then routed along the inner edge of the phenolic sleeve and out the rear of the body. The washers and grids were fixed in place by a spring placed between the collector and a rear cover.

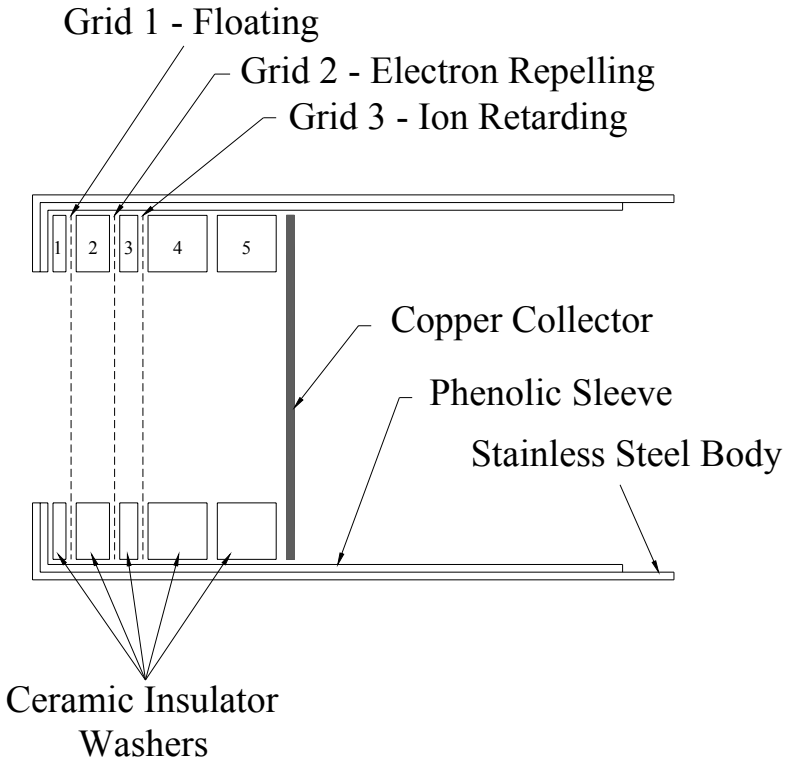

Figure 10-9 Schematic of the RPA.

Figure 10-10 shows the RPA electrical schematic. During operation, grid 1 was electrically isolated from the probe to minimize perturbation between the probe

and ambient plasma. Grid 2 was biased -30 V below ground to repel incident electrons. An electric potential ranging from 0-1100 V relative to ground was applied to grid 3 using a high-voltage power supply. The ion current to the collector was measured using a picoammeter.

Table 10-2 Dimensions of the RPA washers.

Washer	Thickness (mm)	Inner Diameter (mm)
1	1.0	18.6
2	3.4	21.6
3	1.7	21.7
4	6.5	21.4
5	6.5	21.5

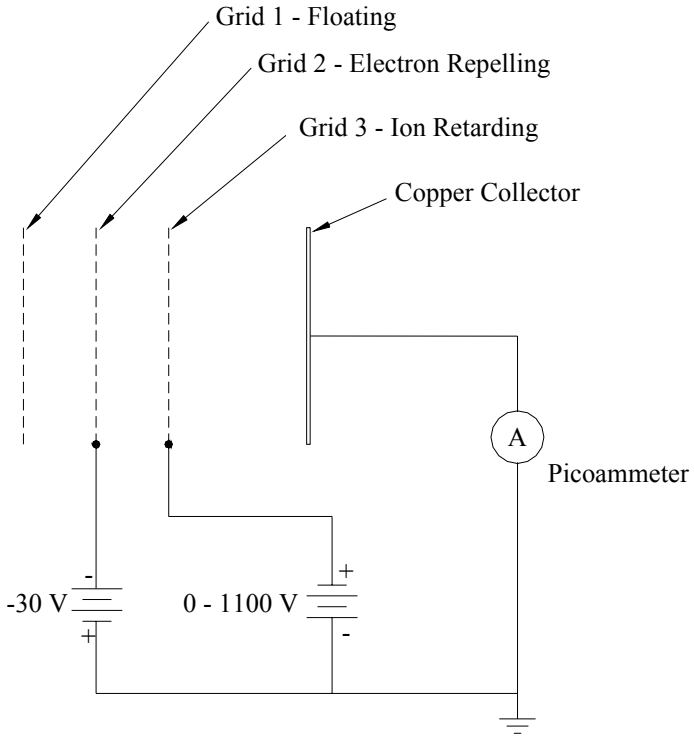

Figure 10-10 Electrical schematic of the RPA.

Figure 10-11 is a photograph of the experimental setup used with the RPA during testing with the NASA-173Mv2 in VF12. A movable shutter was used to protect the RPA grids when the probe was not being used. The thruster is not

shown in Figure 10-11. However, the RPA was placed in the same location relative to the thruster as the ExB probe shown in Figure 6-4. Specifically, the center of grid 1 was placed two meters downstream of the thruster exit plane on thruster centerline, within an accuracy of ±0.5 cm in both the axial and radial directions. The face of grid 1 was aligned parallel to the thruster exit plane to an accuracy of ±0.5°

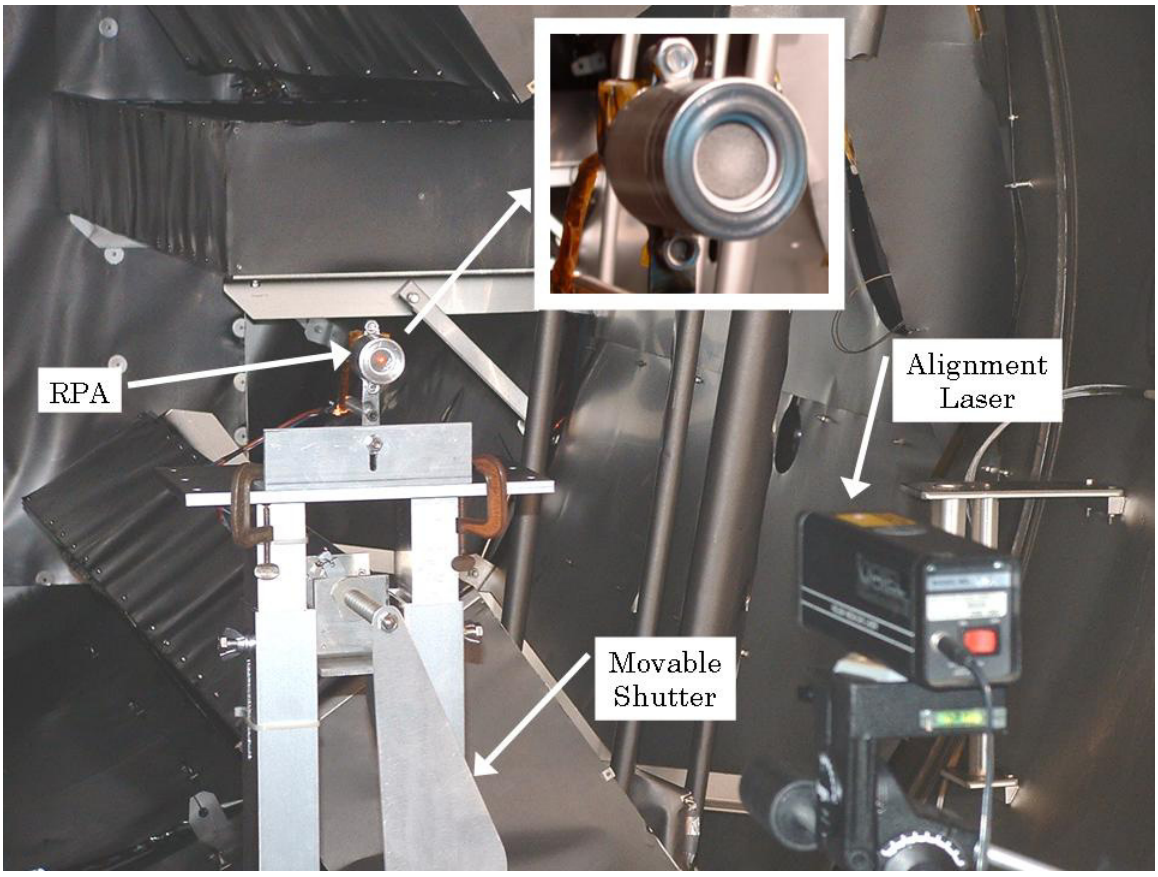

Figure 10-11 Photograph of the RPA in VF12. A movable shutter was used to protect the RPA grids when the probe was not being used. Before testing, a laser was used to align the RPA with respect to the NASA-173Mv2.

10.3.4.3 Data analysis

The RPA measured the ion voltage with respect to facility ground. As shown in the potential diagram of Figure 10-12, the true ion voltage V_{true} was obtained by subtracting the plasma potential from the measured value V_{rpa}

$$V_{true} = V_{rpa} - V_p . \tag{10-17}$$

To characterize the voltage utilization efficiency (see section 4.4.3) given by

$$\eta_v = \frac{V_a}{V_d}, \tag{10-18}$$

(where V_a is the ion voltage averaged over all ion species and V_d is the discharge voltage) the most-probable ion voltage V_{mp} and the loss voltage V_{loss} were found from the ion voltage distribution. As shown in Figure 10-13, the most-probable ion voltage was defined as the voltage where the ion current was greatest. The loss voltage was then computed as the difference between the discharge voltage and the most-probable voltage

$$V_{loss} = V_d - V_{mp} . \tag{10-19}$$

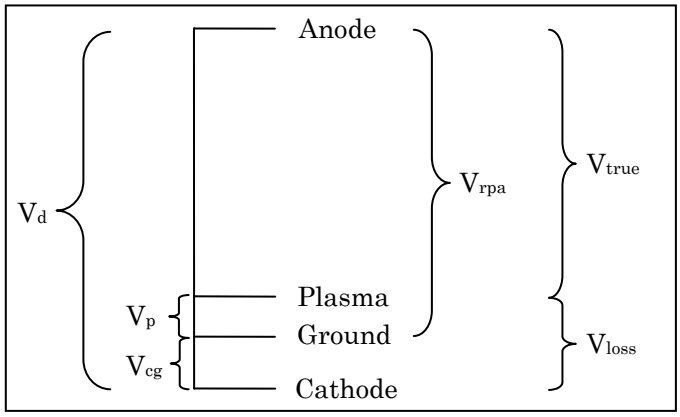

Figure 10-12 Potential diagram showing the relationship between the measured quantities (V_{rpa}, V_p, $V_{c\text{-}g}$, V_d), the true ion voltage (V_{true}), and the loss voltage (V_{loss}).

The most-probable ion voltage and the loss voltage can be used to approximate the voltage utilization efficiency since the average acceleration voltage and the most-probable voltage are nearly equal. In which case, the voltage utilization efficiency is given by

$$\eta_v = \frac{V_a}{V_d} \approx \frac{V_{mp}}{V_d} = 1 - \frac{V_{loss}}{V_d}. \qquad \textbf{(10-20)}$$

Eqn. 10-20 is an approximation because the average acceleration voltage and the most-probable voltage will differ by a few volts due to the effects of multiply-charged ions and collisions. Similarly, the loss voltage from the RPA (V_{loss}) will also differ by a few volts from the average loss voltage V_l used in the performance model (see sections 4.3.3 and 4.4.3).

The spread in ion velocities (or energy) is given by the dispersion efficiency[39]

$$\eta_d = \frac{\langle v_i \rangle^2}{\langle v_i^2 \rangle}, \qquad \textbf{(10-21)}$$

where $\langle v_i \rangle$ is the average ion velocity [2]. The dispersion efficiency was characterized by the full width at half-maximum (FWHM) of the ion voltage distribution. As shown in Figure 10-13, the FWHM was defined as the difference in volts above and below the most-probable voltage where the ion current fell to one-half its maximum value. Measurement uncertainty from probe-induced signal broadening (see section 10.3.4.4) did not allow the ion voltage distributions to be used in calculating the dispersion efficiency. However, the FWHM was still useful in observing the relative variation of the dispersion efficiency with operating point.

[39] Note that the dispersion efficiency does not explicitly appear in the anode efficiency derived in Eqn. 4-67. This is because the dispersion of ion velocities is already accounted for in the acceleration efficiency. (Kim incorrectly includes the dispersion efficiency in his expression for anode efficiency in Ref. [2]). As defined here, the dispersion efficiency is simply a useful means to study the details of the ionization and acceleration processes.

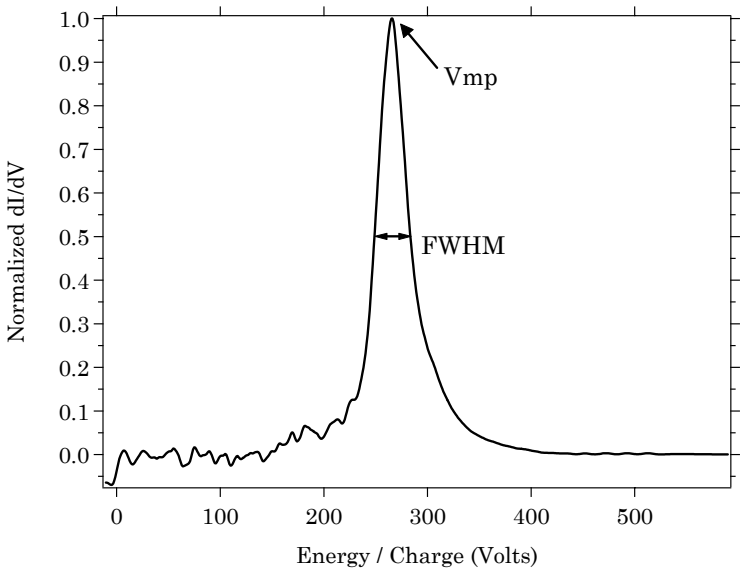

Figure 10-13 Sample ion voltage distribution demonstrating how the most-probable ion voltage (V_{mp}) and the FWHM were defined.

10.3.4.4 Measurement uncertainty

The RPA was compared to a 45° parallel-plate electrostatic energy analyzer (ESA) in Ref.[261]. In those experiments, both instruments collected plume data 0.5 m downstream of a Busek BHT-200-X3 Hall thruster operated at a discharge voltage of 250 V. Figure 10-14 shows the ion voltage distributions measured with respect to facility ground by the RPA and the ESA on thruster centerline. Comparisons of the most-probable voltage and FWHM from the different instruments are used here to assess their relative accuracy.

As Figure 10-14 shows, the most-probable ion voltage measured by the two instruments was in good agreement. The RPA measured a most-probable voltage of 220 V and the ESA was 3.6% higher, or 228 V. In contrast, the FWHM from the two instruments showed significant differences. The FWHM measured by the RPA was 45 V and the ESA was 42% lower, or 26 V. The differences can be attributed to instrument broadening in the RPA and, to a lesser extent, the effects of numerical differentiation and spline curve fitting (see section 11.4). Instrument broadening in

the RPA could have been due to pressure build-up inside the probe and/or the large acceptance half-angle of the probe (45º in the RPA versus 4º in the ESA). Regardless of the exact cause, the FWHM of the RPA was considered an upper bound of the true FWHM. Considering the results in Ref. [261] and the experiments reported here, the uncertainties of the most-probable voltage and the FWHM were estimated as ±10 V and +0/-20 V, respectively.

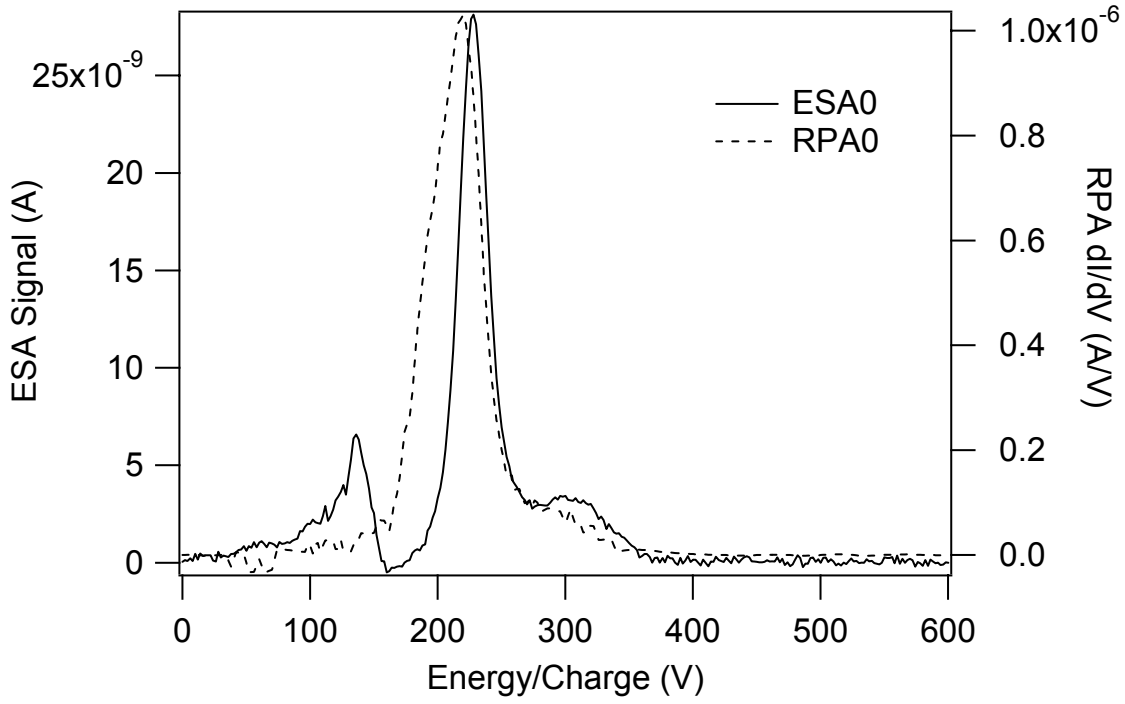

Figure 10-14 Ion voltage distributions measured with the RPA and a parallel-plate energy analyzer (ESA) on the centerline of the Busek BHT-200-X3 Hall thruster, 0.5 m downstream of the exit plane [261].

10.4 Summary

This chapter has described the vacuum facilities, support equipment, and plasma diagnostics used during experiments that continued to characterize the plasma properties of the NASA-173Mv2. The next chapter presents the results from those experiments. In Chapter 12, the results are analyzed and discussed.

Chapter 11

Characterization of the NASA-173Mv2

This chapter describes results from a series of plasma diagnostics used with the NASA-173Mv2 in order to improve understanding of the physical processes affecting Hall thruster performance at high-specific impulse. Section 11.1 reports on measurements of the plasma floating potential that were taken inside the discharge chamber, while sections 11.2-11.4 describe far-field measurements of the ion species fractions, plasma potential, and ion voltage distribution, respectively. Chapter 12 discusses the results from each of these experiments.

All experiments described in this chapter were conducted at an anode mass flow rate of 10 mg/s and a cathode mass flow rate of 1.0 mg/s. During the development phase of the NASA-173Mv2, these flow rates had proven to be an acceptable balance between performance, thermal margin, and stability up to voltages of 1000 V. At these flow rates, the total specific impulse and total efficiency of the NASA-173Mv2 range from 1600-3400 seconds and 51-61%, respectively, over voltages of 300-1000 V (see section 8.4.1).

The effects of changing the magnetic field topography on thruster operation were investigated by energizing the thruster coils in different combinations. The coil combinations are labeled in the figures as:

1. IC, OC – only the inner and outer coils were energized,
2. ITC – the internal trim coil was energized in addition to the inner and outer coils,
3. ITC, ETC – both trim coils were energized in addition to the inner and outer coils, and
4. ETC – the external trim coil was energized in addition to the inner and outer coils.

With the exception of the ETC points, the coil currents were taken directly from the performance characterization in section 8.4.1 that showed these settings maximized thruster efficiency. That characterization usually did not include data with the external trim coil unless the internal trim coil was also energized. The experiments described in sections 11.2-11.4 include data with the external trim coil (i.e., coil combination #4 above). This additional coil combination was included so that the effects of the external trim coil could be investigated separate from the internal trim coil.

Table 11-1 summarizes the thruster operating conditions that were evaluated with the various plasma diagnostics. Thruster telemetry and data from the experiments in this chapter are tabulated in Appendix D.

Before each experiment, the thruster was operated for four hours after initial exposure to vacuum conditions to allow for outgassing of the chamber walls. Upon subsequent thruster shutdowns and restarts or a change in the discharge voltage, the thruster was operated for at least 30-60 minutes before data were acquired. This procedure allowed enough time for the discharge current to reach a steady-state value.

Table 11-1 Thruster operating conditions during the extended plasma characterization of the NASA-173Mv2. Coil combinations are from the numbered list shown in the main text of section 11.1.

	Vd (V)	Anode (mg/s)	Cathode (mg/s)	Coil combinations	Section
Floating potential	300, 600	10.0	1.0	1-3	§11.1
ExB probe	300-900	10.0	1.0	1-4	§11.2
Langmuir probe	300-1000	10.0	1.0	1-4	§11.3
RPA	300-800	10.0	1.0	1-4	§11.4

11.1 Discharge chamber floating potential

This section describes floating potential measurements that were taken over axial sweeps on discharge chamber centerline of the NASA-173Mv2. The experiments were conducted in the LVTF at the University of Michigan, described in section 10.2.1. The floating potential probe and the experimental setup were described in section 10.3.1.

Results from floating potential measurements on discharge chamber centerline (r = 73.7 mm) are presented in Figures 11-1 and 11-2. Only data from probe sweeps into the thruster are shown. Axial positions were referenced from the exit plane, with the anode at z = -38 mm and the cathode plane at z = +30 mm. The thruster was operated at an anode mass flow rate of 10 mg/s, a cathode mass flow rate of 1.0 mg/s, and the discharge voltage was either 300 V or 600 V. Changes to the magnetic field were investigated by using different combinations of the trim coils (see Table 11-1). Thruster telemetry during data collection are tabulated as Table D-1 in Appendix D.

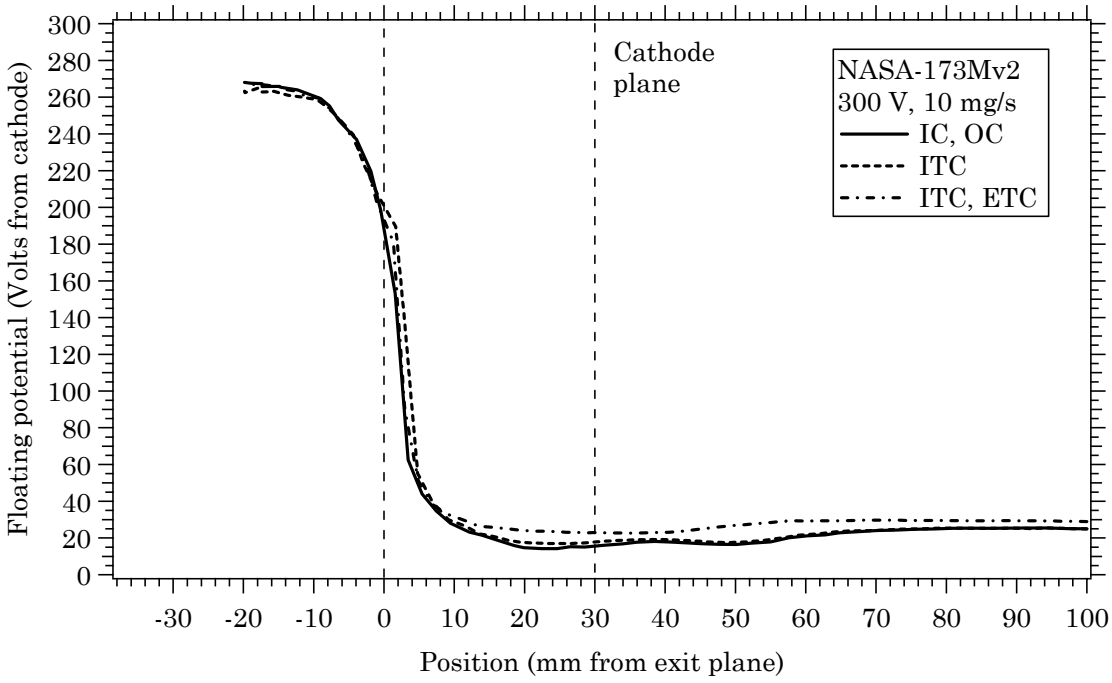

Figure 11-1 Floating potential versus axial position of the NASA-173Mv2 at 300 V, 10 mg/s and different coil combinations.

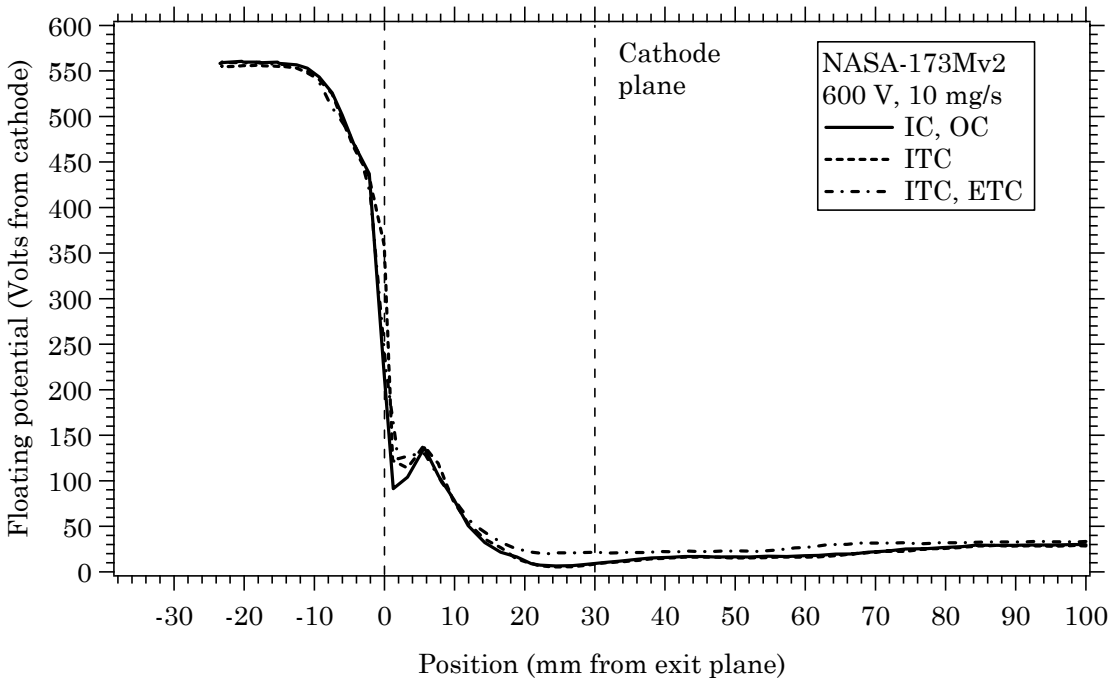

Figure 11-2 Floating potential versus axial position of the NASA-173Mv2 at 600 V, 10 mg/s and different coil combinations.

11.1.1 Probe-induced thruster perturbations

As shown in Figures 11-3 and 11-4, inserting the floating potential probe into the discharge chamber was found to affect thruster operation by increasing the discharge current and the cathode potential. At both 300 and 600 V, the discharge current and cathode potential began to increase when the probe reached z = +15 mm. Upon removal of the probe (not shown), the discharge current and cathode potential returned to their initial steady-state values. At 300 V, the current increased by 45% and at 600 V by 38%.

The percentage change in the discharge current was much greater than expected, based on prior experiments that also used the HARP with the P5 Hall thruster (the P5 was described in section 5.3.1) [135, 142, 143, 247]. In Ref. [143], discharge current perturbations were less than 10% when operating at 10 A, 300 V. The experiments with the P5 and NASA-173Mv2 were similar in three important aspects: first, the thrusters shared discharge chamber geometry. Second, in Ref. [143] a double probe that was 3.2 mm long by 1.6 mm wide was used, which was just slightly smaller than the 3.4 mm diameter floating probe used with the NASA-173Mv2. Third, the probes in Ref. [143] moved more slowly than the floating probe used here. The faster the probe moved, the less susceptible the probe body was to ablation, which is known to affect thruster operation [247].

As discussed in sections 7.2 and 8.2, the major difference between the P5 and the NASA-173Mv2 is the magnetic field topography. It was hypothesized that the magnetic field in the NASA-173Mv2 improved plasma confinement compared to the P5. This would have raised the plasma density in the discharge chamber and made the NASA-173Mv2 more susceptible to disturbances caused by probes. The hypothesis that the plasma density was higher in the NASA-173Mv2 than in the P5

was supported by the improved efficiency and plume characteristics of the NASA-173Mv2 compared to the P5 (see Tables A-1, and C-1 to C-3). Since the NASA-173Mv2 probe was slightly larger than the probe used on the P5, a smaller probe should reduce the magnitude of disturbances. Future experiments with smaller probes will test this hypothesis.

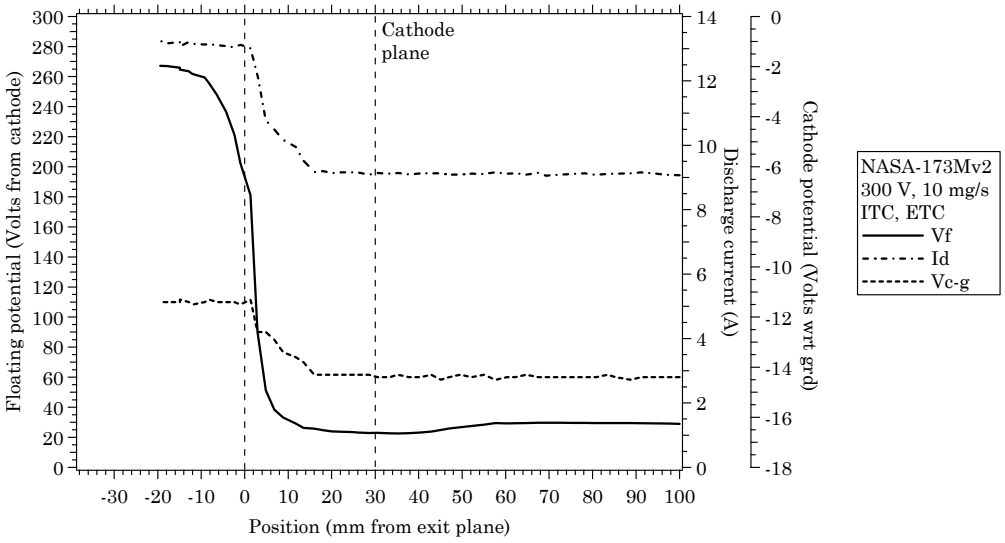

Figure 11-3 Floating potential, discharge current, and cathode potential versus axial position of the NASA-173Mv2 at 300 V, 10 mg/s with both trim coils energized.

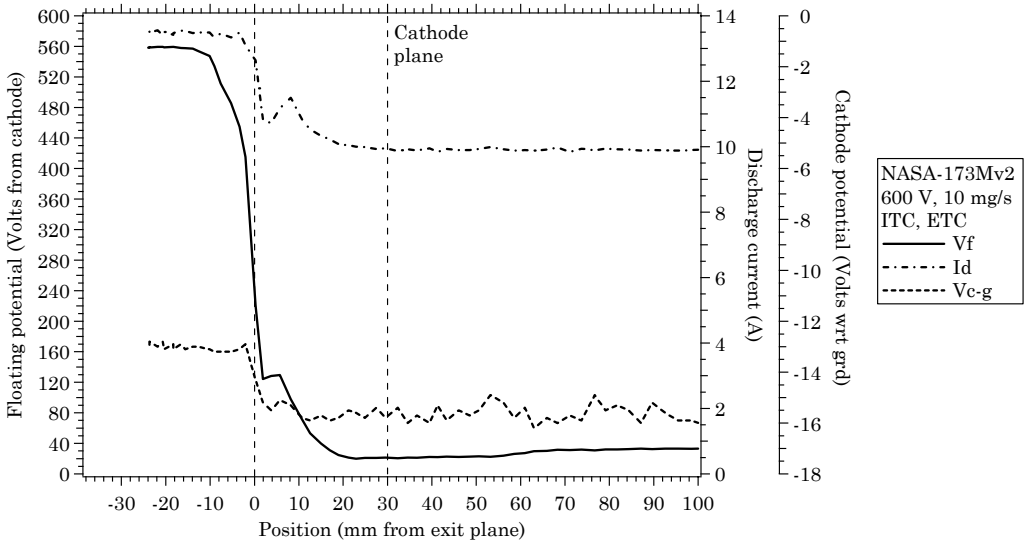

Figure 11-4 Floating potential, discharge current, and cathode potential versus axial position of the NASA-173Mv2 at 600 V, 10 mg/s with both trim coils energized.

The disturbances to thruster operation increased the uncertainty of the floating potential measurements, which was estimated to be ±10%. This included the uncertainty associated with the probe design (see section 10.3.1).

11.2 Far-field ion species fractions

This section describes measurements of the far-field ion species fractions of the NASA-173Mv2 Hall thruster. The experiments were conducted in Vacuum Facility 12 (VF12) at NASA GRC (see section 10.2.2). The ExB probe used to measure ion species fractions was described in section 10.3.2.

Measurements of the species fractions are important because multiply-charged ions affect thruster performance and the lifetime of the thruster and sensitive spacecraft surfaces (*e.g.*, solar arrays and optics). At constant beam current, the presence of multiply-charged ions decreases thruster performance (see section 4.5.2). At high discharge voltages, the importance of multiply-charged ions on Hall thruster performance and lifetime is relatively unknown because measurements have thus far been limited to 300-500 V in xenon Hall thrusters [27, 29, 203, 204, 207, 208].

ExB probe measurements were taken with the thruster operating at an anode flow rate of 10.0 mg/s and a cathode flow rate of 1.0 mg/s. The discharge voltage was varied from 300-900 V. The ExB probe was two meters downstream of the thruster exit plane on the thruster centerline. At each discharge voltage, the effects of the magnetic field were evaluated by using several combinations of the coils (see Table 11-1). Thruster telemetry from the test series are tabulated as Table D-2 in Appendix D.

Figures 11-5 through 11-7 are representative ExB probe traces at 300, 600, and 900 V, respectively, when the inner and outer coils were energized. Each figure is the average of three to five voltage sweeps of the ExB probe. In general, the probe traces yielded distinct and repeatable spectra for the Xe^{+}, Xe^{2+}, and Xe^{3+} peaks. The Xe^{2+} and Xe^{3+} peaks closely corresponded to the expected $\sqrt{Z_i}$ dependence.

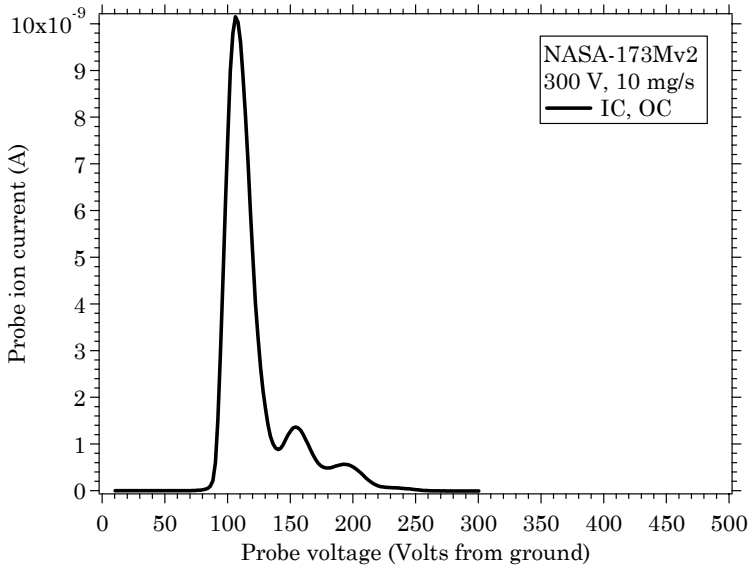

Figure 11-5 ExB probe ion current versus probe voltage of the NASA-173Mv2 at 300 V, 10 mg/s.

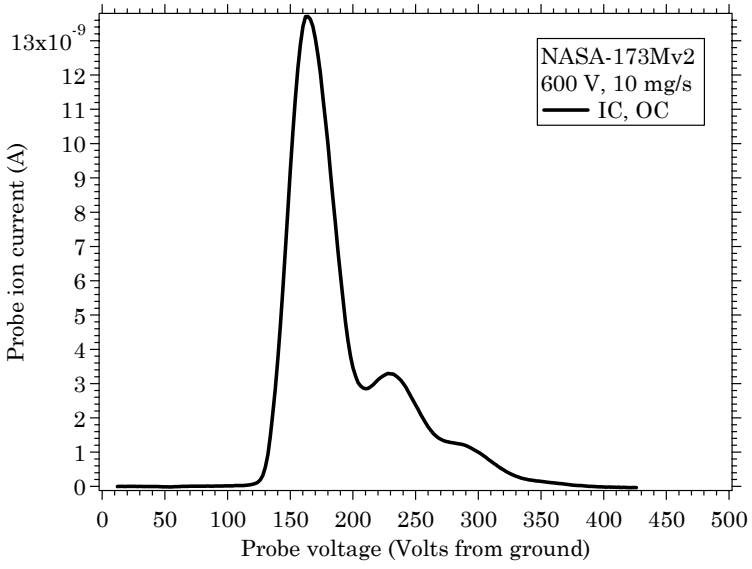

Figure 11-6 ExB probe ion current versus probe voltage of the NASA-173Mv2 at 600 V, 10 mg/s.

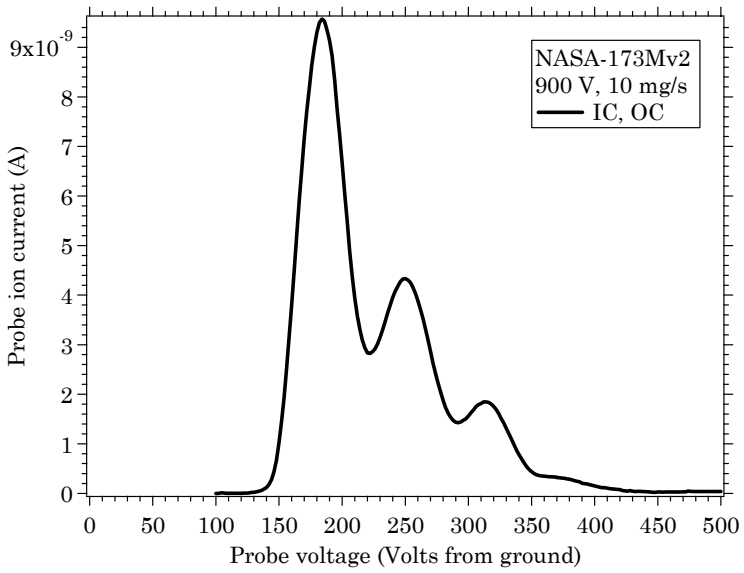

Figure 11-7 ExB probe ion current versus probe voltage of the NASA-173Mv2 at 900 V, 10 mg/s.

The widths of the probe spectra for each species show a clear broadening with discharge voltage. This result correlated with measurements of the ion voltage distribution that showed the same trend (see section 11.4). The implications of these results are discussed further in section 12.4.

The variation of the ion species fractions with discharge voltage and magnetic field configuration is shown in Figure 11-8 and tabulated in Appendix D as Table D-3. While the results indicated a general increase in the fraction of multiply-charged ions with increasing discharge voltage, Xe^+ still dominated the plasma at all discharge voltages. There was no systematic dependence of the species fractions with the magnetic field configuration. Measurement uncertainty, caused by the 7% energy resolution of the ExB probe, likely contributed to this result.

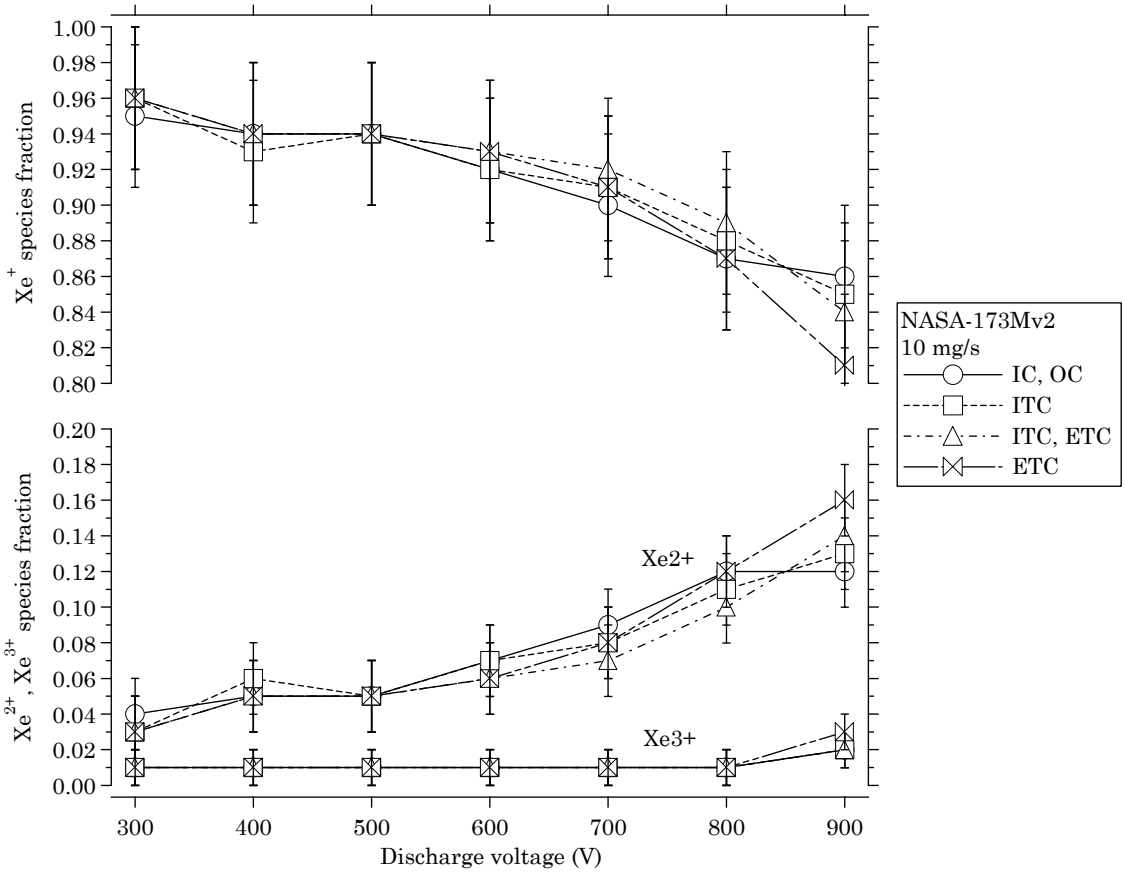

Figure 11-8 Ion species fractions versus discharge voltage of the NASA-173Mv2 at 10 mg/s and different coil combinations.

11.3 Far-field plasma potential

This section describes measurements of the far-field plasma potential of the NASA-173Mv2 Hall thruster. The experiments were conducted in Vacuum Facility 12 (VF12) at NASA GRC (see section 10.2.2). The cylindrical Langmuir probe used to measure plasma potential was described in section 10.3.3. The plasma potential was needed so that the true ion voltage distribution, measured with the RPA in section 11.4, could be calculated (see section 10.3.4.3).

Langmuir probe measurements were taken with the thruster operating at an anode flow rate of 10.0 mg/s and a cathode flow rate of 1.0 mg/s. The discharge voltage was varied from 300-1000 V. The Langmuir probe was two meters

downstream of the thruster exit plane and six centimeters radially away from thruster centerline (see section 10.3.3). At each discharge voltage, the effects of the magnetic field were evaluated by using several combinations of the coils (see Table 11-1). Thruster telemetry from the test series are tabulated as Table D-4 in Appendix D.

Figure 11-9 plots the plasma potential with respect to facility ground versus the discharge voltage and magnetic field. Regardless of the magnetic field, the plasma potential increased 3-4 V as the discharge voltage increased from 300-1000 V. At a given discharge voltage, changing the magnetic field with the external trim coil decreased the plasma potential by 1-2 V while the internal trim coil had no apparent effect.

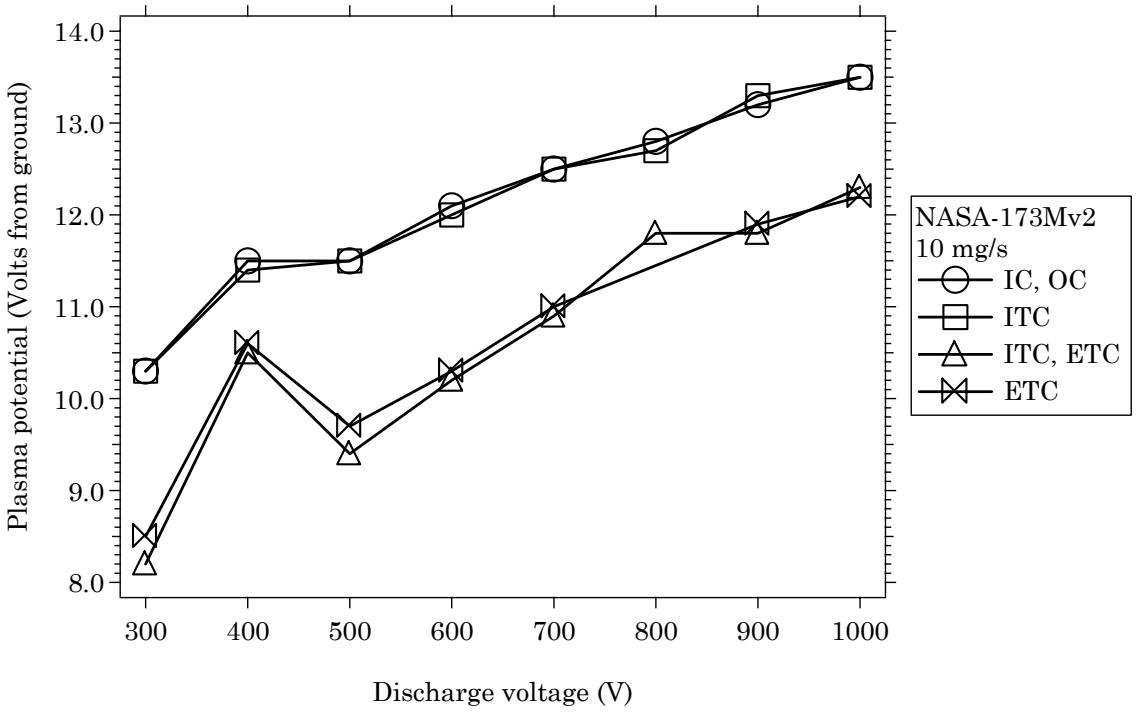

Figure 11-9 Plasma potential versus discharge voltage of the NASA-173Mv2 at 10 mg/s and different coil combinations.

11.4 Far-field ion voltage distribution

This section describes measurements of the far-field ion voltage distribution of the NASA-173Mv2 Hall thruster. The experiments were conducted in Vacuum Facility 12 (VF12) at NASA GRC (see section 10.2.2). A retarding potential analyzer (RPA), described in section 10.3.4, was used to measure the ion voltage distributions. A cylindrical Langmuir probe was also used to obtain the plasma potential so that the true ion voltage distribution could be calculated (see section 11.3).

The ion voltage distribution is of interest because it is used by spacecraft designers to calculate plume impingement on sensitive surfaces (*e.g.*, solar arrays and optics), as well as by thruster designers to quantify how changes to the operating point or thruster hardware affect lifetime and performance. The goal of these experiments was to gain insight on how the ionization and acceleration processes internal to the thruster were affected by changes of the magnetic field and discharge voltage.

RPA measurements were taken with the NASA-173Mv2 operating at an anode flow rate of 10.0 mg/s and a cathode flow rate of 1.0 mg/s. The discharge voltage was varied from 300-800 V. A grid short with the RPA ended testing at 800 V after testing only with the inner and outer coils (IC,OC). The RPA was located two meters downstream of the thruster exit plane on the thruster centerline. At each discharge voltage, the effects of the magnetic field were evaluated by using several combinations of the coils (see Table 11-1). Thruster telemetry from the test series are tabulated as Table D-6 in Appendix D.

At each discharge voltage and magnetic field configuration, three sweeps of the ion retarding voltage were performed with the RPA. The resulting I-V curves were found to be very repeatable. Figure 11-10 shows the raw data from voltage

sweeps when the inner and outer coils were energized (IC, OC). Except for 800 V (where a grid short occurred after one sweep), each curve in Figure 11-10 consists of the data from three separate sweeps.

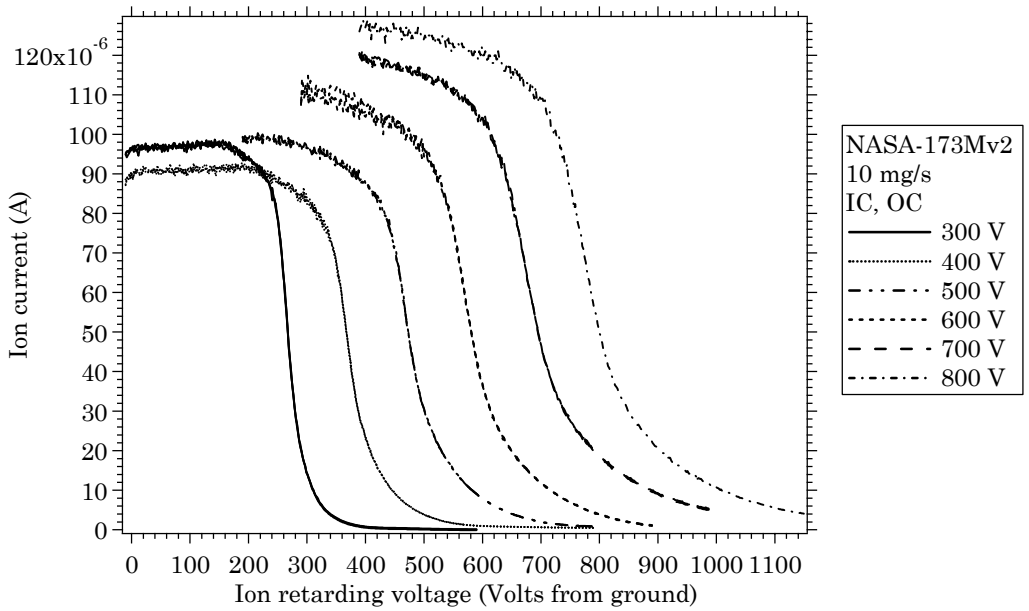

Figure 11-10 Ion current versus retarding voltage from the RPA of the NASA-173Mv2 at 10 mg/s for discharge voltages of 300-800 V. To demonstrate repeatability, data from multiple sweeps are overlaid at each discharge voltage, except 800 V where only one sweep was obtained.

For a given voltage and magnetic field, each sweep of the RPA was averaged together, curve-fit using a smoothing spline algorithm [262], and then numerically differentiated. The spline was used to reduce noise caused by the differentiation. Lastly, the plasma potential obtained from the Langmuir probe measurements in section 11.3 was subtracted from the retarding voltage to yield the true ion voltage distribution. In Figure 11-11, the effects of the spline are compared to the raw data for discharge voltages of 300 and 700 V (IC, OC). The spline operation induced enough smoothing that detailed features (*e.g.*, charge-exchange collision signatures) were not resolved. However, the most-probable ion voltage and the FWHM were relatively insensitive to the smoothing parameters. The uncertainties in the most-

probable ion voltage and the FWHM from the spline operation were estimated as ±0.5% and ±1% of the discharge voltage, respectively. The uncertainty estimates were based on numerical experiments that examined how the two quantities depended on the smoothing parameters. The uncertainty from the spline operation was included in the overall uncertainty estimates discussed in section 10.3.4.4.

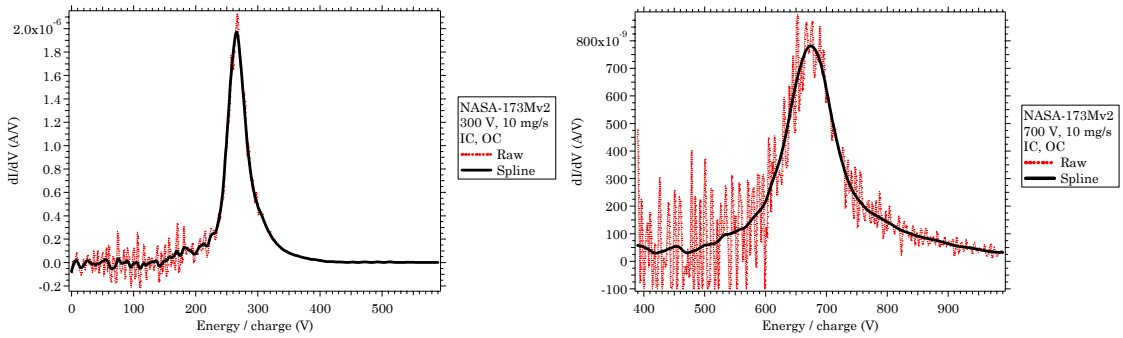

Figure 11-11 Representative ion voltage distributions showing the raw data and the spline fit to the data for discharge voltages of 300 and 700 V.

Figure 11-12 shows the ion voltage distribution (normalized to the peak ion current) at each thruster operating point. The coil configurations are not delineated in the figure because the differences were indistinguishable at the chosen scale.

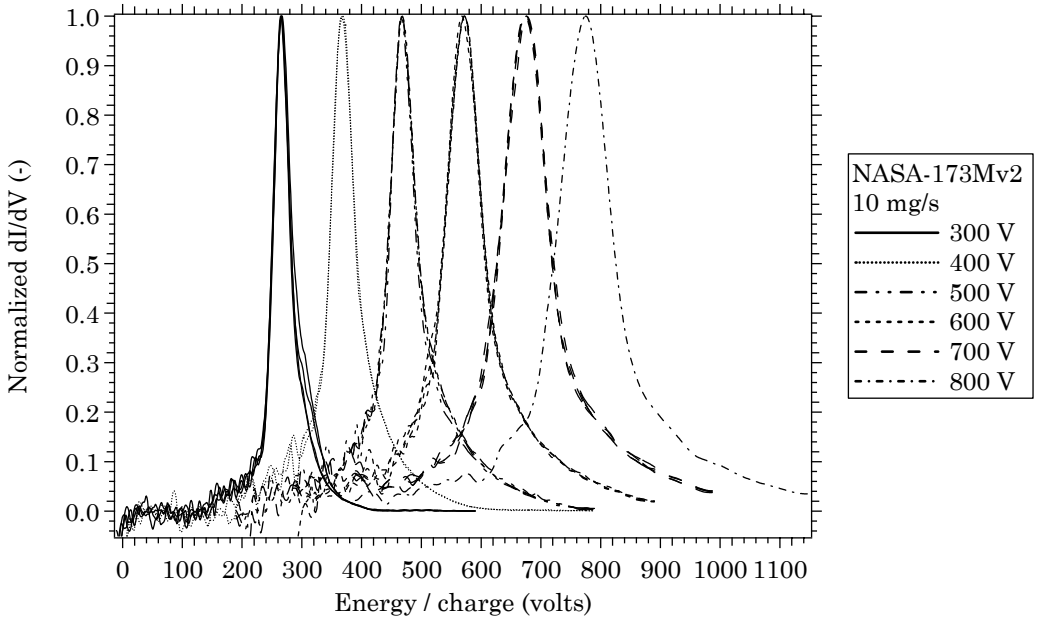

Figure 11-12 Normalized ion voltage distributions versus discharge voltage.

From each of the distributions in Figure 11-12, the most-probable voltage, the loss voltage, and the FWHM were calculated. Figure 11-13 shows the loss voltage and Figure 11-14 shows the FWHM versus discharge voltage and magnetic field. The loss voltage and FWHM data are tabulated in Appendix D as Tables D-7 and D-8, respectively.

There was no systematic dependence of the loss voltage with the magnetic field. The loss voltage decreased with discharge voltage from 35 V at 300 V to 25 V at 800 V, which translated into an increase in the voltage utilization efficiency from 89% at 300 V to 97% at 800 V. The FWHM increased with discharge voltage by over a factor of three from 33 V at 300 V to 105 V at 800 V (*i.e.*, the dispersion efficiency decreased). The increase in the FWHM correlated with measurements using the ExB probe (see section 11.2) that showed the same trend. Changes in the magnetic field due to the external trim coil decreased the FWHM by 3-4 V on average.

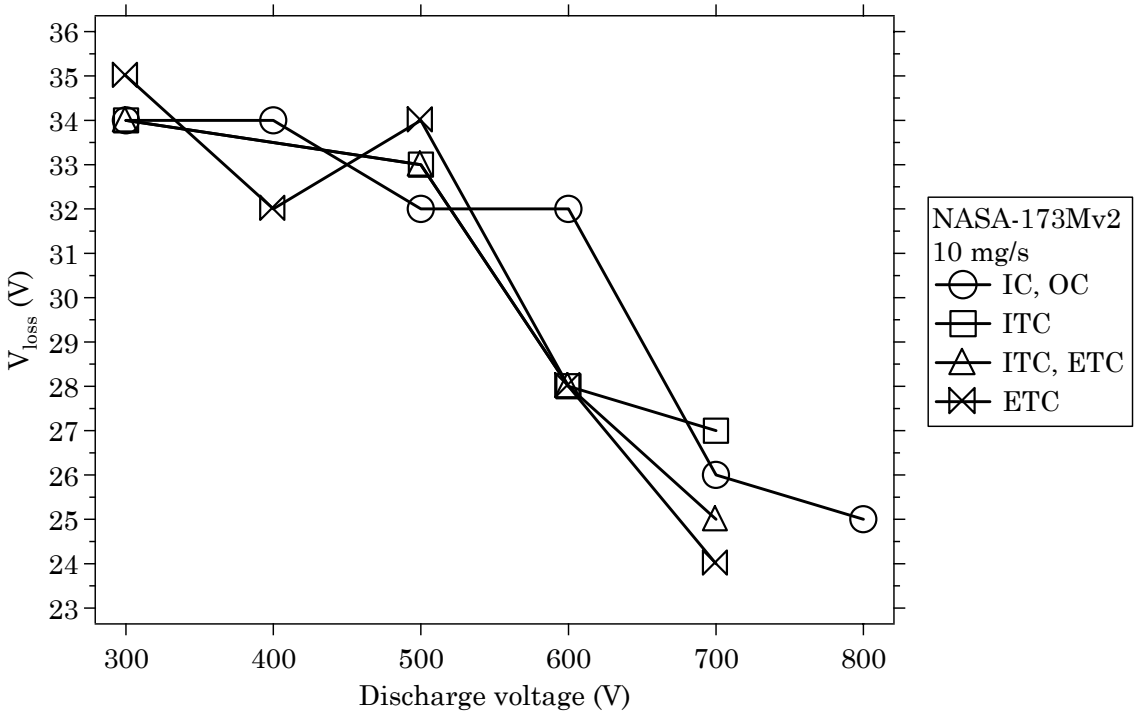

Figure 11-13 Loss voltage versus discharge voltage of the NASA-173Mv2 at 10 mg/s and different coil combination.

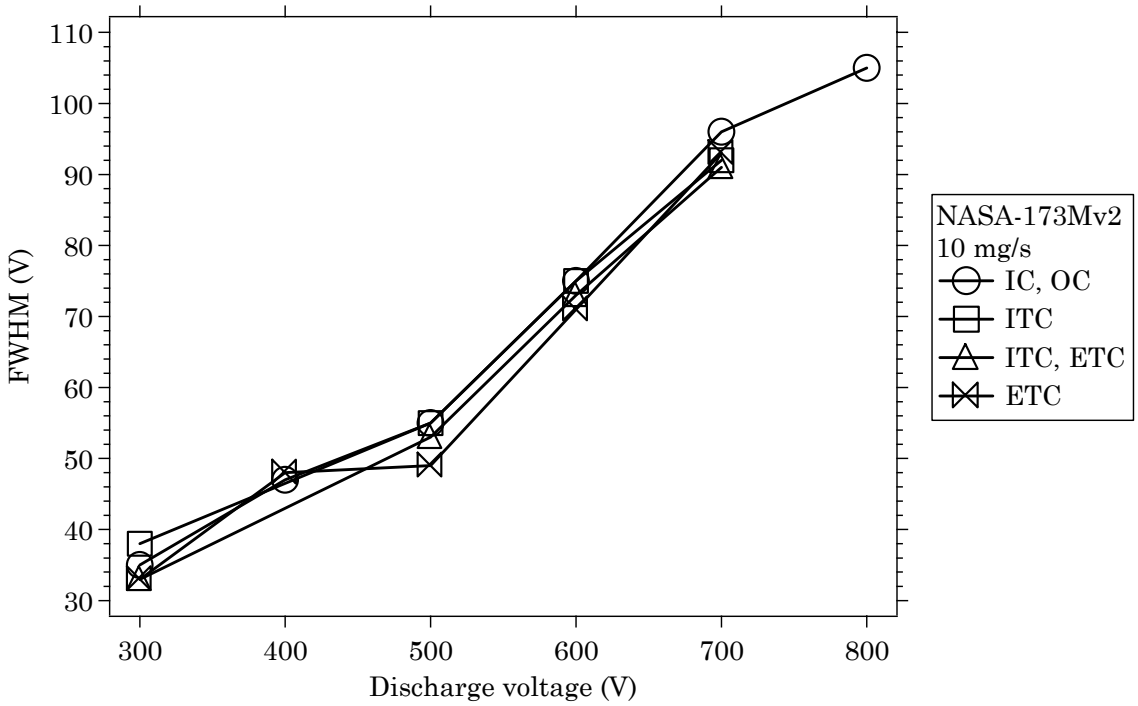

Figure 11-14 The full-width at half-maximum (FWHM) of the ion voltage distributions versus discharge voltage of the NASA-173Mv2 at 10 mg/s and different coil combinations.

11.5 Summary

Internal floating potential and far-field measurements of the ion species fractions, plasma potential, and ion voltage distribution were taken to investigate the plasma state of the high-efficiency, high-specific impulse NASA-173Mv2 Hall thruster. Chapter 12 discusses the results from each of these experiments.

Chapter 12

Discussion II – Plasma properties of the NASA-173Mv2

This chapter discusses results from the extended plasma characterization of the NASA-173Mv2 described in Chapter 11. Section 12.1 discusses the internal floating potential measurements while sections 12.2-12.4 discuss the far-field ion species fractions, plasma potential, and ion voltage distributions, respectively. In section 12.5, the performance model derived in Chapter 4 is combined with the experimental data to compute the utilization efficiencies of the NASA-173Mv2.

12.1 Discharge chamber floating potential

12.1.1 Effects of the magnetic field

Figures 11-1 and 11-2 show how changes to the magnetic field affected the floating potential at 300 and 600 V, respectively. At both voltages, changing the magnetic field with the external trim coil increased the floating potential by 10–15 V at distances greater than z = +10 mm. During the performance characterization at NASA GRC (see section 8.4.1), the external trim coil generally increased the cathode potential[40] (*i.e.*, decreased the magnitude with respect to ground) and increased the plume divergence. This indicated that changes to the external magnetic field were primarily affecting the electron coupling with the discharge, rather than improving

[40] In the PEPL experiments, the cathode potential was more negative when the external trim coil was used (see Tables C-2 and D-1). This was attributed to differences in the vacuum facilities at PEPL and NASA GRC.

ion focusing. The floating potential data taken at the University of Michigan supported this conclusion by demonstrating that the floating potential downstream of the exit plane increased when the external trim coil was energized, which would presumably improve the coupling of the electrons with the discharge chamber plasma.

The effect of the internal trim coil on the potential distribution was less apparent than the external trim coil, mostly likely because of the way the internal trim coil changes the magnetic field. The internal trim coil primarily alters the axial gradient of the radial magnetic field, which changes the radius of curvature of the field lines (see section 5.1.4). Thus, the effects of the internal trim coil would be more noticeable by comparing the potential distribution radially across the discharge chamber. In addition, the internal trim coil reduces the fall potential at the anode by zeroing the magnetic field (see sections 5.1.4 and 7.5.2.5). Neither of these effects can be resolved by the data shown in Figures 11-1 and 11-2.

For the 600 V data shown in Figure 11-2, there was a local maximum in the potential distributions that occurred at z = +6 mm. The trim coils decreased the prominence of this feature. Figure 11-2 also shows disturbances to the discharge current at this same location. Similar results were reported on the P5 Hall thruster with both emissive and floating probes, but a complete explanation for the effect was not determined [142]. Non-perturbing laser diagnostics are ideally suited to diagnose whether or not these features are an artifact of the probe disturbing thruster operation.

12.1.2 Effects of the discharge voltage

Figure 12-1 compares operation at 300 and 600 V when both the internal and external trim coils were energized. The negative first derivative of the floating potential $-dV_f/dz$ was computed by numerical differentiation, under the assumption that this quantity was proportional to the axial electric field E_z (see section 10.3.1.2). As shown in Figure 12-1, the magnitude of $-dV_f/dz$ at 600 V was roughly twice the value at 300 V. Since to first order the axial electric field scales as $E_z \propto V_d/L_a$, where V_d is the discharge voltage and L_a is the thickness of the accelerating layer, these results suggested that **the accelerating layer thickness was weakly dependent on voltage**. This was expected because, at both operating conditions, the position of the anode and cathode were unchanged and the axial gradient of the magnetic field was approximately the same. Recent internal measurements using an emissive probe by Raitses, *et al.* [154] with a 2 kW Hall thruster have also found that the accelerating layer thickness was nearly constant with increased voltage.

After analyzing all the data shown in Figures 11-1 and 11-2, the results indicated that **the acceleration layer thickness was 14±2 mm**, which closely agreed with experimental and theoretical values [2, 98]. There was no strong dependence of the acceleration layer thickness with voltage or magnetic field, but this result may have been obscured by measurement uncertainty. The accelerating layer thickness was defined as the distance separating the points on either side of the maximum value of $-dV_f/dz$ that equaled 10% of the peak, excluding the regions at 600 V where the electric field was negative. Alternatively, if the acceleration layer thickness was defined by the distance separating the points where the electric field initially increased above zero and where it returned back to zero (again excluding the negative regions at 600 V), then the layer thickness was about 40 mm.

Thus, while the bulk of the acceleration occurred over a short distance of 14 mm, the ions reached their maximum velocity over a length of 40 mm. In addition, it was observed that the floating potential reached a minimum at the cathode plane (z = +30 mm). In the P5 Hall thruster, the cathode plane was at z = +50 mm and this was where the plasma potential reached a minimum [143]. This implies that the acceleration layer thickness can be partially controlled by cathode placement, which has implications on controlling divergence, decreasing erosion and improving efficiency.

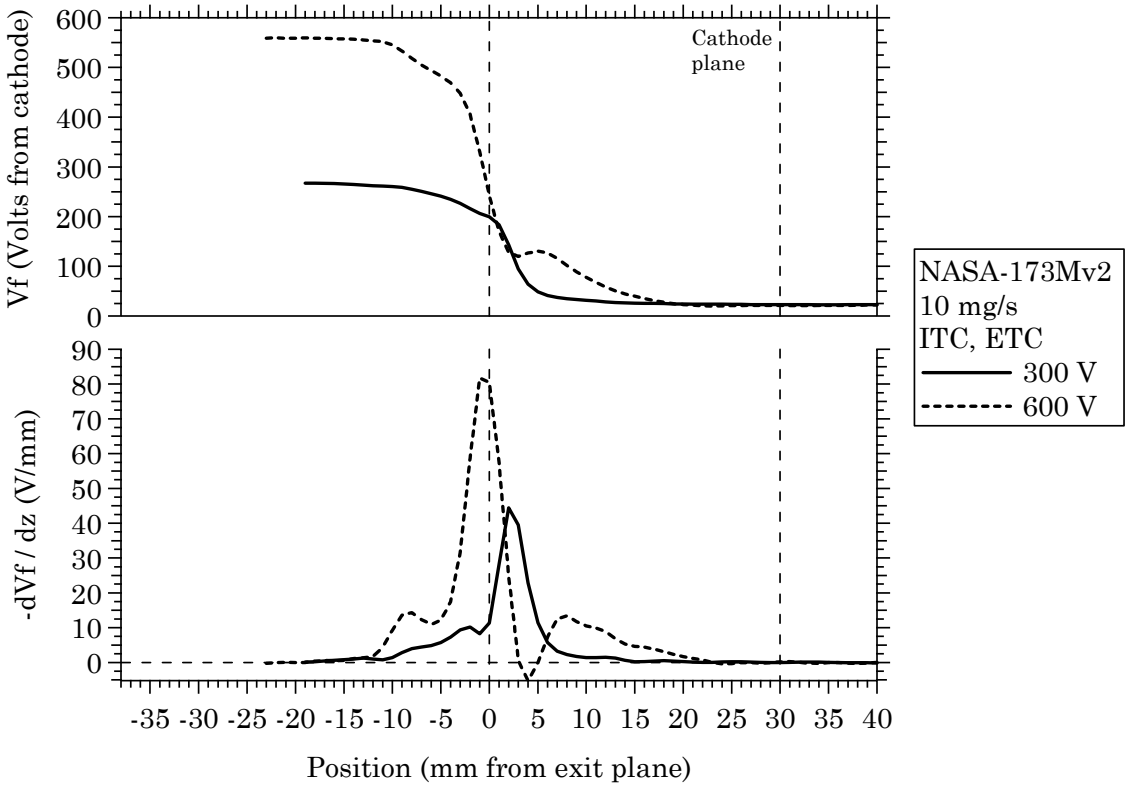

Figure 12-1 Floating potential and its negative first derivative (-dV$_f$/dz) versus axial position of the NASA-173Mv2 at 300 and 600 V with both trim coils energized.

As shown in Figure 12-1, **the acceleration layer shifted closer to the anode at 600 V**, by an average of 3±1 mm when all data were considered. This result was supported by visual observations of the plasma shifting closer to the

anode as the voltage increased (see section 8.4.1.1). A shift in the acceleration layer position affects thruster lifetime because shifts towards the anode increase the likelihood of radial electric fields accelerating ions into the wall. Since efficiency increased between 300 and 600 V (see Figure 8-7), it may be that such effects are offset by improved focusing efficiency at higher voltages so that erosion rates are not significantly changed. This could partially explain why the 500 V T-220 had nearly the same volumetric erosion rates as the 300 V SPT-100 [173].

In section 12.4.2, the results from the floating potential measurements are used to interpret the trends observed in the voltage and dispersion efficiency that were measured by the RPA.

12.2 Far-field ion species fractions

12.2.1 Effects of the magnetic field

Changes in the magnetic field resulted in marginal changes to the ion species fractions shown in Figure 11-8. This was likely the result of the probe resolution, which was 7%. Experiments with a higher resolution ExB probe (similar to the 1% resolution of Kim's probe [27, 208]) are needed to better resolve the effects of the magnetic field.

12.2.2 Effects of the discharge voltage

While the ion species fractions shown in Figure 11-8 indicated a general increase in the fraction of multiply-charged ions with increasing discharge voltage, **Xe^+ still dominated the plasma at all discharge voltages**. Over the range of 300-900 V, the species fraction of Xe^+ decreased from 0.96 to 0.81. Over the same voltage range, the Xe^{2+} species fraction increased from 0.03 to 0.16 and the Xe^{3+} species fraction increased from 0.01 to 0.03. At 300 V, the fractions of Xe^{2+} and Xe^{3+}

were lower, but still consistent with, previous Hall thruster studies using other mass analyzers [27, 29, 203, 204, 207, 208]. These past studies have shown the plume to be composed of 0.06-0.11 Xe^{2+} and 0.01 Xe^{3+}.

The effects of the measured ion species fractions on thruster efficiency are discussed further in section 12.5.

12.3 Far-field plasma potential

12.3.1 Effects of the magnetic field

A remarkable feature of Figure 11-9 is the 1-2 V decrease in plasma potential caused by changing the magnetic field with the external trim coil.[41,42] The decrease in plasma potential might at first seem unlikely because of the relatively large distance involved (~12 thruster diameters) and the small change in the magnetic field caused by the external trim coil (5-10% of the peak field at the exit plane). However, the trends are consistent with numerical modeling by Keidar and Boyd [205], which showed that a decreasing magnetic field would decrease the plasma potential in the thruster plume, albeit at smaller rates (about 0.03 V/G compared to 0.1-0.2 V/G from the results presented here). The ability to influence the plasma potential with external magnetics could be used to control the plasma near the thruster (especially charge-exchange ions). This has important implications regarding spacecraft integration and thruster lifetime. Additional experiments are planned to investigate magnetic field effects on the plasma potential distribution in the thruster plume.

[41] At 400 V, the decrease in plasma potential was smaller than the other discharge voltages most likely because the external trim coil current was less (-2 A at 400 V versus -4 to -6 A at all other voltages).
[42] Plotting the plasma potential with respect to the cathode shows the same trends.

12.3.2 Effects of the discharge voltage

Figure 11-9 shows that the plasma potential ranged from 8.2-13.5 V as the discharge voltage increased from 300-1000 V. While still small compared to the discharge voltage, the plasma potential was a significant fraction of the loss voltage (24-34 V) measured with the RPA (see section 11.4). These findings highlight the importance of knowing the true ion voltage to reduce uncertainty in the loss voltage, *i.e.*, the voltage utilization efficiency.

12.4 Far-field ion voltage distribution

12.4.1 Effects of the magnetic field

Changes in the magnetic field resulted in marginal changes to the ion voltage distribution. Of all the coil combinations that were used, only the external trim coil consistently changed the distributions by decreasing the FWHM. It is likely that the magnetic field dependence of the ion voltage distribution was obscured by measurement uncertainty. Experiments with a high-resolution electrostatic energy analyzer such as those described in Ref. [28, 204, 261], are needed to better resolve the effects of the magnetic field.

12.4.2 Effects of the discharge voltage

Figure 12-2 illustrates the relative positions of the ionization and acceleration zones in a Hall thruster discharge chamber. The voltage and dispersion efficiencies (η_v and η_d, see section 10.3.4.3) are primarily affected by changes to the centroid position (z_i and z_a) or the length (L_i and L_a) of the ionization (i) and acceleration (a) zones. As shown in the figure, the two zones overlap such that η_v and η_d are always less than unity. If L_a and z_a are unchanged, efficiency improvements are possible if L_i decreases and z_i is positioned further upstream of

the acceleration zone. However, due to the competing effects of wall losses, maximum thruster efficiency does not correspond to the complete separation of the two zones. This is because moving the ionization zone away from the acceleration zone can increase the rate at which ions are lost to the walls. Thus, the optimum configuration in a Hall thruster would **seem** to be highly peaked ionization and acceleration zones with the ionization zone located as close to the beginning of the acceleration zone as possible.

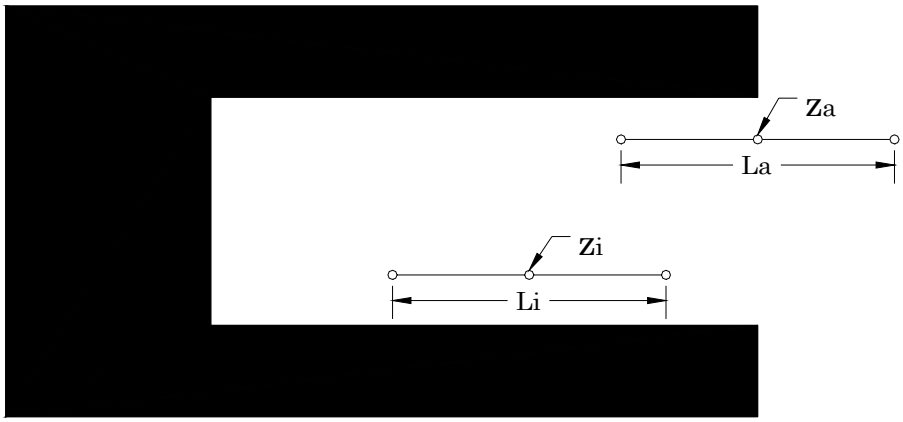

Figure 12-2 Schematic illustrating the relative positions of the ionization (*i*) and acceleration (*a*) zones in a Hall thruster discharge chamber. The length *L*, and centroid *z*, of each zone are indicated. (not to scale)

As the discharge voltage of the NASA-173Mv2 was increased, η_a increased and η_d decreased. There are several ways that z_i, z_a, L_i, and L_a can change to produce these results. Before considering these, it is helpful to review the discharge chamber floating potential results from section 12.1. The floating potential experiments indicated that as the discharge voltage increased:

1) L_a was approximately constant,

2) z_a moved upstream by 3±1 mm, and

3) either z_i moved upstream or L_i increased in length towards the anode. This was inferred from visual observations of the plasma, so it was not

possible to determine if the movement resulted from a shift in z_i or growth of L_i. (Note that an increase of L_i in only one direction must also shift z_i.)

The floating potential experiments are useful in determining the source of changes in η_v and η_d measured with the RPA. In general, an increase in η_v may result if:

a) z_i moves upstream,

b) L_i grows in the direction of the anode,

c) z_a moves downstream, or

d) L_a decreases.

From the floating potential experiments, 1) and 2) eliminate d) and c), respectively, while 3) supports either a) or b). Therefore, the increase in the voltage utilization efficiency can be either attributed to a shift or lengthening of the ionization zone towards the anode.

In general, a decrease in η_d may result if:

i) z_i moves downstream,

ii) L_i increases,

iii) z_a moves upstream, or

iv) L_a increases.

From the floating potential experiments, 1) eliminates iv), 3) eliminates i) and supports ii), and 2) supports iii). Therefore, the decrease in the dispersion efficiency can be attributed either to the movement of the acceleration zone or growth of the ionization zone. However, because a shift in the position of the acceleration zone towards the anode would also decrease the voltage efficiency (the

opposite was observed), it was more likely that **changes to the position and length of the ionization zone were the primary factors driving the observed changes in the voltage and dispersion efficiencie**s.

A simple explanation for the growth and shift of the ionization layer can be attributed to the expected increase of electron temperature with discharge voltage (the electron temperature scaling with voltage inferred from plume measurements in section 8.4.2 was $T_{e,D} \propto V_d^{0.84}$). As the electron temperature increases, the ionization layer can be expected to grow simply because it will take longer for the electrons to liberate their energy through wall collisions and ionization. Internal plasma measurements are needed to verify this claim.

As discussed at the beginning of this section, a longer ionization zone could be detrimental to thruster efficiency and lifetime due to higher wall losses. However, because the total efficiency increased with discharge voltage, additional wall losses may have been reduced by better focusing efficiency. This would be consistent with the decrease of plume divergence from 38º to 28º at voltages of 400-1000 V measured in section 8.4.2.

The effects of the measured ion voltage distributions on thruster efficiency are discussed further in section 12.5.

12.5 Efficiency analysis

The anode efficiency of a Hall thruster can be decomposed into the utilization efficiencies characterizing the physical processes that contribute to the generation of useful thrust. In Chapter 4, the utilization efficiencies were derived as part of the performance model for a multiply-charged, partially-ionized plasma. In this section,

the performance model is used to compute the utilization efficiencies of the NASA-173Mv2 at an anode flow rate of 10 mg/s.

Knowing the functional dependence of the utilization efficiencies at high-specific impulse is useful in understanding which processes dominate the anode efficiency. As shown in section 4.4.4, the electron current fraction largely determines the anode efficiency but, unfortunately, is very difficult to measure with existing diagnostics.[43] While attempts have been made to measure the electron current in Ref. [178] and other unpublished experiments by the author,[44] the following analysis is restricted to applying the performance model to first compute the electron current and then each of the utilization efficiencies.

The anode efficiency in a Hall thruster is given by

$$\eta_a = \frac{T^2}{2\dot{m}_a P_d} = \eta_q \eta_v \eta_b \eta_m , \tag{12-1}$$

where the partial efficiencies are the charge utilization efficiency

$$\eta_q = \frac{\left(\sum \Omega_i / \sqrt{Z_i} \right)^2}{\sum \Omega_i / Z_i} , \tag{12-2}$$

the voltage utilization efficiency

$$\eta_v = \frac{V_a}{V_d} = 1 - \frac{V_l}{V_d} , \tag{12-3}$$

[43] The electron current can be computed by measuring the ion and discharge currents. The ion current has traditionally been measured using a Faraday probe, however, there are several practical limitations with this diagnostic. For example, it is unclear where the sampling plane should be located and it is unclear how to account for ions lost to charge-exchange collisions (or worse, which charge-exchange ions to include!). In short, current methods are, at best, estimates of the "true" ion current. While potentially useful as a means to study the relative variation of the electron current with operating point, these methods, at least in the opinion of the author, do not currently offer the accuracy needed to measure the electron current.

[44] The unpublished experiments used the cathode-plane Faraday probe shown in Figures 6-4 and 6-5.

the current utilization efficiency

$$\eta_b = \frac{I_b}{I_d} = 1 - \varepsilon \,, \tag{12-4}$$

and the mass utilization efficiency

$$\eta_m = \frac{\dot{m}_b}{\dot{m}_a} = \xi \eta_b \sum \frac{\Omega_i}{Z_i} \,. \tag{12-5}$$

(Formal definitions for each of the terms appearing in the utilization efficiencies are given in Chapter 4.) The current, mass, and charge utilization efficiencies are related functions due to their dependence on the ion beam current and the ion species current fractions. Thus, the anode efficiency can also be expressed as

$$\eta_a = \eta_q \eta_v \eta_b \eta_m = \overbrace{\left(1 - \frac{V_l}{V_d}\right)}^{\eta_v} \underbrace{(1-\varepsilon)^2 \xi \left(\sum \frac{\Omega_i}{\sqrt{Z_i}} \right)^2}_{\eta_b \eta_m \eta_q} \,. \tag{12-6}$$

Equation 12-6 is a powerful means by which the electron current fraction and utilization efficiencies can be computed if the anode efficiency, loss voltage, and ion species current fractions are known. Table 12-1 summarizes the diagnostics that were used to compute the electron current fraction. The anode efficiency was computed from the thrust stand measurements in section 8.4.1, the ion current fractions were measured with the ExB probe in section 11.2, and the loss voltage was measured with the RPA in section 11.4 (after correcting the RPA data with the plasma potential measurements from section 11.3).

Table 12-1 Diagnostics used with the performance model to compute the electron current and utilization efficiencies of the NASA-173Mv2 at 10 mg/s.

Diagnostic	Measurement	Data range
Thrust stand	Anode efficiency	300-1000 V
ExB probe	Ion species fractions	300-900 V
Langmuir probe	Plasma potential (to correct RPA)	300-1000 V
Retarding potential analyzer (RPA)	Loss voltage	300-800 V (IC,OC only at 800 V)

12.5.1 Charge utilization efficiency

Figure 12-3 shows the charge utilization efficiency over 300-900 V computed with Eqn. 12-2 by using the ion species fractions measured with the ExB probe in section 11.2. The charge utilization was computed only for the thruster operating points (*i.e.*, coil combinations) that were studied during the performance characterization in section 8.4.1.

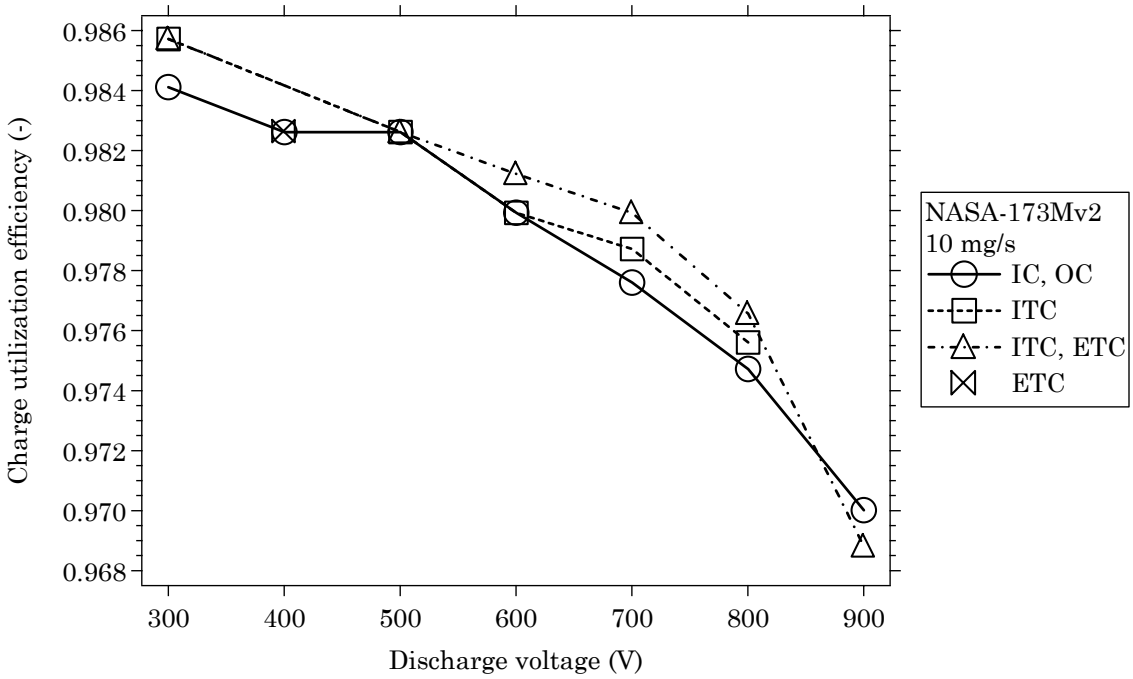

Figure 12-3 Charge utilization efficiency versus discharge voltage of the NASA-173Mv2 at 10 mg/s.

As shown in Figure 12-3, the charge utilization was, on average, 98.5% at 300 V and then decreased at a nearly linear rate to an average value of 97.6% at 800 V. A (relatively) sharp decrease occurred between 800 and 900 V, where the charge utilization dropped to an average of 97.0%. **Thus, the presence of multiply-charged ion species decreased the anode efficiency by 1.5-3.0% over the range of 300-900 V.** Note that the charge utilization does not include the effects of multiply-charged ions on the mass utilization or the current utilization. However, at least with the NASA-173Mv2 at 10 mg/s, the charge utilization is a good measure of the net effect of multiply-charged ions on performance because the current and mass utilization efficiencies were usually increasing or constant with voltage (see section 12.5.4 and 12.5.5 below).

12.5.2 Voltage utilization efficiency

Figure 12-4 shows the voltage utilization efficiency over 300-900 V computed with Eqn. 12-3 by using the loss voltage measured with the RPA in section 11.4. The voltage utilization was computed only for the thruster operating points (*i.e.*, coil combinations) that were studied during the performance characterization in section 8.4.1. The RPA data included all of the thruster operating points from the performance characterization between 300-700 V. However, at 800 V, data with the RPA were acquired only with the inner and outer coils (IC,OC). No data were collected with the RPA at 900 V. Since the voltage utilization showed a clear trend with voltage, the loss voltage was conservatively extrapolated for the missing data points at 800 and 900 V.[45] At 800 V, the loss voltage was set to 25 V for the operating conditions using the trim coils (the same as the measured value at 800 V,

[45] Note from the previous section that the charge utilization was not extrapolated from the last data point at 900 V to 1000 V (the maximum voltage tested during the performance characterization). This was because the uncertainty in the ExB probe measurements did not justify such an extrapolation.

IC,OC). At 900 V, the loss voltage was set to 24 V for each data point, which was consistent with the observed decrease in loss voltage with increasing discharge voltage.

As shown in Figure 12-4, the voltage utilization ranged from 88.7% at 300 V to 96.9% at 800 V (for the extrapolated data at 900 V, the voltage utilization was 97.3%). The substantial increase in the voltage utilization was primarily the result of the discharge voltage increasing, since the decrease in the loss voltage was only minor in comparison.

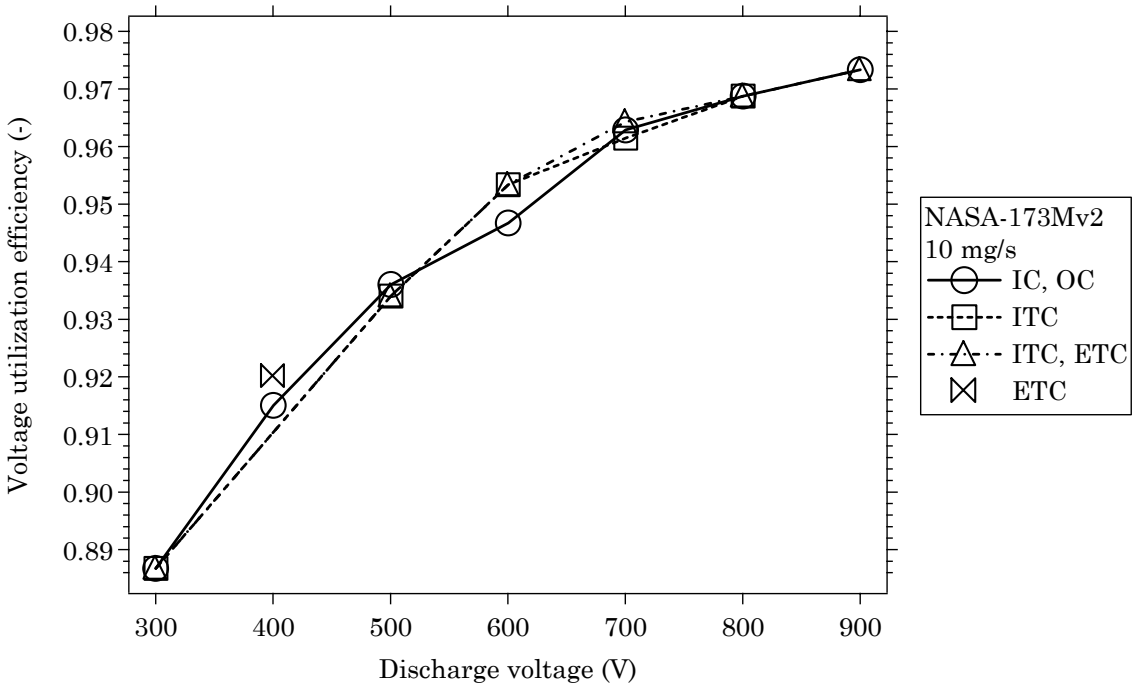

Figure 12-4 Voltage utilization efficiency versus discharge voltage of the NASA-173Mv2 at 10 mg/s. Data at 800-900 V are based on extrapolation of the loss voltage except for the 800 V (IC,OC) point.

12.5.3 Electron and ion current

The electron current fraction ($\varepsilon = I_e/I_d$) was computed from Eqn. 12-6 using the anode efficiency, loss voltage, and ion species fractions. Since the discharge current was also known, this also meant that the electron current and ion current could be computed. Figures 12-5 and 12-6 show the electron current and ion

current, respectively, over 300-900 V. As described in section 12.5.2, data at 800-900 V are based on extrapolation of the loss voltage except for the 800 V (IC,OC) point. The discharge current has also been included in Figure 12-6 for reference.

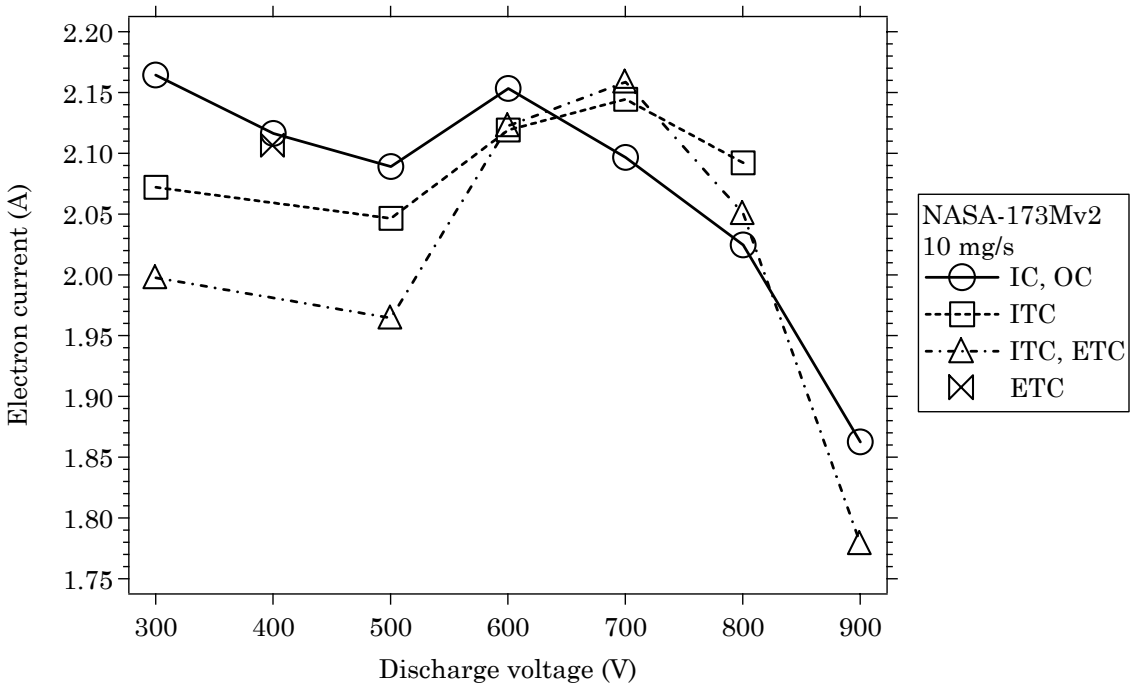

Figure 12-5 Electron current versus discharge voltage of the NASA-173Mv2 at 10 mg/s. Data at 800-900 V are based on extrapolation of the loss voltage except for the 800 V (IC,OC) point.

The electron current was relatively constant over the range of 300-700 V and then decreased between 700-900 V. The average value of the electron current over 300-900 V was 2.06 A with a maximum deviation of +5%/-14% from the average. In contrast, the ion current steadily increased with the discharge voltage from a minimum of 6.79 A at 300 V to a maximum of 8.05 A at 900 V. The same relative increase in the ion current with voltage has been confirmed with a cathode-plane Faraday probe (not shown, the method employed was similar to Ref. [178]). The discharge current also increased with discharge voltage from a minimum of 8.84 A at 300 V to a maximum of 9.83 A at 900 V. **Thus, the increase in the discharge current with voltage was attributed to increased ion current due to the**

increased fraction of multiply-charged ions, rather than an increase of electron current. These results show that:

1. the electron current in a high-specific impulse Hall thruster can be regulated if the magnetic field is of the appropriate shape and strength, and
2. an increasing current-voltage characteristic should not be assumed to be the sole result of increased electron current (see section 3.2.2.1), especially if the thruster is operating efficiently.

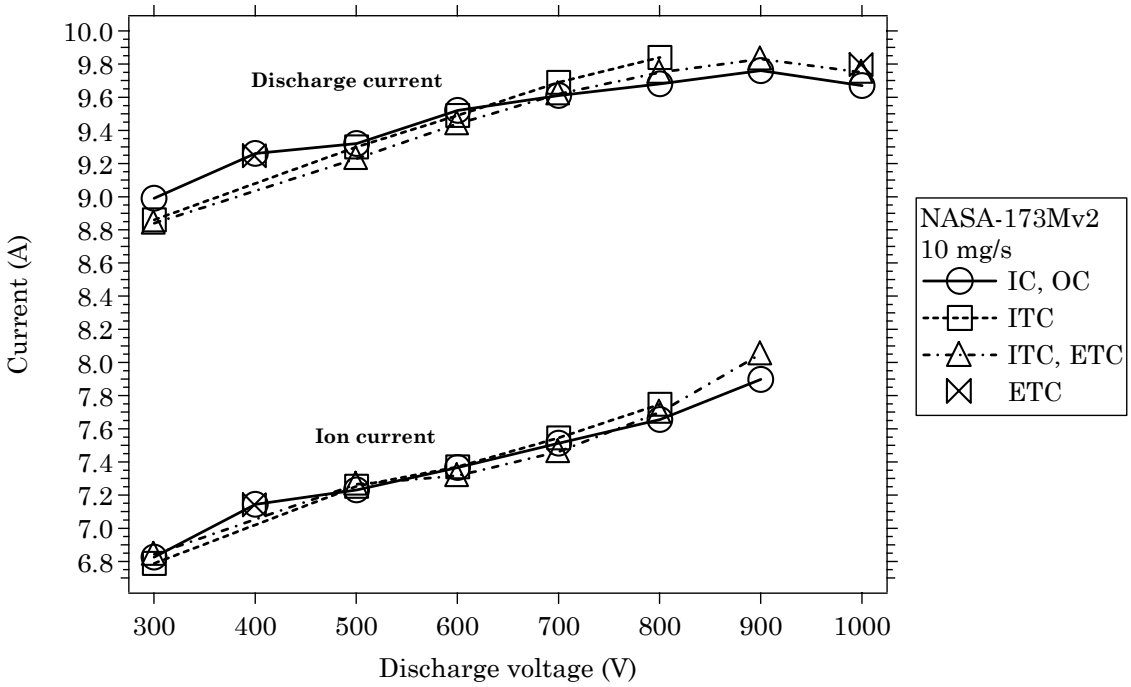

Figure 12-6 Ion current and discharge current versus discharge voltage of the NASA-173Mv2 at 10 mg/s. Data at 800-900 V are based on extrapolation of the loss voltage except for the 800 V (IC,OC) point.

12.5.4 Current utilization efficiency

Figure 12-7 shows the current utilization efficiency over 300-900 V computed with Eqn. 12-4 by using the ion current that was computed in section 12.5.3. As

described in section 12.5.2, data at 800-900 V are based on extrapolation of the loss voltage except for the 800 V (IC,OC) point.

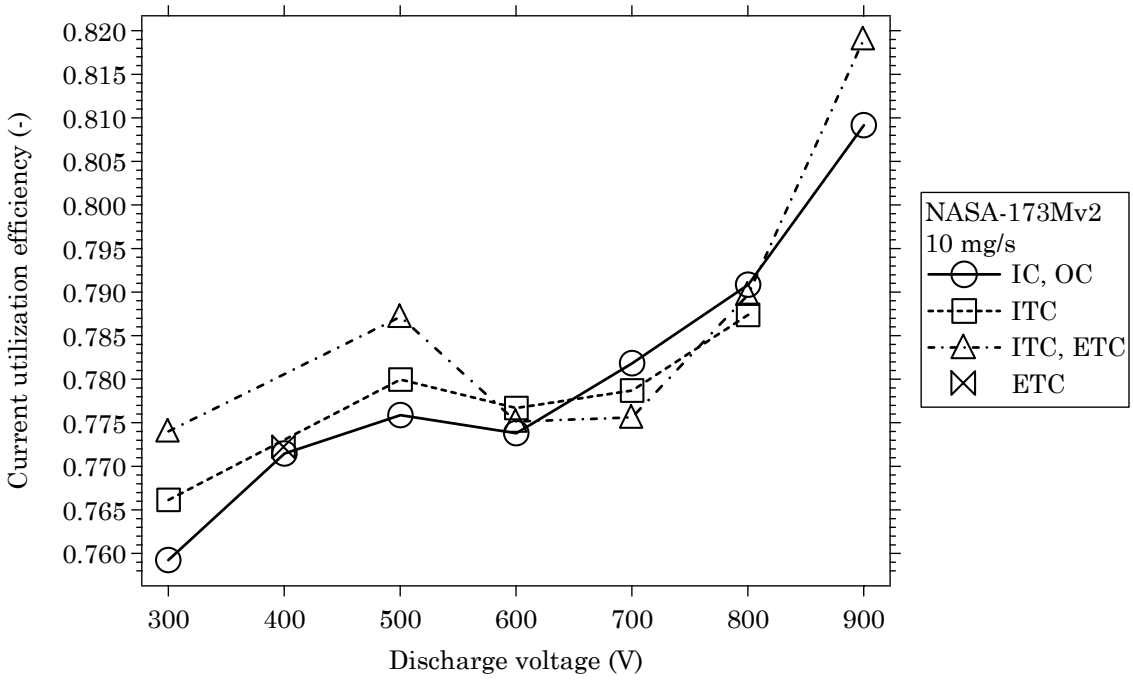

Figure 12-7 Current utilization efficiency versus discharge voltage of the NASA-173Mv2 at 10 mg/s. Data at 800-900 V are based on extrapolation of the loss voltage except for the 800 V (IC,OC) point.

As shown in Figure 12-7, the continuous increase with voltage that was shown in the ion current in Figure 12-6 was not reflected in the current utilization, since the current utilization depends on the ion and electron current. Instead, the current utilization initially increased between 300-500 V, was relatively constant between 500-700 V, and then increased between 700-900 V. The rise in the current utilization beginning at 700 V was largely the result of the sudden decrease in electron current shown in Figure 12-5. Overall, since the electron current was nearly constant between 300-900 V, the current utilization efficiency increased because of the increasing fraction of multiply-charged ions as the voltage increased. The current utilization was, on average, 76.6% at 300 V and increased to an average of 81.4% at 900 V.

12.5.5 Mass utilization efficiency

Figure 12-8 shows the mass utilization efficiency over 300-900 V computed with Eqn. 12-5 by using the ion current that was computed in section 12.5.3. As described in section 12.5.2, data at 800-900 V are based on extrapolation of the loss voltage except for the 800 V (IC,OC) point.

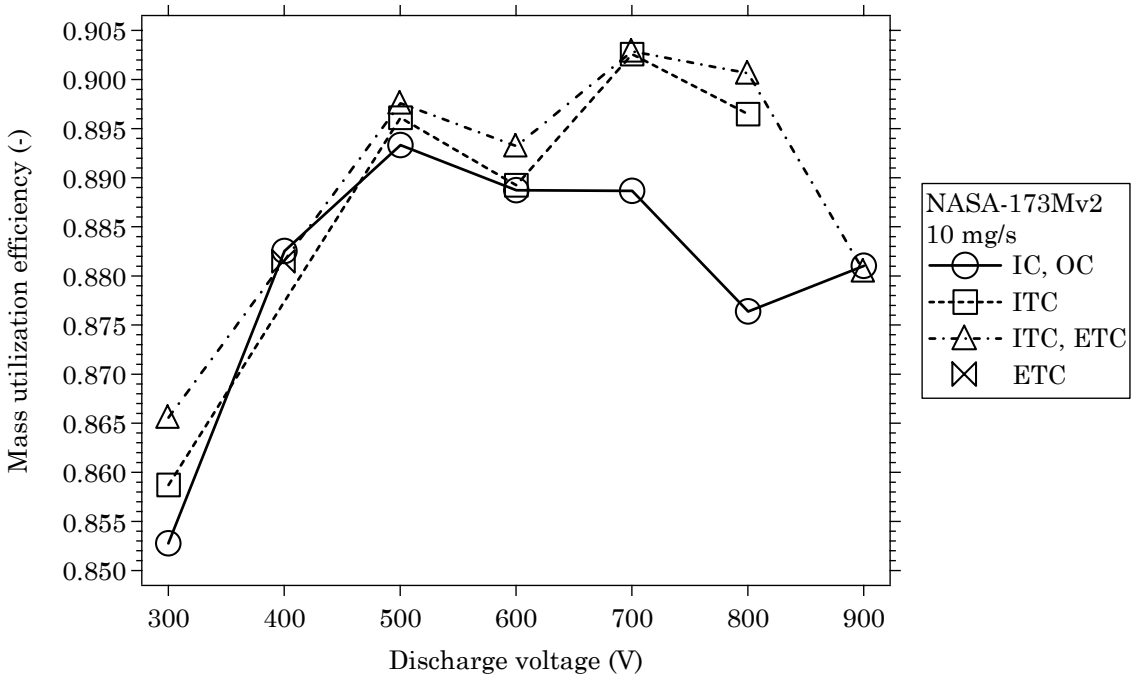

Figure 12-8 Mass utilization efficiency versus discharge voltage of the NASA-173Mv2 at 10 mg/s. Data at 800-900 V are based on extrapolation of the loss voltage except for the 800 V (IC,OC) point.

As shown in Figure 12-8, the mass utilization increased rapidly between 300-500 V, was relatively constant between 500-700 V, and then showed evidence of a decrease between 700-900 V. At 300 V, the mass utilization was, on average, 85.9% at 300 V and 88.1% at 900 V. The maximum mass utilization was 90.3%, which occurred at 700 V.

12.5.6 Anode efficiency

For reference, Figure 12-9 shows the anode efficiency of the NASA-173Mv2 at 10 mg/s from the performance characterization in section 8.4.1. The anode

efficiency, which excludes the cathode flow and the magnet power, ranged from a minimum of 56.5% at 300 V to a maximum of 68.5% at 1000 V. (Total efficiency is shown in Figure 8-7.) Figure 12-10 shows the anode efficiency and the corresponding utilization efficiencies for the coil combinations at each discharge voltage shown in Figure 12-9 that maximized anode efficiency. As described in section 12.5.2, data for the utilization efficiencies at 800-900 V are based on extrapolation of the loss voltage.

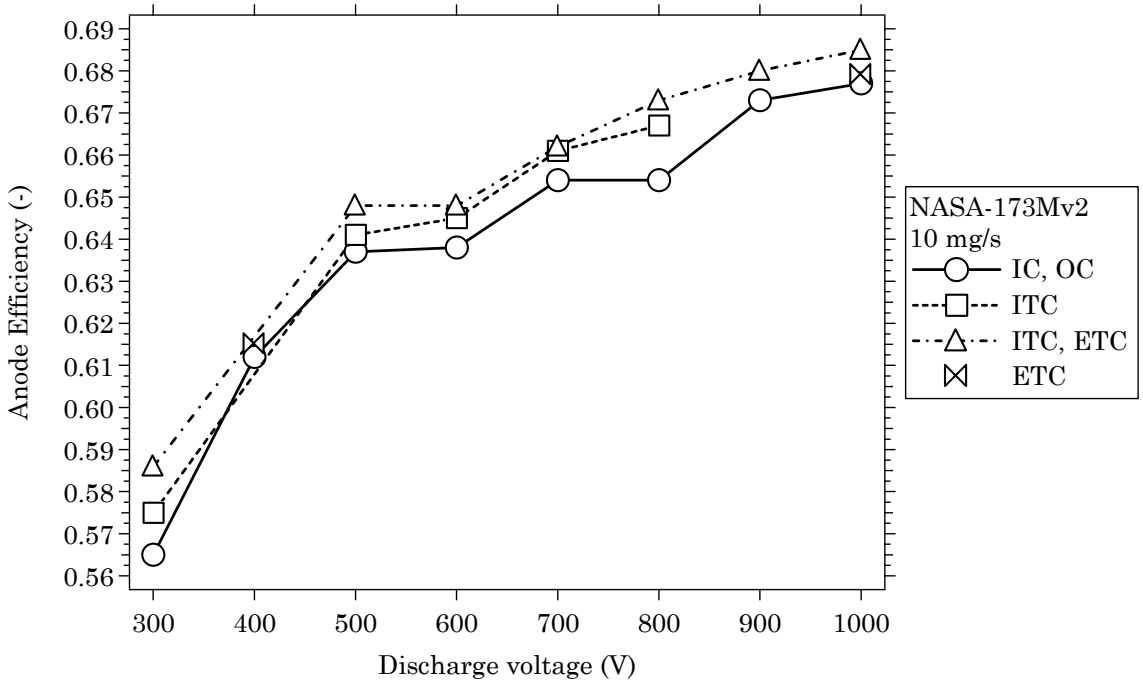

Figure 12-9 Anode efficiency versus discharge voltage of the NASA-173Mv2 at 10 mg/s.

At the optimum coil combinations represented by Figure 12-10, the voltage and current utilization efficiencies increased with discharge voltage, the charge utilization efficiency decreased, and the mass utilization efficiency was nearly constant. Note that the charge utilization is a good measure of the net effect of multiply-charged ions on the anode efficiency since the other terms that are strongly affected by multiply-charged ions, the current and mass utilization, were usually

increasing or constant with voltage. As shown in section 4.4.4, these results confirm that the anode efficiency in a Hall thruster is largely determined by the current utilization.

Since the current utilization was an increasing function of the discharge voltage (and the electron current showed evidence of a decrease above 700 V), these results imply that **the maximum anode efficiency of a Hall thruster has not yet been reached with existing design strategies**. With further design improvements, anode efficiencies can potentially still be increased, perhaps as high as 80%, if the discharge voltage is increased beyond 1000 V. At lower voltages, since the electron current was relatively constant, further efficiency improvements would require a means to minimize the production of multiply-charged ions and to increase the voltage utilization efficiency further.

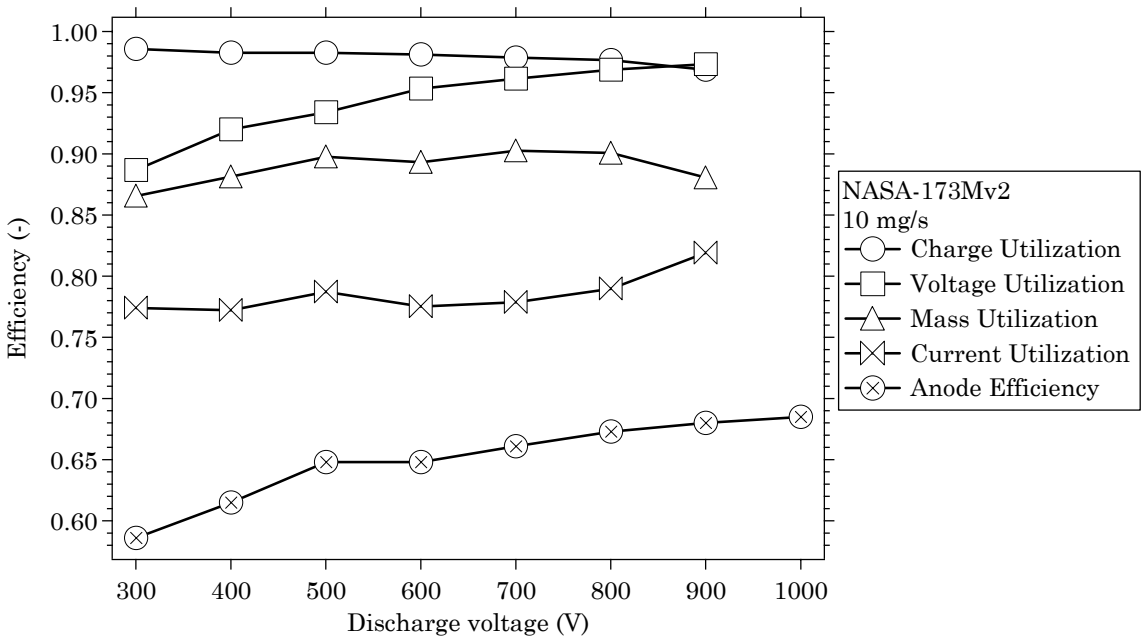

Figure 12-10 Optimized anode efficiency and the corresponding utilization efficiencies versus discharge voltage of the NASA-173Mv2 at 10 mg/s. For the utilization efficiencies, data at 800-900 V are based on extrapolation of the loss voltage.

12.5.7 Electron Hall parameter

The scaling of the axial electron current with voltage provides insight on the electron Hall parameter. The Hall parameter characterizes the number of azimuthal revolutions an electron will complete before reaching the anode and is affected by any process that increases the axial electron mobility (see section 3.1.3). Note that neither a zero nor an infinite Hall parameter are desirable, since a Hall parameter of zero would mean electrons migrate unimpeded to the anode and an infinite Hall parameter would mean electrons never reach the anode. Therefore, there must be a limited range of Hall parameters where the thruster will operate efficiently (see section 3.1.2).

As shown in section 3.1.3, the electron Hall parameter is equal to the ratio of the azimuthal and axial electron current densities given by

$$\Omega_e = \frac{j_{e\theta}}{j_{ez}}. \tag{12-7}$$

From the ExB drift velocity v_{ExB}, the azimuthal electron current density was computed from

$$j_{e\theta} = n_e e v_{ExB} = n_e e \frac{E_z}{B_r}. \tag{12-8}$$

The axial electron current density was computed from the electron current from the performance model (see section 12.5.3) and the annular cross-sectional area of the discharge chamber

$$j_{ez} = \frac{I_e}{A}. \tag{12-9}$$

After applying the quasineutrality condition ($n_e \approx n_b$), the electron Hall parameter was given by

$$\Omega_e = \frac{n_b e E_z A}{B_r I_e}. \tag{12-10}$$

Besides the electron current and channel area, the Hall parameter was estimated from the available data as follows:

1. the axial electric field at 300 V was estimated from typical electric field strengths in modern Hall thrusters and then linearly varied with discharge voltage (based on the results from the floating potential probe and Ref. [154]),
2. the radial magnetic field was given by the measurements taken with the Gaussmeter (see section 8.4.4), and
3. the beam density was computed with Eqn. 4-46 from the performance model.

Figure 12-11 shows the electron Hall parameter over 300-900 V computed with Eqn. 12-10. As described in section 12.5.2, data at 800-900 V are based on extrapolation of the loss voltage except for the 800 V (IC,OC) point.

At 300 V, the electron Hall parameter averaged 210. Between 300-400 V, the electron Hall parameter decreased by 25% and then was nearly constant between 400-900 V. Over 400-900 V, the electron Hall parameter averaged 160 with a maximum deviation from the average of +12%/-7%. The electron Hall parameter computed here is consistent with experimental investigations [2, 135, 136] that have shown that the Hall parameter attains a value of several hundred in the closed-drift region, and with numerical simulations [138,

144] that have found acceptable results when a numerical fitting parameter α_{ano}^{-1} (see Eqn. 3-15), which is equal to the electron Hall parameter if Bohm-like transport dominates, was approximately 100.

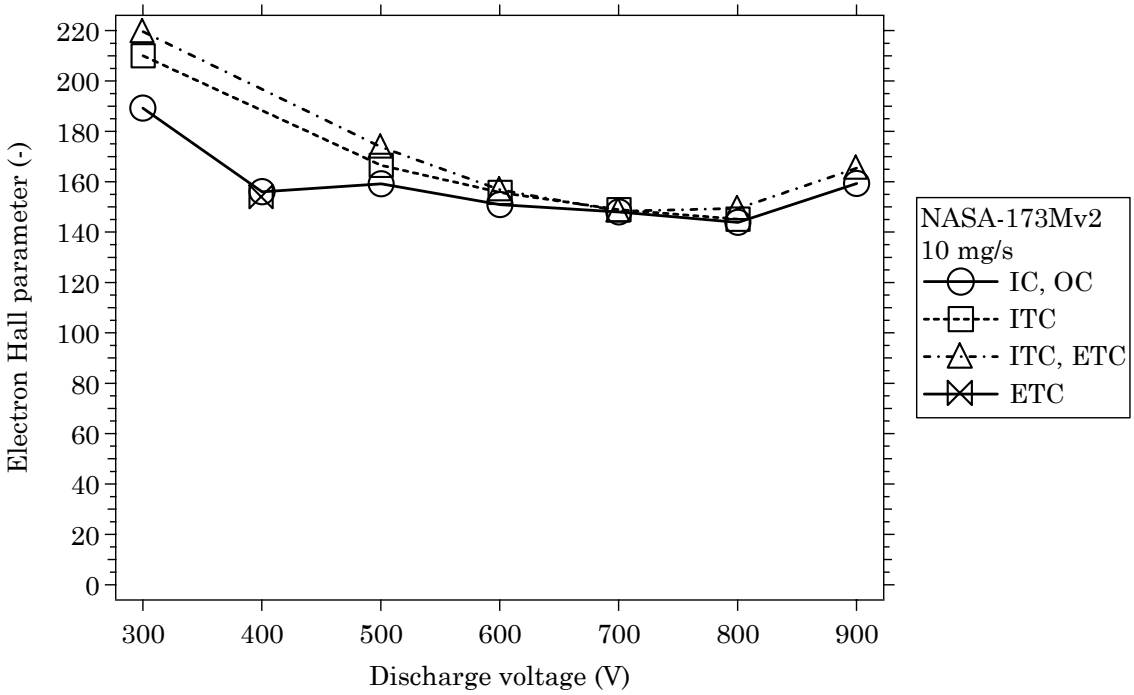

Figure 12-11 Electron Hall parameter versus discharge voltage of the NASA-173Mv2 at 10 mg/s. Data at 800-900 V are based on extrapolation of the loss voltage except for the 800 V (IC,OC) point.

The decrease in the Hall parameter between 300-400 V most likely coincided with the onset of space-charge saturation of the discharge chamber wall sheaths [109, 110]. Although this claim cannot be confirmed directly, there is ample evidence that the thruster is transitioning to a different operating mode beginning around 400 V. For example, consider the large jump in plume divergence and discharge current oscillations between 300-400 V shown in Figures 8-15 and 8-19, respectively. Apparently, the transition to this new regime persists until about 600 V, after which the oscillations suddenly decrease. It seems then that the magnetic

field in the NASA-173Mv2 is effective at controlling oscillations and wall effects above 600 V so that the efficiency does not begin to decrease.

At least over 400-1000 V, maintaining a nearly constant electron Hall parameter over such a large voltage range implied that the balance of all the processes affecting the axial electron mobility were also approximately constant. **This confirms the claim made in section 3.1.2 that efficient thruster operation can only be realized over a limited range of electron Hall parameters.**

12.6 Conclusions

The results from a series of plasma diagnostics used with the NASA-173Mv2 have shown the effects of the magnetic field and discharge voltage on the discharge chamber and far-field plasma properties during high-specific impulse operation.

Discharge chamber floating potential measurements have proven to be useful in understanding relative trends in the acceleration process. The acceleration layer moved upstream 3±1 mm when the voltage increased from 300 V to 600 V. Additionally, the 14±2 mm acceleration layer length was found to be approximately constant with voltage and magnetic field, which in turn implied that the electric field scaled linearly with the discharge voltage.

An ExB probe was used to measure the ion species fractions of Xe^{+}, Xe^{2+}, and Xe^{3+}. Over discharge voltages of 300-900 V, the Xe^{2+} species fractions increased from 0.03 to 0.16 and the Xe^{3+} species fraction increased from 0.01 to 0.03.

A cylindrical Langmuir probe was used to measure the plasma potential and a retarding potential analyzer was employed to measure the ion voltage distribution. The plasma potential was affected by relatively small changes in the external

magnetic field, which suggested a means to control the plasma surrounding the thruster. As the discharge voltage increased, the ion voltage distribution showed that the voltage utilization efficiency increased and the dispersion efficiency decreased. This implied that the ionization zone was growing axially and moving closer to the anode, which could have affected thruster efficiency and lifetime due to higher wall losses. However, wall losses may have been reduced by improved focusing efficiency since the total efficiency increased and the plume divergence decreased with discharge voltage.

Using the experimental data as inputs, the performance model for a multiply-charged, partially-ionized plasma was used to compute the utilization efficiencies of the NASA-173Mv2 over discharge voltages of 300-900 V. With increasing discharge voltage, the net decrease of the anode efficiency due to the increasing fraction of multiply-charged ions was shown to be minor. The electron current was also shown to be approximately constant with increasing discharge voltage, while the ion current increased due to the increased fraction of multiply-charged ions. These results confirmed that the shape and strength of the magnetic field in the NASA-173Mv2 enabled efficient operation at high-specific impulse by effectively regulating the electron current. Further analysis revealed that the anode efficiency was largely determined by the current utilization efficiency, which suggested that the maximum efficiency of Hall thrusters has yet to be reached. Finally, it was shown that the electron Hall parameter was approximately constant with increasing discharge voltage. At 300 V, the electron Hall parameter averaged 210 and then decreased to an average value of 160 +12%/-7% over 400-900 V. This confirmed that efficient thruster operation can be realized only over a limited range of Hall parameters.

Chapter 13

Conclusions

The central aim of this dissertation, the development and characterization of xenon Hall thrusters capable of both high-specific impulse and high-efficiency operation, has been achieved. Through design and experiment, the development of the NASA-173M Hall thrusters established that Hall thrusters can operate efficiently at high-specific impulse if a minimum current density is maintained and the magnetic field topography is properly shaped. During an extended characterization of the NASA-173Mv2, a series of plasma diagnostics were deployed to study the competing mechanisms affecting performance at high-specific impulse. To aid the characterization studies, a performance model accounting for the effects of a multiply-charged, partially-ionized plasma was also derived. Among other results, the characterization phase of the NASA-173Mv2 confirmed how the magnetic field enabled efficient operation at high-specific impulse by effectively regulating the electron current.

In the remainder of this chapter, the major conclusions from this dissertation are summarized and suggestions concerning the future development of high-specific impulse Hall thrusters are proposed.

13.1 The role of magnetic field topography

The NASA-173M Hall thrusters were designed based on the hypothesis that the magnetic field topography required for efficient, high-specific impulse operation

would differ from that employed at 1600 s specific impulse. Experiments with the NASA-173Mv1 confirmed this basic hypothesis by establishing the validity of the plasma lens magnetic field design. In a performance study at low current density, changes to the magnetic field topography at high-specific impulse were shown to be critical to achieving efficient operation. Analysis of the magnetic field identified several factors that contributed to the performance benefits gained by altering the magnetic field topography.

13.2 The role of current density and magnetic field topography

Experiments with the NASA-173Mv2 documented the influence of current density and magnetic field topography on the performance, plume divergence and plasma oscillations at high-specific impulse. Test results showed there was a minimum current density and optimum magnetic field topography at which efficiency monotonically increased with voltage. Between 300-1000 V and an anode mass flow rate of 10 mg/s, the total specific impulse of the NASA-173Mv2 ranged from 1600-3400 s with a corresponding total efficiency of 51-61%. The use of trim coils to modify the magnetic field improved performance while decreasing plume divergence and the frequency and magnitude of plasma oscillations. This may ultimately prove to be the greatest utility of trim coils, since controlling divergence and oscillations is critical to extending thruster lifetime. While enhancing performance overall, trim coils were not required to obtain a monotonic efficiency-voltage characteristic. This demonstrated that traditional magnetic circuits can still be used if the fixed magnetic field topography is properly designed.

13.3 Optimizing the magnetic field for specific impulse

A performance comparison of the NASA-173M Hall thrusters demonstrated that efficiency could be optimized for specific impulse by changing the design of the plasma lens. The magnetic field topography of the NASA-173Mv1 was found to be well suited for low-specific impulse operation, while the improved design of the NASA-173Mv2 optimized at high-specific impulse. These results have shown how the magnetic field of a Hall thruster can be tailored to maximize efficiency for a particular range of specific impulse. In other words, there is no magic magnetic field that will result in maximum efficiency over an infinite range of discharge voltages. This should go without saying, but of course, dispelling such a notion is what motivated this research in the first place.

13.4 Plasma properties at high-specific impulse

Measurements of discharge current oscillations, magnetic field, internal floating potential, and plume measurements of the ion current density, ion species fractions, plasma potential, and ion voltage distributions have improved the existing understanding of Hall thruster operation at high-specific impulse. From these measurements, most of which were taken at an anode mass flow rate of 10 mg/s, some of the major results and conclusions were that:

1. The breathing-mode frequency steadily increased with voltage, from 14.5 kHz at 300 V to 22 kHz at 1000 V. Above 500 V, additional oscillatory modes in the 80–90 kHz band emerged. Trim coils were shown to affect this frequency band.
2. At optimum thruster efficiency, a nearly linear increase of the magnetic field was required with increased discharge voltage.

Between 300-1000 V, the magnetic field increased by a factor of 2.6 for flow rates of 10 mg/s.

3. Plume divergence decreased between 400–1000 V from a maximum of 38° to a minimum of 28°. An increase in divergence from 300 to 400 V was attributed to plasma oscillations.
4. The thickness of the acceleration layer was nearly constant with increased discharge voltage, which implied that the scaling of the electric field with voltage was linear. The position of the acceleration layer also moved upstream with voltage.
5. The loss voltage decreased with discharge voltage from 35 V at 300 V to 25 V at 800 V.
6. The length and position of the ionization layer increased towards the anode with increased discharge voltage.
7. The species fraction of Xe^{+} decreased from 0.96 to 0.81 over 300-900 V, while Xe^{2+} increased from 0.03 to 0.16 and Xe^{3+} increased from 0.01 to 0.03 over the same voltage range.
8. The far-field plasma potential was affected by relatively small changes in the external magnetic field, which suggested a means to control the plasma surrounding the thruster.

13.5 Utilization efficiency analysis

A phenomenological Hall thruster performance model accounting for the effects of a multiply-charged, partially-ionized plasma was derived as a function of the utilization efficiencies of current, mass, voltage, and charge. It was shown how the model could be combined with experimental measurements of the plasma

parameters to compute the electron current and utilization efficiencies. Since the electron current is difficult to measure accurately using probe-based diagnostics, the performance model has proven to be an extremely powerful tool in the study of Hall thruster physics.

Using the experimental data as inputs, the performance model for a multiply-charged, partially-ionized plasma was used to compute the utilization efficiencies of the NASA-173Mv2 over discharge voltages of 300-900 V. With increasing discharge voltage, the net decrease of the anode efficiency due to the increasing fraction of multiply-charged ions was shown to be minor. The electron current was also shown to be approximately constant with increasing discharge voltage, while the ion current increased due to the increased fraction of multiply-charged ions. These results confirmed that the shape and strength of the magnetic field in the NASA-173Mv2 enabled efficient operation at high-specific impulse by effectively regulating the electron current. Further analysis revealed that the anode efficiency was largely determined by the current utilization efficiency, which suggested that the maximum efficiency of Hall thrusters has yet to be reached. Finally, it was shown that the electron Hall parameter was approximately constant with increasing discharge voltage. At 300 V, the electron Hall parameter averaged 210 and then decreased to an average value of 160 +12%/-7% over 400-900 V. This confirmed that efficient thruster operation can be realized only over a limited range of Hall parameters.

13.6 A proposed testing standard for Hall thrusters

Based on the successful application of the performance model in this dissertation, it is hoped that the methods described here will be adopted and refined into a standard characterization procedure for Hall thrusters. If such a procedure

were adopted, this would enable researchers to make quantitative comparisons between thruster designs with unprecedented accuracy, thus enabling a deeper understanding of Hall thruster physics throughout the community. Specifically, the performance model suggests that the following diagnostics should be a part of any laboratory studying Hall thrusters:

1. a thrust stand to measure performance,
2. a retarding potential analyzer (RPA) or electrostatic energy analyzer (ESA) to measure the average ion voltage,
3. a cylindrical Langmuir probe to correct the RPA,
4. an ExB probe to measure the ion species fractions,[46] and
5. a Faraday probe to measure ion current density.

To compute the electron current, the performance model depends on the loss voltage, ion species fractions, and the thruster efficiency. Since the plasma parameters in the model represent global properties of the thruster, the plasma parameters should be measured to account for any spatial dependence so that average values can be computed. While the far-field measurements that were taken during the course of this research were certainly a good indicator of the average plasma properties, the methodology could be refined to decrease the uncertainty in the measurements.

At least in theory, the most accurate method to account for the spatial dependence of the plasma parameters is to make radial measurements of the ion current density and the other plasma parameters at some axial location downstream of the thruster (considering the pumping speed limitations of most vacuum facilities,

[46] Actually, an ExB probe should be capable of measuring the average ion energy. ExB probes used with Hall thrusters usually require calibration because ExB probes are prone to alignment errors that are difficult to quantify. Since this is easily done with an RPA, both probes are included in the list of suggested diagnostics.

one to five thruster diameters is suggested). The current density is used to weight the plasma parameter measurements so that average values can be computed. For example, if the ion voltage was measured at some axial location along radial sweeps from thruster centerline, then at each radial location the average ion voltage $V_a(r)$ could be calculated from the ion voltage distribution $f(r,V)$

$$V_a(r) = \int_0^\infty V f(r,V) dV \,, \tag{13-1}$$

The average ion voltage V_a for the thruster could then be calculated by weighting each radial measurement by the ion current density $j_b(r)$ and then integrating radially

$$V_a = \frac{1}{I_b} \int_0^\infty V_a(r) j_b(r) 2\pi r dr \,, \tag{13-2}$$

where the total ion beam current I_b is given by

$$I_b = \int_0^\infty j_b(r) 2\pi r dr \,. \tag{13-3}$$

Since the ion current density is used only as a weighting function, it is not necessary for this measurement, or the total ion beam current computed from it, to be particularly accurate in terms of absolute quantities. Only the relative change in the ion current density is needed to weight the plasma properties.

In addition, during the experiments changes to the plasma caused by altering the magnetic field were largely unresolved. Improving the resolution of the probes used here should alleviate this shortcoming and improve the overall accuracy of the quantities computed from the performance model. Specifically, it is recommended

that energy probes used in future investigations have an energy resolution of better than 1%.

13.7 Suggestion for future work

The research described in this dissertation has established a solid foundation from which the future development of high-specific impulse Hall thrusters may proceed. While the design of such a thruster by the author and his co-workers is currently in progress at NASA GRC [49], there are several other issues and potential directions that deserve further scrutiny. These topics include, at least:

1. **Numerical simulations of high-specific impulse Hall thrusters.** The plasma measurements presented here have only begun to scratch the surface of a more fundamental explanation of the factors affecting Hall thruster efficiency at high-specific impulse. The recent work by Gascon, *et al.* and Barral, *et al.* [109, 110] concerning the transition to a space-charge saturation regime has been offered here as a likely explanation of the trends observed with the NASA-173M Hall thrusters. However, the NASA-173M data do not allow for definitive conclusions, only indirect inferences are currently possible. It is hoped that the data in this dissertation can be used to validate future numerical models. Such models could presumably lend additional insight necessary to understand the underlying physics of high-specific impulse operation.
2. **Lifetime evaluation of high-specific impulse Hall thrusters.** This dissertation has tacitly assumed that if thruster efficiency is maximized so too is thruster lifetime. While this may prove to be

accurate, there are still unanswered questions concerning the **rate** at which lifetime decreases with voltage. Recent numerical modeling by Garrigues, *et al.* [215] has begun to address some of these lifetime issues by demonstrating how erosion rates in 1600 s thrusters decreases when a plasma lens is used (in lieu of less concave magnetic field lines). Efforts to establish the voltage dependence of lifetime with the use of a plasma lens should be pursued in the near-term.

3. **Characterization of high-specific impulse Hall thrusters with krypton as a propellant**. Besides offering higher specific impulse (at the expense of efficiency), krypton propellant may prove to be a better choice than xenon for high-specific impulse Hall thrusters. While krypton is harder to ionize than xenon (which lowers the efficiency mainly by decreasing the mass utilization), this attribute also decreases the production of multiply-charged ions. If the efficiency of krypton Hall thrusters can be improved, such thrusters would presumably have longer lifetimes than their xenon counterparts due to the decreased fractions of multiply-charged ions.

4. **Influence of neutral flow uniformity on high-specific impulse Hall thrusters.** The azimuthal uniformity of the neutral flow through the anode has proven to be critical to maintaining efficient operation. Unfortunately, this topic rarely receives the attention it deserves, at least in the research community. It is suggested that improved anode designs and better methods to evaluate flow uniformity be developed.

Appendices

Appendix A

UM/AFRL P5 performance data

Table A-1 UM/AFRL P5 performance data at 300-600 V, 5-15 A from section 7.6.2 [200].

Vd (V)	Id (A)	Pd (W)	Anode (mg/s)	Cathode (mg/s)	IC (A)	OC (A)	Pmag (W)	Ptot (W)	Thrust (mN)	Thrust / Pd (mN/kW)	Thrust / Ptot (mN/kW)	Anode Isp (sec)	Anode Efficiency	Total Isp (sec)	Total Efficiency	Vc-g (V)	Pressure (Torr-Xe)
299.9	4.86	1458	5.37	0.60	2.24	1.01	13.1	1471	85.9	58.9	58.4	1630	0.471	1470	0.420	-20.8	3.4E-06
400.0	4.76	1904	5.34	0.60	2.50	1.26	17.1	1921	101.7	53.4	52.9	1940	0.509	1750	0.453	-21.6	3.4E-06
500.0	5.00	2500	5.46	0.60	3.51	1.51	32.3	2532	116.8	46.7	46.1	2180	0.500	1970	0.445	-21.4	3.4E-06
600.0	5.24	3144	5.33	0.60	3.51	2.95	51.0	3195	131.1	41.7	41.0	2510	0.513	2250	0.454	-21.8	3.4E-06
300.0	9.92	2976	10.21	0.60	4.00	2.01	45.5	3021	174.7	58.7	57.8	1740	0.502	1650	0.467	-20.2	5.7E-06
400.0	9.98	3992	10.22	0.60	4.51	2.01	58.0	4050	212.4	53.2	52.4	2120	0.553	2000	0.515	-20.8	5.7E-06
500.0	10.04	5020	10.18	0.60	5.01	2.01	72.9	5093	238.9	47.6	46.9	2390	0.558	2260	0.519	-20.9	5.7E-06
600.0	10.18	6108	10.23	0.60	6.51	2.53	134.5	6243	268.3	43.9	43.0	2670	0.576	2530	0.532	-22.1	5.7E-06
300.1	15.12	4538	14.62	0.60	6.00	1.99	113.3	4651	253.8	55.9	54.6	1770	0.486	1700	0.455	-24.4	7.9E-06
400.0	15.10	6040	14.56	0.60	6.51	1.99	140.8	6181	309.7	51.3	50.1	2170	0.545	2080	0.512	-25.6	7.9E-06
500.0	15.00	7500	14.43	0.60	6.99	1.99	169.3	7669	354.2	47.2	46.2	2500	0.580	2400	0.544	-25.9	7.9E-06
600.0	15.34	9204	14.43	0.60	8.51	1.99	270.8	9475	396.5	43.1	41.8	2800	0.592	2690	0.552	-27.1	7.9E-06

Appendix B

NASA-173Mv1 performance data

Table B-1 NASA-173Mv1 performance data at 300-600 V, 5 mg/s (anode #1) from section 7.4.

Vd (V)	Id (A)	Pd (W)	Anode (mg/s)	Cathode (mg/s)	IC (A)	OC (A)	ITC (A)	Thrust (mN)	Thrust / Pd (mN/kW)	Anode Isp (s)	Anode Eff	Vcg (V)	Pressure (Torr-Xe)
300.1	4.18	1255	5.00	0.54	2.00	1.50	0.00	75.0	59.8	1530	0.449	-12.5	4.6E-06
300.5	4.20	1262	4.98	0.52	2.00	1.50	0.00	75.3	59.7	1542	0.452	-13.5	4.6E-06
300.5	4.18	1257	4.98	0.52	2.00	1.50	-0.12	75.9	60.4	1554	0.461	-13.6	4.6E-06
300.6	4.15	1247	4.98	0.52	2.00	1.50	-0.22	75.6	60.7	1548	0.461	-13.5	4.6E-06
300.6	4.13	1242	4.98	0.52	2.00	1.50	-0.30	75.2	60.5	1539	0.457	-13.2	4.6E-06
300.1	4.17	1250	4.98	1.02	2.00	1.49	-0.44	74.1	59.3	1517	0.441	-12.3	4.8E-06
300.0	4.20	1259	4.98	1.02	2.00	1.49	-0.53	74.2	58.9	1519	0.439	-12.1	4.8E-06
299.9	4.33	1297	4.98	1.02	2.00	1.49	-1.01	71.1	54.8	1454	0.391	-11.4	4.8E-06
400.0	4.18	1674	5.00	0.54	1.99	1.50	0.00	90.3	54.0	1841	0.487	-12.9	4.6E-06
400.4	4.20	1682	4.98	0.52	2.06	2.04	-0.09	91.0	54.1	1862	0.494	-13.3	4.6E-06
400.1	4.26	1706	4.98	1.02	2.06	2.04	-0.27	91.9	53.9	1880	0.497	-12.7	4.8E-06
400.4	4.37	1749	4.98	1.02	2.06	2.04	-0.44	93.6	53.5	1917	0.503	-12.8	4.8E-06
400.1	4.37	1748	4.98	1.02	2.06	2.04	-0.50	92.8	53.1	1900	0.495	-12.8	4.8E-06
400.3	4.44	1779	4.98	1.02	2.06	2.04	-0.60	92.4	51.9	1891	0.482	-12.6	4.8E-06
400.2	4.49	1798	4.98	1.02	2.06	2.04	-0.75	89.1	49.6	1824	0.443	-12.5	4.8E-06
500.4	4.52	2260	4.98	1.02	2.00	2.00	0.00	105.5	46.7	2160	0.495	-12.5	4.8E-06
500.4	4.51	2258	4.98	1.02	2.00	1.99	0.00	106.1	47.0	2171	0.500	-12.4	4.8E-06
500.3	4.46	2231	4.98	1.02	2.00	1.99	-0.09	106.2	47.6	2175	0.508	-12.7	4.8E-06
500.4	4.51	2259	4.98	1.02	2.00	1.99	-0.22	107.1	47.4	2193	0.510	-12.3	4.8E-06
500.2	4.50	2251	4.98	1.02	2.00	1.99	-0.27	107.1	47.6	2192	0.512	-12.4	4.8E-06
500.1	4.59	2297	4.98	1.02	2.00	1.99	-0.40	107.2	46.7	2194	0.502	-12.2	4.8E-06
500.1	4.68	2343	4.98	1.02	2.00	1.99	-0.53	106.6	45.5	2182	0.487	-11.9	4.8E-06
500.1	4.68	2342	4.98	1.02	2.00	1.99	-1.01	102.7	43.9	2102	0.452	-11.7	4.8E-06
600.4	4.63	2780	4.98	0.52	3.03	2.99	0.00	119.0	42.8	2436	0.511	-14.0	4.6E-06
600.5	4.57	2746	4.98	0.52	3.03	2.99	0.00	118.7	43.2	2429	0.515	-13.9	4.6E-06
600.3	4.55	2730	4.98	0.52	3.03	3.00	-0.12	118.0	43.2	2416	0.512	-14.0	4.6E-06
600.2	4.64	2786	4.98	0.52	3.03	2.99	-0.22	120.0	43.1	2455	0.519	-14.1	4.6E-06
600.0	4.75	2851	4.98	0.52	3.03	2.99	-0.37	120.5	42.3	2467	0.511	-13.7	4.6E-06
600.1	4.83	2895	4.98	0.52	3.03	2.99	-0.50	120.1	41.5	2459	0.500	-13.4	4.6E-06
600.0	4.94	2963	4.98	0.52	3.03	2.99	-1.03	118.4	40.0	2424	0.475	-12.9	4.6E-06
600.0	4.93	2956	4.98	0.52	3.03	2.99	-2.03	114.2	38.6	2337	0.443	-12.7	4.6E-06
600.4	4.75	2850	4.98	0.52	3.03	2.99	-3.07	107.7	37.8	2204	0.408	-12.5	4.6E-06

Table B-2 NASA-173Mv1 performance data at 700-1000 V, 5 mg/s (anode #1) from section 7.4.

Vd (V)	Id (A)	Pd (W)	Anode (mg/s)	Cathode (mg/s)	IC (A)	OC (A)	ITC (A)	Thrust (mN)	Thrust / Pd (mN/kW)	Anode Isp (s)	Anode Eff	Vcg (V)	Pressure (Torr-Xe)
700.3	4.77	3342	4.98	0.52	3.52	3.47	0.00	128.2	38.4	2625	0.494	-13.6	4.6E-06
700.3	4.77	3338	4.98	0.52	3.52	3.47	0.00	128.4	38.5	2628	0.496	-13.5	4.6E-06
700.4	4.72	3303	4.98	0.52	3.52	3.48	0.00	128.1	38.8	2622	0.499	-13.9	4.6E-06
700.3	4.76	3334	4.98	0.52	3.52	3.47	-0.27	129.0	38.7	2641	0.501	-13.7	4.6E-06
700.5	4.70	3293	4.98	0.52	3.52	3.47	-0.27	128.4	39.0	2627	0.502	-14.0	4.6E-06
700.6	4.66	3267	4.98	0.52	3.52	3.47	-0.50	128.0	39.2	2620	0.503	-14.0	4.6E-06
700.4	4.74	3317	4.98	0.52	3.52	3.47	-0.52	129.2	39.0	2645	0.505	-13.7	4.6E-06
700.4	4.73	3314	4.98	0.52	3.52	3.47	-0.75	128.7	38.8	2634	0.502	-13.7	4.6E-06
700.5	4.74	3318	4.98	0.52	3.52	3.47	-0.75	128.6	38.8	2633	0.501	-13.8	4.6E-06
700.2	4.91	3439	4.98	0.52	3.51	3.47	-1.03	129.7	37.7	2655	0.491	-13.2	4.6E-06
700.0	5.02	3514	4.98	0.52	3.51	3.47	-1.23	129.2	36.8	2646	0.477	-12.8	4.6E-06
700.0	5.03	3521	4.98	0.52	3.51	3.47	-1.50	128.1	36.4	2623	0.468	-12.6	4.6E-06
799.5	4.75	3799	5.00	0.54	3.50	3.50	0.00	135.0	35.5	2752	0.480	-12.3	4.6E-06
800.5	4.87	3898	4.98	0.52	3.52	3.48	0.00	136.9	35.1	2802	0.483	-12.9	4.6E-06
800.6	4.83	3866	4.98	0.52	3.51	3.49	0.00	136.7	35.3	2797	0.485	-13.1	4.6E-06
800.5	4.86	3894	4.98	0.52	3.52	3.48	-0.27	137.8	35.4	2820	0.489	-12.9	4.6E-06
800.6	4.81	3852	4.98	0.52	3.51	3.48	-0.27	137.0	35.6	2804	0.489	-13.1	4.6E-06
800.7	4.80	3843	4.98	0.52	3.51	3.48	-0.50	137.2	35.7	2809	0.492	-13.2	4.6E-06
800.6	4.85	3882	4.98	0.52	3.52	3.48	-0.50	138.3	35.6	2831	0.495	-13.0	4.6E-06
800.7	4.85	3887	4.98	0.52	3.51	3.48	-0.75	138.0	35.5	2825	0.492	-13.0	4.6E-06
800.7	4.81	3848	4.98	0.52	3.51	3.48	-0.75	137.0	35.6	2805	0.490	-13.2	4.6E-06
800.6	4.95	3965	4.98	0.52	3.51	3.48	-1.00	138.3	34.9	2832	0.485	-12.8	4.6E-06
800.2	5.20	4160	4.98	0.52	3.51	3.48	-1.50	138.5	33.3	2834	0.463	-11.9	4.6E-06
800.5	4.83	3864	4.98	0.52	4.54	4.52	0.00	135.2	35.0	2768	0.475	-13.7	4.6E-06
800.5	4.85	3885	4.98	0.52	4.54	4.52	-1.01	138.3	35.6	2832	0.495	-13.8	4.6E-06
800.4	4.94	3954	4.98	0.52	4.54	4.52	-2.05	140.3	35.5	2871	0.500	-13.6	4.6E-06
800.2	5.12	4097	4.98	0.52	4.54	4.52	-3.05	139.3	34.0	2851	0.475	-13.0	4.6E-06
900.4	5.08	4577	5.00	1.02	5.03	4.99	0.00	146.8	32.1	2994	0.471	-10.8	4.8E-06
900.5	5.07	4569	5.00	1.02	5.03	4.99	-1.05	149.3	32.7	3044	0.488	-10.9	4.8E-06
900.6	5.10	4594	5.00	1.02	5.03	4.99	-2.06	152.0	33.1	3099	0.503	-10.8	4.8E-06
900.4	5.47	4926	5.00	1.02	5.02	4.99	-3.03	153.4	31.1	3127	0.478	-10.0	4.8E-06
900.2	5.51	4962	5.00	1.02	5.03	4.99	-3.03	153.9	31.0	3137	0.477	-9.8	4.8E-06
1003.2	5.20	5217	5.00	1.02	4.98	4.97	0.00	154.9	29.7	3159	0.460	-10.0	4.8E-06
1003.4	5.19	5212	5.00	1.02	4.98	4.97	-1.01	159.8	30.7	3258	0.490	-10.2	4.8E-06
1003.5	5.18	5200	5.00	1.02	4.98	4.97	-1.53	160.3	30.8	3269	0.494	-9.9	4.8E-06
1003.7	5.26	5283	5.00	1.02	4.98	4.97	-2.03	164.9	31.2	3362	0.515	-10.2	4.8E-06
1000.5	5.67	5672	5.00	1.02	5.02	4.99	-3.03	162.1	28.6	3305	0.463	-9.3	4.8E-06
1003.4	5.74	5757	5.00	1.02	5.01	4.98	-3.03	163.2	28.4	3328	0.463	-9.2	4.8E-06

Table B-3 NASA-173Mv1 performance data (anode #2) from section 7.6.2.

Point #	Vd (V)	Id (A)	Pd (W)	Anode (mg/s)	Cathode (mg/s)	IC (A)	OC (A)	ITC (A)	Pmag (W)	Ptot (W)	Thrust (mN)	Thrust / Pd (mN/kW)	Thrust / Ptot (mN/kW)	Anode Isp (s)	Anode Efficiency	Total Isp (s)	Total Efficiency	Vcg (V)	Pressure (Torr-Xe)
5	300.3	4.42	1327	5.37	0.54	1.75	1.75	0.00	18.5	1346	89.1	67.1	66.2	1690	0.557	1540	0.499	-13.7	2.7E-06
6	300.3	4.41	1324	5.37	0.54	1.75	1.75	-0.10	18.6	1343	89.9	67.9	66.9	1710	0.568	1550	0.509	-13.7	2.7E-06
8	500.5	4.72	2362	5.46	0.55	1.75	1.75	0.00	19.0	2381	125.1	53.0	52.5	2340	0.607	2120	0.547	-13.6	2.7E-06
24	500.3	9.49	4748	10.18	1.02	3.00	2.26	0.00	51.5	4799	245.1	51.6	51.1	2450	0.621	2230	0.559	-11.1	4.6E-06
23	500.3	9.22	4613	10.18	1.02	3.00	2.26	-0.50	51.5	4664	246.4	53.4	52.8	2470	0.646	2240	0.581	-11.6	4.6E-06
32	300.4	13.93	4185	14.61	1.46	2.53	1.88	-1.00	40.2	4225	285.6	68.3	67.6	1990	0.667	1810	0.601	-8.7	6.7E-06
33	300.5	14.06	4225	14.61	1.46	2.53	1.88	0.00	38.6	4264	282.6	66.9	66.3	1970	0.647	1790	0.583	-8.5	6.7E-06
38	500.4	14.22	7116	14.43	1.44	3.29	2.62	0.00	80.6	7196	363.6	51.1	50.5	2570	0.644	2340	0.579	-9.9	6.7E-06
39	500.4	14.16	7086	14.43	1.44	3.29	2.62	-1.25	84.9	7171	372.6	52.6	52.0	2630	0.679	2390	0.610	-10.4	6.7E-06

Table B-4 NASA-173Mv1 performance data (anode #2) from section 7.6.3.

Point #	Vd (V)	Id (A)	Pd (W)	Anode (mg/s)	Cathode (mg/s)	IC (A)	OC (A)	ITC (A)	Pmag (W)	Ptot (W)	Thrust (mN)	Thrust / Pd (mN/kW)	Thrust / Ptot (mN/kW)	Anode Isp (s)	Anode Efficiency	Total Isp (s)	Total Efficiency	Vcg (V)	Pressure (Torr-Xe)
1	300.3	4.17	1252	5.00	0.50	1.74	1.74	0.00	17.8	1270	82.6	66.0	65.0	1680	0.545	1530	0.488	-13.9	2.6E-06
2	300.3	4.16	1249	5.00	0.50	1.74	1.74	-0.10	17.9	1267	83.3	66.7	65.7	1700	0.555	1540	0.498	-13.9	2.6E-06
11	400.3	4.17	1669	5.00	0.50	1.65	1.65	0.00	17.3	1687	99.5	59.6	59.0	2030	0.593	1840	0.534	-14.1	2.5E-06
7	500.4	4.37	2187	5.00	0.50	1.75	1.75	0.00	18.7	2205	114.4	52.3	51.9	2330	0.598	2120	0.539	-13.8	2.5E-06
12	600.6	4.38	2631	5.00	0.50	2.20	2.20	0.00	31.2	2662	126.3	48.0	47.4	2580	0.606	2340	0.545	-14.2	2.5E-06
27	300.1	9.10	2731	10.00	1.00	2.15	1.85	0.00	30.6	2761	178.8	65.5	64.7	1820	0.585	1660	0.526	-10.6	4.6E-06
28	300.0	8.70	2610	10.00	1.00	2.15	1.85	-0.40	30.9	2641	178.8	68.5	67.7	1820	0.612	1660	0.550	-11.3	4.6E-06
25	500.3	9.38	4693	10.00	1.00	3.00	2.26	0.00	52.1	4745	239.5	51.0	50.5	2440	0.611	2220	0.549	-11.1	4.6E-06
26	500.3	9.09	4548	10.00	1.00	3.00	2.26	-0.50	53.0	4601	241.9	53.2	52.6	2470	0.643	2240	0.578	-11.7	4.6E-06
52	600.3	9.64	5787	10.00	1.00	2.65	2.39	0.00	58.0	5845	266.1	46.0	45.5	2710	0.612	2470	0.551	-11.0	4.6E-06
51	600.3	9.38	5631	10.00	1.00	2.65	2.39	-0.87	59.5	5690	265.1	47.1	46.6	2700	0.624	2460	0.561	-11.5	4.6E-06
54	700.2	9.62	6736	10.00	1.00	3.32	3.29	0.00	104.3	6840	285.9	42.4	41.8	2910	0.607	2650	0.543	-12.9	4.6E-06
53	700.1	9.36	6553	10.00	1.00	3.32	3.29	-1.17	106.3	6659	287.9	43.9	43.2	2940	0.632	2670	0.566	-13.6	4.6E-06
56	800.4	9.69	7756	10.00	1.00	3.79	3.72	0.00	142.1	7898	304.8	39.3	38.6	3110	0.599	2830	0.535	-13.5	4.6E-06
55	800.4	9.45	7564	10.00	1.00	3.79	3.72	-1.49	145.6	7709	309.9	41.0	40.2	3160	0.635	2870	0.566	-13.9	4.6E-06
57	900.3	9.39	8454	10.00	1.00	4.29	4.21	-1.60	194.7	8648	327.1	38.7	37.8	3330	0.633	3030	0.562	-14.8	4.6E-06
30	300.4	14.58	4380	15.00	1.50	2.53	1.88	0.00	37.8	4418	291.8	66.6	66.1	1980	0.648	1800	0.584	-8.3	6.7E-06
31	300.5	14.53	4366	15.00	1.50	2.53	1.88	-1.00	40.0	4406	296.2	67.8	67.2	2010	0.670	1830	0.603	-8.5	6.7E-06
37	500.2	14.96	7483	15.00	1.50	3.29	2.62	0.00	79.7	7563	384.4	51.4	50.8	2610	0.658	2380	0.592	-9.3	6.7E-06
36	500.2	14.95	7478	15.00	1.50	3.29	2.62	-1.26	82.4	7560	391.7	52.4	51.8	2660	0.684	2420	0.615	-9.4	6.7E-06

Table B-5 NASA-173Mv1 performance data (anode #2) not reported in the main text.

Point #	Vd (V)	Id (A)	Pd (W)	Anode (mg/s)	Cathode (mg/s)	IC (A)	OC (A)	ITC (A)	Pmag (W)	Ptot (W)	Thrust (mN)	Thrust / Pd (mN/kW)	Thrust / Ptot (mN/kW)	Anode Isp (s)	Anode Efficiency	Total Isp (s)	Total Efficiency	Vcg (V)	Pressure (Torr-Xe)
42	150.3	15.72	2363	15.00	1.50	2.26	1.19	-0.64	30.1	2393	192.7	81.6	80.5	1310	0.524	1190	0.470	-7.8	6.7E-06
43	150.2	15.00	2253	14.55	1.45	2.23	1.40	-0.68	31.3	2284	184.7	82.0	80.9	1290	0.520	1180	0.468	-7.7	6.7E-06
44	150.2	14.99	2251	14.59	1.45	2.23	1.40	0.00	30.1	2282	182.7	81.1	80.1	1280	0.508	1160	0.456	-7.7	6.7E-06
45	200.2	14.99	3001	14.90	1.45	2.04	1.42	-0.13	26.9	3028	231.1	77.0	76.3	1580	0.597	1440	0.539	-7.9	6.7E-06
46	250.1	15.00	3752	15.22	1.45	2.39	1.67	-0.46	37.4	3789	271.1	72.3	71.6	1820	0.644	1660	0.582	-8.3	6.7E-06
47	300.0	15.00	4500	15.35	1.45	2.75	2.03	-0.38	51.7	4552	300.9	66.9	66.1	2000	0.655	1830	0.592	-8.6	6.7E-06
48	350.4	12.85	4503	13.62	1.29	2.92	2.02	-0.49	56.6	4559	281.5	62.5	61.7	2110	0.646	1930	0.583	-11.2	7.1E-06

Appendix C

NASA-173Mv2 performance data

Table C-1 NASA-173Mv2 performance data at 300-1000 V, 5 mg/s from section 8.4.1.

Thrust Stand Point #	Vd (V)	Id (A)	Pd (W)	Anode (mg/s)	Cathode (mg/s)	IC (A)	OC (A)	ITC (A)	ETC (A)	Pmag (W)	Ptotal (W)	Thrust (mN)	Thrust / Pd (mN/kW)	Thrust / Ptotal (mN/kW)	Anode Isp (s)	Anode Efficiency	Total Isp (s)	Total Efficiency	Vcg (V)	Pressure (Torr-Xe)
TS_39	300.2	4.23	1270	4.99	0.50	1.50	1.20	0.00	0.00	11.3	1281	80.7	63.6	63.0	1650	0.514	1500	0.463	-11.9	2.6E-06
TS_12	300.1	4.19	1257	5.05	0.51	1.50	1.20	0.00	0.00	9.7	1267	80.9	64.3	63.8	1630	0.515	1480	0.465	-12.2	2.6E-06
TS_19	300.2	4.21	1264	5.00	0.50	1.50	1.20	0.00	0.00	9.7	1274	81.2	64.2	63.8	1660	0.522	1510	0.471	-12.0	2.6E-06
TS_13	300.1	4.20	1260	5.05	0.51	1.50	1.20	0.00	-3.00	16.5	1277	81.3	64.5	63.7	1640	0.519	1490	0.466	-11.3	2.6E-06
TS_20	300.2	4.22	1267	5.00	0.50	1.50	1.20	0.00	-3.00	16.7	1284	81.8	64.6	63.7	1670	0.528	1520	0.474	-11.2	2.6E-06
TS_22	400.2	4.35	1741	5.00	0.50	1.70	1.60	0.00	0.00	15.4	1756	100.1	57.5	57.0	2040	0.576	1860	0.519	-13.0	2.6E-06
TS_23	400.2	4.35	1741	5.00	0.50	1.70	1.60	0.00	-4.00	28.2	1769	100.5	57.7	56.8	2050	0.580	1860	0.519	-11.8	2.6E-06
TS_34	500.3	4.41	2206	4.99	0.50	1.56	1.46	0.00	0.00	14.2	2221	115.1	52.2	51.8	2350	0.602	2140	0.543	-12.9	2.6E-06
TS_35	500.3	4.44	2221	4.99	0.50	1.56	1.46	0.00	-3.00	21.4	2243	115.5	52.0	51.5	2360	0.602	2150	0.542	-11.7	2.6E-06
TS_37	600.4	4.73	2840	5.00	0.50	1.85	1.55	0.00	0.00	17.8	2858	126.9	44.7	44.4	2590	0.567	2350	0.512	-12.2	2.6E-06
TS_38	600.5	4.76	2858	5.00	0.50	1.85	1.55	0.00	0.00	17.8	2876	128.0	44.8	44.5	2610	0.573	2370	0.518	-11.1	2.6E-06
TS_124	600.3	4.68	2809	4.95	0.52	1.83	1.55	0.00	0.00	16.7	2826	126.5	45.0	44.8	2610	0.575	2360	0.518	-11.5	2.6E-06
TS_125	600.3	4.65	2791	4.95	0.52	1.83	1.55	0.27	0.00	16.8	2808	126.5	45.3	45.0	2610	0.579	2360	0.521	-11.7	2.6E-06
TS_127	700.3	4.89	3424	4.95	0.52	2.00	1.70	0.00	0.00	20.3	3445	137.5	40.2	39.9	2830	0.558	2560	0.502	-11.1	2.6E-06
TS_128	700.4	4.80	3362	4.95	0.52	2.00	1.70	0.20	0.00	20.5	3382	137.4	40.9	40.6	2830	0.567	2560	0.510	-11.5	2.6E-06
TS_129	800.2	5.00	4001	4.95	0.52	2.67	1.99	0.00	0.00	32.6	4034	144.8	36.2	35.9	2980	0.529	2700	0.475	-10.7	2.6E-06
TS_130	800.2	4.89	3913	4.95	0.52	2.68	1.99	0.52	0.00	33.6	3947	146.9	37.5	37.2	3030	0.557	2740	0.500	-11.4	2.6E-06
TS_131	900.2	5.36	4825	4.95	0.52	2.88	2.32	0.00	0.00	42.9	4868	155.8	32.3	32.0	3210	0.508	2900	0.456	-9.4	2.6E-06
TS_135	900.2	5.26	4735	4.95	0.52	2.77	2.51	0.00	0.00	48.7	4784	155.3	32.8	32.5	3200	0.514	2890	0.461	-8.9	2.6E-06
TS_136	900.3	5.06	4556	4.95	0.52	2.79	2.17	0.00	0.00	42.9	4598	154.3	33.9	33.6	3180	0.528	2880	0.473	-10.8	2.6E-06
TS_132	900.2	4.88	4393	4.95	0.52	2.88	2.32	0.46	0.00	43.6	4437	157.1	35.8	35.4	3240	0.567	2930	0.508	-12.2	2.6E-06
TS_133	900.2	4.84	4357	4.95	0.52	2.88	2.31	0.56	0.00	44.3	4401	156.9	36.0	35.6	3230	0.571	2920	0.511	-12.3	2.6E-06
TS_134	900.2	4.84	4357	4.95	0.52	2.77	2.51	0.56	0.00	48.1	4405	158.2	36.3	35.9	3260	0.580	2950	0.519	-12.5	2.6E-06
TS_137	1000	5.23	5232	4.95	0.52	2.99	2.41	0.00	0.00	52.5	5284	163.9	31.3	31.0	3380	0.519	3050	0.465	-9.7	2.6E-06
TS_138	1000	4.94	4942	4.95	0.52	2.99	2.41	0.54	0.00	53.7	4996	168.2	34.0	33.7	3460	0.578	3140	0.518	-12.3	2.6E-06
TS_139	1000	4.90	4902	4.95	0.52	2.92	2.42	0.57	0.00	53.9	4956	168.0	34.3	33.9	3460	0.582	3130	0.521	-12.6	2.6E-06

Table C-2 NASA-173Mv2 performance data at 300-1000 V, 10 mg/s from section 8.4.1.

Thrust Stand Point #	Vd (V)	Id (A)	Pd (W)	Anode (mg/s)	Cathode (mg/s)	IC (A)	OC (A)	ITC (A)	ETC (A)	Pmag (W)	Ptotal (W)	Thrust (mN)	Thrust / Pd (mN/kW)	Thrust / Ptotal (mN/kW)	Anode Isp (s)	Anode Efficiency	Total Isp (s)	Total Efficiency	Vcg (V)	Pressure (Torr-Xe)
TS_42	300.1	8.99	2698	10.00	1.00	1.75	1.49	0.00	0.00	14.3	2712	174.6	64.7	64.4	1780	0.565	1620	0.511	-12.4	4.6E-06
TS_14	300.2	8.90	2672	9.98	1.00	1.75	1.50	0.00	0.00	14.4	2686	172.1	64.4	64.1	1760	0.555	1600	0.502	-12.7	4.6E-06
TS_43	300.2	8.86	2660	10.00	1.00	1.75	1.49	-0.54	0.00	14.6	2674	174.9	65.8	65.4	1780	0.575	1620	0.520	-12.7	4.6E-06
TS_44	300.2	8.84	2654	10.00	1.00	1.75	1.50	-0.54	-4.00	27.4	2681	176.3	66.4	65.8	1800	0.586	1630	0.527	-12.1	4.6E-06
TS_49	400.2	9.26	3706	9.99	1.00	2.50	2.26	0.00	0.00	34.0	3740	212.9	57.4	56.9	2170	0.612	1980	0.551	-13.3	4.6E-06
TS_50	400.2	9.24	3698	9.99	1.00	2.52	2.26	0.00	-1.97	38.2	3736	213.2	57.7	57.1	2180	0.615	1980	0.554	-13.2	4.6E-06
TS_57	500.3	9.32	4663	9.99	1.00	3.00	2.20	0.00	0.00	45.7	4709	243.7	52.3	51.8	2490	0.637	2260	0.574	-13.9	4.6E-06
TS_58	500.3	9.30	4653	9.99	1.00	3.00	2.20	-0.35	0.00	46.3	4699	244.2	52.5	52.0	2490	0.641	2270	0.577	-14.1	4.6E-06
TS_59	500.3	9.23	4618	9.99	1.00	3.00	2.20	-0.35	-5.00	69.0	4687	244.6	53.0	52.2	2500	0.648	2270	0.581	-14.3	4.6E-06
TS_61	600.3	9.52	5715	9.99	1.00	3.26	2.49	0.00	0.00	60.1	5775	269.9	47.2	46.7	2750	0.638	2500	0.574	-13.4	4.6E-06
TS_62	600.3	9.49	5697	9.99	1.00	3.24	2.49	-0.26	0.00	61.6	5758	271.0	47.6	47.1	2770	0.645	2510	0.580	-13.8	4.6E-06
TS_63	600.3	9.44	5667	9.99	1.00	3.24	2.49	-0.26	-5.00	85.4	5752	270.8	47.8	47.1	2760	0.648	2510	0.580	-14.0	4.6E-06
TS_141	700.3	9.61	6730	9.96	1.02	3.41	3.06	0.00	0.00	89.6	6819	296.1	44.0	43.4	3030	0.654	2750	0.585	-13.5	4.6E-06
TS_142	700.3	9.69	6786	9.96	1.02	3.41	3.06	-0.20	0.00	90.7	6877	299.0	44.1	43.5	3060	0.661	2780	0.592	-14.1	4.6E-06
TS_143	700.3	9.62	6737	9.96	1.02	3.41	3.06	-0.20	-5.00	116.2	6853	298.0	44.2	43.5	3050	0.662	2770	0.590	-13.4	4.6E-06
TS_144	800.3	9.68	7747	9.96	1.02	3.82	3.30	0.00	0.00	113.6	7861	317.8	41.0	40.4	3250	0.654	2950	0.585	-13.5	4.6E-06
TS_145	800.3	9.84	7875	9.96	1.02	3.81	3.29	-0.21	0.00	116.3	7991	323.5	41.1	40.5	3310	0.667	3000	0.596	-14.3	4.6E-06
TS_146	800.3	9.75	7803	9.96	1.02	3.81	3.29	-0.21	-4.01	134.6	7937	323.4	41.4	40.7	3310	0.673	3000	0.600	-13.5	4.6E-06
TS_152	900.1	9.76	8785	9.96	1.02	3.85	3.61	0.00	0.00	142.0	8927	343.2	39.1	38.4	3510	0.673	3190	0.601	-14.4	4.6E-06
TS_151	900.1	9.83	8848	9.96	1.02	3.85	3.61	-0.04	-5.90	178.4	9026	346.2	39.1	38.4	3540	0.680	3210	0.605	-13.5	4.6E-06
TS_169	1000	9.67	9672	9.96	1.02	4.37	3.81	0.00	0.00	184.1	9856	361.1	37.3	36.6	3700	0.677	3350	0.602	-13.9	4.6E-06
TS_164	1000	9.79	9792	9.96	1.02	4.36	3.81	0.00	-5.01	178.4	9970	363.8	37.2	36.5	3720	0.679	3380	0.604	-13.7	4.6E-06
TS_167	1000	9.75	9752	9.96	1.02	4.36	3.81	-0.16	-5.00	203.5	9955	364.7	37.4	36.6	3730	0.685	3390	0.608	-13.5	4.6E-06

Table C-3 NASA-173Mv2 performance data at 300-600 V, 15 mg/s from section 8.4.1.

Thrust Stand Point #	Vd (V)	Id (A)	Pd (W)	Anode (mg/s)	Cathode (mg/s)	IC (A)	OC (A)	ITC (A)	ETC (A)	Pmag (W)	Ptotal (W)	Thrust (mN)	Thrust / Pd (mN/kW)	Thrust / Ptotal (mN/kW)	Anode Isp (s)	Anode Efficiency	Total Isp (s)	Total Efficiency	Vcg (V)	Pressure (Torr-Xe)
TS_66	300.4	14.82	4452	14.99	1.50	2.15	1.75	0.00	0.00	24.4	4476	291.5	65.5	65.1	1980	0.637	1800	0.576	-8.9	6.7E-06
TS_67	300.5	14.70	4417	14.99	1.50	2.15	1.74	-0.22	0.00	24.6	4442	291.7	66.0	65.7	1980	0.643	1800	0.581	-9.1	6.7E-06
TS_68	300.6	14.67	4410	14.99	1.50	2.15	1.74	-0.22	-6.00	55.3	4465	294.8	66.9	66.0	2010	0.657	1820	0.590	-8.6	6.7E-06
TS_71	400.4	15.17	6074	14.99	1.50	2.51	2.01	0.00	0.00	34.6	6109	344.8	56.8	56.4	2350	0.653	2130	0.590	-9.3	6.7E-06
TS_72	400.5	14.98	5999	14.99	1.50	2.50	2.00	-0.82	0.00	35.4	6035	346.7	57.8	57.4	2360	0.668	2140	0.604	-9.4	6.7E-06
TS_73	400.1	14.96	5985	14.99	1.50	2.50	2.00	-0.82	-6.00	68.9	6054	350.1	58.5	57.8	2380	0.683	2160	0.614	-8.9	6.7E-06
TS_75	500.1	15.47	7737	15.00	1.50	3.24	2.98	0.00	0.00	75.7	7812	389.7	50.4	49.9	2650	0.654	2410	0.589	-10.9	6.7E-06
TS_74	500.1	15.50	7752	15.00	1.50	3.24	2.99	0.00	0.00	74.8	7826	390.7	50.4	49.9	2660	0.656	2410	0.591	-10.9	6.7E-06
TS_76	500.2	15.27	7638	14.99	1.50	3.24	2.98	-1.24	0.00	78.0	7716	395.1	51.7	51.2	2690	0.682	2440	0.613	-10.9	6.7E-06
TS_77	500.3	15.12	7565	14.99	1.50	3.24	2.98	-1.24	-7.94	139.9	7704	401.7	53.1	52.1	2730	0.712	2480	0.635	-9.5	6.7E-06
TS_179	500.4	15.21	7611	15.00	1.50	3.25	2.99	-1.25	-8.00	171.9	7783	397.9	52.3	51.1	2700	0.693	2460	0.616	-9.3	6.7E-06
TS_79	600.4	15.38	9234	15.00	1.50	3.76	3.25	0.00	0.00	98.4	9333	441.6	47.8	47.3	3000	0.704	2730	0.633	-12.3	6.7E-06
TS_78	600.2	15.52	9315	15.01	1.50	3.75	3.25	0.00	0.00	104.4	9419	442.4	47.5	47.0	3000	0.700	2730	0.629	-11.9	6.7E-06

Table C-4 NASA-173Mv2 performance data not reported in the main text.

Thrust Stand Point #	Vd (V)	Id (A)	Pd (W)	Anode (mg/s)	Cathode (mg/s)	IC (A)	OC (A)	ITC (A)	ETC (A)	Pmag (W)	Ptotal (W)	Thrust (mN)	Thrust / Pd (mN/kW)	Thrust / Ptotal (mN/kW)	Anode Isp (s)	Anode Efficiency	Total Isp (s)	Total Efficiency	Vcg (V)	Pressure (Torr-Xe)
TS_111	125.3	15.06	1887	14.53	1.51	2.03	1.50	-0.19	-6.98	81.8	1969	152.7	80.9	77.6	1071	0.425	970	0.369	-7.8	6.5E-06
TS_109	125.4	14.91	1870	14.53	1.51	2.08	1.93	-0.18	-6.98	93.3	1963	152.1	81.3	77.5	1067	0.426	967	0.367	-8.1	6.5E-06
TS_172	300.1	14.99	4498	15.13	1.51	2.15	1.66	0.00	0.00	32.1	4531	296.1	65.8	65.4	1995	0.644	1814	0.581	-8.7	6.8E-06
TS_171	300.1	15.01	4505	15.26	1.51	2.15	1.66	-0.50	-5.00	58.8	4563	301.6	67.0	66.1	2015	0.662	1833	0.594	-8.6	6.8E-06
TS_173	350.3	12.85	4501	13.40	1.32	2.29	1.63	0.00	0.00	33.7	4535	275.1	61.1	60.7	2093	0.627	1905	0.567	-9.6	6.0E-06
TS_175	350.4	12.87	4510	13.55	1.34	2.40	1.94	-0.80	-5.00	68.3	4578	282.4	62.6	61.7	2124	0.653	1933	0.585	-9.0	6.1E-06

Appendix D

NASA-173Mv2 telemetry and plasma data

Table D-1 NASA-173Mv2 telemetry during the floating potential measurements from section 11.1.

Vf Point No.	Vd (V)	Id (A)	Anode (mg/s)	Cathode (mg/s)	IC (A)	OC (A)	ITC (A)	ETC (A)	Vcg (V)	Pressure (Torr-Xe)
Vf_12_01	300	9.20	10.00	1.00	1.75	1.50	0.00	0.00	-12.5	1.3E-05
Vf_11_01	300	9.00	10.00	1.00	1.75	1.50	-0.54	0.00	-12.6	1.3E-05
Vf_10_01	300	9.10	10.00	1.00	1.75	1.50	-0.54	-4.00	-14.4	1.3E-05
Vf_13_01	600	9.80	10.00	1.00	3.26	2.51	0.00	0.00	-15.0	1.3E-05
Vf_14_01	600	9.80	10.00	1.00	3.26	2.51	-0.26	0.00	-14.2	1.3E-05
Vf_15_01	600	9.90	10.00	1.00	3.26	2.51	-0.26	-5.00	-15.5	1.3E-05

Table D-2 NASA-173Mv2 telemetry during the ExB probe measurements from section 11.2.

Point No.	Vd (V)	Id (A)	Anode (mg/s)	Cathode (mg/s)	IC (A)	OC (A)	ITC (A)	ETC (A)	Vcg (V)	Pressure (Torr-Xe)
93	300.4	8.87	10.00	1.00	1.75	1.50	0.00	0.00	-11.8	4.6E-06
94	300.4	8.73	10.00	1.00	1.75	1.50	-0.54	0.00	-11.7	4.6E-06
95	300.4	8.73	10.00	1.00	1.75	1.50	-0.54	-4.00	-11.4	4.6E-06
96	300.4	8.83	10.00	1.00	1.75	1.50	0.00	-4.00	-11.4	4.6E-06
101	400.4	9.24	10.00	1.00	2.50	2.26	0.00	0.00	-13.0	4.6E-06
102	400.3	9.16	10.00	1.00	2.50	2.26	-0.36	0.00	-13.0	4.6E-06
103	400.3	9.16	10.00	1.00	2.50	2.26	-0.36	-2.00	-12.7	4.6E-06
104	400.3	9.22	10.00	1.00	2.50	2.26	0.00	-2.00	-12.7	4.6E-06
105	500.4	9.37	10.00	1.00	3.00	2.20	0.00	0.00	-13.3	4.6E-06
106	500.4	9.30	10.00	1.00	3.00	2.20	-0.35	0.00	-13.3	4.6E-06
107	500.2	9.33	10.00	1.00	3.00	2.20	-0.35	-5.00	-13.0	4.6E-06
108	500.2	9.36	10.00	1.00	3.00	2.20	0.00	-5.00	-13.0	4.6E-06
109	600.2	9.53	10.00	1.00	3.26	2.49	0.00	0.00	-13.4	4.6E-06
110	600.2	9.48	10.00	1.00	3.26	2.49	-0.26	0.00	-13.5	4.6E-06
111	600.2	9.54	10.00	1.00	3.26	2.49	-0.26	-5.00	-12.8	4.6E-06
112	600.2	9.44	10.00	1.00	3.26	2.49	0.00	-5.00	-13.1	4.6E-06
113	700.4	9.71	10.00	1.00	3.41	3.06	0.00	0.00	-14.0	4.6E-06
114	700.4	9.64	10.00	1.00	3.41	3.06	-0.20	0.00	-13.7	4.6E-06
115	700.4	9.61	10.00	1.00	3.41	3.06	-0.20	-5.00	-13.2	4.6E-06
116	700.4	9.60	10.00	1.00	3.41	3.06	0.00	-5.00	-13.3	4.6E-06
117	800.1	9.81	10.00	1.00	3.82	3.30	0.00	0.00	-14.1	4.6E-06
118	800.1	9.94	10.00	1.00	3.82	3.30	-0.21	0.00	-13.7	4.6E-06
119	800.1	9.94	10.00	1.00	3.82	3.30	-0.21	-4.00	-13.3	4.6E-06
120	800.1	9.87	10.00	1.00	3.82	3.30	0.00	-4.00	-13.5	4.6E-06
126	900.1	9.84	10.00	1.00	3.85	3.61	0.00	0.00	-13.8	4.6E-06
131	900.2	9.76	10.00	1.00	3.85	3.61	-0.04	0.00	-13.9	4.6E-06
130	900.2	9.76	10.00	1.00	3.85	3.61	-0.04	-5.90	-13.5	4.6E-06
129	900.1	9.74	10.00	1.00	3.85	3.61	0.00	-5.90	-13.5	4.6E-06

Table D-3 Ion species fractions, measured with the ExB probe, two meters downstream of the NASA-173Mv2 at 10 mg/s from section 11.2.

	Xe^{+} species fraction			
Vd	IC, OC	ITC	ITC, ETC	ETC
300	0.95	0.96	0.96	0.96
400	0.94	0.93	0.94	0.94
500	0.94	0.94	0.94	0.94
600	0.92	0.92	0.93	0.93
700	0.90	0.91	0.92	0.91
800	0.87	0.88	0.89	0.87
900	0.86	0.85	0.84	0.81
	Xe^{2+} species fraction			
Vd	IC, OC	ITC	ITC, ETC	ETC
300	0.04	0.03	0.03	0.03
400	0.05	0.06	0.05	0.05
500	0.05	0.05	0.05	0.05
600	0.07	0.07	0.06	0.06
700	0.09	0.08	0.07	0.08
800	0.12	0.11	0.10	0.12
900	0.12	0.13	0.14	0.16
	Xe^{3+} species fraction			
Vd	IC, OC	ITC	ITC, ETC	ETC
300	0.01	0.01	0.01	0.01
400	0.01	0.01	0.01	0.01
500	0.01	0.01	0.01	0.01
600	0.01	0.01	0.01	0.01
700	0.01	0.01	0.01	0.01
800	0.01	0.01	0.01	0.01
900	0.02	0.02	0.02	0.03

Table D-4 NASA-173Mv2 telemetry during the Langmuir probe measurements from section 11.3.

Point No.	Vd (V)	Id (A)	Anode (mg/s)	Cathode (mg/s)	IC (A)	OC (A)	ITC (A)	ETC (A)	Vcg (V)	Pressure (Torr-Xe)
148	300.3	9.00	10.00	1.00	1.75	1.50	0.00	0.00	-11.3	4.6E-06
149	300.4	8.89	10.00	1.00	1.75	1.50	-0.54	0.00	-11.2	4.6E-06
150	300.4	8.88	10.00	1.00	1.75	1.50	-0.54	-4.00	-10.6	4.6E-06
151	300.4	8.99	10.00	1.00	1.75	1.50	0.00	-4.00	-10.9	4.6E-06
152	400.2	9.32	10.00	1.00	2.50	2.26	0.00	0.00	-12.7	4.6E-06
153	400.2	9.26	10.00	1.00	2.50	2.26	-0.36	0.00	-12.7	4.6E-06
154	400.2	9.25	10.00	1.00	2.50	2.26	-0.36	-2.00	-12.3	4.6E-06
155	400.2	9.32	10.00	1.00	2.50	2.26	0.00	-2.00	-12.2	4.6E-06
156	500.3	9.49	10.00	1.00	3.00	2.20	0.00	0.00	-13.2	4.6E-06
157	500.3	9.34	10.00	1.00	3.00	2.20	-0.35	0.00	-13.4	4.6E-06
158	500.3	9.42	10.00	1.00	3.00	2.20	-0.35	-5.00	-12.7	4.6E-06
159	500.3	9.46	10.00	1.00	3.00	2.20	0.00	-5.00	-12.6	4.6E-06
160	600.3	9.41	10.00	1.00	3.26	2.49	0.00	0.00	-13.0	4.6E-06
161	600.3	9.24	10.00	1.00	3.26	2.49	-0.26	0.00	-13.5	4.6E-06
162	600.3	9.35	10.00	1.00	3.26	2.49	-0.26	-5.00	-12.9	4.6E-06
163	600.3	9.46	10.00	1.00	3.26	2.49	0.00	-5.00	-12.4	4.6E-06
164	700.3	9.40	10.00	1.00	3.41	3.06	0.00	0.00	-14.3	4.6E-06
165	700.3	9.53	10.00	1.00	3.41	3.06	-0.20	0.00	-14.1	4.6E-06
166	700.3	9.51	10.00	1.00	3.41	3.06	-0.20	-5.00	-13.8	4.6E-06
168	700.5	9.54	10.00	1.00	3.41	3.06	0.00	-5.00	-13.3	4.6E-06
170	800.1	9.44	10.00	1.00	3.82	3.30	0.00	0.00	-14.7	4.6E-06
171	800.1	9.55	10.00	1.00	3.82	3.30	-0.21	0.00	-14.5	4.6E-06
172	800.1	9.53	10.00	1.00	3.82	3.30	-0.21	-5.00	-13.9	4.6E-06
175	900.4	9.61	10.00	1.00	3.85	3.61	0.00	0.00	-13.8	4.6E-06
176	900.4	9.72	10.00	1.00	3.85	3.61	-0.04	0.00	-13.8	4.6E-06
177	900.4	9.73	10.00	1.00	3.85	3.61	-0.04	-5.90	-13.3	4.6E-06
178	900.4	9.73	10.00	1.00	3.85	3.61	0.00	-5.90	-13.3	4.6E-06
181	1000.1	9.71	10.00	1.00	4.36	3.81	0.00	0.00	-14.2	4.6E-06
182	1000.1	9.85	10.00	1.00	4.36	3.81	-0.16	0.00	-13.8	4.6E-06
183	1000.1	9.94	10.00	1.00	4.36	3.81	-0.16	-5.00	-13.1	4.6E-06
184	1000.1	10.08	10.00	1.00	4.36	3.81	0.00	-5.00	-12.9	4.6E-06

Table D-5 Plasma potential, measured with the Langmuir probe, two meters downstream of the NASA-173Mv2 at 10 mg/s from section 11.3.

	Plasma Potential (Volts from Ground)			
Vd	IC, OC	ITC	ITC, ETC	ETC
300	10.3	10.3	8.2	8.5
400	11.5	11.4	10.5	10.6
500	11.5	11.5	9.4	9.7
600	12.1	12	10.2	10.3
700	12.5	12.5	10.9	11
800	12.8	12.7	11.8	-
900	13.2	13.3	11.8	11.9
1000	13.5	13.5	12.3	12.2

Table D-6 NASA-173Mv2 telemetry during the RPA measurements from section 11.4.

Point No.	Vd (V)	Id (A)	Anode (mg/s)	Cathode (mg/s)	IC (A)	OC (A)	ITC (A)	ETC (A)	Vcg (V)	Pressure (Torr-Xe)
70	300.2	8.86	10.00	1.00	1.75	1.50	0.00	0.00	-11.9	4.6E-06
71	300.2	8.68	10.00	1.00	1.75	1.50	-0.54	0.00	-11.9	4.6E-06
72	300.1	8.68	10.00	1.00	1.75	1.50	-0.54	-4.00	-11.5	4.6E-06
73	300.2	8.88	10.00	1.00	1.75	1.50	0.00	-4.00	-11.5	4.6E-06
74	400.4	9.24	10.00	1.00	2.50	2.26	0.00	0.00	-12.7	4.6E-06
75	400.4	9.24	10.00	1.00	2.50	2.26	0.00	-2.00	-12.7	4.6E-06
76	500.4	9.38	10.00	1.00	3.00	2.20	0.00	0.00	-13.2	4.6E-06
77	500.3	9.23	10.00	1.00	3.00	2.20	-0.35	0.00	-13.1	4.6E-06
78	500.4	9.29	10.00	1.00	3.00	2.20	-0.35	-5.00	-13.1	4.6E-06
79	500.4	9.43	10.00	1.00	3.00	2.20	0.00	-5.00	-13.3	4.6E-06
82	600.3	9.53	10.00	1.00	3.26	2.49	0.00	0.00	-13.1	4.6E-06
83	600.3	9.47	10.00	1.00	3.26	2.49	-0.26	0.00	-12.8	4.6E-06
84	600.3	9.51	10.00	1.00	3.26	2.49	-0.26	-5.00	-12.5	4.6E-06
85	600.3	9.53	10.00	1.00	3.26	2.49	0.00	-5.00	-12.7	4.6E-06
86	700.1	9.68	10.00	1.00	3.41	3.06	0.00	0.00	-13.1	4.6E-06
87	700.1	9.62	10.00	1.00	3.41	3.06	-0.20	0.00	-13.2	4.6E-06
88	700.1	9.70	10.00	1.00	3.41	3.06	-0.20	-5.00	-12.4	4.6E-06
89	700.1	9.73	10.00	1.00	3.41	3.06	0.00	-5.00	-12.4	4.6E-06
90	800.4	9.89	10.00	1.00	3.82	3.30	0.00	0.00	-13.6	4.6E-06

Table D-7 Loss voltage (V_{loss}) from the ion voltage distribution, measured with the RPA, two meters downstream of the NASA-173Mv2 at 10 mg/s from section 11.4.

	V_{loss} (Volts)			
Vd	IC, OC	ITC	ITC, ETC	ETC
300	34	34	34	35
400	34	-	-	32
500	32	33	33	34
600	32	28	28	28
700	26	27	25	24
800	25	-	-	-

Table D-8 Full-width at half-maximum (FWHM) of the ion voltage distribution, measured with the RPA, two meters downstream of the NASA-173Mv2 at 10 mg/s from section 11.4.

	FWHM (Volts)			
Vd	IC, OC	ITC	ITC, ETC	ETC
300	35	38	33	33
400	47	-	-	48
500	55	55	53	49
600	75	75	73	71
700	96	92	91	93
800	105	-	-	-

Bibliography

[1] Kaufman, H. R., "Technology of closed-drift thrusters," *AIAA Journal*, Vol. 23, No. 1, pp. 78-87, 1985.

[2] Kim, V., "Main physical features and processes determining the performance of stationary plasma thrusters," *Journal of Propulsion and Power*, Vol. 14, No. 5, pp. 736-743, 1998.

[3] Zhurin, V. V., Kaufman, H. R., and Robinson, R. S., "Physics of closed drift thrusters," *Plasma Sources Science and Technology*, Vol. 8, No. 1, pp. R1-R20, 1999.

[4] Lary, E. C., Meyerand, R. G., and Salz, F., "Ion acceleration in a gyro-dominated neutral plasma - theory," *Bulletin of the American Physical Society, Sr. II*, Vol. 7, pp. 441, 1962.

[5] Seikel, G. R. and Reshotko, E., "Hall current accelerator," *Bulletin of the American Physical Society, Sr. II*, Vol. 7, pp. 414, 1962.

[6] Salz, F., Meyerand, R. G., and Lary, E. C., "Ion acceleration in a gyro-dominated neutral plasma - experiment," *Bulletin of the American Physical Society, Sr. II*, Vol. 7, pp. 441, 1962.

[7] Meyer, R. X., "Acceleration of cesium ions by means of a negative space charge sheath," AIAA-66-256, 1966.

[8] Meyer, R. X., "A space-charge-sheath electric thruster," *AIAA Journal*, Vol. 5, No. 11, pp. 2057-2059, 1967.

[9] Pinsley, E. A., Brown, C. O., and Banas, C. M., "Hall-current accelerator utilizing surface contact ionization," *Journal of Spacecraft and Rockets*, Vol. 1, No. 5, pp. 525-531, 1964.

[10] Brown, C. O. and Pinsley, E. A., "Further experimental investigations of a cesium Hall-current accelerator," *AIAA Journal*, Vol. 3, No. 5, 1965.

[11] Morosov, A. I., "Focusing of cold quasineutral beams in electromagnetic fields," *Soviet Physics - Doklady*, Vol. 10, No. 8, 1966.

[12] Morosov, A. I. and Solov'ev, L. S., "A similarity parameter in the theory of plasma flow," *Soviet Physics - Doklady*, Vol. 10, No. 9, 1966.

[13] Zharinov, A. V. and Popov, Y. S., "Acceleration of plasma by a closed Hall current," *Soviet Physics Technical Physics*, Vol. 12, No. 2, 1967.

[14] Bober, A. S. and Maslennikov, N. A., "SPT in Russia - new achievements," IEPC-95-06, 24th International Electric Propulsion Conference, Moscow, Russia, Sept. 19-23, 1995.

[15] Arhipov, B. A., Vinogradov, V. N., Kozubsky, K. N., Kudriavtsev, S. S., *et al.*, "Development and application of electric thrusters at EDB "Fakel"," IEPC-97-004, 25th International Electric Propulsion Conference, Cleveland, OH, Aug. 24-28, 1997.

[16] Morosov, A. I., "Stationary plasma thruster (SPT) development steps and future perspectives," IEPC-93-101, 23rd International Electric Propulsion Conference, Seattle, WA, Sept. 13-16, 1993.

[17] Gallimore, A. D., "Near- and far-field characterization of stationary plasma thruster plumes," *Journal of Spacecraft and Rockets*, Vol. 38, No. 3, pp. 441-453, 2001.

[18] Artsimovich, L. A. and et al., "Development of the stationary plasma thruster (SPT) and its test on Meteor satellite," *Kosmicheskie Issledovanija (in Russian)*, Vol. 7, No. 3, pp. 451-468, 1974.

[19] Kim, V., "Electric propulsion activity in Russia," IEPC-2001-005, 27th International Electric Propulsion Conference, Pasadena, CA, October 14-19, 2001.

[20] Bober, A. S., Kim, V., Kozubsky, K. N., Kolodny, G. Y., *et al.*, "Russian experience of EP application in space and on the ground," AIAA-94-2737, 30th Joint Propulsion Conference, Indianapolis, IN, June 27-29, 1994.

[21] Clauss, C. W., Tilley, D. L., and Barnhart, D. A., "Benefits of low-power stationary plasma thruster propulsion for small satellites," 9th AIAA/USU Conference on Small Satellites, 1995.

[22] Murashko, V., Koryakin, A., Nyatin, A., Kim, V., *et al.*, "State of the art and prospects of electric propulsion in Russia," IEPC-2003-340, 28th International Electric Propulsion Conference, Toulouse, France, March 17-21, 2003.

[23] Oleson, S. R. and Sankovic, J. M., "Advanced Hall electric propulsion for future in-space transportation," NASA-TM-210676, NASA Glenn Research Center, Cleveland, OH, 2001.

[24] Arhipov, B. A., Bober, A. S., Gnizdor, R. Y., Kozubsky, K. N., *et al.*, "The results of 7000-hour SPT-100 life testing," IEPC-95-39, 24th International Electric Propulsion Conference, Moscow, Russia, Sept. 19-23, 1995.

[25] Brophy, J. R., Barnett, J. W., Sankovic, J. M., and Barnhart, D. A., "Performance of the stationary plasma thruster: SPT-100," AIAA-95-3155, 31st Joint Propulsion Conference, San Diego, CA, July 10-12, 1995.

[26] Garner, C. E., Brophy, J. R., Polk, J. E., and Pless, L. C., "A 5730 hr cyclic endurance test of the SPT-100," AIAA-95-2667, 31st Joint Propulsion Conference, San Diego, CA, July 10-12, 1995.

[27] Kim, S.-W. and Gallimore, A. D., "Plume study of a 1.35-kW SPT-100 using an ExB probe," *Journal of Spacecraft and Rockets*, Vol. 39, No. 6, 2002.

[28] King, L. B. and Gallimore, A. D., "Ion-energy diagnostics in the plasma exhaust plume of a Hall thruster," *Journal of Propulsion and Power*, Vol. 16, No. 5, 2000.

[29] King, L. B. and Gallimore, A. D., "Mass spectral measurements in the plume of an SPT-100 Hall thruster," *Journal of Propulsion and Power*, Vol. 16, No. 6, pp. 1086-1092, 2000.

[30] Manzella, D. H., "Stationary plasma thruster plume emissions," IEPC-93-097, 23rd International Electric Propulsion Conference, Seattle, WA, September 13-16, 1993.

[31] Manzella, D. H., "Stationary plasma thruster ion velocity distribution," AIAA-94-3141, 30th Joint Propulsion Conference, Indianapolis, IN, June 27-29, 1994.

[32] Manzella, D. H. and Sankovic, J. M., "Hall thruster ion beam characterization," AIAA-95-2927, 31st Joint Propulsion Conference, San Diego, CA, July 10-12, 1995.

[33] Sankovic, J. M., Hamley, J. A., and Haag, T. W., "Performance evaluation of the Russian SPT-100 at NASA LeRC," NASA-TM-106401, NASA Lewis Research Center, Cleveland, OH, 1993.

[34] Manzella, D., Hamley, J., Miller, J., Clauss, C.*, et al.*, "Operational characteristics of the SPT-140 Hall thruster," AIAA-97-2919, 33rd Joint Propulsion Conference, Seattle, WA, July 6-9, 1997.

[35] Marrese, C. M., Haas, J. M., Domonkos, M. T., Tverdokhlebov, S. O.*, et al.*, "D-100 performance and plume characterization on krypton," AIAA-96-2969, 32nd Joint Propulsion Conference, Lake Buena Vista, FL, July 1-3, 1996.

[36] Sankovic, J. M., Haag, T. W., and Manzella, D. H., "Operating characteristics of the Russian D-55 thruster with anode layer," AIAA-94-3011, 30th Joint Propulsion Conference, Indianapolis, IN, June 27-29, 1994.

[37] Garner, C. E., Tverdokhlebov, S. O., Semenkin, A. V., and Garkusha, V. I., "Evaluation of a 4.5-kW D-100 thruster with anode layer," AIAA-96-2967, 32nd Joint Propulsion Conference, Lake Buena Vista, FL, July 1-3, 1996.

[38] Garner, C. E., Brophy, J. R., Polk, J. E., and Pless, L. C., "Performance evaluation and life testing of the SPT-100," AIAA-94-2856, 30th Joint Propulsion Conference, Indianapolis, IN, June 27-29, 1994.

[39] Garner, C. E., Mueller, J., Vasin, A., Lasinsky, M.*, et al.*, "Experimental evaluation of the T-100-3 stationary plasma thruster and xenon propellant system for the RHETT-1 program," AIAA-96-2968, 32nd Joint Propulsion Conference, Lake Buena Vista, FL, July 1-3, 1996.

[40] Sankovic, J. M., Manzella, D. H., and Osborn, M. F., "RHETT2/EPDM development testing," IEPC-97-102, 25th International Electric Propulsion Conference, Cleveland, OH, Aug. 24-28, 1997.

[41] Peterson, T., Allen, D., Koester, K., Baranov, V.*, et al.*, "The EXPRESS/T-160E Flight hardware development effort," AIAA-98-3328, 34th Joint Propulsion Conference, Cleveland, OH, July 13-15, 1998.

[42] Marrese, C., Polk, J. E., King, L. B., Gallimore, A. D., *et al.*, "Analysis of anode layer thruster guard ring erosion," IEPC-95-196, 24th International Electric Propulsion Conference, Moscow, Russia, Sept. 19-23, 1995.

[43] Pencil, E. J., Randolph, T., and Manzella, D. H., "End-of-life stationary plasma thruster far-field plume characterization," AIAA-96-2709, 32nd Joint Propulsion Conference, Lake Buena Vista, FL, July 1-3, 1996.

[44] Randolph, T., Pencil, E., and Manzella, D., "Far-field plume contamination and sputtering of the stationary plasma thruster," AIAA-94-2855, 30th Joint Propulsion Conference, Indianapolis, IN, June 27-29, 1994.

[45] Domonkos, M. T., Gallimore, A. D., Marrese, C. M., and Haas, J. M., "Very-near-field plume investigation of the anode layer thruster," *Journal of Propulsion and Power*, Vol. 16, No. 1, 2000.

[46] Pote, B., Hruby, V., and Monheiser, J., "Performance of an 8 kW Hall thruster," IEPC-99-080, 26th International Electric Propulsion Conference, Kitakyushu, Japan, Oct. 17-21, 1999.

[47] Manzella, D. H., Jankovsky, R. S., and Hofer, R. R., "Laboratory model 50 kW Hall thruster," AIAA-2002-3676, 38th Joint Propulsion Conference, Indianapolis, IN, July 7-10, 2002.

[48] Jacobson, D. and Manzella, D. H., "50 kW class krypton Hall thruster performance," AIAA-2003-4550, 39th Joint Propulsion Conference, Huntsville, AL, July 20-23, 2003.

[49] Dunning, J. W. and Jankovsky, R. S., "NASA's electric propulsion program," AIAA-2003-4437, 39th Joint Propulsion Conference, Huntsville, AL, July 20-23, 2003.

[50] Hruby, V., "Review of electric propulsion activities in the US industry," AIAA-2003-4441, 39th Joint Propulsion Conference, Huntsville, AL, July 20-23, 2003.

[51] Saccoccia, G. and Gonzalez, J., "European activities in electric propulsion," AIAA-2003-5271, 39th Joint Propulsion Conference, Huntsville, AL, July 20-23, 2003.

[52] Komurasaki, K., "An overview of electric propulsion activities in Japan," AIAA-2003-5272, 39th Joint Propulsion Conference, Huntsville, AL, July 20-23, 2003.

[53] Blandino, J., Gatsonis, N., Cappelli, M. A., Gallimore, A. D., *et al.*, "Overview of electric propulsion research in U.S. academia," AIAA-2003-4442, 39th Joint Propulsion Conference, Huntsville, AL, July 20-23, 2003.

[54] McVey, J. B., Britt, E. J., Engelman, S. F., Gulczinski, F. S., *et al.*, "Characteristics of the T-220HT Hall-effect thruster," AIAA-2003-5158, 39th Joint Propulsion Conference, Huntsville, AL, July 20-23, 2003.

[55] de Grys, K., Rayburn, C., Wilson, F., Fisher, J., *et al.*, "Multi-mode 4.5 kW BPT-4000 Hall thruster qualification status," AIAA-2003-4552, 39th Joint Propulsion Conference, Huntsville, AL, July 20-23, 2003.

[56] Fisher, J., Wilson, A., King, D., Meyer, S., *et al.*, "The development and qualification of a 4.5 kW Hall thruster propulsion system," AIAA-2003-4551, 39th Joint Propulsion Conference, Huntsville, AL, July 20-23, 2003.

[57] Hruby, V., Monheiser, J., Pote, B., Rostler, P., *et al.*, "Development of low power Hall thrusters," AIAA-99-3534, 30th Plasmadynamics and Lasers Conference, Norfolk, VA, June 28 - July 1, 1999.

[58] McLean, C. H., McVey, J. B., and Schappell, D. T., "Testing of a U.S.-built HET system for orbit transfer applications," AIAA-99-2574, 35th Joint Propulsion Conference, Los Angeles, CA, June 20-24, 1999.

[59] Hruby, V., Pote, B., Gamero-Castano, M., Kolencik, g., *et al.*, "Hall thrusters operating in pulsed mode," IEPC-01-66, 27th International Electric Propulsion Conference, Pasadena, CA, Oct. 15-19, 2001.

[60] Lynn, P. R., Osborn, M. F., Sankovic, J. M., and Caveny, L. H., "Electric propulsion demonstration module (EPDM) flight Hall thruster system," IEPC-97-100, 25th International Electric Propulsion Conference, Cleveland, OH, Aug. 24-28, 1997.

[61] Naval Research Laboratory, "Naval Research Laboratory goes operational with United States first Hall thruster electric propulsion system," Press Release, October 29, 1998.

[62] Lyszyk, M., Klinger, E., Secheresse, O., Bugeat, J. P., *et al.*, "Qualification status of the PPS1350 plasma thruster," AIAA 99-2278, 35th Joint Propulsion Conference, Los Angeles, CA, June 20-24, 1999.

[63] Tverkokhlebov, S., Semenkin, A., and Polk, J., "Bismuth propellant option for very high power TAL thruster," AIAA-2002-0348, 40th Aerospace Sciences Meeting & Exhibit, Reno, NV, Jan., 2002.

[64] Jankovsky, R. S., Jacobson, D. T., Pinero, L. R., Sarmiento, C. J., *et al.*, "NASA's Hall thruster program 2002," AIAA-2002-3675, 38th Joint Propulsion Conference, Indianapolis, IN, July 7-10, 2002.

[65] Jankovsky, R. S., Jacobson, D. T., Rawlin, V. K., Manzella, D. H., *et al.*, "NASA's Hall thruster program," AIAA-2001-3888, 37th Joint Propulsion Conference, Salt Lake City, UT, July 8-11, 2001.

[66] Spanjers, G. G., Birkan, M., and Lawrence, T. J., "The USAF electric propulsion research program," AIAA-2000-3146, 36th Joint Propulsion Conference, Huntsville, AL, July 16-19, 2000.

[67] Sutton, G. P. and Biblarz, O., *Rocket propulsion elements*, 7th ed., New York, John Wiley & Sons, 2001.

[68] Stuhlinger, E., *Ion propulsion for space flight*, 1st ed., New York, McGraw-Hill, 1964.

[69] Jahn, R. G., *Physics of electric propulsion*, 1st ed., New York, McGraw-Hill, 1968.

[70] Curran, F. M., Sovey, J. S., and Myers, R. M., "Electric propulsion: An evolutionary technology," IAF-91-241, 42nd Congress of the International Astronautical Federation, Montreal, CA, Oct. 5-11, 1991.

[71] Byers, D. C., "An experimental investigation of a high-voltage electron-bombardment ion thruster," *Journal of the Electrochemical Society*, Vol. 116, No. 1, pp. 9-17, 1969.

[72] Oleson, S. R., Myers, R. M., Kluever, C. A., Riehl, J. P., *et al.*, "Advanced propulsion for geostationary orbit insertion and north-south station keeping," *Journal of Spacecraft and Rockets*, Vol. 34, No. 1, pp. 22-28, 1997.

[73] Knopfler, M. and Sting, "Money for nothing," Performed by The Dire Straits, in *Brothers in Arms*: Warner Bros. Records, 1985. Specifically, a debt is owed to the refrain, "I want my, I want my MTV."

[74] Jahn, R. G. and Choueiri, E. Y., "Electric propulsion," in *Encyclopedia of Physical Science and Technology*, Vol. 5, 3rd ed., Academic Press, 2002, pp. 125-141.

[75] Martinez-Sanchez, M. and Pollard, J. E., "Spacecraft electric propulsion - an overview," *Journal of Propulsion and Power*, Vol. 14, No. 5, pp. 688-693, 1998.

[76] Pollard, J. E., Jackson, D. E., Marvin, D. C., Jenkin, A. B., *et al.*, "Electric propulsion flight experience and technology readiness," AIAA-93-2221, 1993.

[77] Kaufman, H. R. and Robinson, R. S., *Operation of broad-beam sources*, Alexandria, VA, Commonwealth Scientific Corporation, 1987.

[78] Wilbur, P. J., Rawlin, V. K., and Beattie, J. R., "Ion thruster development trends and status in the United States," *Journal of Propulsion and Power*, Vol. 14, No. 5, pp. 708-715, 1998.

[79] Langmuir, D. B., "Low-thrust flight. Constant exhaust velocity in field-free space," in *Space Technology*, Seifert, H., Ed., New York, John Wiley & Sons, 1959.

[80] Auweter-Kurtz, M. and Kurtz, H., "Optimization of electric thrusters for primary propulsion based on the rocket equation," *Journal of Propulsion and Power*, Vol. 19, No. 3, pp. 413-423, 2003.

[81] Vaughan, C. E. and Cassady, R. J., "An updated assessment of electric propulsion technology for near-earth space missions," AIAA-92-3202, July, 1992.

[82] Gulczinksi, F. S. and Spores, R. A., "Analysis of Hall-effect thrusters and ion engines for orbit transfer missions," AIAA-96-2973, 32nd Joint Propulsion Conference, Lake Buena Vista, FL, July 1-3, 1996.

[83] Oleson, S. R., "Electric propulsion for low earth orbit communication satellites," IEPC-97-148, 25th International Electric Propulsion Conference, Cleveland, OH, Aug. 24-28, 1997.

[84] Oleson, S. R., "Advanced electric propulsion for RLV launched geosynchronous spacecraft," IEPC-99-185, 26th International Electric Propulsion Conference, Kitakyushu, Japan, Oct. 17-21, 1999.

[85] Oleson, S. R., "Advanced electric propulsion for space solar power satellites," AIAA-99-2872, 35th Joint Propulsion Conference, Los Angeles, CA, June 20-24, 1999.

[86] Oleson, S. R., "Mission advantages of constant power, variable Isp electrostatic thrusters," AIAA-2000-3413, 36th Joint Propulsion Conference, Huntsville, AL, July 17-19, 2000.

[87] Raitses, Y., Guelman, M., Ashkenazy, J., and Appelbaum, G., "Orbit transfer with a variable thruster Hall thruster under drag," *Journal of Spacecraft and Rockets*, Vol. 36, No. 6, pp. 875-881, 1998.

[88] Porte, F., Saint Aubert, P., and Buthion, C., "Benefits of electric propulsion for orbit injection of communication spacecraft," AIAA-92-1955, March, 1992.

[89] Spitzer, A., "Near optimal transfer orbit trajectory using electric propulsion," AAS-95-215, AAS/AIAA Spaceflight Mechanics Conference, Albuquerque, NM, Feb., 1995.

[90] Free, B., "High altitude orbit raising with on-board electric power," IEPC-93-205, 23rd International Electric Propulsion Conference, Seattle, WA, Sept. 13-16, 1993.

[91] Gulczinksi, F. S. and Schilling, J. H., "Comparison of orbit transfer vehicle concepts utilizing mid-term power and propulsion options," IEPC-2003-022, 28th International Electric Propulsion Conference, March 17-21, 2003.

[92] Oleson, S. R. and Benson, S. W., "Electric propulsion for international space station reboost: a fresh look," AIAA-2001-3644, 37th Joint Propulsion Conference, Salt Lake City, UT, July 8-11, 2001.

[93] Brophy, J. R. and Noca, M., "Electric propulsion for solar system exploration," *Journal of Propulsion and Power*, Vol. 14, No. 5, pp. 700-707, 1998.

[94] Dudzinski, L. A., Hack, K. J., Gefert, L. P., Kerslake, T. W.*, et al.*, "Design of a solar electric propulsion transfer vehicle for a non-nuclear human mars exploration architecture," IEPC-99-181, 26th International Electric Propulsion Conference, Kitakyushu, Japan, Oct. 17-21, 1999.

[95] Fiehler, D. and Oleson, S., "A comparison of electric propulsion systems for Mars exploration," AIAA-2003-4574, 39th Joint Propulsion Conference, Huntsville, AL, July 20-23, 2003.

[96] Gefert, L. P., Hack, K. J., and Kerslake, T. W., "Options for the human exploration of mars using solar electric propulsion," AIP Conference Proceedings No. 458, Space Technology and Applications International Forum (STAIF), Albuquerque, NM, Jan. 31 - Feb. 4, 1999.

[97] Noca, M. and Brophy, J. R., "Over powering solar system exploration," AIAA-97-2914, 33rd Joint Propulsion Conference, Seattle, WA, July 6-9, 1997.

[98] Belan, N. V., Kim, V. P., Oranskiy, A. I., and Tikhonov, V. B., *Stationary Plasma Engines*, Khar'kov Karh'kovskiy Aviatsionnyy Institut, 1989.

[99] Grishin, S. D. and Leskov, L. V., *Electric rocket engines for spacecraft*, Moscow, Machinostroenie, 1989.

[100] Schmidt, D. P., Meezan, N. B., Hargus, W. A., and Cappelli, M. A., "A low-power, linear-geometry Hall plasma source with an open electron-drift," *Plasma Sources Science and Technology*, Vol. 9, No. 1, pp. 68-76, 2000.

[101] Hargus, W. A. and Cappelli, M. A., "Development of a linear Hall thruster," AIAA-98-3336, 34th Joint Propulsion Conference, Cleveland, OH, July 13-15, 1998.

[102] Beal, B. E. and Gallimore, A. D., "Development of the linear gridless ion thruster," AIAA-2001-3649, 37th Joint Propulsion Conference, Salt Lake City, UT, July 8-11, 2001.

[103] Kaufman, H. R., Robinson, R. S., and Seddon, R. I., "End-Hall ion source," *Journal of Vacuum Science and Technology A*, Vol. 5, No. 4, pp. 2081-204, 1987.

[104] Raitses, Y., Fisch, N. J., Ertmer, K. M., and Burlingame, C. A., "A study of cylindrical Hall thruster for low power space applications," AIAA-00-3421, 36th Joint Propulsion Conference, Huntsville, AL, July 17-19, 2000.

[105] Smirnov, A., Raitses, Y., and Fisch, N. J., "Parametric investigation of miniaturized cylindrical and annular Hall thrusters," *Journal of Applied Physics*, Vol. 92, No. 10, pp. 5673-5679, 2002.

[106] Tverdokhlebov, S. O., "Study of double-stage anode layer thruster using inert gases," IEPC-93-232, 23rd International Electric Propulsion Conference, Seattle, WA, Sept. 13-16, 1993.

[107] Garkusha, V. I., Lyapin, E. A., Semenkin, A. V., and Tverdokhlebov, S. O., "Anode layer thrusters, state-of-the-art and perspectives," IEPC-93-228, 23rd International Electric Propulsion Conference, Seattle, WA, Sept. 13-16, 1993.

[108] Yasui, S., Kumakura, K., Yamamoto, N., Komurasaki, K.*, et al.*, "Function of a hollow anode for an anode layer type Hall thruster," AIAA-2003-4702, 39th Joint Propulsion Conference, Huntsville, AL, July 20-23, 2003.

[109] Gascon, N., Dudeck, M., and Barral, S., "Wall material effects in stationary plasma thrusters I: Parametric studies of an SPT-100," *Physics of Plasmas*, Vol. 10, No. 10, pp. 4123-4136, 2003.

[110] Barral, S., Makowski, K., Peradzynski, Z., Gascon, N.*, et al.*, "Wall material effects in stationary plasma thrusters II: Near-wall and in-wall conductivity," *Physics of Plasmas*, Vol. 10, No. 10, pp. 4137-4152, 2003.

[111] Garnier, Y., Viel, V., Roussel, J. F., Pagnon, D.*, et al.*, "Investigation of xenon ion sputtering of one ceramic material used in SPT discharge chamber," IEPC-99-083, 26th International Electric Propulsion Conference, Kitakyushu, Japan, October 17-21, 1999.

[112] Kim, V., Kozlov, V., Semenov, A., and Shkarban, I., "Investigation of the boron nitride based ceramics sputtering yield under its bombardment by Xe and Kr ions," IEPC-01-073, 27th International Electric Propulsion Conference, Pasadena, CA, Oct. 15-19, 2001.

[113] Peterson, P. Y. and Manzella, D. H., "Investigation of the erosion characteristics of a laboratory Hall thruster," AIAA-2003-5005, 39th Joint Propulsion Conference, Huntsville, AL, July 20-23, 2003.

[114] Garnier, Y., Viel, V., Roussel, J. F., and Bernard, J., "Low-energy xenon ion sputtering of ceramics investigated for stationary plasma thrusters," *Journal of Vacuum Science and Technology A*, Vol. 17, No. 6, 1999.

[115] Kim, V., Kozlov, V., Skrylnikov, A., Veselovzorov, A.*, et al.*, "Investigation of operation and characteristics of small SPT with discharge chamber walls made of different ceramics," AIAA-2003-5002, 39th Joint Propulsion Conference, Huntsville, AL, July 20-23, 2003.

[116] Raitses, Y., Ashkenazy, J., and Appelbaum, G., "Experimental investigation of the effect of channel material on Hall thruster characteristics," IEPC-97-056, 25th International Electric Propulsion Conference, Cleveland, OH, Aug. 24-28, 1997.

[117] Raitses, Y., Keidar, M., Staack, D., and Fisch, N. J., "Effects of segmented electrode in Hall current plasma thrusters," *Journal of Applied Physics*, Vol. 92, No. 9, 2002.

[118] Kim, V., Grdlichko, D., Kozlov, V., Lazourenko, A.*, et al.*, "Local plasma parameter measurements by nearwall probes inside the SPT accelerating channel under thruster operation with Kr," AIAA-2002-4108, 38th Joint Propulsion Conference, Indianapolis, IN, July 7-10, 2002.

[119] Bugrova, A. I., Morozov, A. I., Lipatov, A. S., Bishaev, A. M.*, et al.*, "Integral and spectral characteristics of ATON stationary plasma thruster operating on krypton and xenon," IEPC-2003-366, 28th International Electric Propulsion Conference, Toulouse, France, March 17-21, 2003.

[120] Kim, V., Popov, G., Kozlov, V., Skrylnikov, A.*, et al.*, "Investigation of SPT performance and particularities of its operation with Kr and Kr/Xe mixtures," IEPC-01-065, 27th International Electric Propulsion Conference, Pasadena, CA, Oct. 15-19, 2001.

[121] Gavryushin, V. M., Kim, V., Kozlov, V. I., and Maslennikov, N. A., "Physical and technical bases of the modern SPT Development," IEPC-95-38, 24th International Electric Propulsion Conference, Moscow, Russia, Sept. 19-23, 1995.

[122] Semenkin, A. V., Tverdokhlebov, S. O., Garcousha, V. I., and Grishin, S. D., "Non-propulsive application of the TAL technology," IEPC-97-164, 25th International Electric Propulsion Conference, August 24-28, 1997.

[123] Kulagin, S. N., Statsenko, I. N., Serebryansky, V. N., and Semenkin, A. N., "Some results of investigation of anode design influence of anode layer thruster characteristics," IEPC-95-52, 24th International Electric Propulsion Conference, Moscow, Russia, Sept. 19-23, 1995.

[124] Loyan, A. V. and Oghienko, S. A., "Investigation of possibility to increase the thruster efficiency, discharge efficiency, and the SPD life-time by influence to the speed of the neutral propellant gas stream," IEPC-99-117, 26th International Electric Propulsion Conference, Kitakyushu, Japan, October 17-21, 1999.

[125] Vial, V., Lazurenko, A., Laure, C., Bouchoule, A., *et al.*, "Xenon gas injection in SPT thrusters," IEPC-2003-221, 28th International Electric Propulsion Conference, Toulouse, France, March 17-21, 2003.

[126] Guerrini, G., Michaut, C., Bacal, M., Vesselovzorov, A. N., *et al.*, "An intense Hall-type ion source for satellite propulsion," *Review of Scientific Instruments*, Vol. 69, No. 2, 1998.

[127] Tverdokhlebov, S. O., Semenkin, A., Shoumkin, B., and Kotchergin, A., "Evaluation of TAL technology applicability to high power (10kW and above) EP Systems," AIAA-2001-3892, 37th Joint Propulsion Conference, Salt Lake City, UT, July 8-11, 2001.

[128] Patterson, M. J., Domonkos, M. T., Carpenter, C., and Kovaleski, S. D., "Recent development activities in hollow cathode technology," IEPC-01-270, 27th International Electric Propulsion Conference, Pasadena, CA, Oct. 15-19, 2001.

[129] Domonkos, M. T., Gallimore, A. D., Williams, G. J., and Patterson, M. J., "Low-current hollow cathode evaluation," AIAA-99-2575, 35th Joint Propulsion Conference, Los Angeles, CA, June 20-24, 1999.

[130] Hofer, R. R. and Jankovsky, R. S., "The influence of current density and magnetic field topography in optimizing the performance, divergence, and plasma oscillations of high specific impulse Hall thrusters," IEPC-2003-142, 28th International Electric Propulsion Conference, Toulouse, France, March 17-21, 2003.

[131] Jacobson, D. T. and Jankovsky, R. S., "Performance evaluation of a 50 kW Hall thruster," AIAA-99-0457, 37th Aerospace Sciences Meeting and Exhibit, Reno, NV, Jan. 11-14, 1999.

[132] Solodukhin, A. E., Semenkin, A. V., Tverdokhlebov, S. O., and Kochergin, A. V., "Parameters of D-80 anode layer thruster in one- and two-stage operation modes," IEPC-2001-032, 27th International Electric Propulsion Conference, Pasadena, CA, October 15-19, 2001.

[133] Jacobson, D. T., Jankovsky, R. S., Rawlin, V. K., and Manzella, D. H., "High voltage TAL performance," AIAA-2001-3777, 37th Joint Propulsion Conference, Salt Lake City, UT, July 8-11, 2001.

[134] Morozov, A. I., Esipchuk, Y. V., Kapulkin, A. M., Nevrovskii, V. A., *et al.*, "Effect of the magnetic field on a closed-electron-drift accelerator," *Soviet Physics Technical Physics*, Vol. 17, No. 3, 1972.

[135] Haas, J. M., "Low-perturbation interrogation of the internal and near-field plasma structure of a Hall thruster using a high-speed probe positioning system," Ph.D. Dissertation, Dept. of Aerospace Engineering, University of Michigan, Ann Arbor, MI, 2001.

[136] Bishaev, A. M. and Kim, V., "Local plasma properties in a Hall-current accelerator with an extended acceleration zone," *Soviet Physics Technical Physics*, Vol. 23, No. 9, 1978.

[137] Ahedo, E., Martinez-Cerezo, P., and Martinez-Sanchez, M., "One-dimensional model of the plasma flow in a Hall thruster," *Physics of Plasmas*, Vol. 8, No. 6, 2001.

[138] Ahedo, E., Gallardo, J. M., and Martinez-Sanchez, M., "Effects of the radial plasma-wall interaction on the Hall thruster discharge," *Physics of Plasmas*, Vol. 10, No. 8, pp. 3397-3409, 2003.

[139] Boeuf, J. P. and Garrigues, L., "Low frequency oscillations in a stationary plasma thruster," *Journal of Applied Physics*, Vol. 84, No. 7, 1998.

[140] Boeuf, J. P., Garrigues, L., and Pitchford, L. C., "Modeling of a magnetized plasma: the stationary plasma thruster," in *Electron kinetics and applications of glow discharges*, Kortshagen, U. and Tsendin, L., Eds., Plenum Press, 1998.

[141] Choueiri, E. Y., "Plasma oscillations in Hall thrusters," *Physics of Plasmas*, Vol. 8, No. 4, pp. 1411-1426, 2001.

[142] Haas, J. M. and Gallimore, A. D., "Internal plasma potential profiles in a laboratory-model Hall thruster," *Physics of Plasmas*, Vol. 8, No. 2, 2001.

[143] Haas, J. M. and Gallimore, A. D., "Considerations on the role of the Hall current in a laboratory-model thruster," *IEEE Transactions on Plasma Science*, Vol. 30, No. 2, 2002.

[144] Fife, J. M., "Hybrid-PIC modeling and electrostatic probe survey of Hall thrusters," Ph.D. Dissertation, Dept. of Aeronautics and Astronautics, Massachusetts Institute of Technology, Cambridge, MA, 1998.

[145] Morosov, A. I., Esipchuk, Y. V., Tilinin, G. N., Trofimov, A. V., *et al.*, "Plasma accelerator with closed electron drift and extended acceleration zone," *Soviet Physics Technical Physics*, Vol. 17, No. 1, 1972.

[146] Ivanov, A. A., Ivanov, A. A., and Bacal, M., "Effect of plasma-wall recombination on the conductivity in Hall thrusters," *Plasma Physics and Controlled Fusion*, Vol. 44, pp. 1463-1470, 2002.

[147] Hagelaar, G. J. M., Bareilles, J., Garrigues, L., and Boeuf, J. P., "Two-dimensional model of a stationary plasma thruster," *Journal of Applied Physics*, Vol. 91, No. 9, 2002.

[148] Janes, G. S. and Lowder, R. S., "Anomalous electron diffusion and ion acceleration in a low-density plasma," *Physics of Fluids*, Vol. 9, No. 6, 1966.

[149] Meezan, N. B., Hargus, W. A., and Cappelli, M. A., "Anomalous electron mobility in a coaxial Hall discharge plasma," *Physical Review E*, Vol. 63, No. 026410, pp. 1-7, 2001.

[150] Meezan, N. B. and Cappelli, M. A., "Kinetic study of wall collisions in a coaxial Hall discharge," *Physical Review E*, Vol. 66, No. 036401, pp. 1-10, 2002.

[151] Dunaevsky, A., Raitses, Y., and Fisch, N. J., "Secondary electron emission from dielectric materials of a Hall thruster with segmented electrodes," *Physics of Plasmas*, Vol. 10, No. 6, pp. 2574-2577, 2003.

[152] Choueiri, E. Y., "Fundamental difference between the two Hall thruster variants," *Physics of Plasmas*, Vol. 8, No. 11, pp. 5025-5033, 2001.

[153] Viel-Inguimbert, V., "Secondary electron emission of ceramics used in the channel of SPT," IEPC-2003-258, 28th International Electric Propulsion Conference, Toulouse, France, March 17-21, 2003.

[154] Raitses, Y., Staack, D., Dorf, L., and Fisch, N. J., "Experimental study of acceleration region in a 2 kW Hall thruster," AIAA-2003-5153, 39th Joint Propulsion Conference, Huntsville, AL, July 20-23, 2003.

[155] Syage, J. A., "Electron-impact cross sections for multiple ionization of Kr and Xe," *Physical Review A*, Vol. 46, No. 9, 1992.

[156] Tverdokhlebov, S. O. and Garkusha, V. I., "High-voltage mode of a TAL thruster operation," IEPC-97-023, 25th International Electric Propulsion Conference, Cleveland, OH, Aug. 24-28, 1997.

[157] Grishin, S. D., Erofeev, V. S., Zharinov, A. V., Naumkin, V. P.*, et al.*, "Characteristics of a two-stage ion accelerator with an anode layer," *Journal of Applied Mathematics & Technical Physics*, No. 2, pp. 28-36, 1978.

[158] Kim, V., Popov, G., Tikhonov, V., Garkusha, V. I.*, et al.*, "Modern trends in electric propulsion activity in Russia," IEPC-99-004, 26th International Electric Propulsion Conference, Kitakyushu, Japan, October 17-21, 1999.

[159] Morozov, A. I., Shubin, A. P., and Elizarov, L. I., "Modern state and future of electric propulsion thrusters," Anniversary Specialist Conference on Nuclear Power and Engineering in Space, Obninsk, May 15-19, 1990.

[160] Garner, C. E., Brophy, J. R., Polk, J. E., Semenkin, S.*, et al.*, "Experimental evaluation of a Russian anode layer thruster," 3rd Russian-German Conference on Electric Propulsion, Stuggart, July 19-23, 1994.

[161] Garkusha, V. I., Mironov, S. G., Semenkin, A. V., Grishin, S. D.*, et al.*, "Electric propulsion activity in TsNIIMASH," IEPC-95-009, 24th International Electric Propulsion Conference, Moscow, Russia, Sept. 19-23, 1995.

[162] "Plasma accelerators (a collection of papers from the 1st All-Union Conference on Plasma Accelerators)," Artsimovich, L. A., Grishin, S. D., Grodzovsky, G. L., Leskov, L. V., Morozov, A. I., Porotnikov, A. A., Dorodnov, A. M., Padalka, V. G., and Pergament, M. I., Eds. Moscow: Mashinostroenie, 1973.

[163] Zubkov, I. P., Kislov, A. Y., and Morosov, A. I., "Experimental study of a two-lens accelerator," *Soviet Physics - Technical Physics*, Vol. 15, No. 11, pp. 1796-1800, 1971.

[164] Knauer, W., "Mechanism of the Penning discharge at low pressures," *Journal of Applied Physics*, Vol. 33, No. 6, 1962.

[165] Yerofiev, V. S. and Safronov, I. N., "Working features of two-stage accelerator with anode layer on cesium," Abstracts for IV All-Union Conference on Plasma Accelerators and Ion Injectors, 1978.

[166] Mironov, O. N., "Investigation of working characteristics of thruster stage on cesium in two-stage thruster with anode layer," Abstracts for IV All-Union Conference on Plasma Accelerators and Ion Injectors, 1978.

[167] Antipov, A. T., Grushkevyc, A. D., Ignatenko, V. V., Kapulkyn, A. M., *et al.*, "Two-stage accelerator with closed drift of electrons," Abstracts for IV All-Union Conference on Plasma Accelerators and Ion Injectors, 1978.

[168] Bardadimov, N. A., Ivashkin, A. B., Leskov, L. V., and Trofimov, A. V., "Hybrid accelerator with closed drift of electrons," Abstracts for IV All-Union Conference on Plasma Accelerators and Ion Injectors, 1978.

[169] Hofer, R. R., Peterson, P. Y., Gallimore, A. D., and Jankovsky, R. S., "A high specific impulse two-stage Hall thruster with plasma lens focusing," IEPC-01-36, 27th International Electric Propulsion Conference, Pasadena, CA, October 15-19, 2001.

[170] Manzella, D. H. and Jacobson, D., "Investigation of low-voltage/high-thrust Hall thruster operation," AIAA-2003-5004, 39th Joint Propulsion Conference, Huntsville, AL, July 20-23, 2003.

[171] Jankovsky, R., Tverdokhlebov, S., and Manzella, D., "High power Hall thrusters," AIAA-99-2949, 35th Joint Propulsion Conference, Los Angeles, CA, June 20-24, 1999.

[172] Jankovsky, R. S., McLean, C., and McVey, J., "Preliminary evaluation of a 10 kW Hall thruster," AIAA-99-0456, 37th Aerospace Sciences Meeting and Exhibit, Reno, NV, Jan. 11-14, 1999.

[173] Mason, L. S., Jankovsky, R. S., and Manzella, D. H., "1000 hours of testing on a 10 kilowatt Hall effect thruster," AIAA-2001-3773, 37th Joint Propulsion Conference, Salt Lake City, UT, July 8-11, 2001.

[174] Jacobson, D. T., "High voltage TAL erosion characterization," AIAA-2002-4257, 38th Joint Propulsion Conference, Indianapolis, IN, July 7-10, 2002.

[175] Pote, B. and Tedrake, R., "Performance of a high specific impulse Hall thruster," IEPC-01-35, 27th International Electric Propulsion Conference, Pasadena, CA, Oct. 15-19, 2001.

[176] Manzella, D. H., Jacobson, D. T., and Jankovsky, R. S., "High Voltage SPT Performance," AIAA-2001-3774, 37th Joint Propulsion Conference, Salt Lake City, UT, July 8-11, 2001.

[177] Hofer, R. R. and Gallimore, A. D., "The role of magnetic field topography in improving the performance of high-voltage Hall thrusters," AIAA-2002-4111, 38th Joint Propulsion Conference, Indianapolis, IN, July 7-10, 2002.

[178] Hofer, R. R. and Gallimore, A. D., "Recent results from internal and very-near-field plasma diagnostics of a high specific impulse Hall thruster," IEPC-2003-037, 28th International Electric Propulsion Conference, Toulouse, France, March 17-21, 2003.

[179] Hofer, R. R. and Gallimore, A. D., "Ion species fractions in the far-field plume of a high-specific impulse Hall thruster," AIAA-2003-5001, 39th Joint Propulsion Conference, Huntsville, AL, July 20-23, 2003.

[180] Hofer, R. R., Haas, J. M., and Gallimore, A. D., "Ion voltage diagnostics in the far-field plume of a high-specific impulse Hall thruster," AIAA-2003-4556, 39th Joint Propulsion Conference, Huntsville, AL, July 20-23, 2003.

[181] Solodukhin, A. E. and Semenkin, A. V., "Study of discharge channel erosion in multi mode anode layer thruster," IEPC-2003-204, 28th International Electric Propulsion Conference, Toulouse, France, March 17-21, 2003.

[182] Semenkin, A. V., "External anode layer thruster parameters at a high specific impulse regimes," IEPC-97-055, 25th International Electric Propulsion Conference, Cleveland, OH, Aug. 24-28, 1997.

[183] Arhipov, B., Krochak, L., and Maslennikov, N. A., "Investigation of the operating characteristics of a high-power Hall effect thruster," *Journal of Propulsion and Power*, Vol. 16, No. 5, 2000.

[184] Bouchoule, A., Lazurenko, A., Vial, V., Kim, V., *et al.*, "Investigation of the SPT operation under high discharge voltages," IEPC-2003-211, 28th International Electric Propulsion Conference, Toulouse, France, March 17-21, 2003.

[185] Kim, V., Kozlov, V., Lazurenko, A., Popov, G., *et al.*, "Development and characterization of small SPT," AIAA-98-3335, 34th Joint Propulsion Conference, Cleveland, OH, July 13-15, 1998.

[186] Marcucci, M. G. and Polk, J. E., "NSTAR xenon ion thruster on deep space 1: ground and flight tests (invited)," *Review of Scientific Instruments*, Vol. 71, No. 3, pp. 1389-1400, 2000.

[187] Szabo, J. J., Warner, N. Z., and Martinez-Sanchez, M., "Instrumentation and modeling of a high Isp Hall thruster," AIAA-2002-4248, 38th Joint Propulsion Conference, Indianapolis, IN, July 7-10, 2002.

[188] Szabo, J. J., Rostler, P. S., McElhinney, S. A., and Warner, N. Z., "One and two dimensional modeling of the BHT-1000," IEPC-2003-231, 28th International Electric Propulsion Conference, Toulouse, France, March 17-21, 2003.

[189] Warner, N. Z., Szabo, J. J., and Martinez-Sanchez, M., "Characterization of a high specific impulse Hall thruster using electrostatic probes," IEPC-2003-82, 28th International Electric Propulsion Conference, Toulouse, France, March 17-21, 2003.

[190] Britton, M., Waters, D., Messer, R., Sechkar, E., *et al.*, "Sputtering erosion measurement on boron nitride as a Hall thruster material," NASA TM-2002-211837, NASA, Cleveland, OH, 2002.

[191] Boyd, I. D., "Review of Hall thruster plume modeling," *Journal of Spacecraft and Rockets*, Vol. 38, No. 3, pp. 381-387, 2001.

[192] Dorval, N., Bonnet, J., Marque, J. P., Rosencher, E., *et al.*, "Determination of the ionization and acceleration zones in a stationary plasma thruster by optical spectroscopy study: Experiments and model," *Journal of Applied Physics*, Vol. 91, No. 8, pp. 4811-4817, 2002.

[193] Cohen-Zur, A., Fruchtman, A., Ashkenazy, J., and Gany, A., "Analysis of the steady-state axial flow in the Hall thruster," *Physics of Plasma*, Vol. 9, No. 10, 2002.

[194] Boyd, I. D., Garrigues, L., Koo, J., and Keider, M., "Progress in development of a combined device/plume model for Hall thrusters," AIAA-2000-3520, 36th Joint Propulsion Conference, Huntsville, AL, July 17-19, 2000.

[195] Bugrova, A. I., Lipatov, A. S., Morozov, A. I., and Churbanov, D. V., "On a similarity criterion for plasma accelerators of the stationary plasma thruster type," *Technical Physics Letters*, Vol. 28, No. 10, pp. 821-823, 2002.

[196] Bugrova, A. I., Maslennikov, N. A., and Morozov, A. I., "Similarity laws for the global parameters of a Hall accelerator," *Soviet Physics Technical Physics*, Vol. 36, No. 6, pp. 612-615, 1991.

[197] Hofer, R. R. and Jankovsky, R. S., "A Hall thruster performance model incorporating the effects of a multiply-charged plasma," AIAA-2001-3322, 37th Joint Propulsion Conference, Salt Lake City, UT, July 8-11, 2001.

[198] Biagioni, L., Saverdi, M., and Andrenucci, M., "Scaling and performance prediction of Hall effect thrusters," AIAA-2003-4727, 39th Joint Propulsion Conference, Huntsville, AL, July 20-23, 2003.

[199] Tilley, D. L., de Grys, K. H., and Myers, R. M., "Hall thruster - cathode coupling," AIAA-99-285, 35th Joint Propulsion Conference, Los Angeles, CA, June 20-24, 1999.

[200] Hofer, R. R., Peterson, P. Y., and Gallimore, A. D., "Characterizing vacuum facility backpressure effects on the performance of a Hall thruster," IEPC-01-45, 27th International Electric Propulsion Conference, Pasadena, CA, October 15-19, 2001.

[201] Declercq, H., Bourguignon, E., Scalais, T., and Digoin, J. J., "Power processing unit for stationary plasma thruster," IEPC-99-059, 26th International Electric Propulsion Conference, Kitakyushu, Japan, Oct. 17-21, 1999.

[202] Skelly, P. T. and Kay, R. J., "RHETT/EPDM power processing unit," IEPC-97-104, 25th International Electric Propulsion Conference, Cleveland, OH, Aug. 24-28, 1997.

[203] Gulczinski, F. S., "Examination of the structure and evolution of ion energy properties of a 5 kW class laboratory Hall effect thruster at various operational conditions," Ph.D. dissertation, Dept. of Aerospace Engineering, University of Michigan, Ann Arbor, MI, 1999.

[204] King, L. B., "Transport-property and mass spectral measurements in the plasma exhaust plume of a Hall effect space propulsion system," Ph.D. Dissertation, Dept. of Aerospace Engineering, University of Michigan, Ann Arbor, MI, 1998.

[205] Keidar, M. and Boyd, I. D., "Effect of a magnetic field on the plasma plume from Hall thrusters," *Journal of Applied Physics*, Vol. 86, No. 9, pp. 4786-4791, 1999.

[206] King, L. B., Gallimore, A. D., and Marrese, C. M., "Transport-property measurements in the plume of an SPT-100 Hall thruster," *Journal of Propulsion and Power*, Vol. 14, No. 3, pp. 327-335, 1998.

[207] Gulczinksi, F. S. and Gallimore, A. D., "Near-field ion energy and species measurements of a 5-kW Hall thruster," *Journal of Propulsion and Power*, Vol. 17, No. 2, pp. 418-427, 2001.

[208] Kim, S. W., "Experimental investigations of plasma parameters and species-dependent ion energy distribution in the plasma exhaust plume of a Hall thruster," Ph.D. dissertation, Dept. of Aerospace Engineering, University of Michigan, Ann Arbor, MI, 1999.

[209] Vahrenkamp, R. P., "Measurement of double charged ions in the beam of a 30-cm mercury bombardment thruster," AIAA-73-1057, 10th International Electric Propulsion Conference, Lake Tahoe, NV, Oct. 31-Nov. 2, 1973.

[210] Griffiths, D. J., *Introduction to Electrodynamics*, 2nd ed., Upper Saddle River, NJ, Prentice Hall, 1989.

[211] Nasar, S. A., *Schaum's outline of theory and problems of electric machines and electromechanics*, New York, McGraw-Hill, 1998.

[212] Chen, C.-W., *Magnetism and metallurgy of soft magnetic materials*, New York, Dover Publications, Inc., 1986.

[213] Jiles, D., *Introduction to Magnetism and Magnetic Materials*, 1st ed., London, Chapman & Hall, 1991.

[214] Garkusha, V. I. and Semenkin, A. V., "Magnetic system for Hall thrusters evaluation and design," IEPC-2001-029, 27th International Electric Propulsion Conference, Pasadena, CA, October 15-19, 2001.

[215] Garrigues, L., Boniface, C., Bareilles, J., Hagelaar, G. J. M., *et al.*, "Parametric study of Hall thruster operation based on a 2D hybrid model: influence of the magnetic field on the thruster performance and lifetime," IEPC-2003-183, 28th International Electric Propulsion Conference, Toulouse, France, March 17-21, 2003.

[216] Kim, V., Grdlichko, D., Kozlov, V., and Lazurenko, A., "SPT-115 development and characterization," AIAA-99-2568, 35th Joint Propulsion Conference, Los Angeles, CA, June 20-24, 1999.

[217] King, D. Q. and de Grys, K. H., "Multi-mode Hall Thruster Development," AIAA-2001-3778, 37th Joint Propulsion Conference, Salt Lake City, UT, July 8-11, 2001.

[218] Bugeat, J. P. and Koppel, C., "Development of a second generation of SPT," IEPC-95-35, 24th International Electric Propulsion Conference, Moscow, Russia, Sept. 19-23, 1995.

[219] Day, M., Kim, V., Kozlov, V., Lazurenko, A., *et al.*, "Investigation of the possibility to reduce SPT plume divergence by optimization of the magnetic field topology in the accelerating channel," IEPC-97-154, 25th International Electric Propulsion Conference, Cleveland, OH, Aug. 24-28, 1997.

[220] Belikov, M. B., Gorshkov, O. A., Rizakhanov, R. N., Shagayda, A. A., *et al.*, "Hall-type low- and mean-power thrusters output parameters," AIAA-99-2571, 35th Joint Propulsion Conference, Los Angeles, CA, June 20-24, 1999.

[221] Bugrova, A. I., Morozov, A. I., Popkov, G. B., and Kharchevnikov, V. K., "Characteristics of a plasma lens," *Soviet Physics Technical Physics*, Vol. 31, No. 2, 1986.

[222] Valentian, D., Bugrova, A., and Morozov, A., "Development status of the SPT MK II thrusters," IEPC-93-223, 23rd International Electric Propulsion Conference, Seattle, WA, Sept. 13-16, 1993.

[223] Bareilles, J., Hagelaar, G. J. M., Garrigues, L., Boniface, C., *et al.*, "Critical assessment of a 2D model of Hall thrusters - comparisons with experiments," IEPC-2003-184, 28th International Electric Propulsion Conference, Toulouse, France, March 17-21, 2003.

[224] Gavryushin, V. M., Kim, V. P., Kozlov, V. I., Kozubsky, K. N., *et al.*, "Study of the effect of magnetic field variation, channel geometry change and its walls contamination upon the SPT performance," AIAA-94-2858, 30th Joint Propulsion Conference, Indianapolis, IN, June 27-29, 1994.

[225] Haas, J. M., Gulczinksi, F. S., Gallimore, A. D., Spanjers, G. G., *et al.*, "Performance characteristics of a 5 kW laboratory Hall thruster," AIAA-98-3503, 34th Joint Propulsion Conference, Cleveland, OH, July 13-15, 1997.

[226] Williams, G. J., Smith, T. B., Gulczinksi, F. S., Beal, B. E., *et al.*, "Laser induced fluorescence measurements of ion velocities in the plume of a Hall effect thruster," AIAA-99-2424, 35th Joint Propulsion Conference, Los Angeles, CA, June 20-24, 1999.

[227] Hargus, W. A., Fife, J. M., Mason, L. S., Jankovsky, R. S., *et al.*, "Preliminary performance results of the high performance Hall system SPT-140," AIAA-2000-3250, 36th Joint Propulsion Conference, Huntsville, AL, July 17-19, 2000.

[228] Hofer, R. R., Walker, M. L. R., and Gallimore, A. D., "A comparison of nude and collimated faraday probes for use with Hall thrusters," IEPC-01-20, 27th International Electric Propulsion Conference, Pasadena, CA, October 15-19, 2001.

[229] Dushman, S., *Scientific foundations of vacuum technique*, Vol. 4, New York, Wiley, 1958.

[230] Biagioni, L., Kim, V., Nicolini, D., Semenkin, A. V., *et al.*, "Basic issues in electric propulsion testing and the need for international standards," IEPC-2003-230, 28th International Electric Propulsion Conference, Toulouse, France, March 17-21, 2003.

[231] Sovey, J. S., Vetrone, R. H., Grisnik, S. P., Myers, R. M., *et al.*, "Test facilities for high-power electric propulsion," *Journal of Propulsion and Power*, Vol. 10, No. 1, pp. 18-24, 1994.

[232] Haag, T. and Osborn, M., "RHETT/EPDM performance characterization," IEPC-97-107, 25th International Electric Propulsion Conference, Cleveland, OH, Aug. 24-28, 1997.

[233] Haag, T. W., "Thrust stand for high-power electric propulsion devices," *Review of Scientific Instruments*, Vol. 62, No. 5, 1991.

[234] Walker, M. L. R., Hofer, R. R., and Gallimore, A. D., "The effects of nude Faraday probe design and vacuum facility backpressure on the measured ion current density profile of Hall thruster plumes," AIAA-2002-4253, 38th Joint Propulsion Conference, Indianapolis, IN, July 7-10, 2002.

[235] Mikami, K., Komurasaki, K., and Fujiwara, T., "Optimization of channel configuration of Hall thrusters," IEPC-95-33, 24th International Electric Propulsion Conference, Moscow, Russia, Sept. 19-23, 1995.

[236] Cohen-Zur, A., Fruchtman, A., Ashkenazy, J., and Gany, A., "Channel length and wall recombination effects in the Hall thruster," AIAA-2000-3654, 36th Joint Propulsion Conference, Huntsville, AL, July 17-19, 2000.

[237] Fife, J. M., Hargus, W. A., Jaworske, D. A., Sarmiento, C. J., *et al.*, "Spacecraft interaction test results of the high performance Hall system SPT-140," AIAA-2000-3521, 36th Joint Propulsion Conference, Huntsville, AL, July 17-19, 2000.

[238] VanGilder, D. B., Boyd, I. D., and Keidar, M., "Particle simulations of a Hall thruster plume," *Journal of Spacecraft and Rockets*, Vol. 37, No. 1, 2000.

[239] Bondar, Y. A., Markelov, G. N., Schweigert, V. A., and Ivanov, M. S., "Modeling of the plume of an ATON-Hall thruster," AIAA-2001-3357, 37th Joint Propulsion Conference, Salt Lake City, UT, July 8-11, 2001.

[240] Ashkenazy, J., Raitses, Y., and Appelbaum, G., "Parametric studies of the Hall current plasma thruster," *Physics of Plasmas*, Vol. 5, No. 5, 1998.

[241] Martinez-Sanchez, M., Personal Communication, Dec. 2002.

[242] Ahedo, E., Gallardo, J. M., and Martinez-Sanchez, M., "Model of the plasma discharge in a Hall thruster with heat conduction," *Physics of Plasma*, Vol. 9, No. 9, pp. 4061-4070, 2002.

[243] Khayms, V. and Martinez-Sanchez, M., "Design of a miniaturized Hall thruster for microsatellites," AIAA-96-3291, 32nd Joint Propulsion Conference, Lake Buena Vista, FL, July 1-3, 1996.

[244] Esipchuk, Y. B., Morosov, A. I., Tilinin, G. N., and Trofimov, A. V., "Plasma oscillations in closed-drift accelerators with an extended acceleration zone," *Soviet Physics - Technical Physics*, Vol. 18, No. 7, 1974.

[245] Raitses, Y., Ashkenazy, J., and Appelbaum, G., "Probe measurements of plasma properties inside an experimental Hall thruster," AIAA-98-3640, 34th Joint Propulsion Conference, Cleveland, OH, July 13-15, 1998.

[246] Hutchinson, I. H., *Principles of plasma diagnostics*, 1st ed., Cambridge, Cambridge University Press, 1987.

[247] Haas, J. M., Gallimore, A. D., McFall, K., and Spanjers, G., "Development of a high-speed, reciprocating electrostatic probe system for Hall thruster interrogation," *Review of Scientific Instruments*, Vol. 17, No. 11, 2000.

[248] Leal-Quiros, E. and Prelas, M. A., "New tilted-poles Wien filter with enhanced performance," *Review of Scientific Instruments*, Vol. 60, No. 3, 1989.

[249] Leal-Quiros, E. and Prelas, M. A., "Focused high-intensity proton beam from a lithium source by using an ExB stigmatic selector," *Review of Scientific Instruments*, Vol. 61, No. 1, 1990.

[250] Batson, P. E., "High-energy resolution electron spectrometer for 1-nm spatial analysis," *Review of Scientific Instruments*, Vol. 57, No. 1, 1986.

[251] Seliger, R. L., "ExB mass-separator design," *Journal of Applied Physics*, Vol. 43, No. 5, 1972.

[252] Quiros, E. L., "Some experimental facts that indicate the elimination of astigmatism in ion beams with separators using crossed electric and magnetic fields," *Journal of Applied Physics*, Vol. 52, No. 3, 1981.

[253] Guan, S. and Marshall, A. G., "A mass- and velocity-broadband ion deflector for off-axis ion injection into a cyclotron resonance ion trap," *Review of Scientific Instruments*, Vol. 67, No. 2, 1996.

[254] Anderson, J. R. and Fitzgerald, D., "Fullerene propellant research for electric propulsion," AIAA-96-3211, 1996.

[255] Wrenger, B. and Meiwes-Broer, K. H., "The application of a Wien filter to mass analysis of heavy clusters from a pulsed supersonic nozzle source," *Review of Scientific Instruments*, Vol. 68, No. 5, 1997.

[256] Williams, G. J., Domonkos, M. T., and Chavez, J. M., "Measurement of doubly charged ions in ion thruster plumes," IEPC-01-310, 27th International Electric Propulsion Conference, Pasadena, CA, Oct. 15-19, 2001.

[257] Hagstrum, H. D., "Auger ejection of electrons from tungsten by noble gas ions," *Physical Review*, Vol. 96, No. 2, 1954.

[258] Miller, J. S., Pullins, S. H., Levandier, D. J., Chiu, Y., *et al.*, "Xenon charge exchange cross sections for electrostatic thruster models," *Journal of Applied Physics*, Vol. 91, No. 3, 2002.

[259] Schott, L., "Electrical probes," in *Plasma diagnostics*, Lochte-Holtgreven, W., Ed., 1st ed., New York, American Elsevier Publishing Company, 1968, pp. 668-731.

[260] Prioul, M., Bouchoule, A., Roche, S., Magne, L., *et al.*, "Insights on physics of Hall thrusters through fast current interruptions and discharge transients," IEPC-2001-59, 27th International Electric Propulsion Conference, Pasadena, CA, Oct. 15-19, 2001.

[261] Beal, B. E. and Gallimore, A. D., "Energy analysis of a Hall thruster cluster," IEPC-2003-035, 28th International Electric Propulsion Conference, Toulouse, France, March 17-21, 2003.

[262] Reinsch, C. H., "Smoothing by spline functions," *Numerische Mathematic*, Vol. 10, pp. 177-183, 1967.